Development of Polymeric Materials for Heterogeneous (Photo)catalytic Applications

John Michael Tobin, MSc

Submitted for the degree of Doctor of Philosophy

Heriot-Watt University

School of Engineering and Physical Sciences

Institute of Chemical Sciences

Edinburgh, United Kingdom

October 2018

ABSTRACT

Demand for both renewable energy and sustainable chemical processes as a result of anthropogenic climate change in our society has never been greater. As we attempt to understand and develop new materials to address this need, the principles of 'green' chemistry help shape this journey. One method that has shown great promise to meet this demand is the utilisation of (photo)catalytic processes, which has been a driving force behind the development of many new materials. Among these materials, conjugated porous polymers (CPPs) have received much attention as (photo)catalytic materials due to their high specific surface area, extended π-conjugation and ability to act as light harvesters. This thesis presents a series of published works highlighting the research performed, including synthetic design and a wide scope of applications, and ideas towards how these materials will shape the way forward.

Chapter 2 presents two CPPs with a broad range of absorbances from 520-550 nm which were utilised as efficient heterogeneous photosensitisers under visible light irradiation for singlet oxygen generation. Chapter 3 expands the scope of applications by introducing a CPP with both broad visible light absorbance and active bipyridyl groups within the polymer framework. This allowed for its use as both a (photo)catalysts for Knoevenagel reactions and photooxidation of benzylamines as well as a chelating agent for Pb uptake. Chapter 4 focuses on polymer-supported photosensitisers based on a repeat unit found in other CPPs. These polystyrene-based photosensitisers were used to generate reactive oxygen species under irradiation at 420 nm and helped demonstrate the significance of continuous flow chemistry compared to traditional batch procedures. Chapter 5 completes the story with a post-synthetically modified CPP used for Ag uptake. The silver-loaded polymers were then employed as heterogeneous catalysts for the heterocyclisation of 4-pentynoic acid. Overall, the results presented demonstrate a potential way forward to help meet the energy and sustainability demands in society.

ACKNOWLEDGEMENTS

First and foremost, I would like to thank my supervisor Dr. Filipe Vilela. Without his motivation, compassion and guidance, successfully completing my PhD would not have been possible. Filipe always encouraged me to be a better scientist, collaborator, writer and presenter, no matter how well I thought I was doing. He consistently provided me with opportunities and routes to help me become a more well-rounded scientist. The help from my second supervisor, Dr. Valeria Arrighi, cannot go unmentioned as well. Valeria always made time for me and was always willing to lend an ear when in over my head. I cannot express my gratitude enough to both Filipe and Valeria as my supervisors during my PhD.

For a small group such as ours, collaborative efforts increase our ability to carry out research that is not our specialty. I would like to thank all the individuals and groups that I had the pleasure of working with throughout my PhD. In particular, Professor Zhengtao Xu and his group (LJ, Sarah, Wilson, MQ) at City University of Hong Kong have been exceptional collaborators and it has been a pleasure to work with them. Being able to visit their lab for 6 weeks in Hong Kong and work alongside them was an unforgettable experience and I hope to have the opportunity again one day.

The rest of the academic staff at Heriot-Watt also helped to make the journey as painless as possible. I would like to personally thank Dr. Arno Kraft, Dr. Gareth Lloyd, and Dr. David Ellis for their technical and professional guidance during my PhD. Furthermore, a place like this does not (and cannot) run without the help of support staff. Mary (stores), Koenraad, Brian and Tom (undergraduate teaching labs), and Susan (secretary) always kept things running smoothly.

I am unable to write this without giving a good deal of credit to my parents, Stan and Judy. Throughout my life, they have always encouraged and supported my decisions and choices. Without them, I would not be where I am today. Finally, I must thank my wife and best friend, Rachael. To be blunt, she put up with me through the entirety of my PhD and has taken it in stride. She has given me unconditional support, love and care during this time and I could not be more grateful. This journey would not have been possible without you.

SUMMARY OF CONTENTS

Chapter 1 will present a brief introduction to polymers and photocatalysis as well as provide context regarding the development of new materials. To help aid in the understanding of current literature, a review regarding the use of a new class of polymeric materials, conjugated porous polymers (CPPs), and their applications as heterogeneous photocatalysts will be presented. This chapter will describe state-of-the-art CPPs along with their advantages and drawbacks as heterogeneous photocatalysts. Applications will include photosensitisation, photooxidation, photodegradation, coupling reactions, photopolymerisations and hydrogen production.

Chapter 2 will explore new CPPs possessing a bathochromic shift as heterogeneous photosensitisers for the production of singlet oxygen under continuous flow conditions. By employing different synthetic methodologies (either traditional Pd-catalysed cross coupling or metal-free procedures), two polymers exhibiting high surface areas, high thermal/photo stability and absorbance in the visible spectrum will be described. These polymers will be shown as efficient heterogeneous photosensitisers in a variety of organic and 'green' solvents upon visible-light irradiation at 530 nm. Furthermore, utilisation of continuous flow chemistry and how it can be beneficial over tradition batch methods will also be discussed.

Chapter 3 will focus on the synthesis of a CPP through a metal-free synthetic procedure and how it can be employed in a variety of applications. Through the inclusion of multiple bipyridyl functional groups in the repeat unit of the polymer, both Pb ion uptake from water and heterogeneous catalysis of Knoevenagel reactions will be presented. Furthermore, the polymer will be shown as an effective heterogeneous photocatalyst utilising white light ($\lambda > 400$ nm) for the aerobic photooxidation of benzylamines under continuous flow conditions.

Chapter 4 continues to explore new alternative photoactive materials produced in a metal-free environment. The development and design of a novel photoactive monomer will be described, along with its subsequent incorporation into a polystyrene matrix as a crosslinker through free-radical polymerisation methods. Three physical formats of the polymer (gels, beads and a monolith) will be shown as efficient and

stable heterogeneous triplet photosensitisers for the production of singlet oxygen and superoxide radical anions.

Chapter 5 returns to the synthesis of CPPs, examining morphology using a modified Sonogashira-Hagihara coupling reaction under mild conditions to create a monolithic material. Post-modification chemistry will also be addressed through the addition of sulphur moieties to alkynes in the polymer backbone. These sulphur groups will be shown as good chelators for several metal species, with a selectivity towards Ag(I). The silver-loaded CPP demonstrates the ability to use an immobilised metal species as a catalytic material. In this instance, the heterocyclisation of 4-pentynoic acid is examined.

Lastly, Chapter 6 will present a conclusion to the primary research outcomes for the chapters described above. Design philosophy and how this was employed to develop many of the materials presented here will be briefly discussed as well. An outlook will be presented towards how conjugated porous polymers and other new photocatalytic materials can be further established, along with their potential for alternative applications.

TABLE OF CONTENTS

LIST OF ABBREVIATIONS

AIBN	Azobisisobutylnitrile
BOC	*Tert*-butyl carboxylate
BODIPY	4,4-difluoro-4-bora-3a,4a-diaza-s-indacene
BTZ	2,1,3-Benzothiadiazole
CMP	Conjugated microporous polymer
CP-MAS	Cross-polarisation magic angle spinning
CPP	Conjugated porous polymer
COF	Covalent-organic framework
DVB	Divinylbenzene
EDX	Energy dispersive X-ray spectroscopy
FT-IR	Fourier-transform infrared spectroscopy
HIPE	High internal phase emulsion
HOMO	Highest occupied molecular orbital
HPLC	High performance liquid chromatography
ICP-AES	Inductively coupled plasma atomic emission spectroscopy
LED	Light emitting diode
LUMO	Lowest unoccupied molecular orbital
MOF	Metal-organic framework
NMR	Nuclear magnetic resonance
NP	Nanoparticle
$^1O_2$	Singlet oxygen
$^3O_2$	Ground state triplet oxygen
$O_2^{\cdot -}$	Superoxide radical
PDT	Photodynamic therapy
PXRD	Powder x-ray diffraction
Py	Pyrene
QSDFT	Quenched solid state functional theory
SA	Strong electron acceptor
S_{BET}	Brunauer–Emmett–Teller surface area
SEM	Scanning electron microscopy
SET	Single electron transfer
Sp	Spirobifluorene
TEM	Transmission electron microscopy
TGA	Thermogravimetric analysis
TLC	Thin layer chromatography
TPE	Tetraphenylethylene
UV	Ultraviolet light
Vis	Visible light
WD	Weak electron donor

LIST OF PUBLICATIONS

Accepted:

J. Liu, **J. M. Tobin**, Z. Xu, F. Vilela, *Facile synthesis of a conjugated microporous polymeric monolith via copper-free Sonogashira–Hagihara cross-coupling in water under aerobic conditions*, Polym. Chem., **6**, 7251-7255 (2015)

J. Shen, R. Steinbach, **J. M. Tobin**, M. M. Nakata, M. Bower, M. R. S. McCoustra, H. Bridle, V. Arrighi, F. Vilela, *Photoactive and metal-free polyamide-based polymers for water and wastewater treatment under visible light irradiation*, Appl. Catal. B-Environ., **193**, 226-233 (2016)

Y.-L. Wong, **J. M. Tobin**, Z. Xu, F. Vilela, *Conjugated porous polymers for photocatalytic applications*, J. Mater. Chem. A, **4**, 18677-18686 (2016)

J. M. Tobin, J. Liu, H. Hayes, M. Demleitner, D. Ellis, V. Arrighi, Z. Xu, F. Vilela, *BODIPY-based conjugated microporous polymers as reusable heterogeneous photosensitisers in a photochemical flow reactor*, Polym. Chem., **7**, 6662-6670 (2016)

J. M. Tobin, T. J. D. McCabe, A. W. Prentice, S. Holzer, G. O. Lloyd, M. J. Paterson, V. Arrighi, P. A. G. Cormack, F. Vilela, *Polymer-Supported Photosensitizers for Oxidative Organic Transformations in Flow and under Visible Light Irradiation,* ACS Catal., **7**, 4602-4612 (2017)

R. Xiao, **J. M. Tobin**, M. Zha, Y.-L. Hou, J. He, F. Vilela, Z. Xu, *A nanoporous graphene analog for superfast heavy metal removal and continuous-flow visible-light photoredox catalysis*, J. Mater. Chem. A, **5**, 20180-20187 (2017)

C. J. C. Lamb, B. G. Nderitu, G. McMurdo, **J. M. Tobin**, F. Vilela, A.-L. Lee, *Auto-Tandem Catalysis: Pd^{II}-Catalysed Dehydrogenation/Oxidative Heck Reaction of Cyclopentane-1,3-diones*, Chem. Eur. J., **23**, 18282-18288 (2017)

J. M. Tobin, F. Vilela, *Application Note 58 – Visible Light Singlet Oxygen*, 2018, Vapourtec Ltd., accessed September 2018, <https://www.vapourtec.com/flow-chemistry-resource-centre/application-note-58-visible-light-singlet-oxygen/>

C. H. A. Tsang, **J. Tobin**, J. Xuan, F. Vilela, H. Huang, D. Y. C. Leung, *BTZ-copolymer loaded graphene aerogel as new type Green and metal-free visible light photocatalyst*, Appl. Catal. B-Environ., **240**, 50-63 (2019)

M. Z. C. Hatit, L. F. Reichenbach, **J. M. Tobin**, F. Vilela, G. A. Burley, A. J. B. Watson, *A flow platform for degradation-free CuAAC bioconjugation*, Nat. Commun. **9**, 4021 (2018)

K. Kinastowska, J. Liu, **J. M. Tobin**, Y. Rakovich, F. Vilela, Z. Xu, W. Bartkowiak, M. Grzelczak, *Photocatalytic cofactor regeneration involving triethanolamine revisited: The critical role of glycolaldehyde*, Appl. Catal. B-Environ., **243**, 686-692 (2019)

CHAPTER 1: General Introduction

Since the advent of the industrial revolution in the mid-1700s, the usage of fossil fuels including coal, oil, and natural gas has increased exponentially. Consequently, the use of these fuel sources has contributed to a sharp rise in the concentration of atmospheric greenhouse gases. These gases, such as CO_2, CH_4, and NO_2, have nearly doubled in concentration over the past 200 years [1.1]. As a result, overwhelming scientific consensus has concluded that these relatively sudden fluctuations have contributed extensively towards the onset of global warming [1.2]. As the concentration of these greenhouse gases continue to rise and their effects become more severe, it has become a global priority to research and develop new materials and processes in a renewable and sustainable fashion.

Concerns over the accelerated use of fossil fuels and their limited supply have been raised for over 100 years. As energy is fundamental to the global economy and everyday life, explorations into alternative energy sources, such as wind, solar, and hydro power, have been conducted. Through continued understanding and research into the way plants harness solar energy *via* photosynthesis, the idea of using solar light as a direct energy source has become increasingly pervasive. In a paper published in *Science* in 1912, Giacomo Ciamician ruminates:

> "*And if in a distant future the supply of coal becomes completely exhausted, civilization will not be checked by that, for life and civilization will continue as long as the sun shines! If our black and nervous civilization, based on coal, shall be followed by a quieter civilization based on the utilization of solar energy, that will not be harmful to progress and to human happiness*" [1.3].

Figure 1.1 depicts the spectrum of light that reaches the Earth from the Sun and its corresponding irradiance [1.4]. While this light covers a broad spectrum of wavelengths, the highest intensity light occurs within the visible spectrum (400-700 nm). Therefore, materials that absorb in this region are advantageous as they can utilise the most intense region of the solar spectrum. One way to harness this near limitless supply of energy is to use light harvesting materials. While these materials can be used for the

generation of electricity *via* solar cells [1.5], they can also be used as photocatalysts to help drive chemical processes. The search for alternative methods to generate electricity also coincides with the development of sustainable and reusable materials in an effort to reduce our rapid (and increasing) consumption of natural resources.

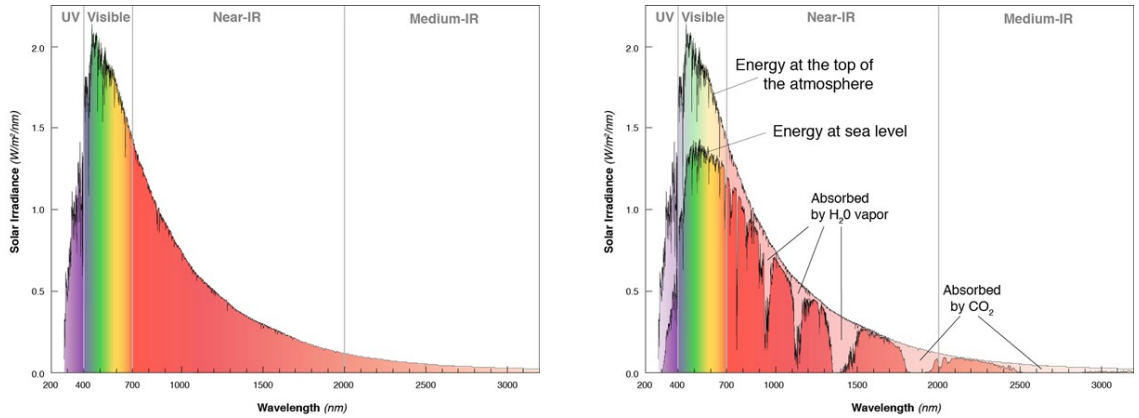

Figure 1.1 Solar spectrum of irradiation from the Sun (left) and the corresponding spectrum after passing through the atmosphere (right) [1.4].

Green chemistry is a concept that focuses on sustainability, aiming to slow and ultimately end our dependence on fossil fuels as well as other environmentally harmful chemical processes and products. The principles of green chemistry, as outlined by Anastas and Warner in 1998 (Figure 1.2), were developed as a framework to address the reduction of environmental and health impacts brought about by the use and production of harmful chemicals [1.6]. Furthermore, these principles are used to inform new avenues of research to make safe, renewable, reusable, and highly efficient materials. Although it is difficult to address each principle individually when designing a new material, the concept as a whole must be preserved. For example, as we look to develop new photocatalysts, the raw materials, synthetic routes, and product safety must be examined carefully. Moreover, the overall efficiency as well as chemical and photostability of the materials are vital to maintain these principles.

Photocatalytic reactions have been explored to great depths with the range and diversity of photocatalytic materials continuing to grow [1.7]. However, one of the more prominent discoveries did not occur until the 1970s where Fujishima and Honda reported photocatalytic water splitting on TiO_2 electrodes [1.8]. This breakthrough facilitated a renewed growth in the field of photocatalysis where the importance of semiconductors as photocatalytic materials was realised. As semiconductors have a narrow energy gap

between their valence and conduction bands (otherwise known as the band gap), the absorption of energy (*i.e.* light) equal to or greater than this gap allows for photocatalysis to proceed. By altering this so-called band gap through careful selection and design of the photocatalytic materials, the light absorbance required for photoactivity can be adjusted. Even today, research regarding band gap control remains pervasive within the photocatalysis community.

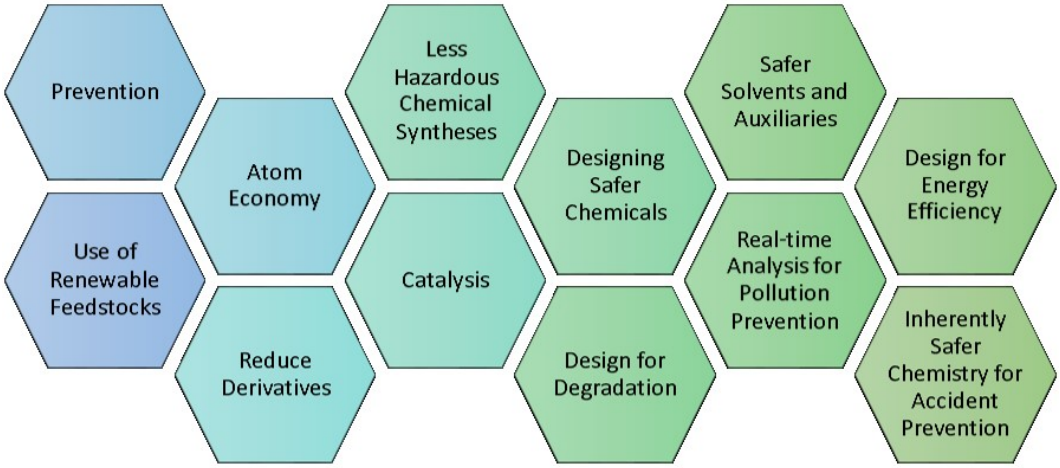

Figure 1.2 The twelve principles of green chemistry as developed by Anastas and Warner [1.6].

In the past, most catalysis research (including photocatalysis) has been centred on inorganic materials [1.9, 1.10] or metal-organic complexes [1.11], the majority of which absorb in the UV region of the spectrum (*i.e.* $\lambda_{max} < 400$ nm). It was not until 2000 that McMillan coined the term *"organocatalysis"* [1.12]. Organocatalysis presents several advantages over conventional metal-based catalysis, not only because of the vast scope of synthetic reactions where it can be employed, but also for environmental and economic reasons. The absence of metals in an organocatalyst offers an undeniable advantage when considering the principles of green chemistry and sustainability. More recently, organic photocatalysts have attracted interest as a potential alternative to expensive, toxic, and unstable inorganic and metal-organic counterparts.

Organic dyes, such as eosin Y and methylene blue [1.13, 1.14], as well as porphyrins and phthalocyanines [1.15] have been extensively employed in visible-light photocatalysis and photosensitising reactions (Figure 1.3, top). These small molecules are largely soluble in most organic solvents and therefore act as homogeneous photocatalysts. By designing insoluble materials, we can further address the principles

of green chemistry as these materials have advantages such as ease of recovery and reusability. While most metal oxides are entirely insoluble in conventional solvents, purely organic photocatalytic materials can fill this gap through the development of macromolecules. Heterogeneous photocatalysts such as silica gel [1.16] and polymer-supported photosensitisers [1.17], polymeric carbon nitride [1.18, 1.19], and hyper crosslinked polymers [1.20] are now gaining traction in this topical field (Figure 1.3, bottom). Moreover, both organic dyes and heterogeneous polymeric photocatalysts have been shown to primarily absorb light in the visible region ($\lambda_{max} > 400$ nm), providing yet another advantage when compared to many metal-based photocatalysts. As we continue to develop these alternative photocatalytic materials, it is essential to understand potential design and synthesis strategies. This is particularly true for the ever-expanding field of polymer chemistry.

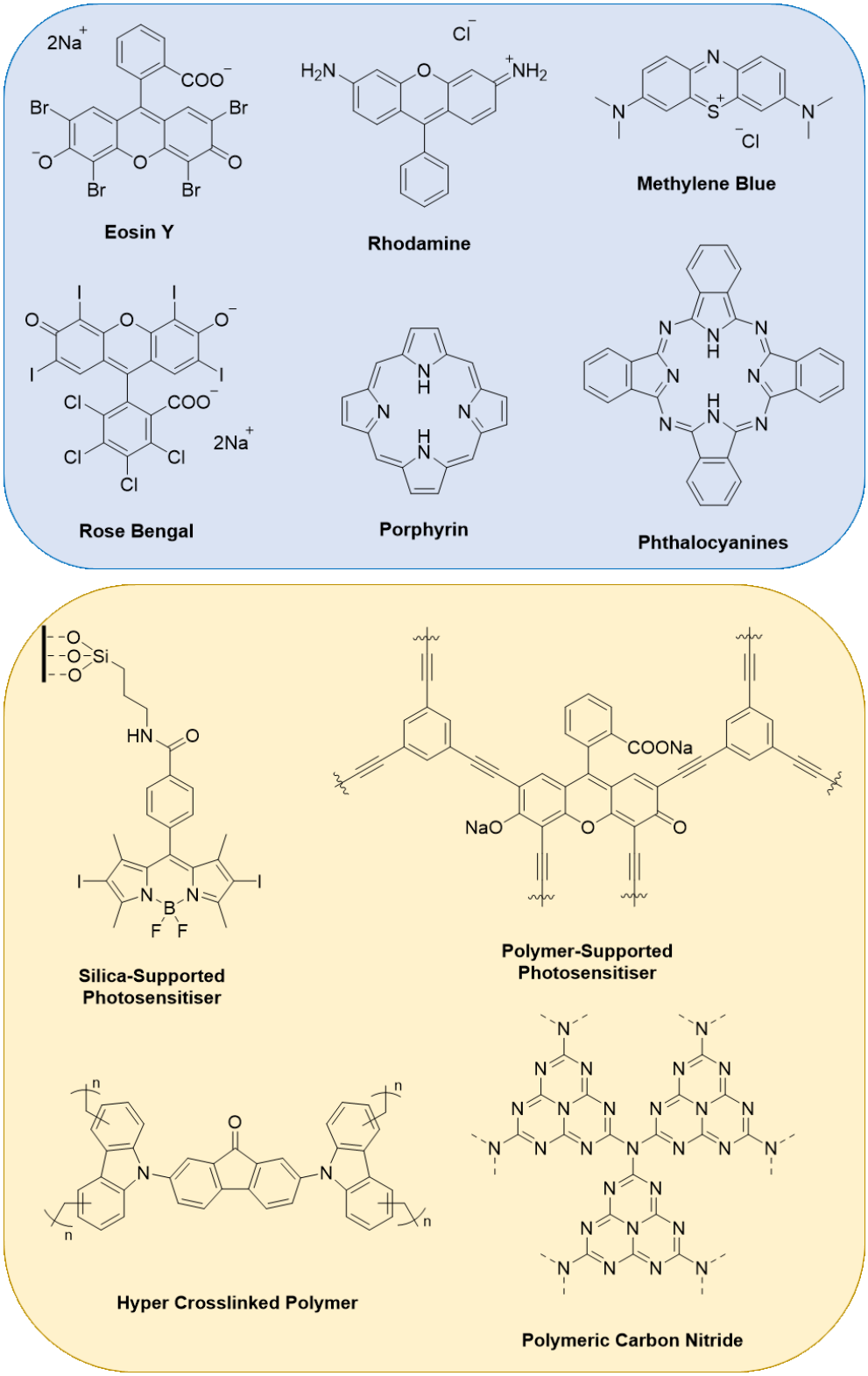

Figure 1.3 Examples of homogeneous photocatalysts (top, blue) and heterogeneous photocatalysts (bottom, orange).

1.1 Polymer Chemistry

While the idea of macromolecular entities existed since the mid-1800s, it wasn't until 1927 that Nobel Prize winner Hermann Staudinger accurately described the molecular make-up and characteristics of polymeric materials [1.21]. Since then, the development and innovation of polymer chemistry has had a profound impact on the world, contributing to the advancement of new industrial processes, a host of invaluable commercial products, and everyday household items.

Though the procedures used to create polymers can differ greatly, the polymerisation process results in long chains of repeating monomers with relatively high molecular weights compared to the starting monomer. More traditional polymer syntheses tend to use methods such as free-radical or ionic polymerisation techniques [1.22]. In Figure 1.4, an example of the free-radical polymerisation of styrene is presented using azobisisobutylnitrile (AIBN) as the initiator. Although this method can terminate through either combination or disproportionation, styrene tends to terminate through a combination mechanism [1.22, 1.23]. While some polymer chains can result in a linear orientation of repeating monomeric units, it is also possible to achieve other architectures, which can be exploited for their physical and morphological properties. As seen in Figure 1.5, these architectures can include linear, branched, star, and crosslinked (or network) configurations. Furthermore, it is possible to synthesise polymers with more than one monomeric unit. A copolymer, consisting of two or more different monomers, can distribute the different monomers in multiple ways, including alternating, statistical (random), block, and graft, just to name but a few (Figure 1.6) [1.22].

Due to the enormous range of physical and chemical characteristics exhibited by different polymer architectures and compositions, their applications are nearly limitless. As most polymers tend to be carbon-based materials (*i.e.* free from metals), they have great potential as green materials for catalytic applications. With the ability to include catalytic monomers (*e.g.* catalytic sites) within the polymer chain, their use as organocatalysts has been described [1.24]. Furthermore, through the addition of crosslinkers within the polymer chain, the polymer can be rendered insoluble, allowing the organocatalyst to be used as heterogeneous materials.

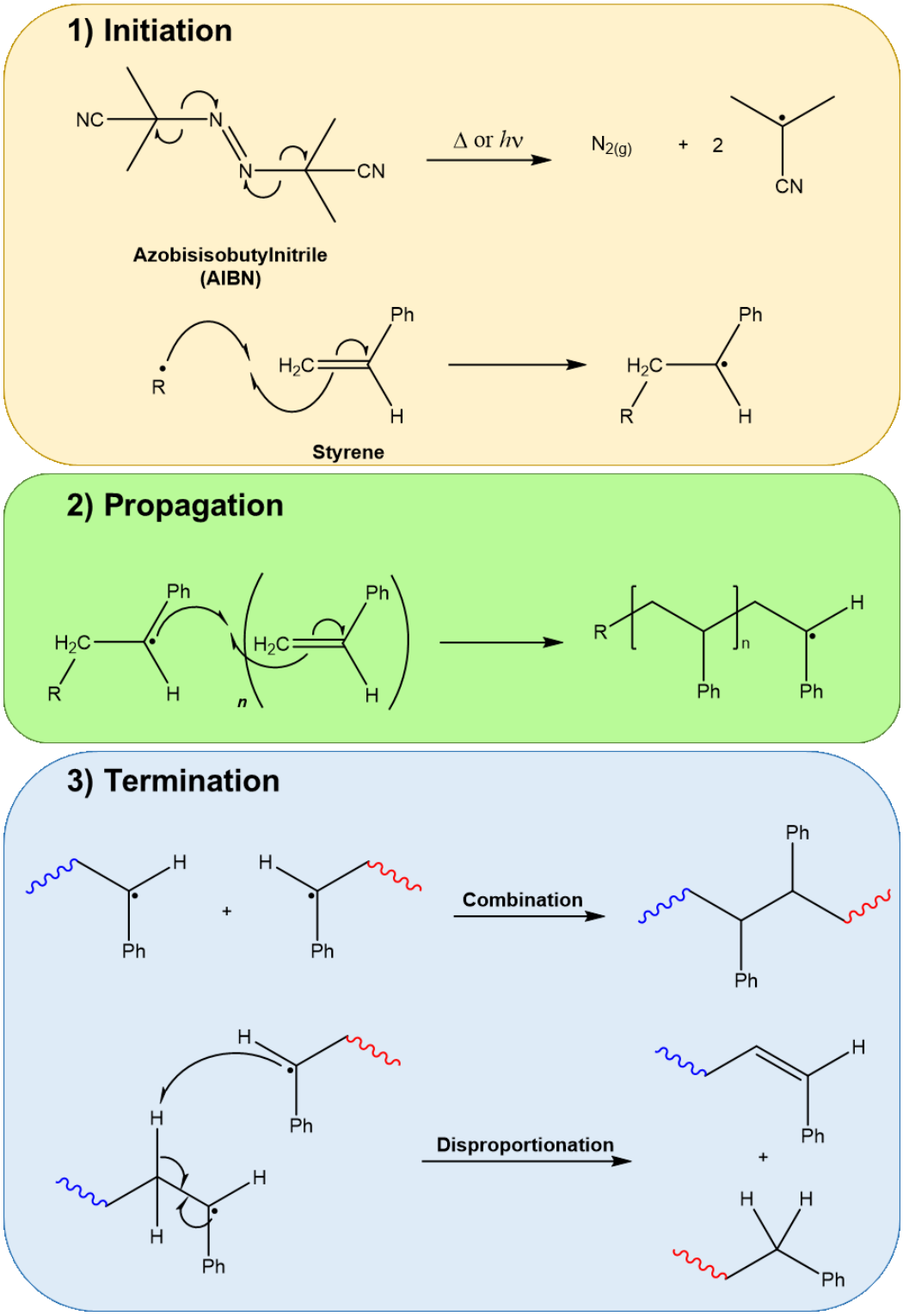

Figure 1.4 Example of free-radical polymerisation of styrene *via* initiation, propagation and termination (R = initiator radical product; Ph = phenyl).

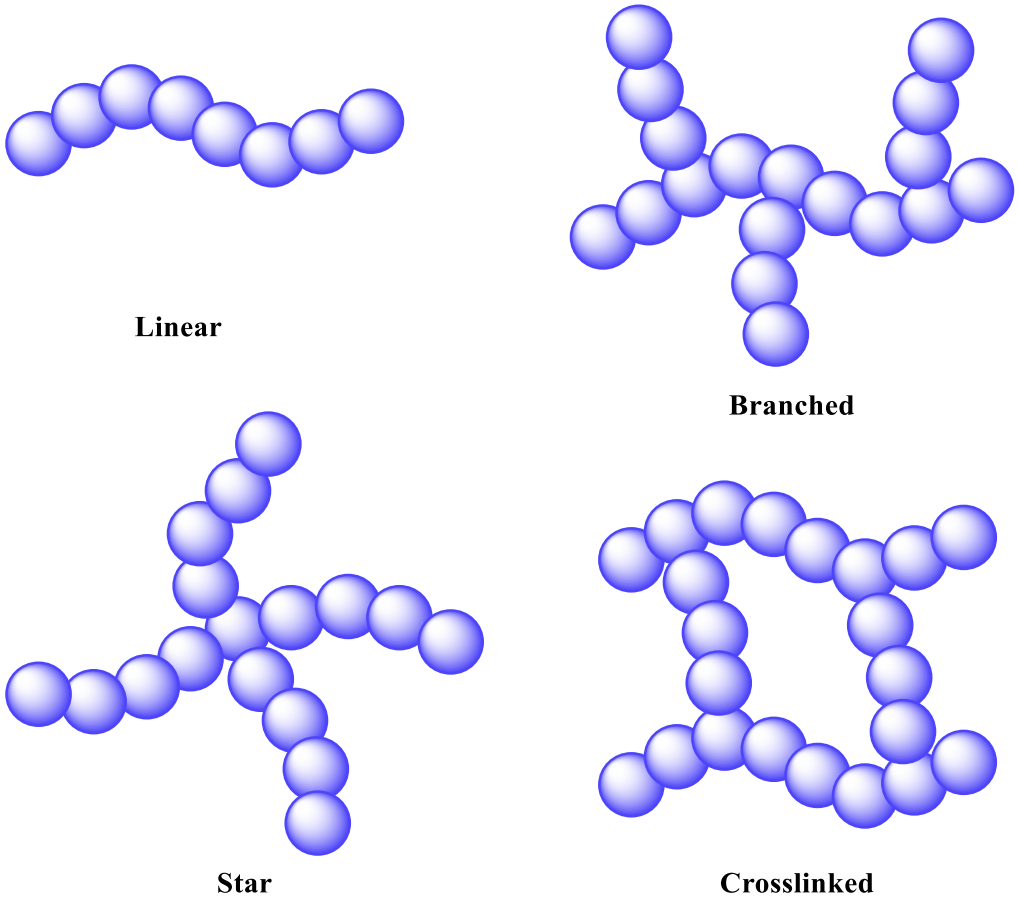

Figure 1.5 Examples of various polymer structures and architectures.

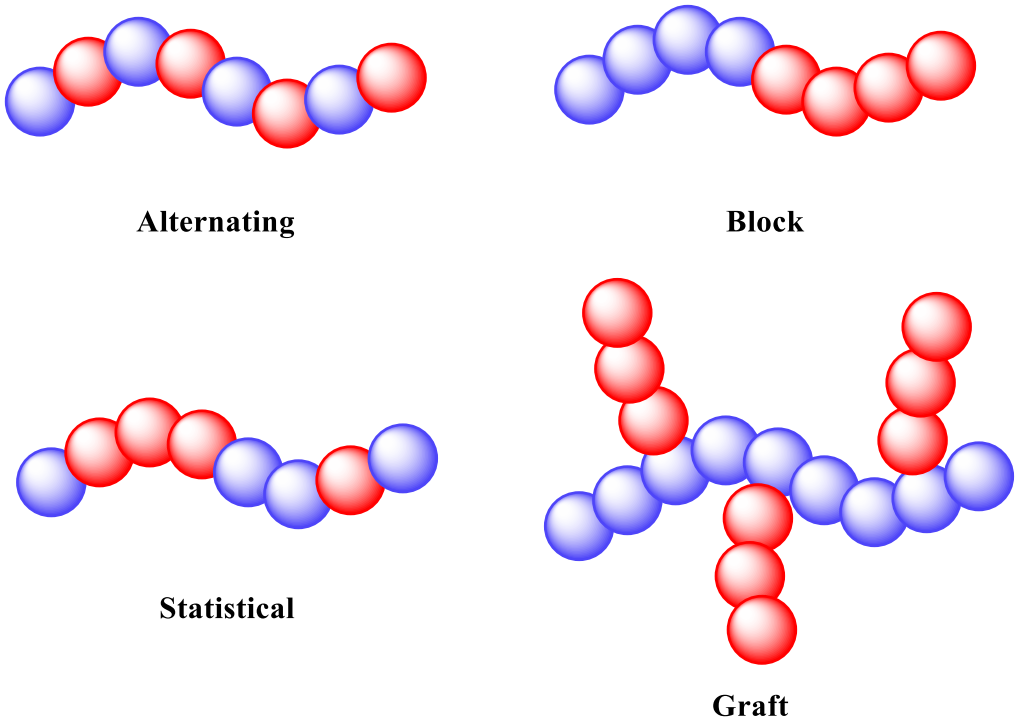

Figure 1.6 Examples of copolymer classifications using a two-monomer system, denoted by the red and blue monomeric units.

Through careful design and selection of monomers, polymeric materials can also be constructed with semiconducting properties. Designing these polymers with alternating double bonds creates a band gap which allows for the materials to act as semiconductors (or photocatalysts) upon irradiation at the appropriate wavelength. By crosslinking these semiconducting polymers, network polymers are created allowing the materials to be employed as heterogeneous photocatalysts. One class of polymers that has recently experienced a surge in popularity regarding their ability to act as heterogeneous photocatalytic materials are conjugated microporous polymers (CMPs). This popularity is a result of CMPs exhibiting unique characteristics and a wide scope of applications.

1.2 Conjugated Microporous Polymers

CMPs, first described by Cooper *et al*. [1.25], are fully crosslinked polymers with characteristic trademarks such as good thermal and chemical stability, along with high Brunauer–Emmett–Teller surface areas (S_{BET}) resulting from their microporosity (pore size < 2 nm; as defined by IUPAC) [1.26]. Furthermore, the extended π-π conjugated nature of CMPs allows them to act as organic semiconductors and light harvesters, with applications reported in areas such as gas sorption and separation, energy storage, and (photo)catalysis [1.27, 1.28]. The wide range of applications can be attributed to the combination of electronic and morphological properties of CMPs. While the advantageous properties of CMPs may not individually surpass those of other porous materials, such as zeolites, metal oxides, metal-organic frameworks (MOFs), and covalent-organic frameworks (COFs), the combination of the thermal and chemical stability, functionality, conductivity, and porosity are what make CMPs stand out from the rest [1.28, 1.29].

Due to being highly crosslinked polymers by design, this renders CMPs insoluble in conventional solvents and allows them to be used as heterogeneous materials in (photo)catalytic applications. While this has benefits regarding ease of recovery and recyclability when compared to homogeneous materials, their insoluble nature also leads to inherent difficulties regarding processability. In general, the synthetic techniques used to make CMPs results in the formation of amorphous powders and solids whereby solution processing (*e.g.* film casting) is not possible. While there are exceptions [1.30,

1.31], it is rare to encounter CMPs in different physical formats. Chapter 5 will address this subject in greater depth by describing the synthesis and characterisation of a monolithic CMP.

1.2.1 Synthesis and Characterisation of CMPs

To achieve both the characteristic extended π-π conjugation and high S_{BET} found in CMPs, direct coupling of aromatic species to create a rigid polymer network is the most common method described for CMP syntheses. These can include metal-catalysed reactions such as Yamamoto coupling [1.32, 1.33], Glaser coupling [1.34], Suzuki-Miyaura coupling [1.35], and Sonogashira-Hagihara coupling [1.25, 1.36]; or polycondensation and metal-free reactions such as nitrile cyclisation [1.37], imidization [1.38], Schiff base chemistry [1.39, 1.40], and thermal polycondensation [1.18]. Two of the more common metal-based methodologies used from the list above has been Pd-catalysed Suzuki-Miyaura and Sonogashira-Hagihara carbon-carbon cross-coupling reactions.

As seen in Figure 1.7, Suzuki-Miyaura coupling is performed between an aryl halide and an aryl boronic acid or ester in the presence of Pd^0 through three distinctive steps: *i*) oxidative addition; *ii*) transmetalation; *iii*) reductive elimination. Upon formation of the product (reductive elimination) the Pd catalyst is regenerated [1.41]. Depicted in Figure 1.8 is the predicted mechanism for Sonogashira coupling which is performed between an aryl halide and a terminal alkyne. Again, Pd^0 is required for oxidative addition of the aryl halide. However, transmetalation requires a separate Cu cycle for the addition of the alkyne group. After this step, a trans-cis isomerisation occurs within the complex, leading to reductive elimination of the product and regeneration of the Pd^0 catalyst [1.42].

While different polymerisation techniques can be used to control structure, porosity, and S_{BET}, the choice of monomers is also a key factor in designing CMPs [1.36]. Both the synthetic route and monomer selection is largely dependent on the end application for the polymer. For example, by designing an electronic 'push-pull' system with aromatic building-blocks (alternating a strong electron acceptor and weak electron donor) within the repeat unit of the polymer, electronic control can be asserted (Figure 1.9). This facilitates electron delocalisation and allows for optimisation (narrowing) of the optical band gap to tune the material for better photocatalytic performance, preferably

in the visible spectrum. Although the idea of this electronic 'push-pull' system has been traditionally used for (small) molecular-based organic electronics, the same can be applied to macromolecular structures such as polymers [1.43].

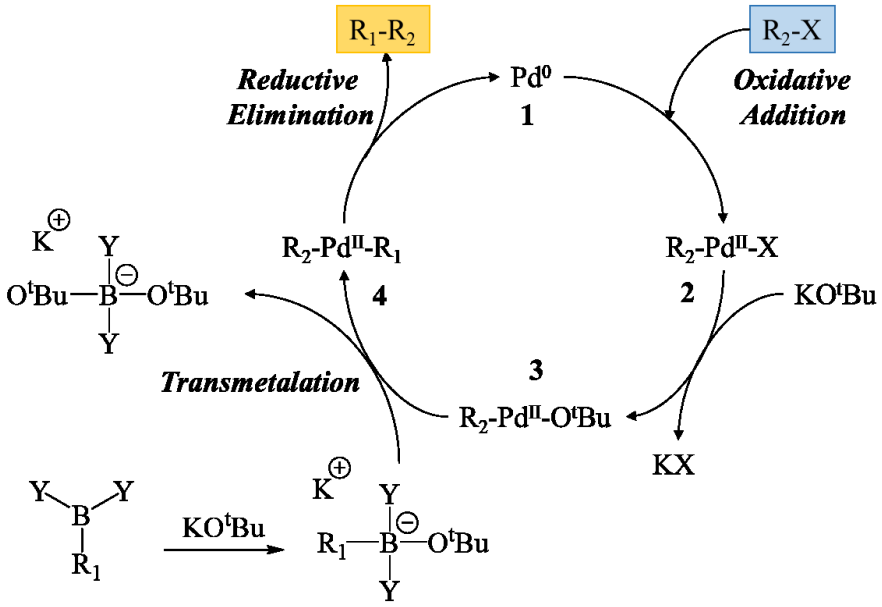

Figure 1.7 Palladium cycle for Suzuki-Miyaura cross-coupling [1.41].

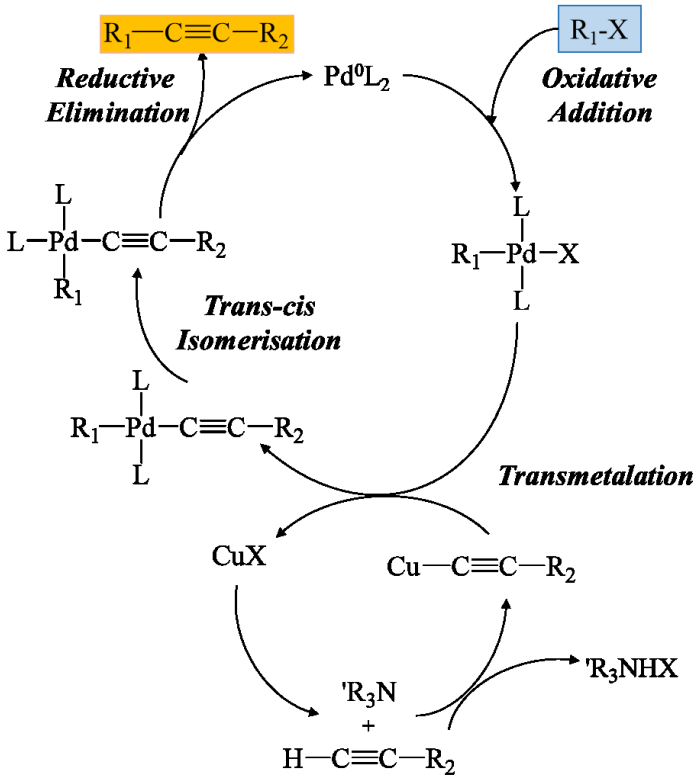

Figure 1.8 Palladium-Copper catalytic cycle for Sonogashira-Hagihara cross-coupling [1.42].

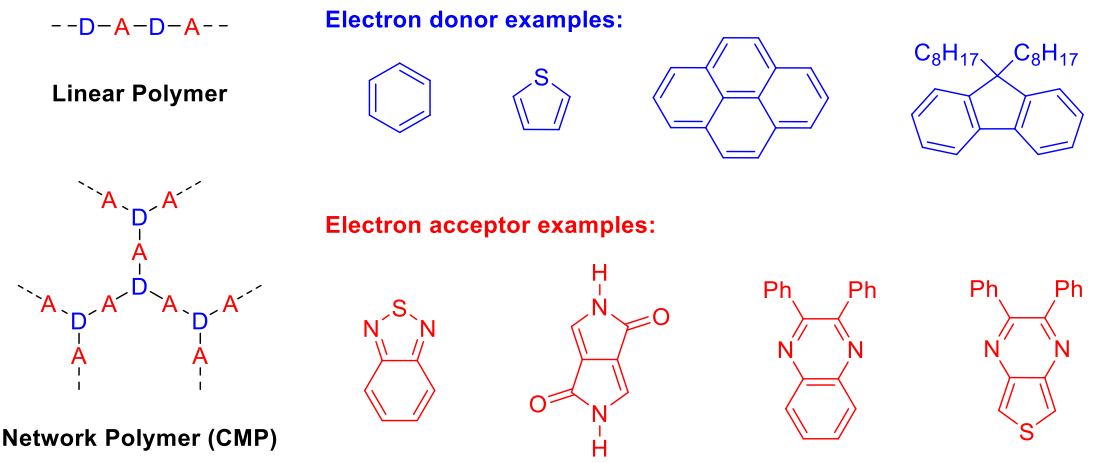

Figure 1.9 Simplified example of an electronic 'push-pull' system found in low band gap linear polymers and CMPs. The blue 'D' indicates an electron donor while a red 'A' indicates an electron acceptor [1.43].

Molecular and physical characterisation of CMPs can be a difficult task to accomplish due to their insoluble nature. Solution state characterisation techniques such as ^{1}H and ^{13}C nuclear magnetic resonance (NMR) spectroscopy, and UV-Visible spectroscopy are generally unfeasible. Fortunately, it is possible to perform both ^{13}C NMR and UV-Vis spectroscopic methods in the solid state. Other characterisations that can be performed in the solid state include Fourier-transform infrared (FT-IR) spectroscopy, Brunauer–Emmett–Teller surface area (S_{BET}) analysis, thermogravimetric analysis (TGA), and scanning and transmission electron microscopy (SEM/TEM) imaging. Techniques such as NMR and FT-IR spectroscopy help characterise the chemical structure of the polymer. To study the physical characteristics of CMPs, UV-Vis spectroscopy, TGA, BET surface area analysis, and SEM/TEM imaging are generally employed.

The proceeding section will focus on CMPs and similar materials towards their application as heterogeneous photocatalysts. The introduction and use of 'conjugated microporous polymer' (CMP) above can be thought of as a more specific nomenclature regarding these materials. The term 'conjugated porous polymer' (CPP) is a broader yet equally correct description and will be used henceforth for the sake of clarity.

1.3 Conjugated Porous Polymers for Photocatalytic Applications (Publication, *Journal of Materials Chemistry A*, RSC)

This section presents a comprehensive review of current state-of-the-art CPPs focusing on their use in heterogeneous photocatalytic applications. Through a combination of high surface area and porosity, extended π-conjugation and their insoluble nature, CPPs display beneficial properties which show them as good potential alternatives to traditional homogeneous photocatalytic materials. The review is presented as a publication titled '*Conjugated Porous Polymers for Photocatalytic Applications*' published in *Journal of Materials Chemistry A* in 2016. This work is summarised and discussed below and can be found in its entirety at the end of this chapter. Contributions and work performed by other students, collaborators or academics are presented throughout the chapter in the appropriate sections.

1.3.1 Background

The development of porous materials, such as zeolites [1.44-1.46], silica [1.47, 1.48], metal oxides [1.49-1.52], metal-organic frameworks (MOFs) [1.53-1.58], and covalent-organic frameworks (COFs) [1.59-1.62], has advanced chemical processes as they have demonstrated great sustainability and reusability. These promising materials have been implemented as clean and renewable resources for applications in gas storage, sensing and (photo)catalysis. Among them is an emerging class of materials labelled conjugated porous polymers (CPPs), which have shown a similarly diverse range of applications. Moreover, due to extended π-conjugation and light harvesting capabilities, CPPs offer photophysical and electronic properties allowing for their use in photocatalytic applications [1.27]. Moving away from materials that utilise destructive UV light as an energy source allows for reactions to be performed under milder conditions (wavelengths in the visible region of the electromagnetic spectrum of light). This widens the scope of potential for CPPs as photocatalytic materials.

Current research regarding CPPs as photocatalysts continues to revolve around the design of new materials with regards to both their physical and photophysical properties. Control of physical properties such as pore size and S_{BET} have been demonstrated as an effective method to increase photocatalytic activity [1.63].

Combining electronic control with an extended delocalised backbone, CPPs allow for greater light harvesting capabilities and energy transfer to acceptor molecules, triggering the chemical or physical change required for the desired reaction to proceed [1.35].

CPPs offer an attractive alternative when compared to commonly used homogeneous photocatalysts, such as organic dyes, and other inorganic and organometallic small molecules [1.64]. In a homogeneous system, product separation and purification along with catalyst regeneration can be cumbersome and time consuming. Conversely, a heterogeneous system allows for facile isolation, recovery and recycling of the photocatalytic material. Owing to the generally rigid backbone associated with CPPs, they also offer greater photostability and are comparatively less prone to photodegradation *via* photobleaching, a common problem for many homogeneous photocatalysts [1.65]. While heterogeneous photocatalytic reactions do tend to exhibit lower rates of reaction, this can be alleviated to some degree through the morphological and electronic control as described above. Due to the properties and characteristic demonstrated by CPPs, a surge of heterogeneous photocatalytic applications has been described and will be discussed below. The introduction and background section of the manuscript was edited with the help of Professor Zhengtao Xu, City University of Hong Kong.

1.3.2 Aim/Objectives

A comprehensive review of the literature regarding CPPs and their applications as photocatalysts is presented, summarising the key areas of development and the greater potential these materials offer. Through a critical analysis of this literature, a wide variety of CPPs have proven to be effective photocatalysts. Furthermore, a perspective upon their ideal design criteria and potential for new polymers was presented. The primary aim of this literature review was to present the reader with a contextual overview of CPPs with a focus on their performance as heterogeneous photocatalysts when compared to mainstream photocatalytic materials. This includes identifying any disadvantages and providing potential directions for further research. As this field is still in relative infancy, the outlook focuses on the design of new CPPs and how some issues may be mitigated, rather than new photocatalytic processes to explore.

1.3.3 Findings

The following outlines a range of selected photocatalytic applications for which CPPs have been employed. These applications include photosensitisation and photodegradation, photooxidations, coupling reactions, photopolymerisations and hydrogen production. Within each section, different CPPs will be presented for each application, showcasing a variety of polymer architectures and designs. The applications regarding photodegradation, coupling reactions and photopolymerisations were written by Yan Lung Wong at City University of Hong Kong.

1.3.3.1 CPPs for Photosensitisation

Photosensitisers are a class of photocatalytic materials used in the production of singlet oxygen ($^1O_2$), a highly reactive electronic state of oxygen used in applications such as photodynamic therapy (PDT) for cancer treatment [1.66, 1.67], wastewater treatment [1.68, 1.69] and synthesis of fine chemicals [1.70]. As much of the work presented in the proceeding chapters investigates polymeric materials as photosensitisers, the mechanism is described below.

The process of generating $^1O_2$ works through the absorption of light at a specific wavelength by a photosensitiser, promoting it to a higher energy singlet state (^{1}PS). Through an intersystem crossing (ISC) mechanism, the spin paring of electrons become parallel resulting in a lower energy triplet state (^{3}PS). If this intersystem crossing is either inefficient or does not occur, the energy is dissipated through either fluorescence or non-radiative decay. Furthermore, if ^{3}PS is unable to interact with a target molecule either through rate of relaxation or absence of substrate, the photosensitiser will return to the ground state (PS) through either phosphorescence or non-radiative decay. However, in the presence of oxygen at its ground state ($^3O_2$), an energy transfer *via* physical collision between $^3O_2$ and ^{3}PS can occur resulting in the production of $^1O_2$ and the photosensitiser relaxing back to its ground state [1.64]. This process is depicted using a Jablonski diagram as seen in Figure 1.10.

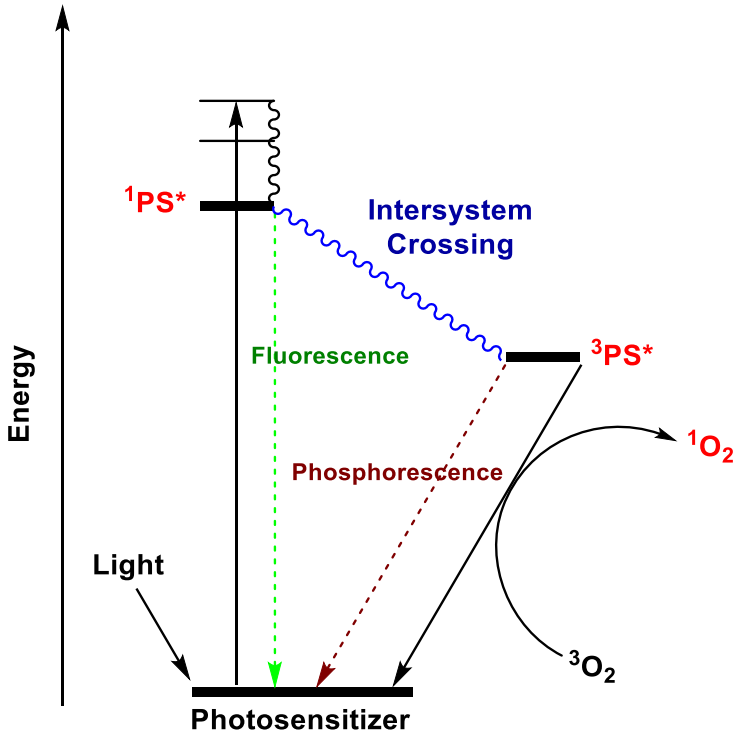

Figure 1.10 Jablonski diagram describing the photosensitisation of $^3O_2$.

Distinguishing between the electronic structure of $^3O_2$ and $^1O_2$ is important to understanding the difference in their reactivity. As depicted in the molecular orbital diagram (Figure 1.11), $^3O_2$ ($^3\Sigma^-_g$) contains two unpaired electrons occupying two degenerate anti-bonding (π^*) orbitals. Upon excitation, two accessible excited states can be formed, $^1\Delta_g$ and $^1\Sigma^+_g$, which have energies of 95 and 158 kJ mol^{-1} above the ground state, respectively. The second singlet state, $^1\Sigma^+_g$, presents with a similar electronic configuration with the exception of an antiparallel spin between the two π^* electrons. This electronic state is highly unstable and is not the reactive $^1O_2$ referred to in this section as it is a spin allowed transition and relaxes back to the ground state too quickly to interact with a substrate. However, the first singlet state, $^1\Delta_g$, presents with the π^* electrons as a pair leaving the other orbital unfilled. The transition from $^1\Delta_g$ to $^3\Sigma^-_g$ is spin forbidden and therefore is relatively long-lived (10^{-6} to 10^{-3} s in solvent), allowing its use as an electrophilic reagent [1.64].

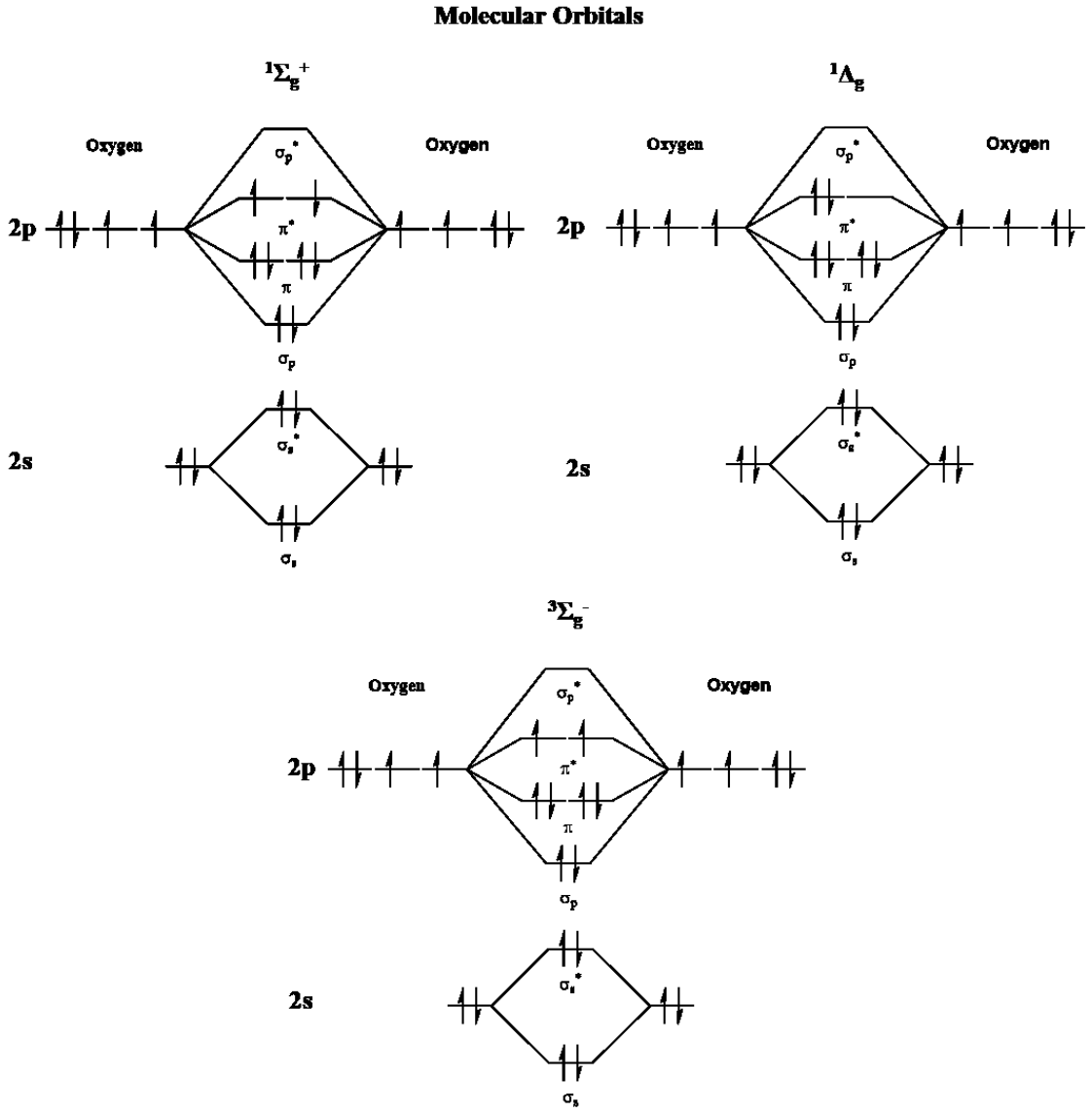

Figure 1.11 Molecular orbital diagram of the triplet ($^3\Sigma^-_g$) and accessible singlet ($^1\Delta_g$ and $^1\Sigma^+_g$) electronic states of oxygen. Lower energy 1s orbitals have been omitted for simplicity.

Many common photosensitisers are employed under homogeneous conditions and include a variety of organic dyes, porphyrins, and cyanines, just to name a few [1.13]. Recently, however, CPPs have been demonstrated as effective heterogeneous photosensitisers for $^1O_2$ production. A CPP containing alternating benzene and benzothiadiazole units separated by alkynes acted as a photosensitiser in chloroform when irradiated at a wavelength of 420 nm [1.63, 1.71]. To monitor this reaction qualitatively, *α*-terpinene was added to the mixture as it produces ascaridole in the presence of $^1O_2$. This reaction was used as it will not proceed with other reactive forms of oxygen, indicating a positive test for $^1O_2$ production [1.72, 1.73]. The same CPP was

also synthesised in the presence of silica nanoparticles to demonstrate how surface area can have a significant effect on catalytic performance [1.63]. This showed that both the electronic and morphological properties of CPPs can be influenced through carefully selected synthetic methodologies resulting in a highly tuneable photocatalyst.

As CPPs are rigid, carbon-based structures they tend to be incompatible in water, showing poor overall performance. To create a more water compatible material, a hydrophilic mercaptopropionic acid moiety was added to the repeat units of the CPP *via* post-synthetic thiol-yne chemistry (Figure 1.12) [1.74, 1.75]. This resulted in a polymer with much greater compatibility in water, and in turn, demonstrated a heightened ability for $^1O_2$ production in water when compared to the unaltered polymer.

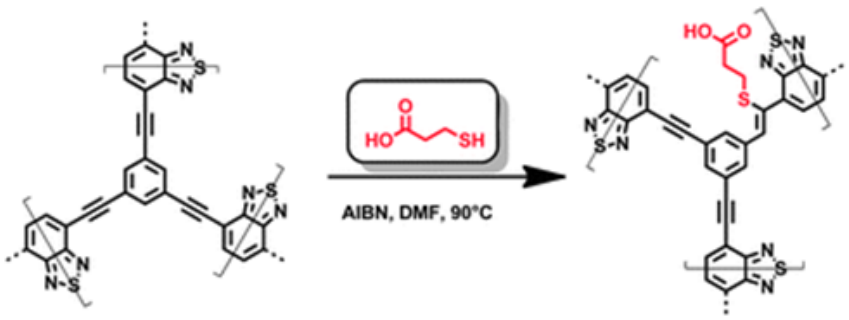

Figure 1.12 Post-synthetically modified CPP using thiol-yne chemistry [1.74].

While CPPs are traditionally designed to be metal-free, this is not always the case. Metallophthalocyanine-based CPPs have been synthesised *via* Schiff base polycondensation with different metal centres [1.76]. These materials also demonstrated remarkable efficiency for $^1O_2$ production, albeit they were irradiated with much less energetic wavelengths (700 nm). In this example, the implementation of metals and the resulting bathochromic shift presents an important trade off to consider when designing CPPs. Ideally, no metals should be present when implementing these materials as photocatalysts as they can be expensive and can result in environmental and toxicity issues due to leeching effects. However, this may be offset by the enhanced or altered properties and may need to be considered where more traditional CPP methodologies do not yield sufficient results for the required task. This issue is addressed through the work presented in this thesis.

1.3.3.2 Photodegradation

Literature has provided several examples of CPPs used in the photodegradation of harmful or toxic chemicals. While the mechanisms of this process can vary greatly depending on the reaction conditions and target reactant, the generation of reactive oxygen species or other radical species tends to be the most common route. Visible-light irradiation ($\lambda > 400$ nm) of graphitic carbon nitride, a specific class of CPP, resulted in accelerated degradation of imidacloprid in an aqueous solution [1.77]. Imidacloprid (Figure 1.13) is one of the most widely used insecticides worldwide and commonly contaminates water sources, requiring the potential need for water purification. While not overly harmful to humans, it is fatal to honey bees, other insects and some aquatic life [1.78].

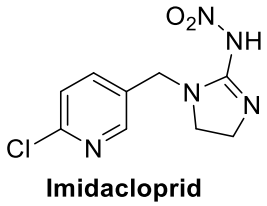

Figure 1.13 Chemical structure of the insecticide imidacloprid.

Polymer-supported dyes in microporous organic polymers have also been shown as effective in the photodegradation of 4-chlorophenol when irradiated with visible light ($\lambda > 420$ nm) [1.79]. While not strictly a CPP due to the break in conjugation, this material demonstrated many of the characteristics associated with photocatalytic CPPs (high surface area, insoluble, visible-light absorbance) and its ability to act as a visible light harvester. The concept of polymer-supported photosensitisers will be addressed further as new materials are presented in Chapter 4.

1.3.3.3 Oxidation

Reactive oxygen species are often seen as a common theme when discussing CPPs as photocatalytic materials. The way in which these species are used, however, is a much more intriguing concept. For example, oxidation of benzyl alcohols for the selective formation of ketones and aldehydes have been shown with mesoporous graphitic carbon nitride [1.80]. Through a templating method with silica nanoparticles, the surface area

was greatly enhanced and consequently demonstrated 10 times the catalytic efficiency when compared to unmodified graphitic carbon nitride.

Another group of CPPs containing cleavable *tert*-butyl carboxylate (BOC) units were used for the photooxidation of organic sulphides to sulfoxides [1.81]. While the removal of the BOC units resulted in materials with greater surface areas, their photocatalytic activity was unchanged when compared to the BOC-equipped CPPs. Although changes in the surface area did not affect the reaction, it is important to explore these avenues. Alteration of existing CPP design methodologies through both electronic and morphological pathways show how these materials may be explored in the future.

1.3.3.4 Coupling Reactions

Organic reactions, predominantly coupling reactions, for the synthesis of fine chemicals has been explored to great depths. As we look to address the issues surrounding sustainability and implementation of 'green' materials, CPPs have begun to arise as potential photocatalytic solutions to these problems. Mesoporous graphitic carbon nitride, as described above, has shown excellent results as a visible-light photocatalyst for a variety of oxidative coupling reactions including the coupling syntheses of amines, benzoxazoles, benzimidazoles and benzothiazoles [1.82]. A benzodifuran-based CPP also demonstrated good photocatalytic activity for the oxidative coupling of amines. However, the reaction was thought to proceed through a photoredox mechanism as opposed to the reductive activation of molecular oxygen as suggested for the mesoporous graphitic carbon nitride [1.83]. Furthermore, CPPs equipped with a common Rose Bengal dye functionality were successfully used as heterogeneous photocatalysts in Aza-Henry reactions, which proceeds through a single electron transfer (SET) mechanism [1.84]. These examples presented in literature exhibit the potential for photocatalytic CPPs and how they can be used under a wide variety of reaction conditions and mechanistic pathways.

The substitution of metal-based photocatalysts for more environmentally friendly materials is a continuing theme for CPPs. However, where CPPs are unable to meet the energetic or mechanistic requirements of more demanding reactions, the incorporation of the appropriate metal into the polymer framework can lead to a more sustainable and easily reused photocatalyst. One such reaction is the Pd-catalysed Suzuki-Miyaura cross

coupling reaction. To address this, a network containing benzoxadiazole-benzene units with immobilised Pd nanoparticles was employed as a visible-light photocatalyst for Suzuki coupling reactions at room temperature [1.85]. Mild reaction conditions and the highly resuable Pd-loaded CPP resulted in a distinct improvement when compared to the standard reaction conditions required (*i.e.* high temperature and soluble Pd-catalyst).

1.3.3.5 Photopolymerisations

Polymers have become and continue to be one of the most important industries worldwide. Although many initiators and polymer growth methods have been described, further development of photoinitiators allows for polymerisations to be carried out under milder conditions (*e.g.* room temperature). To this point, CPPs have been described as heterogeneous visible-light photoinitiators for both free radical and cationic polymerisations. As these CPPs are employed under heterogeneous conditions, ease of separation and reusability along with mitigating unwanted side effects arising from homogeneous photoinitiators (*e.g.* colouration) offer a promising group of materials.

Literature shows that photoinitiating CPPs proceed through a type II mechanism whereby a co-initiator, such as triethylamine (Et_3N), is required for the polymerisation to proceed [1.86]. Three different examples of CPPs have been described as photoinitiators for the polymerisation of methyl methacrylate (MMA). These include a phenolphthalein-based CPP [1.86], mesoporous graphitic carbon nitride [1.87, 1.88] and a benzene-carbazole-benzoxadiazole CPP system [1.89]. While all the materials were successfully recovered and reused, photocatalytic activity varied upon consecutive runs. The scale at which polymers are produced within an industrial setting (tonnes per year) allows for the fervent discovery of new heterogeneous CPP photoinitiators to replace those commonly used. Furthermore, mechanistic studies of CPPs to determine other potential polymerisation pathways is a prudent step to understanding their true scope as photoinitiators.

1.3.3.6 Hydrogen Production

In general, the photocatalytic applications of CPPs presented thus far have had a basis within the synthesis (or destruction) of chemical species. However, CPPs can also be implemented in energy production through the generation of hydrogen *via*

photocatalytic water splitting. As conventional energy sources such as fossil fuels become less sustainable, the implementation of the 'Hydrogen Economy' is a potential remedy to this issue. Thus far, most materials used for photocatalytic hydrogen production have been inorganic semiconductors, such as metal oxides [1.10, 1.90, 1.91]. However, structural and photophysical control of inorganic semiconductors is a difficult task to accomplish. Application of photoactive CPPs can solve these issues as they are highly tuneable allowing them to be designed for more restrictive requirements.

Graphitic carbon nitride was the first reported use of a CPP for photocatalytic hydrogen production whereby both a non-doped and Pt-doped sample was used [1.18, 1.92]. While both materials demonstrated good hydrogen evolution and reusability, the Pt-doped polymer exhibited much greater photocatalytic activity. Polymeric nanorods composed of triphenylamine and a diacrylonitrile monomer were also templated with a TiO_2-Pt composite and used [1.93]. When compared to homogeneous alternatives (Eosin-Y and a Ru-based photocatalyst), the nanorods presented equal or lesser photocatalytic activity. Upon repeated usage, significant degradation and decreased efficiency was observed in the nanorods, hereby nullifying a major selling point of CPPs as heterogeneous photocatalysts.

As seen in the above examples, all of the reaction conditions required the presence of a metal co-catalyst to achieve efficient hydrogen evolution. While this is necessary in many cases, issues associated with increased cost and environmental concerns begin to arise, not to mention a key property of CPPs as being metal-free materials being negated. Furthermore, these metals can introduce instability to the system and affect the reusability potential of these materials (*i.e.* sterilisation of Pd *via* CO poisoning) [1.94].

More recently, a series of CPPs containing benzene-pyrene networks has been reported as materials for photocatalytic hydrogen evolution under visible light irradiation ($\lambda > 420$ nm) [1.95]. All the materials presented varying physical and photophysical properties and therefore had differing results when comparing hydrogen evolution rates. Most importantly, the CPPs were tested in the absence of a metal co-catalyst whereby the most efficient polymers still demonstrated exceptional rates of hydrogen evolution. Conversely, as these CPPs were synthesised through traditional Pd-based Suzuki coupling, it was suggested that residual metals remaining from the polymerisation process may be aiding in this photocatalytic process. After further testing, this concern was

alleviated as addition of a co-catalyst had no effect. The primary factor affecting the process was the optical band gap as it showed the strongest correlation to the rate of hydrogen production. While these materials show great promise for photocatalytic hydrogen production, in depth mechanistic studies are required to acquire a better understanding of this process, particularly regarding the removal of a metal co-catalyst from the equation.

1.3.4 Conclusion

Heterogeneous photocatalytic applications utilising CPPs have begun to emerge and grow in recent years. With the ability to control both electronic and morphological properties, CPPs have been shown as effective substitutes to traditional homogeneous photocatalysts within many applications. As issues can arise regarding light penetration with an increasing scale of reaction, we envisaged CPPs to be integrated into continuous flow technology. An application note written for Vapourtec Ltd. is available on their website regarding the use of CPPs and other photocatalytic polymers under continuous flow conditions and can also be found in Appendix A [1.96]. The application note details the advantages of flow chemistry compared to traditional batch reactions and describes some of the materials used thus far in our laboratory.

As previously mentioned, a primary goal of CPPs as metal-free heterogeneous photocatalysts is to create more sustainable and less toxic alternatives to reactions which tend to use metal-rich photocatalysts. While not all photoinduced reactions were successful without some form of metal co-catalyst, most applications excelled with the CPP alone. The removal of metals from these reactions solves the issues of trace metal contamination, a serious concern surrounding pharmaceutical synthesis [1.97, 1.98]. While CPPs have shown tremendous progress and innovation, the scope for new applications and material design continues to grow at an increasing rate.

With a focus towards CPP synthesis and design, this perspective outlines three major challenges, which must be addressed to compete with the well-established photocatalysts used today. The first issue concerns the synthetic routes for CPPs as they largely consist of metal catalysed coupling reactions. Due to economic and environmental factors, these synthetic routes may limit their production at larger commercial and industrial scales. Furthermore, by developing metal-free polymerisation

techniques for CPPs, more sustainable processes for both the synthesis and application can be envisioned. Secondly, continued investigation into electronic control of CPPs allows for a potential bathochromic shift in absorbance to lower energy (longer wavelength) light irradiation. This is much preferred as UV and near-UV irradiation is problematic with regards to photodegradation of reagents and products as well as unwanted side reactions. Lastly, it must be acknowledged that CPPs will not always be able to meet the energetic demands or environmental conditions required to act as a (photo)catalyst where metal-based materials are used. This may be caused by an unreachable energy barrier (inadequate energetic state of the CPP) or potential mechanistic consideration (*e.g.* Cu click reactions) whereby a reaction is unable to proceed with a CPP alone. Therefore, in situations where a CPP is unable to fulfil the role of a (photo)catalyst alone, metal-loading *via* synthetic design or post synthetic modification can be performed to immobilise the metal species. This will allow for materials that can be easily recovered and reused, along with the potential for greater photostability when compared to the metal catalyst alone.

1.3.5 Impact on Literature and Research

For the advancement of research in a particularly young and growing field such as CPPs, accessibility to concise information is of paramount importance. While CPPs have shown the ability to be employed in a variety of applications, this review focused solely on literature describing their broad range of photocatalytic capabilities. Furthermore, current obstacles which need to be addressed have been presented, along with a perspective towards how this may be achieved. To date, this paper has 30 citations, indicating its impact on the scientific community and the growing interest of CPPs as photocatalytic materials. This work has not only encouraged the continued investigation of CPPs in a broader context, it has also helped nurture the growth and discovery of these materials [1.28, 1.99].

The work that will be presented throughout the remaining chapters was influenced greatly by the literature cited within the review below. This is true not only in terms of potential applications but also with regards to polymer design. By investigating and understanding the available materials, this allowed a perspective to be formed on how to proceed. Specifically, the notion of electronic control of absorbance values and metal-

free synthetic procedures permeate throughout this work. The concept of morphological control and post-synthetic modification will also be addressed.

1.4 References

[1.1] *Changes since the industrial revolution,* 2013, American Chemical Society, accessed September 2018, <https://www.acs.org/content/acs/en/climatescience/greenhousegases/industrialrevolution.html>

[1.2] J. Cook, N, Oreskes, P. T. Doran, W. R. L. Anderegg, B. Verheggen, E. W. Maibach, J. S. Carlton, S. Lewandowsky, A. G. Skuce, S. A. Green, D. Nuccitelli, P. Jacobs, M. Richardson, B. Winkler, R. Painting, K. Rice, *Consensus on consensus: a synthesis of consensus estimates on human-caused global warming*, Environ. Res. Lett., **11**, 048002 (1-7), (2016)

[1.3] G. Ciamician, *The Photochemistry of the Future*, Science, **36**, 385-394, (1912)

[1.4] *Factors that Control Earth's Temperature*, 2016, J. Rosen, A. E. Egger, accessed September 2018**,** <https://www.visionlearning.com/en/library/Earth-Science/6/Factors-that-Control-Earths-Temperature/234>

[1.5] T. D. Lee, A. U. Ebong, *A Review of thin film solar cell technologies and challenges*, Renew. Sust. Energ. Rev., **70**, 1286-1297, (2017)

[1.6] P. T. Anastas, J. Warner, *Green Chemistry: Theory and Practice*, Oxford University Press, USA, (1998)

[1.7] J. Schneider, D. Bahnemann, J. Ye, G. Li Puma. D. D. Dionysiou, *Photocatalysis: Fundamentals and Perspectives*, The Royal Society of Chemistry, UK, (2016)

[1.8] A. Fujishima, K. Honda, *Electrochemical Photolysis of Water at a Semiconductor Electrode*, Nature, **238**, 37-38 (1972)

[1.9] M. R. Hoffmann, S. T. Martin, W. Choi, D. W. Bahnemann, *Environmental Applications of Semiconductor Photocatalysis*, Chem. Rev., **95**, 69-96 (1995)

[1.10] A. Kudo, Y. Miseki, *Heterogeneous photocatalyst materials for water splitting*, Chem. Soc. Rev., **38**, 253-278 (2009)

[1.11] A. J. Esswein, D. G. Nocera, *Hydrogen Production by Molecular Photocatalysis,* Chem. Rev., **107**, 4022-4047 (2007)

[1.12] K. A. Ahrendt, C. J. Borths, D. W. C. Macmillan, *New Strategies for Organic Catalysis: The First Highly Enantioselective Organocatalytic Diels-Alder Reaction*, J. Am. Chem. Soc., **122**, 4243-4244 (2000)

[1.13] R. W. Redmond, J. N. Gamlin, *A compilation of singlet oxygen yields from biologically relevant molecules,* Photochem. Photobiol., **70**, 391-475 (1999)

[1.14] V. Srivastava, P. P. Singh, *Eosin Y catalysed photoredox synthesis: a review*, RSC Adv., **7**, 31377-31392 (2017)

[1.15] M. L. Marin, L. Santos-Juanes, A. Arques, A. M. Amat, M. A. Miranda, *Organic Photocatalysis for the Oxidation of Pollutants and Model Compounds*, Chem. Rev., **112**, 1710-1750 (2012)

[1.16] S. Guo, H. Zhang, L. Huang, Z. Guo, G. Xiong, J. Zhao, *Porous material-immobilized iodo-Bodipy as an efficient photocatalyst for photoredox catalytic organic reaction to prepare pyrrolo[2,1-a]isoquinoline*, Chem. Commun., **49**, 8689-8691 (2013)

[1.17] C-A. Wang, Y-W. Li, X-L. Cheng, J-P. Zhang, Y-F. Han, *Eosin Y dye-based porous organic polymers for highly efficient heterogeneous photocatalytic dehydrogenative coupling reaction*, RSC Adv., **7**, 408-414 (2017)

[1.18] X. Wang, K. Maeda, A. Thomas, K. Takanabe, G. Xin, J. M. Carlsson, K. Domen, M. Antonietti, *A metal-free polymeric photocatalyst for hydrogen production from water under visible light*, Nat. Mater., **8**, 76–80 (2009)

[1.19] Y. Wang, X. Wang, M. Antonietti, *Polymeric graphitic carbon nitride as a heterogeneous organocatalyst: from photochemistry to multipurpose catalysis to sustainable chemistry*, Angew. Chem., Int. Ed., **51**, 68–89 (2012)

[1.20] Y. Zhi, K. Li, H. Xia, M. Xue, Y. Mu, X. Liu, *Robust porous organic polymers as efficient heterogeneous organo-photocatalysts for aerobic oxidation reactions*, J. Mater. Chem. A., **5**, 8697-8704 (2017)

[1.21] H. Staudinger, *Über Polymerisation*, Ber. Dtsch. Chem. Ges., **53**, 1073-1085 (1920)

[1.22] J. M. G. Cowie, V. Arrighi, *Polymers: Chemistry and Physics of Modern Materials*, 3rd Ed., CRC Press: Boca Raton, FL, (2008)

[1.23] H. Catalgil-Giz, A. Giz, A. Oncul-Koc, *Termination mechanism of polymethyl methacrylate and polystyrene studied by ultrasonic degradation technique*, Polym. Bull., **43**, 215-222 (1999)

[1.24] S. Itsuno, M. M. Parves, N. Haragushi, *Polymeric chiral organocatalysts*, Polym. Chem., **2**, 1942-1949 (2011)

[1.25] J.-X. Jiang, F. Su, A. Trewin, C. D. Wood, N. L. Campbell, H. Niu, C. Dickinson, A. Y. Ganin, M. J. Rosseinsky, Y. Z. Khimyak, A. I. Cooper, *Conjugated Microporous Poly(aryleneethynylene) Networks*, Angew. Chem., Int. Ed., **46**, 8574-8578 (2007)

[1.26] K. S. W. Sing, D. H. Everett, R. A. W. Haul, L. Moscou, R. A. Pierotti, J. Rouquerol, T. Siemieniewska, *Reporting physisorption data for gas/solid systems with special reference to the determination of surface area and porosity*, Pure & Appl. Chem., **4**, 603-619 (1985)

[1.27] F. Vilela, K. Zhang, M. Antonietti, *Conjugated porous polymers for energy applications*, Energy Environ. Sci., **5**, 7819-7832 (2012)

[1.28] N. Chaoui, M. Trunk, R. Dawson, J. Schmidt, A. Thomas, *Trends and challenges for microporous polymers*, Chem. Soc. Rev., **46**, 3302-3321 (2017)

[1.29] Q. Huo, *Synthetic Chemistry of the Inorganic Ordered Porous Materials.* In: Modern Inorganic Synthetic Chemistry, Elsevier, Amsterdam (2011)

[1.30] P. Lindemann, A. Schade, L. Monnereau, W. Feng, K. Batra, H. Gliemann, P. Levkin, S. Brase, C. Woll, M. Tsotsalas, *Surface functionalization of conjugated microporous polymer thin films and nanomembranes using orthogonal chemistries*, J. Mater. Chem. A, **4**, 6815-6818 (2016)

[1.31] C. Gu, N. Huang, Y. Chen, L. Qin, H. Xu, S. Zhang, F. Li, Y. Ma, D. Jiang, *π-Conjugated Microporous Polymer Films: Designed Synthesis, Conducting Properties, and Photoenergy Conversions*, Angew. Chem., Int. Ed., **46**, 13594-13598 (2015)

[1.32] K. Zhang, B. Tieke, J. C. Forgie, P. J. Skabara, *Electrochemical Polymerisation of N-Arylated and N-Alkylated EDOT-Substituted Pyrrolo[3,4-c]pyrrole-1,4-dione (DDP) Derivatives: Influence of Substitution Pattern on Optical and Electronic Properties*, Macromol. Rapid. Commun., **30**, 1834-1840 (2009)

[1.33] J. Schmidt, M. Werner, A. Thomas, *Conjugated Microporous Polymer Networks via Yamamoto Polymerization*, Macromolecules, **42**, 4426-4429 (2009)
4426–4429

[1.34] J.-X. Jiang, F. Su, H. Niu, C. D. Wood, N. L. Campbell, Y. Z. Khimyak, A. I. Cooper, *Conjugated microporous poly(phenylenebutadiynylene)s*, Chem. Commun., **4**, 486-488 (2008)

[1.35] L. Chen, Y. Honsho, S. Seki, D. Jiang, *Light-Harvesting Conjugated Microporous Polymers: Rapid and Highly Efficient Flow of Light Energy with a Porous Polyphenylene Framework as Antenna*, J. Am. Chem. Soc., **132**, 6742–6748 (2010)

[1.36] J.-X. Jiang, F. Su, A. Trewin, C. D. Wood, H. Niu, J. T. A. Jones, Y. Z. Khimyak, A. I. Cooper, *Synthetic Control of the Pore Dimension and Surface Area in Conjugated Microporous Polymer and Copolymer Networks*, J. Am. Chem. Soc., **130**, 7710–7720 (2008)

[1.37] P. Kuhn, M. Antonietti, A. Thomas, *Porous, Covalent Triazine-Based Frameworks Prepared by Ionothermal Synthesis*, Angew. Chem., Int. Ed., **47**, 3499–3502 (2008)

[1.38] J. Weber, O. Su, M. Antonietti, A. Thomas, *Exploring Polymers of Intrinsic Microporosity – Microporous, Soluble Polyamide and Polyimide*, Macromol. Rapid Commun., **28**, 1871-1876 (2007)

[1.39] M. G. Schwab, B. Fassbender, H. W. Spiess, A. Thomas, X. Feng, K. Mullen, *Catalyst-free preparation of melamine-based microporous polymer networks through Schiff base chemistry,* J. Am. Chem. Soc., **131**, 7216-7217 (2009)

[1.40] P. Pandey, A. P. Katsoulidis, I. Eryazici, Y. Wu, M. G. Kanatzidis, S. T. Nguyen, *Imine-Linked Microporous Polymer Organic Frameworks*, Chem. Mater., **22**, 4974-4979 (2010)

[1.41] N. Miyaura, A. Suzuki, *Palladium-Catalyzed Cross-Coupling Reactions of Organoboron Compounds*, Chem. Rev., **95**, 2457-2483 (1995)

[1.42] R. Chinchilla, C. Najera, *Recent advances in Sonogashira reactions*, Chem. Soc. Rev., **40**, 5084-5121 (2011)

[1.43] Y.-J. Cheng, S.-H. Yang, C.-S. Hsu, *Synthesis of Conjugated Polymers for Organic Solar Cell Applications*, Chem. Rev., **109**, 5868-5923 (2009)

[1.44] M. Zaarour, B. Dong, I. Naydenova, R. Retoux, S. Mintova, *Progress in zeolite synthesis promotes advanced applications*, Microporous Mesoporous Mater., **189**, 11–21 (2014)

[1.45] M. E. Davis, *New vistas in zeolite and molecular sieve catalysis*, Acc. Chem. Res., **26**, 111–115 (1993)

[1.46] A. K. Cheetham, G. Ferey, T. Loiseau, *Open-Framework Inorganic Materials*, Angew. Chem., Int. Ed., **38**, 3268–3292 (1999)

[1.47] J. G. Croissant, X. Cattoen, M. Wong Chi Man, J.-O. Durand, N. M. Khashab, *Syntheses and application of periodic mesoporous organosilica nanoparticles*, Nanoscale, **7**, 20318–20334 (2015)

[1.48] V. C. Menon, S. Komarneni*, Porous Adsorbents for Vehicular Natural Gas Storage: A Review*, J. Porous Mater., **5**, 43–58 (1998)

[1.49] M. Nolan, A. Iwaszuk, A. K. Lucid, J. J. Carey, M. Fronzi, *Design of Novel Visible Light Active Photocatalyst Materials: Surface Modified TiO_2,* Adv. Mater., **27**, 5425–5446 (2016)

[1.50] C. N. R. Rao, S. Dey, *Generation of H_2 and CO by solar thermochemical splitting of H_2O and CO_2 by employing metal oxides*, J. Solid State Chem., **242***,* 107–115 (2016)

[1.51] Z. Zhang, Z. Jiang, W. Shangguan, *Low-temperature catalysis for VOCs removal in technology and application: A state-of-the-art review*, Catal. Today, **264**, 270–278 (2016)

[1.52] M. Tiemann, *Porous Metal Oxides as Gas Sensors*, Chem.–Eur. J., **13**, 8376–8388 (2007)

[1.53] M. C. So, G. P. Wiederrecht, J. E. Mondloch, J. T. Hupp, O. K. Farha, *Metal-Organic framework materials for light-harvesting and energy transfer*, Chem. Commun., **51**, 3501–3510 (2015)

[1.54] I. Senkovska, S. Kaskel, *Ultrahigh porosity in mesoporous MOFs: promises and limitation*, Chem. Commun., **50**, 7089–7098 (2014)

[1.55] N. J. Hinks, A. C. McKinlay, B. Xiao, P. S. Wheatley, R. E. Morris, *Metal organic frameworks as NO delivery materials for biological applications*, Microporous Mesoporous Mater., **129**, 330–334 (2010)

[1.56] W. Cai, C.-C. Chu, G. Liu, Y.-X. J. W′ang, *Metal-Organic Framework-Based Nanomedicine Platforms for Drug Delivery and Molecular Imaging*, Small, **11**, 4806–4822 (2015)

[1.57] J. Gascon, A. Corma, F. Kapteijn, F. X. Llabres i Xamena, *Metal Organic Framework Catalysis: Quo vadis?*, ACS Catal., **4**, 361–378 (2014)

[1.58] R. Sabouni, H. Kazemian, S. Rohani, *Carbon dioxide capturing technologies: a review focusing on metal organic framework materials (MOFs)*, Environ. Sci. Pollut. Res., **21**, 5427–5449 (2013)

[1.59] A. P. Cote, A. I. Benin, N. W. Ockwig, M. O'Keeffe, A. J. Matzger, O. M. Yaghi, *Porous, Crystalline, Covalent Organic Frameworks,* Science, **310**, 1166–1170 (2005)

[1.60] E. L. Spitler, W. R. Dichtel, *Lewis acid-catalysed formation of two-dimensional phthalocyanine covalent organic frameworks*, Nat. Chem., **2**, 672–677 (2010)

[1.61] X. Feng, L. Chen, Y. Dong, D. Jiang, *Porphyrin-based two-dimensional covalent organic frameworks: synchronized synthetic control of macroscopic structures and pore parameters*, Chem. Commun., **47**, 1979–1981 (2011)

[1.62] J. W. Colson, W. R. Dichtel, *Rationally synthesized two-dimensional polymers*, Nat. Chem., **5**, 453–465 (2013)

[1.63] K. Zhang, D. Kopetzki, P. H. Seeberger, M. Antonietti, F. Vilela, *Angew. Chem. Int. Ed.*, **2013**, *52*, 1432-1436.

[1.64] M. C. DeRosa, R. J. Crutchley, *Coord. Chem. Rev*., **2002**, *233–234*, 351-371.

[1.65] J. M. Tobin, T. J. D. McCabe, A. W. Prentice, S. Holzer, G. O. Lloyd, M. J. Paterson, V. Arrighi, P. A. G. Cormack, F. Vilela, *Polymer-Supported Photosensitizers*

for Oxidative Organic Transformations in Flow and under Visible Light Irradiation, ACS Catal., **7**, 4602-4612 (2017)

[1.66] R. Bonnett, *Photosensitizers of the porphyrin and phthalocyanine series for photodynamic therapy*, Chem. Soc. Rev., **24**, 19−33 (1995)

[1.67] S. G. Awuah, Y. You, *Boron dipyrromethene (BODIPY)-based photosensitizers for photodynamic therapy,* RSC Adv., **2**, 11169−11183 (2012)

[1.68] S. Canonica, P. G. Tratnyek, *Quantitative structure-activity relationships for oxidation reactions of organic chemicals in water*, Environ. Toxicol. Chem., **22**, 1743−1754 (2003)

[1.69] J. Shen, R. Steinbach, J. M. Tobin, M. M. Nakata, M. Bower, M. R. S. McCoustra, H. Bridle, V. Arrighi, F. Vilela, *Photoactive and metal-free polyamide-based polymers for water and wastewater treatment under visible light irradiation*, Appl. Cat. B - Environ., **193**, 226-233 (2016)

[1.70] E. L. Clennan, *New Mechanistic and Synthetic Aspects of Singlet Oxygen Chemistry*, Tetrahedron, **56**, 9151-9179 (2000)

[1.71] K. Zhang, Z. Vobecka, K. Tauer, M. Antonietti, F. Vilela, *π-Conjugated polyHIPEs as highly efficient and reusable heterogeneous photosensitizers,* Chem. Commun., **49**, 11158–11160 (2013)

[1.72] S. Ogawa, S. Fukui, Y. Hanasaki, K. Asano, H. Uegaki, F. Sumiko, S. Ryosuke, *Determination method of singlet oxygen in the atmosphere by use of α-terpinene,* Chemosphere, **22**, 1211-1225 (1991)

[1.73] D. Choi, M. Jung, *Protective activities of catechins on singlet oxygen induced photooxidation of α-terpinene in methanol: structure and singlet oxygen quenching activity relationship*, Food Sci. Biotechnol., **22**, 249-256 (2013)

[1.74] H. Urakami, K. Zhang, F. Vilela, *Modification of conjugated microporous poly-benzothiadiazole for photosensitized singlet oxygen generation in water*, Chem. Commun., **49**, 2353-2355 (2013)

[1.75] B. Kiskan, J. Weber, *Versatile Postmodification of Conjugated Microporous Polymers Using Thiol-yne Chemistry*, ACS Macro Lett., **1**, 37-40 (2012)

[1.76] X. Ding, B.-H. Han, *Metallophthalocyanine-Based Conjugated Microporous Polymers as Highly Efficient Photosensitizers for Singlet Oxygen Generation*, Angew. Chem., Int. Ed., **54**, 6536-6539 (2015)

[1.77] X. Liu, X. Wu, Z. Long, C. Zhang, Y. Ma, X. Hao, H. Zhang, C. Pan, *Photodegradation of Imidacloprid in Aqueous Solution by the Metal-Free Catalyst*

Graphitic Carbon Nitride using an Energy-Saving Lamp, J. Agric. Food Chem., **63**, 4754–4760 (2015)

[1.78] *Imidacloprid General Fact Sheet*, 2010, National Pesticide Information Center, accessed June 2018**,** <http://npic.orst.edu/factsheets/imidagen.html>

[1.79] N. Park, D. Kang, M. C. Ahn, S. Kang, S. M. Lee, T. K. Ahn, J. Y. Jaung, H.-W. Shin, S. U. Son, *Hollow and sulfonated microporous organic polymers: versatile platforms for non-covalent fixation of molecular photocatalysts*, RSC Adv., **5**, 47270–47274 (2015)

[1.80] F. Su, S. C. Mathew, G. Lipner, X. Fu, M. Antonietti, S. Blechert, X. Wang, *mpg-C_3N_4-Catalyzed Selective Oxidation of Alcohols Using O_2 and Visible Light*, J. Am. Chem. Soc., **132**, 16299–16301 (2010)

[1.81] Z. J. Wang, S. Ghasimi, K. Landfester, K. A. I. Zhang, *Highly porous conjugated polymers for selective oxidation of organic sulfides under visible light*, Chem. Commun., **50**, 8177–8180 (2014)

[1.82] F. Su, S. C. Mathew, L. Mohlmann, M. Antonietti, X. Wang, S. Blechert, *Aerobic Oxidative Coupling of Amines by Carbon Nitride Photocatalysis with Visible Light,* Angew. Chem., Int. Ed., **50**, 657–660 (2011)

[1.83] N. Kang, J. H. Park, K. C. Ko, J. Chun, E. Kim, H.-W. Shin, S. M. Lee, H. J. Kim, T. K. Ahn, J. Y. Lee, S. U. Son, *Tandem Synthesis of Photoactive Benzodifuran Moieties in the Formation of Microporous Organic Networks*, Angew. Chem., Int. Ed., **52**, 6228–6232 (2013)

[1.84] J.-X. Jiang, Y. Li, X. Wu, J. Xiao, D. J. Adams, A. I. Cooper, *Conjugated Microporous Polymers with Rose Bengal Dye for Highly Efficient Heterogeneous Organo-Photocatalysis*, Macromolecules, **46**, 8779–8783 (2013)

[1.85] Z. J. Wang, S. Ghasimi, K. Landfester, K. A. I. Zhang, *Photocatalytic Suzuki Coupling Reaction Using Conjugated Microporous Polymer with Immobilized Palladium Nanoparticles under Visible Light*, Chem. Mater., **27**, 1921–1924 (2015)

[1.86] B. Kiskan, M. Antonietti, J. Weber, *Teaching New Tricks to an Old Indicator: pH-Switchable, Photoactive Microporous Polymer Networks from Phenolphthalein with Tunable CO_2Adsorption Power,* Macromolecules, **45**, 1356–1361 (2012)

[1.87] B. Kiskan, J. Zhang, X. Wang, M. Antonietti, Y. Yagci, *Mesoporous Graphitic Carbon Nitride as a Heterogeneous Visible Light Photoinitiator for Radical Polymerization*, ACS Macro Lett., **1**, 546–549 (2012)

[1.88] S. Dadashi-Silab, H. Bildirir, R. Dawson, A. Thomas, Y. Yagci, *Microporous Thioxanthone Polymers as Heterogeneous Photoinitiators for Visible Light Induced Free Radical and Cationic Polymerizations*, Macromolecules, **47**, 4607–4614 (2014)

[1.89] Z. J. Wang, K. Landfester, K. A. I. Zhang, *Hierarchically porous π-conjugated polyHIPE as a heterogeneous photoinitiator for free radical polymerization under visible light*, Polym. Chem., **5**, 3559–3562 (2014)

[1.90] X. Chen, S. Shen, L. Guo, S. S. Mao, *Semiconductor-based Photocatalytic Hydrogen Generation*, Chem. Rev., **110**, 6503–6570 (2010)

[1.91] X. Li, J. Yu, J. Low, Y. Fang, J. Xiao, X. Chen, *Engineering heterogeneous semiconductors for solar water splitting*, J. Mater. Chem. A, **3**, 2485–2534 (2015)

[1.92] K. Kailasam, J. Schmidt, H. Bildirir, G. Zhang, S. Blechert, X. Wang, A. Thomas, *Room Temperature Synthesis of Heptazine-Based Microporous Polymer Networks as Photocatalysts for Hydrogen Evolution*, Macromol. Rapid Commun., **34**, 1008–1013 (2013)

[1.93] J. H. Park, K. C. Ko, N. Park, H.-W. Shin, E. Kim, N. Kang, J. Hong Ko, S. M. Lee, H. J. Kim, T. K. Ahn, J. Y. Lee, S. U. Son, *Microporous organic nanorods with electronic push–pull skeletons for visible light-induced hydrogen evolution from water*, J. Mater. Chem. A, **2**, 7656–7661 (2014)

[1.94] D. Y. Chung, H.-i. Kim, Y.-H. Chung, M. J. Lee, S. J. Yoo, A. D. Bokare, W. Choi, Y.-E. Sung, *Inhibition of CO poisoning on Pt catalyst coupled with the reduction of toxic hexavalent chromium in a dual-functional fuel cell,* Sci. Rep., **4**, 7450 (2014)

[1.95] R. S. Sprick, J.-X. Jiang, B. Bonillo, S. Ren, T. Ratvijitvech, P. Guiglion, M. A. Zwijnenburg, D. J. Adams, A. I. Cooper, *Tunable Organic Photocatalysts for Visible-Light-Driven Hydrogen Evolution*, J. Am. Chem. Soc., **137**, 3265–3270 (2015)

[1.96] *Application Note 58 – Visible Light Singlet Oxygen*, 2018, Vapourtec Ltd., accessed September 2018 <https://www.vapourtec.com/flow-chemistry-resource-centre/application-note-58-visible-light-singlet-oxygen/>

[1.97] M. Lamblin, L. Nassar-Hardy, J.-C. Hierso, E. Fouquet, F.-X. Felpin, *Recyclable Heterogeneous Palladium Catalysts in Pure Water: Sustainable Developments in Suzuki, Heck, Sonogashira and Tsuji–Trost Reactions*, Adv. Synth. Catal., **352**, 33-79 (2010)

[1.98] C. E. Garrett, K. Prasad, *The Art of Meeting Palladium Specifications in Active Pharmaceutical Ingredients Produced by Pd-Catalyzed Reactions*, Adv. Synth. Catal., **346**, 889-900 (2004)

[1.99] Y.-B. Zhou, Z.-P. Zhan, *Conjugated Microporous Polymers for Heterogeneous Catalysis*, Chem. Asian J., **13**, 9-19 (2018)

DECLARATION

As equal primary author of this publication, I can confirm a significant portion of the work to be my own, with sections written by collaborators as outlined in section 1.3.3.

Signature: _____

PUBLICATION 1

Conjugated porous polymers for photocatalytic applications

Y.-L. Wong, J. M. Tobin, Z. Xu, F. Vilela

DOI: 10.1039/c6ta07697a

J. Mater. Chem. A, **2016**, *4*, 18677-18686

Abstract

Conjugated porous polymers (CPPs) are a class of fully crosslinked polymers defined by high surface area and porosity in the nanometer range, having been traditionally developed for applications such as gas storage, sensing and (photo)catalysis. As these materials are comprised of extended π-conjugation, their ability to act as light harvesters, and in turn photocatalysts, has come to prominence. The insoluble nature of CPPs allows them to be employed as photocatalysts under heterogeneous conditions, replacing traditional homogeneous systems. This Perspective highlights the current state-of-the-art CPPs along with a view to their applications as heterogeneous photocatalysts for a wide range of chemical transformations including hydrogen production, organic synthesis and photopolymerization, just to name but a few.

1. Introduction

The development of clean and renewable energy resources as well as more sustainable chemical processes has been in recent years the major driving force behind the advancement of materials science. In particular, porous materials ranging from the traditional zeolites [1-3], silica [4, 5], and metal oxides [6-9] to the more recent metal-organic frameworks (MOFs) [10-15], and crystalline covalent-organic frameworks (COFs) [16-19] are actively pursued for promising applications in gas storage, sensing, separation, and catalysis. In this context, the emerging class of conjugated porous polymers (CPPs), with potentially versatile photophysical and electronic properties arising from their extensive π-conjugation, offers salient advantages for light harvesting and photocatalysis applications. The diverse organic π-systems allow for flexible tuning of the absorbance and band-gap attributes, so as to optimize energy transfer and photocatalytic performances (e.g., for better utilizing visible light in lieu of the commonly used, more destructive UV light).

In general, CPPs can be assembled by directly polymerizing the molecular building blocks via strong covalent links (e.g., aryl-aryl bond), and therefore offers ease of preparation and excellent chemical/thermal stability as compared with many MOFs and COFs, which build on reversible and less robust bonding linkages (e.g., B-O and C=N), and often involve extensive crystallization efforts. Moreover, the pore sizes and morphologies of CPPs can be rationally controlled by monomer size/shape and employing various templating agents, e.g., silica/metal oxide nanoparticles (NPs), cleavable functional groups, and surfactants [20-22]. By polymerizing around silica NPs, the resultant polymer products (after chemically etching away the SiO_2 spheres) exhibited microporosity features with surface areas of 500-850 $m^2\ g^{-1}$ (as in N_2 sorption). Also, various technologically important morphologies can be accessed by adjusting the synthetic conditions, with examples including: the surfactant-assisted miniemulsion (oil-in-water, o/w) synthesis of CMP nanoparticles for better dispersibility and water compatibility [23], organic sol-gel methods for better processability [24], and thin films (as made by electro-polymerization) for potential device applications [25].

The large surface areas and tunable pore features of CPPs, together with their ability to accept and transport light energy throughout the delocalized backbone, stand to boost light harvesting and energy transfer onto an adsorbed acceptor molecule to trigger

physical/chemical changes towards the end product (Figure 1) [26]. Indeed, CPPs as heterogeneous photocatalysts are attracting ever more attention. Unlike the commonly used homogeneous photocatalysts (organic dyes, such as rose bengal, methylene blue, and eosin-Y, along with inorganic and organometallic small molecules) [27], which entail cumbersome product separation/purification, CPP solids can be easily isolated and recycled. Moreover, catalyst photo-degradation (e.g., via photobleaching), a major issue in the free-flowing homogeneous systems, can be ameliorated through the rigid confinement of the CPP backbone. Besides better stability, the metal-free CPPs eliminate metal contamination (an important issue for pharmaceuticals), whereas photoactive MOFs often run the risk of metal leaching from the host net.

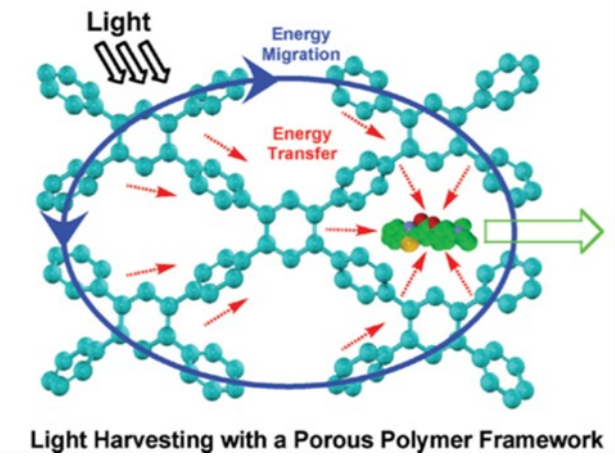

Figure 1 A polyphenylene-based CPP illustrating the nature of light harvesting. Reproduced with permission from Ref. [26]. Copyright (2010) American Chemical Society.

Overall, photocatalysis remains a young topic for CPPs, and much effort is clearly needed for further exploration. With a succinct overview of the field, this perspective aims to highlight the unique fundamental and practical importance of CPP photocatalysis. We will present the fundamental workings, selected case studies and outstanding issues, so as to help impart a working knowledge of this open and growing field.

2. Photochemical Applications of CPPs

2.1 CPPs for Photosensitization

CPPs with low-band-gap character and high photon absorption capability are particularly suited for light-harvesting applications. Singlet oxygen ($^1O_2$) generation, for example, is of great interest because of the important applications of $^1O_2$ in photodynamic therapy (PDT) of cancer, photo-oxidative degradation of toxic chemicals and synthesis of fine chemicals [27]. Photosensitizers have included commonly known organic dyes such as methylene blue, rose bengal and fluorescein, but spans a wide range of molecular types and derivatives [28].

A photosensitizer absorbs light at a specific wavelength and is promoted to a higher energy state ($^1PS^*$). This energy can be dissipated through fluorescence, non-radiative decay, or undergoes an intersystem crossing mechanism where the spin paring of electrons become parallel, creating the triplet state photosensitizer ($^3PS^*$). To reach the ground state, the energetic photosensitizer can return to the ground state through phosphorescence or non-radiative decay. Conversely, an energy transfer via a physical collision between the energized photosensitizer and $^3O_2$ can occur to produce $^1O_2$.

Strong electron-accepting moieties such as benzothiadiazole (Figure 2) and weak electron-donating units (such as benzene and fluorene), when coupled in CPP backbones, have been found to be efficient photosensitizers that generate $^1O_2$ under UV-vis irradiation (e.g., with blue light at 420 nm for the poly(benzothiadiazole) network in Figure 2) [29, 30]. As a hydrophobic CPP, the poly(benzothiadiazole) network does not perform ideally as a photosensitizer in water, for example, only 50% yield was achieved in the $^1O_2$-induced conversion of 2-furoic acid when water was used as the solvent. To enhance water compatibility, hydrophilic mercaptopropionic acid units were attached to the CPP backbone via postsynthetic thiol-yne reaction (Figure 3). The CPP thus modified became much more water-dispersible, and accordingly, better performance of $^1O_2$-induced conversion of 2-furoic acid (~90% yield) was achieved [31].

Visible light harvesting within metal-encapsulated CPPs was observed in a series of metallophthalocyanine (MPc) based conjugated microporous polymers (MPc-CMPs, see Figure 4) which was synthesized *via* Schiff base condensation [32]. The resultant polymer networks showed long-wavelength absorption capability in visible light region and remarkable efficiency for $^1O_2$ generation under visible light irradiation at 700 nm (bandpass filter from a xenon lamp).

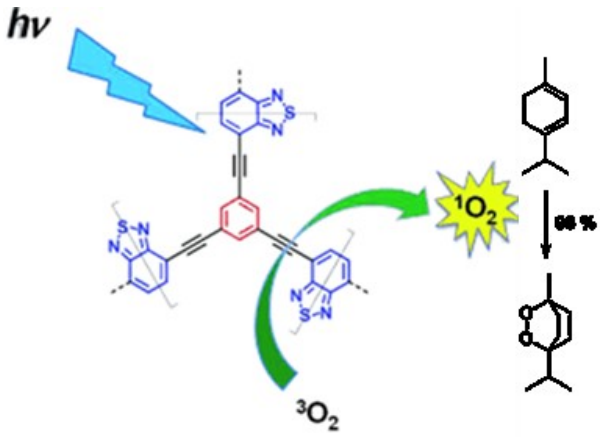

Figure 2 *In-situ* $^1O_2$ generation and subsequent conversion of α-terpinene into ascaridole with a photosensitizing poly(benzothiadiazole) network. The benzothiadiazole units are indicated by blue color. Reproduced from Ref. [29]. Copyright (2013) WILEY-VCH Verlag GmbH & Co. KGaA.

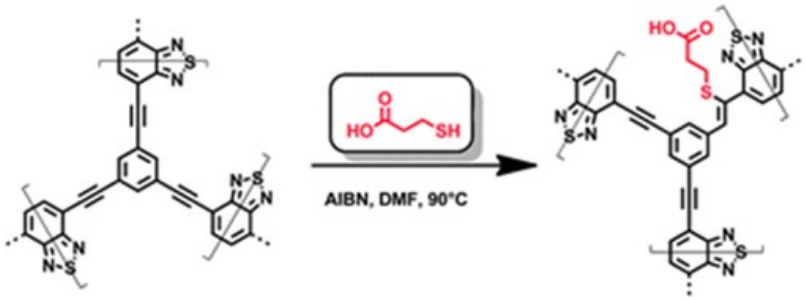

Figure 3 Thiol-yne modification of the poly(benzothiadiazole) network. Reproduced from Ref. [31] with permission from The Royal Society of Chemistry.

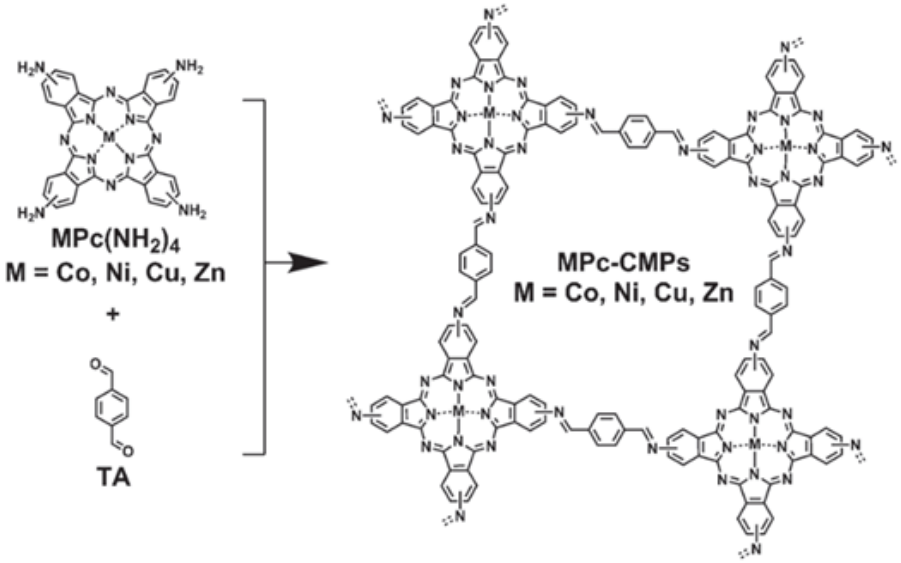

Figure 4 Synthetic scheme for the synthesis of MPc-CMPs. Reproduced from Ref. [32]. Copyright (2015) WILEY-VHC Verlag GmbH & Co. KGaA.

2.2 CPPs for Photocatalysis

2.2.1 Photodegradation

Metal-free, photoactive CPPs are capable of catalysing pesticide degradation. For example, under visible-light irradiation ($\lambda > 400$ nm), a graphitic carbon nitride (g-C_3N_4) solid (50 mg; prepared from urea) was found to degrade over 80% of the imidacloprid (2 mg, 7.8 mmol) in an aqueous solution (100 mL) within 5 hours [33]. The photocatalytic degradation mechanisms (see Figure 5) were attributed to the photogenerated hole (h+) of the polymer surface, rather than hydroxyl free radical (•OH) and superoxide radical (•O_2-).

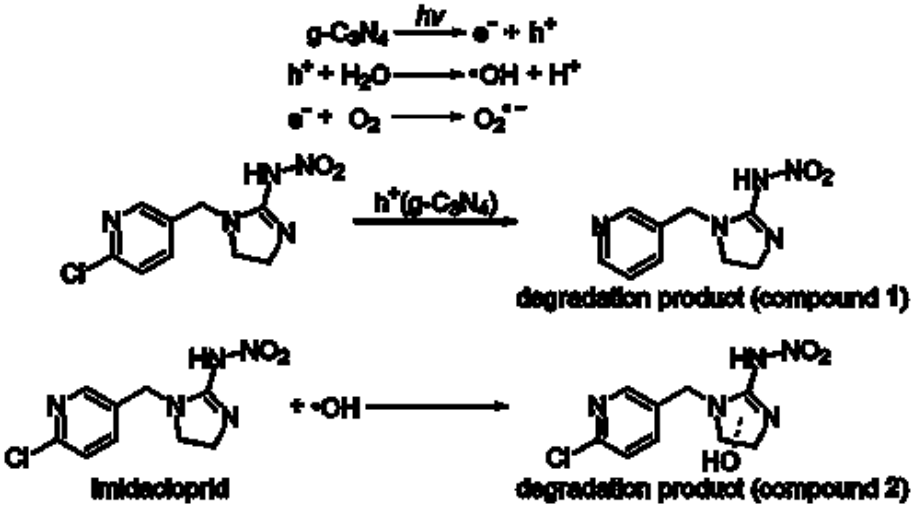

Figure 5 Proposed imidacloprid degradation mechanism over a g-C_3N_4 photocatalyst. Adapted with permission from Ref. [33]. Copyright (2015) American Chemical Society

Cationic dyes were also anchored via ionic interaction, onto a sulfonate-functionalized hollow microporous organic polymer (HMOP, Figure 6) [34] to provide significant photocatalytic activities, as seen in the room-temperature degradation of 4-chlorophenol in water (irradiation by a 200-W xenon lamp; $\lambda > 420$ nm). $^1O_2$-mediated oxidative dechlorination was proposed to account for the detected benzoquinone products.

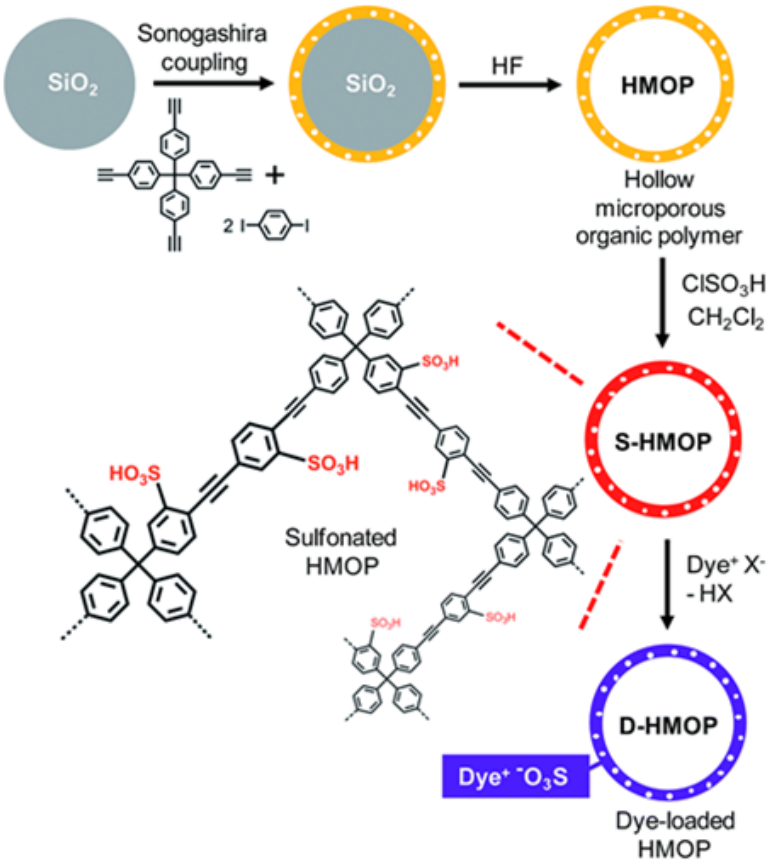

Figure 6 Synthetic scheme for the preparation of the sulfonated hollow microporous organic polymer (S-HMOP) and the heterogeneization of ionic dyes. Reproduced from Ref. [34] with permission from The Royal Scoiety of Chemistry.

2.2.2 Oxidations

CPP photocatalysts are also used in photooxidizing fine molecules and organic dyes. Mesoporous graphitic carbon nitrides, for example, acted as an effective photocatalyst in O_2 oxidation of benzyl alcohols to selectively form ketones/aldehydes [35]. The mesoporosity of mesoporous graphitic carbon nitride (mpg-C_3N_4) was generated by the silica NP template method (e.g., surface area: 200 m^2 g^{-1}), with enhanced the catalytic efficiency over 10 times higher than bulk g-C_3N_4. Reactivation of the mpg-C_3N_4 photocatalyst was effected by a simple wash with aqueous NaOH.

CPPs (Figure 7; prepared by high internal phase emulsion polymerization, polyHIPEs) with cleavable tert-butyl carboxylate (Boc) units were studied in a continuous flow setting [36]. Both Boc-laced and Boc-removed polymers exhibited similar photocatalytic efficiencies and high selectivity (*i.e.*, 99%) in photooxidation of organic sulfides to sulfoxides under blue LED irradiation (4.5 W cm^{-2}) at 460 nm and room

temperature in air. Photogenerated of $^1O_2$ was suggested to be responsible for the selective oxidation.

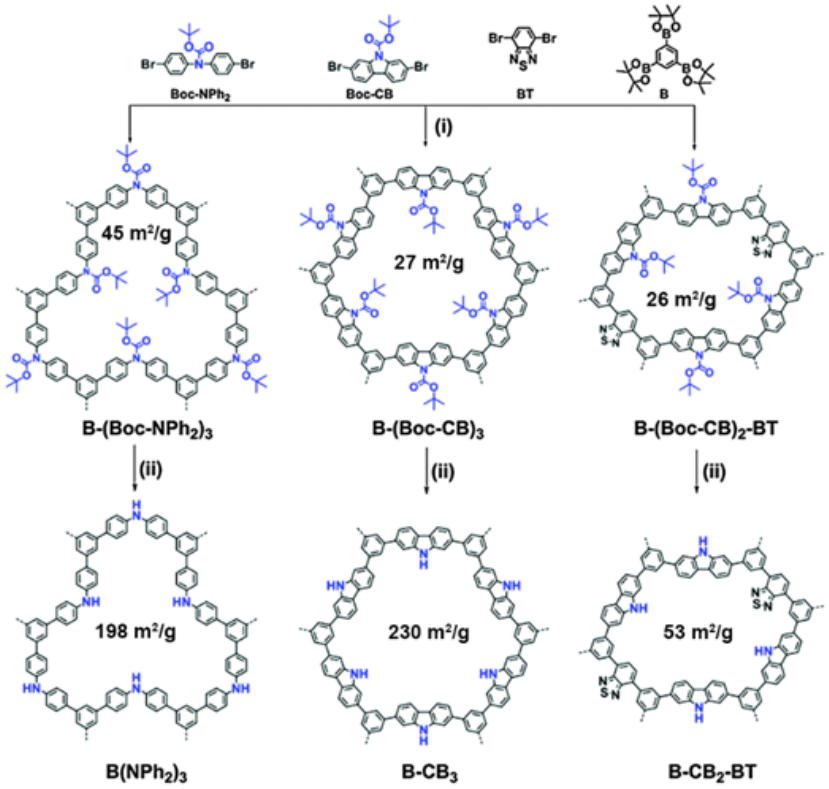

Figure 7 Idealized structures with corresponding BET surface areas of CPPs. (i) Suzuki-Miyaura coss-coupling polyHIPEs and (ii) thermal cleavage of the Boc spacer. Reproduced from Ref. [36] with permission from The Royal Society of Chemistry.

2.2.3 Coupling Reactions

Metal-free or metal-encapsulated CPPs can be photocatalytically active in coupling reactions (e.g., C-C or C-N formation) [37]. For example, aerobic oxidative coupling of amines to imines was achieved using mpg-C_3N_4 as the photocatalyst (under visible light irradiation, $\lambda > 420$ nm; yields over 90%) [38]. Photogenerated electron-hole pairs were suggested to be key in the reductive activation of molecular oxygen and the ensuing electron transfer processes. The mpg-C_3N_4 photocatalyst also exhibited efficient one-pot oxidative coupling synthesis of benzoxazoles, benzimidazoles, and benzothiazoles under similar conditions.

Similar amine oxidation was also studied with a benzodifuran-based CPP as a heterogeneous photocatalyst (irradiation by a blue LED; λ_{max} = 460 nm) [39]. The

electron-rich, redox-active benzodifuran moieties were formed in situ *via* intramolecular cyclization during the Sonogashira coupling polymerization (see Figure 8A). Photophysical studies suggested a photoredox mechanism (see Figure 8B) rather than the singlet-oxygen pathway. Cooper *et al*. succeeded in building the Rose Bengal dye function into CPP backbones [40]. The two polymers of RB-CMP1 and RB-CMP2 (Figure 9A) showed high porosity (833 and 801 $m^2 g^{-1}$, respectively) and are photoactive in heterogeneous Aza-Henry reactions at room temperature for various tertiary amines (Figure 9B; light source: a 60-W household bulb). Notably, the more photoactive RB-CMP1 can be recycled over ten times with well-retained photoactivity.

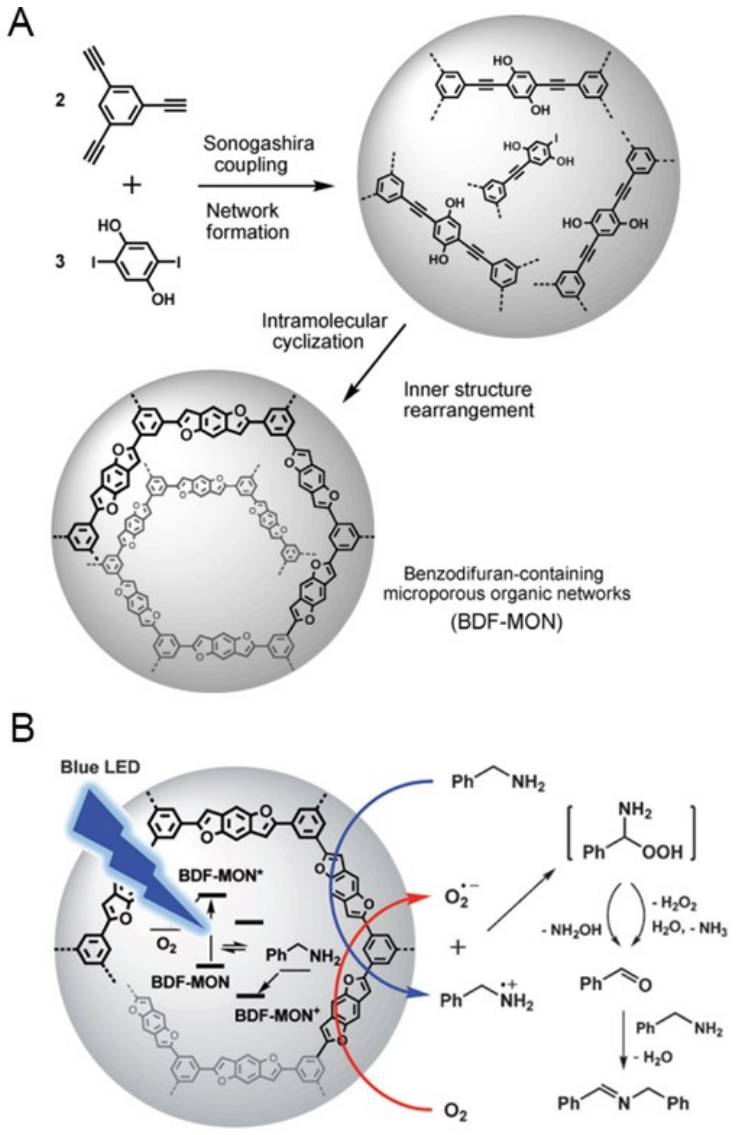

Figure 8 (A) Synthetic scheme for the benzodifuran-based CCP (BDF-MON). (B) The proposed mechanism for photooxidizing benzylamine into imine as catalysed by BDF-MON. Adapted from Ref. [39]. Copyright (2013) WILEY-VCH Verlag GmbH & Co. KGaA.

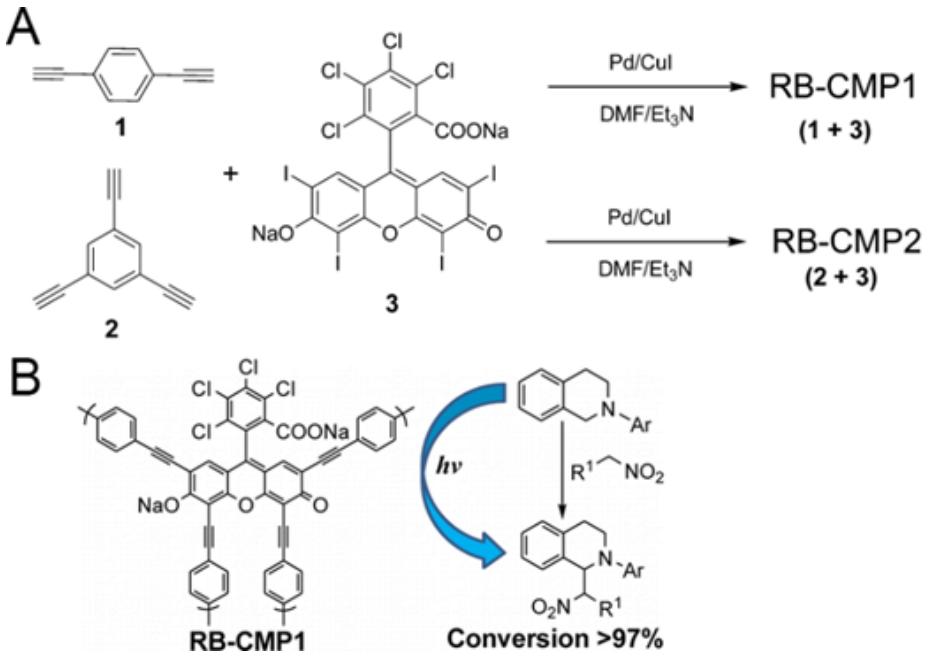

Figure 9 (A) Synthetic scheme for the Rose Bengal-based conjugated microporous polymer (RB-CMP) networks. (B) Room-temperature Aza-Henry reaction with RB-CMP1 photocatalyst under irradiation with a 60 W household bulb in air. Adapted with permission from Ref. [40]. Copyright (2015) American Chemical Scoiety.

A conjugated microporous poly(benzoxadiazle) network (B-BO_3, Figure 10A) with immobilized Pd nanoparticles (NPs) was found to be a heterogeneous visible-light photocatalyst for room-temperature Suzuki coupling reaction [41]. The Pd-immobilized polymer (Pd@B-BO_3) has a BET surface area of 176 m^2 g^{-1} with the Pd NPs ranging from 5 to 10 nm. The suggested mechanism (Figure 10B) involves photogeneration of electron-hole pairs inside the semiconductive network and the migration of photoexcited electrons from the polymer to the Pd metal center under visible light irradiation by a white LED lamp (1.2 W cm^{-2}). The photocatalyst can be recycled without significant loss in activity as demonstrated in five consecutive runs of coupling between iodobenzene and phenylboronic acid. Moreover, the metal-free B-BO_3 polymer exhibited enhanced photocatalytic activity towards oxidative coupling of benzylamines when compared to two other similar networks of lower redox potentials [42]. Tuning and optimization of band gaps of CPPs for achieving enhanced photocatalysis was elegantly demonstrated in poly(benzobisthiadiazole) networks [43].

Versatile photocatalyses were recently reported of a metal-free, highly porous carbazolic CPP (Cz-POF-1, Figure 11) [44]. The photoactive carbazole-based polymer was prepared by oxidative polymerization with a high specific surface area (2065 m^2 g^{-1})

and shown to be photocatalytically active in α-alkylation of aldehydes, dehalogenation of phenacyl bromides, and hydroxylation of arylboronic acids under illumination with a 14 W household lamp or a blue LED (0.135 W, 465 nm) at room temperature.

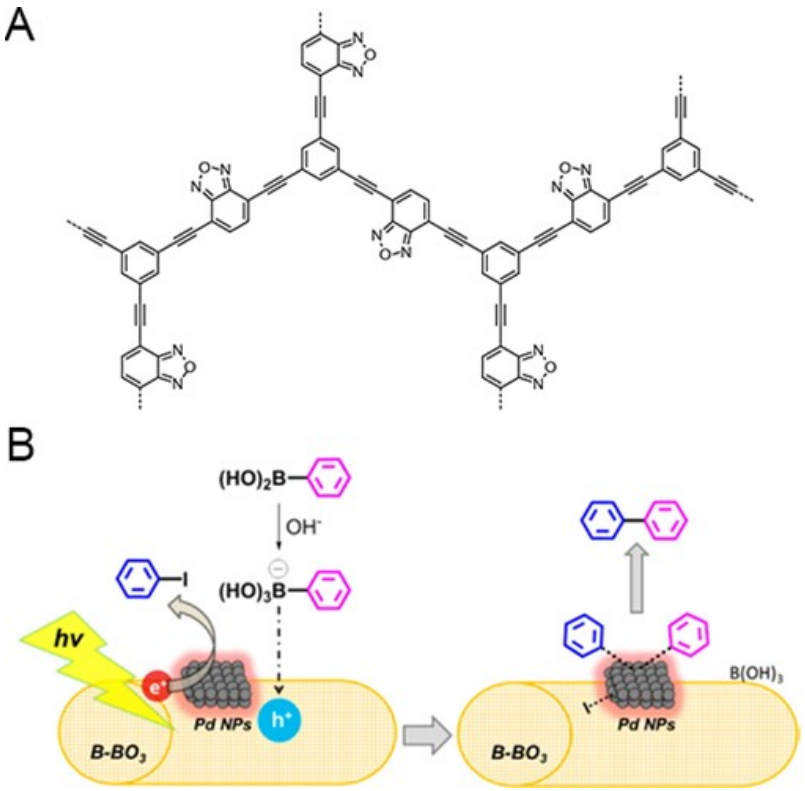

Figure 10 (A) Polymer backbone structure of B-BO_3. (B) The proposed mechanism for the photocatalytic Suzuki coupling at the interface of B-BO_3 and Pd NPs. Adapted with permission from Ref. [41]. Copyright (2015) American Chemical Scoiety.

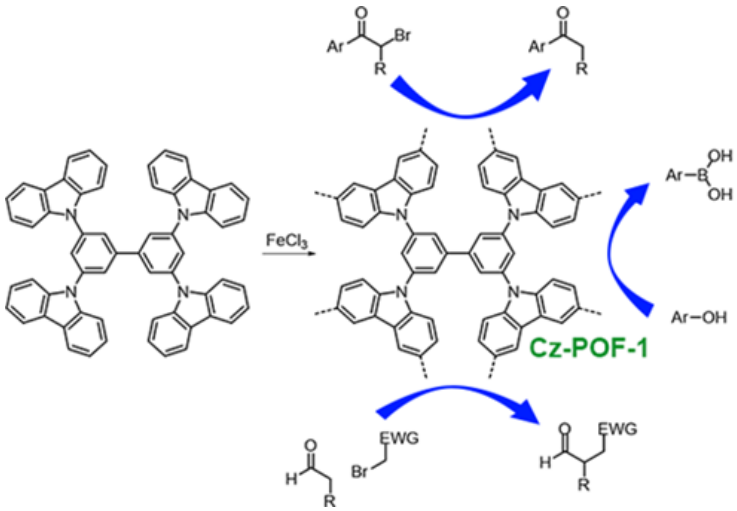

Figure 11 Synthetic scheme for the carbazolic porous organic polymer (Cz-POF-1) as photocatalysts for selected organic reactions. Adapted with permission from Ref. [44]. Copyright (2015) American Chemical Society.

2.2.4 Photopolymerizations

Photopolymerization are of great importance for various industrial uses such as coatings, adhesives, optical waveguides, microelectronics [45], acrylate dental fillings [46] and other biomaterials [47, 48]. CPPs can be used as heterogeneous photoinitiators in free radical and cationic polymerizations, offering multiple advantages of easy separation and reusability, and avoiding unwanted coloring of the polymer products—such coloring is a common issue when soluble sensitizing dyes are used as initiators. For example, a phenolphthalein-based microporous CPP acted as a heterogeneous photoinitiator in polymerizing methyl methacrylate (MMA) under visible light ($\lambda > 420$ nm) [49]. The pH-switchable phenolphthalein moieties allowed fine-tuning of the microporosity and light-harvesting ability of the polymer net; and a NaOH-treated CCP presumably photoinitiates via a type-II (H abstraction) mechanism, with trimethylamine (Et_3N) acting as a co-initiator (Figure 12). The photoinitiator can be separated from the reaction product by centrifugation and filtration without color contamination of the polymer product. The second use of this photoinitiator exhibited reduced conversion (e.g., down to 25%) but still comparable with most reported homogeneous molecular photoinitiators.

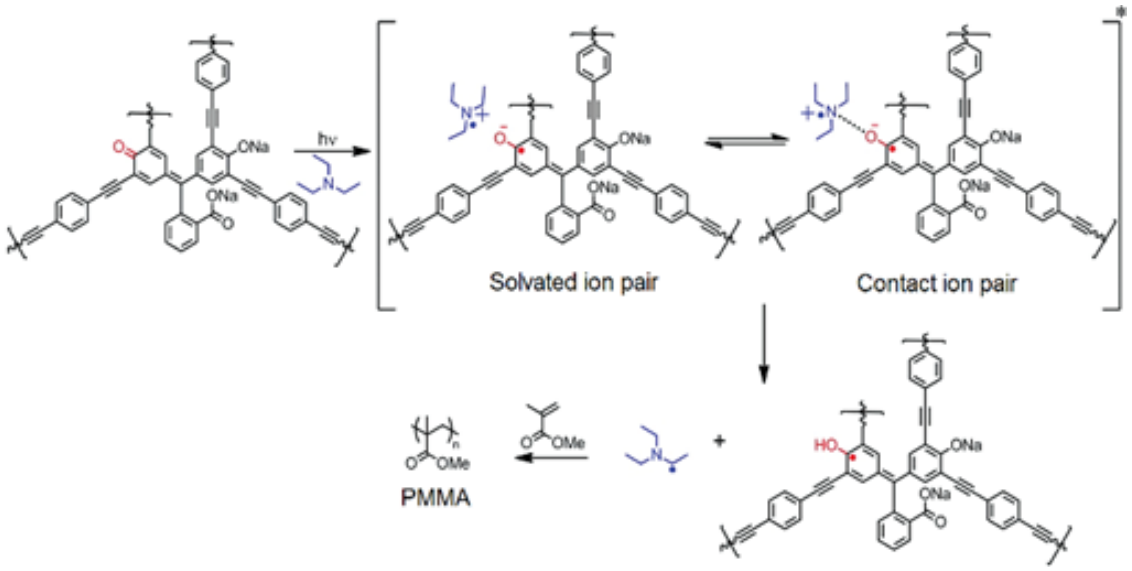

Figure 12 The proposed photoinitiation mechanism of a NaOH-treated phenolphthalein-based polymer. Adapted with permission from Ref. [49]. Copyright (2012) American Chemical Society.

The type II photoinitiation mechanism was also proposed for mpg-C_3N_4 as a visible-light photoinitiator in MMA polymerization [50]. Also, a thioxanthone(TX)-based CPP (Figure 13A), with BET surface areas of 500–750 m^2 g^{-1}, was photocatalytically active for MMA and cyclohexene oxide (CHO) polymerizations under visible light or sunlight at room temperature, with, e.g., Et_3N or $(C_6H_5)_2I(PF_6)$ as co-initiators [51]. The hydrogen abstraction (type-II) for the Et_3N co-initiator and electron transfer for the iodonium co-initiator were proposed for MMA polymerization (Figure 13B). The insoluble CPP photoinitiators are easily collected by dissolving the PMMA product in THF and filtering and retained similar activity in three runs.

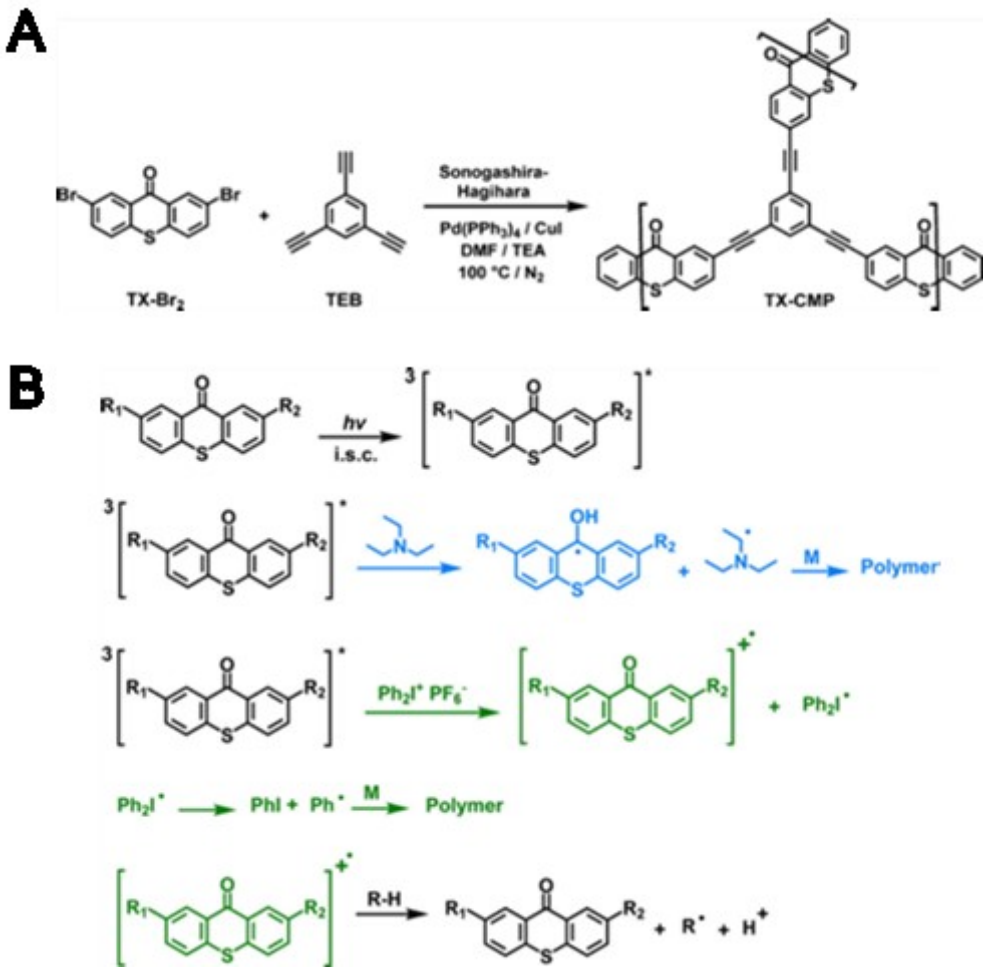

Figure 13 (A) Synthetic scheme for the preparation of TX-based polymers. (B) Proposed initiation mechanisms for the free radical polymerization of MMA over TX-based polymer photocatalysts in the presence of Et_3N or iodonium salt co-initiators under visible light or sunlight irradiation. Adapted with permission from Ref. [51]. Copyright (2014) American Chemical Society.

Also of interest is a hierarchically porous polymer synthesized within high internal phase emulsions (polyHIPE) as a heterogeneous photoinitiator for room-temperature, free-radical polymerization of MMA under a 23 W household energy saving light bulb [52]. The polymer material was prepared by Suzuki cross-coupling (Figure 14) using a dibromocarbazole (Boc-CB), 1,3,5-benzenetriboronate (B) as the cross-linker and dibromobenzoxadiazole (BO) as a strong electron acceptor. The resultant polymer, B–(Boc-CB)$_2$–BO, exhibited a BET surface area of 82 m^2 g^{-1} and reusability over three successive runs in MMA polymerization. The photopolymerization mechanism was also suggested to be a type-II free radical initiation with the Et_3N co-initiator. Simple separation of the photoinitiator from the mixture was achieved by filtration and the polymer catalyst exhibited reusability.

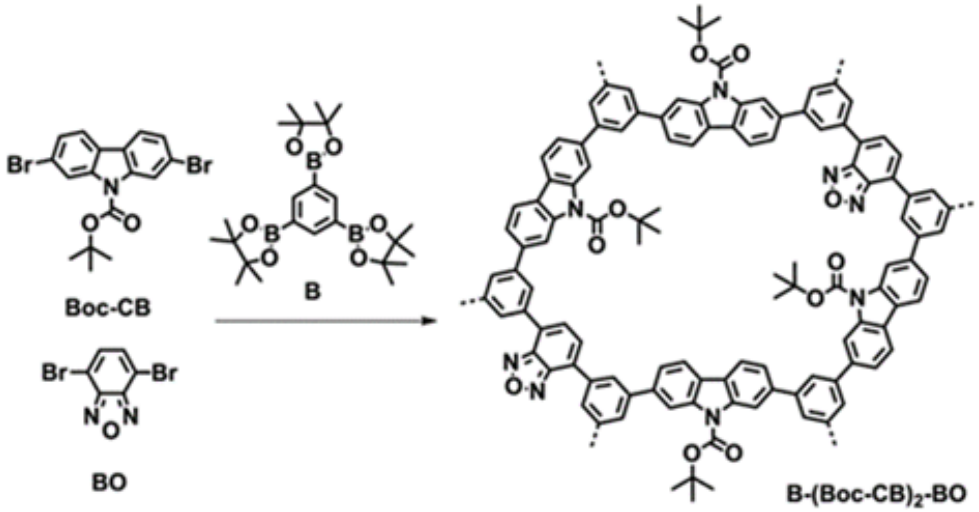

Figure 14 Synthetic scheme for the B–(Boc-CB)$_2$–BO polymer. Adapted from Ref. [52] – Published by the American Chemical Society.

2.2.5 Hydrogen Production

As conventional energy sources such as fossil fuels become scarcer, alternatives must be considered. One of the more adventurous ideas under investigation is the use of hydrogen as a source and storage mechanism for energy production. Photocatalytic hydrogen production from water has been explored largely with inorganic semiconductors as a photocatalyst [53-55]. However, organic semiconducting CPPs have recently been demonstrated in photocatalytic water splitting. The mechanism by which this process proceeds is similar for both types of materials where the semiconductor absorbs photons at a specific wavelength (equal to or greater than its bandgap) resulting

in excited electrons and electron holes (Figure 15). The vast majority of inorganic semiconductors developed thus far have been inorganic metal oxides, often incorporating metal cations with d^0 and d^{10} electronic configurations [56]. One of the main drawbacks with these materials is their high bandgap, and therefore, requirement for light in the UV range ($\lambda < 400$ nm). It is also difficult to adjust the structure and properties of inorganic semiconductors on a molecular level, while CPPs can be easily designed and tuned to fit specific and narrow requirements. An important thermodynamic property of water splitting is the energy required for the reaction to proceed is 237 kJ mol^{-1} (1.23 eV). Therefore, the minimum band gap required for this process should theoretically be 1.23 eV or higher [55]. This value is paramount in the design of novel CPPs for water splitting.

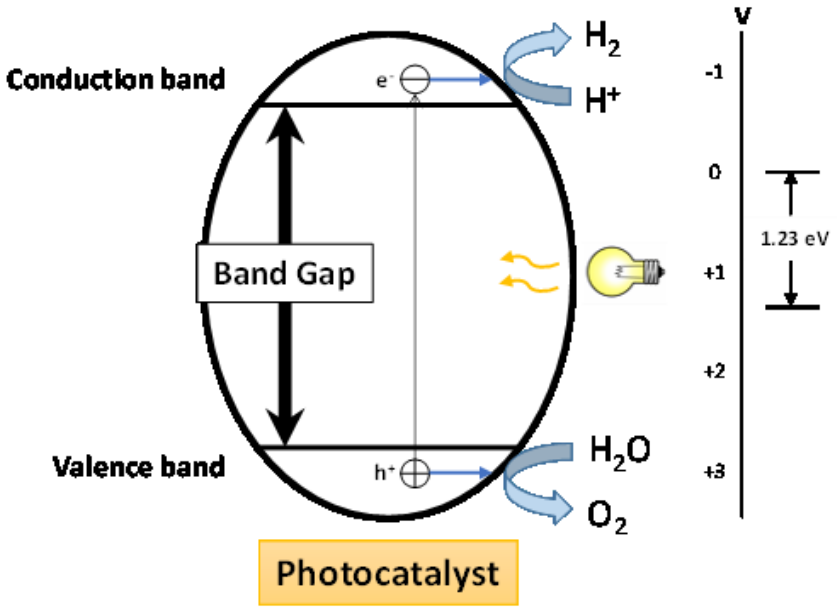

Figure 15 Principle of semiconductor-based photocatalytic water splitting for the production of hydrogen.

Graphitic carbon nitride (g-C_3N_4) and its analogues (Figure 16) have been among the first reported CPPs to be used in this application under visible light [57, 58]. Synthesized *via* thermal polycondensation of cyanamide (673 to 873 K) or heptazine (298 K), these materials have relatively low BET surface area (10-185 m^2 g^{-1}). However, both demonstrated the capability to act as photocatalysts for hydrogen production in water. Hydrogen evolution was tested with both pure g-C_3N_4 and Pt-deposited g-C_3N_4 (2-4%) where the Pt-doped material showed significantly more activity over a 24 h period. Both materials also demonstrated no degradation in output over repeated trials, indicating good reusability. Other prominent phenyl-triazine materials for hydrogen generation have been

described by Lotsch *et al* [59, 60]. For further information on g-C_3N_4-based materials for photocatalysis, we can direct towards reviews from Cao *et al* [61, 62].

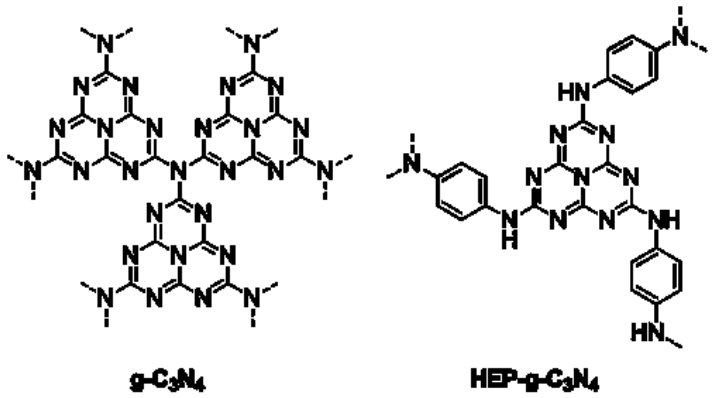

Figure 16 Graphitic carbon nitride (g-C_3N_4) and heptazine-based g-C_3N_4 (HEP-g-C_3N_4).

Son *et al*. have reported the preparation of polymeric nanorods through Knoevenagel condensation of triphenylamine and 2,2'-(biphenyl-4,4'-diyl)diacrylonitrile where the resultant polymer was templated with TiO_2-Pt [63]. Due to a 50 wt% content and low surface area TiO_2-Pt, the BET surface area of the nanorod composite reduced from 474 $m^2\ g^{-1}$ to 237 $m^2\ g^{-1}$ after the adsorption of TiO_2-Pt. These nanorods exhibited hydrogen production from water under visible light irradiation (200 W Xe lamp, <420 nm cutoff, 4.6 mW cm^{-2}), maintaining a stable output of hydrogen (45-52 μmol over 5 hours) for 5 separate runs. The nanorod composite was compared to Eosin-Y and a Ru-based small molecule (N719) composites with adsorbed TiO_2-Pt under the same conditions. Initially, other methods presented greater or equal hydrogen evolution over time. However, repeated uses demonstrated significant degradation and decreased quantum efficiencies. There are many examples in literature where C_3N_4 based materials have been successfully employed as photocatalysts, for the purpose of this perspective, we mainly focus on CPPs.

One major issue with many inorganic and CPP-based materials for hydrogen production is the need for metals as either the main component or as a co-catalyst. These co-catalysts are added largely to enhance the absorption of visible light due to the formation of localized or delocalized electronic states. In small quantities, this addition can also result in a narrowing of the bandgap, enhancing the photocatalytic activity of the material in the visible region [55]. Aside from the obvious environmental and cost issues associated with many of these metals, instability may also present further issues, such as

reusability. In particular, Pd co-catalysts are highly susceptible to CO poisoning, rendering the catalysis no longer feasible and requires addition loading of the metal [64].

To combat this issue, Cooper *et al.* have recently reported the synthesis of a series of metal-free CPP's comprised of benzene-pyrene networks *via* Suzuki-Miyaura cross-coupling using varying monomeric molar ratios [65]. These CPP's exhibited high BET surface areas (597 to 1710 m^2 g^{-1}) along with a wide range of absorbance photoluminescence values, largely in the visible spectrum (Figure 17). All of these materials were tested for hydrogen evolution in water in the absence of a metal co-catalyst. They demonstrated varying rates with respect to their optical band gap (1.94 to 2.95 eV) where the copolymer with the greatest activity had an optical band gap at 2.33 eV and evolved 100 μmol of hydrogen over a 6-hour period under visible light irradiation (300 W Xe lamp, $\lambda > 420$ visible filter). Based on these results and further testing, it was suggested that these copolymers were effective in the evolution of hydrogen without the need for a metal co-catalyst and in fact showed a strong correlation with the optical gap. It is unclear why a co-catalyst was not required nor showed any improvement in hydrogen production upon addition to the CPP. It was suggested that the photocatalytic activity of these polymers may be affected by parameters outside of their optical bandgap and Pt content. This group has studied this topic further with a greater variety of CPP designs, exhibiting greater photocatalytic activities whilst requiring UV light over visible light irradiation [66]. CPPs designed through similar methods have been reported by Wang *et al*., although it should be noted that Pt co-catalysts were used in this instance [67].

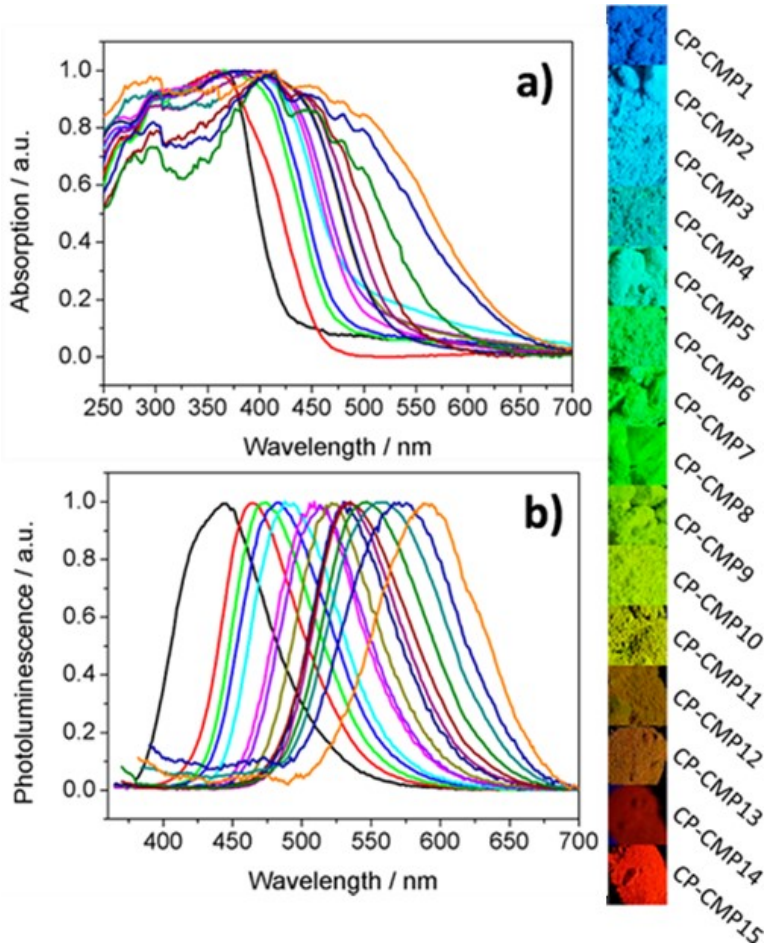

Figure 17 Series of benzene-pyrene copolymers and their associated photophysical properties. Photographs of the 15 copolymers under 365 nm irradiation (right); (a) UV-visible absorption spectra of the 15 copolymers; (b) Photoluminescence spectra of the 15 copolymers with excitation at 360 nm. Adapted from Ref. [65] – Published by the American Chemical Society.

3. Conclusions and Outlook

Application of CPPs as heterogeneous photocatalysts has seen a significant increase, particularly within the last five years. As described above, a paradigm shift where promising CPPs have replaced traditional homogeneous photocatalysts has proven to be effective in a wide variety of applications. Furthermore, development of these materials beyond simple amorphous powders, such as macroscopic monoliths, thin films and nanoparticles, has established their versatility and further increased the potential of device integration of CPPs for light harvesting applications. In particular, we envisage the integration of CPPs within flow technologies where issues such as light penetration

(photon flux) and continuous production are addressed. Recently, we have also demonstrated this combination of materials and technology where we describe two new low-bandgap BODIPY-based CPPs with a bathochromic shift in absorbance (λ_{max} = 520-550 nm) and their application as a photosensitizer under continuous flow conditions in a commercial photoreactor from Vapourtec Ltd. One of these polymers was synthesized via metal-free synthetic protocol and further functionalized with the BODIPY dye also in the absence of metals. These materials are compatible with a multitude of solvents (including green solvents, with the exception of water) in the flow reactor and are highly effective in producing singlet oxygen at a less energetic wavelength (530 nm) [68].

Designed as metal-free materials, many CPPs have seen success where reactions requiring metal-based catalysts are generally employed. This not only removes potential issues such as metal contamination, particularly problematic in pharmaceutical synthesis, but can also reduce the energy required for catalysis. Many CPPs have been strategically constructed to utilize visible light, where a bathochromic shift in absorption compared to traditional photocatalysts uses less energy, which in turn creates the potential for greater photostability, less photodegradation and more durable materials. While there has been great progress in all aspects of these photocatalytic materials, more effort is needed to compete with more conventional and well-established photocatalysts, particularly on larger scales. We have narrowed the challenges in need of greater attention to the following:

A. Metal-Free Synthesis

Synthetic routes for the majority of CPPs involves metal catalyzed carbon-carbon cross coupling reactions, limiting the commercial and industrial applications due to cost, reaction conditions and the ever-receding supply of these metals. Trace amounts of these metals left behind on CMPs after purification may also be problematic. However, there is evidence that these traces do not significantly contribute to any photocatalytic activity [65]. Nonetheless, polymerization techniques that do not require metal catalysts would be beneficial. While there exists examples of metal-free synthetic procedures via Knoevenagel condensation, Schiff base and imidazole chemistry, it is imperative to continue exploring these avenues [63, 69]. Alternatively, we have recently described the synthesis and implementation of a photoactive repeat unit, as seen in previous work, into a well-known polyamide system [70]. This allowed for a metal-free synthetic route using

an industrial scale polymerization technique whilst retaining photoactivity of the polymer.

B. Bathochromic Shift in Absorbance

Electronic control of CPPs not only allows for band gap control but also dictates at which wavelengths the materials will absorb. Currently, most of these polymers are designed to absorb in the visible spectrum (>400 nm), leaving the UV range which is typically employed by metal-based catalysts. However, the range of visible light absorption for CPPs tends to be in the 400-500 nm region, leaving a large portion of the spectrum unused. Photoactivation at less energetic wavelengths (>500 nm) is much preferred as reagents and synthesis products are more susceptible to photodegradation at higher energy wavelengths, resulting from side reactions or simple photodecomposition. To this end, photocatalytic materials absorbing in the visible red to near IR may be a solution.

C. Metal-Loading for More Demanding Applications

Finally, we must also acknowledge that certain systems exist where a metal-free CPP does not provide the appropriate environment or energy to act as the photocatalyst. As CPPs gain more attention, investigations into their reaction mechanisms during the photocatalytic process will play a vital role in determining how they will be used in the future. However, these properties have yet to be examined on a large scale and must be understood fully before CPPs can be used in a larger setting. In cases where CPPs cannot meet the requirements as a photocatalyst, metal-loading *via* synthetic design or post synthetic modification would allow for these materials to be employed in a similarly heterogeneous manner while simplifying the recovery process of the metals. However, this method presents its own set of complications, primarily the leaching of metal from the polymer backbone. Preventing this would help maintain the photoactivity of the material over an extended period and potentially increase its economic viability in the long-term, and ultimately access a wider range of photocatalytic reactions.

Nonetheless, with an ever-expanding field, CPPs as a whole and as photocatalysts in particular, have demonstrated tremendous growth and importance. In our perspective,

this class of polymeric materials shows great promise in both the applications described above as well as new potential synthetic procedures and designs.

References

[1] M. Zaarour, B. Dong, I. Naydenova, R. Retoux and S. Mintova, *Microporous Mesoporous Mater.*, 2014, **189**, 11-21.

[2] M. E. Davis, *Acc. Chem. Res.*, 1993, **26**, 111-115.

[3] A. K. Cheetham, G. Férey and T. Loiseau, *Angew. Chem., Int. Ed.*, 1999, **38**, 3268-3292.

[4] J. G. Croissant, X. Cattoen, M. Wong Chi Man, J.-O. Durand and N. M. Khashab, *Nanoscale*, 2015, **7**, 20318-20334.

[5] V. C. Menon and S. Komarneni, *J. Porous Mater.*, 1998, **5**, 43-58.

[6] M. Nolan, A. Iwaszuk, A. K. Lucid, J. J. Carey and M. Fronzi, *Adv. Mater.*, 2016, **27**, 5425-5446.

[7] C. N. R. Rao and S. Dey, *J. Solid State Chem.*, 2016, **242**(2), 107-115.

[8] Z. Zhang, Z. Jiang and W. Shangguan, *Catal. Today*, 2016, **264**, 270-278.

[9] M. Tiemann, *Chem. – Eur. J.*, 2007, **13**, 8376-8388.

[10] M. C. So, G. P. Wiederrecht, J. E. Mondloch, J. T. Hupp and O. K. Farha, *Chem. Commun.*, 2015, **51**, 3501-3510.

[11] I. Senkovska and S. Kaskel, *Chem. Commun.*, 2014, **50**, 7089-7098.

[12] N. J. Hinks, A. C. McKinlay, B. Xiao, P. S. Wheatley and R. E. Morris, *Microporous Mesoporous Mater.*, 2010, **129**, 330-334.

[13] W. Cai, C.-C. Chu, G. Liu and Y.-X. J. Wáng, *Small*, 2015, **11**, 4806-4822.

[14] J. Gascon, A. Corma, F. Kapteijn and F. X. Llabrés i Xamena, *ACS Catal.*, 2014, **4**, 361-378.

[15] R. Sabouni, H. Kazemian and S. Rohani, *Environ. Sci. Pollut. Res.*, 2013, **21**, 5427-5449.

[16] A. P. Côté, A. I. Benin, N. W. Ockwig, M. O'Keeffe, A. J. Matzger and O. M. Yaghi, *Science*, 2005, **310**, 1166-1170.

[17] E. L. Spitler and W. R. Dichtel, *Nat. Chem.*, 2010, **2**, 672-677.

[18] X. Feng, L. Chen, Y. Dong and D. Jiang, *Chem. Commun.*, 2011, **47**, 1979-1981.

[19] J. W. Colson and W. R. Dichtel, *Nat. Chem.*, 2013, **5**, 453-465.

[20] N. Kang, J. H. Park, M. Jin, N. Park, S. M. Lee, H. J. Kim, J. M. Kim and S. U. Son, *J. Am. Chem. Soc.*, 2013, **135**, 19115-19118.

[21] J. Jin, B. Kim, M. Kim, N. Park, S. Kang, S. M. Lee, H. J. Kim and S. U. Son, *Nanoscale*, 2015, **7**, 11280-11285.

[22] B. Lim, J. Jin, J. Yoo, S. Y. Han, K. Kim, S. Kang, N. Park, S. M. Lee, H. J. Kim and S. U. Son, *Chem. Commun.*, 2014, **50**, 7723-7726.

[23] B. C. Ma, S. Ghasimi, K. Landfester, F. Vilela and K. A. I. Zhang, *J. Mater. Chem. A*, 2015, **3**, 16064-16071.

[24] S.-Y. Moon, J.-S. Bae, E. Jeon and J.-W. Park, *Angew. Chem., Int. Ed.*, 2010, **49**, 9504-9508.

[25] C. Gu, N. Huang, J. Gao, F. Xu, Y. Xu and D. Jiang, *Angew. Chem., Int. Ed.*, 2014, **53**, 4850-4855.

[26] L. Chen, Y. Honsho, S. Seki and D. Jiang, *J. Am. Chem. Soc.*, 2010, **132**, 6742-6748.

[27] M. C. DeRosa and R. J. Crutchley, *Coord. Chem. Rev.*, 2002, **233-234**, 351-371.

[28] R. W. Redmond and J. N. Gamlin, *Photochem. Photobiol.*, 1999, **70**, 391-475.

[29] K. Zhang, D. Kopetzki, P. H. Seeberger, M. Antonietti and F. Vilela, *Angew. Chem., Int. Ed.*, 2013, **52**, 1432-1436.

[30] K. Zhang, Z. Vobecka, K. Tauer, M. Antonietti and F. Vilela, *Chem. Commun.*, 2013, **49**, 11158-11160.

[31] H. Urakami, K. Zhang and F. Vilela, *Chem. Commun.*, 2013, **49**, 2353-2355.

[32] X. Ding and B.-H. Han, *Angew. Chem., Int. Ed.*, 2015, **54**, 6536-6539.

[33] X. Liu, X. Wu, Z. Long, C. Zhang, Y. Ma, X. Hao, H. Zhang and C. Pan, *J. Agric. Food Chem.*, 2015, **63**, 4754-4760.

[34] N. Park, D. Kang, M. C. Ahn, S. Kang, S. M. Lee, T. K. Ahn, J. Y. Jaung, H.-W. Shin and S. U. Son, *RSC Adv.*, 2015, **5**, 47270-47274.

[35] F. Su, S. C. Mathew, G. Lipner, X. Fu, M. Antonietti, S. Blechert and X. Wang, *J. Am. Chem. Soc.*, 2010, **132**, 16299-16301.

[36] Z. J. Wang, S. Ghasimi, K. Landfester and K. A. I. Zhang, *Chem. Commun.*, 2014, **50**, 8177-8180.

[37] J. H. Ko, N. Kang, N. Park, H.-W. Shin, S. Kang, S. M. Lee, H. J. Kim, T. K. Ahn and S. U. Son, *ACS Macro Lett.*, 2015, **4**, 669-672.

[38] F. Su, S. C. Mathew, L. Möhlmann, M. Antonietti, X. Wang and S. Blechert, *Angew. Chem., Int. Ed.*, 2011, **50**, 657-660.

[39] N. Kang, J. H. Park, K. C. Ko, J. Chun, E. Kim, H.-W. Shin, S. M. Lee, H. J. Kim, T. K. Ahn, J. Y. Lee and S. U. Son, *Angew. Chem., Int. Ed.*, 2013, **52**, 6228-6232.

[40] J.-X. Jiang, Y. Li, X. Wu, J. Xiao, D. J. Adams and A. I. Cooper, *Macromolecules*, 2013, **46**, 8779-8783.

[41] Z. J. Wang, S. Ghasimi, K. Landfester and K. A. I. Zhang, *Chem. Mater.*, 2015, **27**, 1921-1924.

[42] Z. J. Wang, S. Ghasimi, K. Landfester and K. A. I. Zhang, *Adv. Mater.*, 2015, **27**, 6265-6270.

[43] Z. J. Wang, S. Ghasimi, K. Landfester and K. A. I. Zhang, *Adv. Synth. Catal.*, 2016, **358**, 2576-2582.

[44] J. Luo, X. Zhang and J. Zhang, *ACS Catal.*, 2015, **5**, 2250-2254.

[45] J. Kloosterboer, *Adv. Polym. Sci.*, 1988, **84**, 1-61.

[46] K. S. Anseth, S. M. Newman and C. N. Bowman, in *Adv. Polym. Sci.*, ed. N. Peppas and R. Langer, Springer, Berlin Heidelberg, 1995, vol. 122, ch. 4, pp. 177-217.

[47] J. P. Fisher, D. Dean, P. S. Engel and A. G. Mikos, *Annu. Rev. Mater. Res.*, 2001, **31**, 171-181.

[48] Y. Yagci, S. Jockusch and N. J. Turro, *Macromolecules*, 2010, **43**, 6245-6260.

[49] B. Kiskan, M. Antonietti and J. Weber, *Macromolecules*, 2012, **45**, 1356-1361.

[50] B. Kiskan, J. Zhang, X. Wang, M. Antonietti and Y. Yagci, *ACS Macro Lett.*, 2012, **1**, 546-549.

[51] S. Dadashi-Silab, H. Bildirir, R. Dawson, A. Thomas and Y. Yagci, *Macromolecules*, 2014, **47**, 4607-4614.

[52] Z. J. Wang, K. Landfester and K. A. I. Zhang, *Polym. Chem.*, 2014, **5**, 3559-3562.

[53] X. Chen, S. Shen, L. Guo and S. S. Mao, *Chem. Rev.*, 2010, **110**, 6503-6570.

[54] A. Kudo and Y. Miseki, *Chem. Soc. Rev.*, 2009, **38**, 253-278.

[55] X. Li, J. Yu, J. Low, Y. Fang, J. Xiao and X. Chen, *J. Mater. Chem. A*, 2015, **3**, 2485-2534.

[56] X. Wang, G. Zhang and Z.-A. Lan, *Angew. Chem., Int. Ed.*, 2016, **55**, 15712-15727.

[57] X. Wang, K. Maeda, A. Thomas, K. Takanabe, G. Xin, J. M. Carlsson, K. Domen and M. Antonietti, *Nat. Mater.*, 2009, **8**, 76-80.

[58] K. Kailasam, J. Schmidt, H. Bildirir, G. Zhang, S. Blechert, X. Wang and A. Thomas, *Macromol. Rapid Commun.*, 2013, **34**, 1008-1013.

[59] K. Schwinghammer, S. Hug, M. B. Mesch, J. Senker and B. V. Lotsch, *Energy Environ. Sci.*, 2015, **8**, 3345-3353.

[60] V. S. Vyas, F. Haase, L. Stegbauer, G. Savasci, F. Podjaski, C. Ochsenfeld and B. V. Lotsch, *Nat. Commun.*, 2015, **6**, 8508.

[61] S. Cao and J. Yu, *J. Phys. Chem. Lett.*, 2014, **5**, 2101-2107.

[62] S. Cao, J. Low, J. Yu and M. Jaroniec, *Adv. Mater.*, 2015, **27**, 2150-2176.

[63] J. H. Park, K. C. Ko, N. Park, H.-W. Shin, E. Kim, N. Kang, J. Hong Ko, S. M. Lee, H. J. Kim, T. K. Ahn, J. Y. Lee and S. U. Son, *J. Mater. Chem. A*, 2014, **2**, 7656-7661.

[64] D. Y. Chung, H.-i. Kim, Y.-H. Chung, M. J. Lee, S. J. Yoo, A. D. Bokare, W. Choi and Y.-E. Sung, *Sci. Rep.*, 2014, **4**, 7450.

[65] R. S. Sprick, J.-X. Jiang, B. Bonillo, S. Ren, T. Ratvijitvech, P. Guiglion, M. A. Zwijnenburg, D. J. Adams and A. I. Cooper, *J. Am. Chem. Soc.*, 2015, **137**, 3265-3270.

[66] R. S. Sprick, B. Bonillo, M. Sachs, R. Clowes, J. R. Durrant, D. J. Adams and A. I. Cooper, *Chem. Commun.*, 2016, **52**, 10008-10011.

[67] C. Yang, B. C. Ma, L. Zhang, S. Lin, S. Ghasimi, K. Landfester, K. A. I. Zhang and X. Wang, *Angew. Chem., Int. Ed.*, 2016, **55**, 9202-9206.

[68] J. M. Tobin, J. Liu, H. Hayes, M. Demleitner, D. Ellis, V. Arrighi, Z. Xu and F. Vilela, *Polym. Chem.,* 2016, **7**, 6662-6670.

[69] Q. Liu, Z. Tang, M. Wu and Z. Zhou, *Polym. Int.*, 2014, **63**, 381-392.

[70] J. Shen, R. Steinbach, J. M. Tobin, M. Mouro Nakata, M. Bower, M. R. S. McCoustra, H. Bridle, V. Arrighi and F. Vilela, *Appl. Catal., B*, 2016, **193**, 226-233.

CHAPTER 2: BODIPY-based Conjugated Microporous Polymers as Reusable Heterogeneous Photosensitisers in a Photochemical Flow Reactor (Publication, *Polymer Chemistry,* RSC)

The following section outlines the development of new 4,4-difluoro-4-bora-3a,4a-diaza-s-indacene (BODIPY)-equipped conjugated porous polymers (CPPs) and their application as heterogeneous photosensitisers for the generation of singlet oxygen ($^1O_2$). These materials exhibited a broad range of absorbances ranging from 520-550 nm, prompting their use as photosensitisers activated *via* visible light. The new polymers were fully characterised and then tested for the generation of $^1O_2$ in a variety of solvents, and under continuous flow conditions. This chapter will outline and discuss the publication titled '*BODIPY-based Conjugated Microporous Polymers as Reusable Heterogeneous Photosensitisers in a Photochemical Flow Reactor*' which was published in *Polymer Chemistry* and can be found in its entirety (including supporting information) at the end of this chapter. Any contributions and work performed by other students, collaborators or academics are presented throughout the chapter in the appropriate sections.

2.1 Background

The development of CPPs, as discussed in the previous chapter, concentrates primarily on low band gap materials and their potential for new photocatalytic applications. In this work, the implementation of a new strong electron acceptor (SA)/weak electron donator (WD) system was introduced, using BODIPY (Figure 2.1) to replace the well-established benzothiadiazole (BTZ) moiety. While BODIPY can act as both a SA and WD [2.1, 2.2], in this instance it was employed as a SA. The introduction of BODIPY into a CPP through traditional synthetic methods, such as Suzuki-Miyaura cross coupling, results in a repeat unit with a familiar electron donor-acceptor system and allows for the new material to act as a low band gap light harvesting material for the production of $^1O_2$ [2.3]. BODIPY was chosen as a monomer in the polymer network as it is known to have a bathochromic shift in light absorbance when compared to more common organic light harvesters [2.4]. This allows for the use of a less energetic (longer

wavelength) light source, mitigating photodecomposition of starting materials and/or products, and unwanted side reactions when compared to the use of more energetic (shorter wavelength) light sources, such as UV light.

The newly synthesised CPPs were designed as photosensitisers for the production of $^1O_2$ due to the extensive documentation describing BODIPY and its derivatives as effective photosensitisers, particularly in biological systems [2.5]. Whilst $^1O_2$ has been known and studied for over 100 years, it still has a wide reach as a synthetic reagent in applications such as organic synthesis [2.6], environmental water treatment [2.7], and photodynamic therapy (PDT) as a cancer treatment [2.8]. Presented below are two new BODIPY-equipped CPPs synthesised through two different pathways (traditional and metal-free). These CPPs were subsequently implemented as heterogeneous photosensitisers for the production of $^1O_2$ in a variety of organic solvents using a commercial flow system.

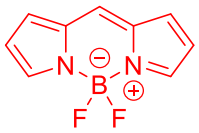

4,4-difluoro-4-bora-3a,4a-diaza-s-indacene (BODIPY)

Figure 2.1 Chemical structure of the BODIPY core. For simplicity, the charged atoms (B anion and N cation) will not be shown as such in further depictions of BODIPY.

2.2 Aim/Objectives

The primary aim of this study was to explore how optoelectronic control of CPPs can be achieved by designing repeat unit cells to contain the BODIPY moiety. Two novel CPPs were designed through either a traditional cross-coupling method or a metal-free post-synthetic modification of an aldehyde-equipped CPP. While designed through separate routes, both materials were expected to present a bathochromic shift when compared to many CPPs presented in literature [2.9]. This shift to less energetic wavelengths is important as we move away from traditional photocatalytic materials absorbing in the UV or near UV range. The two materials were employed in a variety of solvent systems, including 'green' solvents, for investigations into their use as $^1O_2$

photosensitisers. Furthermore, continuous flow chemistry, as opposed to more commonly used batch chemistry, was utilised to demonstrate the versatility, stability and robust nature of the materials under atypical conditions.

2.3 Synthesis of Materials/Methodology

The methodologies used for the preparation and characterisation of the BODIPY-equipped CPPs as well as their implementation as photosensitisers under continuous flow, is described in this section. The polymer powders were characterised using FT-IR spectroscopy, solid state ^{13}C NMR cross-polarisation magic angle spinning (CP-MAS) spectroscopy, solid state UV-Vis spectroscopy, fluorescence spectroscopy, thermogravimetric analysis (TGA), BET surface area (S_{BET}) analysis, energy dispersive X-ray spectroscopy (EDX), and scanning/transmission electron microscopy (SEM/TEM). All solid state ^{13}C NMR CP-MAS measurements were carried out by Dr David Ellis at Heriot-Watt University.

2.3.1 Synthesis of Traditional Pd-catalysed BODIPY CPP (BDP_CMP)

A direct assembly approach for the synthesis of BDP_CMP was employed utilising a palladium-catalysed Suzuki-Miyaura cross-coupling reaction whereby 1,3,5-tris(4,4,5,5-tetramethyl-1,3,2-dioxaborolan-2-yl)benzene, a tritopic cross-linker, was reacted with the 2,6-dibromo-1,3,5,7-tetramethyl-8-phenyl-BODIPY monomer (Scheme 2.1). Both the benzene and BODIPY monomers used in this reaction were synthesised through known literature procedures [2.10-2.12]. The resulting red powder was purified *via* Soxhlet extraction and dried *in vacuo* for 24 h to remove residual solvent from the porous material. A monomeric analogue to BDP_CMP was also synthesised (labelled Ph_BDP) under the same reaction conditions for comparison as a photocatalyst. The initial synthesis of BDP_CMP was performed by Martin Demleitner (Erasmus student) under my supervision. S_{BET}, TGA, EDX, SEM and TEM measurements of this material were carried out by our collaborator Jie Liu, City University of Hong Kong, Hong Kong.

2.3.2 Synthesis of Metal-free BODIPY CPP (PHTT_BDP)

An approach through post-synthetic functionalisation of a previously described porous polymer [2.13] was utilised through the conversion of chemically available aldehyde groups into BODIPY (Scheme 2.2). This procedure was performed *via* modified literature methods [2.11] along with additional heating (50 °C) to facilitate progress of the reactions. Furthermore, due to the insoluble nature of both initial and modified polymers, the intermediate products were easily isolated. Each intermediate along with the final product was purified *via* Soxhlet extraction and analysed to compare the chemical and physical changes. Both the initial aldehyde-equipped polymer and the post-synthetic modification method used synthetic routes without the need for any metal catalysts. Synthesis of PHTT_BDP as well as S_{BET}, TGA, EDX, SEM and TEM measurements of these materials was carried out by our collaborator Jie Liu, City University of Hong Kong, Hong Kong.

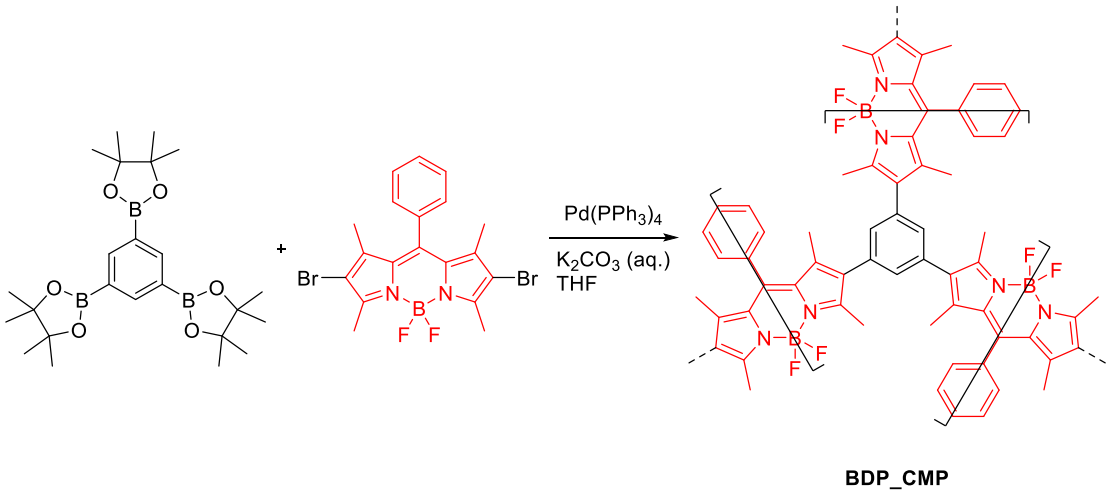

Scheme 2.1 Synthesis and theoretical repeat unit of BDP_CMP.

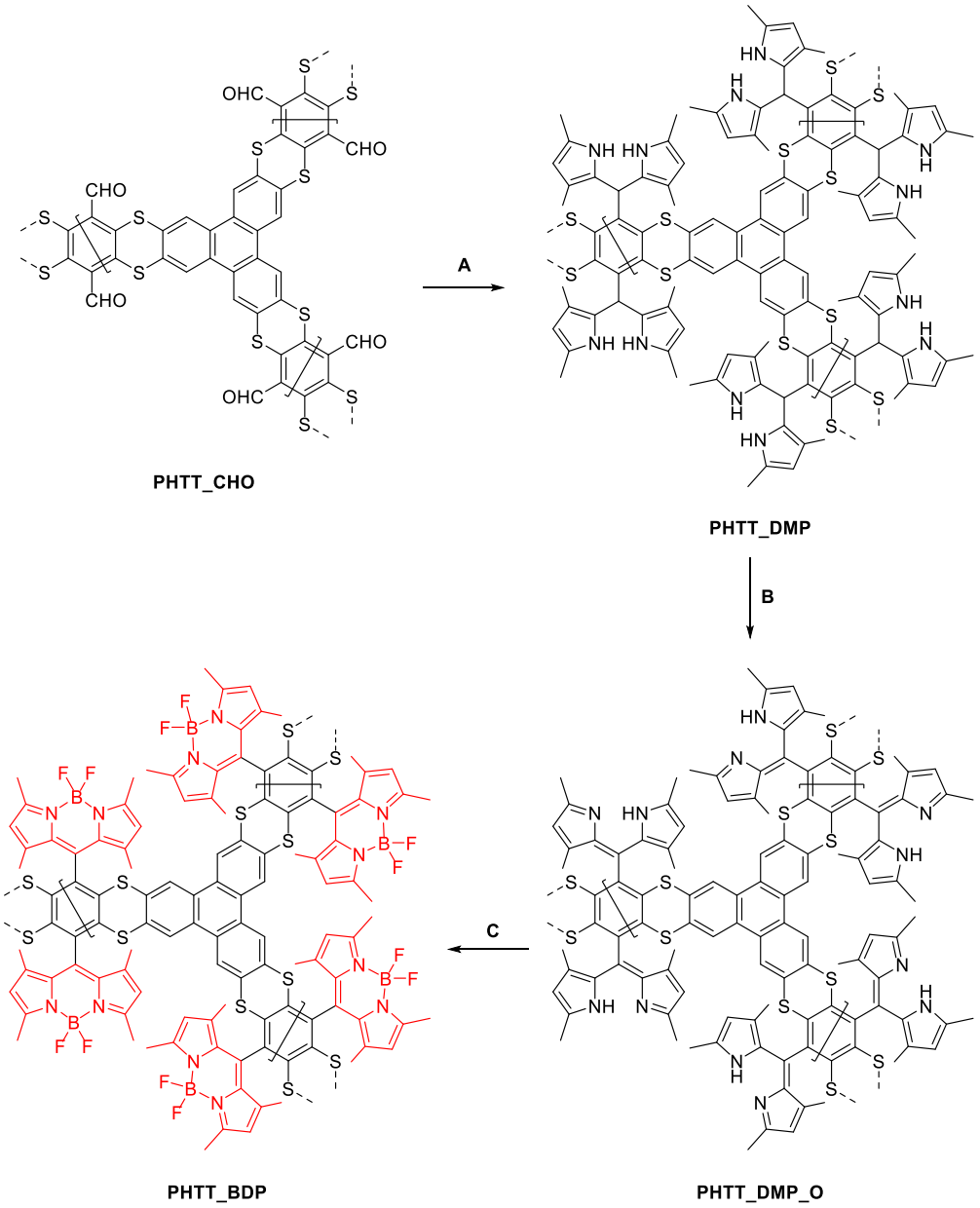

Scheme 2.2 Post-synthetic modification of PHTT_CHO through a three-step process.

2.3.3 Photosensitisation Reactions for $^1O_2$ Generation

The general experimental and qualitative techniques used for the detection of $^1O_2$ were carried out as discussed in the introduction and described in past work [2.9], through the conversion of α-terpinene to ascaridole monitored *via* ^{1}H NMR spectroscopy. In general, reaction mixtures consisted of the polymer (5 mg) dispersed in a solvent (15 mL) containing α-terpinene (136 mg, 1 mmol). Initially, a larger concentration of polymer was used (1 mg/1 mL), however this resulted in severe flow issues as the material quickly aggregated to create blockages. A smaller concentration of the polymeric material was then used (1 mg/3 mL) to create a better dispersion of the polymers, avoiding aggregation

and subsequent blockages. This dispersion was pumped through the photochemical flow reactor equipped with peristaltic pumps at a flow rate of 1 mL min^{-1}. The flow rate was chosen as the most optimal as it reduced aggregation whilst allowing for extended periods of irradiation and subsequent formation of $^1O_2$. Concurrently, air (the oxygen source), was propelled through a second pump at the same flow rate, meeting the dispersion at a T-junction prior to entering the photochemical reactor (Figure 2.2). The photochemical reactor (10 mL total volume) was equipped with a 530 nm LED module, ensuring complete irradiation of any reactants present. The mixture was continuously cycled through the reactor until full conversion to ascaridole was observed. All flow experiments and ^1H NMR spectroscopic analyses were aided by Heather Hayes (MChem project student) under my supervision.

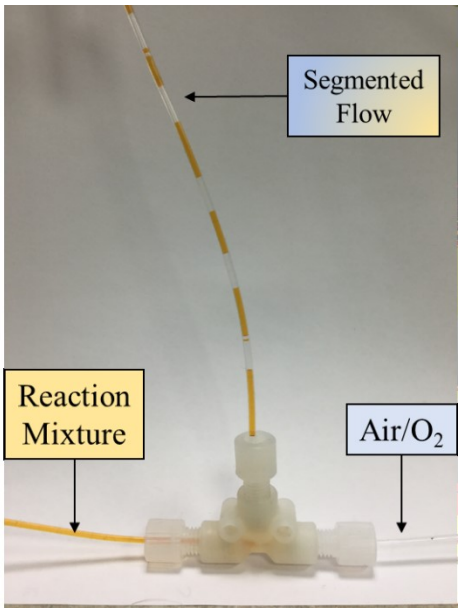

Figure 2.2 Photograph of the T-junction employed showing gas/liquid segmented pattern exhibited for singlet oxygen reactions under continuous flow conditions.

2.4 Results

2.4.1 Characterisation of BDP_CMP and PHTT_BDP

Initial analysis of the CPPs focused on spectroscopic properties, specifically UV-Vis absorption and fluorescence spectroscopy. As anticipated, BDP_CMP presented a significant bathochromic shift when compared to previously published materials

presented in Chapter 1, with a maximum absorbance at 550 nm (Figure 2.3a). Furthermore, PHTT_BDP presented with a broad absorbance between 500-600 nm with a maximum absorption peak at 520 nm (Figure 2.3b). As solid-state UV-Vis was used for these measurements, the optical band gap for both polymers was calculated to be 1.77 eV.

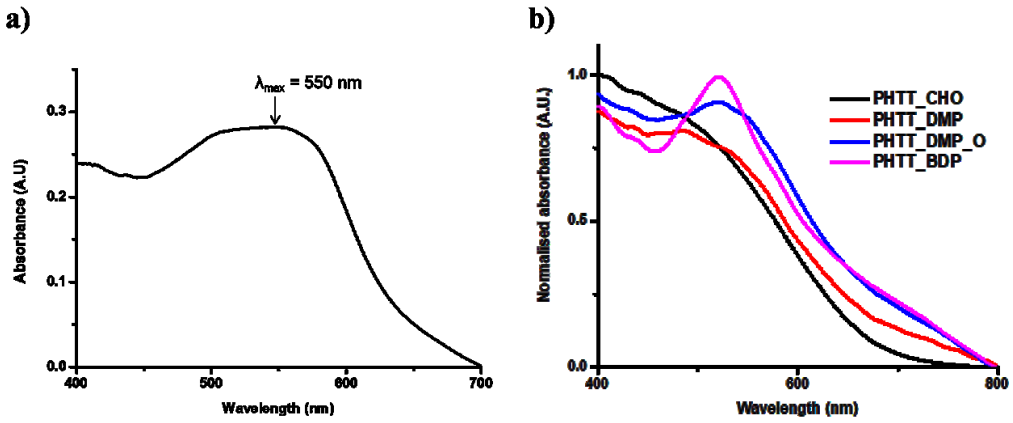

Figure 2.3 Solid state UV-Vis spectra of a) BDP_CMP, b) PHTT_CHO, PHTT_DMP, PHTT_DMP_O, and PHTT_BDP.

As expected for most BODIPY-based compounds, both BDP_CMP and its monomeric analogue Ph_BDP exhibited intense fluorescence when irradiated at 520 nm. Fluorescence spectra at this excitation wavelength showed sharp emissions and a weak Stokes shift of 21 nm for BDP_CMP and 24 nm for Ph_BDP. Surprisingly, PHTT_BDP did not exhibit fluorescence at any excitation wavelength. Whilst not conclusive, and more photophysical studies would have been required, this may indicate a more readily populated and/or stable triplet state when compared to BDP_CMP and Ph_BDP. Fluorescence occurs as a result of a photoexcited material transitioning from the excited singlet state directly back to its ground state, emitting light as the energy is lost. As a result, highly fluorescent materials can be indicative of low quantum yields in the triplet state if relaxation from the singlet state to the ground state occurs too readily [2.14].

Structural elements of the polymers were measured primarily through FT-IR and ^{13}C NMR CP-MAS spectroscopy. A C=N stretch at ~1700 cm^{-1} was observed for BDP_CMP while the disappearance of the aldehyde peak near the same wavenumber can be seen for the transition of PHTT_CHO to PHTT_BDP. Investigations into ^{13}C NMR CP-MAS for BDP_CMP showed aromatic carbons between 142-128 ppm along with a

signal at 155, indicative of the C=N bonds. The presence of methyl groups was also indicated with a signal at 12.5 ppm. For PHTT_BDP, the appearance of signals at 11.3, 15.22 and 14.2 ppm for the intermediate polymers indicates the presence of CH_3 groups found on the dimethylpyrrole groups. Furthermore, the disappearance of the aldehyde signal found in PHTT_CHO shows the successful addition of the pyrrole groups. Physical characterisations of both materials were also performed to determine their effective surface area and thermal stability. S_{BET} analysis of BDP_CMP and PHTT_BDP presented with relatively high surface areas at 769 $m^2 g^{-1}$ and 484 $m^2 g^{-1}$, respectively. Interestingly, post-synthetic addition of BODIPY to PHTT_CHO decreased the measured surface area from 686 $m^2 g^{-1}$ to 484 $m^2 g^{-1}$. This is not surprising as the decrease in surface area can be attributed to the addition of the sterically bulky BODIPY group. TGA measurements under a nitrogen stream of both polymers demonstrated high thermal stability up to 300 °C.

Finally, SEM and TEM imaging (p. 118-120) techniques of the polymers showed highly textured and amorphous materials, indicative of a porous yet unstructured framework. Coupled with SEM imaging, EDX analysis was also performed to illustrate the difference between the synthetic routes used to create each polymer. BDP_CMP was found to contain trace amounts of Pd (0.94 wt.%), indicating the presence of Pd that was not removed from the polymer matrix after purification. Conversely, as the synthesis of PHTT_BDP did not require a metal catalyst, there was no trace metal species present in the EDX analysis.

2.4.2 Heterogeneous Photosensitisation of $^1O_2$ using BDP_CMP and PHTT_BDP

Initial investigations into $^1O_2$ production with the synthesised CPPs were performed under continuous flow conditions with chloroform (Figure 2.4). ^{1}H NMR spectroscopy, used to monitor the conversion of α-terpinene to ascaridole, showed that both BDP_CMP and PHTT_BDP photosensitisers achieved full conversion within 1 hour. This experiment verified the ability for both polymers to act as promising photosensitisers, prompting further examination.

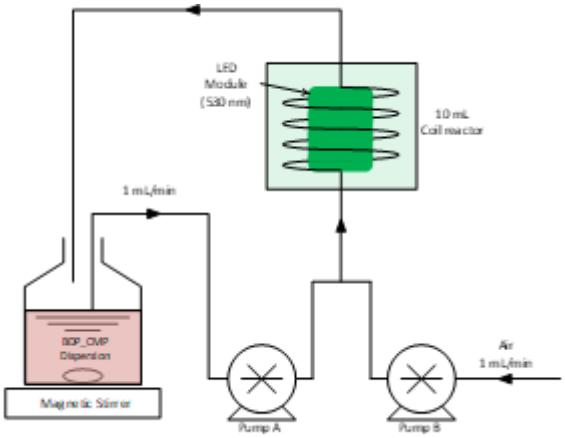

Figure 2.4 Schematic representation of the experimental set-up for the photocatalytic production of $^1O_2$ under continuous flow conditions.

To ensure the photo and chemical stability of the CPPs, a similar experiment for the generation of $^1O_2$ was performed. However, prior to the addition of α-terpinene the dispersed polymers were allowed to cycle under the same reaction conditions for 5 hours. After this time, α-terpinene was added and the reaction was carried out for 1 hour and the mixture analysed every 10 minutes to determine the rate of conversion. While BDP_CMP showed no degradation in photocatalytic activity (Figure 2.5a), conversion of α-terpinene to ascaridole decreases by 10% with PHTT_BDP when compared to the initial reaction rate (Figure 2.5b). Whilst slight, the difference in performance may be attributed to how BODIPY is incorporated into the respective polymers. With BDP_CMP, the BODIPY monomer is an integral part of the polymer backbone and may contribute to the enhanced stability. However, the same BODIPY monomer in PHTT_BDP has been post-synthetically grafted onto the polymer, where it may be at greater risk of photobleaching or open to interaction with other reactive species. Regardless, both polymers clearly share excellent photo and chemical stability under continuously harsh conditions.

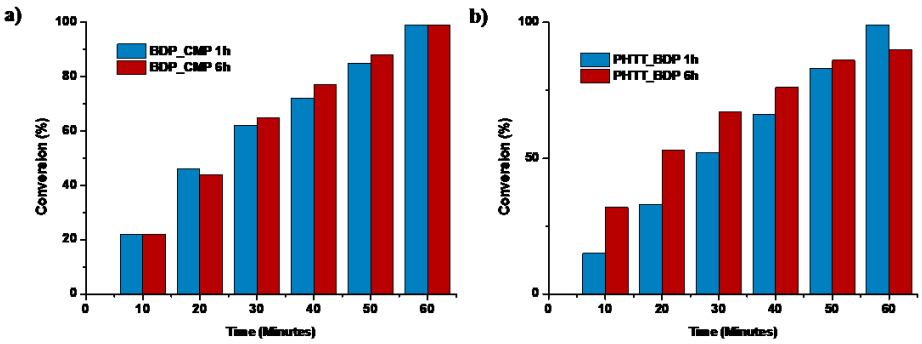

Figure 2.5 Conversion of α-terpinene to ascaridole over 60 minutes with a) BDP_CMP and b) PHTT_BDP.

Upon examination of the kinetics, we expect a second-order reaction [2.15] as the conversion rate is dependent on the concentration of both reactants (α-terpinene and $^1O_2$). However, as most photocatalytic studies are performed under batch conditions, the concentration of the substrate is much greater than that of the short lived $^1O_2$, resulting in a pseudo-first-order rate model [2.16-2.18]. The kinetic studies were fitted to a pseudo-first-order model which the PHTT_BDP polymer followed very closely. However, the same was not observed for BDP_CMP as the conversion, which occurred after 60 minutes, was greater than expected. It can be argued that the continuous flow of air (oxygen) resulted in the continued generation of $^1O_2$ to a point where its concentration greatly exceeded that of α-terpinene. Due to this, the same model could no longer fit the reaction kinetics. Furthermore, the increase in conversion rate highlights an advantage of continuous flow over traditional batch chemistry, as overall oxygen penetration into the reaction mixture is much greater.

2.4.3 Control Experiments and Validation of BODIPY as a Photoactive Moiety

To better understand and validate how the BODIPY-based polymers act as photosensitisers, control experiments were performed. While perhaps obvious, no change occurred to α-terpinene in reactions either in the absence of O_2 or the polymers under the reaction conditions stated above. Furthermore, a change in the irradiation wavelength to 420 nm showed poor conversion, 9% after 90 minutes reaction time. In the absence of light, no conversion was observed. These results underline the optical control demonstrated in the synthesis of these materials and a desirable shift to photosensitisation reactions performed using less energetic wavelengths.

Further validation of the BODIPY core as the fundamental component for these reactions was performed where Ph_BDP was employed as the monomeric equivalent to BDP_CMP. Experiments under the same reaction conditions were carried out and no variation in the time to reach full conversion after both 1 hour and 6 hours was observed. Furthermore, as demonstrated with BDP_CMP, no apparent degradation of the monomer occurred after 6 hours under the reaction conditions. The result of this experiment is two-fold: *i*) the BODIPY core of BDP_CMP is a vital component regarding its application as a photosensitiser; *ii*) it can be surmised that any residual palladium within the BDP_CMP matrix (as seen in the EDX measurements) had negligible effect on its photocatalytic activity.

As PHTT_CHO and the intermediate structures (PHTT_DMP and PHTT_DMP_O, Scheme 2.2) leading up to PHTT_BDP demonstrated some amount of absorption at 530 nm (Figure 2.3b), each step was isolated and tested as photosensitisers under the same reaction conditions. While PHTT_CHO showed only minimal photoactivity, the addition of the pyrrole groups and subsequent oxidation resulted in 77% conversion after 1 hour. This is not entirely surprising as the absorbance around 530 nm increased after each reaction step. However, only the PHTT_BDP product was able to achieve full conversion within 1 hour, validating the complete formation of BODIPY.

2.4.4 Heterogeneous Photosensitisation of $^1O_2$ in Different Solvents

The entirety of the reactions described up to this point were performed in chloroform. While this is an ideal solvent, due to extended $^1O_2$ lifetimes [2.14], it is also hazardous and an environmental pollutant. To exhibit the versatility of the photosensitisers as well as a move towards more sustainable solvent systems, a variety of common organic solvents as well as 'green' solvents (2-methyltetrahydrofuran, dimethyl carbonate, and water) were examined under the same reactions conditions. As expected, most of the common organic solvents presented with a decrease in conversions after 1 hour for both materials, most likely due to the decreased $^1O_2$ lifetimes. However, it should be noted that these decreases were relatively low with conversions reaching no less than 81% when compared to the initial reaction in chloroform.

Examination of the 'green' solvents exhibited similar conversions to the common organic solvents after 1 hour, demonstrating their potential as alternate solvent choices for these reactions. Water was also chosen as the ultimate green solvent, however due to the incompatible nature of the polymers in water they showed poor dispersion and quickly agglomerated, causing severe blockages in the reactor tubing. As a result, water could not be examined in this case.

Throughout this scope of solvents, it is prudent to remark on the photoactive nature of both BDP_CMP and PHTT_BDP and how they compare to each other. No appreciable difference was observed in the comparisons between solvent systems, although it could be argued that PHTT_BDP works better in some cases. As the fundamental distinction between the two polymers resides in how they were synthesised,

the similar photoactivity further denotes the benefits of developing and employing metal-free synthetic methods for the production of CPPs.

2.5 Conclusion

Two distinct BODIPY-based conjugated porous polymers have been prepared through either traditional palladium catalysed cross-coupling or post-synthetic modification of an aldehyde-equipped CPP host in the absence of metals. By coupling BODIPY (strong electron acceptor) to benzene (weak electron donor), a bathochromic shift occurred where the maximum absorbance of the CPPs were observed at less energetic wavelengths (~530 nm). The polymers were then examined as heterogeneous photosensitising materials in a commercial photochemical flow reactor, equipped with a LED lamp irradiating at 530 nm, in a variety of organic solvent systems. Overall, both polymers demonstrated high photocatalytic activity for $^1O_2$ production, indicating adequately long-lived triplet excited states. Furthermore, high photo and chemical stability, along with ease of recovery, allowed for the materials to be reused with little to no degradation in photocatalytic activity. Through the combination of band gap tuning, metal-free synthesis, and flow chemistry, these novel materials have demonstrated a distinct progression for the development of photocatalytic CPPs.

2.6 Impact on Literature and Research

This research has provided new avenues towards the synthesis of porous organic-based materials with an aim towards heterogeneous photocatalytic applications, an important and growing field focusing on sustainability and green chemical processes. To date, this paper has been cited 10 times, denoting the impact and continued interest in this field. By demonstrating tuneable absorbance values, a shift away from absorbance values at UV and near UV wavelengths was accomplished. Moving away from highly energetic UV light has several advantages, primarily with regards to the detrimental effects it can have on reactants, products, and/or photocatalytic materials. However, it must be noted that there is a limit to which a bathochromic shift is useful. As the maximum absorbance of a material shifts to longer wavelengths, less energic light is required for photoactivity. A potential result of this is the promotion of electrons to less energetic excited states,

particularly the triplet state. In the case of $^1O_2$ production, the energy required to promote $^3O_2$ to this electronic state is 95 kJ mol^{-1}. If the energy transferred from the triplet excited state to $^3O_2$ does not exceed or match this energy, $^1O_2$ will not be formed [2.19].

Another key aspect of this work is the formation of PHTT_BDP through a metal-free methodology while retaining comparable photoactivity to that of the palladium catalysed BDP_CMP. Not only does this ensure the absence of any residual metal catalyst within the polymer matrix, it also demonstrates a more sustainable synthetic route, both environmentally and economically. This sustainability is of paramount importance when determining the long-term and/or industrial viability of CPPs. The success and potential scope of these materials, especially PHTT_BDP, has helped shape the goals and outlook for our own research. The proceeding chapter expands on the idea of metal-free synthesis with the introduction of a CPP with applications beyond photocatalysis.

2.7 References

[2.1] M. D. Yilmaz, O. A. Bozdemir, E. U. Akkaya, *Light Harvesting and Efficient Energy Transfer in a Boron-dipyrrin (BODIPY) Functionalized Perylenediimide Derivative*, Org. Lett., **8**, 2871-2873 (2006)

[2.2] R. Ziessel, C. Goze, G. Ulrich, M. Cesario, P. Retailleau, A. Harriman, J. P. Rostron, *Intramolecular Energy Transfer in Pyrene–Bodipy Molecular Dyads and Triads*, Chem. Eur. J., **11**, 7366-7378 (2005)

[2.3] F. Vilela, K. Zhang, M. Antonietti, *Conjugated porous polymers for energy applications*, Energy Environ. Sci., **5**, 7819-7832 (2012)

[2.4] G. Ulrich, R. Ziessel, A. Harriman, *The chemistry of fluorescent bodipy dyes: versatility unsurpassed*, Angew. Chem., Int. Ed., **47**, 1184-1201 (2008)

[2.5] S. O. McDonnell, M. J. Hall, L. T. Allen, A. Byrne, W. M. Gallagher, D. F. O'Shea, *Supramolecular Photonic Therapeutic Agents*, J. Am. Chem. Soc., **127**, 16360-16361 (2005)

[2.6] E. L. Clennan, *New Mechanistic and Synthetic Aspects of Singlet Oxygen Chemistry*, Tetrahedron, **56**, 9151-9179 (2000)

[2.7] J. Shen, R. Steinbach, J. M. Tobin, M. M. Nakata, M. Bower, M. R. S. McCoustra, H. Bridle, V. Arrighi, F. Vilela, *Photoactive and metal-free polyamide-based polymers*

for water and wastewater treatment under visible light irradiation, Appl. Cat. B - Enviorn., **193**, 226-233 (2016)

[2.8] R. Bonnett, *Photosensitizers of the porphyrin and phthalocyanine series for photodynamic therapy*, Chem. Soc. Rev., **24**, 19-33 (1995)

[2.9] Y. L. Wong, J. M. Tobin, Z. Xu, F. Vilela, *Conjugated porous polymers for photocatalytic applications*, J. Mat. Chem. A, **4**, 18677-18686 (2016)

[2.10] P. V. Dau, K. K. Tanabe, S. M. Cohen, *Functional group effects on metal–organic framework topology*, Chem. Commun., **48**, 9370-9372 (2012)

[2.11] A. Vazquez-Romero, N. Kielland, M. J. Arevalo, S. Preciado, R. J. Mellanby, Y. Feng, R. Lavilla, M. Vendrell, *Multicomponent Reactions for de Novo Synthesis of BODIPY Probes: In Vivo Imaging of Phagocytic Macrophages*, J. Am. Chem. Soc., **135**, 16018-16021 (2013)

[2.12] L. Wang, J-W. Wang, A-J. Cui, X-X. Cai, Y. Wan, Q. Chen, M-Y. He, W. Zhang, *Regioselective 2,6-dihalogenation of BODIPYs in 1,1,1,3,3,3-hexafluoro-2-propanol and preparation of novel meso-alkyl polymeric BODIPY dyes*, RSC Adv., **3**, 9219-9222 (2013)

[2.13] J. Liu, J. Cui, F. Vilela, J. He, M. Zeller, A. D. Hunter, Z. Xu, *In situ production of silver nanoparticles on an aldehyde-equipped conjugated porous polymer and subsequent heterogeneous reduction of aromatic nitro groups at room temperature*, Chem. Commun., **51**, 12197-12200 (2015)

[2.14] U. E. Steiner, *Fundamentals of Photophysics, Photochemistry, and Photobiology*, In: M. Abdel-Kader (ed.), *Photodynamic Therapy*, Springer, Berlin, (2014)

[2.15] E. Appiani, R. Ossola, D. E. Latch, P. R. Erickson, K. McNeill, *Aqueous singlet oxygen reaction kinetics of furfuryl alcohol: effect of temperature, pH, and salt content*, Envrion. Sci.: Processes Impacts, **19**, 507-516 (2017)

[2.16] H. Kim, W. Kim, Y. Mackeyev, G.-S. Lee, H.-J. Kim, T. Tachikawa, S. Hong, S. Lee, J. Kim, L. J. Wilson, T. Majima, P. J. J. Alvarez, W. Choi, J. Lee, *Selective Oxidative Degradation of Organic Pollutants by Singlet Oxygen-Mediated Photosensitization: Tin Porphyrin versus C_{60} Aminofullerene Systems*, Environ. Sci. Technol., **46**, 9606–9613 (2012)

[2.17] T. Zhang, Y. Ding, H. Tang, *Generation of singlet oxygen over Bi(V)/Bi(III) composite and its use for oxidative degradation of organic pollutants*, Chem. Eng. J., **264**, 681–689 (2015)

[2.18] J. Lee, Y. Mackeyev, M. Cho, L. J. Wilson, J.-H. Kim, P. J. J. Alvarez, *C_{60} Aminofullerene Immobilized on Silica as a Visible-Light-Activated Photocatalyst*, Environ. Sci. Technol., **44**, 9488–9495 (2010)

[2.19] M. C. DeRosa, R. J. Crutchley, *Photosensitized singlet oxygen and its applications*, Coord. Chem. Rev., **233-234**, 351-371 (2002)

DECLARATION

As primary author of this publication, I can confirm the majority of the work to be my own. Work carried out by other students or collaborators has been outlined above.

Signature: _____

PUBLICATION 2

BODIPY-based conjugated microporous polymers as reusable heterogeneous photosensitisers in a photochemical flow reactor

J. M. Tobin, J. Liu, H. Hayes, M. Demleitner, D. Ellis, V. Arrighi, Z. Xu, F. Vilela

DOI: 10.1039/c6py01393g

Polym. Chem., **2016**, *7*, 6662-6670

Abstract

BODIPY-based conjugated microporous polymers (BDP_CMP and PHTT_BDP) have been synthesised via two distinct methods of assembly: high-yielding Suzuki-Miyaura cross-coupling of BODIPY-containing building blocks, and post-synthetic conversion of an aldehyde-equipped CMP host that was synthesised in the absence of metal-based catalysts. Both approaches yielded BODIPY-based materials featuring high BET surface area (484-769 m^2 g^{-1}) and a bathochromic shift in the maximum light absorbance (520-550 nm). Singlet oxygen production employing the BODIPY-based materials at 530 nm was carried out heterogeneously in a commercial photochemical flow reactor.

Introduction

Anthropogenic climate change as a result of our current energy demands is of great concern in today's society. The need for new sources of clean and renewable energy alongside with improved sustainable chemical processes has been the driving force behind the development of many new materials. One class of materials that has recently gained a great deal of attention from the research community consist of systems with inherent porosity [1]. These materials have the potential to provide a means to store and separate chemical entities such as gases [2]; participate in (photo)catalytic processes such as hydrogen evolution from water [3]; and in the storage and delivery of energy [4]. Conjugated microporous polymers (CMPs) fall into this class of materials.

As first described by Cooper *et al.* [5, 6], CMPs have been investigated as counterparts to zeolites, metal-organic frameworks, covalent-organic frameworks and other microporous polymers [7]. Combining high surface areas, microporosity and photoactivity, CMPs have also shown applications in gas sorption and separation [8], light harvesting [9], and heterogeneous (photo)catalysis [10-13], amongst others. One important application where CMPs have recently gained traction is in the heterogeneous photoactivation of singlet oxygen ($^1O_2$) [11, 14, 15].

Unlike most natural compounds, molecular oxygen has triplet multiplicity ($^3O_2$) in the ground state and two excited singlet states [16]. The most common and widely used generation of $^1O_2$ is based on homogenous photosensitisers [17, 18]. This simple method requires only an oxygen source, light of an appropriate wavelength and a photosensitiser possessing an energetically suitable excited triplet state. Through the absorption of light, the photosensitiser is excited to its singlet state and *via* a subsequent intersystem crossing mechanism it populates into a triplet state. The excited sensitiser can then transfer energy and spin to the ground state $^3O_2$, thus forming the excited $^1O_2$ [18]. Given its strong electrophilic and oxidising character, it has been widely used as a versatile synthetic reagent in a range of applications including organic synthesis [19], environmental water treatment [20] or photodynamic therapy of cancer [21].

One particular dye that is effective in the production of singlet oxygen is BODIPY (4,4-difluoro-4-bora-3a,4a-diaza-s-indacene), Fig. 1 [22]. Due to its strong absorption–emission and fluorescence properties, as well as chemical robustness [23-25], BODIPY

derivatives have also been widely employed for different applications such as biological tags with visible to near-IR emission, molecular rotors, lasing, dye-sensitised solar cells, electroluminescence and chemical photosensitisation reactions [25-35]. This strong electron-accepting dye has therefore the necessary properties for photosensitisation at higher wavelengths of $^1O_2$ when incorporated into a CMP.

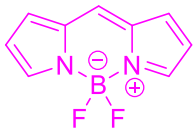

Fig. 1 Chemical structure of the BODIPY core.

As part of our ongoing efforts to develop versatile synthetic strategies for functional CMP solids, herein we report the chemical synthesis and characterisation of two novel BODIPY-based CMPs, which exhibits high surface areas and a bathochromic shift with their maximum light absorbance at 520-550 nm. These polymers were tested in a commercial photochemical flow reactor [36] for the production of $^1O_2$ in multiple solvents, and simply using air as the source of oxygen.

The BODIPY-based CMPs prove to be efficient photosensitisers under the conditions tested and can be easily recovered and isolated *via* simple filtration and then conveniently reused multiple times. Furthermore, in photocatalytic reactions, a photosensitiser that absorbs light at higher wavelengths is desirable as it mitigates photodecomposition of starting materials and/or products whilst also avoiding undesirable side reactions when more energetic light sources such as UV are employed.

Experimental

Instrumentation and Measurements

All reagents and starting materials employed in this work were commercially available and used without further purification unless otherwise stated. ^1H NMR and ^{13}C NMR were recorded on a 400 MHz Bruker superconducting-magnet high-field NMR spectrometer at room temperature with tetramethylsilane as the internal standard or a 300 MHz Bruker AV-III300 spectrometer at room temperature. Solid state ^{13}C NMR CP-

MAS measurements were carried out using a Bruker Advance 400 spectrometer operating at 100.6 MHz for ^{13}C NMR using a Bruker 4 mm double resonance probe-head operating at a spinning rate of 10-12.5 kHz. Solution UV-Vis spectra were recorded on a PerkinElmer Lambda 25 system using 10 mm quartz cuvettes with CH_2Cl_2 as the solvent. Solid-state UV-Vis spectra were recorded on the same system using a Labsphere RSA-PE-20 reflectance spectroscopy integration sphere. Fluorescence spectra were recorded on a Perkin Elmer LS 55 spectrometer using 10 mm quartz fluorescence cell with CH_2Cl_2 as the solvent. FT-IR spectra were recorded on a Nicolet Avatar 360 FT-IR spectrophotometer or an ATR-FTIR spectrometer *Thermo Scientific Nicolet iS5*. Thermogravimetric analysis (TGA) of the BDP_CMP sample was carried out in a nitrogen stream using TA Instruments Q50 Thermogravimetric Analyser with a heating rate of 3 °C min^{-1} and a heating range of 30 °C to 950 °C. TGA of the PHTT_BDP sample was carried out in a nitrogen stream using PerkinElmer Thermal analysis equipment (STA 6000) with a heating rate of 3 °C min^{-1}, with an empty Al_2O_3 crucible being used as the reference. BET Surface area was carried out using a Quantachrome Autosorb iQ gas sorption analyser. Each sample was outgassed at 0.03 torr with a 2 °C min^{-1} ramp to 100 °C and held at 100 °C for 12 hours. The sample was then held at vacuum until the analysis was run. Pore analysis was performed using N_2 at 77 K (P/P_0 range of 1×10^{-5} to 0.995) and CO_2 at 273 K (P range of 8×10^{-3} to 780 mmHg). Scanning electron microscopy (SEM) was carried out on Philips XL30 Esem-FEG, (FEI Company, The Netherlands) equipped with an energy-dispersive x-ray microanalysis (EDX) system (EDAX Phoenix system, EDAX Inc., Mahwah NJ, USA). Transmission electronic microscopy (TEM) was conducted on a Philips Technai 12 Transmission Electron Microscope with an accelerating voltage of 120 KV.

Syntheses

Two distinct synthetic strategies were examined. First, in a direct assembly approach, BDP_CMP was obtained using a palladium-catalysed Suzuki-Miyaura cross-coupling reaction, whereby 1,3,5-tris(4,4,5,5-tetramethyl-1,3,2-dioxaborolan-2-yl)benzene was used as the cross-linker reacting with 2,6-dibromo-1,3,5,7-tetramethyl-8-phenyl-BODIPY monomer (Scheme 1). Tetrakis(triphenylphosphine) palladium(0), 1,3,5-tris(4,4,5,5-tetramethyl-1,3,2-dioxaborolan-2-yl)benzene and 2,6-dibromo-1,3,5,7-tetramethyl-8-phenyl-BODIPY were synthesised *via* literature methods [37-40] which can be found in the ESI. A monomeric version of the repeat unit, 2,6-diphenyl-1,3,5,7-

tetramethyl-8-phenyl-BODIPY (BDP_Ph), was also synthesised through a similar cross-coupling reaction and compared to results found in literature [41]. The scheme and structure for BDP_Ph is presented in the ESI. Second, in a post-synthetic functionalisation approach, the aldehyde groups of a known polymer system PHTT-_CHO, as described in our previous work [13], were converted into the BODIPY function *via* the classical protocol of condensation with 2,4-dimethylpyrrole, followed by oxidation via 2,3-dichloro-5,6-dicyano-1,4-benzoquinone (DDQ) and boron trifluoride diethyl etherate ($BF_3{\cdot}O(Et)_2$) treatment (Scheme 2). Along with the synthesis of the known PHTT_CHO polymer, this method also employed a metal-free synthetic procedure. The result of these methods allowed for the entirety of the target material PHTT_BDP to be produced in the absence of metals. The scheme and structure of each intermediate is presented in the ESI.

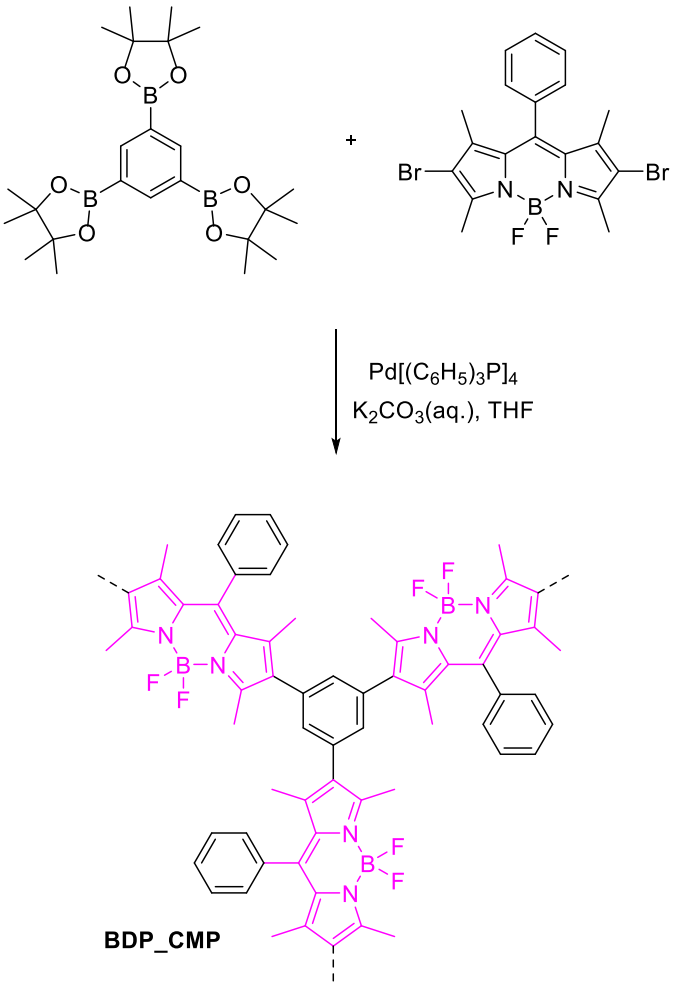

Scheme 1 Synthesis and proposed structure of BDP_CMP.

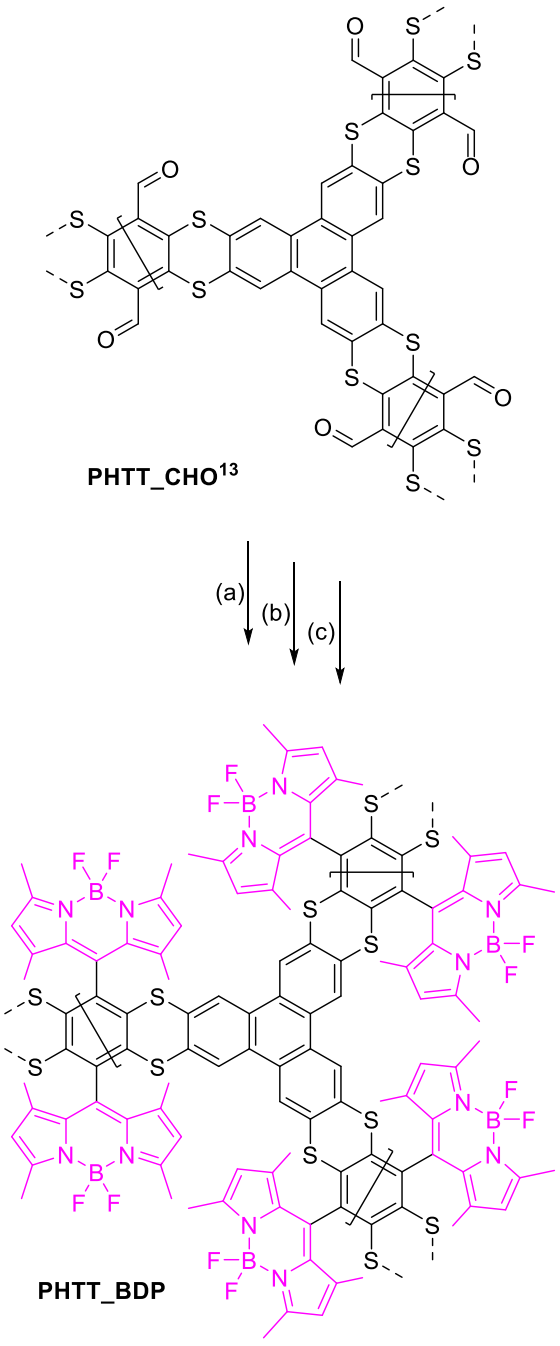

Scheme 2 Synthesis and proposed structure of PHTT_BDP. Reactions conditions: (a) Dimethylpyrrole, 50 °C, TFA. (b) DDQ, DCM, r.t. (c) Triethyleamine, $BF_3{\cdot}O(Et)_2$, DCM, 50 °C.

2,6-Diphenyl-1,3,5,7-tetramethyl-8-phenyl-BODIPY (BDP_Ph). To a dry 100 mL-flask equipped with a magnetic stirring bar, a septum inlet, and a reflux condenser was placed a mixture of $Pd[(C_6H_5)_3P]_4$ (5 mg, 0.003 mmol), 2,6-dibromo-1,3,5,7-tetramethyl-8-phenyl-BODIPY (50 mg, 0.10 mmol) and phenylboronic acid (24 mg, 0.20 mmol). This flask was connected to a Schlenk line, evacuated and back-filled with N_2 three times for purging. In the flask, whilst under N_2 dry THF (15 mL) was added to

dissolve the reagents. An aqueous solution was prepared with K_2CO_3 (55 mg, 0.4 mmol) and degassed with nitrogen for 10 minutes. The aqueous solution was added through a syringe and the solution was heated to 70°C and stirred overnight. After 16 h, the bright orange reaction mixture was allowed to cool to room temperature before adding approximately 40 mL of water and transferring to a separating funnel with 50 mL of dichloromethane. The organic layer was washed with deionised water (50 mL x 3) and dried over $MgSO_4$. The crude mixture was filtered and a short column using silica gel was used to remove excess catalyst and by-products. Bright orange crystals precipitated from the solution which were filtered, washed with small amount of cold acetone and allowed to dry in air (30 mg, yield: 63%). ^{1}H NMR (300 MHz, $CDCl_3$): δ 7.54-7.49 (m, 3H), 7.44-7.36 (m, 8H), 7.21 (t, 2H), 7.18 (t, 2H), 2.58 (s, 6H), 1.34 (s, 6H).

BDP_CMP. To a dry 100 mL-flask equipped with a magnetic stirring bar, a septum inlet, and a reflux condenser was placed a mixture of $Pd[(C_6H_5)_3P]_4$ (30 mg, 0.03 mmol), 2,6-dibromo-1,3,5,7-tetramethyl-8-phenyl-BODIPY (248 mg, 0.51 mmol) and 1,3,5-tris(4,4,5,5-tetramethyl-1,3,2-dioxaborolan-2-yl)benzene (160 mg, 0.34 mmol). This flask was connected to a Schlenk line, evacuated and back-filled with N_2 three times. In the flask whilst under N_2 dry THF (40 mL) was added to dissolve the solid reagents. An aqueous solution was then prepared with K_2CO_3 (181 mg, 1.03 mmol) and degassed with nitrogen for 10 minutes. The aqueous solution was added to the organic solution, heated to 70°C and stirred overnight. After refluxing for 24 h, a precipitate formed and was filtered and washed three times with MeOH, THF and H_2O. The precipitate was purified *via* soxhlet extraction with THF and $CHCl_3$ for 4 h. The solid reddish powder was dried for 24 h *in vacuo* (176 mg, yield: 72.5%). ^{13}C NMR CP-MAS (100.6 MHz): δ 155.0, 142.0, 134.6, 131.3, 128.5, 12.53.

PHTT_DMP (Step 1). PHTT_CHO (102 mg, 0.17 mmol) and a stir bar were loaded into a 5-mL Schlenk tube. The Schlenk tube was connected to a Schlenk line, evacuated and back-filled with N_2 three times for purging. 2,4-Dimethylpyrrole (1.43 g, 15 mmol, bubbled with N_2 for 5 min beforehand) was transferred into the tube *via* cannula. Trifluoroacetic acid (TFA) (2 drops) was then added into the reaction mixture under N_2. After the mixture was stirred at 50 °C for one day, a brown red solid was collected on a Buchner funnel after the reaction mixture was cooled down to the room temperature, washed with Na_2CO_3/DI water solution, deionised water (10 mL × 4, pH~7), MeOH (10 mL × 2), DCM (10 mL) and dried under vacuum at room temperature for 3 h

to afford the as-made product PHTT_DMP as brown-red solid (152 mg). The crude product was purified *via* Soxhlet extraction in refluxing MeOH for 48 h, and then evacuated by pump at 50 °C for 5 h to provide an activated solid product PHTT_DMP (brown-red solid, 145 mg, yield: 76.9%). ^{13}C NMR CP-MAS (100.6 MHz): δ 135.0, 128.6, 110.1, 11.31.

*PHTT_DMP_O (Step 2)***.** PHTT_DMP (120 mg, 0.11 mmol), 2,3-dichloro-5,6-dicyano-1,4-benzoquinone (DDQ) (110 mg, 0.48 mmol) and dry DCM (5 mL) were added into a 7.5 mL glass vial. The reaction mixture was stirred at room temperature for 24 h. The black-brown solid was then collected on a Buchner funnel, washed with DCM (10 mL x 3) and dried under vacuum at room temperature for 5 h to afford the product PHTT_DMP_O (115 mg) as a black-brown solid. ^{13}C NMR CP-MAS (100.6 MHz): δ 130.39 (broad 110 – 140), 15.22.

PHTT_BDP (Step 3). PHTT_DMP_O (110 mg, 0.10 mmol) and a stir bar were loaded into a 10 mL Schlenk tube. The Schlenk tube was connected to a Schlenk line, evacuated and back-filled with N_2 three times for purging. Triethylamine (320 mg, 3.2 mmol) in dry DCM (2 mL) (bubbled with N_2 for 2 minutes beforehand) was transferred into the flask via cannula. After the reaction mixture was stirred at room temperature for 10 minutes, $BF_3{\cdot}O(Et)_2$ (670 mg, 4.72 mmol) was added into the reaction mixture under nitrogen protection. The reaction mixture was then stirred at 50 °C for 24 h. The black-brown solid was collected on a Buchner funnel, washed with DCM (10 mL × 5) and dried under vacuum at room temperature for 5 h to afford the product PHTT_BDP (116 mg) as black-brown solid. ^{13}C NMR CP-MAS (100.6 MHz): δ 149.9, 138.4, 129.7, 124.5, 14.20.

Photosensitisation Reactions

General procedure and experimental conditions for photosensitisation reactions in flow are exemplified as follows: BDP_CMP (5 mg) was dispersed into a solution containing $CHCl_3$ (15 mL) and *α*-terpinene (136 mg, 1 mmol). This dispersion (ESI Fig. S1-right) was then pumped using a peristaltic pump through the commercial photochemical reactor employing 1 mm I.D. PTFE tubing at a flow rate of 1 mL min^{-1}. Concurrently, air was pumped through a second pump at the same flow rate. In order to simplify the experimental setup, we chose to use air rather than pure oxygen. The use of two peristaltic pumps allowed for (i) a heterogeneous mixture to pass easily through the

system and (ii) air to be pumped through the reactor coil. The dispersion and the air were mixed through a T-junction prior entering to the photochemical coil reactor (10 mL total volume) equipped with a 530 nm LED module. The LED module contains six small arrays and sits in the middle of the coil reactor to ensure full irradiation of the photochemical reactor [36]. This mixture was cycled through several times until full conversion was observed.

Due to the risk of polymer agglomeration and consequent blockage, care was taken to minimise this issue. The polymers were ground into a fine powder before dispersal in solvent, ensuring that the particles are small enough to travel uninhibited through the 1 mm I.D. of the tubing as well as aiding in an even dispersion in each of the solvents tested. A magnetic stirrer was also used to ensure that the dispersion was uniform throughout the experiment. Employing a minimal amount of the photoactive polymer to the reaction mixtures also ensured an appropriately dilute dispersion and further reduced the risk of blockages. It is noted that the dispersion did not increase the flow pressure throughout the experiment indicating that any viscosity increase was negligible.

Results and Discussion

Spectroscopic Properties

The solid-state UV-Vis absorption spectra of BDP_CMP shows a maximum at 550 nm (ESI Fig. S9). Interestingly, the intermediate steps between PHTT_CHO and PHTT_BDP present with increased broadening of the absorption wavelength and a more intense absorbance between 500-600 nm. The absorbance reaches a peak with the PHTT_BDP product developing a pronounced λ_{max} at 520 nm (ESI Fig. S11). These materials are slightly red-shifted in comparison with the synthesised 1,3,5,7-tetramethyl-8-phenyl-BODIPY monomer, which has an absorption maximum at around 500 nm [39]. This red-shift occurs due to the enhanced delocalisation of the electrons in the polymer [9, 42].

Since the BODIPY-based polymers mainly absorb light at a lower energetic region of the electromagnetic spectrum chances of photodecomposition of the material and/or reagents are in principle greatly reduced. The absorption edges of both polymers

at approximately 700 nm allows for the optical band-gap to be approximately calculated according to the Planck-Einstein relation as shown in Eq. (1):

$$Eg_{(opt.)} = h\frac{c}{\lambda} \qquad (1)$$

where $Eg_{(opt.)}$ (J) is the optical band-gap of the polymer, *h* being the Planck constant (6.63 x 10^{-34} Js), *c* the speed of light in vacuum (3.00 x 10^{8} m s^{-1}), and λ being the wavelength (m) at the absorption edge. With an absorption edge at 700 nm, the optical band-gap of both polymers thus calculated equates to 1.77 eV (1 eV = 1.60 x 10^{-19} J). This is not surprising as BODIPY derivatives exhibit variable redox chemistry, and they have been used as electron donors and acceptors [43, 44]. In the latter case, BODIPY co-monomers have the potential of lowering the band gap of conjugated polymers (and stabilising their reduced states), since donor and acceptor units within conjugated structures are able to bring the HOMO/LUMO energy levels closer together [45, 46].

Absorption and fluorescence spectra of BDP_CMP and its monomeric version Ph_BDP can be in Fig. S10. Both materials were examined first using UV-Vis absorption measurements to determine the maximum absorption wavelengths. BDP_CMP and Ph_BDP presented with a λ_{max} at 520 nm and 527 nm, respectively. We note that due to the insoluble nature of BDP_CMP, it was suspended in CH_2Cl_2 for both the absorption and fluorescence measurements. Excitation at these wavelengths presented with sharp emission spectra showing a weakly Stokes-shifted band of mirror image shape when compared to the absorption spectra. A red shift of both BDP_CMP and Ph_BDP absorption and emission spectra presented with a maximum at 541 and 551 nm, respectively. This can be attributed to the extended π conjugation, particularly in BDP_CMP. Similar characterisation was also performed on PHTT_BDP but no fluorescence was observed.

FT-IR measurements of BDP_CMP were compared to that of the 1,3,5,7-tetramethyl-8-phenyl-BODIPY small molecule (ESI Fig. S12). A characteristic peak at ~1700 cm^{-1} pertaining to a C=N stretch can be seen in both spectra, indicating the presence of the BODIPY moiety within the polymer. PHTT_BDP was also measured *via* FT-IR and compared against the three preceding steps (ESI Fig. S13). The characteristic aldehyde stretch at 1700 cm^{-1} is seen in the initial polymer PHTT_CHO. However, the

addition of pyrroles to the aldehyde functionality was supported by the regression of this peak.

Solid-state ^{13}C NMR CP-MAS was also employed to BDP_CMP and PHTT_BDP along with the PHTT_DMP and PHTT_DMP_O intermediates (ESI Fig. S5-8). BDP_CMP presented primarily with aromatic carbons between 142-128 ppm with a smaller signal at 155 which was attributed to the C=N bonds. A signal at 12.5 ppm was also seen, indicating the presence of CH_3 groups. Data for PHTT_BDP and the intermediates was difficult to differentiate, as much of the structures distinctive functional groups are not affected throughout the synthesis. Each showed grouping of broad signals in the 110 – 150 ppm range which can be attributed to large quantity of aromatic carbons in all of these materials. However, the appearance of signals at 11.3, 15.22 and 14.2 ppm for PHTT_DMP, PHTT_DMP_O and PHTT_BDP, respectively, indicates the presence of CH_3 groups found on the dimethylpyrrole groups. The disappearance of the aldehyde signal also indicates the pyrrole groups have replaced this functional group, thus confirming the addition of dimethylpyrrole to PHTT_CHO was successful.

Physical and Thermal Analysis

Considerable porosity of the BODIPY-based and intermediate polymers was seen in both N_2 sorption (at 77 K, ESI Fig. S18-25) and CO_2 sorption (at 273 K, ESI Fig. S26-33) experiments. Typical type-I N_2 adsorption isotherms were observed, with BET measurements showing relatively high surface areas of 769 $m^2\ g^{-1}$ for BDP_CMP and 484 $m^2\ g^{-1}$ for PHTT_BDP, which is in line with most reported CMPs [9]. QSDFT analysis on pore size distribution and pore volume indicated for BDP_CMP an average pore width of 0.545 nm and pore volume of 0.563 $cm^3\ g^{-1}$ and for PHTT_CMP an average pore width of 1.096 nm and pore volume of 0.523 $cm^3\ g^{-1}$. Interestingly, an increase in pore volume was observed from 0.374 $cm^3\ g^{-1}$ for PHTT_CHO to 0.448 $cm^3\ g^{-1}$ for PHTT_DMP_O and finally to 0.523 $cm^3\ g^{-1}$ for PHTT_BDP. A summary of surface area and pore size/volume values for all synthesised polymers can be found in Table S2.

Since the BODIPY moiety was grafted onto PHTT_CHO post-synthetically, it is worth noting the decrease in surface area from 686 $m^2\ g^{-1}$ for the aldehyde-equipped precursor to 484 $m^2\ g^{-1}$ [13]. This is not surprising given that BODIPY is a bulky molecule that contributes to the decrease in surface area and as expected is also observed in the intermediate polymers. Nevertheless, both materials present high surface areas and

we have previously demonstrated the importance of surface area in photocatalytic processes [11]. In general, as surface area of the photocatalyst increases, the interface between the polymeric material and the medium also increases, thus resulting in greater photocatalytic efficiencies. Both BODIPY-based CMPs, in this instance, fulfil the requirements for an efficient photosensitiser for the production of $^1O_2$.

TGA for all products was also performed. TGA for BDP_CMP (ESI Fig. S14) showed good thermal stability up to 300 °C and with 40% weight percentage remaining at 950 °C. TGA measurements of PHTT_BDP and its intermediates (ESI Fig. S15-17) also showed high thermal stability up to 300 °C. When compared to the PHTT_CHO starting material [13], decreased thermal stability at higher temperatures is observed in the intermediate products while the final PHTT_BDP product regains some of this stability. When comparing to BDP_CMP, at 950 °C only 20% weight percent of the product remained, exhibiting PHTT_BDP as the less stable of the two BODIPY-based polymers at elevated temperatures.

SEM and TEM images (ESI Fig. S34-41) established the target polymers as highly textured, amorphous surfaces, indicating the potential for high surface areas. EDX analysis (ESI Fig. S42-45) demonstrates the primary difference between the two BODIPY-based polymers and their respective synthetic methods. While the Pd catalysed Suzuki cross-coupling reaction presents with minute traces of Pd metal (0.94 wt.%) remaining within the polymer matrix, the metal-free synthetic procedure clearly shows no presence of trace metal species.

Heterogeneous Photosensitisation at 530 nm

Using the BODIPY-based CMPs as heterogeneous photosensitisers, $^1O_2$ production was carried out in a commercial photochemical flow reactor equipped with an LED module with narrow emission at 530 nm (easy-Photochem from Vapourtec, Fig. S2) as described above. The setup used is illustrated in the schematic diagram in Fig. 2.

The progress of the Diels-Alder reaction (Scheme 3) was followed by ^{1}H NMR spectroscopy, and the conversion calculated from the ratio of peaks assigned to the starting material (α-terpinene) and the product (ascaridole) (ESI Fig. S3). This Alder-ene reaction was chosen as it is well-established that α-terpinene is extremely susceptible to

photosensitised $^1O_2$ oxidation while being rather stable against other oxidants such as ozone (O_3), hydrogen peroxide (H_2O_2) and hydroxyl radical ($OH^{\bullet}$) [47, 48].

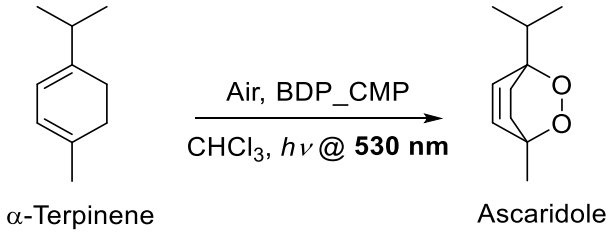

Scheme 3 Synthesis of ascaridole from *α*-terpinene *via* the photosensitisation of $^1O_2$ under green light irradiation.

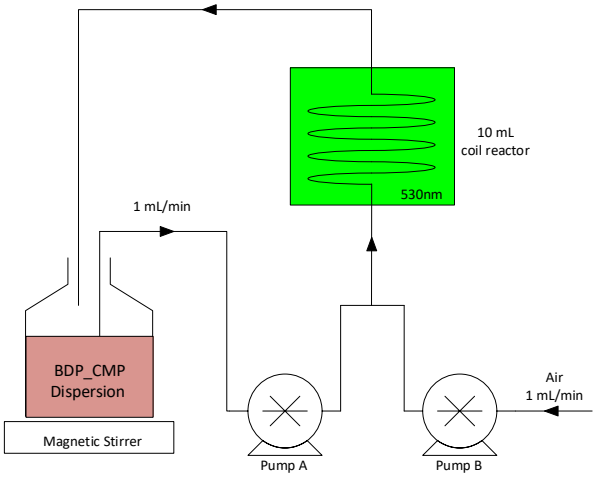

Fig. 2 Schematic representation of the experimental set-up using the easy-Photochem flow reactor from Vapourtec.

After a 1 h period, both the BDP_CMP and PHTT_BDP polymers were able to fully convert (>99%) *α*-terpinene into ascaridole in chloroform. This confirms that both materials can act as photosensitisers for the production of $^1O_2$. In order to further verify the photostability of the BODIPY-based CMPs and using the same conditions as described above (of light and air), we cycled in the absence of *α*-terpinene a new dispersion for 5 hours after which *α*-terpinene (136 mg, 1 mmol) was added. The dispersion was then cycled through the photochemical reactor for another 60 min. Samples were taken every 10 min and the conversions were calculated and plotted (Fig. 3). The tabulated values can be found in the ESI Table S1.

BDP_CMP shows enhanced photostability when compared to PHTT_BDP. This may be attributed to the fact that within BDP_CMP the BODIPY moiety is an integral

part of the backbone of the polymer repeat unit whereas PHTT_BDP has the BODIPY grafted onto the polymer backbone without benzene ring attached to it. This may contribute to an enhanced photobleaching of the BODIPY core. Nevertheless, and given that $^1O_2$ was produced during the initial 5 hour-experiment, we also demonstrate that the BDP_CMP polymer is not affected by this powerful oxidant whereas for PHTT_BDP we observed a loss of 10% in its photoactivity. Slight deviations to the initial results can be attributed to experimental error associated to ^{1}H NMR integrations and/or due to the fact that more air was dissolved in the latter experiment since it was aerated for 5 consecutive hours.

The photochemical reaction between $^1O_2$ and the substrate, in this case *α*-terpinene, is essentially a second-order reaction, where the rate of the reaction is dependent on the concentration of both reactants. However, most studies conducting these photochemical reactions do so under batch conditions where the concentration of the substrate is much greater than the concentration of $^1O_2$. Therefore, the kinetics of reactions between $^1O_2$ and the substrate can be simplified by the pseudo-first-order model [49-51]. This model is expressed as Eq. (2):

$$-\frac{dC}{dt} = kC \qquad (2)$$

where C is the concentration of substrate (mM or mg/L), t is the reaction time (h), and k is the pseudo-first-order rate constant (h^{-1}). If the initial concentration of substrate is C_0, Eq. (2) can be integrated as follows:

$$\ln C - \ln C_0 = -kt \qquad (3)$$

Eq. (3) can be further presented in exponential form as follows:

$$\frac{C}{C_0} = e^{-kt} \qquad (4)$$

The kinetics of *α*-terpinene conversion were fitted to the pseudo-first-order model by non-linear regression of concentration versus time data for the 6 h experiments (Fig. 3). Results show that the conversion of *α*-terpinene generally followed this model.

However, for the BDP_CMP, conversion near the 60 min mark was greater than expected based on the pseudo-first-order model. This may be explained by the continuous addition of air (and therefore oxygen) being supplied to the flow reactor, leading to a continuous generation of $^1O_2$. At this point in the reaction, the concentration of $^1O_2$ is much greater than that of *α*-terpinene, hereby not fulfilling the pseudo-first-order model any longer. Therefore, with actual conversion higher than that of the model, a major advantage is highlighted of the continuous flow reaction over the batch method.

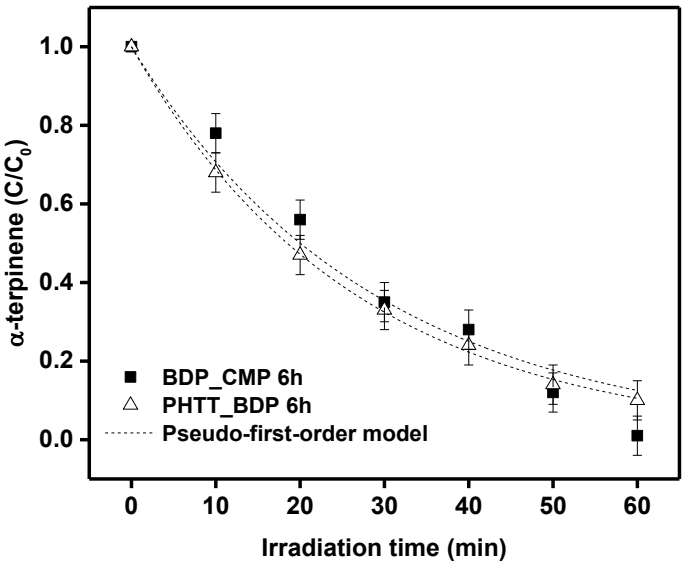

Fig. 3 Conversion of *α*-terpinene to ascaridole *via* BDP_CMP and PHTT_BDP in chloroform after 6h irradiation at 530 nm. Curves represent non-linear regression fits to the pseudo-first-order model. Error bars indicate potential error in ^1H NMR integration values.

Controls and Validation of BODIPY

A control experiment was performed under similar conditions using visible light at 420 nm as the source of photons. After 90 minutes, only 9% conversion of *α*-terpinene into ascaridole was observed, demonstrating the essential need for a light source at 530 nm, which is more suitable for application in photochemical reactions where reagents and/or products are susceptible to photodecomposition at more energetic wavelengths.

Validation of the BODIPY core as the photoactive component within these polymers was performed by employing the synthesised BDP_Ph monomer and testing

under the same conditions as the polymeric counterparts. After both 1 hour and 6 hours, full conversion of *α*-terpinene into ascaridole was observed with no apparent degradation of the monomer, demonstrating the BODIPY core as the essential photoactive component.

To ensure the post modification of PHTT_CHO to PHTT_BDP was required to perform as a photosensitiser at 530 nm, all intermediates of PHTT_BDP were isolated and employed under the same experimental conditions. Table 1 shows the intermediate material conversion values after 1h and how they compare to the other BODIPY-containing materials synthesised. Only a 77% conversion of α-terpinene into ascaridole was observed for the PHTT_DMP and PHTT_DMP_O intermediates while PHTT_BDP showed 100% conversion. While the addition of pyrrole groups to PHTT_CHO demonstrated good photoactivity, this is not surprising as this modification resulted in an increased absorbance at 530 nm. Despite this, only the PHTT_BDP polymer was able to achieve full conversion after 60 minutes thereby validating the addition of the BODIPY core to PHTT_CHO.

Photosensitisation Reactions in Different Solvents

To verify the versatility of the BODIPY-based CMPs in the production of $^1O_2$, different solvents were tested with the same experimental set-up. Life-time of $^1O_2$ varies considerably in different solvents and it is not surprising that some solvents are in effect better than others to perform $^1O_2$ reactions [47]. Nevertheless, and due to different solvation requirements for given substrates, having a wide range of solvents in which $^1O_2$ can be produced heterogeneously further validates the BODIPY-based CMPs as universal $^1O_2$ photosensitisers in a variety of organic transformations. Commonly used organic solvents that were tested in this study, along with the corresponding lifetime of $^1O_2$ in the respective solvents, are tabulated in Table 2. In general, as the lifetime of $^1O_2$ in a solvent decreases, the percent conversion of α-terpinene to ascaridole also declines. Ethanol presents as the one slight outlier, showing an enhanced conversion when comparing to the $^1O_2$ lifetime in this solvent. Water was also tested in the same conditions, however, due to the hydrophobicity of both CMPs, a uniform dispersion was not achievable and polymer aggregates were observed, which invariably led to the blockage of the flow reactor. Since water is a “green” solvent, two other solvents under the same classification, dimethylcarbonate (DMC) and 2-methyltetrahydrofuran (2-MeTHF) were also tested.

These exhibited comparable results to those of the commonly used organic solvents, demonstrating their potential to replace more environmentally harmful solvent systems.

Table 1 Conversion of α-terpinene into ascaridole in chloroform after 60 min employing different photosensitisers using the described photochemical reactor.

Photosensitiser	Conversion (%)[a]
PHTT_DMP	77
PHTT_DMP_O	77
PHTT_BDP	>99
BDP_Ph	>99
BDP_CMP	>99

[a] Percent conversion calculated from integrated ^{1}H NMR signals.

Table 2 Conversion of α-terpinene into ascaridole in chloroform after 60 min in different solvents using the described photochemical reactor.

Solvent	Conv. w/ BDP_CMP (%)[a]	Conv. w/ PHT_BDP (%)[a]	Lifetime (s)[52]
Chloroform	>99	>99	$2.5 \cdot 10^{-4}$
Acetonitrile	98	99	$7.5 \cdot 10^{-5}$
Ethanol	88	92	$1.2 \cdot 10^{-5}$
THF	87	92	$3 \cdot 10^{-5}$
Toluene	85	81[d]	$2.5 \cdot 10^{-5}$
Acetone	83	92	$1.2 \cdot 10^{-5}$
Green Solvents:			
2-Methyl THF	93	81	-[e]
DMC[b]	92	91	-[e]
Water[c]	-	-	$4.2 \cdot 10^{-6}$

[a] Percent conversion calculated from integrated ^{1}H NMR signals. [b] Dimethylcarbonate. [c] Aggregation of BDP_CMP and PHTT_BDP in water impeded the flow process. [d] PHTT_BDP dispersed poorly in toluene, impeding flow of the photosensitiser and therefore decreasing potential for $^1O_2$ generation. [e] No available data.

DMC and 2-MeTHF can be classed as green solvents as they are derived from renewable resources such as biomass rather than petroleum. DMC is attractive as an alternative solvent because it can be produced by the catalytic oxidative carbonylation of methanol, a method that avoids the use of toxic phosgene [53]. Furthermore, in 2009 DMC was made exempt under the definition of volatile organic compounds (VOCs) by the United States Environmental Protection Agency [54]. 2-MeTHF can be obtained from agricultural by-products and has been shown to give good results in a variety of synthetic process, having already been applied in industry [55].

Conclusions

In conclusion, BODIPY-based conjugated microporous polymers with high surface areas (484-769 m^2 g^{-1}) have been prepared by two distinct methods: direct assembly *via* a palladium-catalysed Suzuki-Miyaura cross-coupling reaction and a post-synthetic transformation of an aldehyde-equipped CMP host that overall was synthesised in the absence of metals. Employing a strategy whereby a strong electron acceptor (BODIPY) is coupled to weak electron donors (benzene), we were able to bathochromically shift the maximum absorbance of the CMPs towards a less energetic wavelength (530 nm) of the visible spectrum. The polymer products were then tested in a commercial photochemical flow reactor (Vapourtec Ltd) equipped with an LED module at 530 nm as the source of photons for the production of $^1O_2$ in a variety of solvents. $^1O_2$ production was monitored *via* ^{1}H NMR *via* the conversion of α-terpinene into ascaridole. Overall, the polymers demonstrated high photostability, especially with BDP_CMP showing no loss in photoactivity. These materials were easily recoverable *via* simple filtration and reused for further $^1O_2$ reactions. This work shows that conjugated porous polymers represent a new promising family of recyclable heterogeneous photocatalysts, with tuneable light absorption and which will significantly simplify the handling and purification of sensitive reactions, presenting itself as a more sustainable class of materials that potentially can be applied to different photocatalytic processes.

Moreover, the successful deployment of the above two synthetic schemes points to a number of broad-scope advantages. First, the robust aryl-aryl links of the BDP_CMP backbone provides outstanding compatibility and stability properties (e.g., compared with the more fragile and reactive alkyne-based link) for real-world applications. Such stability is well illustrated in the above extensive investigations on photochemical catalysis properties, wherein highly reactive species (e.g., $^1O_2$) is constantly being generated, and long-term stability of the host backbone is crucial for reusable, sustainable applications. Second, the post-synthetic approach for preparing PHTT_BDP involves no transition or heavy metal reagents at any step, and thus minimises health and environmental concerns. Moreover, the post-synthetic transformation of the aldehyde groups offers functional flexibility. For example and in future work, the dipyrrin precursor can chelate to metal centres other than the boron unit, and thereby imparting onto the CMP backbone the diverse and versatile reactivities of metal-dipyrrin complexes.

Acknowledgements

We would like to acknowledge Vapourtec Ltd for their valuable technical support. F. Vilela would like to thank Heriot-Watt University and the Royal Society for financial support (RG140169). M. Demleitner would like to thank the ERASMUS programme for financial support. Z. Xu would like to thank the Research Grants Council of HKSAR for financial support (City U 11303414).

References

[1] N. B. McKeown and P. M. Budd, *Chem. Soc. Rev*., 2006, **35**, 675-683.

[2] J. Germain, J. M. J. Frechet and F. Svec, *Small*, 2009, **5**, 1098-1111.

[3] R. S. Sprick, J.-X Jiang, B. Bonillo, S. Ren, T. Ratvijitvech, P. Guiglion, M. A. Zwijnenburg, D. J. Adams and A. I. Cooper, *J. Am. Chem. Soc*., 2015, **137**, 3265-3270.

[4] F. Vilela, K. Zhang and M. Antonietti, *Energy Environ. Sci*., 2012, **5**, 7819-7832.

[5] J.-X. Jiang, F. Su, A. Trewin, C. D. Wood, N. L. Campbell, H. Niu, C. Dickinson, A. Y. Ganin, M. J. Rosseinsky, Y. Z. Khimyak, and A. I. Cooper, *Angew. Chem., Int. Ed*., 2007, **46**, 8574-8578.

[6] J. X. Jiang, C. Wang, A. Laybourn, T. Hasell, R. Clowes, Y. Z. Khimyak, J. Xiao, S. J. Higgins, D. J. Adams and A. I. Cooper, *Angew. Chem., Int. Ed*., 2011, **50**, 1072-1075.

[7] J.-X. Jiang and A. Cooper, *Top. Curr. Chem.*, 2010, **293**, 1-33.

[8] X. Liu, S. A, Y. Zhang, X. Luo, H. Xia, H. Li and Y. Mu, *RSC Adv*., 2014, **4**, 6447-6453.

[9] Y. Xu, S. Jin, H. Xu, A. Nagai and D. Jiang, *Chem. Soc. Rev*., 2013, **42**, 8012-8031.

[10] J.-X. Jiang, Y. Li, X. Wu, J. Xiao, D. J. Adams and A. I. Cooper, *Macromolecules*, 2013, **46**, 8779-8783.

[11] K. Zhang, D. Kopetzki, P. H. Seeberger, M. Antonietti and F. Vilela, *Angew. Chem., Int. Ed.*, 2013, **52**, 1432-1436.

[12] J. Liu, J. M. Tobin, Z. Xu and F. Vilela, *Polym. Chem*., 2015, **6**, 7251-7255.

[13] J. Liu, J. Cui, F. Vilela, J. He, M. Zeller, A. D. Hunter and Z. Xu, *Chem. Commun*., 2015, **51**, 12197-12200.

[14] K. Zhang, Z. Vobecka, K. Tauer, M. Antonietti and F. Vilela, *Chem. Commun*., 2013, **49**, 11158-11160.

[15] H. Urakami, K. Zhang and F. Vilela, *Chem. Commun*., 2013, **49**, 2353-2355.

[16] G. Herzberg, *Molecular Spectra and Molecular Structure I: Spectra of Diatomic Molecules*; 2nd Ed. VonNostrand, New York, 1950.

[17] T. Nyokong and V. Ahsen, *Photosensitizers in Medicine, Environment and Security*; Springer, London, 2012.

[18] M. C. DeRosa and R. J. Crutchley, *Coord. Chem. Rev*., 2002, **233-234**, 351-371.

[19] E. L. Clennan, *Tetrahedron*, 2000, **56**, 9151-9179.

[20] J. Shen, R. Steinbach, J. M. Tobin, M. M. Nakata, M. Bower, M. R. S. McCoustra, H. Bridle, V. Arrighi and F. Vilela, *Appl. Catal. B*, 2016, **193**, 226-233.

[21] R. Bonnett, *Chem. Soc. Rev*., 1995, **24**, 19-33.

[22] S. O. McDonnell, M.J. Hall, L. T. Allen, A. Byrne, W. M. Gallagher and D. F. O'Shea, *J. Am. Chem. Soc*., 2005, **127**, 16360-16361.

[23] A. Loudet and K. Burgess, *Chem. Rev*., 2007, **107**, 4891-4932.

[24] G. Ulrich, R. Ziessel and A. Harriman, *New J. Chem*., 2007, **31**, 496-501.

[25] G. Ulrich, R. Ziessel and A. Harriman, *Angew. Chem., Int. Ed*., 2008, **47**, 1184-1201.

[26] Q. D. Zheng, G. X. Xu and P. N. Prasad, *Chem.-Eur. J*., 2008, **14**, 5812-5819.

[27] Y. Ikawa, S. Moriyama and H. Furuta, *Anal. Biochem*., 2008, **378**, 166-170.

[28] M. A. H. Alamiry, A. C. Benniston, G. Copley, K. J. Elliott, A. Harriman, B. Stewart and Y. G. Zhi, *Chem. Mater*., 2008, **20**, 4024-4032.

[29] O. Garcia, L. Garrido, R. Sastre, A. Costela and I. Garcia-Moreno, *Adv. Funct. Mater*., 2008, **18**, 2017-2025.

[30] A. Costela, I. Garcia-Moreno, M. Pintado-Sierra, M. Amat-Guerri, M. Liras, R. Sastre, F. L. Arbeloa, J. B. Prieto and I. L. Arbeloa, *J. Photochem. Photobiol*. *A*, 2008, **198**, 192-198.

[31] S. Mula, A. K. Ray, M. Banerjee, T. Chaudhuri, K. Dasgupta and S. Chattopadhyay*, J. Org. Chem*., 2008, **73**, 2146-2154.

[32] S. Erten-Ela, M. D. Yilmaz, B. Icli, B. Y. Dede, S. Icli and E. U. Akkaya, *Org. Lett*., 2008, **10**, 3299-3302.

[33] L. Bonardi, H. Kanaan, F. Camerel, P. Jolinat, P. Retailleau and R. Ziessel, *Adv. Funct. Mater*., 2008, **18**, 401-413.

[34] M. M. Sartin, F. Camerel, A. J. Ziessel and J. Bard, *J. Phys. Chem. C*, 2008, **112**, 10833-10841.

[35] S. G. Awuah and Y. You, *RSC Adv*., 2012, **2**, 11169-11183.

[36] Vapourtec, http://www.vapourtec.co.uk/, accessed August 2016.

[37] M. Ranger, D. Rondeau and M. Leclerc, *Macromolecules*, 1997, **30**, 7686-7691.

[38] P. V. Dau, K. K. Tanabe and S. M. Cohen, *Chem. Commun*., 2012, **48**, 9370-9372.

[39] A. Vazquez-Romero, N. Kielland, M. J. Arevalo, S. Preciado, R. J. Mellanby, Y. Feng, R. Lavilla and M. Vendrell, *J. Am. Chem. Soc*., 2013, **135**, 16018-16021.

[40] L. Wang, J-W. Wang, A-j, Cui, X-X. Cai, Y. Wan, Q. Chen, M-Y. He and W. Zhang, *RSC Adv*., 2013, **3**, 9219-9222.

[41] Y. Chen, J. Zhao, H. Guo and L. Xie, *J. Org. Chem*., 2012, **77**, 2192-2206.

[42] M. Liras, M. Iglesias and F. Sanchez, *Macromolecules*, 2016, **49**, 1666-1673.

[43] M. D. Yilmaz, O. A. Bozdemir and E. U. Akkaya, Org. Lett., 2006, 8, 2871-2873.

[44] R. Ziessel, C. Goze, G. Ulrich, M. Cesario, P. Retailleau, A. Harriman and J. P. Rostron, *Chem.–Eur. J*., 2005, **11**, 7366-7378.

[45] J. C. Forgie, P. J. Skabara, I. Stibor, F. Vilela and Z. Vobecka, *Chem. Mater*., 2009, **21**, 1784-1786.

[46] D. C.-Lacalle, C. T. Howells, S. Gambino, F. Vilela, Z. Vobecka, N. J. Findlay, A. R. Inigo, S. A. J. Thomson, P. J. Skabara and I. D. W. Samuel, *J. Mater. Chem*., 2012, **22**, 14119-14126.

[47] S. Ogawa, S. Fukui, Y. Hanasaki, K. Asano, H. Uegaki, F. Sumiko and S. Ryosuke, *Chemosphere*, 1991, **22**, 1211-1225.

[48] D. Choi and M. Jung, *Food Sci. Biotechnol*., 2013, **22**, 249-256.

[49] H. Kim, W. Kim, Y. Mackeyev, G.-S. Lee, H.-J. Kim, T. Tachikawa, S. Hong, S. Lee, J. Kim, L. J. Wilson, T. Majima, P. J. J. Alvarez, W. Choi and J. Lee, *Environ. Sci. Technol*., 2012, **46**, 9606–9613.

[50] T. Zhang, Y. Ding and H. Tang, *Chem. Eng. J*., 2015, **264**, 681–689.

[51] J. Lee, Y. Mackeyev, M. Cho, L. J. Wilson, J.-H. Kim and P. J. J. Alvarez, *Environ. Sci. Technol*., 2010, **44**, 9488–9495.

[52] F. Wilkinson, W. P. Helman and A. B. Ross, *J. Phys. Chem. Ref. Data*, 1995, **24**, 663-1021.

[53] L. Rossi, S. Grego, A. E. Rosamilia, F. Arico and P. Tundo, *Green Chemical Reactions*, Springer Link, 2008, pp. 213-232.

[54] US-EPA, https://www3.epa.gov/ttn/oarpg/t1pfpr.html, Accessed August 2016.

[55] V. Antonucci, J. Coleman, J. B. Ferry, N. Johnson, M. Mathe, J. P. Scott and J. Xu, *Org. Process Res. Dev*., 2011, **15**, 939-941.

Supporting Information

Experimental Section

Synthesis of Tetrakis(triphenylphosphine) palladium(0) Catalyst

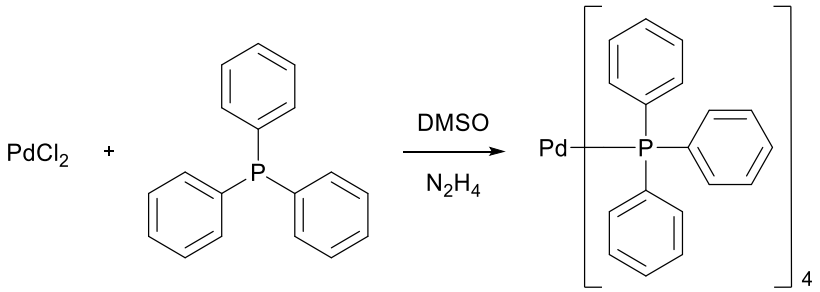

Tetrakis(triphenylphosphine) palladium(0) ($Pd[(C_6H_5)_3P]_4$) was prepared *via* modified literature methods [1] by dissolving palladium chloride (350 mg, 2 mmol) and triphenylphosphine (2.62 g, 10 mmol) in 25 mL of anhydrous dimethyl sulphoxide. The mixture was stirred and heated to 140-160 °C under nitrogen until an orange solution was formed and stirring continued for 15 minutes thereafter. Hydrazine hydrate (0.39 mL, 8 mmol) was charged quickly into the orange solution and taken from heat and left to cool to room temperature. During this time, yellow crystals formed and were then filtered through a sintered glass adaptor under nitrogen. The crystals were washed with dry methanol and dry diethyl ether and left to dry under nitrogen. The product was used without further purification.

Synthesis of 1,3,5-tris(4,4,5,5-tetramethyl-1,3,2-dioxaborolan-2-yl)benzene.

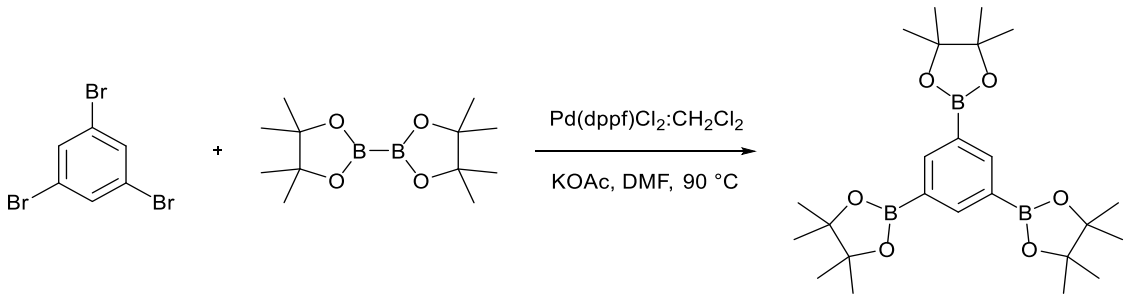

1,3,5 Tris(4,4,5,5-tetramethyl-1,3,2-dioxaborolan-2-yl)benzene was synthesised *via* literature methods [2] by dissolving 1,3,5-Tribromobenzene (3.0 g, 9.5 mmol), bis(pinacolato)diboron (7.7 g, 30.4 mmol), 1,1'-bis(diphenylphosphino) ferrocenepalladium (II) dichloride dichloromethane (0.24 g, 0.29 mmol), and KOAc (5.6 g, 57 mmol) in Dimethylformamide (DMF) (30 mL) in a 2-necked flask. The mixture was heated to 90 ºC under N_2 and left to react for 16 h. Deionised water (200 mL) was

added to the cooled mixture resulting in a dark brown precipitate. Upon filtration, the product was obtained as a brown solid. Product was recrystallised from minimal MeOH to give a light brown solid. Product was dried *in vaco*. ^{1}H NMR was used to compare the product with literature and deemed to be pure [2]. (Dried yield: 2.9 g; 67%)

Synthesis of tetramethylphenyl-BODIPY and dibromotetramethylphenyl-BODIPY.

1,3,5,7-Tetramethyl-8-phenyl-4,4-difluoro-4-bora-3a,4a-diaza-s-indacene (**1,3,5,7-tetramethyl-8-phenyl-BODIPY**) and 2,6-dibromo-1,3,5,7-tetramethyl-8-phenyl-4,4-difluoro-4-bora-3a,4a-diaza-s-indacene (**2,6-dibromo-1,3,5,7-tetramethyl-8-phenyl-BODIPY**) were synthesised using literature methods [3, 4].

Step 1

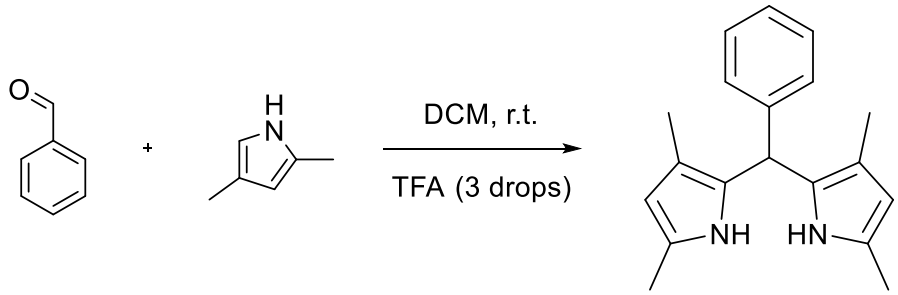

2,4-Dimethylpyrrole (1.05 g, 11 mmol) and benzaldehyde (0.58g, 5.5 mmol) were dissolved in 50 mL dry dichloromethane (DCM) under a nitrogen atmosphere. Three drops of trifluoroacetic acid (TFA) was added to the solution and the reaction mixture was stirred at room temperature overnight. The crude product was used in the following step without purification.

Step 2

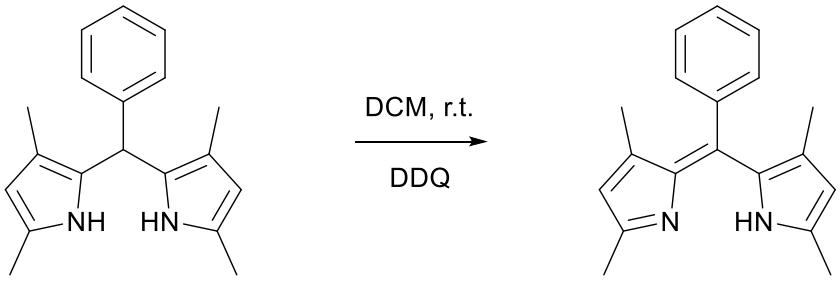

After this time, 2,3-dichloro-5,6-dicyano-1,4-benzoquinone (DDQ) (5 mmol, 1.14 g) was dissolved in approximately 75 mL of DCM and added slowly by pipette to the reaction mixture. This mixture was then left to stir at room temperature under a nitrogen atmosphere for 15 minutes. The crude product was used in the following step without purification.

Step 3

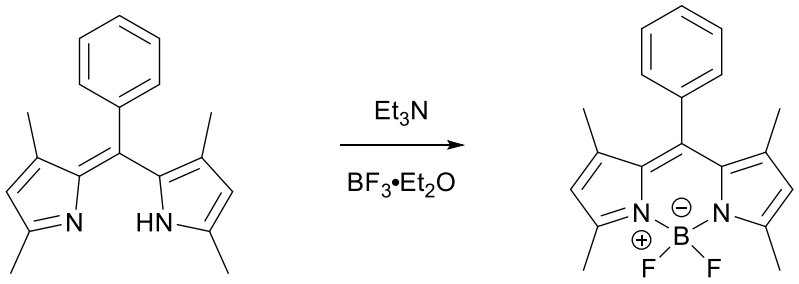

Triethylamine (10 mL, excess) and boron trifluoride diethyl etherate (BF_3OEt_2) (10 mL, excess) were then added to the reaction and left to stir at room temperature under a nitrogen atmosphere for 3 hours. The solution was then diluted in 100 mL of dichloromethane and washed with deionised water three times. The organic phase was dried over $MgSO_4$ and filtered. The crude product was purified through silica gel column chromatography with a DCM : hexane (1:1) eluent to yield a red-green solid (420 mg, 24%). ^{1}H NMR was used to compare the product with literature and deemed to be pure [3].

Step 4

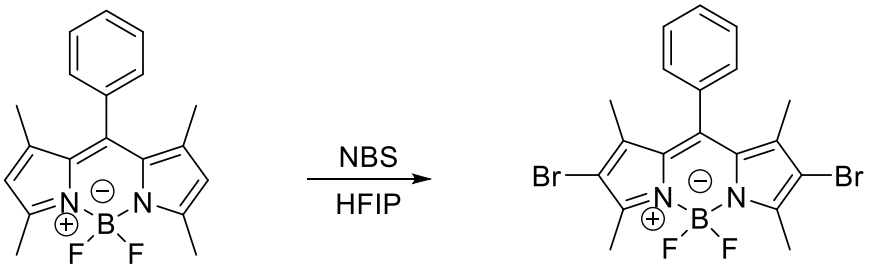

1,3,5,7-tetramethyl-8-phenyl-BODIPY

2,6-dibromo-1,3,5,7-tetramethyl-8-phenyl-BODIPY

A mixture of **1,3,5,7-tetramethyl-8-phenyl-BODIPY** (0.2 mmol, 64.8 mg) and *n*-bromosuccinimide (NBS) (0.48 mmol, 85.5 mg) in 2 mL of 1,1,1,3,3,3-hexafluoro-2-propanol (HFIP) was stirred at room temperature for 10 minutes. A colour change from

yellow/orange to dark red occurred and TLC was used to confirm reaction completion. The residue was extracted with 25 mL of DCM and washed with deionised water three times. The organic phase was dried over Na_2SO_4 and evaporated to give a crude product. The crude product was further purified using silica gel column chromatography with a DCM: hexane (1:1) eluent to afford a dark red solid product (76 mg, 85%). ^{1}H NMR was used to compare the product with literature and deemed to be pure [4].

Synthesis of PHTT_BDP and Proposed Intermediate Structures

Step 1

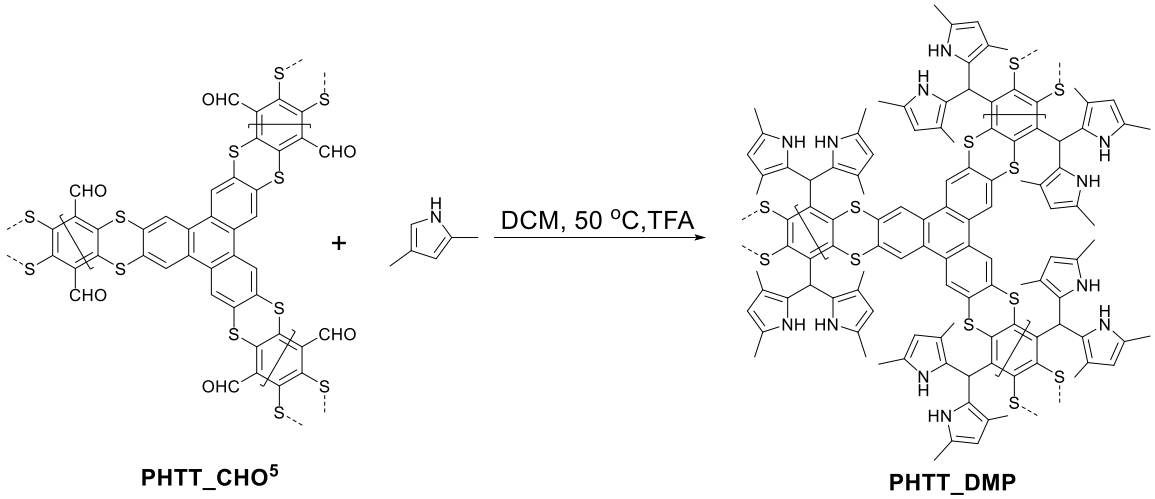

PHTT_CHO[5] **PHTT_DMP**

Step 2

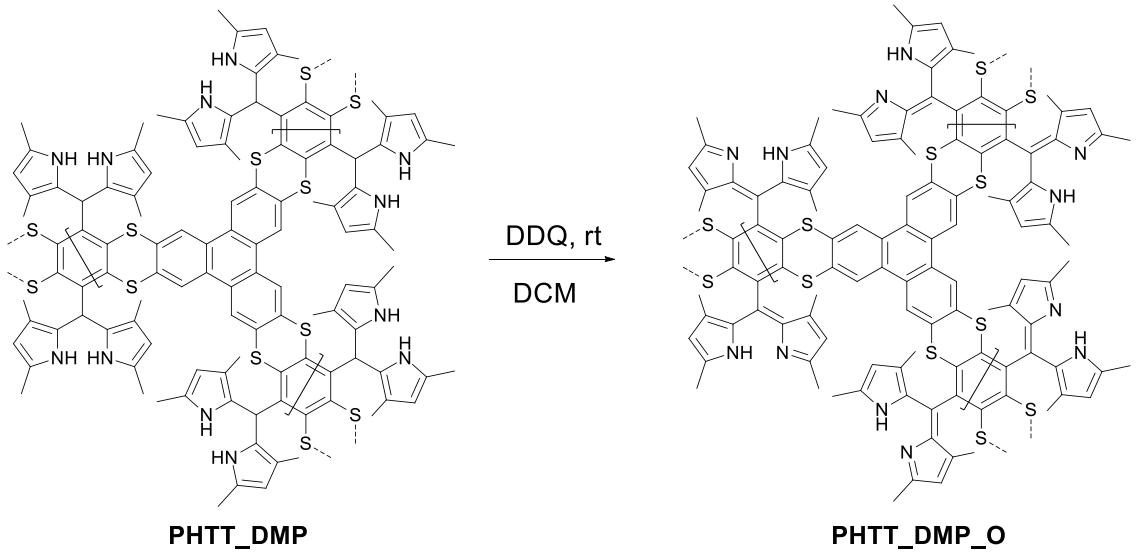

PHTT_DMP **PHTT_DMP_O**

Step 3

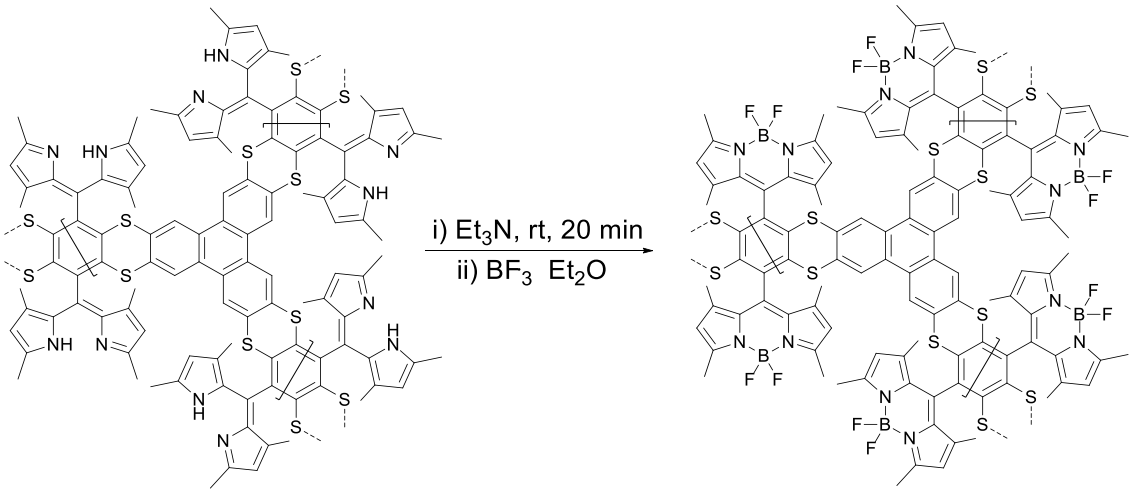

PHTT_DMP_O **PHTT_BDP**

Synthesis of 2,6-diphenyl-1,3,5,7-tetrametyl-8-phenyl-BODIPY.

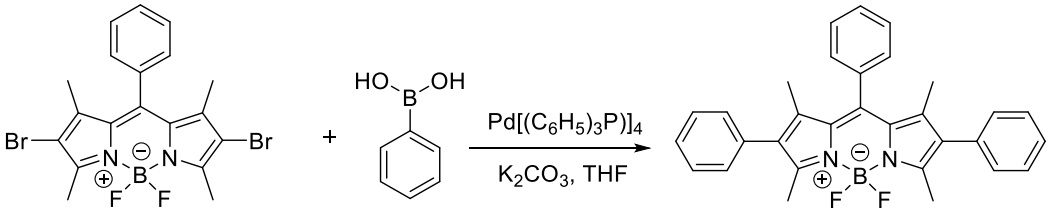

2,6-dibromo-1,3,5,7-tetramethyl-8-phenyl-BODIPY

2,6-diphenyl-1,3,5,7-tetramethyl-8-phenyl-BODIPY

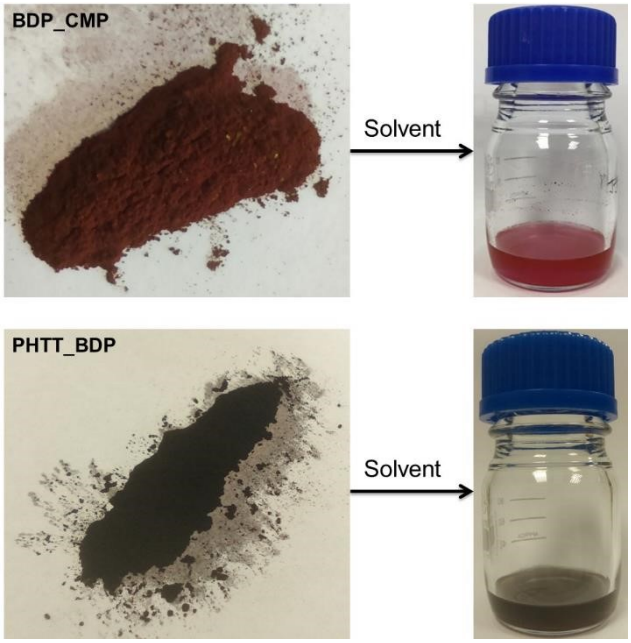

Fig. S1 BDP_CMP (top left) and **PHTT_BDP** (bottom left) as solids and as a dispersion in solvent (right).

Fig. S2 Easy-Photochem flow system from Vapourtec equipped with visible light LED module emitting light at 530nm.

Table S1 Conversion of *α*-terpinene to ascaridole *via* ^{1}H NMR over time with a flow rate of 1mL.min^{-1} in the easy-Photochem flow reactor from Vapourtec.

Time (min)	***BDP_CMP 1h Conv. (%)***	***BDP_CMP 6h Conv. (%)***	***PHTT_CMP 1h Conv. (%)***	***PHTT_CMP 6h Conv. (%)***
0	0	0	0	0
10	22	22	15	28
20	46	44	33	59
30	62	65	52	69
40	72	77	66	80
50	86	88	83	83
60	99	99	99	90

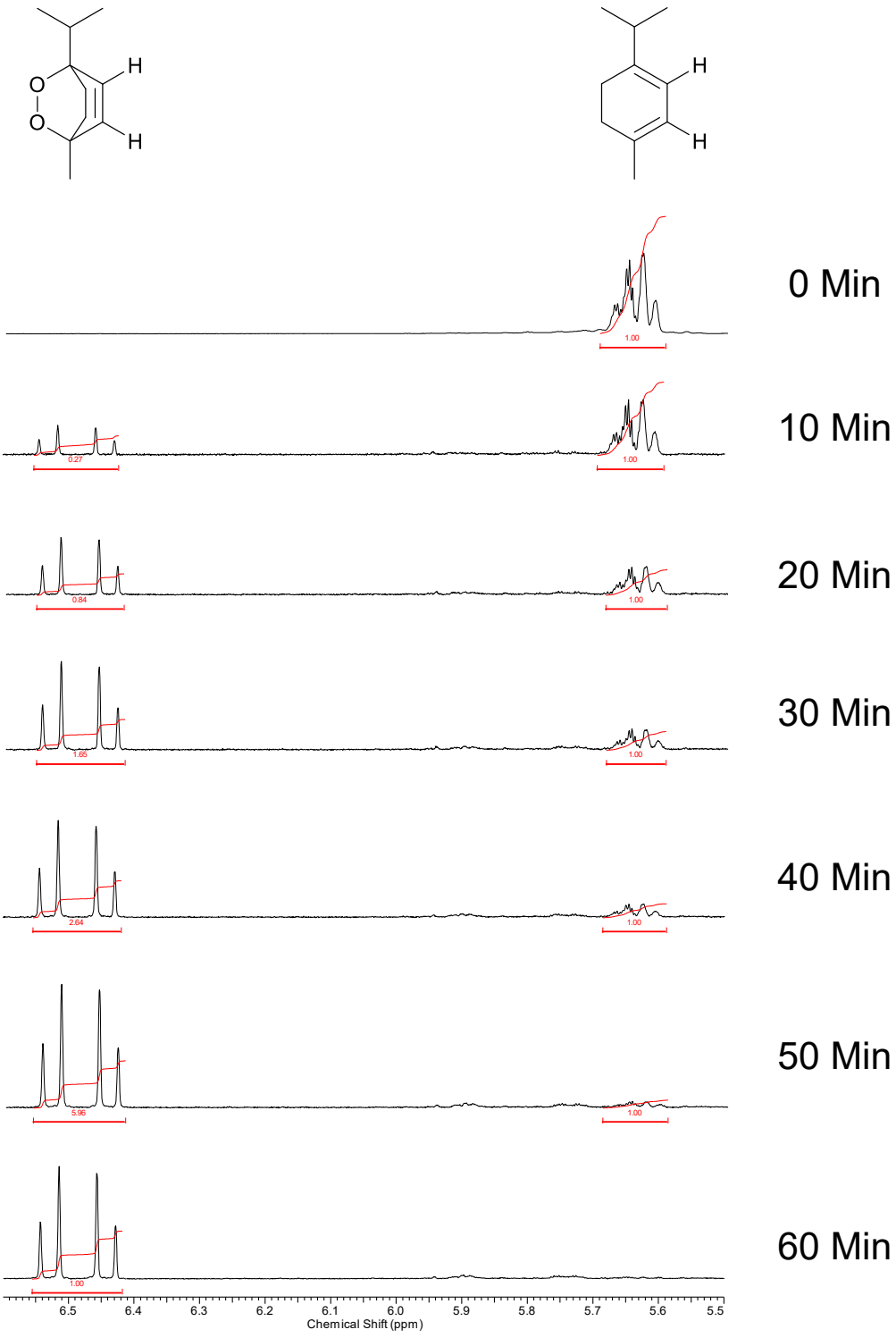

Fig. S3 Progress of the Alder-ene reaction in chloroform followed by ^{1}H NMR spectroscopy.

Spectroscopic Analysis

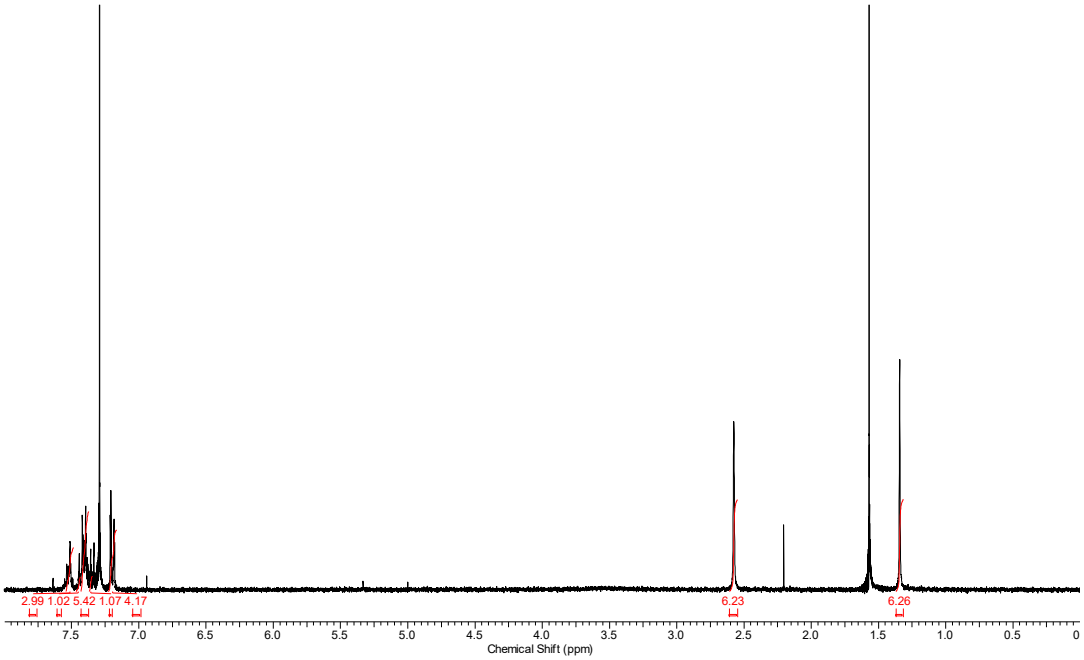

Fig. S4 ^{1}H NMR of 2,6-diphenyl-1,3,5,7-tetramethyl-8-phenyl-BODIPY(**BDP_Ph**).

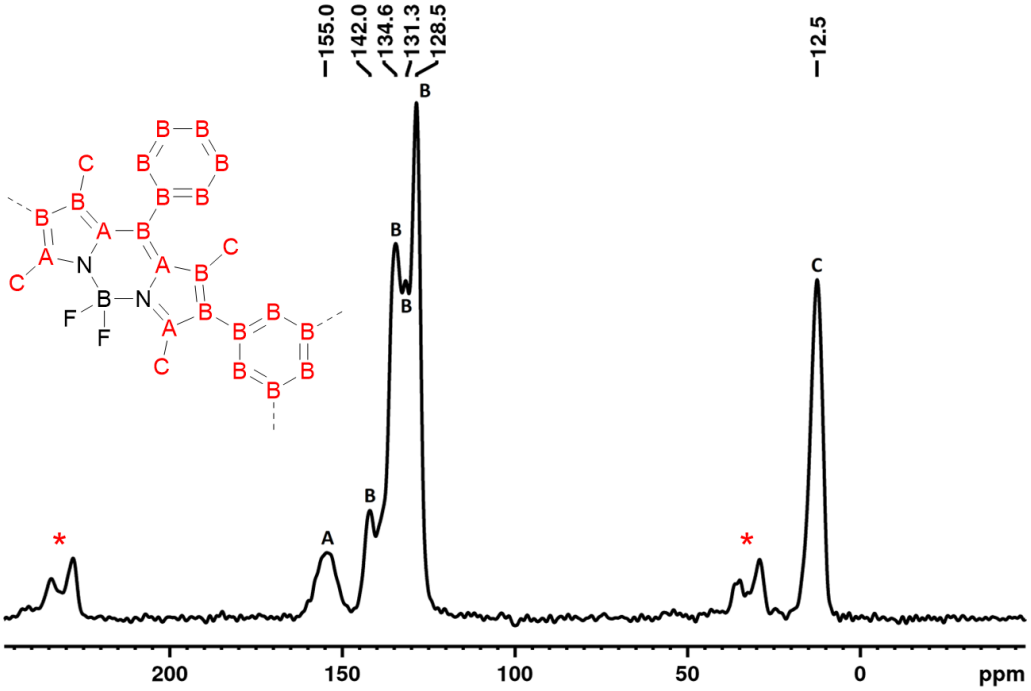

Fig. S5 Solid state ^{13}C NMR of **BDP_CMP** (δ155.0 (N-*C*), 142.0, 134.6, 131.3, 128.5 (other aromatic-*C*), 12.53 (methyl-*C*)). Peaks denoted by (*) indicate the presence of side bands.

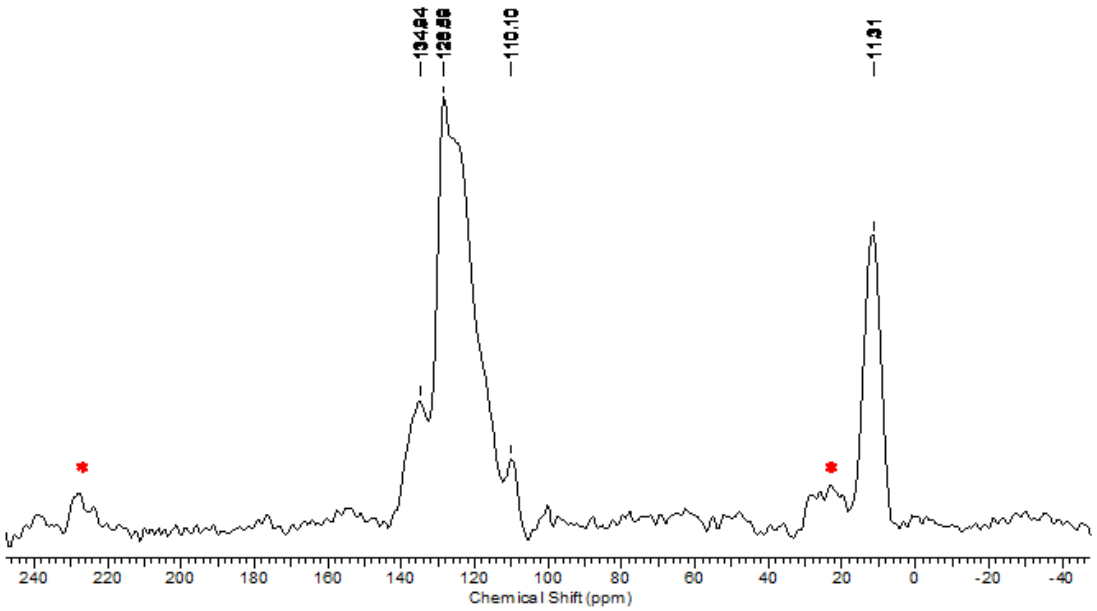

Fig. S6 Solid state ^{13}C NMR of **PHTT_DMP** (δ134.94, 128.59, 110.10, 11.31). Peaks denoted by (*) indicate the presence of side bands.

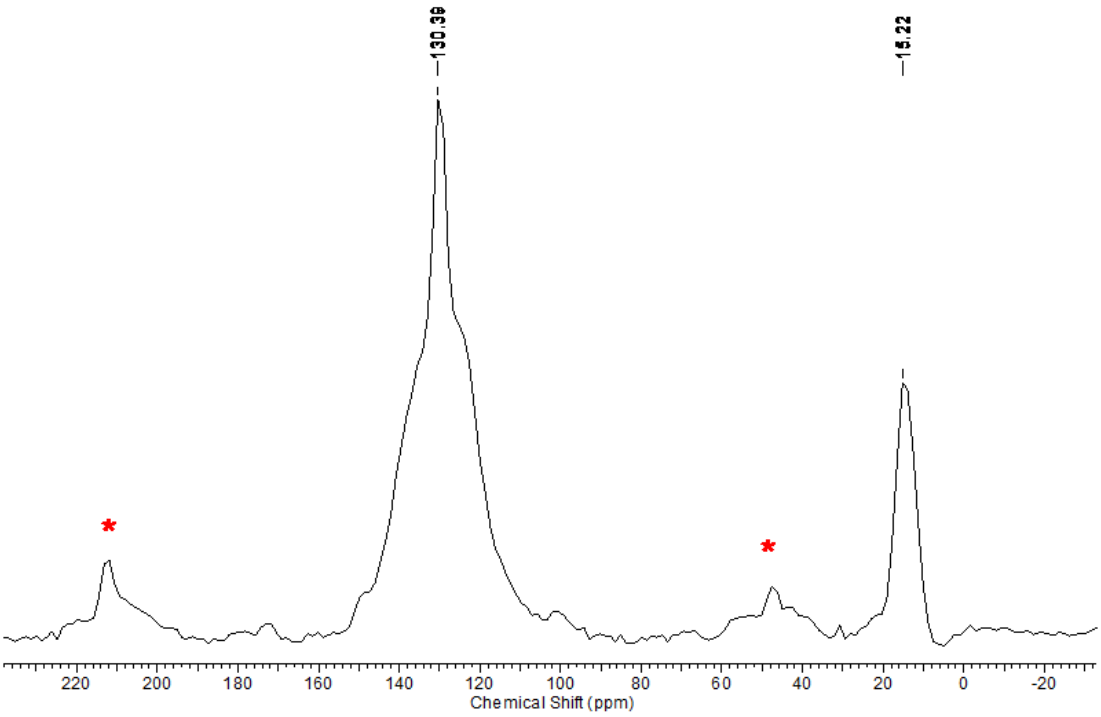

Fig. S7 Solid state ^{13}C NMR of **PHTT_DMP_O** (δ130.39, 15.22). Peaks denoted by (*) indicate the presence of side bands.

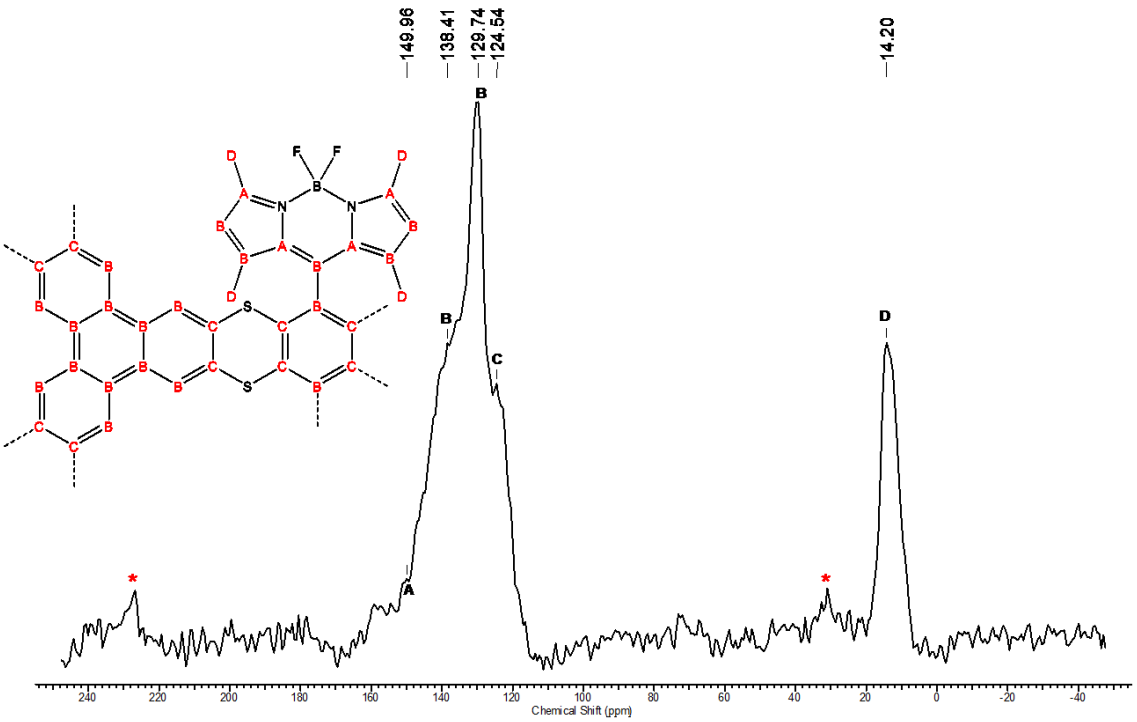

Fig. S8 Solid state ^{13}C NMR of **PHTT_BDP** (δ149.96, 138.41, 129.74 (aromatic-*C*), 124.54 (S-C), 14.20 (methyl-*C*)). Peaks denoted by (*) indicate the presence of side bands.

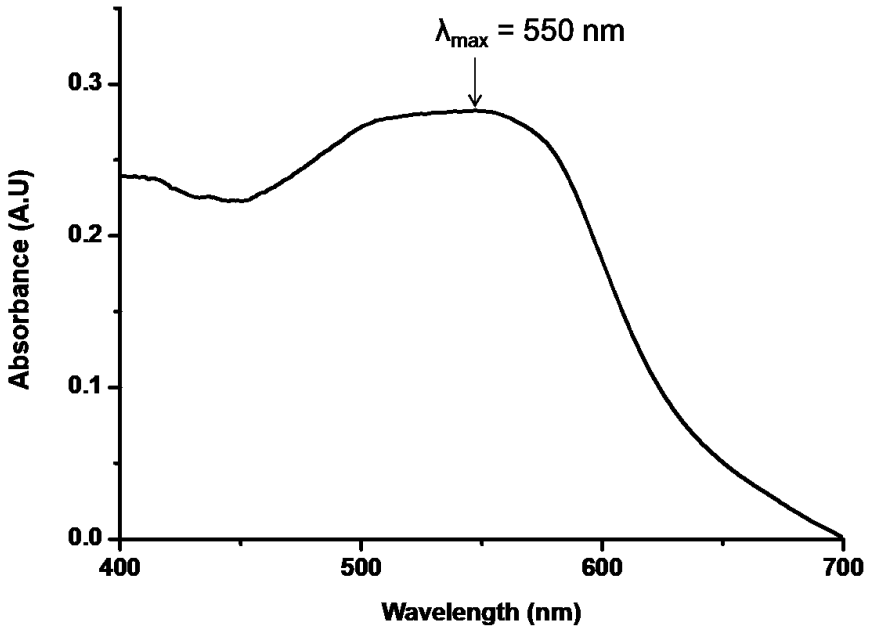

Fig. S9 Solid state UV-Vis spectrum of the **BDP_CMP** polymer with a λ_{max} = 550 nm and absorption edge ≈ 700 nm.

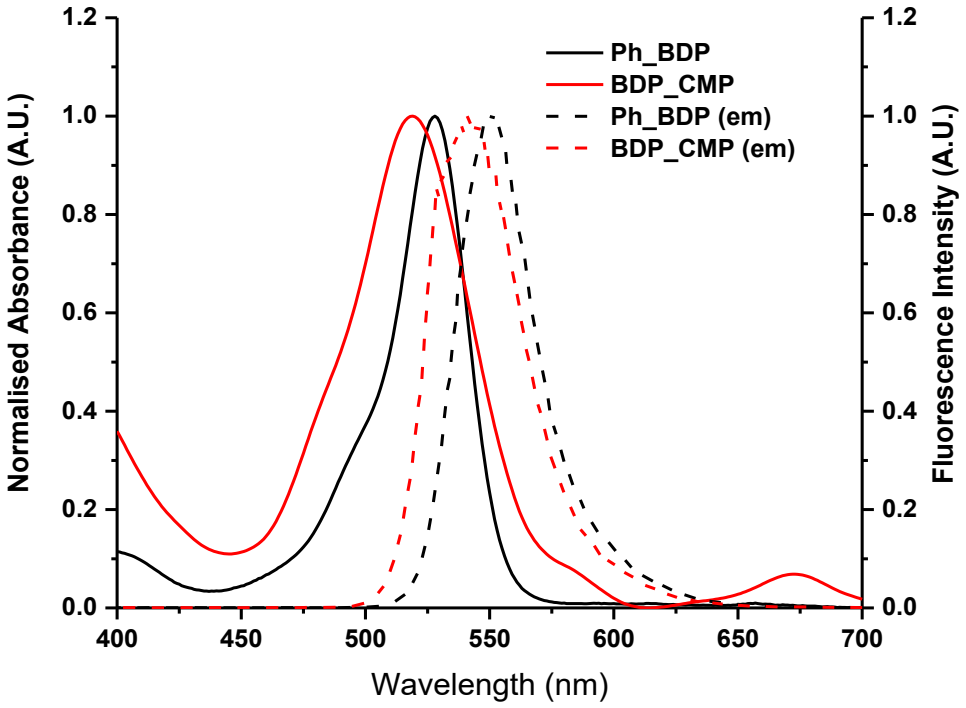

Fig. S10 UV-Vis (solid lines) and fluorescence (dashed lines) spectra of **Ph_BDP** and **BDP_CMP** with an excitation wavelength at 527 and 520 nm, respectively.

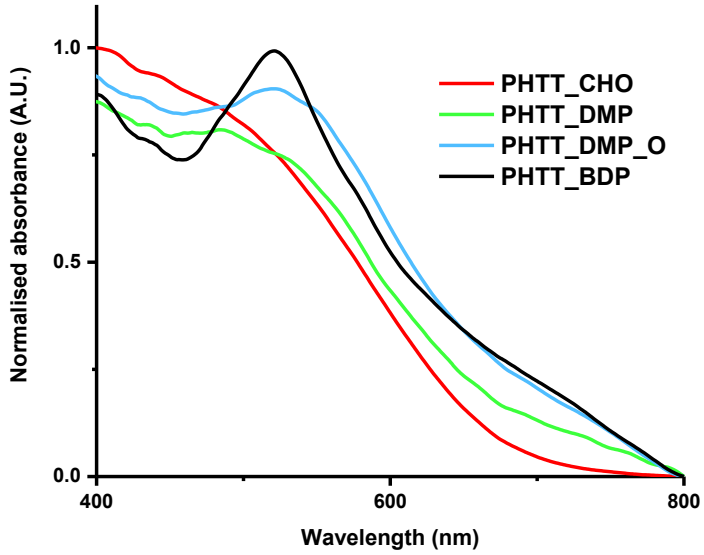

Fig. S11 Solid state UV-Vis spectrum of the **PHTT_CHO**, **PHTT_DMP**, **PHTT_DMP_O** and **PHTT_BDP** polymers. **PHTT_BDP** λ_{max} = 520 nm.

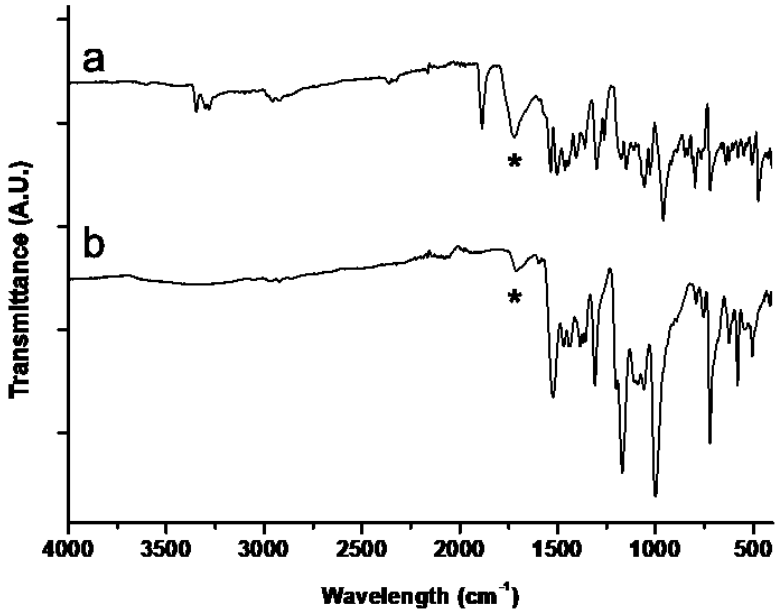

Fig. S12 FT-IR spectra of (a) 1,3,5,7-tetramethyl-8-phenyl-BODIPY and (b) **BDP_CMP**. The asterisked peak at ~1700 cm^{-1} is ascribed to the C=N bond.

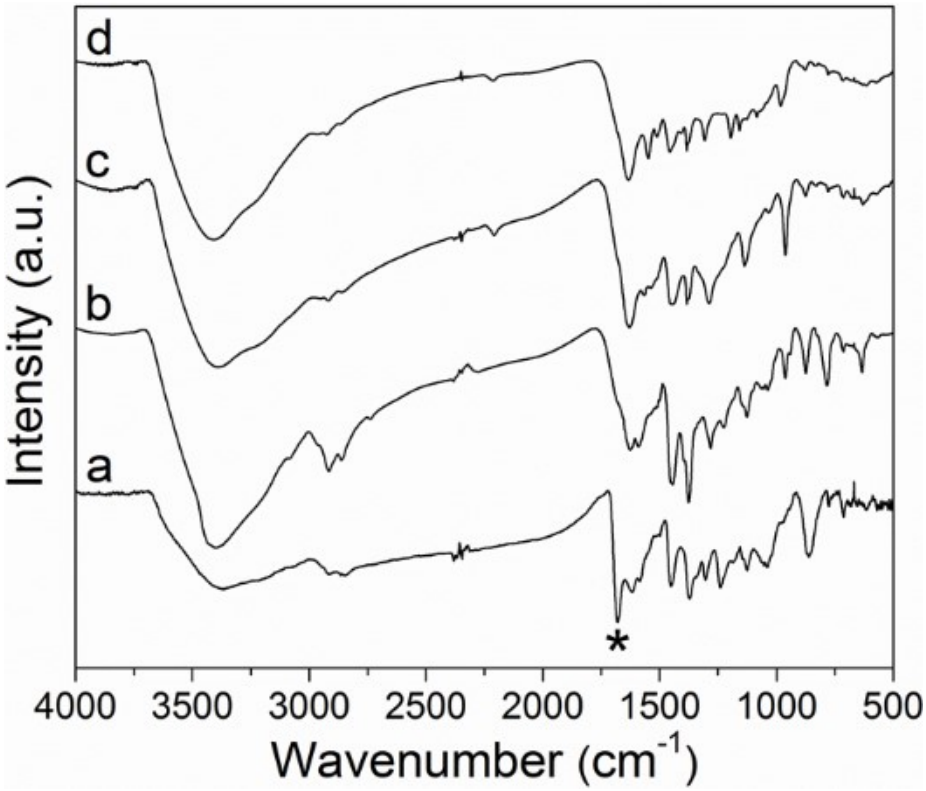

Fig. S13 FT-IR spectra of (a) a sample of **PHTT_CHO**, (b) a sample of **PHTT_DMP**, (c) a sample of **PHTT_DMP_O** and (d) a sample of **PHTT_BDP**. The asterisked peak is ascribed to the aldehyde group.

Physical and Thermal Analysis

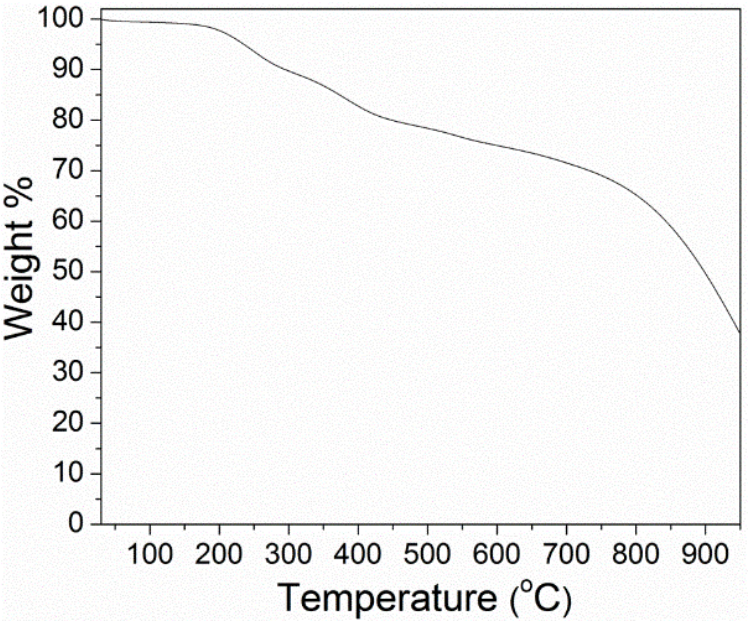

Fig. S14 Thermogravimetric analysis (TGA) of a sample of **BDP_CMP**.

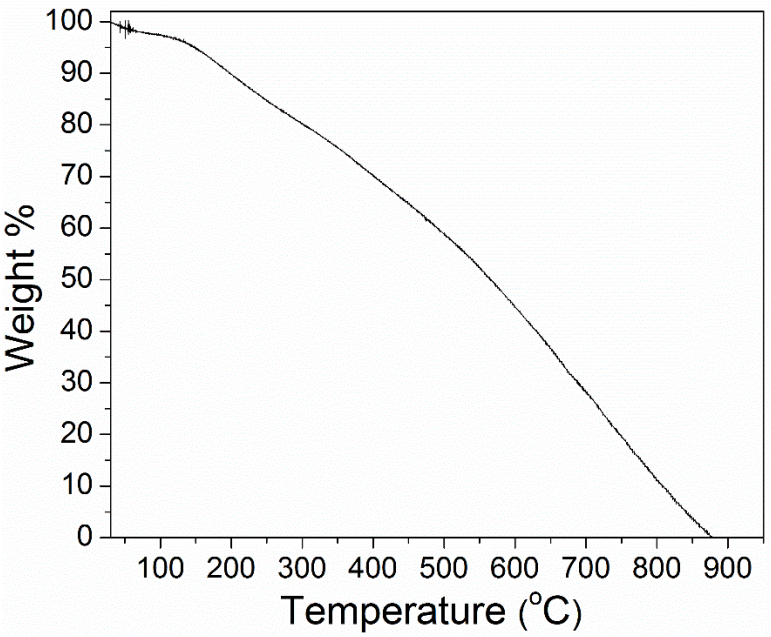

Fig. S15 Thermogravimetric analysis (TGA) of a sample of **PHTT_DMP**.

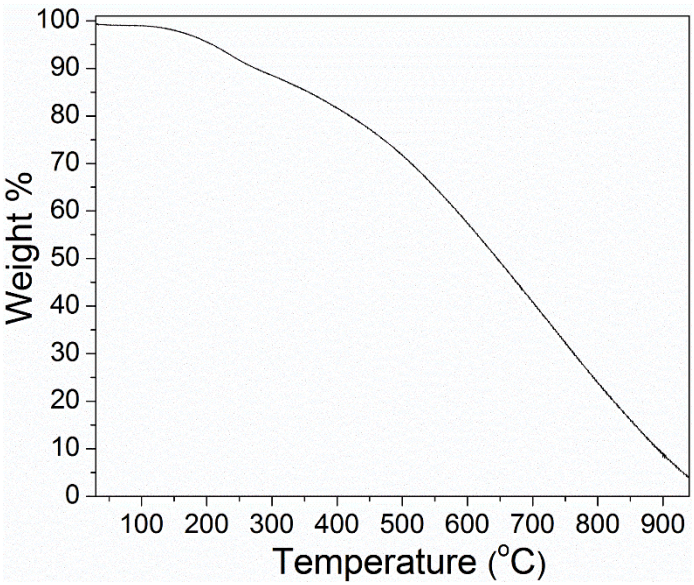

Fig. S16 Thermogravimetric analysis (TGA) of a sample of **PHTT_DMP_O**.

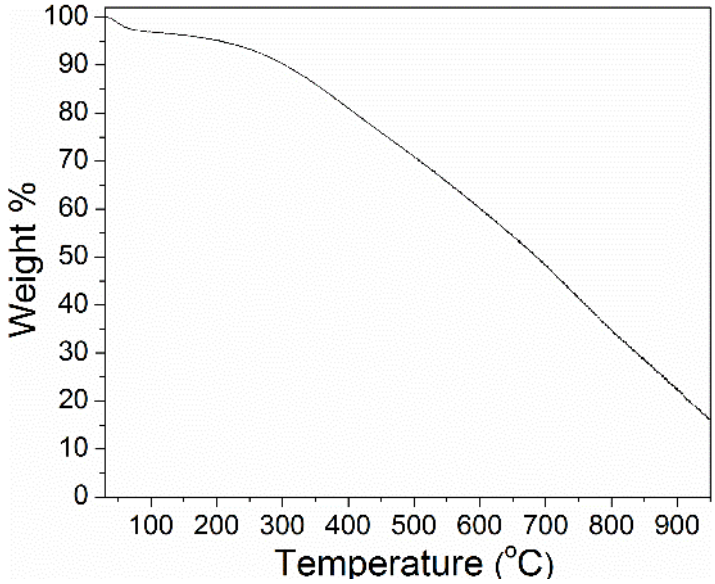

Fig. S17 Thermogravimetric analysis (TGA) of a sample of **PHTT_BDP**.

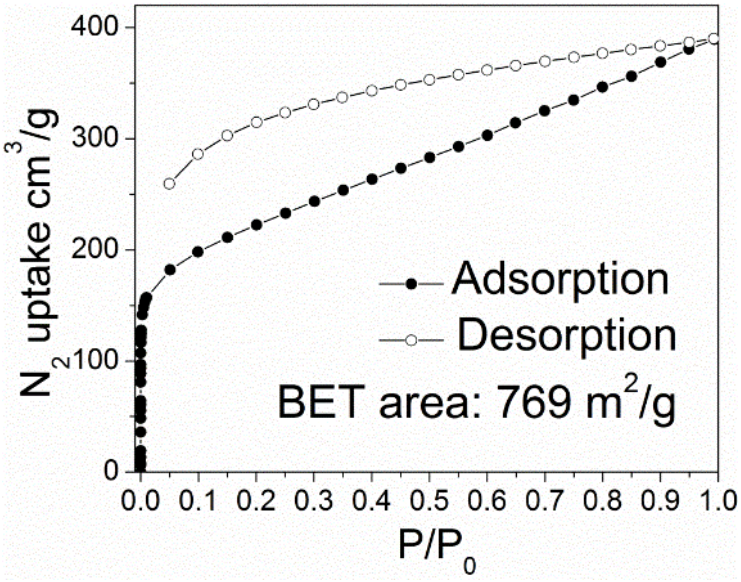

Fig. S18 N_2 sorption isotherm at 77 K for an activated **BDP_CMP** sample

.

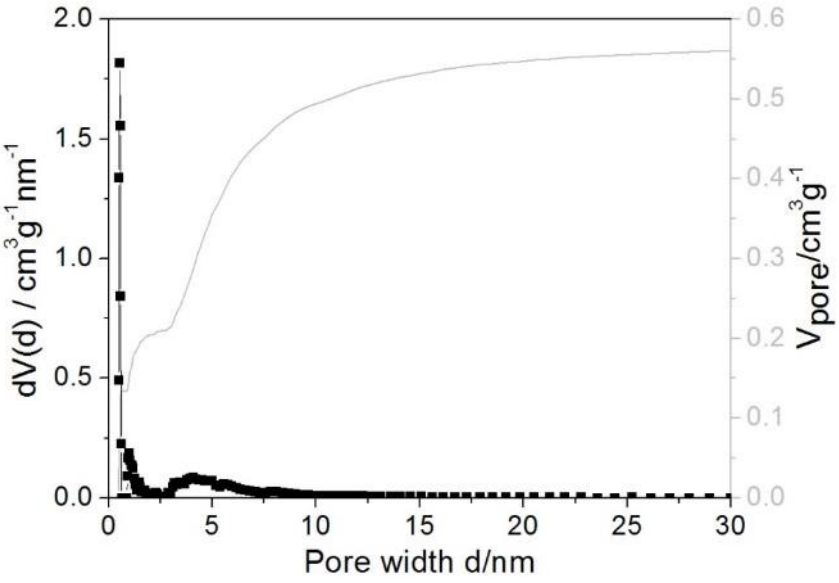

Fig. S19 Pore size distribution and pore volume of an activated **BDP_CMP** sample (N_2 gas at 77 K; QSDFT model). (Average pore width 0.545 nm, pore volume 0.563 cm^3/g).

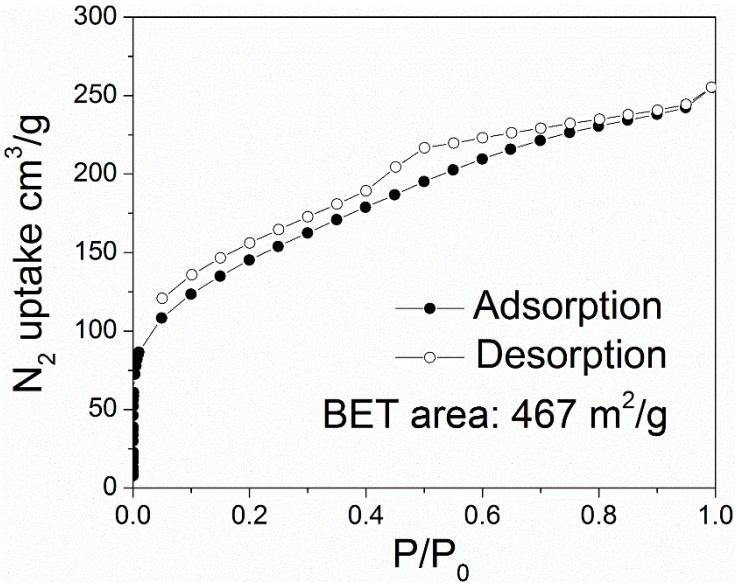

Fig. S20 N_2 sorption isotherm at 77 K for the activated solid sample of **PHTT_DMP**.

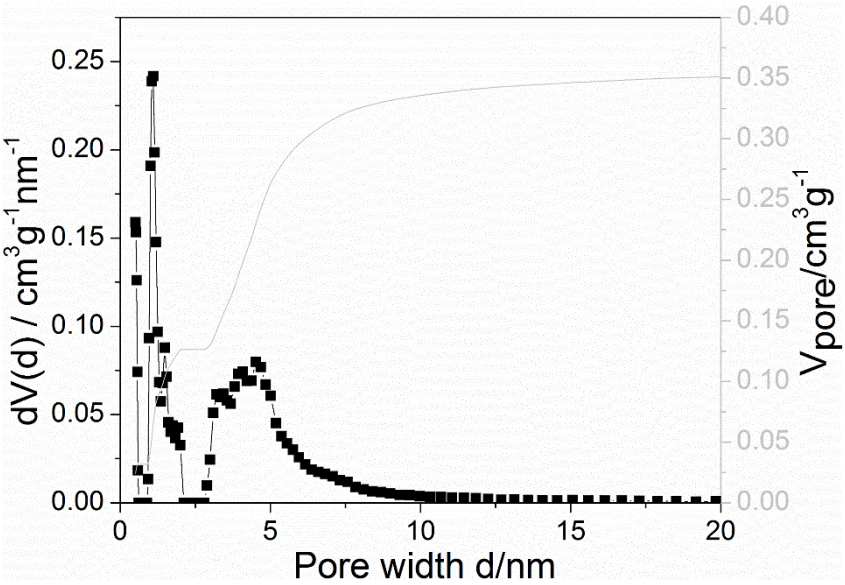

Fig. S21 Pore size distribution and pore volume of an activated **PHTT_DMP** sample (N_2 gas at 77 K; QSDFT model). (Average pore width 1.096 nm, pore volume 0.364 cm^3/g).

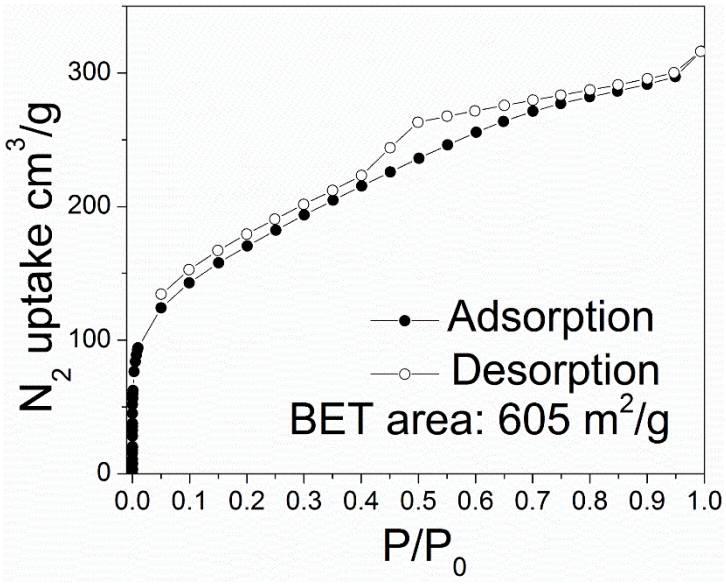

Fig. S22 N_2 sorption isotherm at 77 K for the activated solid sample of **PHTT_DMP_O**.

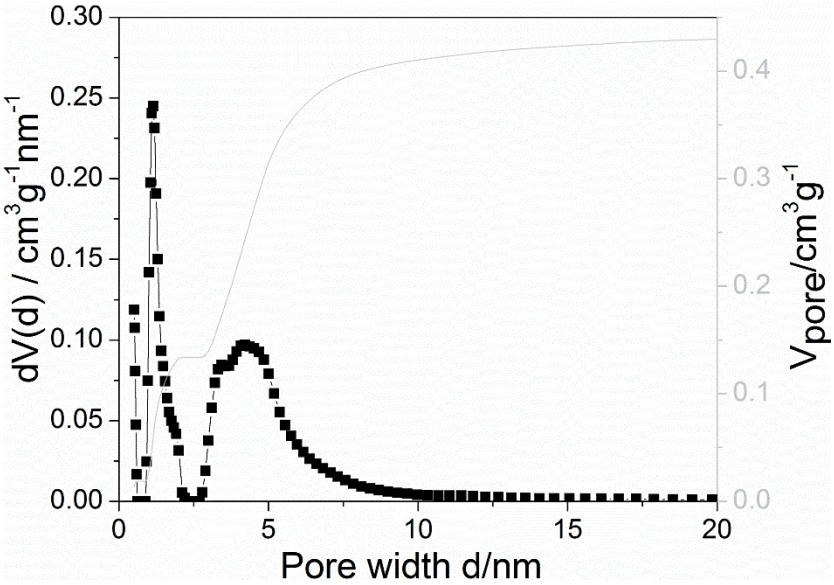

Fig. S23 Pore size distribution and pore volume of an activated **PHTT_DMP_O** sample (N_2 gas at 77 K; QSDFT model). (Average pore width 1.144 nm, pore volume 0.448 cm^3/g).

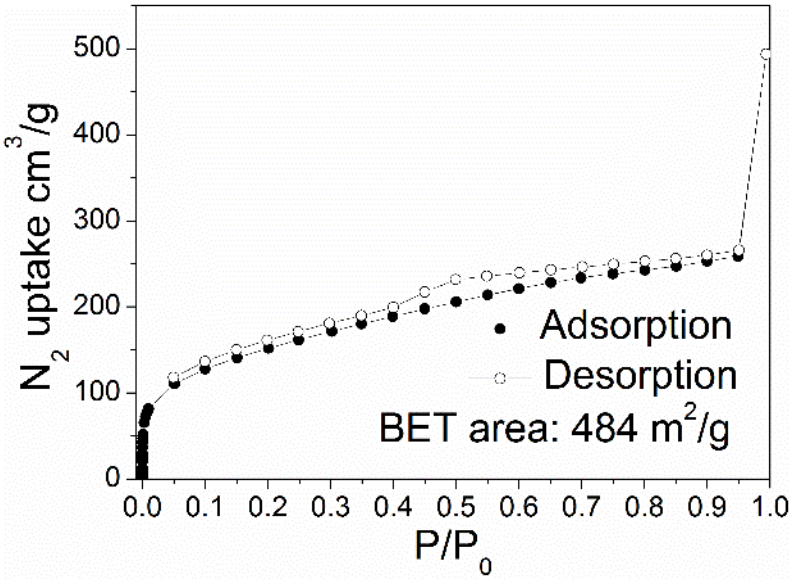

Fig. S24 N_2 sorption isotherm at 77 K for the activated solid sample of **PHTT_BDP**.

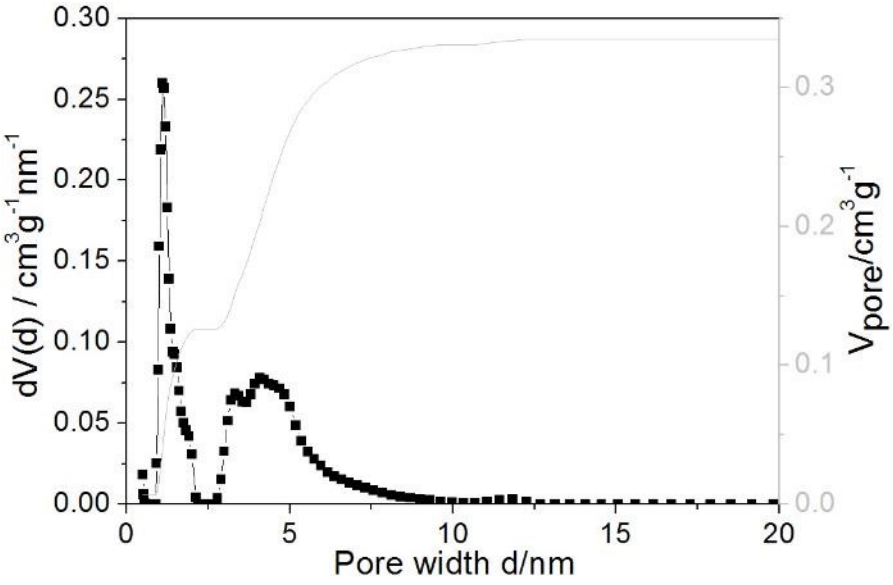

Fig. S25 Pore size distribution and pore volume of an activated **PHTT_BDP** sample (N_2 gas at 77 K; QSDFT model). (Average pore width 1.096 nm, pore volume 0.523 cm^3/g).

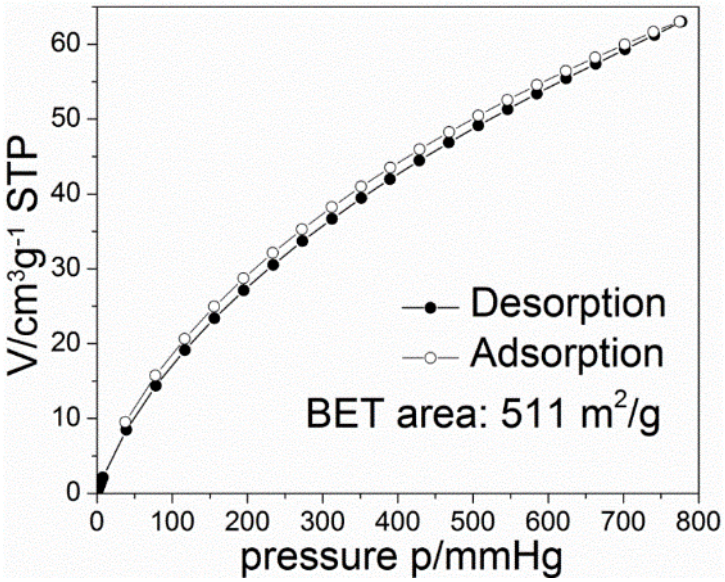

Fig. S26 CO_2 sorption isotherm at 273 K for an activated **BDP_CMP** sample.

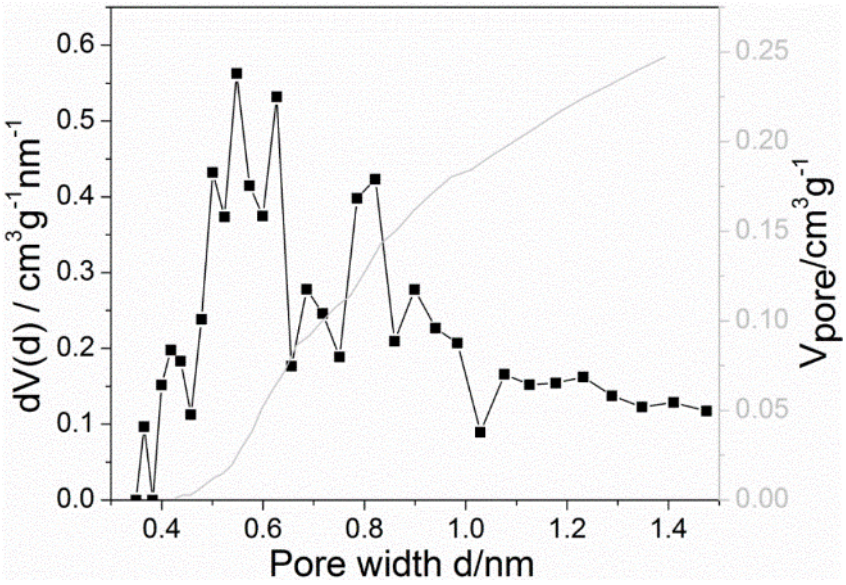

Fig. S27 Pore size distribution and pore volume of an activated **BDP_CMP** sample (CO_2 gas at 273 K; Monte-Carlo model). (Average pore width: 0.548 nm, micropore volume: 0.247 cm^3/g).

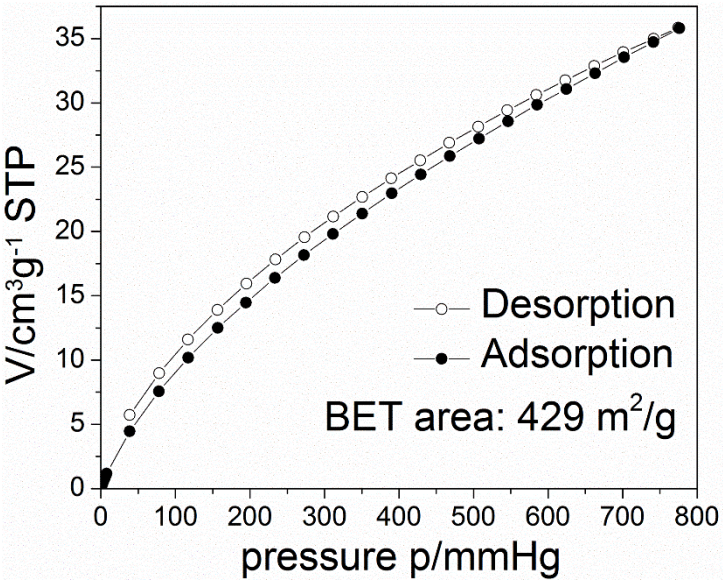

Fig. S28 CO_2 sorption isotherm at 273 K for an activated **PHTT_DMP** sample.

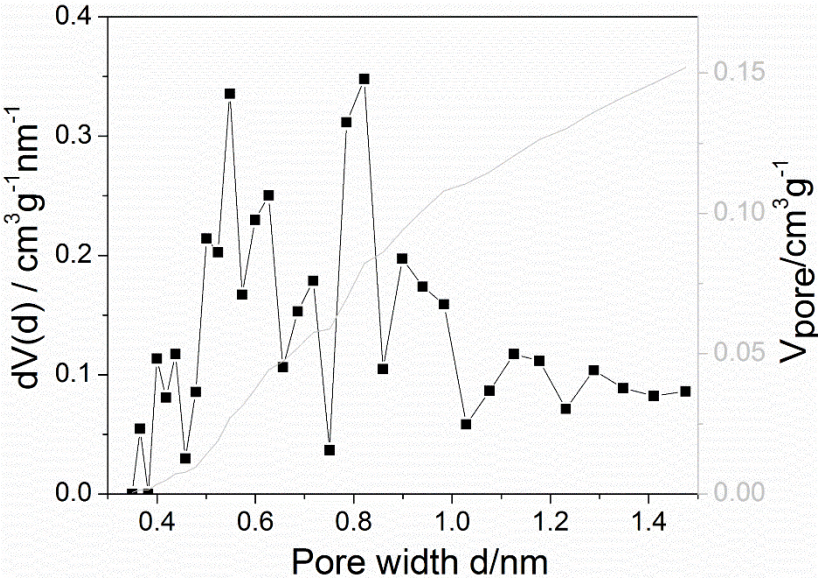

Fig. S29 Pore size distribution and pore volume of an activated **PHTT_DMP** sample (CO_2 gas at 273 K; Monte-Carlo model). (Average pore width: 0.822 nm, micropore volume: 0.152 cm^3/g).

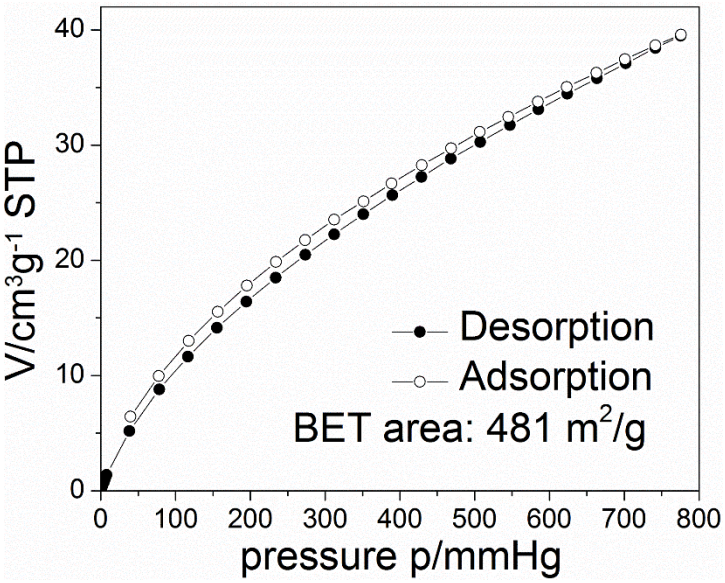

Fig. S30 CO_2 sorption isotherm at 273 K for an activated **PHTT_DMP_O** sample.

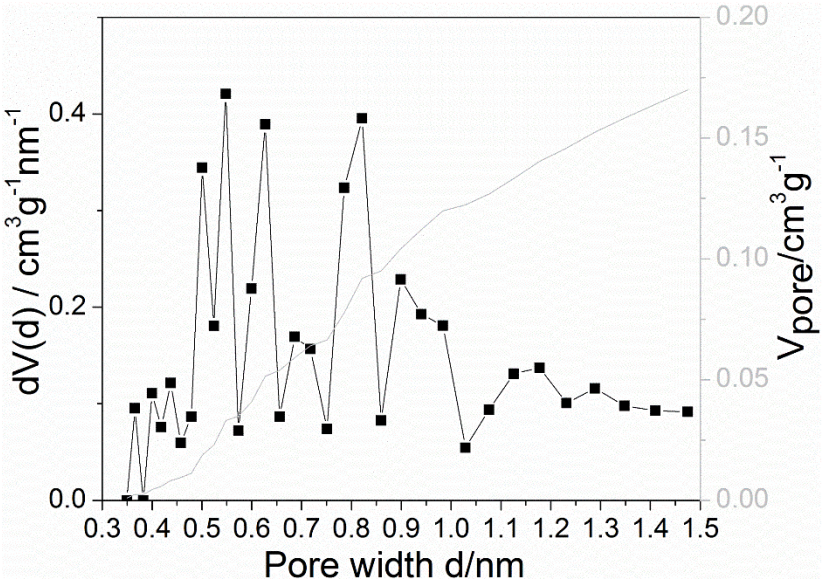

Fig. S31 Pore size distribution and pore volume of an activated **PHTT_DMP_O** sample (CO_2 gas at 273 K; Monte-Carlo model). (Average pore width: 0.548 nm, micropore volume: 0.170 cm^3/g).

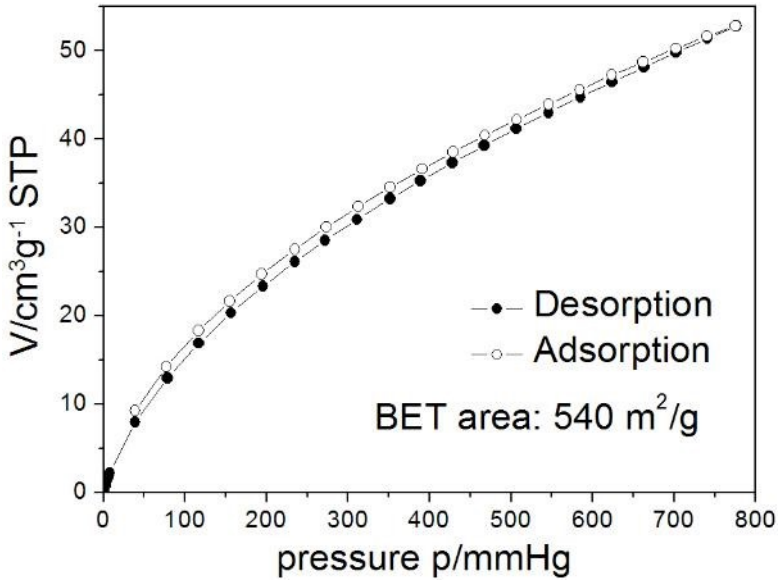

Fig. S32 CO_2 sorption isotherm at 273 K for the activated solid sample of **PHTT_BDP**.

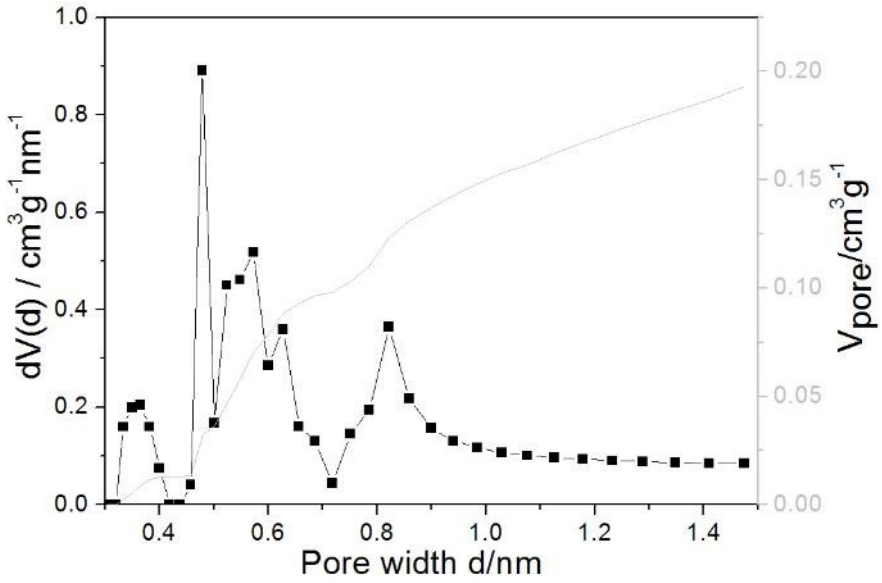

Fig. S33 Pore size distribution and pore volume of an activated **PHTT_BDP** sample (CO_2 gas at 273 K; Monte-Carlo model). (Average pore width: 0.479 nm, micropore volume: 0.193 cm^3/g).

Table S2 Summary of surface area and porosity measurement values for the synthesised polymers.

Polymer	*SA_{BET} (m^2 g^{-1})[a]*	*Pore Width (nm)[b]*	*V_{micro} (cm^3 g^{-1})[b]*
BDP_CMP	769	0.545	0.563
PHTT_CHO[c]	686	1.030	0.374
PHTT_DMP	467	1.096	0.364
PHTT_DMP_O	605	1.144	0.448
PHTT_BDP	484	1.096	0.523

[a] Surface area calculated from the N_2 adsorption isotherm using the Brunauer-Emmett-Teller method. [b] The micropore size and micropore volume were derived using density functional theory. [c] Data obtained from Ref [5].

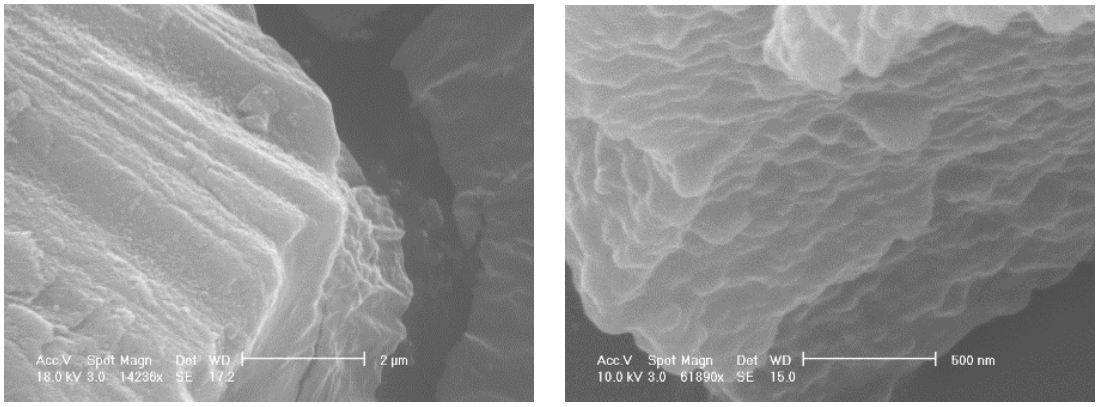

Fig. S34 SEM images of **BDP_CMP**.

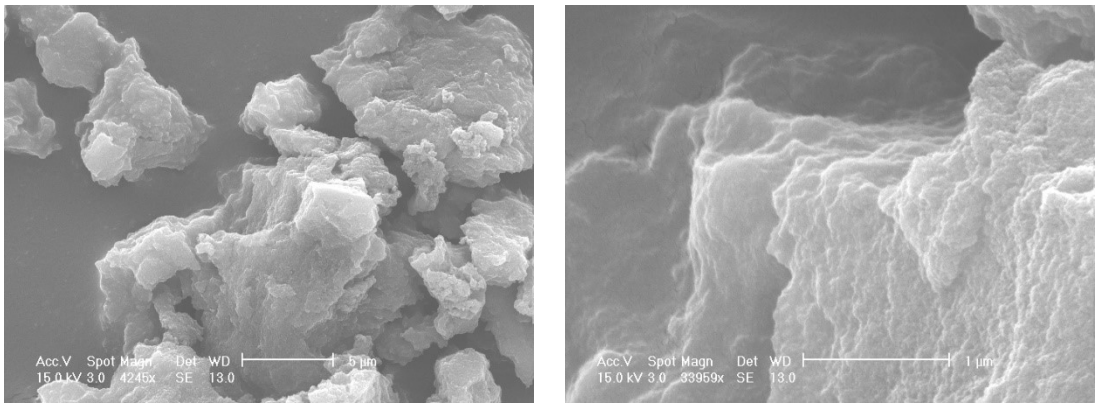

Fig. S35 SEM images of **PHTT_DMP**.

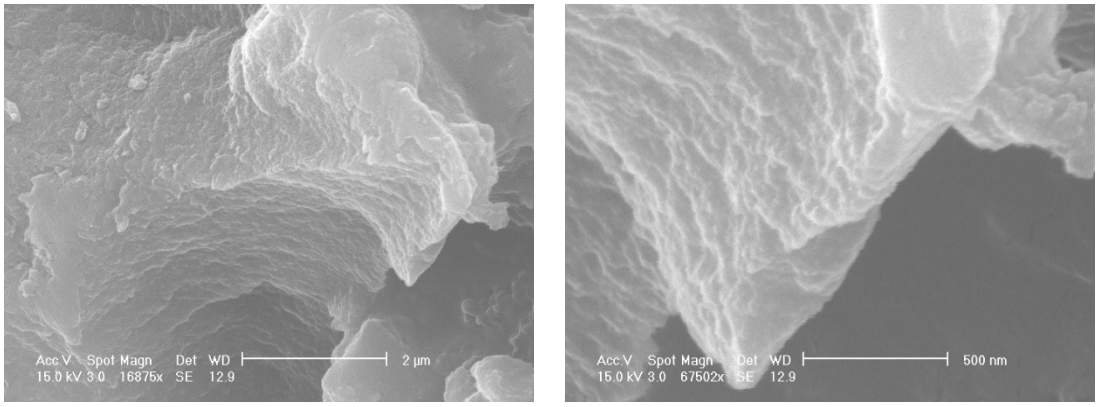

Fig. S36 SEM images of **PHTT_DMP_O**.

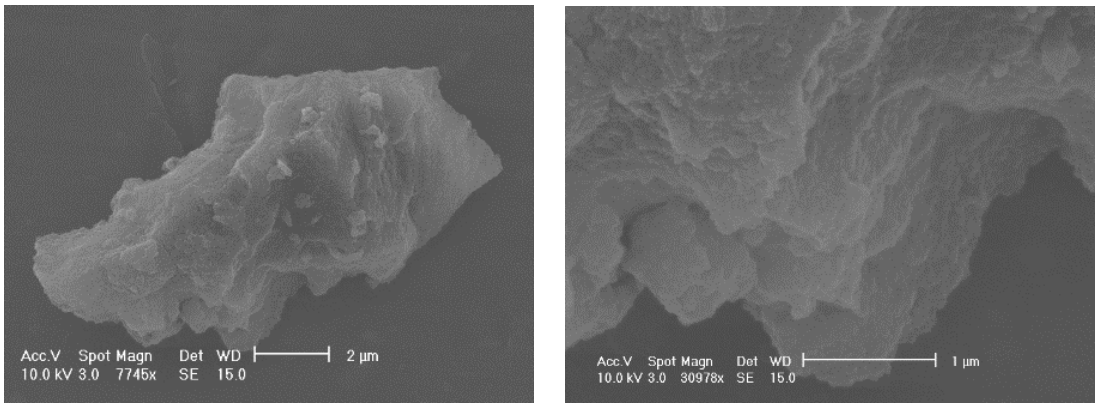

Fig. S37 SEM images of **PHTT_BDP**.

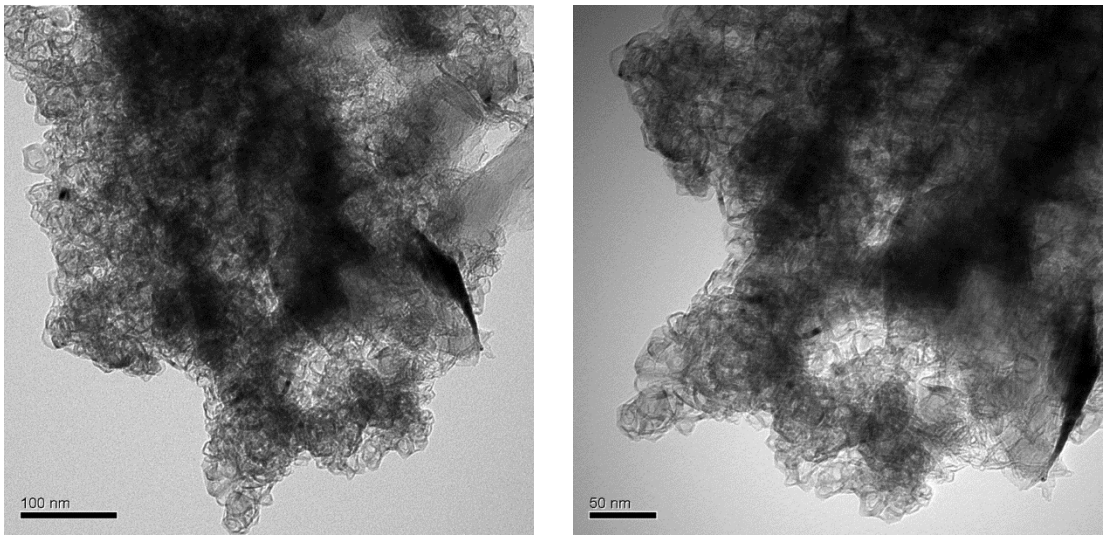

Fig. S38 TEM images of **BDP_CMP**.

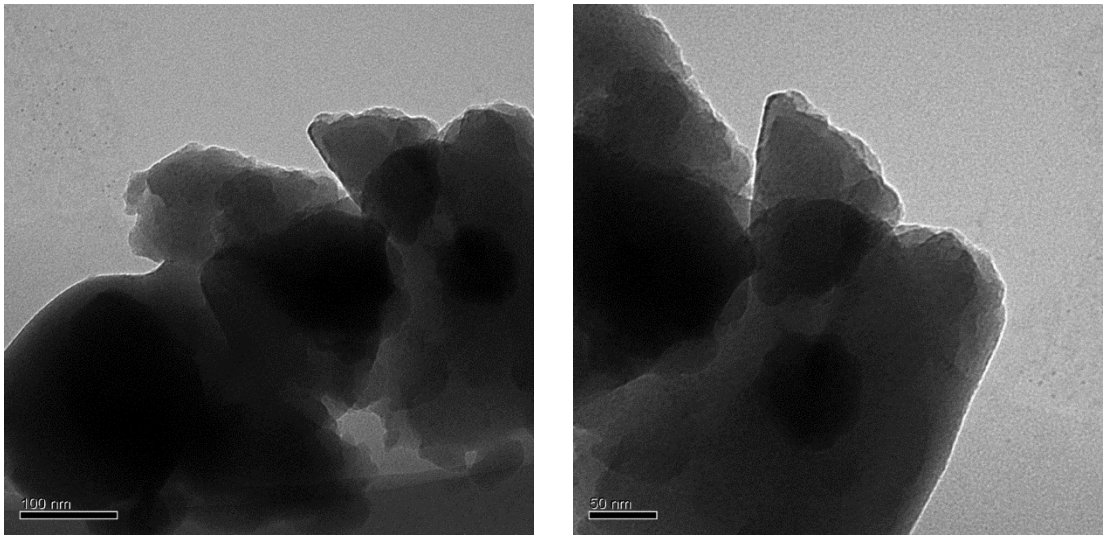

Fig. S39 TEM images of **PHTT_DMP**.

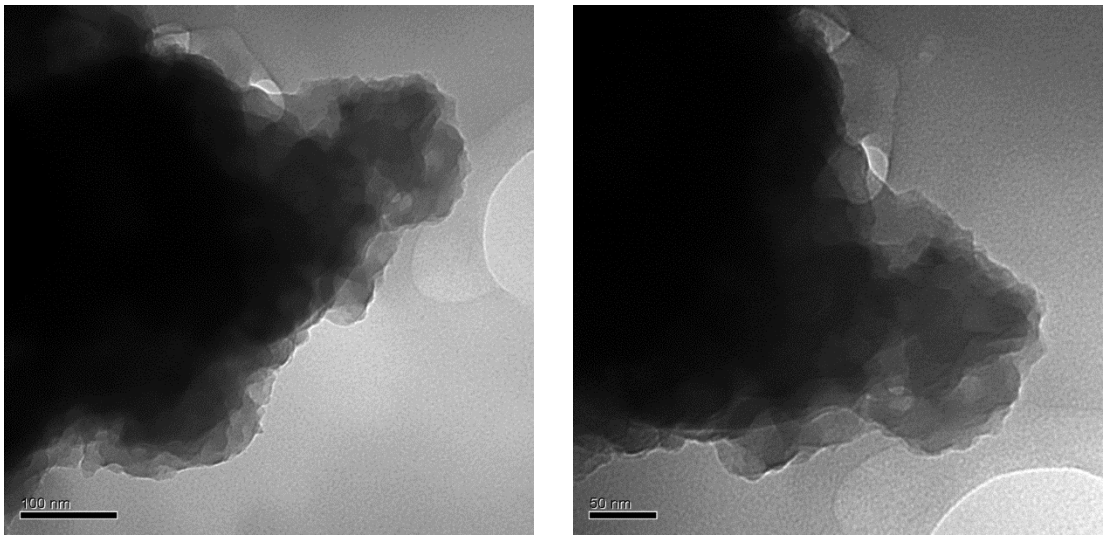

Fig. S40 TEM images of **PHTT_DMP_O**.

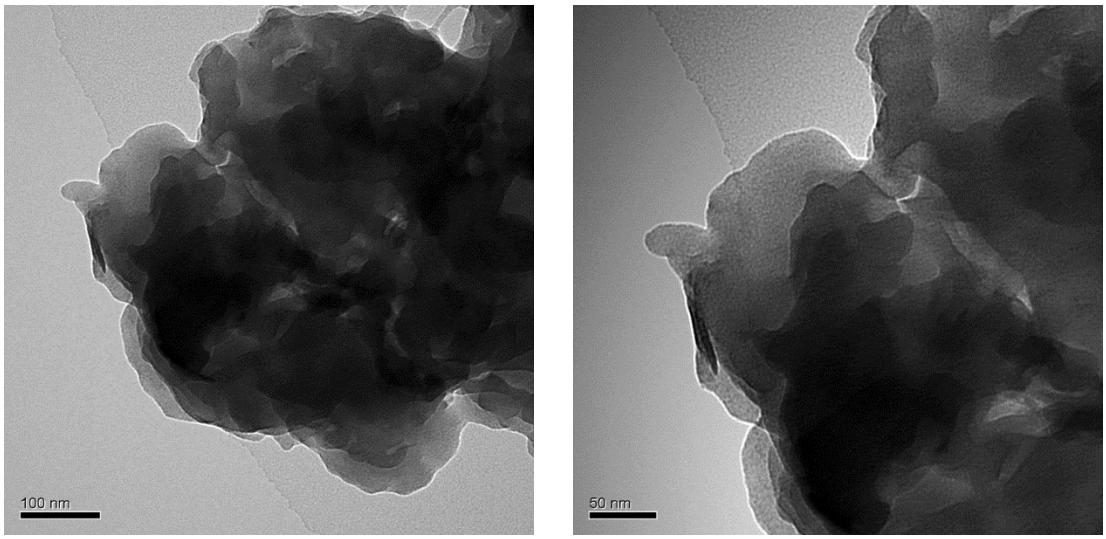

Fig. S41 TEM images of **PHTT_BDP**.

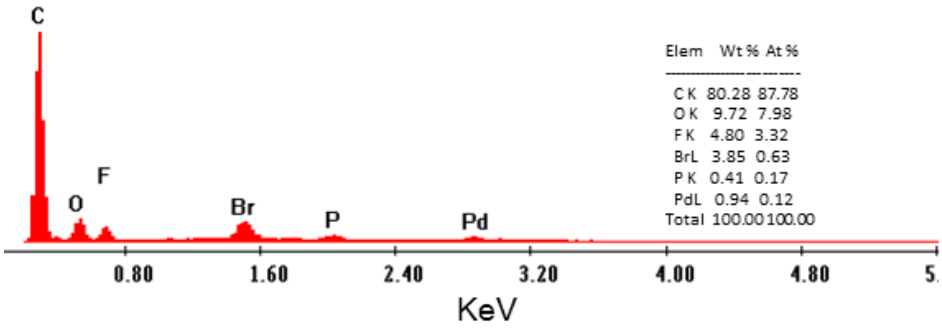

Fig. S42 EDX spectrum of **BDP_CMP**.

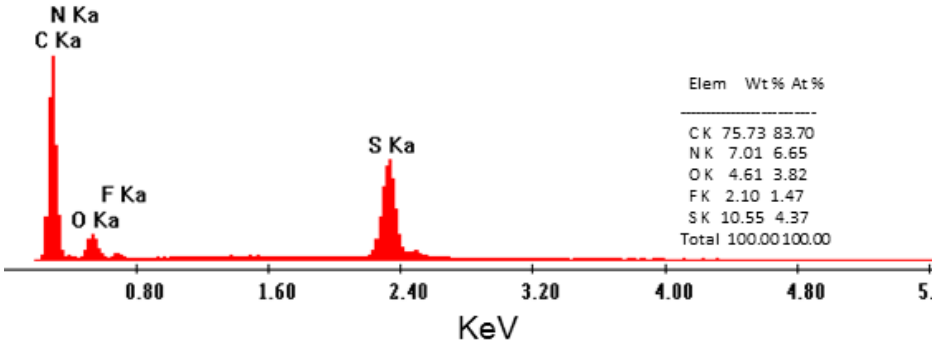

Fig. S43 EDX spectrum of **PHTT_DMP**.

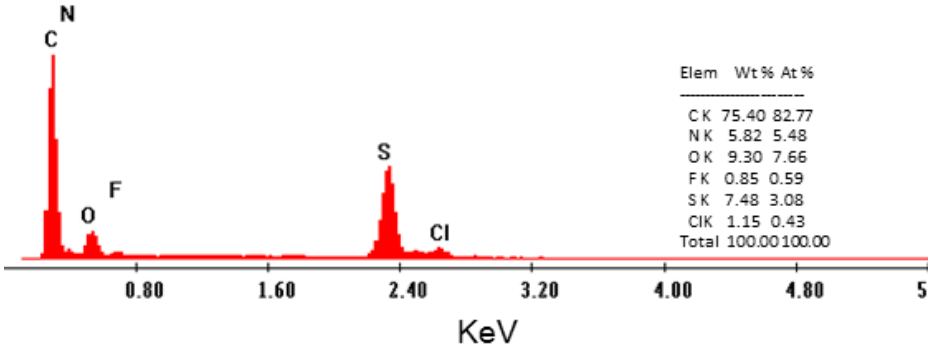

Fig. S44 EDX spectrum of **PHTT_DMP_O**.

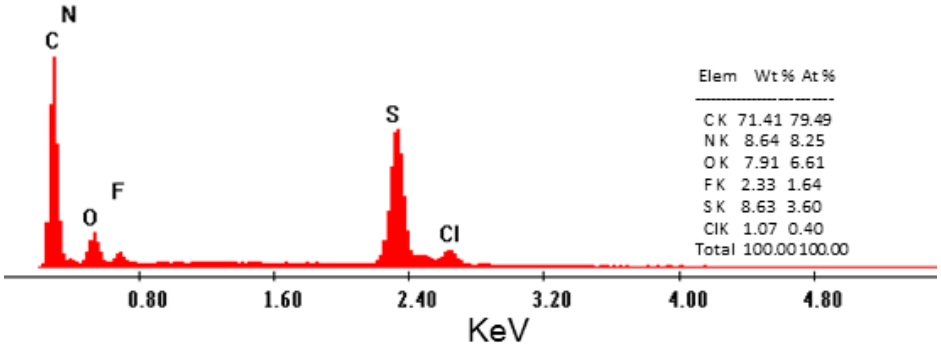

Fig. S45 EDX spectrum of **PHTT_BDP**.

References

[1] M. Ranger, D. Rondeau, M. Leclerc, *Macromolecules*, 1997, **30**, 7686-7691.

[2] P. V. Dau, K. K. Tanabe, S. M. Cohen, *Chem. Commun.*, 2012, **48**, 9370-9372.

[3] A. Vazquez-Romero, N. Kielland, M. J. Arevalo, S. Preciado, R. J. Mellanby, Y. Feng., R. Lavilla, M. Vendrell, *J. Am. Chem. Soc.*, 2013, **43**, 16018-16021.

[4] L. Wang, J-W. Wang, A-j. Cui, X-X. Cai, Y. Wan, Q. Chen, M-Y. He, W. Zhang, *RSC Adv.*, 2013, **3**, 9219-9222.

[5] J. Liu, J. Cui, F. Vilela, J. He, M. Zeller, A. D. Hunter, Z. Xu, *Chem. Commun.*, 2015, **51**, 12197-12200.

CHAPTER 3: A Nanoporous Graphene Analog for Superfast Heavy Metal Removal and Continuous-Flow Visible-Light Photoredox Catalysis (Publication, *Journal of Materials Chemistry A,* RSC)

The following section will focus on the design, synthesis, and characterisation of a novel CPP framework using a metal-free methodology. Designed with bipyridyl units within the polymer backbone, the material was employed for Pb uptake in water. Furthermore, the alkaline N-heterocycles were used as a heterogeneous catalyst for Knoevenagel condensation reactions. Lastly, the CPP also exhibited broad absorbance in the visible light region, prompting its use as a heterogeneous photocatalyst for the photooxidation of benzylamines. This chapter will outline and discuss the publication titled '*A nanoporous graphene analog for superfast heavy metal removal and continuous-flow visible-light photoredox catalysis*' which was published in *Journal of Materials Chemistry A* and can be found in its entirety (including supporting information) at the end of this chapter. Any contributions and work performed by other students, collaborators or academics are presented throughout the chapter in the appropriate sections. Much of the synthesis, characterisation and initial metal chelation studies (unpublished work) was performed during a 6-week secondment with Professor Zhengtao Xu and his group at City University of Hong Kong. Continuous flow experiments along with solid state ^{13}C NMR measurements were performed at Heriot-Watt University.

3.1 Background

The development of novel metal-free polymerisation techniques for the synthesis of CPPs is becoming more attractive as these materials continue to gain attention. Using 'green' synthetic procedures, such as Schiff base [3.1, 3.2] and imidization [3.3] reactions, it is possible to eliminate the need for metal-catalysed methods whilst retaining the desired properties (*i.e.* surface area, porosity, light harvesting) of CPPs. While there are some examples in the literature demonstrating metal-free methodologies for synthesising CPPs [3.4], they remain limited with a narrow scope of application.

As CPPs tend to be designed for a singular purpose towards a specific application, such as photocatalysis [3.5] or heavy metal removal [3.6], there remains a substantial void for versatile and multipurpose CPPs [3.7]. By combining the ideas of metal-chelating bipyridyl groups and electron donating/accepting components, a CPP can offer multiple capabilities for a variety of applications. This work presents a CPP designed to be synthesised through a metal-free procedure utilising two simple building blocks whereby the inclusion of alternating bipyridyl and oxo groups in a conjugated system allows for the potential for multiple applications. Applications regarding water purification and light harvesting for photocatalysis are prominent areas where development of sustainable materials continues to thrive.

3.2 Aim/Objectives

The primary aim of this study was to explore a metal-free route towards the synthesis of a CPP. By moving away from expensive and potentially toxic metal species towards more sustainable synthetic routes, we strived to develop materials with enhanced 'green' characteristics. Using monomers containing either oxygen or bipyridyl groups, the target polymer was also designed with a distinct electron donor-acceptor system. By combining hexahydroxytriphenylene (HOTT) monomers with hexaazatrinaphthylene (HATN) units in an alternating fashion (Scheme 3.1), the new CPP was anticipated to act as a light harvester, and subsequently used as a photocatalyst for the aerobic photooxidation of benzylamines. Furthermore, inclusion of well-known bipyridyl chelating units allowed base-catalysed reactions and the ability for aqueous metal uptake.

3.3 Synthesis of Materials/Methodology

The graphene-like CPP (herein referred to as HOTT-HATN) was prepared, characterised, and employed for a variety of applications discussed in this chapter. The preparation of HOTT-HATN, along with its initial monomers, was performed through metal-free synthetic routes. HOTT-HATN was characterised using FT-IR spectroscopy, solid state ^{13}C NMR CP-MAS spectroscopy, solid state UV-Vis spectroscopy, elemental analysis, thermogravimetric analysis (TGA), BET surface area (S_{BET}) analysis, energy dispersive X-ray spectroscopy (EDX), powder x-ray diffraction (PXRD),

scanning/transmission electron microscopy (SEM/TEM), and inductively coupled plasma atomic emission spectroscopy (ICP-AES). Solid state ^{13}C NMR CP-MAS measurements were carried out by Dr David Ellis at Heriot-Watt University. TGA, S_{BET} and PXRD measurements were carried out by Ran Xiao at City University of Hong Kong.

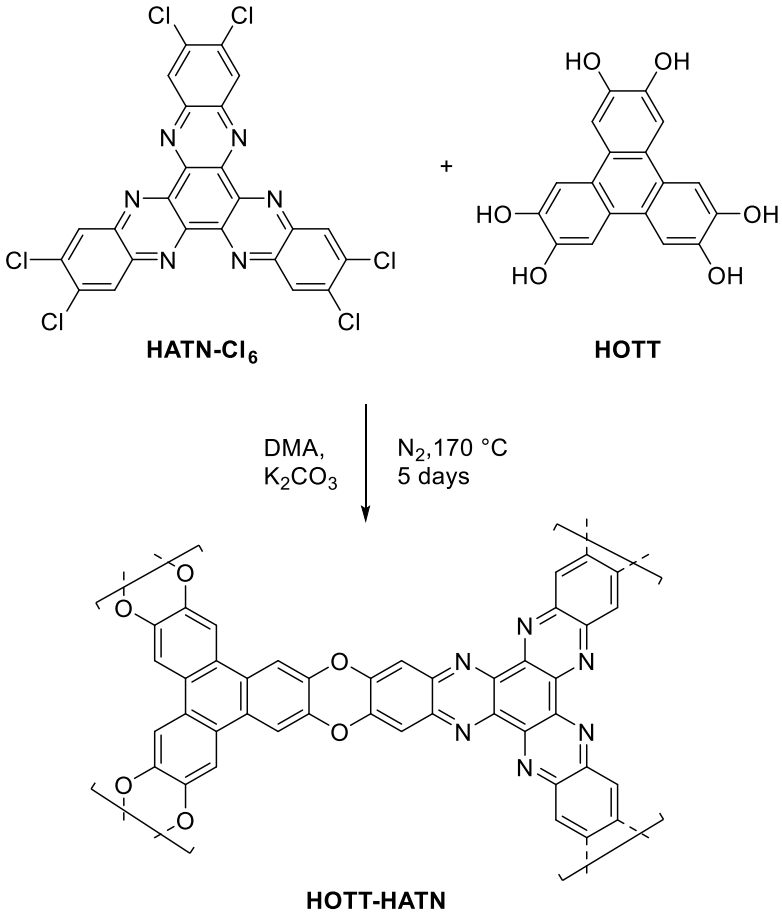

Scheme 3.1 Synthetic procedure for HOTT-HATN polymer. The brackets indicate the theoretical boundary of the repeat unit.

3.3.1 Synthesis of HOTT-HATN Polymer

The assembly of HOTT-HATN was performed through metal-free aromatic nucleophilic substitution [3.7, 3.8] whereby the two monomers, 2,3,6,7,10,11-hexahydroxytripheneylene (HOTT) and 2,3,8,9,14,15-hexachloro-5,6,11,12,17,18-hexaazatrinaphthylene (HATN-Cl_6), were linked *via* an oxygen bridge (Scheme 3.1). While HOTT is commercially available, HATN-Cl_6 was synthesised through a known literature procedure [3.9, 3.10]. The resultant dark red/brown polymer was purified *via* Soxhlet extraction and dried in air. Synthesis of HOTT-HATN was performed by Ran Xiao at City University of Hong Kong.

3.3.2 Kinetic and Isotherm Studies of Pb(II) Sorption using HOTT-HATN

All studies regarding metal uptake by HOTT-HATN were performed in water using Pb^{+2} (supplied from $Pb(NO_3)_2$) as the source of metal ions. For kinetic studies, 20 mg of HOTT-HATN were added to a 50 mL solution containing 10 ppm Pb and stirred at room temperature. Samples were removed from the mixture at given time intervals, filtered, and measured *via* ICP-AES to determine the remaining Pb concentration. For isotherm studies, a series of 5 mL aqueous solutions were prepared with 5 mg of HOTT-HATN and various concentrations of $Pb(NO_3)_2$ (10-150 mg L^{-1}). Each solution was shaken for 270 minutes at room temperature, filtered, and analysed *via* ICP-AES to determine the remaining Pb concentration. All metal chelation studies were performed by the Xu group at City University of Hong Kong.

3.3.3 Heterogeneous Catalytic Knoevenagel Condensations using HOTT-HATN

The general reaction mixtures for HOTT-HATN based-catalysed Knoevenagel reactions included an aldehyde substrate (0.25 mmol), malononitrile (0.375 mmol), deionised water (1 mL), and HOTT-HATN (5 mg). For aldehyde substrates with poor solubility in water, a minimal amount of $CHCl_3$ (0.2 mL) was added. The mixtures were shaken at 40 °C for 2.5-12 hours, filtered, and extracted with CH_2Cl_2. The crude product was then analysed *via* ^1H NMR spectroscopy to determine conversion to the condensation product. Regeneration of the HOTT-HATN catalyst was performed by washing with CH_2Cl_2 and acetone, and subsequently dried *in vacuo*. All catalytic Knoevenagel condensation studies were performed by the Xu group at City University of Hong Kong.

3.3.4 Aerobic Photooxidation of Benzylamines with HOTT-HATN

The general reaction mixtures for the aerobic photooxidation of benzylamines included a benzyl amine (0.5 mmol) and HOTT-HATN (5 mg) dispersed in acetonitrile (10 mL). To ensure a uniform suspension, the mixtures were sonicated for 3 minutes prior to the start of the reaction. This dispersion was pumped through a commercial photochemical reactor (10 mL total volume) equipped with a white light LED lamp ($\lambda >$ 400 nm, Figure 3.1) at a flow rate of 1 mL min^{-1}. The flow rate was chosen as the most optimal as it reduced aggregation whilst allowing for extended periods of irradiation. Concurrently, oxygen was propelled through a second pump at the same flow rate,

meeting the dispersion at a T-junction prior to entering the photochemical reactor. The mixture was cycled through the system until no starting material remained as determined *via* thin layer chromatography (TLC). After the reaction was completed, the mixture was filtered, evaporated, and the crude product was analysed *via* ^{1}H NMR spectroscopy to determine conversion to the desired product.

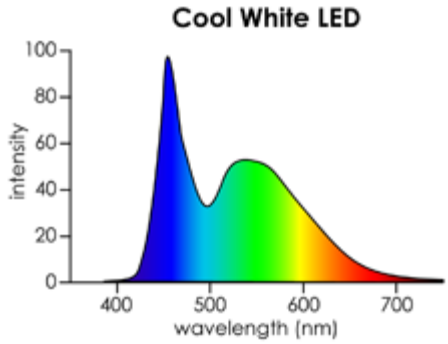

Figure 3.1 Irradiation spectrum produced by the white light LED lamp for aerobic photooxidations of benzylamines.

3.4 Results

3.4.1 Characterisation of HOTT-HATN

Initial analysis of HOTT-HATN focused on its structural characteristics which were examined using a variety of techniques. Elemental CHN and EDX analysis demonstrated a high correlation to the repeat unit of the polymer (Scheme 3.1). FT-IR measurements showed characteristic peaks at 1600 cm^{-1} and 1200-1250 cm^{-1} which correspond to C=N and C-O stretching vibrations, respectively. ^{13}C NMR CP-MAS analysis indicated a fully aromatic system with four resolved peaks at 110.68, 126.27, 142.45 and 147.07 ppm, each of which correspond to a different carbon atom. As the repeat unit of the polymer shows seven distinct aromatic carbons, not all carbons were resolved in the spectrum. However, this is not surprising as the individual carbons in the naphthalene group of HOTT would be expected to demonstrate a similar chemical shift. Spectroscopic measurements were also performed on HOTT-HATN in the form of solid-state UV-Vis spectroscopy. A very broad absorbance in the visible spectrum was observed with a local λ_{max} range between 450-500 nm.

Physical characterisation of HOTT-HATN was also performed to determine its surface area, thermal stability, and morphology. S_{BET} analysis of the polymer presented a relatively high surface area of 526.5 $m^2 g^{-1}$. Furthermore, pore size distribution and pore volume analysis showed an average pore width of 0.52 nm and pore volume of 0.579 $cm^3 g^{-1}$, indicating a microporous material (pore size < 2 nm). TGA measurements showed that HOTT-HATN is highly stable up to temperatures reaching 250 °C under a nitrogen stream. The presence of water was also observed due to significant weight loss at lower temperatures (< 200 °C) and is consistent with the water indicated in the CHN analysis. As expected, PXRD, SEM, and TEM imaging of the polymer showed an amorphous and highly textured morphology (p. 166). Most importantly, these physical properties are consistent with those found in many other CPPs [3.11], despite the use of metal-free synthetic methodology in the formation of HOTT-HATN.

During the synthesis and purification of HOTT-HATN, it was observed that the polymer readily formed a suspension in water. This hydrophilicity most likely arises from the polar aza and oxo groups that make up the polymeric backbone. Interestingly, it is rare for CPPs to exhibit hydrophilicity without specific modifications or design parameters (Figure 3.2) [3.12-3.14]. Such a characteristic, along with the metal-free synthetic design, shows great promise for HOTT-HATN as a material for green applications.

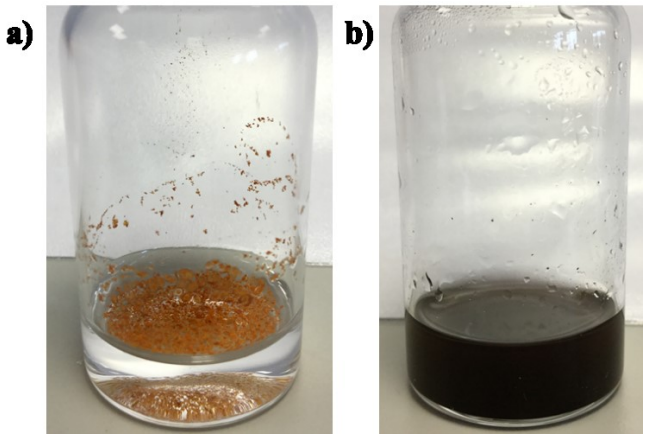

Figure 3.2 A visual comparison between a (a) typical hydrophobic CPP unable to interact with water and (b) HOTT-HATN as a dispersion in water.

3.4.2 Removal of Lead Ions from Water

As HOTT-HATN was designed with several bipyridyl groups within the repeat unit of the polymer backbone, initial investigations focused on metal chelation. Specifically, the aim was to use the materials as easily recoverable and reusable heterogeneous supports for metal-catalysed reactions. Three different metals (Ir, Pd and Cu) were chosen for chelation studies as they are well-known catalysts that use bipyridyl-type ligands. These reactions include Cu-catalysed 'click' reactions [3.15], Ir-catalysed C-H borylation of arenes [3.16] and Pd-catalysed carbon-carbon cross-coupling reactions, such as Suzuki-Miyaura coupling [3.17]. Unfortunately, both Ir and Pd exhibited very poor loading to the bipyridyl sites (< 1 wt.%) as confirmed by EDX measurements. This resulted in little to no catalytic activity when employed in the reactions stated above. Conversely, Cu chelation showed much greater efficiency with a concentration around 10 wt.% in the HOTT-HATN sample as measured *via* EDX analysis. However, when used as a Cu-based catalyst for 'click' reactions, the conversion rates and reaction times required were not comparable to similar catalytic materials [3.15]. Therefore, employing HOTT-HATN as a heterogeneous support for metal-based catalysis was not explored further.

To further examine the metal chelating abilities of HOTT-HATN, it was suggested to use the polymer as an adsorbent for the removal of heavy metal ions from water. Specifically, lead is exceptionally poisonous to humans, with young children and pregnant women being the most susceptible to its negative health effects. Therefore, the removal of lead and other toxic heavy metals from water sources continues to demand high priority within the public health sector with regards to clean drinking water [3.18].

To first understand the efficiency of Pb uptake by HOTT-HATN, a kinetic study was performed with an aqueous $Pb(NO_3)_2$ solution (10 ppm in 50 mL water). Analysis of the water sample *via* ICP-AES showed a 94 % decrease in Pb content after 100 seconds. Within 5 minutes, the Pb content remaining in the solution dropped below the detectable limits of the instrument (15-20 ppb). This is an important value as it is the allowable concentration of Pb in drinking water as dictated by the US Environmental Protection Agency [3.19].

While demonstrating remarkably fast uptake of Pb, an isotherm study was also performed to determine the total adsorption capacity of HOTT-HATN. It was calculated that the adsorbed amount of Pb at equilibrium was 66.8 mg g^{-1}, which is equivalent to 0.28 Pb(II) ions per polymer repeat unit (three bipyridyl units). Upon calculation of the distribution coefficient, we determined that for 1 L of water with a Pb concentration of 150 ppb, only 4.5 mg of HOTT-HATN is required to decrease the concentration of lead ions below the 15 ppb threshold necessary for potable water [3.19]. Comparisons to other adsorption materials for Pb removal show HOTT-HATN as largely superior in both kinetics and affinity for Pb [3.20].

Lastly, a selectivity study using a solution of various heavy metals (Hg^{+2}, Pb^{+2}, Cu^{+2}, Cd^{+2} and Zn^{+2}) and naturally occurring metals (Ca^{+2} and Na^{+}) ions was performed to better understand the affinity of HOTT-HATN for different metal species. Notable preferences were observed for Hg^{+2}, Pb^{+2} and Cu^{+2} where at least 90 % removal from the aqueous solution was achieved within one hour. The non-toxic metal species, Ca^{+2} and Na^{+} showed no more than a 2% decrease in concentration after one hour while Zn^{+2} showed a moderate decrease (25%) within the same time frame. The toxic Cd^{+2} ions, however, presented only a modest 35% decrease under these conditions. By demonstrating the selectivity parameters for certain metal species, superior kinetic performance, and adsorption capacity of HOTT-HATN, we can envision its use as a green material for the treatment of drinking water.

3.4.3 HOTT-HATN Catalysed Knoevenagel Condensation Reactions

After understanding the chelating properties of HOTT-HATN, our focused shifted to the exploration of the polymer as a green heterogeneous catalyst in chemical synthesis. The inherent metal-free nature of HOTT-HATN makes it an ideal candidate as an organocatalyst as it removes any issues regarding metal leeching and contamination which are critical in the electronic and pharmaceutical industries [3.21]. Due to the bipyridyl group's ability to act as an organic base and the proven hydrophilicity of HOTT-HATN, aqueous Knoevenagel condensation reactions offered a robust catalytic test. Furthermore, as Knoevenagel reactions are vital for C-C bond formations in the synthesis of fine chemical and pharmaceuticals [3.22, 3.23], the development of efficient and environmentally benign catalytic materials remains a worthy endeavour.

Knoevenagel condensation reactions were performed in water under mild conditions whereby a selection of aromatic aldehyde compounds was coupled with malononitrile in the presence of the basic HOTT-HATN (Scheme 3.2). The benchmark reaction with benzaldehyde showed full conversion to the benzylidenemalononitrile product *via* ^{1}H NMR spectroscopy after 2.5 hours. The same reaction performed in common organic solvents ($CDCl_3$ and acetonitrile) in the absence of water resulted in a significant increase in the required reaction time. Even after 12 hours, the reaction in $CDCl_3$ showed only 67% conversion and in acetonitrile 80% conversion was observed. When the benchmark reaction was performed in the absence of HOTT-HATN, 62% conversion to the product was observed after 2.5 hours. This suggests that water not only plays an important role in this reaction but can also act as a mild base in the absence of HOTT-HATN, albeit much less efficiently. Nevertheless, the polymer has clearly demonstrated enhanced catalytic capabilities. Excellent chemical stability was also observed as repeated use of HOTT-HATN (5 cycles) showed no decline whatsoever in catalytic efficiency.

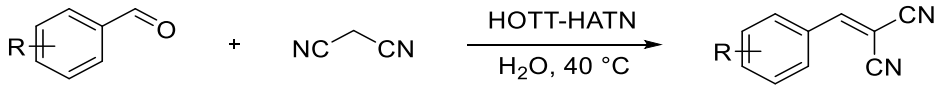

Scheme 3.2 General reaction scheme for HOTT-HATN catalysed Knoevenagel condensation reactions.

As seen in Figure 3.3, an array of substituted benzaldehydes (4-fluoro, 4-hydroxy, 2-bromo and 2-bromo-4,5-dimethoxy) were also examined under optimised conditions. Each of these reactions were comparative to the benchmark reaction, achieving full conversion within 3 hours. However, the use of a bulkier aldehyde (3,5-bis(benzyloxy)-benzaldehyde, Figure 3.3) resulted in a much slower reaction, reaching 82% conversion after 15 hours. This is most likely due to the inability for the sterically hindered aldehyde to penetrate the polymer matrix. The scope of Knoevenagel reactions, along with the properties and characteristics of the polymer, has established HOTT-HATN as an efficient, green and reusable heterogeneous catalyst.

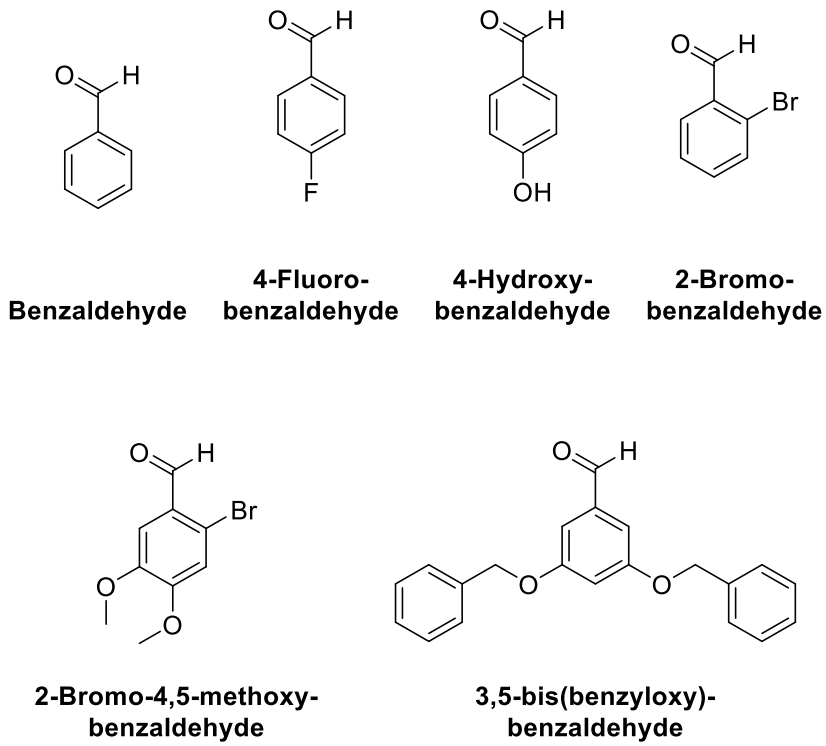

Figure 3.3 Scope of benzaldehydes used for HOTT-HATN catalysed Knoevenagel condensation reactions.

3.4.4 Aerobic Photooxidation of Benzylamines

As HOTT-HATN exhibited broad light absorption within the visible spectrum (400 – 800 nm), we were interested in its potential as a light harvesting material and photocatalyst. As previously described, the use of light, along with a suitable photocatalyst, offers a desirable green alternative to traditional synthetic routes that use direct heating as a source of energy. While Chapter 1 examines the current scope of CPPs available for photocatalytic applications, there remains room to expand upon CPPs synthesised through metal-free procedures for similar applications. HOTT-HATN fits this description and exhibits the properties found in other efficient photocatalytic CPPs [3.5]. Therefore, HOTT-HATN was employed as a photocatalyst under continuous flow conditions to produce imines from benzyl amines, a synthetic procedure which has garnered interest when investigating the synthesis of nitrogen-rich biological molecules [3.24, 3.25].

The photooxidation reactions were carried out under continuous flow conditions in a solution of acetonitrile with a benzyl amine and HOTT-HATN (Scheme 3.3). The mixture was irradiated with a visible light LED module (4 W cm^{-1}; $\lambda > 400$ nm) in the

presence of oxygen until consumption of the starting materials was observed *via* TLC. A benchmark reaction was first attempted with benzylamine showed full conversion to the imine *via* ^{1}H NMR spectroscopy after 6 hours of continuous flow. Interestingly, the use of a narrow wavelength LED module (λ = 420 nm) under the same conditions achieved full conversion after only 4 hours. While this wavelength is more in line with the local λ_{max} of HOTT-HATN, we opted to continue with broad spectrum light as it more accurately simulates common light sources, such as household bulbs and sunlight. Furthermore, to establish that the photooxidation was indeed proceeding under the set of conditions presented, a series of control experiments were performed. When performed in the absence of light, the absence of HOTT-HATN or under a nitrogen atmosphere, little to no conversion was observed, thereby validating the reaction conditions and the need for light, oxygen, and the photocatalytic polymer. While this reaction can proceed through several mechanistic pathways [3.26, 3.27], it was determined that the most likely route this reaction proceeded was through a $^1O_2$ mechanism.

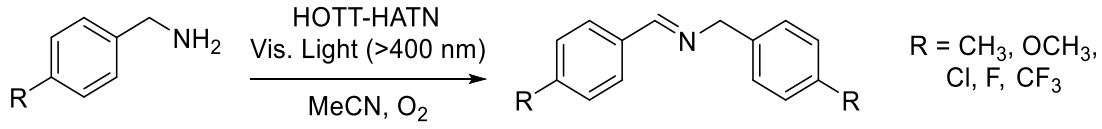

Scheme 3.3 General reaction scheme for aerobic photooxidation of benzylamines using cool white light (wavelength spectrum presented in Figure 3.1).

A variety of substituted benzyl amines (4-methoxy, 4-methyl, 4-chloro, 4-fluoro, and 4-trifluoromethyl) were also examined to demonstrate the scope of imines that can be produced through this reaction method (Figure 3.4). Each substituted benzyl amine showed full conversion within a similar timeframe to that of the benchmark reaction. However, it was noted that benzyl amines with electron donating groups (4-methyl, 4-methoxy) took slightly less time (5 hours) to reach full conversion. Conversely, the benzyl amine with a strong electron withdrawing trifluoromethyl group took slightly longer, requiring 7 hours to reach full conversion.

Finally, to demonstrate the robust nature of HOTT-HATN, the photostability of the polymer was investigated. This was examined by adding the polymer to acetonitrile and subjecting the mixture to the same reaction conditions for a 30-hour period. After this time, benzylamine was added and the benchmark reaction was performed whereby 92% conversion to the imine product was observed after 6 hours. This, along with post-

reaction FT-IR measurements, established HOTT-HATN as highly photostable under prolonged exposure to high intensity irradiation. Furthermore, under the stated reaction conditions it is noted that $^1O_2$ is continuously generated during this time, reinforcing the polymer as not only photostable, but also unaffected when subjected to highly oxidative conditions.

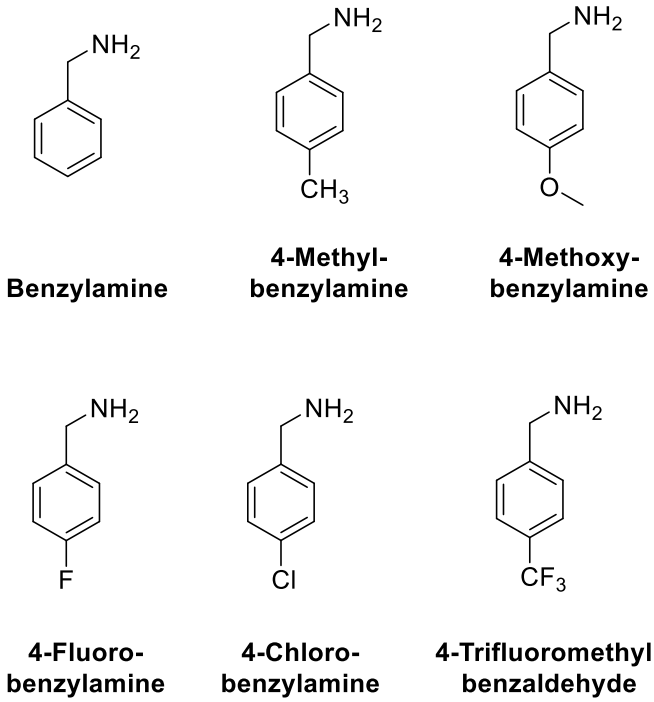

Figure 3.4 Scope of benzylamines used for HOTT-HATN photocatalysed aerobic oxidation experiments.

3.5 Conclusion

A highly robust CPP has been designed and synthesised through an entirely metal-free procedure *via* a nucleophilic substitution reaction between two building blocks, HOTT and HATN-Cl_6. Through electron donor-acceptor interactions between the oxo and aza sites within the polymer backbone, HOTT-HATN was demonstrated as an efficient and stable heterogeneous photocatalyst for the photooxidation of benzylamines under continuous flow conditions and visible light irradiation. This electronic interaction also exhibited a significant effect on basicity of the bipyridyl groups, leading HOTT-HATN to act as both an effective heterogeneous catalyst for Knoevenagel reactions in water and as a 'sponge' for the rapid removal of Pb from water to acceptable drinking levels. With an impressive array of applications, water compatibility, and a metal-free

synthetic procedure, HOTT-HATN has exhibited many of the properties that are highly sought after with respect to green materials.

3.6 Impact on Literature and Research

This research provides a novel and robust CPP developed entirely in the absence of a metal catalyst. Due to the functional groups within the polymer backbone, it was shown as a multifaceted green material with applications in water treatment and (photo)catalysis. Due to broad absorbance in the visible spectrum, narrow wavelength light irradiation was not necessary and more readily available 'white' light ($\lambda > 400$ nm) was used as a source of photons. As this broad spectrum of light closely replicates that provided by the Sun, we can easily envision solar radiation as a legitimate energy source for photocatalytic applications using HOTT-HATN. Along with being metal-free and water compatible, this offers an insight into the range of green credentials exhibited by the polymer.

Moving forward, this work will undoubtedly have an impact on the ideology behind the design methodologies of CPPs. This is true not only for investigations into metal-free synthetic procedures, but also for how these materials can perform multiple tasks through careful selection of the building blocks. We have begun to investigate this idea through the synthesis of polysquaraine-based CPPs as a new class of metal-free polymers (Scheme 3.4). Squaraine-based dyes have shown potential as materials which absorb in the near infrared (NIR) range and are able to undergo condensation reactions with indoles, pyrroles and aniline derivatives [3.28, 3.29]. Materials incorporating NIR-absorbing dyes have been described for applications such as photovoltaics [3.30], medical imaging and light-based therapy [3.31, 3.32].

All three polymers were fully characterised and demonstrated similar properties found in other CPPs (*i.e.* high S_{BET}, insoluble, microporosity, good thermal stability) [3.5]. As expected, the polymers also exhibited an outstanding bathochromic shift with local maxima ranging from 690 to 850 nm. While these materials show promise as insoluble NIR-absorbing polymers, they have so far demonstrated little to no activity as photocatalysts for the generation of reactive oxygen species. Further work is currently being carried out by Professor Zhengtao Xu and his group at City University of Hong

Kong to determine metal absorption capabilities as well as other potential catalytic processes where the polymers may be utilised. Full synthetic methods and characterisation of these materials can be found in Appendix B.

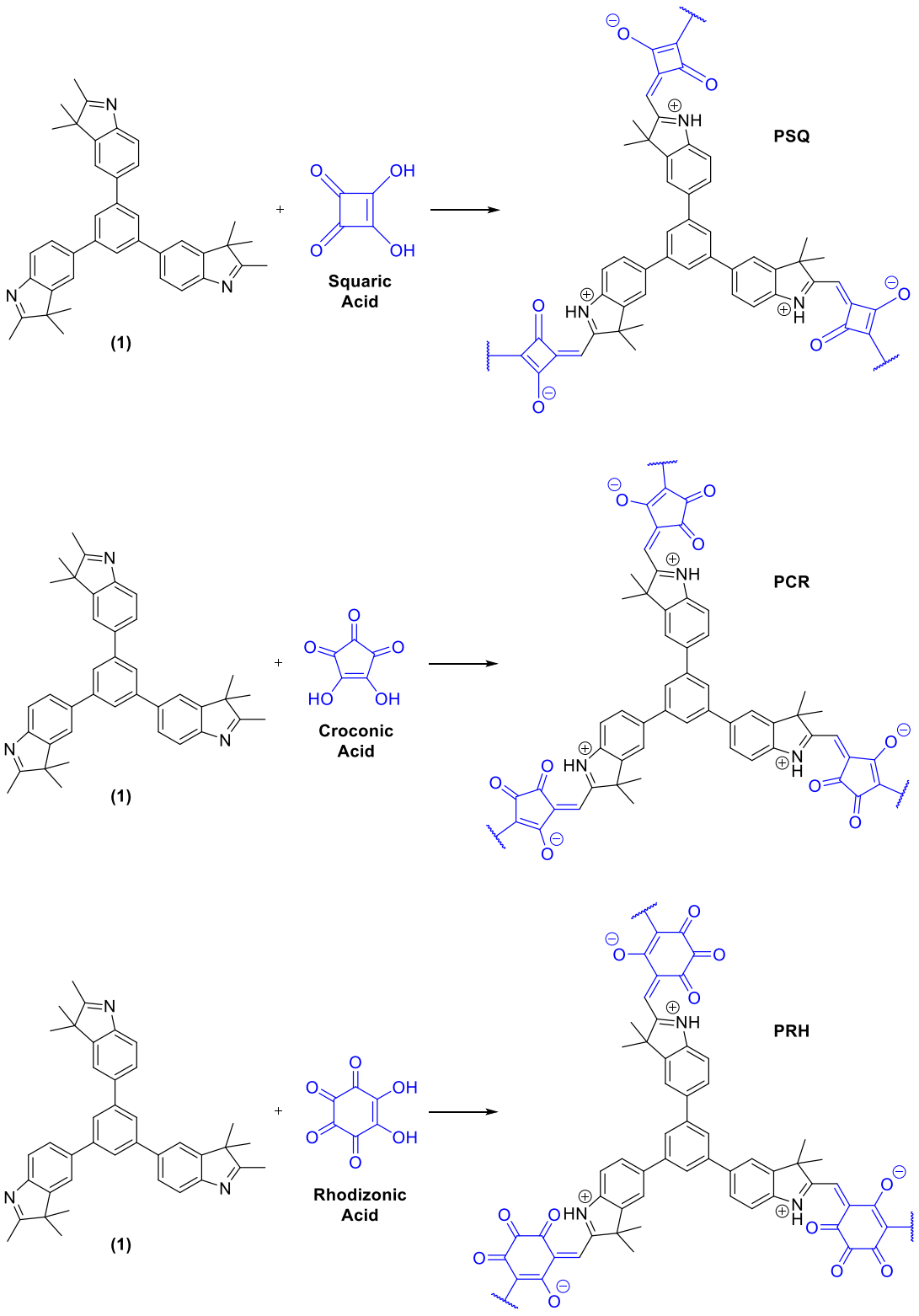

Scheme 3.4 Reaction scheme for the synthesis of a polysquaraine-based CPPs.

While CPPs have clearly exhibited their merit as heterogeneous materials in many applications, other polymeric materials can also fulfil these roles. For example, traditional homogeneous photocatalysts (such as rose Bengal) have been integrated into a polymer matrix to then act as a heterogeneous photocatalytic material [3.33]. The proceeding chapter broadens the scope of potential photoactive materials using free radical polymerisation, a metal-free synthetic technique, to introduce a crosslinking photosensitiser into a polystyrene backbone.

3.7 References

[3.1] J. Weber, O. Su, M. Antonietti, A. Thomas, *Exploring Polymers of Intrinsic Microporosity – Microporous, Soluble Polyamide and Polyimide*, Macromol. Rapid Commun., **28**, 1871-1876 (2007)

[3.2] M. G. Schwab, B. Fassbender, H. W. Spiess, A. Thomas, X. Feng, K. Mullen, *Catalyst-free preparation of melamine-based microporous polymer networks through Schiff base chemistry,* J. Am. Chem. Soc., **131**, 7216-7217 (2009)

[3.3] P. Pandey, A. P. Katsoulidis, I. Eryazici, Y. Wu, M. G. Kanatzidis, S. T. Nguyen, *Imine-Linked Microporous Polymer Organic Frameworks*, Chem. Mater., **22**, 4974-4979 (2010)

[3.4] Q. Liu, Z. Tang, M. Wu, Z. Zhou, *Design preparation and application of conjugated microporous polymers*, Polym. Int., **63**, 381-392 (2014)

[3.5] Y.-L. Wong, J. M. Tobin, Z. Xu, F. Vilela, *Conjugated porous polymers for photocatalytic applications*, J. Mater. Chem. A, **4**, 18677-18686 (2016)

[3.6] Q. Sun, B. Aguila, J. Perman, L. D. Earl, C. W. Abney, Y. Cheng, H. Wei, N. Nguyen, L. Wojtas, S. Ma, *Postsynthetically Modified Covalent Organic Frameworks for Efficient and Effective Mercury Removal*, J. Am. Chem. Soc., **139**, 2786-2793 (2017)

[3.7] J. Liu, K.-K. Yee, K. K.-W. Lo, K. Y. Zhang, W.-P. To, C.-M. Che, Z. Xu, *Selective Ag(I) Binding, H_2S Sensing, and White-Light Emission from an Easy-to-Make Porous Conjugated Polymer*, J. Am. Chem. Soc., **136**, 2818-2824 (2014)

[3.8] P. M. Budd, B. Ghanem, K. Msayib, N. B. McKeown, C. Tattershall, *A nanoporous network polymer derived from hexaazatrinaphthylene with potential as an adsorbent and catalyst support*, J. Mater. Chem., **13**, 2721-2726 (2003)

[3.9] S. Barlow, Q. Zhang, B. R. Kaafarani, C. Risko, F. Amy, C. K. Chan, B. Domercq, Z. A. Starikova, M. Y. Antipin, T. V. Timofeeva, *Synthesis, Ionisation Potentials and*

Electron Affinities of Hexaazatrinaphthylene Derivatives, Chem. Eur. J., **13**, 3537-3547 (2007)

[3.10] S. Skujins, G. Webb, *Spectroscopic and structural studies of some oxocarbon condensation products—I: Preparation and characterization of some substituted phenazines and quinoxalines*, Tetrahedron, **25**, 3935-3945 (1969)

[3.11] Y. Xu, S. Jin, H. Xu, A. Nagai, D. Jiang, *Conjugated microporous polymers: design, synthesis and application*, Chem. Soc. Rev., **42**, 8012-8031 (2013)

[3.12] J. Liu, J. Cui, F. Vilela, J. He, M. Zeller, A. D. Hunter, Z. Xu, *In situ production of silver nanoparticles on an aldehyde-equipped conjugated porous polymer and subsequent heterogeneous reduction of aromatic nitro groups at room temperature*, Chem. Commun., **51**, 12197-12200 (2015)

[3.13] N. Du, G. P. Robertson, I. Pinnau, M. D. Guiver, *Polymers of Intrinsic Microporosity Derived from Novel Disulfone-Based Monomers*, Macromolecules, **42**, 6023-6030 (2009)

[3.14] A. R. Oveisi, K. Zhang, A. Khorramabadi-zad, O. K. Farha, J. T. Hupp, *Stable and catalytically active iron porphyrin-based porous organic polymer: Activity as both a redox and Lewis acid catalyst*, Sci. Rep., **5**, 10621 (2015)

[3.15] S. Chassaing, V. Beneteau, P. Pale, *When CuAAC 'Click Chemistry' goes heterogeneous*, Catal. Sci. Technol., **6**, 923-957 (2016)

[3.16] K. Manna, T. Zhang, F. X. Greene, W. Lin, *Bipyridine- and Phenanthroline-Based Metal–Organic Frameworks for Highly Efficient and Tandem Catalytic Organic Transformations via Directed C–H Activation*, J. Am. Chem. Soc., **137**, 2665-2673 (2015)

[3.17] I. Maluenda, O. Navarro, *Recent Developments in the Suzuki-Miyaura Reaction: 2010–2014*, Molecules, **20**, 7528-7557 (2015)

[3.18] P. B. Tchounwou, C. G. Yedjou, A. K. Patlolla, D. J. Sutton, *Heavy Metals Toxicity and the Environment*, EXS, **101**, 133-164 (2012)

[3.19] *Lead Free Water, World Standards for allowable levels of lead in water*, 2015, accessed June 2018, <http://leadfreewater.com/world-standards/>

[3.20] S. De Gisi, G. Lofrano, M. Grassi, M. Notarnicola, *Characteristics and adsorption capacities of low-cost sorbents for wastewater treatment: A review*, Sustainable Materials and Technologies, **9**, 10-40 (2016)

[3.21] R. S. Sprick, J.-X. Jiang, B. Bonillo, S. Ren, T. Ratvijitvech, P. Guiglion, M. A. Zwijnenburg, D. J. Adams, A. I. Cooper, *Tunable Organic Photocatalysts for Visible-Light-Driven Hydrogen Evolution*, J. Am. Chem. Soc., **137**, 3265–3270 (2015)

[3.22] C. A. Martinez, S. Hu, Y. Dumond, J. Tao, P. Kelleher, L. Tully, *Development of a Chemoenzymatic Manufacturing Process for Pregabalin*, Org. Process Res. Dev., **12**, 392–398 (2008)

[3.23] L. R. Madivada, R. R. Anumala, G. Gilla, S. Alla, K. Charagondla, M. Kagga, A. Bhattacharya, R. Bandichhor, *An Improved Process for Pioglitazone and Its Pharmaceutically Acceptable Salt*, Org. Process Res. Dev., **13**, 1190-1194 (2009)

[3.24] B. Chen, L. Wang, S. Gao, *Recent Advances in Aerobic Oxidation of Alcohols and Amines to Imines*, ACS Catal., **5**, 5851-5876 (2015)

[3.25] S.-I. Murahashi, *Synthetic Aspects of Metal-Catalyzed Oxidations of Amines and Related Reactions*, *Angew. Chem., Int. Ed. Engl*., **34**, 2443-2465 (1995)

[3.26] A. Berlicka, B. Konig, *Porphycene-mediated photooxidation of benzylamines by visible light*, Photochem. Photobiol. Sci., **9**, 1359-1366 (2010)

[3.27] N. Kang, J. H. Park, K. C. Ko, J. Chun, E. Kim, H.-W. Shin, S. M. Lee, H. J. Kim, T. K. Ahn, J. Y. Lee, S. U. Son, *Tandem Synthesis of Photoactive Benzodifuran Moieties in the Formation of Microporous Organic Networks*, Angew. Chem., Int. Ed., **52**, 6228-6232 (2013)

[3.28] S. Kuster, T. Geiger, *Strategies and investigations on bridging squaraine dye units*, Dyes and Pigments, **95**, 657-670 (2012)

[3.29] L. Beverina, P. Salice, *Squaraine Compounds: Tailored Design and Synthesis towards a Variety of Material Science Applications*, Eur. J. Org. Chem., **2010**, 1207-1225 (2010)

[3.30] S. S. Pandey, T. Mizuno, S. K. Das, Y. Ogomi, S. Hayase, *Solution processable thin film organic photovoltaic cells based on far red sensitive soluble squaraine dyes*, Thin Solid Films, **522**, 401-406 (2012)

[3.31] M. Wainwright, *Therapeutic applications of near-infrared dyes*, Coloration Technology, **126**, 115-126 (2010)

[3.32] A. Yuan, J. Wu, X. Tang, L. Zhao, F. Xu, Y. Hu, *Application of near-infrared dyes for tumor imaging, photothermal, and photodynamic therapies*, J. Pharm. Sci., **102**, 6-28 (2013)

[3.33] A. Volkov, F. Nakonechny, M. Nisnevitch, *Polymer-Immobilized Photosensitizers for Continuous Eradication of Bacteria*, Int. J. Mol. Sci., **15**, 14984-14996 (2014)

DECLARATION

As equal primary author of this publication, I can confirm that a significant portion of the work to be my own. Work carried out by other students or collaborators has been outlined above.

Signature: _____

PUBLICATION 3

A nanoporous graphene analog for superfast heavy metal removal and continuous-flow visible-light photoredox catalysis

R. Xaio, J. M. Tobin, M. Zha, Y.-L. Hou, J. He, F. Vilela, Z. Xu

DOI: 10.1039/c7ta05534j

J. Mater. Chem. A, **2017**, *5*, 20180-20187

Abstract

We report a highly recyclable, 2D aromatic framework that offers a unique and versatile combination of photocatalytic activity and heavy metal uptake capability, as well as other attributes crucial for green and sustainable development technologies. The graphene-like open structure consists of fused tritopic aromatic building blocks (*i.e.,* hexaoxotriphenylene and hexaazatrinaphthylene) that can be assembled from readily available industrial materials without the need for transition metal catalysts. Besides fast and strong binding for Pb(II) ions (e.g., removing aqueous Pb ions below the drinkable limit within minutes), the alkaline N-heterocycle units of the robust and porous host is able to catalyse quantitatively Knoevenagel reactions in water. Furthermore, the fused donor-acceptor aromatic π-systems enable environmentally friendly photoredox catalyses (PRC) utilizing the safe and abundant visible light in a commercial flow reactor. Also discussed is a new metric for benchmarking the kinetic performance of sorbents in the context of heavy metal removal from drinking water.

Introduction

Due to their large surface areas, functional diversity and robust reusability, porous polymer frameworks (PPFs) are poised to address critical topics concerning clean environment, renewable energy and sustainable chemical processes [1]. Compared with coordination networks (aka MOFs) [2], the covalent PPFs offer better stability, and can be conveniently assembled without the need of crystallization. Besides the common uses of PPFs in gas sorption/storage and as catalysis supports [3], conjugated PPFs [1d, 4], with their extended π-systems, offer distinct advantages for energy storage/delivery [5], photocatalytic H_2 production [6], heterogeneous photocatalysis [7], and other light harvesting applications [7a, 8].

In spite of the rich functionality, most PPFs were designed to target a single, specific type of application, and a clear gap exists in the research of versatile PPFs that offer multiple capabilities for applications [9]. For example, even though heavy metal removal [10] and photocatalysis [7c, d] have been separately accomplished in some PPF systems, none has been reported to simultaneously address these two key sustainability topics on water purification and light harvesting. To promote the development of versatile PPFs for green applications, we here present an easy-to-make system (HOTT-HATN, Fig. 1) that features a broad array of green credentials, making for a notable example in integrating multiple sustainability criteria into the development of porous materials.

Besides cleaning up lead ions from water and capturing the safe and abundant visible light for the topical photoredox catalysis (PRC), the HOTT-HATN framework is simply assembled from low-cost building blocks without using toxic or expensive metal catalysts. In addition, the alkaline N donors of the polymer backbone also enables acid-base catalysis using water as a green reaction medium. Moreover, this robust framework can also be deployed as a highly efficient heterogeneous photocatalyst in a commercial flow reactor for optimal separation and recycling advantages. To our knowledge, such a wide-ranging green-chemistry profile remains unprecedented among PPF materials.

At a fundamental level, the fused, fully conjugated aromatic π-system of HOTT-HATN promotes electronic communication throughout the net, providing a versatile 2D electronic platform reminiscent of graphene. Unlike the all-carbon graphene system, the

O and N heteroatoms here constitute distinct electron donor-acceptor units. Such D-A units generally exhibit intense photoactivities (e.g., for light harvesting), and were utilized herein to drive photoredox reactions in quantitative yields. Moreover, the chelating pyridinyl N donors on the backbone π-system stand to anchor various metal species, so as to enrich the optical and electronic properties for wider applications.

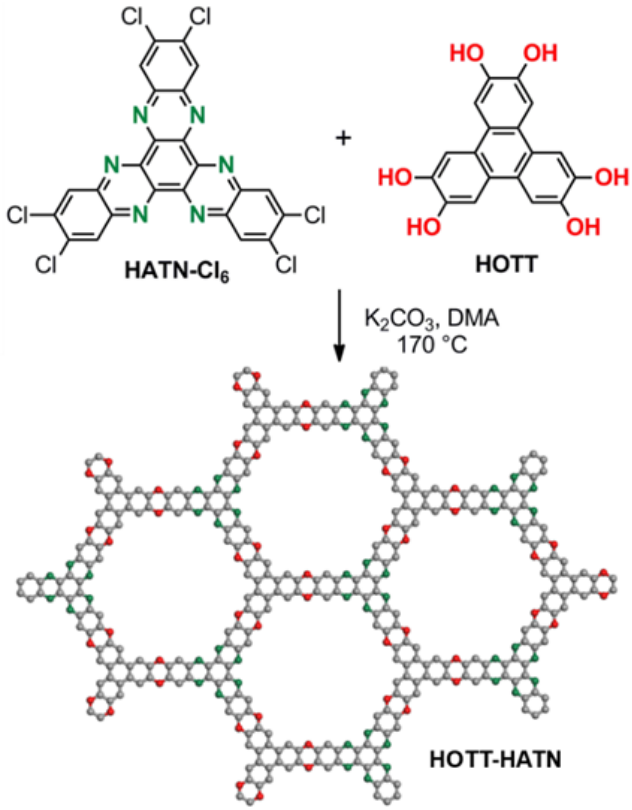

Fig. 1 The synthetic scheme of the honeycomb network of HOTT-HATN (shown in a ball-stick model; red sphere, O; green, N; grey, C).

Results

Preparation and Analysis of HOTT-HATN

HOTT-HATN was assembled using a high-yield, metal-free aromatic nucleophilic substitution [9-11], and simply involves heating the two monomers 2,3,6,7,10,11-hexahydroxytriphenylene (HOTT) and 2,3,8,9,14,15-hexachloro-5,6,11,12,17,18-hexaazatrinaphthylene (HATN-Cl_6, Fig. 1) under N_2 at 170°C for five days using K_2CO_3 as the base and DMA as the solvent. After purification *via* Soxhlet extraction, a dark red brown solid was recovered in a high yield (89%).

Results of CHN elemental analysis fits the composition $(C_{42}H_{12}O_6N_6)\cdot(H_2O)_{10}$, with $C_{42}H_{12}O_6N_6$ being that of the 2D net of Fig. 1 (see ESI for details). Energy dispersive X-ray spectra (EDX) reveals only a trace amount of Cl (< 0.2 atom %, Fig. S3), indicating the efficient displacement of the chloro groups [10a]. Thermogravimetric analysis (TGA, Fig. S4) reveals a stable mass up to 250°C, indicating a good thermal stability comparable to other PPFs [12]. The FT-IR peaks (Fig. S5) at 1600 cm^{-1} and at 1200 and 1250 cm^{-1} correspond to the C=N and C-O stretches, respectively. Solid state ^{13}C NMR CP-MAS analysis (Fig. S6) confirmed the fully aromatic system with four dominant peaks at 110.68, 126.27 142.45 and 147.07 ppm, indicating some of the 7 different carbon atoms of HOTT-HATN were not resolved in this measurement. Solid state UV-Vis analysis of the polymer features broad absorbance in the visible spectrum with a λ_{max} at 460 nm (Fig. S7).

PXRD established HOTT-HATN as an amorphous solid (Fig. S8), while SEM and TEM images (Fig. S9, S10) revealed highly textured, layer-like morphology. N_2 sorption (at 77 K) experiments confirm the porous character of HOTT-HATN, with a typical type-II N_2 gas adsorption isotherm (Fig. 2) revealing a BET surface area of 526.5 $m^2\cdot g^{-1}$. QSDFT analysis on pore size distribution and pore volume showed an average pore width of 0.52 nm and a micropore volume of 0.579 $cm^3\cdot g^{-1}$ (Fig. S11).

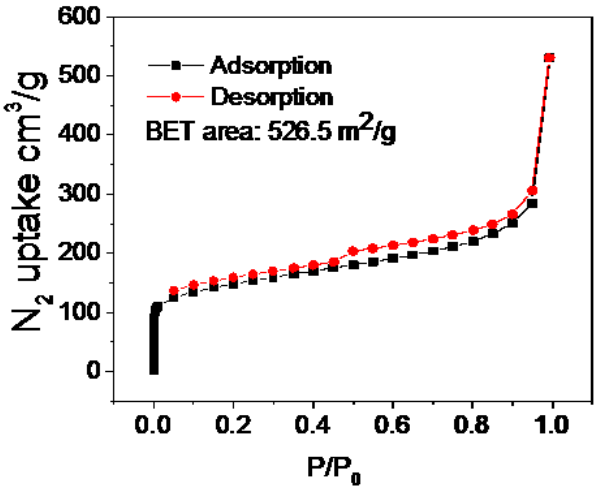

Fig. 2 N_2 isotherm at 77 K of an activated sample of HOTT–HATN.

Removal of Lead from Water

Lead is a cumulative poisonous pollutant that can affect nearly every system in the body. Children under 6 and pregnant women are most susceptible to the negative

health effects of lead exposure. The removal of lead and other toxic heavy metals from water sources therefore remains a high priority in the public health sector [13]. In this regard, HOTT-HATN, with its dense array of bipyridine donors (e.g., these are commonly used for metal chelation and catalysis in solution chemistry [14]) offers clear potential. Moreover, the HOTT-HATN powder is freely dispersible in water, which further facilitates green chemistry applications. Such hydrophilicity can be attributed to the polar aza and oxo groups built into the polymer grid. Incidentally, hydrophilicity is rare among PPFs and often has to be achieved through special synthetic design or modification [15].

The metal uptake studies here follow our long-standing interest in developing metal-binding frameworks for environmental and catalytic applications [3g, 11a]. To probe lead sorption kinetics, a powder sample of HOTT-HATN (20 mg) was added to an aqueous solution of $Pb(NO_3)_2$ (10 ppm; 50 ml) and stirred at room temperature (rt). The Pb remaining in the solution was quantified at specific time intervals *via* ICP-AES. Within 100 seconds the Pb content already dropped below 0.60 ppm, with over 94% of the total Pb removed by the polymer sorbent; within 5 minutes, the Pb content was already reduced beyond the detection limit (15-20 ppb) of the instrument (Table S2, Fig. S12). Such superfast kinetics is on par with a thiol-equipped PPF system for Hg removal (e.g., removing over 99.8% of heavy metal within 5 min, in similar conditions regarding the solvent/sorbate/sorbent ratio) [10b], and can be attributed to the large porosity as well as the distinct hydrophilicity of the O and N components that help the water phase better permeate the polymer matrix. Compared with the thiol-laced PPF systems [10b, c], HOTT-HATN is easier to prepare, and offers better stability, being less prone to oxidation.

Correct interpretation of kinetics data in adsorption studies is of topical interests [16]. The present PPF system, with its large porosity and well-defined binding sites, appears fitting for the Langmuir model. The kinetic data indeed fit the first order equation $\ln(C_t) = -k_1 t + \ln(C_i)$ (Fig. 3a inset), which can be rationalized using the Langmuir model $dC_t/dt = kq_tC_t$ [17], where C_t ($mg \cdot L^{-1}$) refers to the remaining Pb in the solution, $q_t$the number of unoccupied sites of the adsorbent at time t (min), and k ($g^{-1}min^{-1}$) the rate constant—with q_t approximated to be a constant.

Such an approximation is justified in the present condition, in which excess adsorbent was used so that the sorption sites greatly outnumber the Pb ions, e.g., in the above test the sorbent (20 mg) offers sites for 1.34 mg of Pb uptake, over 2.6 times the Pb ions present (0.5 mg). In general, drinking water treatment usually involves heavy metal pollutants at very low concentrations (e.g., sub-ppm), and the adsorbent is deployed in large excess to fully suppress the residual heavy metal content. In other words, only a small fraction of the binding sites of the adsorbent will be occupied, which further justifies the first order assumption. The linear plot based on the first five data points (the Pb became undetectable by the 5th point) yields a k_1 of 1.86 min^{-1} (Fig. 3a inset), with the corresponding half-life being 0.37 min.

The kinetic data also fit the pseudo-second-order kinetic model [10c, 18] $dq_t/dt = k_{p2}(q_e - q_t)^2$ with the following linear fit:

$$\frac{t}{q_t} = \frac{1}{k_2 q_e^2} + \frac{t}{q_e} \qquad (1)$$

where q_t (mg.g^{-1}) is the amount of Pb adsorbed at time t (min), and q_e (mg.g^{-1}) is the Pb adsorbed at equilibrium, and k_2 (g.mg^{-1}min^{-1}) is the adsorption rate constant (Fig. S13).

Such a fit, however, should be taken with caution [16a, c]. Theoretically, the pseudo second order model works best when the total number of the metal ions equals that of the adsorption sites, i.e., $C_iV = q_e$, namely $C_tV = C_iV - q_t = q_e - q_t$, so that $(q_e-q_t)^2 = (C_iV-q_t)(q_e-q_t) = (1/V)(C_i-q_t/V)(q_e-q_t) = (1/V)(C_t)(q_e-q_t)$. When excess sorbent was used (as is often the case), we have $C_iV \ll q_e$ and the first order description instead becomes physically more meaningful.

Second, the linearity between t/q_t and t/q_e is often gratuitous, especially in fast kinetics where $1/(k_2q_e^2)$ is of small, negligible values, rendering $t/q_t \approx t/q_e$. At longer time points, t/q_e becomes ever greater than $1/(k_2q_e^2)$, making the linearity trivial; also at longer times, the adsorption approaches equilibrium, and the reverse process—the desorption—becomes significant, further invalidating the one-way pseudo second order assumption [16a]. Indeed, with excess adsorbent (*i.e.*, $C_iV \ll q_e$), the q_e value derived from superficially linear plot between t/q_t and t/q_e is simply the total meal ions present, having nothing to do with the number of available adsorption sites physically present.

To properly assess the sorbent kinetics in connection with the removal of trace heavy metal contaminants, we suggest that excess adsorbent be used in order to mimic the actual deployment of the adsorbent, and to simplify the kinetics to the first order regime. Also, data points should be collected at the early stage so as to avoid the complication from desorption. For example, with the distribution quotient $Q_d = (C_i - C_t)V/C_t m < K_d/100$, the desorption rate is no greater than 1% that of adsorption, and can thus be omitted. As adsorption isotherm is routinely measured, adsorption capacity q_e and K_d derived thereby provide valuable guidance and cross-check for the kinetic studies. For benchmarking the kinetic performance, the first order rate constant k_1 can be divided by the amount of sorbent m (g). In the above case, k_1/m=1.86/0.020=93 $min^{-1} \cdot g^{-1}$.

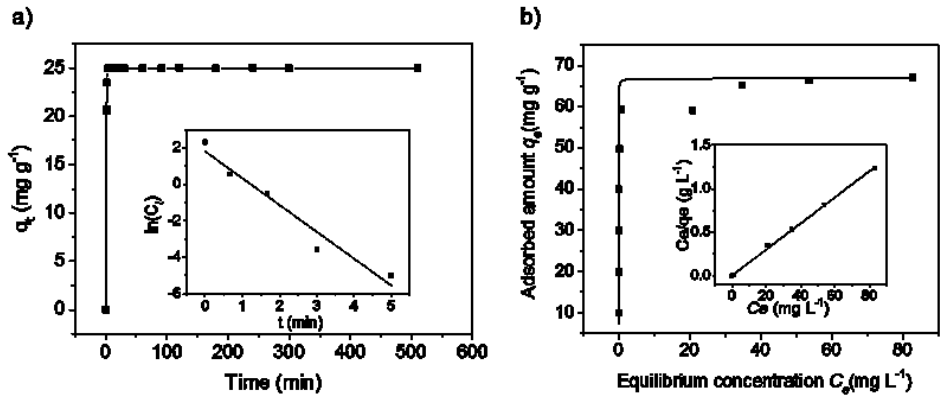

Fig. 3 a) Adsorption curve of Pb(II) versus contact time with HOTT-HATN in aqueous solution. Inset: linear first-order kinetics plot for the initial four points (the Pb levels are below detection limit starting from t = 5 min). b) A Pb (II) Langmuir sorption isotherm for HOTT-HATN. Inset: linear expression fitted with the Langmuir model.

In the isotherm study, a series of 5.0 mL aqueous $Pb(NO_3)_2$ solutions were loaded into glass vials (each containing 5.0 mg HOTT-HATN). The mixtures were shaken at 200 rpm for 4.5 h at rt, then filtered by PTFE membrane. The filtrates were tested *via* ICP-AES. The adsorbed amount of Pb at equilibrium (q_e, $mg \cdot g^{-1}$) was calculated with the data in Table S3:

$$q_e = \frac{(C_i - C_e) \times V}{m} \qquad (2)$$

where C_i and C_e correspond to initial and equilibrium concentration of Pb in water ($mg \cdot L^{-1}$), V stands for the solution volume (mL) and m the sorbent mass (g). The

adsorption isotherm plots fit the Langmuir isotherm model (with a correlation coefficient above 0.998; see also Figure 3b):

$$\frac{C_e}{q_e} = C_e \times \frac{1}{q_{max}} + \frac{1}{K_L q_{max}} \qquad (3)$$

where a plot of C_e/q_e to C_e (see Figure 3b inset) yields the sorption capacity q_{max} (mg·g^{-1}) as the reciprocal of the slope. The q_{max} value thus obtained (66.8 mg·g^{-1}) is equivalent to 0.28 Pb(II) ion per HATN core, suggesting that a large fraction of bipy donors remain unbonded under these conditions.

The strong affinity for Pb(II) ions is demonstrated by the distribution coefficient (K_d), which is defined as:

$$K_d = \frac{C_i - C_f}{C_f} \times \frac{V}{m} \qquad (4)$$

with C_i and C_f being the initial and final Pb concentrations, V the volume of the solution (mL) and m the amount of sorbent (g). From the isotherm data (e.g., Table S3, Entry 4), K_d was estimated to be greater than 2×10^6 mL·g^{-1}. The effective Pb removal capability is consistent with the strong donor character of the chelating pyridinyl groups. Specifically, such chelating ability is greatly enhanced by the strongly electron-releasing dioxin-like oxo groups built into the conjugated backbone. To better demonstrate the essential role of the nitrogen donors in Pb uptake, a sample of the HOTT–HATN polymer was treated with acetic acid to help mask the alkaline pyridinyl sites; consequently, the Pb uptake capacity was found to drop down to about 30 mg g^{-1} (see Fig. S14), being less than half that of the pristine sample. Such sensitivity of the Pb uptake properties to acid treatment indicates that the Pb uptake is affected mostly through the alkaline N donor functions.

Compared with other sorbent systems for Pb removal [19], the fast kinetics and high K_d value of HOTT–HATN clearly rank among the best, even though the uptake capacity is modest. The extraordinary K_d value, however, is especially useful for removing Pb from drinking water (e.g., down to 15 ppb as is set by the US Environmental Protection Agency) [20]. Specifically, with $K_d = 2 \times 10^6$ ml g^{-1}, for one liter of water with

Pb at 150 ppb (*i.e.,* 10 times the legal limit), only 4.5 mg of the HOTT–HATN polymer is needed to reduce the Pb content to 15 ppb. Further to the advantage of product economics, the HOTT–HATN sorbent can be reactivated after stripping off the trapped Pb by sequential washing with the household items of HCl (e.g., 10%), ammonia (5%) and water (see the ESI for details, *e.g.*, Fig. S15).

The selectivity of heavy metal uptake was examined using a solution containing Hg^{2+}, Pb^{2+}, Cu^{2+}, Cd^{2+} and Zn^{2+} at 4.8–6.4 ppm (see Tables S4 and S5), together with Ca^{2+} and Na^{+} at 20 and 53 ppm (to mimic the higher natural occurrence of these two metals), respectively. As shown in Fig. S16, the strongest preferences were observed for Hg^{2+} and Cu^{2+} with over 95% removal achieved within one hour, while the adsorption of Pb^{2+} continues to be effective, with about 90% removal achieved in spite of the various competing ions present at higher concentrations. Notably, a large majority of the low-toxicity ions of Zn^{2+}, Ca^{2+} and Na^{+} were not adsorbed, pointing to further relevance for drinking water treatment. The uptake of the toxic Cd^{2+} ions, however, was only modest, with 65% of the Cd^{2+} ions found to persist in the solution under these experimental conditions.

Knoevenagel Condensation Reactions

We now explore HOTT-HATN for green and sustainable uses in chemical syntheses. Besides convenient product separation (generally associated with heterogeneous catalysts), its metal-free nature resolves the metal leaching and contamination issue that besets especially electronic and pharmaceutical industries [6b]. The hydrophilicity of HOTT-HATN (e.g., dispersible in water), together with its oxo-strengthened pyridinyl donors, also makes for efficient water-based heterogeneous organocatalysis. The well-known Knoevenagel condensation offers a useful test reaction, because it is amenable to base catalysis, and it is an important C-C bond formation method for fine chemicals and pharmaceuticals [21].

The Knoevenagel condensations involved adding an aryl aldehyde (0.25 mmol), malononitrile (0.375 mmol) and HOTT-HATN (5.0 mg) to 1.0 mL of deionized water (with 0.2 mL of $CHCl_3$ added for substrates with poor water solubility). The reaction vessel was then heated to 40 °C and shaken at 250 rpm for 2.5-3 hours, and the conversion rate determined *via* ^1H NMR (see ESI). A benchmark reaction was first performed with

benzaldehyde, resulting in 100% conversion after 2.5 hours. Also examined are controls for solvents (chloroform and acetonitrile) in the absence of water as well as a reaction in the absence of HOTT-HATN (Table 1). Interestingly, replacing water with pure $CDCl_3$ dramatically slows down the reaction, *e.g.*, even after 12 hours, only 67% conversion was observed, while straight acetonitrile resulted in (slightly higher) 80% conversion in similar conditions. Also, the absence of HOTT-HATN resulted in a much lower yield (*i.e.,* cf entries 1 and 4), verifying HOTT-HATN as a useful organocatalyst.

Table 1 Knoevenagel condensation of aldehydes with malononitrile catalyzed by HOTT-HATN.[a]

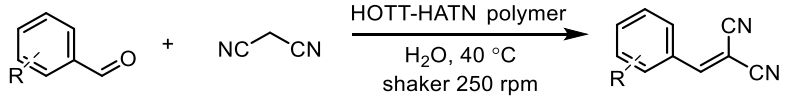

Entry	Aldehyde	Reaction time (h)	Conversion (%)[b]
1	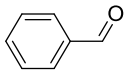	2.5	>99
2[c]	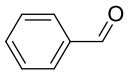	12	67
3[d]	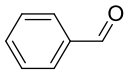	12	80
4[e]	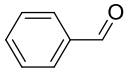	2.5	62
5[f]	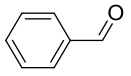	2.5	>99
6	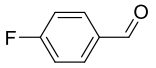	2.5	>99
7	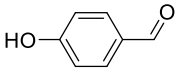	3	>99
8	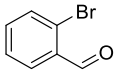	3	>99
9	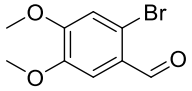	3	>99
10	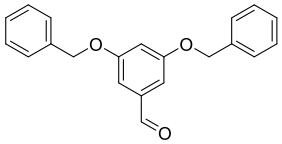	15	82

[a]Reaction conditions: aldehyde (0.25 mmol), malononitrile (0.375 mmol), H_2O (1.0 mL), $CHCl_3$ (0-0.2 mL), HOTT-HATN (5 mg), mechanical shaker (250 rpm), 40 °C. [b]Conversion calculated *via* ^1H NMR analysis. [c]$CDCl_3$ (no water added), 50 °C by heating block, stirring. [d]Acetonitrile (no water added), 50 °C by heating block, stirring. [e]In water without HOTT-HATN. [f]HOTT-HATN polymer re-used in the 5th cycle.

Substituted benzaldehydes (4-fluoro, 2-bromo, 4-hydroxy and 2-bromo-4,5-dimethoxy) were also tested to open the scope of application. Each of these showed full conversion within 3 hours. The bulkier substrate (3,5-bis(phenylmethoxy)-benzaldehyde,

entry 10), however, showed a lower conversion of 82% even after 15 hours, presumably due to its difficulty in penetrating the HOTT-HATN matrix. Finally, HOTT-HATN was recovered, washed and reused throughout five catalytic cycles of the model reaction. No significant decrease in catalytic activity was observed therein, further establishing HOTT-HATN as a green and reusable heterogeneous catalyst with efficiency comparing favorably with various other systems [22].

Aerobic Photooxidation of Benzylamines

Provided with appropriate photocatalysts, light—especially abundant sunlight—offers an attractive alternative energy input (*vis-à-vis* heat) for driving chemical transformations. In spite of various CMP solids studied as photocatalyts for organic reactions, the field remains wide open [23]. For example, rigorously metal-free CMP photocatalysts are rare, and the continuous flow reactors, well-suited to enable scale-up and to overcome other operational challenges of photochemistry, are curiously often left out in CMP photocatalysis studies.

The oxo and aza functions built into the fully conjugated backbone of HOTT-HATN constitute distinct donor-acceptor units that give rise to broad intense absorption in the visible region (Fig. S7), indicating potential photocatalytic activities. The following continuous-flow synthesis using HOTT-HATN as a photocatalyst aims to combine a unique set of green-chemistry merits. The efficient production of imines thus achieved is also of practical interest in the synthesis of nitrogen-rich biologically active molecules [23, 24].

For the photooxidation, a benzyl amine (0.5 mmol) and HOTT-HATN (5.0 mg, *ca* 6.5 μmol of the HATT unit) were added to 10 mL of acetonitrile. The suspension was then cycled through a commercial photochemical flow reactor at rt (Vapourtec Ltd., Fig. S15) in the presence of oxygen and visible light (>400 nm, Cool White LED module, Fig. 4) until the amine was consumed. The conversion rate was measured *via* ^{1}H NMR spectroscopy (see ESI).

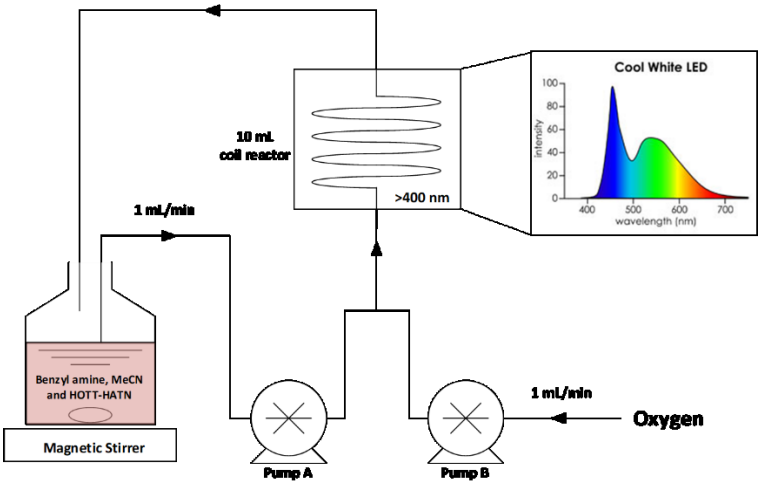

Fig. 4 Schematic representation of the experimental set-up using the easy-Photochem flow reactor from Vapourtec Ltd. with the spectrum for the Cool White LED module (>400 nm).

As seen in Table 2, a series of benzylic amines were examined. A screening was first performed with benzylamine, resulting in full conversion to the imine product within 6 hours. Control experiments, removing light, photocatalyst or oxygen, were also performed to verify the role of each of these components. Furthermore, heating (at 60°C) under the initial reaction conditions did not significantly change the final conversion of the reactions. The use of a narrow wavelength light source (420 ± 2 nm) reduced the reaction time to 4 h. However, due to the abundance of white light sources (as in household lighting), we opted to continue with the Cool White LED module.

Substituted benzyl amines (4-methoxy, 4-methyl, 4-fluoro, 4-chloro, and 4-trifluoromethyl) were also tested to probe scope of substrates. While we note some variation in the time required for full conversion, the differences in these times were not greatly significant. Specifically, benzyl amines with electron-donating groups took slightly less time to reach full conversion (5 hours), while those with strong electron-withdrawing groups took longer (7 h).

Recently, the photooxidation of benzylamine has been described as proceeding through either a photoredox or singlet oxygen ($^1O_2$) mechanism [25]. Through a photoredox mechanism, the amine substrate transfers an electron to the triplet excited state of HOTT-HATN. The photoreduced HOTT-HATN subsequently interacts with O_2 to form a superoxide radical anion ($O_2^{\bullet-}$), and thus returning to the ground state. The amine radical is then oxidized *via* $O_2^{\bullet-}$, where the intermediate amine is able to react with

the initial amine substrate to form the desired product. Conversely, the production of $^1O_2$ proceeds *via* an energy transfer between O_2 and the triplet excited state of HOTT-HATN. The amine substrate is then oxidized by $^1O_2$ and proceeds to the product in a similar manner as described for the photoredox mechanism.

Table 2. Aerobic oxidative coupling of benzyl amines photocatalyzed by HOTT-HATN.[a]

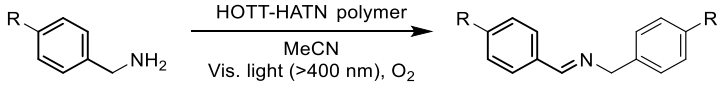

Entry	Amine	Reaction time (h)	Conversion (%)[b]
1	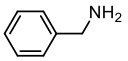	6	>99
2[c]	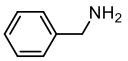	6	2
3[d]	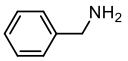	6	14
4[e]	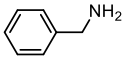	6	-
5[f]	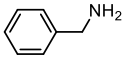	4	>99
6[g]	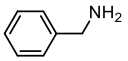	6	92
7	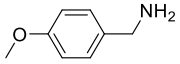	5	>99
8	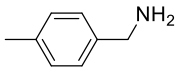	5	>99
9	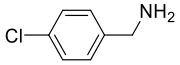	6	>99
10	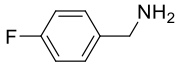	6	>99
11	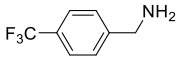	7	>99

[a]Reaction conditions: benzyl amine (0.5 mmol), HOTT-HATN (5.0 mg), acetonitrile (10 mL), 30 °C, visible cool white led module (>400 nm), in flow (1 mL.min^{-1}), O_2 (1 mL.min^{-1}). [b]Conversion calculated *via* ^{1}H NMR spectroscopy. [c]Reaction performed in the absence of light. [d]Reaction performed in the absence of HOTT-HATN. [e]Reaction performed in the absence of O_2, under N_2 atmosphere. [f]Reaction performed using a 420 nm led module. [g]HOTT-HATN in acetonitrile irradiated for 30 h open to air prior to addition of benzylamine.

To better understand how the reaction proceeds, the ability for HOTT-HATN to be used for the production of $^1O_2$ was investigated through the conversion of *α*-terpinene to ascaridole, as described in our previous work [26]. After 2 h irradiation with a Cool

White LED Module (>400 nm), the reaction showed a 62 % conversion to the ascaridole product *via* ^{1}H NMR spectroscopy, indicating $^1O_2$ production under experimental conditions similar to those presented for the photooxidation experiments. Therefore, we can reasonably conclude that the photooxidation of benzylamines is most likely proceeding through a $^1O_2$ mechanism.

Finally, we investigated both the photostability and productivity of HOTT-HATN. To test the material for photostability, HOTT-HATN was added to acetonitrile and irradiated for 30 hours in the presence of oxygen. The irradiated suspension was then used for the model reaction where 92% conversion was achieved within 6 h, establishing that HOTT-HATN maintains high catalytic activity, and therefore photostability, even after prolonged exposure to high intensity light. FTIR analysis of the polymer before and after 36 h of intense irradiation (Fig. S31) presented with virtually no change, further indicating the stability of HOTT-HATN. We also note that $^1O_2$ is generated throughout the entirety of the irradiation period, cementing HOTT-HATN as not only photostable, but also inert under highly oxidative conditions. Furthermore, with the same amounts of HOTT-HATN (5.0 mg) and solvent, the benzylamine can be raised in concentration (from 0.05) up to 0.08 mmol·mL^{-1} and still demonstrate full conversion within 6 hours (higher concentrations require longer reaction time), equivalent to a TON above 120. Overall, the photocatalytic activity of HOTT-HATN compares well with other photocatalysts (both metal-rich and metal-free) for oxidative coupling of benzyl amines [23].

Conclusions

In conclusion, an impressive array of green credentials has been achieved from a highly reusable, fused-aromatic framework efficiently assembled via a transition-metal-free substitution reaction between the building blocks of HOTT and HATN-Cl$_6$. In particular, the oxo and the aza sites built into the conjugated polymer backbone provide a powerful electron donor-acceptor couple that effects the photocatalysis of aerobic amine oxidation using visible light when applied in a commercial flow reactor. Moreover, the oxo units also enhance the basicity of the pyridinyl aza units, so as to effectively catalyze the Knoevenagel reaction in water, and aid in the speedy removal of Pb from water to acceptable drinking levels set by worldwide environmental organizations. This latter capability is especially of note not only because of the convenient recyclability of the

polymer matrix (e.g., by washing with HCl), but also because of the widespread presence of lead as a pollutant in the environment.

Acknowledgements

This work is supported by a GRF grant of the Research Grants Council of Hong Kong SAR (Project 11303414), the National Natural Science Foundation of China (21471037) and the Guangdong Natural Science Funds for Distinguished Young Scholars (15ZK0307). We acknowledge Vapourtec Ltd for their technical support.

References

[1] *(a)* S. Das, P. Heasman, T. Ben and S. Qiu, *Chem. Rev.*, 2017, **117**, 1515-1563; *(b)* D. Wu, F. Xu, B. Sun, R. Fu, H. He and K. Matyjaszewski, *Chem. Rev.*, 2012, **112**, 3959-4015; *(c)* P. Kaur, J. T. Hupp and S. T. Nguyen, *ACS Catal.*, 2011, **1**, 819-835; *(d)* Y. Xu, S. Jin, H. Xu, A. Nagai and D. Jiang, *Chem. Soc. Rev.*, 2013, **42**, 8012-8031; *(e)* N. Chaoui, M. Trunk, R. Dawson, J. Schmidt and A. Thomas, *Chem. Soc. Rev.*, 2017, **46**, 3302-3321.

[2] *(a)* C. Wang, D. Liu and W. Lin, *J. Am. Chem. Soc.*, 2013, **135**, 13222-13234; *(b)* M. Zhang, Z.-Y. Gu, M. Bosch, Z. Perry and H.-C. Zhou, *Coord. Chem. Rev.*, 2015, **293-294**, 327-356; *(c)* V. Guillerm, D. Kim, J. F. Eubank, R. Luebke, X. Liu, K. Adil, M. S. Lah and M. Eddaoudi, *Chem. Soc. Rev.*, 2014, **43**, 6141-6172; *(d)* P. Deria, J. E. Mondloch, O. Karagiaridi, W. Bury, J. T. Hupp and O. K. Farha, *Chem. Soc. Rev.*, 2014, **43**, 5896-5912; *(e)* D. J. Tranchemontagne, Z. Ni, M. O'Keeffe and O. M. Yaghi, *Angew. Chem., Int. Ed.*, 2008, **47**, 5136-5147; *(f)* J. He, M. Zeller, A. D. Hunter and Z. Xu, *CrystEngComm*, 2015, **17**, 9254-9263.

[3] *(a)* F. Goettmann, A. Fischer, M. Antonietti and A. Thomas, *Angew. Chem. Int. Ed.*, 2006, **45**, 4467-4471; *(b)* Y. Zhang, Y. Zhang, Y. L. Sun, X. Du, J. Y. Shi, W. D. Wang and W. Wang, *Chem. Eur. J.*, 2012, **18**, 6328-6334; *(c)* C. Lu, T. Ben and S. Qiu, *Macromol. Chem. Phys.*, 2016, **217**, 1995-2003; *(d)* L. Chen, Y. Yang and D. Jiang, *J. Am. Chem. Soc.*, 2010, **132**, 9138-9143. *(e)* L. Chen, Y. Yang, Z. Guo and D. Jiang, *Adv. Mater.*, 2011, **23**, 3149-3154; *(f)* R. Palkovits, M. Antonietti, P. Kuhn, A. Thomas and F. Schüth, *Angew. Chem., Int. Ed.*, 2009,

48, 6909-6912; *(g)* J. Liu, J. M. Tobin, Z. Xu and F. Vilela, *Polym. Chem.*, 2015, **6**, 7251-7255; *(h)* P. Zhang, Z. Weng, J. Guo and C. Wang, *Chem. Mater.*, 2011, **23**, 5243-5249.

[4] J.-X. Jiang, F. Su, A. Trewin, C. D. Wood, N. L. Campbell, H. Niu, C. Dickinson, A. Y. Ganin, M. J. Rosseinsky, Y. Z. Khimyak and A. I. Cooper, *Angew. Chem., Int. Ed.*, 2007, **46**, 8574-8578.

[5] F. Vilela, K. Zhang and M. Antonietti, *Energy Environ. Sci.*, 2012, **5**,7819-7832.

[6] *(a)* G. Zhang, Z.-A. Lan and X. Wang, *Angew. Chem., Int. Ed.*, 2016, **55**, 15712-15727; *(b)* R. S. Sprick, J.-X. Jiang, B. Bonillo, S. Ren, T. Ratvijitvech, P. Guiglion, M. A. Zwijnenburg, D. J. Adams and A. I. Cooper, *J. Am. Chem. Soc.*, 2015, **137**, 3265-3270; *(c)* K. Kailasam, M. B. Mesch, L. Moehlmann, M. Baar, S. Blechert, M. Schwarze, M. Schroeder, R. Schomaecker, J. Senker and A. Thomas, *Energy Technol.*, 2016, **4**, 744-750.

[7] *(a)* Y.-L. Wong, J. M. Tobin, Z. Xu and F. Vilela, *J. Mater. Chem. A*, 2016, **4**, 18677- 18686; *(b)* Z. Xie, C. Wang, K. E. de Krafft and W. Lin, *J. Am. Chem. Soc.*, 2011, **133**, 2056-2059; *(c)* J. Luo, X. Zhang and J. Zhang, *ACS Catal.*, 2015, **5**, 2250-2254; *(d)* J.-X. Jiang, Y. Li, X. Wu, J. Xiao, D. J. Adams and A. I. Cooper, *Macromolecules*, 2013, **46**, 8779-8783.

[8] C. Gu, N. Huang, Y. Chen, L. Qin, H. Xu, S. Zhang, F. Li, Y. Ma and D. Jiang, *Angew. Chem., Int. Ed.*, 2015, **54**, 13594-13598.

[9] J. Liu, K.-K. Yee, K. K.-W. Lo, K. Y. Zhang, W.-P. To, C.-M. Che and Z. Xu, *J. Am. Chem. Soc.*, 2014, **136**, 2818-2824.

[10] *(a)* P. M. Budd, B. Ghanem, K. Msayib, N. B. McKeown and C. Tattershall, *J. Mater. Chem.*, 2003, **13**, 2721-2726; *(b)* B. Li, Y. Zhang, D. Ma, Z. Shi and S. Ma, *Nat. Commun.*, 2014, **5**, 5537; *(c)* Q. Sun, B. Aguila, J. Perman, L. D. Earl, C. W. Abney, Y. Cheng, H. Wei, N. Nguyen, L. Wojtas and S. Ma, *J. Am. Chem. Soc.*, 2017, **139**, 2786-2793; *(d)* N. Huang, L. Zhai, H. Xu and D. Jiang, *J. Am. Chem. Soc.*, 2017, **139**, 2428-2434.

[11] *(a)* J. Liu, J. Cui, F. Vilela, J. He, M. Zeller, A. D. Hunter and Z. Xu, *Chem. Commun.*, 2015, **51**, 12197-12200; *(b)* N. Du, G. P. Robertson, I. Pinnau and M. D. Guiver, *Macromolecules*, 2009, **42**, 6023-6030; *(c)* A. R. Oveisi, K. Zhang, A. Khorramabadi-zad, O. K. Farha and J. T. Hupp, *Sci. Rep.*, 2015, **5**, 10621.

[12] Y. Xu, S. Jin, H. Xu, A. Nagai and D. Jiang, *Chem. Soc. Rev.*, 2013, **42**, 8012-8031.

[13] P. B. Tchounwou, C. G. Yedjou, A. K. Patlolla and D. J. Sutton, *EXS*, 2012, **101**, 133-164.

[14] C. Kaes, A. Katz and M. W. Hosseini, *Chem. Rev.*, 2000, **100**, 3553-3590.

[15] *(a)* H. Urakami, K. Zhang and F. Vilela, *Chem. Commun.*, 2013, **49**, 2353-2355; *(b)* B. C. Ma, S. Ghasimi, K. Landfester, F. Vilela and K. A. I. Zhang, *J. Mater. Chem. A*, 2015, **3**, 16064-16071; *(c)* S. Ghasimi, K. Landfester and K. A. I. Zhang, *ChemCatChem*, 2016, **8**, 694-698.

[16] *(a)* H. N. Tran, S.-J. You, A. Hosseini-Bandegharaei and H.-P. Chao, *Water Res.*, 2017, **120**, 88-116; *(b)* W. Plazinski, W. Rudzinski and A. Plazinska, *Adv. Colloid Interface Sci.*, 2009, **152**, 2-13; *(c)* G. Alberti, V. Amendola, M. Pesavento and R. Biesuz, *Coord. Chem. Rev.*, 2012, **256**, 28-45.

[17] S. Azizian, *J. Colloid Interface Sci.*, 2004, **276**, 47-52.

[18] *(a)* R. Rostamian, M. Najafi and A. A. Rafati, *Chem. Eng. J.*, 2011, **171**, 1004-1011; *(b)* Y.-S. Ho, *J. Hazard. Mater.*, 2006, **136**, 681-689.

[19] *(a)* J. Li, X. Liu, Q. Han, X. Yao and X. Wang, *J. Mater. Chem. A*, 2013, **1**, 1246–1253; *(b)* A. Mahapatra, B. Mishra and G. Hota, *J. Hazard. Mater*., 2013, **258**, 116–123; *(c)* W. Li, D. Chen, F. Xia, J. Z. Tan, J. Song, W.-G. Song and R. A. Caruso, *Chem. Commun*., 2016, **52**, 4481–4484; (d) S. Zhang, H. Yang, H. Huang, H. Gao, X. Wang, R. Cao, J. Li, X. Xu and X. Wang, *J. Mater. Chem. A*, 2017, **5**, 15913–15922; *(e)* H. Saleem, U. Rafique and R. P. Davies, *Microporous Mesoporous Mater*., 2016, **221**, 238–244; *(f)* Y. Ni, L. Jin, L. Zhang and J. Hong, *J. Mater. Chem*., 2010, **20**, 6430–6436.

[20] Lead Free Water, World Standards for allowable levels of lead in water, http://leadfreewater.com/world-standards/, accessed March 16, 2017.

[21] *(a)* L. R. Madivada, R. R. Anumala, G. Gilla, S. Alla, K. Charagondla, M. Kagga, A. Bhattacharya and R. Bandichhor, *Org. Process Res. Dev.*, 2009, **13**, 1190-1194; *(b)* C. A. Martinez, S. Hu, Y. Dumond, J. Tao, P. Kelleher and L. Tully, *Org. Process Res. Dev*, 2008, **12**, 392-398; *(c)* S. D. Walker, C. J. Borths, E. DiVirgilio, L. Huang, P. Liu, H. Morrison, K. Sugi, M. Tanaka, J. C. S. Woo and M. M. Faul, *Org. Process Res. Dev*, 2011, **15**, 570-580.

[22] *(a)* B. Li, M. Chrzanowski, Y. Zhang and S. Ma, *Coord. Chem. Rev.*, 2016, **307**, 106-129; *(b)* W. Ge, X. Wang, L. Zhang, L. Du, Y. Zhou and J. Wang, *Catal. Sci. Technol.*, 2016, **6**, 460-467; *(c)* E. M. Schneider, M. Zeltner, N. Kranzlin, R. N. Grass and W. J. Stark, *Chem. Commun.*, 2015, **51**, 10695-10698; *(d)* J. Gascon, U. Aktay, M. D. Hernandez-Alonso, G. P. M. van Klink and F. Kapteijn, *J. Catal.*,

2009, **261**, 75-87; *(e)* T. I. Reddy and R. S. Varma, *Tetrahedron Lett.*, 1997, **38**, 1721-1724.

[23] B. Chen, L. Wang and S. Gao, *ACS Catal.*, 2015, **5**, 5851-5876.

[24] S.-I. Murahashi, *Angew. Chem., Int. Ed. Engl.*, 1995, **34**, 2443-2465.

[25] *(a)* A. Berlicka and B. Konig, *Photochem. Photobiol. Sci.*, 2010, **9**, 1359-1366; *(b)* N. Kang, J. H. Park, K. C. Ko, J. Chun, E. Kim, H.-W. Shin, S. M. Lee, H. J. Kim, T. K. Ahn, J. Y. Lee and S. U. Son, *Angew. Chem., Int. Ed.*, 2013, **52**, 6228-6232.

[26] J. M. Tobin, J. Liu, H. Hayes, M. Demleitner, D. Ellis, V. Arrighi, Z. Xu and F. Vilela, *Polym. Chem.*, 2016, **7**, 6662-6670.

Supporting Information

General Procedure

All reagents and starting materials employed in this work are purchased from commercial sources (Aldrich, Acros, TCI, Riedel-de Haën, Fluorochem, and J&K; solvents from Merck, RCI, and ACS), and used without further purification. ^{1}H NMR and ^{13}C NMR measurements were performed on a 400 and a 300 MHz Bruker superconducting-magnet high-field NMR spectrometer at room temperature. Solid State ^{13}C CP-MAS measurements were carried out using a Bruker Avance 400 spectrometer operating at 100.6 MHz using a Bruker 4 mm double resonance probe-head operating at a spinning rate of 7 kHz. Elemental Analysis (CHN) was obtained with an Elementar VARIO Micro Cube Carbon-Hydrogen- Nitrogen Analyzer. Infrared Spectroscopy (FT-IR) spectra were recorded on a Nicolet Avatar 360 FT-IR spectrophotometer. Powder X-ray Diffraction (PXRD) data for the polymer solid were collected in reflection mode at room temperature on an Inel Equinox 1000 X-ray diffractometer (Inel, France) equipped with a CPS 180 detector using monochromated Cu-Kα1 (λ = 1.5406 Å) radiation. The X-ray tube operated at a voltage of 30 kV and a current of 30 mA. Solid State UV/Vis absorption spectra were measured on a PerkinElmer Lambda 25 system using a Labsphere RSA-PE-20 reflectance spectroscopy integration sphere. Thermogravimetric analysis (TGA) of the HOTT-HATN was carried out with a PerkinElmer STA6000 under nitrogen flow (20 mL·min^{-1}). A heating rate of 2 °C·min^{-1} was applied and an empty Al_2O_3 crucible being used as the reference. Gas sorption and porosity analysis were carried out using a Quantachrome Autosorb iQ gas sorption analyser. Scanning electron microscopy (SEM) was carried out on Philips XL30 Esem-FEG, (FEI Company, The Netherlands) equipped with an energy-dispersive x-ray microanalysis (EDX) system (EDAX Phoenix system, EDAX Inc., Mahwah NJ, USA). Transmission electronic microscopy (TEM) was conducted on a Philips Technai 12 Transmission Electron Microscope with an accelerating voltage of 120 KV.

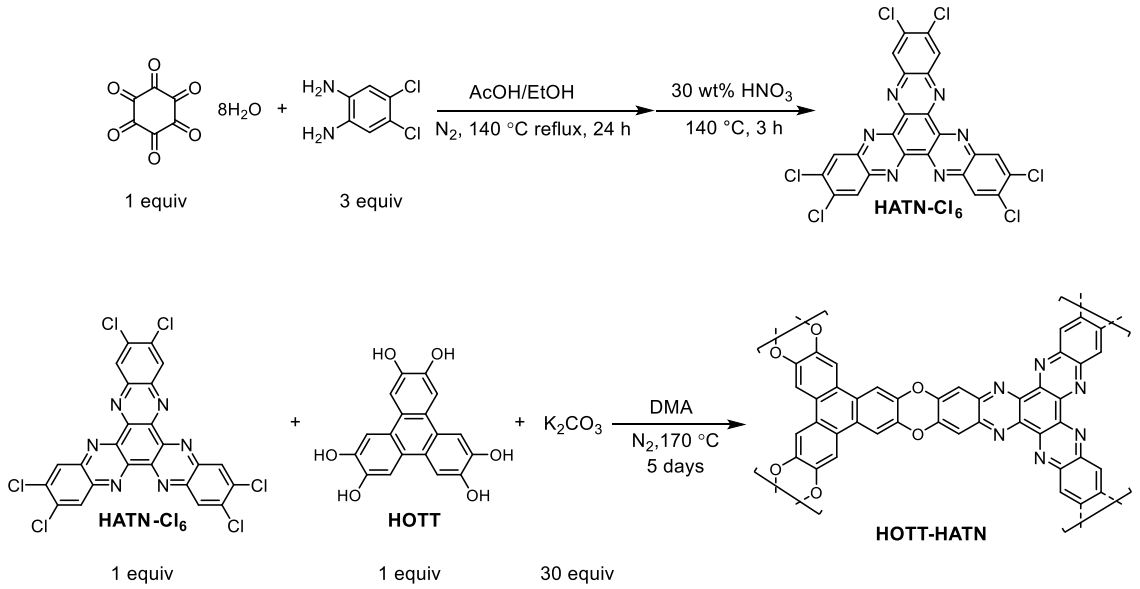

Scheme S1 Synthetic procedure of HOTT-HATN polymer.

Synthesis of 2,3,8,9,14,15-Hexachloro-5,6,11,12,17,18-hexaazatrinaphthylene (HATN-Cl_6)

Hexaketocyclohexane octahydrate (529 mg, 1.69 mmol), 4,5-dichloro-1,2-phenylenediamine (900 mg, 5.08 mmol) and a magnetic stirrer were loaded into a 25ml two-neck round-bottom flask fitted with a condenser and connected to a Schlenk line, evacuated and back-filled with N_2 (three times for purging). Glacial acetic acid and ethanol (12 mL, 1:1 v/v), previously bubbled with N_2 for 5 min, was then transferred into the flask under N_2 via cannula. After refluxed under N_2 at 140 °C for 24 hours, the reaction mixture was filtered and washed with 20 mL hot glacial acetic acid. The solid was then refluxed with 15 mL of 30% nitric acid for 3 hours at 140 °C. The solid of the reaction mixture was filtered, washed with 10 mL deionized water and ethanol, and dried under vacuum. The product HATN-Cl_6 is yellow-green solid (780 mg, 78% yield). ^{1}H NMR (300MHz, $CDCl_3$): δ 8.80 (6H, s) [1, 2].

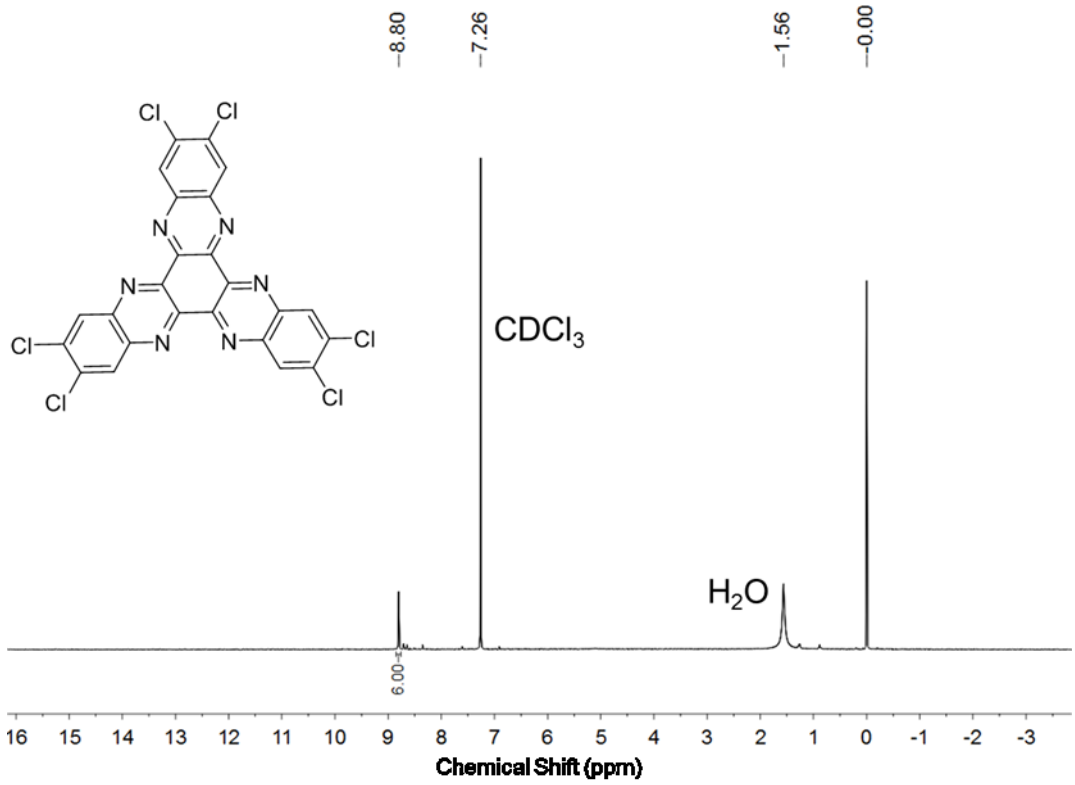

Fig. S1 ^{1}H NMR spectrum of HATN-Cl_6 with a singlet at 8.80 ppm indicating 6 equivalent aromatic hydrogen nuclei.

Synthesis of HOTT-HATN Polymer

2,3,6,7,10,11-Hexahydroxytriphenylene (HOTT) (130 mg, 0.40 mmol), HATN-Cl_6 (236 mg, 0.40 mmol), potassium carbonate (1.66 g, 12.0 mmol) and a magnetic stirrer were loaded into a 50 mL two-neck round bottom flask fitted with a condenser and connected to a Schlenk line, evacuated and back-filled with N_2 (three times for purging). N,N-Dimethylacetamide (10 mL) was bubbled with N_2 for 5 min before injected into the flask *via* cannula under N_2. The reaction was heated to 170 °C in an oil bath under reflux for 5 days. The reaction mixture was then poured into 300 mL deionized water and stirred at 50 °C for 2h before collection by centrifuge. The polymer was washed for several cycles until a pH of 7 was obtained. The mixture was filtered and washed with deionized water (50 mL), ethanol (50 mL) and CH_2Cl_2 (50 mL). A dark reddish brown powder was obtained after drying [3].

Activation of HOTT-HATN Polymer

A thimble (e.g., made from folding filter paper) containing the HOTT-HATN solid sample (400 mg) was loaded into the main chamber of a Soxhlet extractor. The Soxhlet extractor was connected onto a 250-mL round bottom flask S4 containing methanol (150 mL), and then equipped with a condenser. The flask was heated to 130 °C with a heating block for 2 days. The solvent was then replaced by clean tetrahydrofuran and extract heated at 130 °C for 1 day. The filter paper was then taken out and the solid was dried in air to give the activated HOTT-HATN sample (248 mg, 89.2% yield). Solid state ^{13}C NMR CP-MAS (100 MHz): δ 147.07, 142.45, 126.27, 110.68.

Elemental Analysis

A very small amount of Cl can be detected by EDX with atom number ratio lower than 0.2%. CHN elemental analysis of the activated sample found [C (57.14%), H (4.72%), N (10.70%)]. A fitting formula $(C_{42}H_{12}O_6N_6)\cdot(H_2O)_{10}$ gives a calculated profile as [C (57.54%), H (3.68%), N (9.59%)], which is largely consistent with the formation of the HOTT-HATN polymer as depicted in Fig. S2. The presence of water guests is also consistent with the TGA plot, which features significant weight loss at the low temperature region (e.g., <200 °C); however, the water content is likely to be rather variable due to the porous nature of the polymer solid, as well as air humidity and other experimental conditions

Table S1 CHN analysis of activated HOTT-HATN sample.

Entry	N [%]	C [%]	H [%]	C/N ratio	C/H ratio
1	10.72	57.11	4.724	5.3272	12.0899
2	10.67	57.17	4.725	5.3579	12.0978
Average	10.70	57.14	4.72	5.34	12.09

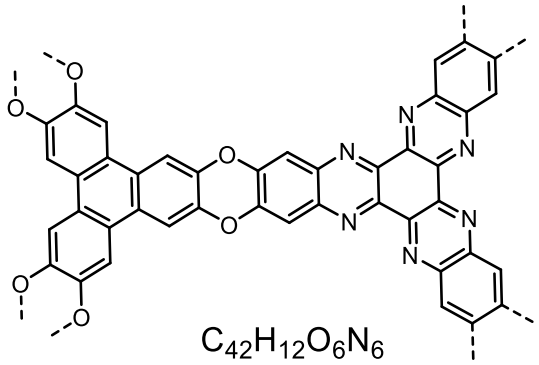

Fig. S2 A repeating unit of the HOTT-HATN polymer framework, with the composition shown also in a condensed formula.

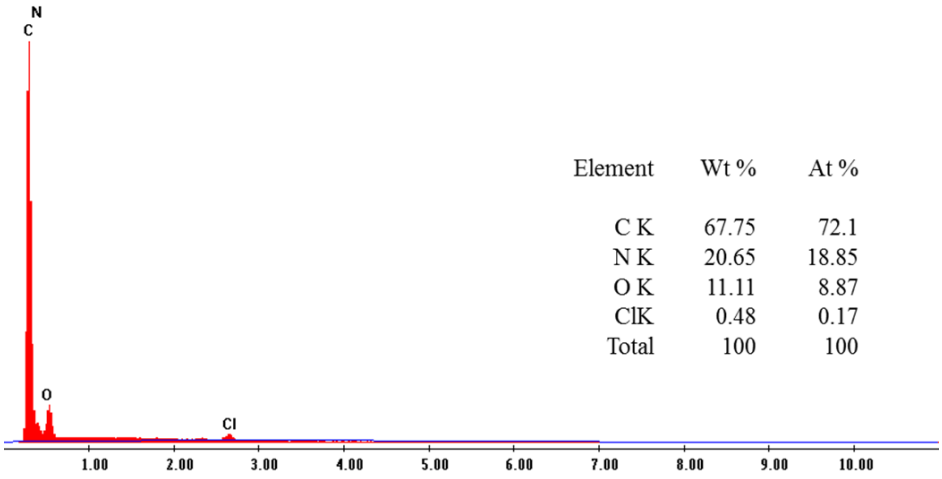

Element	Wt %	At %
C K	67.75	72.1
N K	20.65	18.85
O K	11.11	8.87
ClK	0.48	0.17
Total	100	100

Fig. S3 An EDX spectrum of an activated HOTT-HATN polymer.

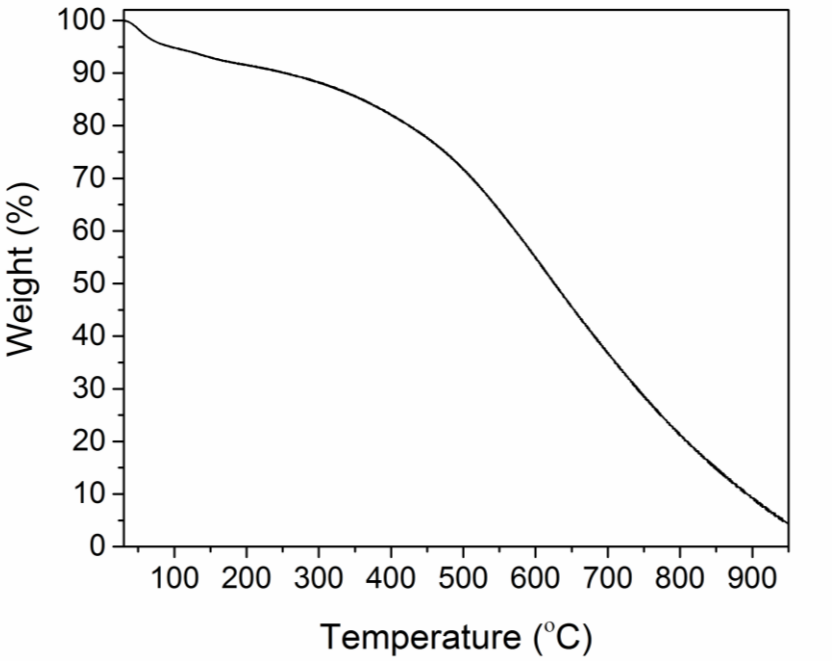

Fig. S4 A thermogravimetric analysis (TGA) plot of an activated sample of HOTT-HATN under N_2 stream (flow rate: 20 ml.min^{-1}). The heating rate is 2 °C.min^{-1}.

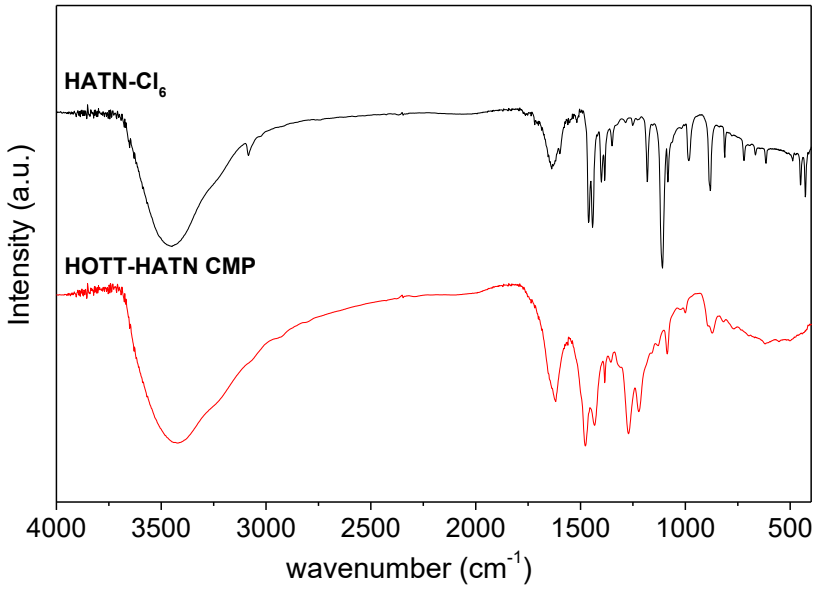

Fig. S5 FT-IR spectra of HATN-Cl_6 and the polymer solid HOTT-HATN.

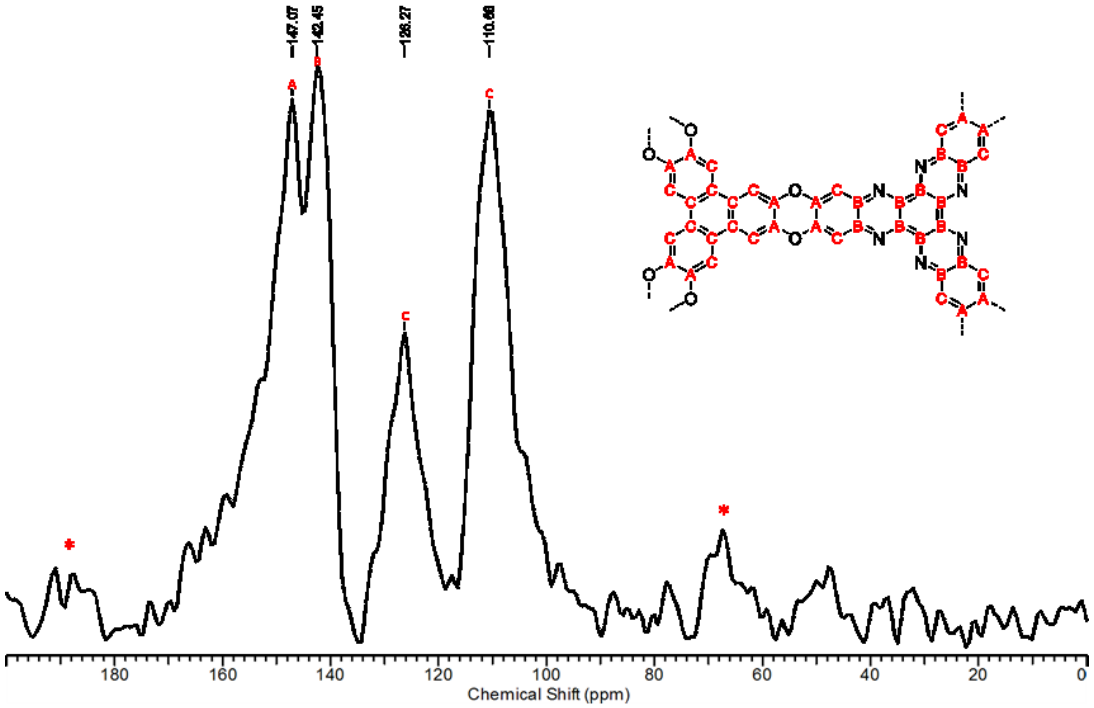

Fig. S6 Solid state ^{13}C NMR of HOTT-HATN (δ147.07 (C-O), 142.45 (C-N), 126.27, 110.68 (aromatic-*C*)). Peaks denoted by (*) indicate the presence of side bands.

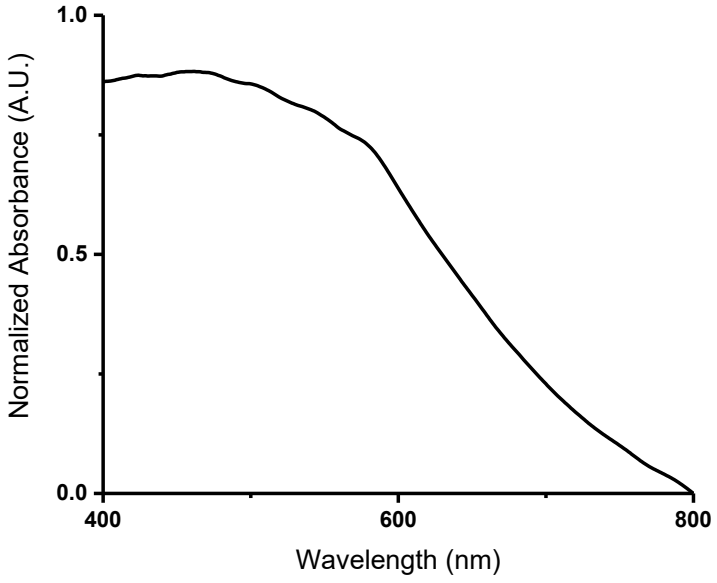

Fig. S7 A solid state UV-Vis spectrum of the HOTT-HATN polymer.

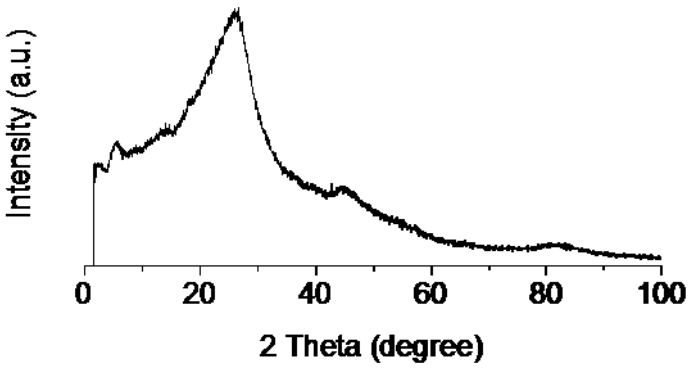

Fig. S8 An X-ray powder pattern (Cu Kα λ= 1.5418 Å) of an activated HOTT-HATN sample.

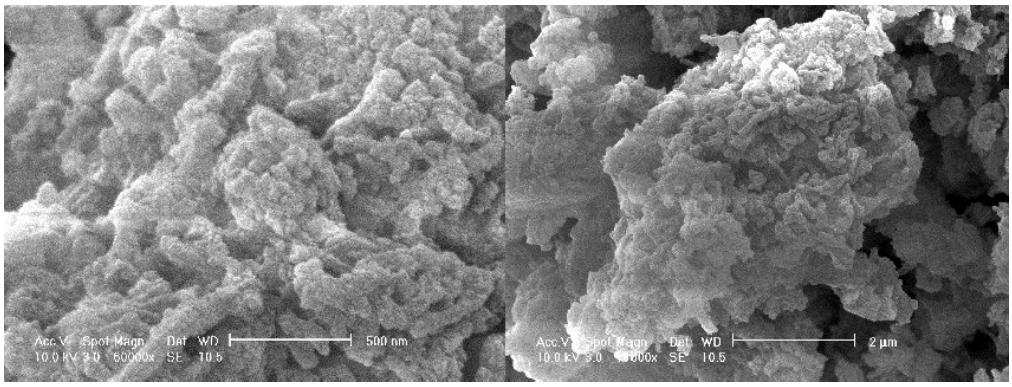

Fig. S9 Two SEM images of the activated HOTT-HATN polymer (with the magnification factors included).

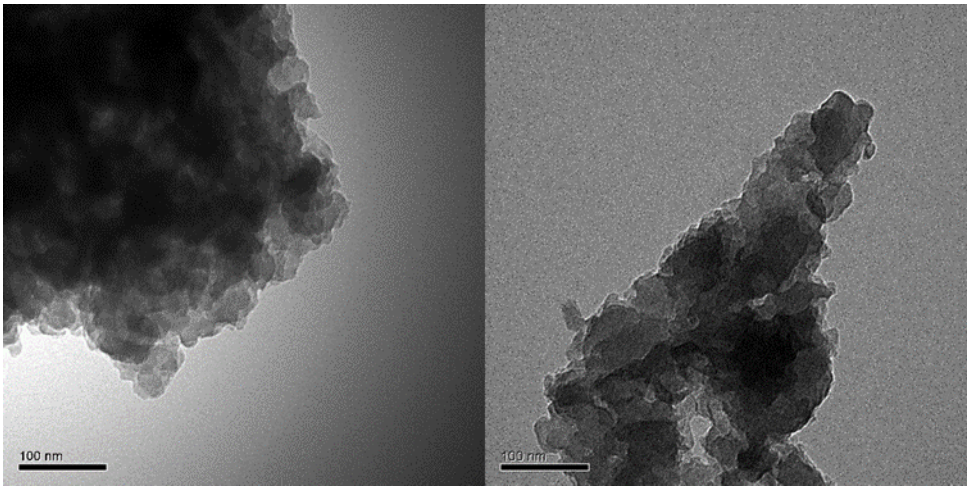

Fig. S10 Two TEM images of the activated HOTT-HATN polymer.

Gas Sorption

Pore analysis of the activated HOTT-HATN sample was performed both using N_2 at 77 K (P/P_0 range of 1×10^{-5} to 0.995). Initial data analysis was done using AS1Win and QuadraWin 5.05 software. The activated HOTT-HATN sample displayed a typical type-II gas adsorption isotherm for N_2 with a Brunauer-Emmett-Teller (BET) surface area of 526 $m^2\ g^{-1}$ (Fig. 2). QSDFT analysis (Pore Size Distribution and Pore Volume) of the N_2 adsorption isotherm (77 K) was performed using a commercialized model (N_2 at 77K on silica; cylinder pore; QSDFT equilibrium model). The PSD and pore volume analysis of N_2 showed an average pore width of 0.52 nm and a micropore volume of 0.579 $cm^3\ g^{-1}$ (Fig. S11).

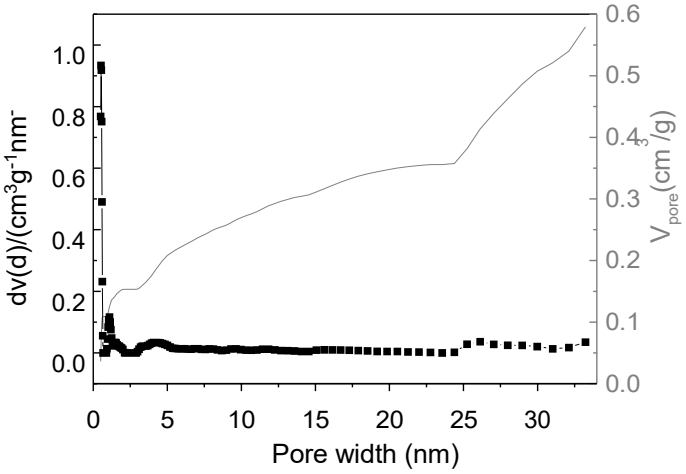

Fig. S11 Pore size distribution and pore volume of an activated HOTT-HATN solid.

Removal of Lead from Water – Kinetic and Isotherm Studies

Kinetic Study of Pb(II) Sorption

A 50 mL solution containing 10 ppm Pb [in form of $Pb(NO_3)_2$] was prepared with deionized water and loaded into a round bottom flask with a magnetic stirrer. HOTT-HATN (20 mg) was added and the solution was stirred vigorously at room temperature. Samples were removed from the suspension with a dropper at intervals and quickly filtered over 0.45-μm membrane filter. The concentration of Pb remaining in the sample was determined by ICP-AES.

Table S2 Pb concentrations at various times observed in a kinetic study of Pb uptake by the HOTT-HATN absorbent.

Time (min)	Concentration of Pb (ppm)
0	10.0
0.67	1.74
1.67	0.585
3	0.029
5	0.007*
7	-0.002*
10	-0.006*
15	-0.004*
20	-0.004*
30	-0.006*
60	-0.005*
90	-0.007*
120	-0.004*
180	-0.006*
240	-0.004*
300	-0.004*
510	-0.004*

* Lead concentration below the detection limit of ICP-AES (15-20 ppb).

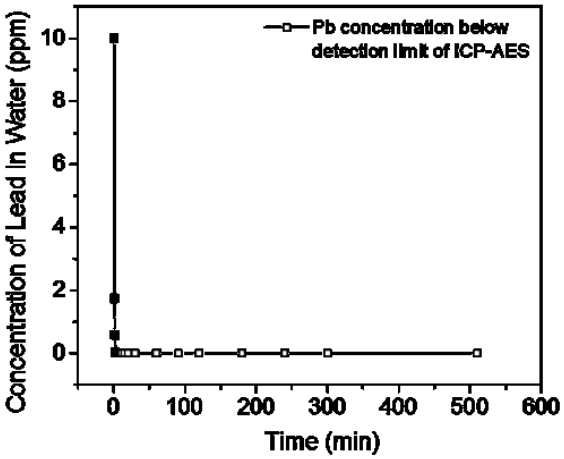

Fig. S12 A kinetic study plot (concentration vs. time) of Pb uptake by the HOTT-HATN polymer. The neighboring data points are manually connected for easier visualization. The black and empty boxes represent instrument readouts above and below the detection limits of the instrument.

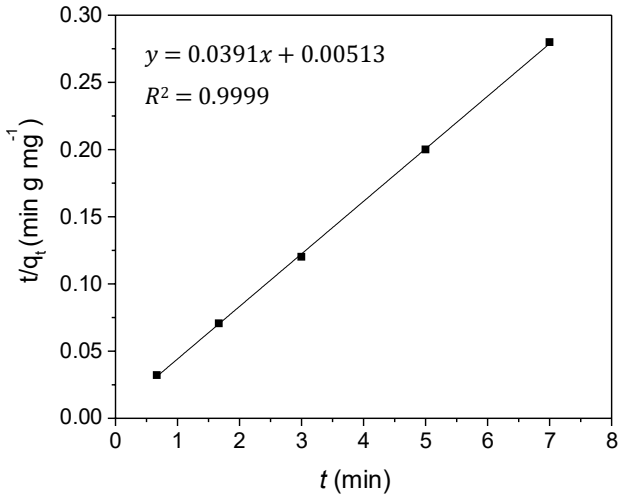

Fig. S13 A pseudo-second-order kinetic plot for Pb(II) adsorption. Starting from the 5th point (t = 7.0 min), C_t drops below ICP detection limit, the q_t value of 25 mg·g^{-1} is used here for the point at (t = 7.0 min).

Isotherm Study of Pb(II) Sorption

A series of 5.0 mL aqueous $Pb(NO_3)_2$ solutions (as listed in Table S3) were loaded into glass vials where 5.0 mg HOTT-HATN polymer was added. The vials were shaken at 200 rpm for 4.5 h at room temperature, then separated over a filter membrane separately. The filtrates were tested *via* ICP-AES.

Table S3. Tabulated isotherm data of Pb sorption by the HOTT-HATN polymer

Entry	Initial concentration (C_i) ($mg.L^{-1}$)	Equilibrium concentration (C_e) ($mg.L^{-1}$)
1	10	0.005
2	20	0.001
3	30	0.003
4	40	0.001
5	50	0.149
6	60	0.644
7	80	20.82
8	100	34.82
9	120	53.63
10	150	82.85

* Lead concentration below the detection limit of ICP-AES.

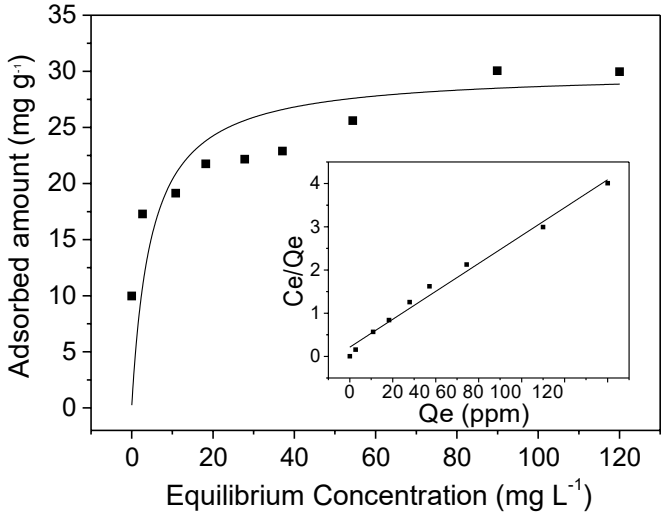

Fig. S14 A Pb(II) Langmuir sorption isotherm of an acetic acid-treated HOTT-HATN sample for illustrating the key role of the alkaline N donors: after treating HOTT-HATN with acetic acid, the Langmuir sorption isotherm as shown here indicates that Pb sorption capacity q_{max} was reduced to be 30 $mg \cdot g^{-1}$, which is less than half of the pristine sample (66.8 $mg \cdot g^{-1}$). Inset: linear expression fitted with the Langmuir model.

Stripping of Pb from Pb-loaded HOTT-HATN

HOTT-HATN polymer (10 mg) with Pb previously loaded (67.6 $mg \cdot g^{-1}$) was loaded in a glass vial. A 10% w/w HCl aqueous solution (3.0 mL) was added. The glass vial was covered and shaken at 200 rpm at room temperature for 4 h and then filtered. The powder was washed with deionized water until the pH was neutral. This was followed by an acetone wash and the polymer was dried *in vacuo*. The extracted sample was characterized *via* EDX analysis (Fig. S10). The EDX spectrum indicates that most of Pb is successfully stripped from the polymer matrix with only a trace amount (0.03 atom%) of Pb left. The Pb-stripped polymer thus obtained, after activated by stirring in a 5 wt% ammonia solution, and washing by water, continues to feature strong heavy metal uptake capabilities (*e.g.*, removing over 95% of Hg(II) within 1.5 hours from a water sample originally containing Hg(II) at about 5.0 ppm).

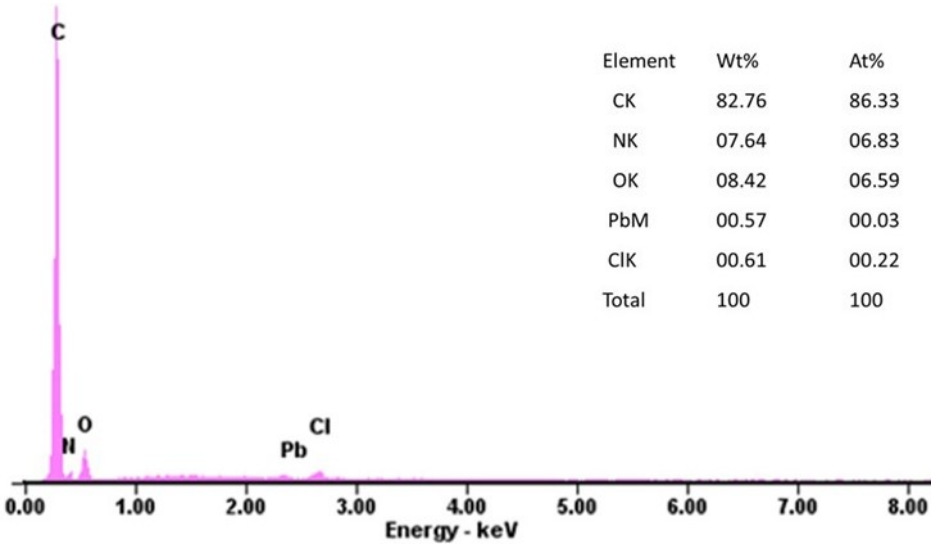

Fig. S15 An EDX spectrum of a Pb-loaded HOTT-HATN polymer sample after being stripped of Pb by HCl washing.

Selectivity Study

100 mL of a mixed solution of Hg^{2+}, Pb^{2+}, Cu^{2+}, Zn^{2+}, Cd^{2+}, Ca^{2+}, Na^{+} nitrate or chloride was loaded into a 250-mL round bottom flask with a magnetic stirrer. The solution was under vigorous stirring while 100 mg of HOTT-HATN polymer was added. Samples were taken out at intervals and quickly filtered over syringe filter membrane and tested by ICP-AES.

Table S4 Tabulated metal concentrations at various times observed in a selectivity study of the HOTT-HATN polymer as absorbent.

t	Zn	Hg	Cu	Na	Pb	Cd	Ca
min	mg/L	mg/L	mg/L	mg/L	mg/L	mg/L	mg/L
0	5.650	5.900	6.358	53.336	4.880	5.952	20.141
2	4.254	1.753	3.478	55.217	2.605	4.522	20.000
6	4.169	0.937	2.582	54.300	2.008	4.398	20.326
10	4.108	0.602	1.886	54.591	1.548	4.103	20.127
30	4.238	0.351	1.049	53.090	1.084	3.920	19.995
60	4.200	0.236	0.658	52.237	0.841	3.901	19.782
210	4.284	0.141	0.295	51.985	0.611	3.890	19.333
450	4.284	0.109	0.209	50.996	0.575	3.870	18.998

Table S5 Tabulated remaining metal percentage at various times observed in a selectivity study of the HOTT-HATN polymer as absorbent.

t	Zn	Hg	Cu	Na	Pb	Cd	Ca
min	%	%	%	%	%	%	%
0	100.0	100.0	100.0	100.0	100.0	100.0	100.0
2	75.3	29.7	54.7	103.5	53.4	76.0	99.3
6	73.8	15.9	40.6	101.8	41.1	73.9	100.9
10	72.7	10.2	29.7	102.4	31.7	68.9	99.9
30	75.0	6.0	16.5	99.5	22.2	65.9	99.3
60	74.3	4.0	10.3	97.9	17.2	65.5	98.2
210	75.8	2.4	4.6	97.5	12.5	65.4	96.0
450	75.8	1.8	3.3	95.6	11.8	65.0	94.3

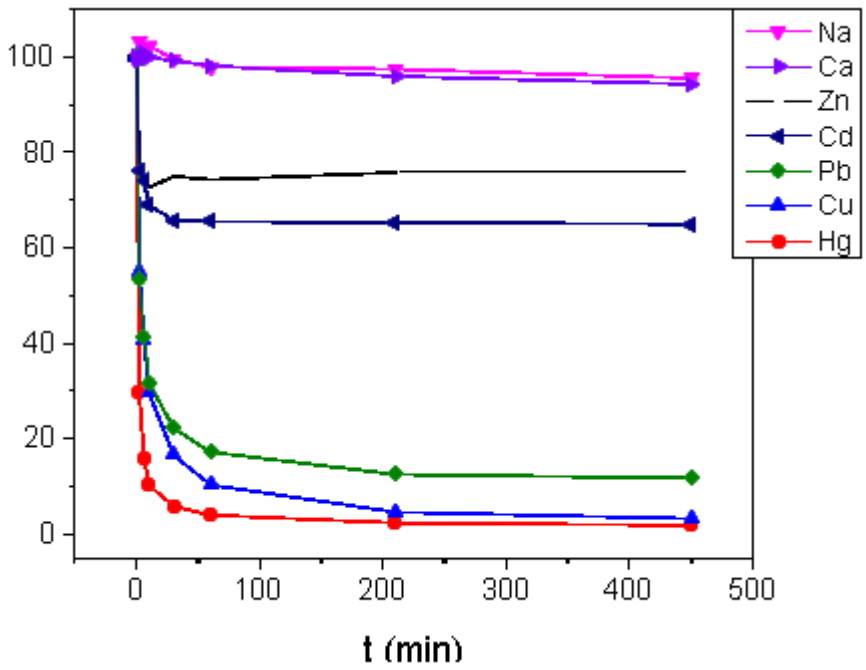

Fig. S16 A kinetic study plot (remained percentage vs. time) of selectivity test by the HOTT-HATN polymer adsorbent.

Typical Conditions for Heterogeneous Catalytic Knoevenagel Condensation

An aldehyde substrate (0.25 mmol), malononitrile (25 mg, 0.375 mmol), deionized water (1.0 mL) and HOTT-HATN polymer (5.0 mg) were loaded in a glass vial. Note that a small amount of chloroform (0.2 mL) was also added for solid aldehyde substrates or aldehyde substrates with poor solubility in water, e.g., entries 8, 9 and 10 of Table 1. The vial was then sealed and shaken at 250 rpm at 40 °C for several hours (as specified in Table 1). The polymer was separated *via* filtration and washed with dichloromethane (3 mL x 3). The filtrated was extracted with dichloromethane three times, and the combined organic layer were washed with deionized water three times and dried over anhydrous $MgSO_4$. The mixture was then filtered and solvent was removed under vacuum to give the crude product. Conversion of the condensation reaction was determined by ^1H NMR analysis.

General Procedure for Recycling HOTT-HATN

After finishing the catalytic reaction, HOTT-HATN polymer was recovered by washing with acetone, then filtered, washed with acetone again and dried under vacuum. A new batch of starting materials were loaded into a glass vial for the next catalytic cycle. The

recyclability of HOTT-HATN heterogeneous catalyst was tested at least five times *via* this method without any significant decreases in catalytic activity.

Aerobic photooxidation of benzylamine and derivatives

A benzylamine (0.5 mmol), HOTT-HATN (5.0 mg) and acetonitrile (MeCN, 10 mL) were added to a flask equipped with a magnetic stir bar. The mixture was sonicated for 3 minutes to ensure even dispersion of the polymer. The dispersion was pumped using a peristaltic pump through the commercial photochemical reactor (Vapourtec Ltd.) equipped with a white light LED lamp (λ > 400 nm, Fig. S15) at a flow rate of 1 mL·min^{-1}. Concurrently, oxygen was pumped through a second pump at the same flow rate. The dispersion and the oxygen then mixed *via* a T-junction prior entering the photochemical reactor. The reaction mixture was cycled through the system until consumption of the benzyl amine was determined *via* TLC (EtOAc:Hexane v/v 1:1). When starting material was no longer present the reaction was stopped. The reaction mixture was filtered *via* syringe filter and evaporated and the residue diluted with $CDCl_3$ for ^{1}H NMR analysis.

Continuous Flow Chemistry Equipment (Vapourtec, Ltd.)

Fig. S17 Easy-Photochem flow system from Vapourtec Ltd. equipped with cool white light LED module emitting light at >400 nm.

^{1}H NMR spectra of Knoevenagel Condensation Products

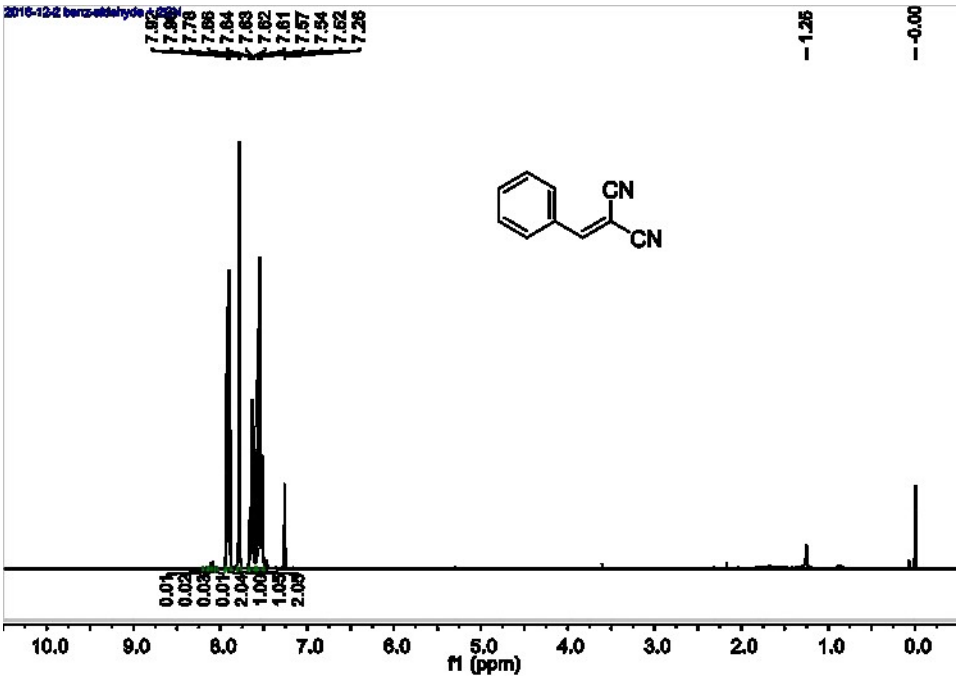

Fig. S18 ^{1}H NMR spectrum of 2-benzylidenemalononitrile (300 MHz, 30 °C, $CDCl_3$): δ = 7.91 (d, *J* = 7.4 Hz, 2H), 7.78 (s, 1H), 7.68 – 7.60 (m, 1H), 7.52 – 7.57 (m, 2H).

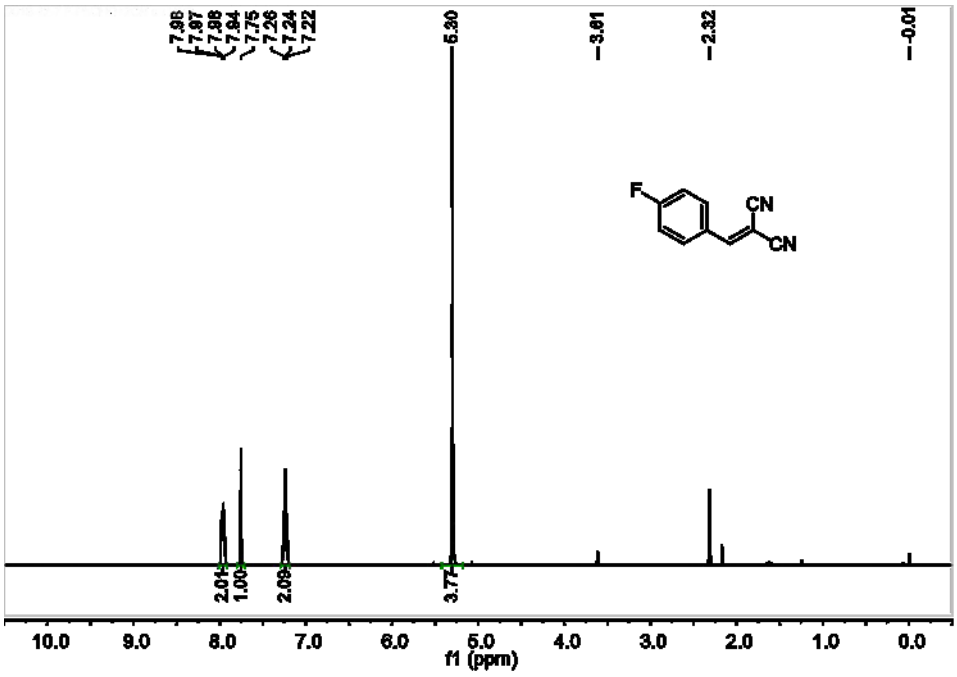

Fig. S19 ^{1}H NMR spectrum of 2-(4-fluorobenzylidene)malononitrile (400 MHz, 30 °C, $CDCl_3$): δ = 7.96 (dd, *J* = 8.7, 5.3 Hz, 2H), 7.75 (s, 1H), 7.24 (t, *J* = 8.5 Hz, 2H).

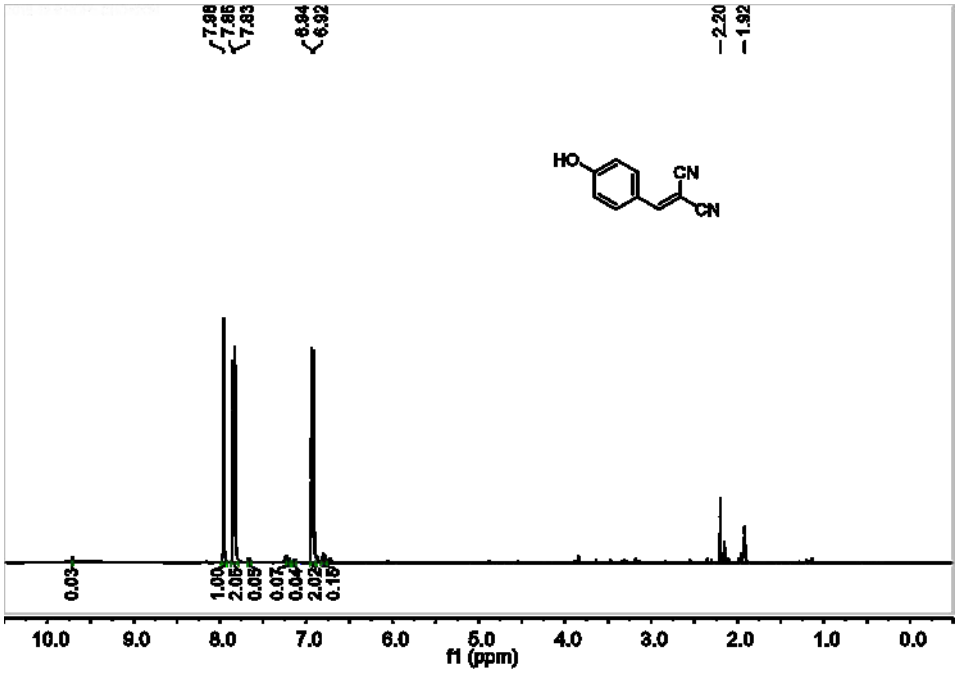

Fig. S20 ^{1}H NMR spectrum 2-(4-hydroxybenzylidene)malononitrile (400 MHz, 30 °C, acetone-D_6): δ = δ 7.96 (s, 1H), 7.84 (d, *J* = 8.8 Hz, 2H), 6.93 (d, *J* = 8.8 Hz, 2H).

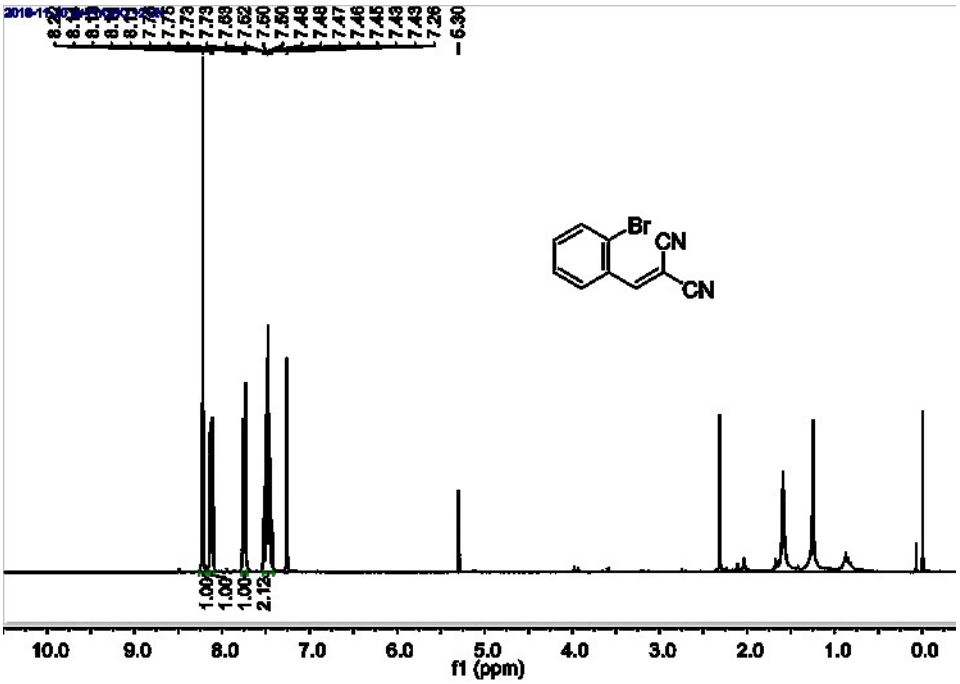

Fig. S21 ^{1}H NMR spectrum of 2-(2-bromobenzylidene)malononitrile (300 MHz, 30 °C, $CDCl_3$): δ = 8.22 (s, 1H), 8.12 (dd, *J* = 2.09, 7.36 Hz, 1H), 7.74 (dd, *J* = 1.66, 7.59 Hz, 1H), 7.43-7.53 (m, 2H).

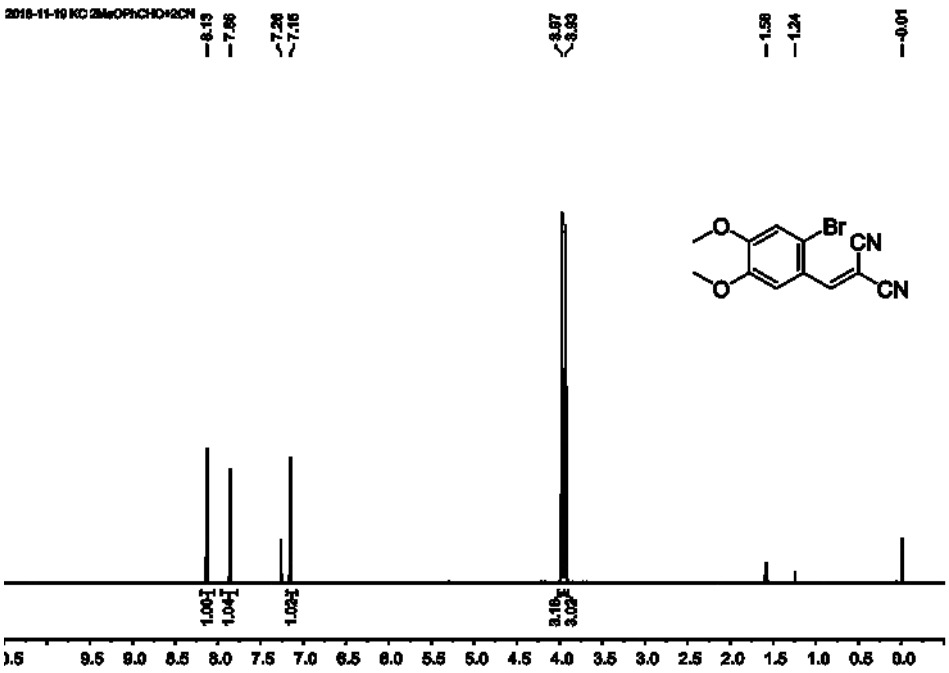

Fig. S22 ^{1}H NMR spectrum of 2-(2-bromo-4,5-dimethoxybenzylidene)malononitrile (300 MHz, 30 °C, $CDCl_3$): δ = 8.13 (s, 1H), 7.86 (s, 1H), 7.15 (s, 1H), 3.97 (s, 3H), 3.93 (s, 3H).

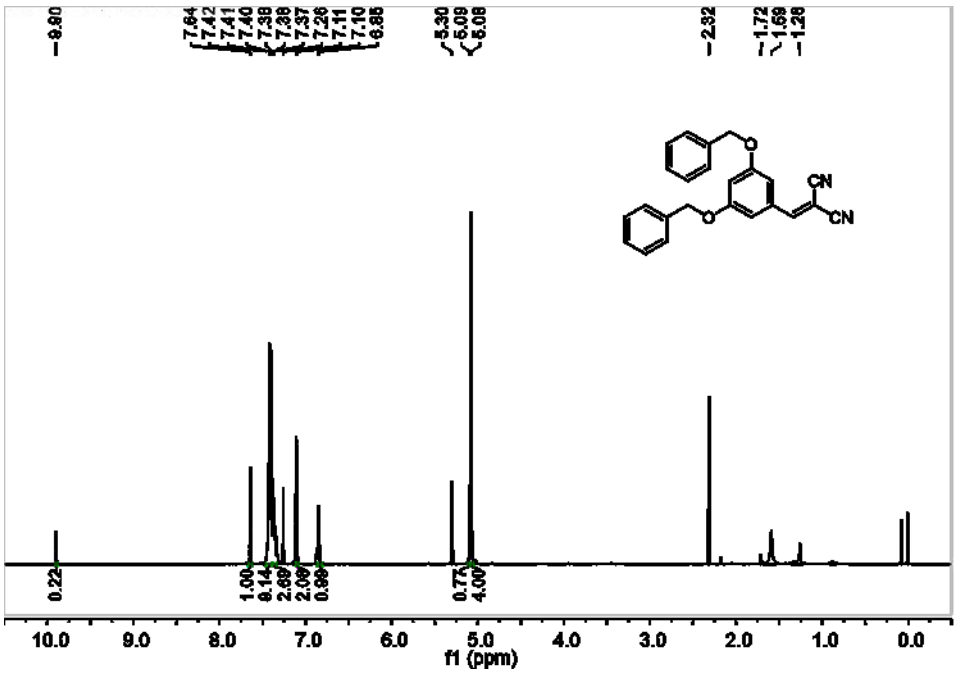

Fig. S23 ^{1}H NMR spectrum of 2-(3,5-bis(benzyloxy)benzylidene)malononitrile (300 MHz, 30 °C, $CDCl_3$): δ_{ppm} = 7.64 (s, 1H), 7.46 – 7.39 (m, 8H), 7.38 (t, *J* = 2.2 Hz, 2H), 7.11 (s, 2H), 7.10 (s, 2H), 6.85 (t, 1H), 5.09 (s, 1H), 5.08 (s, 4H).

^{1}H NMR analysis of aerobic Photooxidation of benzylamine and derivatives.

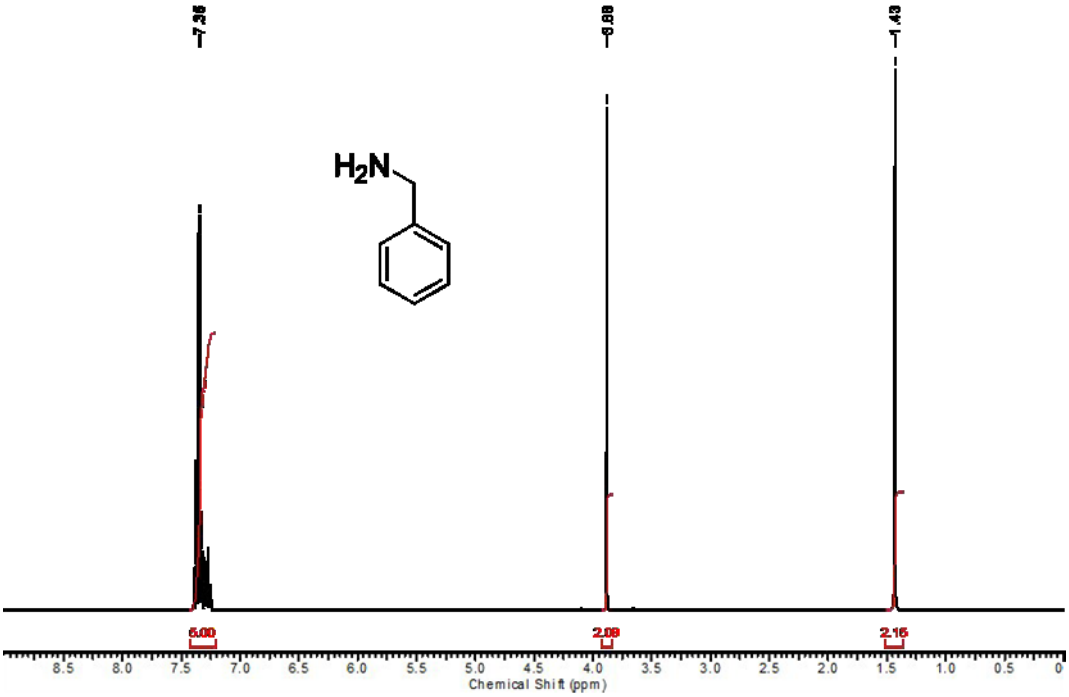

Fig. S24 ^{1}H NMR spectrum of benzyl amine (300 MHz, 30 °C, $CDCl_3$): δ = 1.42 (s, 2H), 3.86 (s, 2H), 7.27-7.39 (m, 5H).

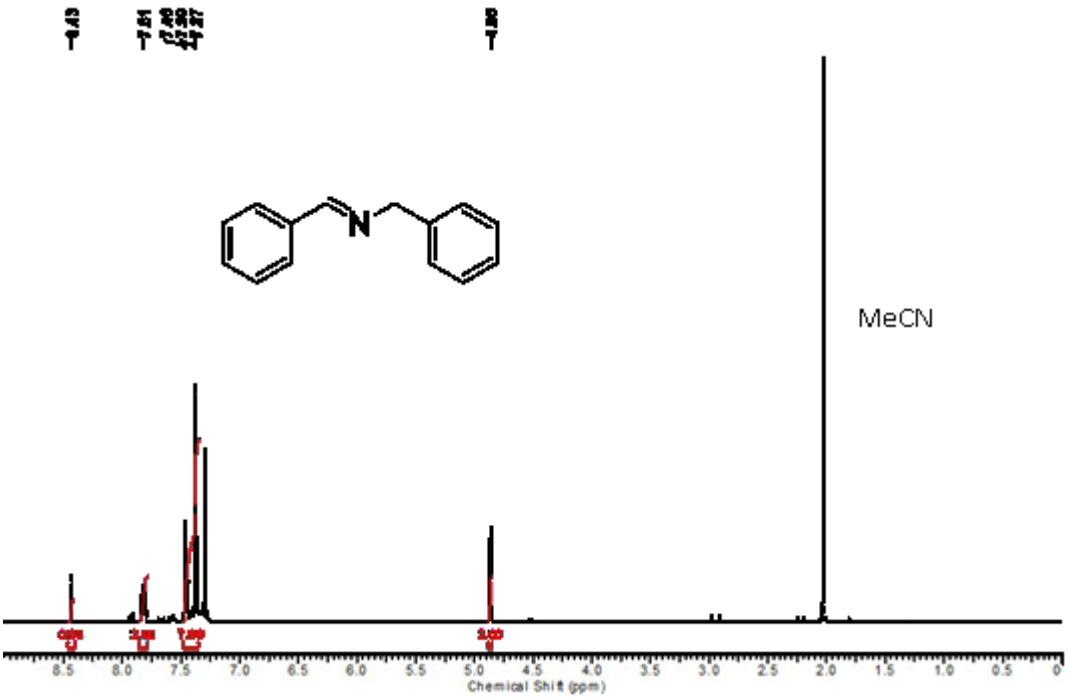

Fig. S25 ^{1}H NMR spectrum of N-benzyl-1-phenylmethanimine (300 MHz, 30 °C, $CDCl_3$): δ = 4.86 (s, 2H), 7.37-7.46 (m, 8H), 7.81 (dd, 2H), 8.43 (s, 1H).

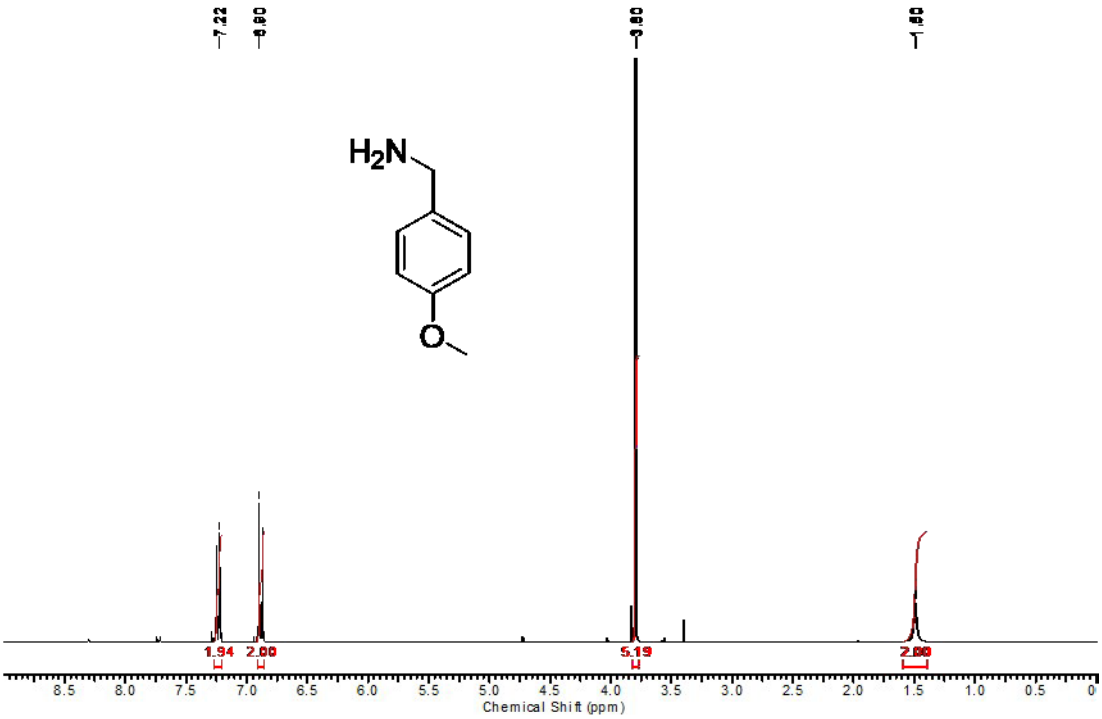

Fig. S26 ^{1}H NMR spectrum of 4-methoxybenzylamine (300 MHz, 30 °C, $CDCl_3$): δ = 1.50 (s, 2H), 3.80 (s, 2H+3H), 6.90 (d, 2H), 7.22 (d, 2H).

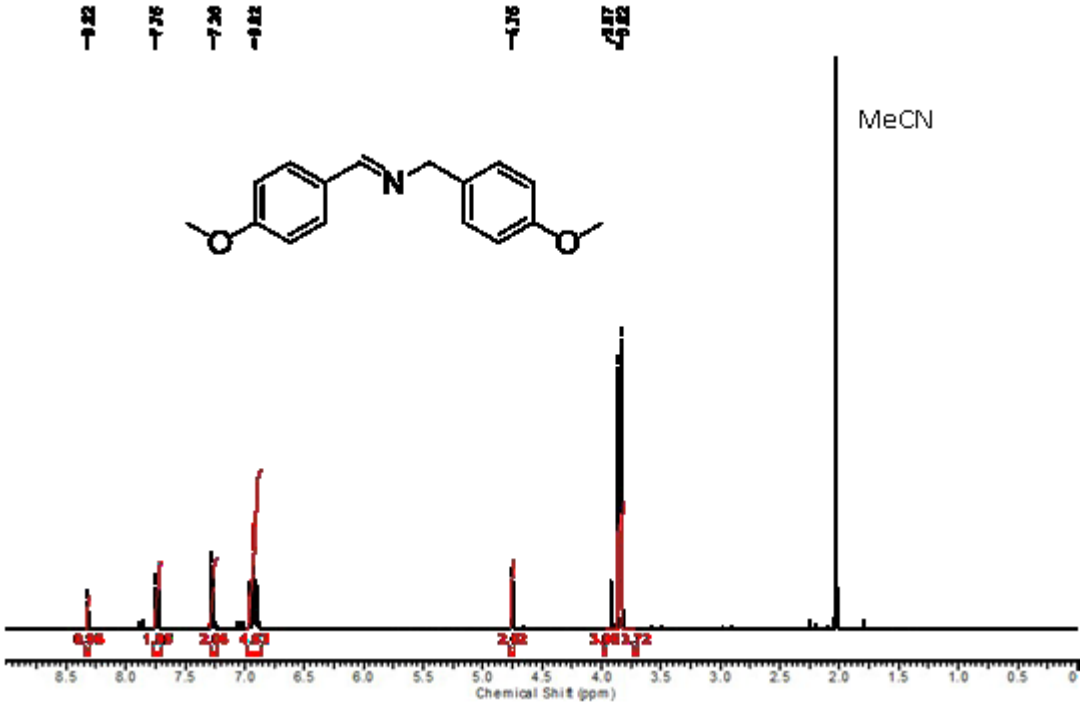

Fig. S27 The ^{1}H NMR spectrum of (*E*)-N-(4-methoxybenzyl)-1-(4-methoxyphenyl) methanimine (300 MHz, 30 °C, $CDCl_3$): δ = 3.82 (s, 3H), 3.87 (s, 3H), 4.75 (s, 2H), 6.91 (d, 2H), 6.93 (d, 2H), 7.26 (d, 2H), 7.75 (d, 2H), 8.32 (s, 1H).

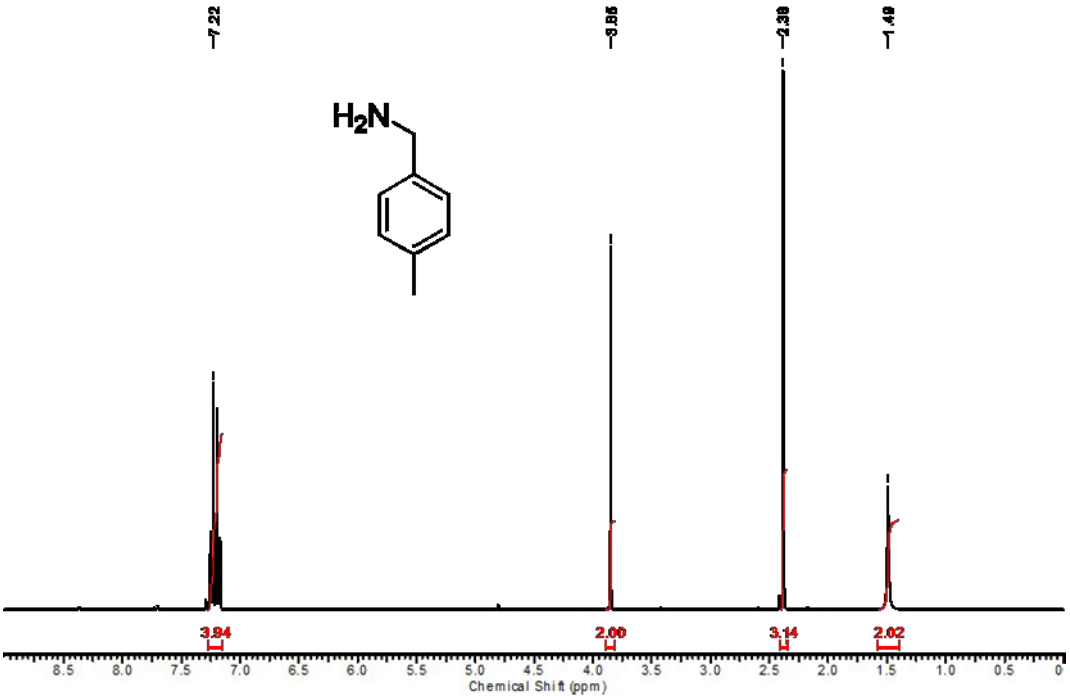

Fig. S28 ^{1}H NMR spectrum of 4-methylbenzylamine (300 MHz, 30 °C, $CDCl_3$): δ = 1.49 (s, 2H), 2.38 (s, 3H), 3.85 (s, 2H), 7.20 (d, 2H), 7.24 (d, 2H).

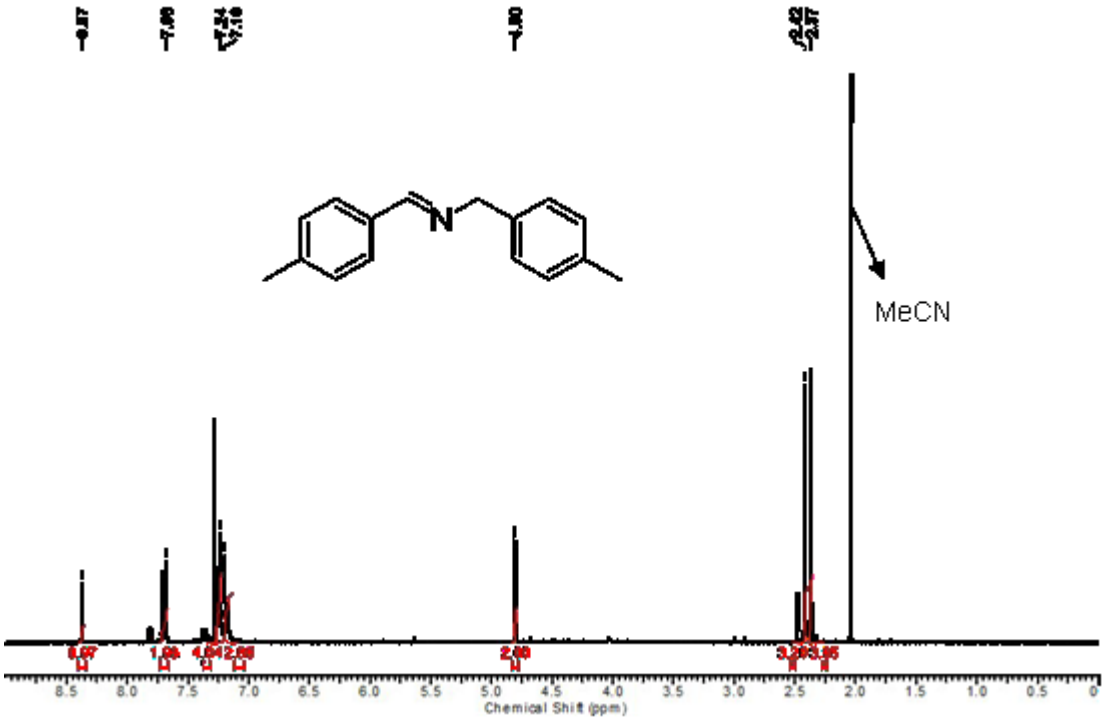

Fig. S29 ^{1}H NMR spectrum of (*E*)-N-(4-methylbenzyl)-1-(4-methylphenyl)methanimine (300 MHz, 30 °C, $CDCl_3$): δ = 2.37 (s, 3H), 2.47 (s, 3H), 4.80 (s, 2H), 7.19 (d, 2H), 7.22 (d, 2H), 7.26 (d, 2H), 7.68 (d, 2H), 8.37 (s, 1H).

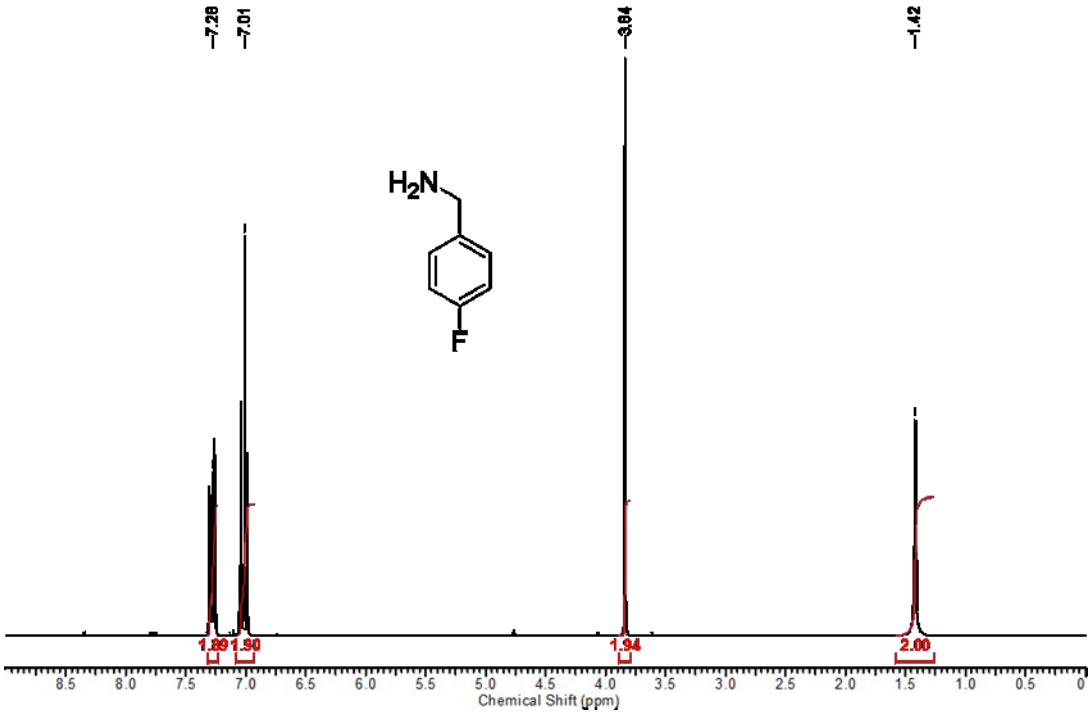

Fig. S30 ^{1}H NMR spectrum of 4-fluorobenzylamine (300 MHz, 30 °C, $CDCl_3$): δ = 1.42 (s, 2H), 3.84 (s, 2H), 7.01 (distorted doublet, 2H), 7.28 (distorted doublet, 2H).

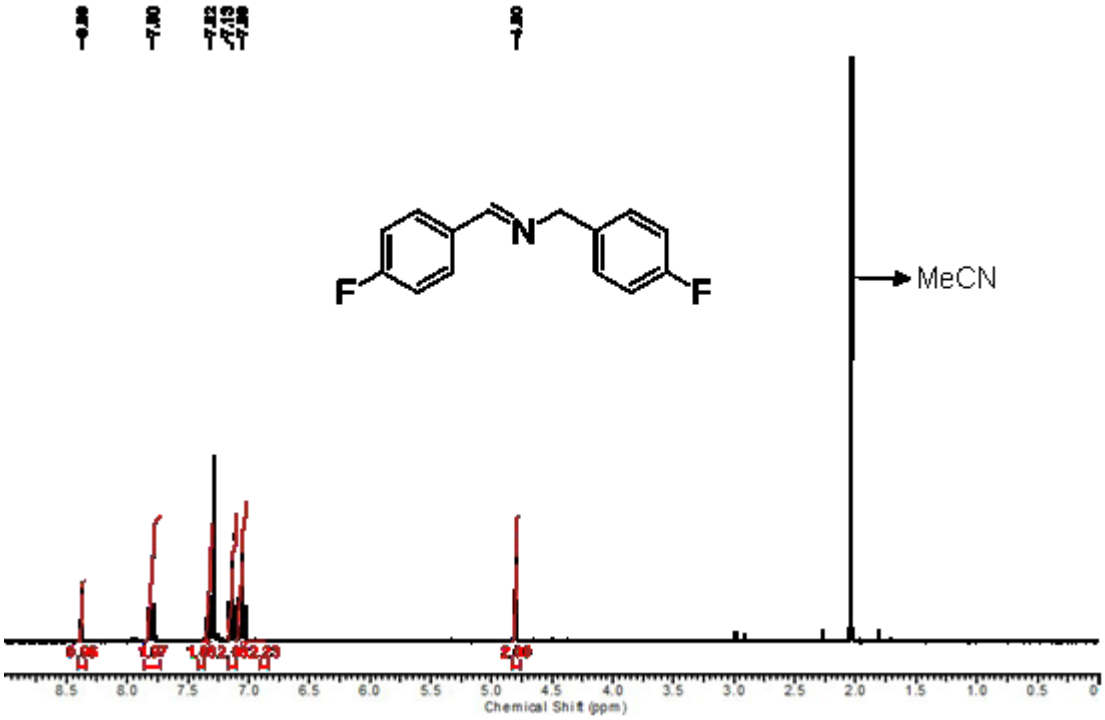

Fig. S31 ^{1}H NMR spectrum of (*E*)-N-(4-fluorobenzyl)-1-(4-fluorophenyl)methanimine (300 MHz, 30 °C, $CDCl_3$): δ = 4.80 (s, 2H), 7.06 (distorted doublet, 2H), 7.13 (distorted doublet, 2H), 7.32 (distorted doublet, 2H), 7.80 (distorted doublet, 2H), 8.38 (s, 1H).

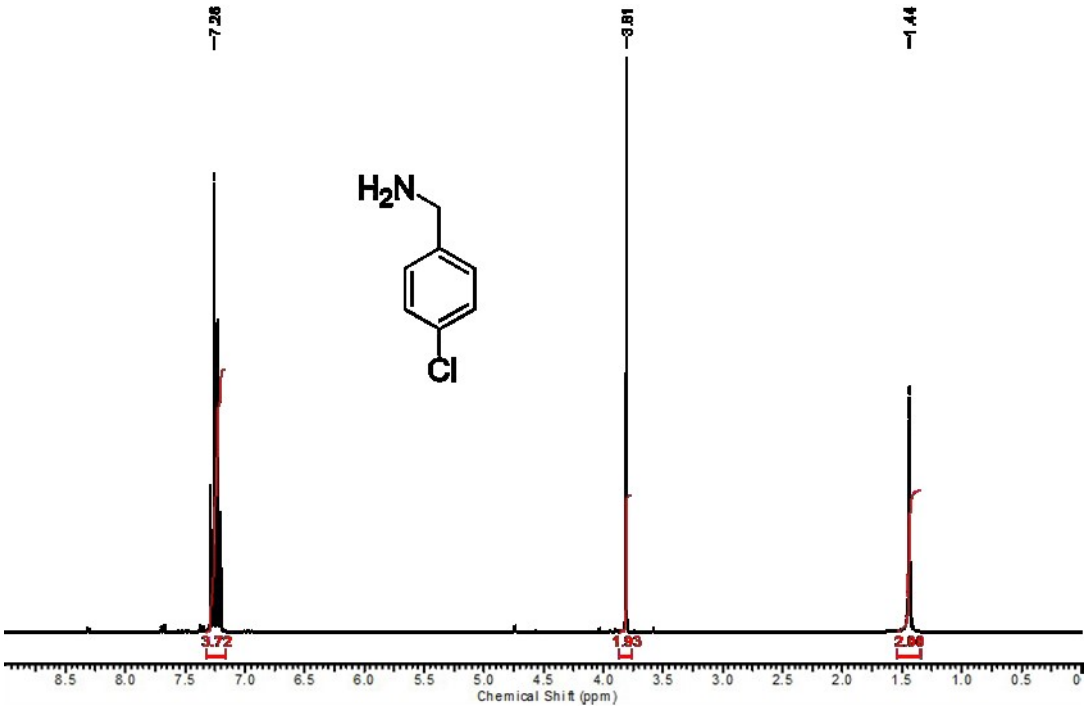

Fig. S32 ^{1}H NMR spectrum of 4-chlorobenzylamine (300 MHz, 30 °C, $CDCl_3$): δ = 1.44 (s, 2H), 3.81 (s, 2H), 7.24 (d, 2H), 7.28 (d, 2H).

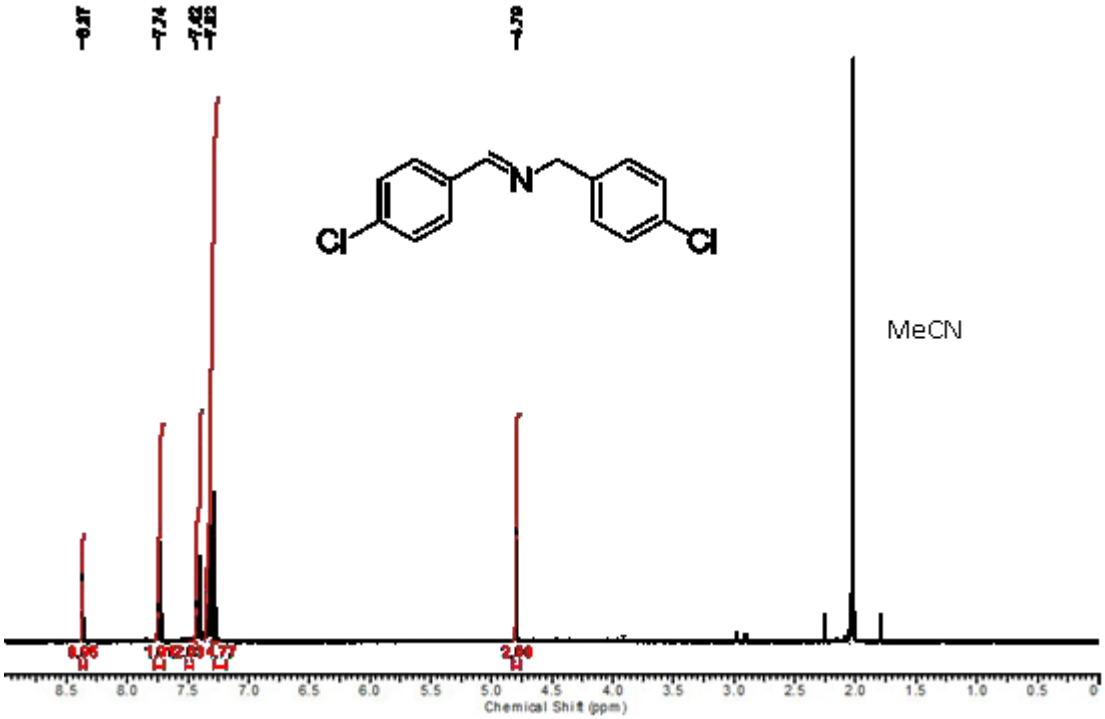

Fig. S33 ^{1}H NMR spectrum of (*E*)-N-(4-chlorobenzyl)-1-(4-chlorophenyl)methanimine (300 MHz, 30 °C, $CDCl_3$): δ = 4.79 (s, 2H), 7.31 (d, 2H), 7.33 (d, 2H), 7.42 (d, 2H), 7.74 (d, 2H), 8.37 (s, 1H).

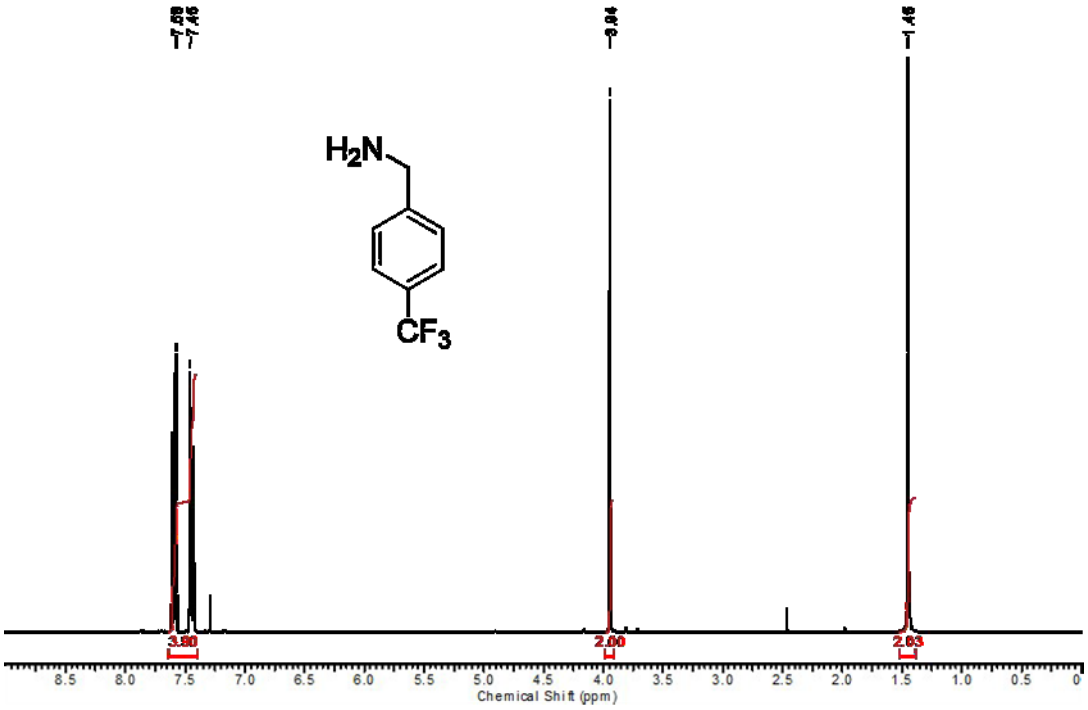

Fig. S34 ^{1}H NMR spectrum of 4-(trifluoromethyl)benzylamine (300 MHz, 30 °C, $CDCl_3$): δ = 1.45 (s, 2H), 3.94 (s, 2H), 7.45 (d, 2H), 7.58 (d, 2H).

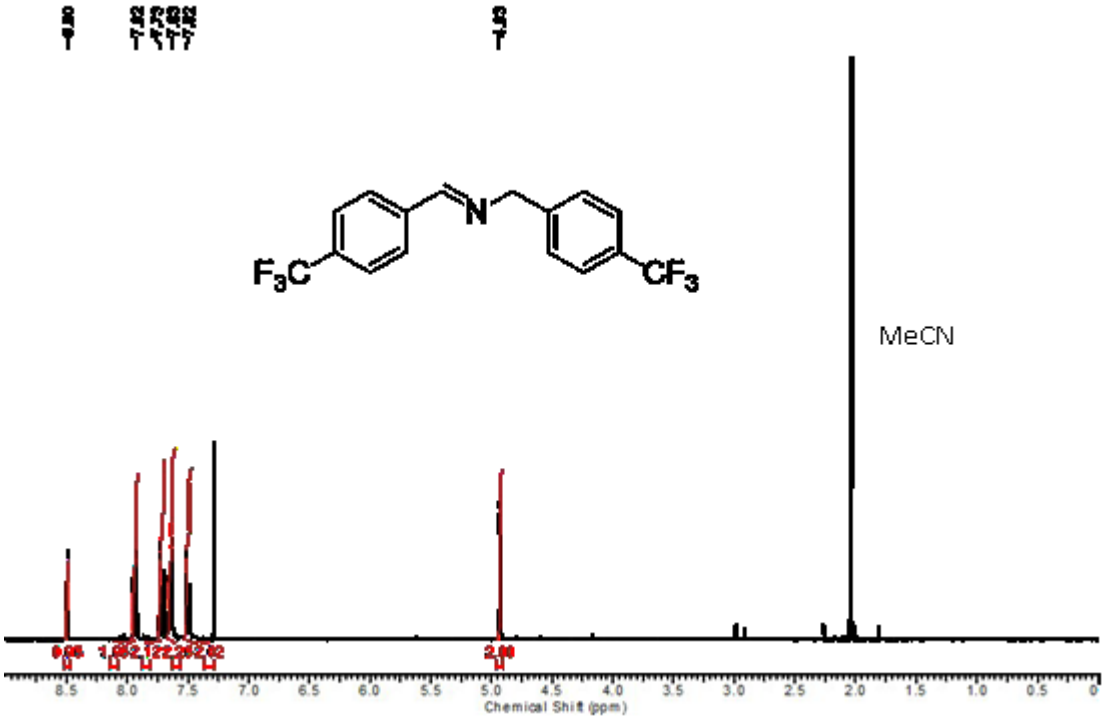

Fig. S35 ^{1}H NMR spectrum of (*E*)-N-(4-(trifluoromethyl)benzyl)-1-(4- (trifluoromethyl) phenyl)methanimine (300 MHz, 30 °C, $CDCl_3$): δ = 4.93 (s, 2H), 7.52 (d, 2H), 7.63 (d, 2H), 7.73 (d, 2H), 7.92 (d, 2H), 8.50 (s, 1H).

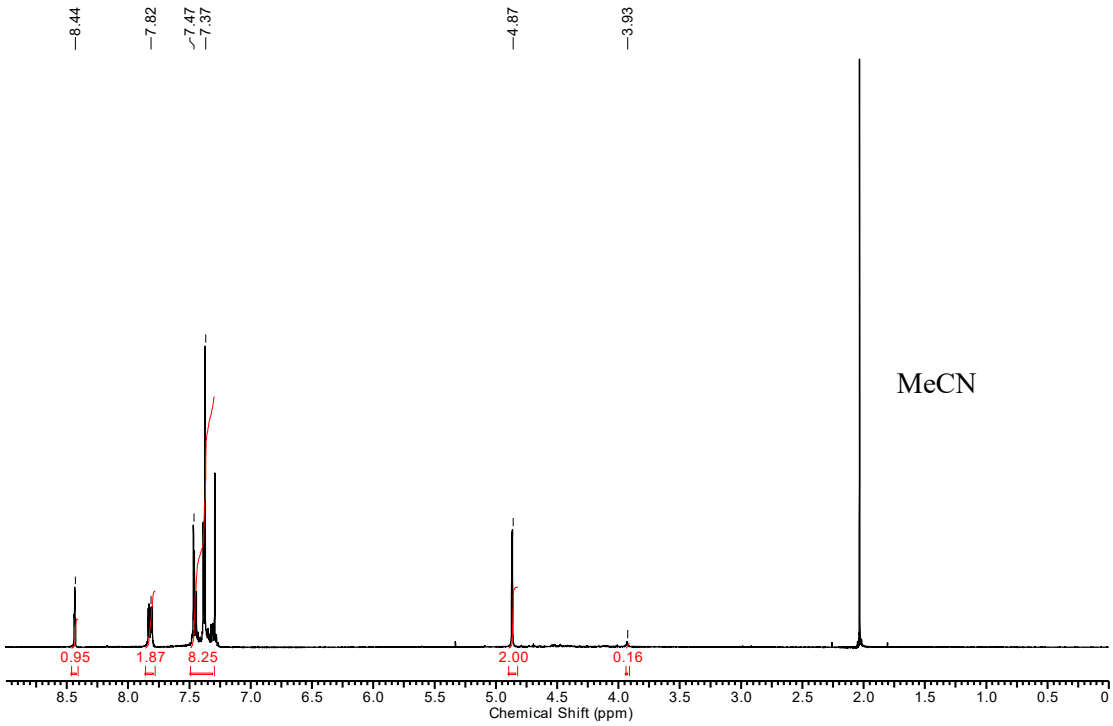

Fig. S36 ^{1}H NMR spectrum of the model reaction after prolonged irradiation of HOTT-HATN (300 MHz, 30 °C, $CDCl_3$): δ_{ppm} = 4.87 (s, 2H), 7.37-7.47 (m, 8H), 7.82 (dd, 2H), 8.44 (s, 1H).

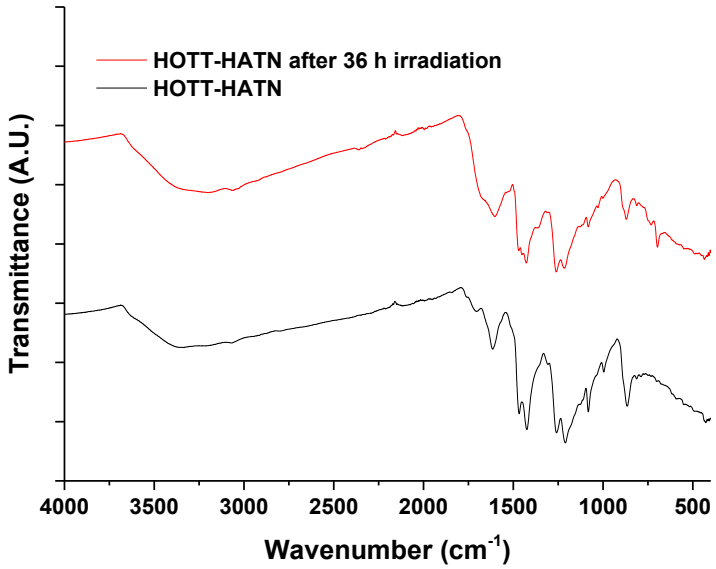

Fig. S37 FTIR anaylsis of HOTT-HATN before and after photocatalytic experiment with a total irradiation time of 36 h.

References

[1] S. Barlow, Q. Zhang, B. R. Kaafarani, C. Risko, F. Amy, C. K. Chan, B. Domercq, Z. A. Starikova, M. Y. Antipin and T. V. Timofeeva, *Chem. Eur. J.*, 2007, **13**, 3537-3547.

[2] S. Skujins and G. Webb, *Tetrahedron*, 1969, **25**, 3935-3945.

[3] P. M. Budd, B. Ghanem, K. Msayib, N. B. McKeown and C. Tattershall, *J. Mater. Chem.*, 2003, **13**, 2721-2726.

CHAPTER 4: Polymer-Supported Photosensitizers for Oxidative Organic Transformations in Flow and under Visible Light Irradiation (Publication, *ACS Catalysis,* ACS)

The following section outlines the design and development of a novel 2,1,3-benzothiadiazole (BTZ)-based photoactive monomer and its subsequent incorporation into a polystyrene matrix as a crosslinker. Three physical formats were synthesised (gels, beads, and a monolith), characterised and subsequently employed as heterogeneous triplet photosensitisers to produce two reactive oxygen species: singlet oxygen ($^1O_2$) and superoxide radical anions ($O_2^{\cdot-}$). This chapter will outline and discuss the publication titled '*Polymer-Supported Photosensitisers for Oxidative Organic Transformations in Flow and under Visible Light Irradiation*' which was published in *ACS Catalysis* and can be found in its entirety (including supporting information) at the end of this chapter. Any contributions and work performed by other students, collaborators or academics are presented throughout the chapter in the appropriate sections.

4.1 Background

The vast majority of the work presented thus far has focused primarily around fully conjugated polymeric materials. While these polymers demonstrated excellent photocatalytic performance and stability, they can be hindered by the need for metal-based synthetic routes. This introduces the potential for trace amounts of these metals to be trapped within the polymer matrix, even after purification [4.1]. Both Chapter 2 and 3 address this issue by focusing on the synthesis of CPPs through metal-free methodologies. The proceeding work continues to explore the synthesis of polymeric photocatalysts without the need for metal-based procedure by introducing an alternative to fully conjugated materials. This is accomplished by applying the concept of alternating a strong electron acceptor with a weak electron donor, as seen in the Ph-BTZ CPP repeat unit [4.2, 4.3], and how it can be diluted as a crosslinker into a more common polymer matrix (Figure 4.1).

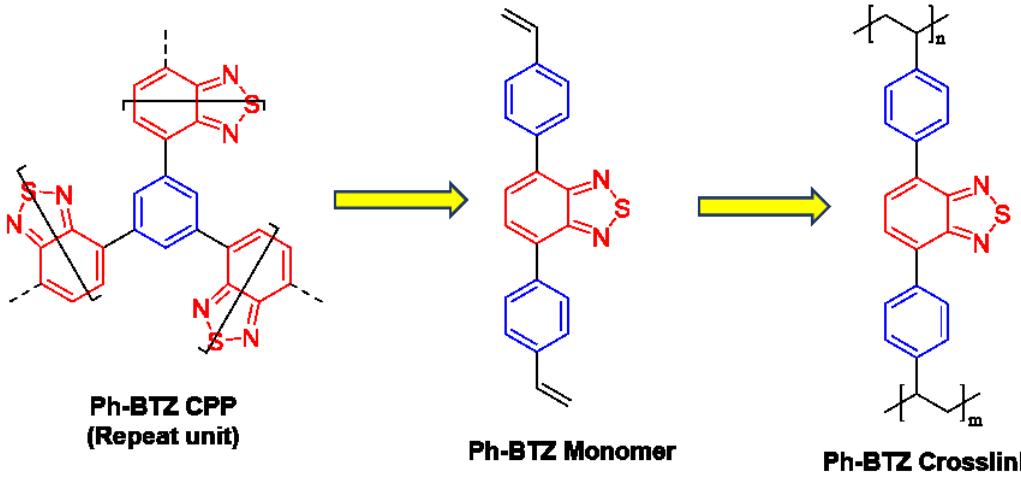

Figure 4.1 Monomeric representation of a Ph-BTZ CPP and its implementation as a crosslinker in a polymer chain.

The use of free radical polymerisation techniques fulfils the requirement of a metal-free synthesis whereby vinyl-substituted monomers can be readily polymerised in the presence of a source of radicals. Styrene fits this category of monomer as it contains a vinyl group. Styrene is readily available, cheap and widely used in both laboratory and industrial settings for the synthesis of polystyrene, with world-wide production exceeding 25 million tonnes every year [4.4]. Furthermore, styrene has shown a high degree of versatility as a monomer as it can be implemented in a variety of polymer architectures (linear, branch, crosslinked, etc.) [4.5]. Due to the benzene groups on the proposed photoactive crosslinker, it is expected to have good compatibility as a copolymer with styrene which further supports the choice of a polystyrene support.

4.2 Aim/Objectives

The aim of this study was to develop a photoactive crosslinking monomer based on the BTZ-benzene donor-acceptor electronic system found in previously published CPPs [4.2]. Designed with two styrene units, the monomer can act as a crosslinker in free radical polymerisation reactions. The BTZ-based monomer was subsequently exploited as a comonomer with styrene and/or divinylbenzene (DVB) to form a range of polystyrene-based heterogeneous photosensitisers. Using traditional as well as more specialised free radical polymerisation techniques, three insoluble formats were synthesised using only 3-5 mol % of the photoactive monomer: gels, beads, and a monolithic high internal phase emulsion polymer (polyHIPE). These three materials were

employed as heterogeneous triplet photosensitisers for the generation of reactive oxygen species, $^1O_2$ and $O_2^{\cdot -}$. Furthermore, utilisation of continuous flow chemistry established the versatility of design of these materials and their use as heterogeneous photocatalysts.

4.3 Synthesis of Materials/Methodology

A BTZ-based crosslinking monomer was synthesised and subsequently copolymerised with styrene and/or divinylbenzene to form three distinct polymers. These materials were fully characterised and employed as heterogeneous triplet photosensitisers for the production of $^1O_2$ or $O_2^{\cdot -}$ under batch and continuous flow procedures. The monomer was characterised using FT-IR spectroscopy, UV-Vis spectroscopy, ^1H and ^{13}C NMR spectroscopy, and X-ray crystallography. The subsequent crosslinked polymers were characterised using FT-IR spectroscopy, solid state ^{13}C NMR CP-MAS spectroscopy, solid state UV-Vis spectroscopy, and scanning electron microscopy (SEM). All solid state ^{13}C NMR CP-MAS measurements were carried out by Dr David Ellis at Heriot-Watt University. X-ray crystallography measurements were carried out by Dr Gareth Lloyd at Heriot-Watt University. Computational modelling studies were also performed by Dr Martin Paterson and Andrew Prentice at Heriot-Watt University.

4.3.1 Synthesis of 4,7-Distyrene-2,1,3-benzothiadiazole (St-BTZ)

Synthesis of St-BTZ was carried out through a palladium-catalysed Suzuki-Miyaura cross-coupling reaction whereby 4,7-dibromo-2,1,3-benzothiadiazole was coupled with 4-vinylphenylboronic acid. The reaction was purified *via* silica gel column chromatography to yield a bright yellow crystalline solid (96 mg, 56 %).

4.3.2 General Synthesis of Styrene-St-BTZ Copolymers via Free Radical Polymerisation (Gel (M%))

Through traditional free-radical polymerisation techniques using AIBN as the initiator, styrene was copolymerised with St-BTZ as a crosslinker. To test the degree of crosslinking required to form an insoluble gel, St-BTZ was added as a comonomer in small, incremental amounts (2, 3 or 5 mol %). While the reaction with 2 mol % St-BTZ remained soluble, both the 3 and 5 mol % St-BTZ reactions formed insoluble, bright

yellow gels (Figure 4.2). The insoluble copolymers were purified *via* Soxhlet extraction with THF and MeOH and dried *in vacuo*. This resulted in two amorphous copolymers, Gel (3%) and Gel (5%), containing different amounts of the photoactive St-BTZ monomer.

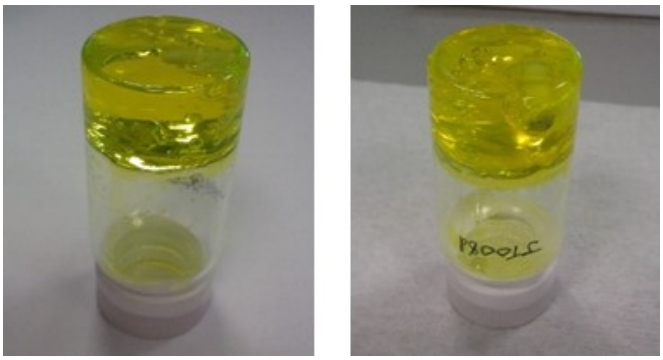

Figure 4.2 Post-polymerisation images of the bright yellow Gel (3%) (left) and Gel (5%) (right) as insoluble polymers in toluene.

4.3.3 Synthesis of Styrene-DVB-St-BTZ Copolymer via Precipitation Polymerisation (Bead-BTZ)

An approach using a more specialised free-radical polymerisation technique was employed for the formation of well-defined polymer beads. Precipitation polymerisation was use by combing DVB-55, styrene, St-BTZ (4 mol %), AIBN in acetonitrile and heating to 60 °C for 48 hours under a nitrogen atmosphere. During this time, the flask was rolled to facilitate the formation of microbeads. The precipitated product was filtered, washed with acetonitrile, toluene, MeOH and acetone and dried *in vacuo*. This resulted in the micrometre-sized yellow beads Bead-BTZ (120 mg, 12 %). Synthesis and SEM measurements of these materials was carried out by our collaborator Professor Peter Cormack and his PhD student Timothy McCabe, University of Strathclyde, Glasgow.

4.3.4 Synthesis of Styrene-DVB-St-BTZ Copolymer via High Internal Phase Emulsion Polymerisation (pHIPE-BTZ)

The third polymer format was designed to act as an immobilised photosensitiser in continuous flow reactors. The formation of a monolithic polyHIPE was achieved by combining styrene, DVB-80, St-BTZ (3 mol %), and Span 80 into a vial. An aqueous mixture of potassium persulfate and NaCl was then added slowly to the organic phase

while the reaction was emulsified using an electric mixer. Upon completion (*i.e.* the aqueous phase no longer combined with the emulsion), the emulsion was delivered into a transparent glass column, sealed and heated to 60 °C for 24 hours. The resulting polymer was flushed with THF, CH_2Cl_2 and $CHCl_3$ resulting in a bright yellow monolith (35 mm length x 7 mm diameter).

4.3.5 General Procedure for Photocatalytic Reactions under Batch Conditions

All photosensitising reactions carried out in batch were performed with either Gel (3 or 5 %) or Bead-BTZ at a concentration of 1mg/1 mL of solution. The solution (5 – 10 mL) was placed in a vial with the appropriate photosensitiser and stirred for 10 minutes to aerate the mixture. The vial was then placed 7 cm from a 420 nm LED module and irradiated open to air until the consumption of the starting material was observed *via* TLC and/or ^{1}H NMR spectroscopy.

4.3.6 General Procedure for Photocatalytic Reactions in Flow Employing Bead-BTZ

Reactions performed under continuous flow conditions utilised Bead-BTZ as a suspension. In general, reaction mixtures consisted of the Bead-BTZ (5 mg) dispersed in a 15 mL solution of α-terpinene in chloroform. This dispersion was pumped through the photochemical reactor at a flow rate of 1 mL min^{-1}. Concurrently, air (the source of oxygen) was propelled through a second pump at the same flow rate, meeting the dispersion at a T-junction prior to entering the photochemical reactor. The photochemical reactor (10 mL total volume) was equipped with a 420 nm LED module, ensuring complete irradiation of any reactants present. The mixture was continuously cycled through the reactor until full conversion to the desired product was observed *via* TLC and/or ^{1}H NMR spectroscopy.

4.3.7 General Procedure for Photocatalytic Reactions in Flow Employing pHIPE-BTZ

While Bead-BTZ was used as a suspension under continuous flow conditions, pHIPE-BTZ was employed as an immobilised photosensitiser under the same conditions (Figure 4.3). The monolith was fitted into a transparent glass column and irradiated with a LED light source (λ = 420 nm). The required solution (10 mL) was pumped through

the column at 0.5 – 1.0 mL min^{-1}. Concurrently, oxygen was propelled through a second pump at the same flow rate, meeting the dispersion at a T-junction prior to entering the column. The solution was cycled through the column until consumption of the starting materials was observed *via* TLC and/or ^{1}H NMR spectroscopy.

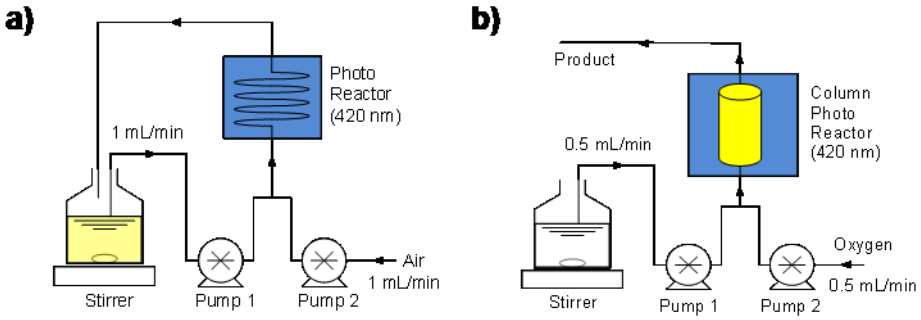

Figure 4.3 Schematic representation of the experimental setup under continuous flow conditions for a) Bead-BTZ and b) pHIPE-BTZ.

4.4 Results

4.4.1 Characterisation of St-BTZ

Structural characterisation of St-BTZ was performed first to determine the success of the reaction. FT-IR, ^{1}H and ^{13}C NMR spectroscopy indicated the target product was indeed synthesised. Further examination using X-ray crystallography supported this data and was fully consistent with the structure of St-BTZ. As expected, UV-Vis spectroscopy showed a broad absorption at 350 – 450 nm with a maximum absorbance at 400 nm. This absorption maximum correlates well to those reported from BTZ-based CPPs [4.2]. Due to the available vinyl groups, St-BTZ was next employed as a crosslinker in a copolymerisation with styrene.

4.4.2 Synthesis and Properties of Polystyrene-based Copolymers

St-BTZ was copolymerised with styrene due to increased compatibility between the monomers and the stability of polystyrene under oxidative conditions [4.6]. Through traditional free radical polymerisation, two bright yellow copolymers, Gel (3%) and Gel (5%), were synthesised. To retain the desired insolubility necessary for a heterogeneous

photosensitiser, it was observed that at least 3 mol % of St-BTZ was required to sufficiently crosslink the polymer chains. This dilute crosslinking resulted in a gel rather than a soluble or rigid polymer. When in contact with the appropriate solvent system the liquid is dispersed throughout the solid gels, resulting in highly swollen materials where the majority of the gel weight is composed of the solvent.

Both optical and structural characterisations were performed to determine the success of the polymerisation. As observed in the St-BTZ monomer, UV-Vis spectroscopy indicated a broad absorption of both gels (350 – 450 nm) with a maximum absorption at 400 nm. FT-IR spectroscopy showed peaks corresponding to St-BTZ (825 and 887 cm^{-1}) that do not appear in pure polystyrene. Solid-state ^{13}C NMR CP-MAS spectroscopy on Gel (3%) indicated two primary aromatic signals at 128 ppm (C-C) and 146 ppm (C-N) as well as signals in the alkyl region at 40-45 ppm as expected from the aliphatic backbone in polystyrene. While all spectroscopic data indicates the successful integration of St-BTZ into the polystyrene matrix, we note that any weak signals most likely arise from the high ratio of styrene to St-BTZ within the copolymer.

Using more complex heterogeneous phase polymerisations [4.5] and free radical initiators, we can demonstrate the versatility of the photoactive crosslinker. We can show this versatility through implementation of St-BTZ in free radical polymerisation techniques to yield polymers with the same photoactive properties as the monomer. For this study, we explored precipitation polymerisation and high internal phase emulsion (HIPE) polymerisation. This results in the synthesis of the polymers in different physical formats derived from the same monomer set: micrometre-sized beads from precipitation polymerisations and monolithic structures from HIPE polymerisations. A polyHIPE was chosen as one of the physical formats due to their high degree of porosity and high specific surface area [4.7]. These characteristics are achieved through an emulsion-templated synthetic procedure whereby an aqueous internal phase is distributed as droplets throughout an oil (organic) external phase. This forms a highly viscous emulsion where the monomers in the external phase can polymerise around the dispersed aqueous droplets. Subsequently, the internal phase can be easily removed *via* heating or solvent extraction to result in a highly porous structure (Figure 4.4).

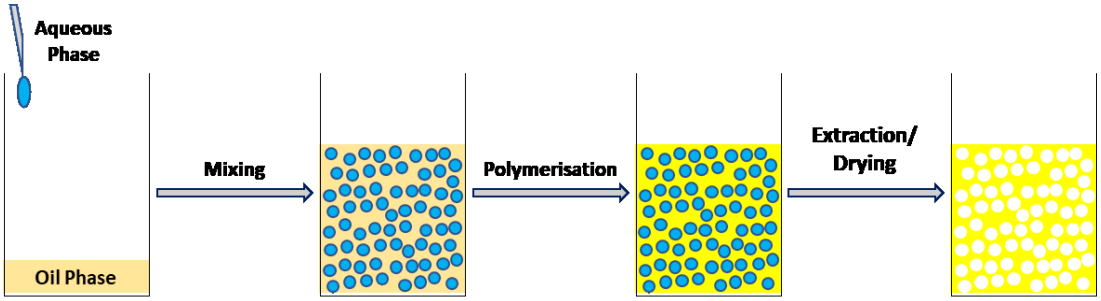

Figure 4.4 Representative depiction of the formation of a polyHIPE using an aqueous internal phase.

Both the beads and polyHIPE were synthesised using primarily styrene along with 3 – 4 mol % of St-BTZ and DVB. The incorporation of DVB as a non-photoactive crosslinker into both Bead-BTZ and pHIPE-BTZ was done so to increase both the rigidity and mechanical robustness of the polymers while having no effect on photocatalytic performance. UV-Vis spectroscopy of both polymers again showed a broad absorption with maximum absorption at 420 nm and exhibited the bright yellow colour seen in both the St-BTZ monomer and the gels described above. Both polymers showed weak signals in the FT-IR spectrum corresponding to the St-BTZ monomer (825 and 887 cm^{-1}). This indicates that St-BTZ was successfully incorporated into both Bead-BTZ and pHIPE-BTZ. As seen in Figure 4.5, SEM imaging of both materials was also performed. Bead-BTZ (Figure 4.5, top) was observed as polymer microspheres with a size range around 1 – 2 μm. The monolithic pHIPE-BTZ (Figure 4.5, bottom) images showed a highly porous, sponge-like material with the pore sizes ranging from <1 μm to 4 μm.

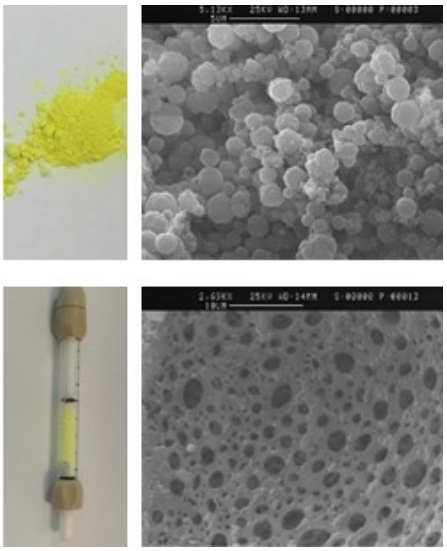

Figure 4.5 Synthesised copolymers and the corresponding SEM images of (top) Bead-BTZ and (bottom) pHIPE-BTZ.

Overall, three polymer formats incorporating the St-BTZ crosslinker were successfully synthesised through metal-free polymerisation techniques. This not only demonstrated a versatility of design but also the robust nature of St-BTZ as a monomer for free radical polymerisations. To fully understand the potential of these materials as photosensitisers, computational modelling was also performed on the singlet and triplet state geometries for both the monomer and within polymeric integration. We observed a high potential for both monomeric and polymeric materials to occupy the triplet state, indicating their capacity to act as triplet photosensitisers. Therefore, investigations into the production of $^1O_2$ were performed.

4.4.3 Homogeneous Photosensitisation with St-BTZ

Initial examinations into St-BTZ as a photosensitiser were performed using the conversion of *α*-terpinene to ascaridole to quantitatively measure the photocatalytic production of $^1O_2$. Full conversion from *α*-terpinene to ascaridole was observed after 90 minutes *via* ^{1}H NMR spectroscopy. However, incremental measurements every 15 minutes showed a sudden decrease in the rate of conversion after 45 minutes. Furthermore, a distinct colour change was noted whereby the solution transitioned from bright yellow to a reddish-orange colour (Figure 4.6). Investigations *via* ^{1}H NMR spectroscopy indicated a clear decrease in the characteristic peaks for St-BTZ, verifying the degradation of the monomer.

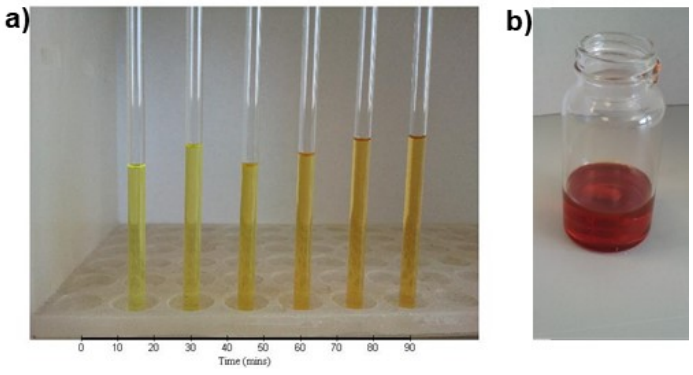

Figure 4.6 St-BTZ as a photosensitiser for $^1O_2$ production and the corresponding colour change: a) at 15-minute intervals and b) at the 90-minute mark.

Upon further review, it was clear that interactions between $^1O_2$ and vinylarenes result in the formation of monoadducts and endoperoxides (Scheme 4.1) [4.8] which

explains the instability of St-BTZ under the highly oxidative conditions. However, due to the stability of polystyrene and various BTZ-based CPPs in the presence of $^1O_2$ [4.2, 4.3, 4.9-4.11], it was postulated that incorporation of the monomer into the polymer matrix would mitigate any photodegradation or oxidative effects.

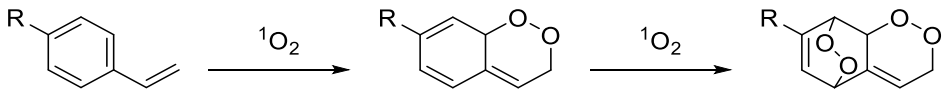

Scheme 4.1 Formation of monoadduct and subsequent *bis*-endoperoxide from styrene in the presence of $^1O_2$ [4.8].

4.4.4 Heterogeneous Photosensitisation with Gel (M %)

The same procedure was employed for the production of $^1O_2$ with Gel (3 %) and Gel (5 %) as a heterogeneous photosensitiser. Both polymers showed excellent catalytic performance reaching near full conversion within 60 minutes with Gel (5 %) performing marginally better than Gel (3 %). More importantly neither polymer showed any colour change or indication of chemical/photo instability. Control experiments were also performed, and established the need for light, oxygen, and the appropriate photocatalyst for the reaction to proceed.

While the gels demonstrated exceptional photoactivity and stability, we note that their use under continuous flow conditions was impractical due to aggregation and coagulation of the tubing. To combat this, both Bead-BTZ and pHIPE-BTZ were designed specifically for applications in flow. The micrometre-size beads were uniformly dispersed in chloroform and showed no signs of aggregation, allowing them to be employed as a 'mobile' photosensitiser and flow through a photochemical reactor as a suspension with negligible effects on the pressure build-up within the reactor. Conversely, pHIPE-BTZ can act as a stationary 'immobilised' photosensitiser allowing the reagent mixture to flow through the porous structure with only a minimal increase in pressure. Due to the oxygen flow required for the experiment, back pressure was added to the system with an optimal operation pressure at 1.3 bar. This ensured a more steady and controllable flow rate through the immobilised photosensitiser.

4.4.5 Heterogeneous Photosensitisation with Bead-BTZ and pHIPE-BTZ in Flow

To compare the photoactivity of Bead-BTZ to the gels, a batch photosensitisation reaction was first performed under the same conditions as Gel (3 %). Unsurprisingly, conversion rates were observed as near identical to that of Gel (3 %) and confirmed that the inclusion of DVB into the polymer structure had no appreciable effect (positive or negative) on the photoactivity of Bead-BTZ. The same reaction was then performed under continuous flow conditions using Bead-BTZ as the photosensitiser, resulting in a similar conversion rate as observed in the batch reaction with full conversion occurring after 60 minutes corresponding to a production rate of 136 mg h^{-1}.

The monolithic pHIPE-BTZ was also employed as a heterogeneous photosensitiser with the distinct difference of being immobilised in a glass column rather than as a free-flowing suspension. Due to the changes in contact time between the photosensitiser and the reaction mixture, the opportunity for α-terpinene to interact with $^1O_2$ decreased greatly, resulting in lower conversion rates. Furthermore, technical limitations were initially difficult to overcome as only one LED module was available (Figure 4.7a). Interested in our work with immobilised photocatalysts, Vapourtec Ltd. offered an opportunity to collaborate in the design of a new column photoreactor. The first iteration provided greater coverage of light to pHIPE-BTZ by using a three-module set-up (Figure 4.7b). This general design model along with our feedback helped inform the final product as seen in Figure 4.7c, which can be found on the Vapourtec Ltd. website [4.12]. After further optimisation of the reaction conditions, the use of the immobilised column photoreactor showed an immense improvement over the initial system with a production rate for the conversion of α-terpinene to ascaridole of 192 mg h^{-1}.

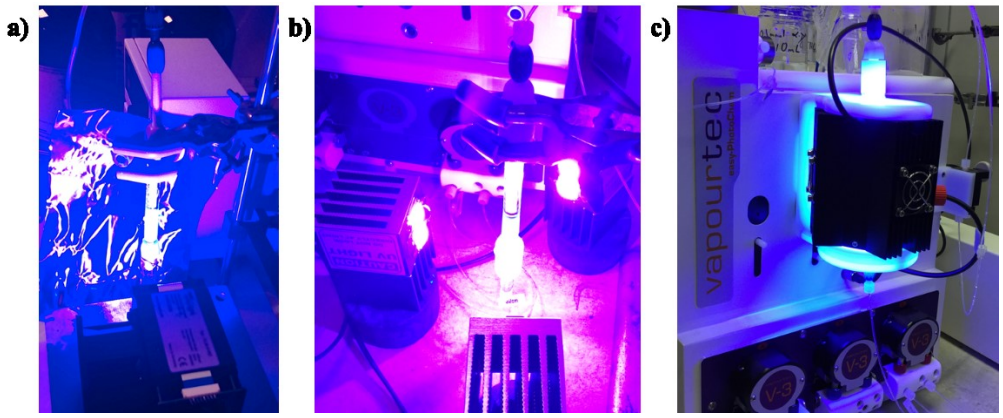

Figure 4.7 Iterations of the pHIPE-BTZ flow set-up: a) single LED module; b) Three LED modules surrounding the column; c) Immobilised photocatalytic reactor from Vapourtec Ltd.

4.4.6 Production of $^1O_2$ under Sunlight Irradiation

The polymers presented thus far have been exhibited as efficient and stable photosensitisers for $^1O_2$ under strict laboratory conditions. However, to establish the robust and versatile nature of these materials, the production of $^1O_2$ was also carried out in batch with Gel (3 %) and Bead-BTZ under direct sunlight irradiation as opposed to the 420 nm LED modules. These reactions were performed under clear skies and during the months of July and August. Full conversion to the ascaridole product was observed after 90 minutes with Gel (3 %) and after 60 minutes with Bead-BTZ. As the conversion rates were comparable with those performed under the narrow wavelength 420 nm LED modules, the robust nature of the photoactive polymers was validated. Furthermore, as we continue to investigate and design new photoactive materials, it is important to recognise that the ideas surrounding photocatalysis revolve around the use of sunlight as a free and abundant source of energy [4.13]. Through the successful implementation of these polymers under sunlight irradiation, we have demonstrated their potential for applications with low environmental impact.

4.4.7 Aerobic Oxidative Hydroxylation of Arylboronic Acids

Thus far, the polystyrene-based material described above have been demonstrated as exceptional triplet state photosensitisers. While the generation of $^1O_2$ has been useful for comparisons to other photosensitising materials, this success also prompted the investigation into other applications that can utilise a triplet photosensitiser [4.14]. One

of these applications is the generation of another reactive oxygen species, superoxide ($O_2^{\cdot -}$). To test this assertion, the conversion of aryl boronic acids to phenols was performed [4.15, 4.16]. It should be noted that a major component for the generation $O_2^{\cdot -}$ when compared to $^1O_2$ generation is the requirement of an amine base as it acts as a sacrificial electron donor. The mechanism describing the difference between $^1O_2$ and $O_2^{\cdot -}$ can be seen in Figure 4.8 [4.15, 4.16].

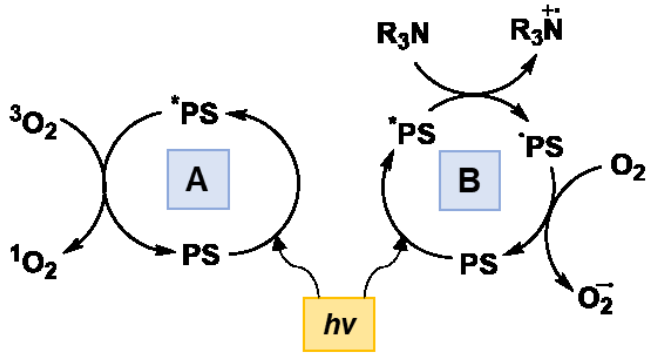

Figure 4.8 Mechanisms depicting (A) the photosensitised generation of $^1O_2$ and (B) the amine-mediated photosensitised generation of $O_2^{\cdot -}$.

From the initial model reaction in batch with phenylboronic acid and Gel (5 %) as the photosensitiser, full conversion of the optimised reaction was observed *via* ^{1}H NMR spectroscopic analysis after 24 h. Control experiments were also performed, indicating the requirement for light, air (O_2), base, and the photosensitiser for the reaction to proceed. The scope for substituted phenylboronic acids was also tested under the optimised conditions (Figure 4.9) where it was observed that aryl boronic acids with electron-withdrawing substituents showed full conversion to the phenol product at an accelerated rate. The exception to this was the ester-substituted phenylboronic acid which required a longer reaction time compared to the unsubstituted reagent. Conversely, aryl boronic acids with electron-donating substituents tended to require extended reaction times to reach full conversion.

The Bead-BTZ and pHIPE-BTZ photosensitisers were also implemented under similar reaction conditions using continuous flow chemistry. While pHIPE-BTZ showed an increase in time to reach full conversion to the phenol product (30 h) when compared to the standard batch reaction with Gel (5 %), it is noted that the total usage time for the polyHIPE was in excess of 80 h. During this time, pHIPE-BTZ was exposed to intense light irradiation, harsh chemicals and solvents, and highly oxidative conditions.

Regardless, it continued to demonstrate good photocatalytic activity and illustrates the highly robust nature of the polymer-supported photosensitiser. The stability shown by St-BTZ when incorporated into a polymer backbone is outstanding, especially when compared to the soluble monomer.

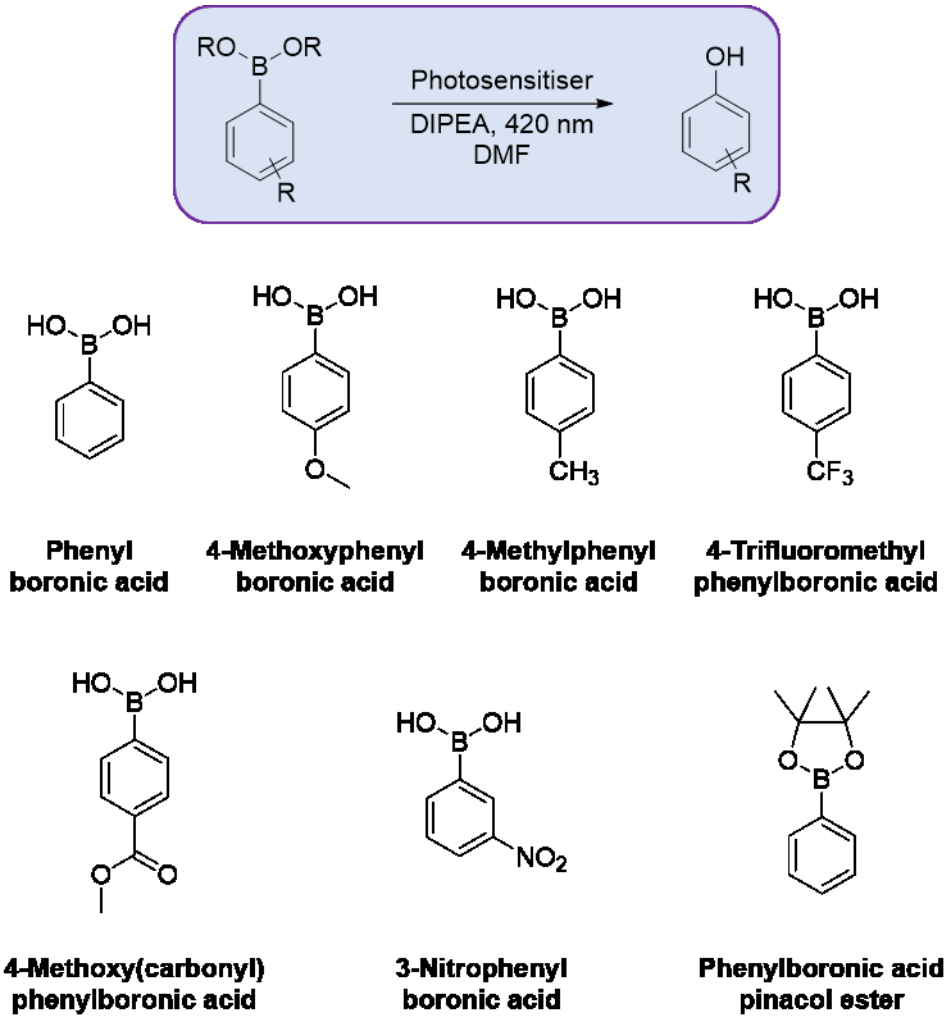

Figure 4.9 General reaction scheme of the conversion of aryl boronic acids to phenols *via* BTZ-based photosensitisation along with the scope of boronic acids used.

Bead-BTZ was studied using the optimised standard reaction with phenylboronic acid in both batch and continuous flow conditions. In batch, a decrease in the time to reach full conversion to the phenol product (10 h) was noted, showing enhanced photoactivity when compared to 24 h required for Gel (5 %). Furthermore, the same reaction carried out under continuous flow conditions demonstrated an even greater decrease in reaction time where full conversion was observed after only 5 h. Further testing also showed Bead-BTZ as reusable and stable to both light and oxidative conditions.

4.5 Conclusion

A novel BTZ-based crosslinking monomer has been designed, synthesised and employed in a copolymerisation with styrene. Using various free radical polymerisation techniques, three insoluble polystyrene-based photosensitisers were synthesised in different formats: gels, beads, and a monolithic polyHIPE. Through utilisation of the coupling between benzene (weak electron donor) and BTZ (strong electron acceptor), both the photoactive monomer and subsequent polymers exhibited absorbance within the visible spectrum (400 – 450 nm). Both past research and computational studies indicated the ability of these materials to occupy a triplet excited state and were subsequently examined as photosensitisers for the formation of reactive oxygen species ($^1O_2$ and $O_2^{\cdot -}$). While photoactive, the St-BTZ monomer demonstrated instability in the presence of $^1O_2$. However, incorporation into the polystyrene matrix as a crosslinker resulted in a dramatic increase in chemical stability and photocatalytic performance. The gels proved efficient in batch but were unsuitable in flow due to their tendency to swell and agglomerate. Both the beads and polyHIPE were employed under continuous flow conditions as mobilised and immobilised photosensitisers, respectively, exhibiting exceptional performance and stability. While more work is required to better understand these materials and the full scope of their capabilities, the work presented provides a proof of concept towards a new class of polymer-supported photocatalysts.

4.6 Impact on Literature and Research

This research focuses primarily on the synthesis of a new photoactive monomer and its dilution into a polymer matrix. By minimising the photoactive component required and retaining similar stability and photocatalytic capabilities compared to other heterogeneous photocatalysts, we have taken a step towards more sustainable and low-impact materials. Furthermore, through control of the vinyl groups on the Ph-BTZ monomer (Figure 4.1), we envisage its use as a photoactive component in any number of polymer systems. To validate this concept, the Ph-BTZ monomer has since been implemented into a polyamide-based material as a water-based photosensitiser for the degradation of two emerging wastewater contaminants, cimetidine and bisphenol A. Moreover, it was also used as a disinfectant for the excystation of chlorine-resistant Cryptosporidium from contaminated water sources [4.17]. This work again demonstrated

the ability for the polymer-supported material to act as a robust photosensitiser for the generation of $^1O_2$ whilst integrated into a different polymer framework.

The success of these materials has also inspired the use of the St-BTZ crosslinker as a comonomer for 3D printed structures (Figure 4.10). While this work is still in an early phase, it has provided an insight into how development of bespoke photoactive resins can enable the application of stereolithography for the fabrication of continuous flow photoreactors with the St-BTZ unit directly incorporated within the polymer matrix. Figure 4.10b depicts the successful incorporation of St-BTZ into a commercially available stereolithography resin, which was subsequently used to fabricate 3D photosensitizing continuous flow reactor prototype for singlet oxygen generation. Preliminary results indicate that the even with small concentration of St-BTZ (0.5 wt%), stereolithography fabricated small scale (0.1 ml) photoactive continuous flow reactor shows activity in singlet oxygen synthesis reaction under visible light irradiation (420 nm). Future work will involve design and fabrication of larger volume photoreactors with intricate flow features, and development of stereolithography resins to produce structure with greater resistance to organic solvents.

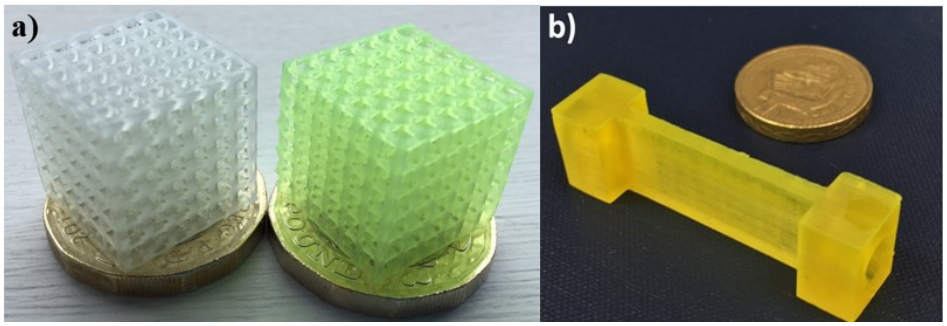

Figure 4.10 3D printed structures incorporating the photoactive St-BTZ monomer into the polymer: a) initial print test with (right) and without (left) St-BTZ; b) small-scale continuous flow reactor with 0.5 mol % St-BTZ.

4.7 References

[4.1] R. S. Sprick, J.-X. Jiang, B. Bonillo, S. Ren, T. Ratvijitvech, P. Guiglion, M. A. Zwijnenburg, D. J. Adams, A. I. Cooper, *Tunable Organic Photocatalysts for Visible-Light-Driven Hydrogen Evolution*, J. Am. Chem. Soc., **137**, 3265-3270 (2015)

[4.2] R. Li, J. Byun, W. Huang, C. Ayed, L. Wang, K. A. I. Zhang, *Poly(benzothiadiazoles) and Their Derivatives as Heterogeneous Photocatalysts for Visible-Light-Driven Chemical Transformations*, ACS Catal., **8**, 4735-4750 (2015)

[4.3] B. C. Ma, S. Ghasimi, K. Landfester, F. Vilela, K. A. I. Zhang, *Conjugated microporous polymer nanoparticles with enhanced dispersibility and water compatibility for photocatalytic applications*, J. Mater. Chem. A, **3**, 16064-16071 (2015)

[4.4] *Global Styrene Production Exceeded 26.4 Million Tonnes in 2012*, Merchant Research and Consulting Ltd., 2013, accessed September 2018, <https://mcgroup.co.uk/news/20130830/global-styrene-production-exceeded-264-million-tonnes.html>

[4.5] J. M. G. Cowie, V. Arrighi, *Polymers: Chemistry and Physics of Modern Materials*, 3rd Ed., CRC Press: Boca Raton, FL, (2008)

[4.6] G. Geuskens, K. David, In *The Photo-oxidation of Polymers. A Comparison with Low Molecular Weight Compounds*, Plenary Lectures Presented at the Seventh Symposium on Photochemistry, Leuven, Belgium, July 24-28, 1978; A. Reiser, Ed.; Elsevier: London, (1979)

[4.7] M. S. Silverstein, *Emulsion-templated porous polymers: A retrospective perspective*, Polymer, **55**, 304-320 (2014)

[4.8] J. F. Rabek, *Photodegradation of Polymers*, Springer-Verlag: Berlin, (1996)

[4.9] K. Zhang, D. Kopetzki, P. H. Seeberger, M. Antonietti, F. Vilela, *Surface Area Control and Photocatalytic Activity of Conjugated Microporous Poly(benzothiadiazole) Networks*, Angew. Chem., Int. Ed., **52**, 1432−1436 (2013)

[4.10] H. Urakami, K. Zhang, F. Vilela, *Modification of conjugated microporous poly-benzothiadiazole for photosensitized singlet oxygen generation in water*, Chem. Commun. **49**, 2353−2355 (2013)

[4.11] K. Zhang, Z. Vobecka, K. Tauer, M. Antonietti, F. Vilela, *π-Conjugated polyHIPEs as highly efficient and reusable heterogeneous photosensitizers*, Chem. Commun., **49**, 11158−11160 (2013)

[4.12] *Illuminating immobilised photo catalysts*, Vapourtec Ltd., 2018, accessed September 2018, <https://www.vapourtec.com/products/flow-reactors/immobilised-photo-catalysts-features/>

[4.13] J. Schneider, D. Bahnemann, J. Ye, G. Li Puma. D. D. Dionysiou, *Photocatalysis: Fundamentals and Perspectives*, The Royal Society of Chemistry, UK, (2016)

[4.14] J. Zhao, W. Wu, J. Sun, S. Guo, *Triplet photosensitizers: from molecular design to applications*, Chem. Soc. Rev., **42**, 5323−5351 (2013)

[4.15] Y.-Q. Zou, J.-R. Chen, X.-P. Liu, L.-Q. Lu, R. L. Davis, K. A. Jorgensen, W.-J. Xiao, *Highly Efficient Aerobic Oxidative Hydroxylation of Arylboronic Acids: Photoredox Catalysis Using Visible Light*, Angew. Chem., Int. Ed., **51**, 784−788 (2012)

[4.16] J. Luo, X. Zhang, J. Zhang, *Carbazolic Porous Organic Framework as an Efficient, Metal-Free Visible-Light Photocatalyst for Organic Synthesis*, ACS Catal., **5**, 2250−2254 (2015)

[4.17] J. Shen, R. Steinbach, J. M. Tobin, M. Mouro Nakata, M. Bower, M. R. S. McCoustra, H. Bridle, V. Arrighi, F. Vilela, *Photoactive and metal-free polyamide-based polymers for water and wastewater treatment under visible light irradiation*, Appl. Catal. B, **193**, 226-233 (2016)

DECLARATION

As primary author of this publication, I can confirm the majority of the work to be my own. Work carried out by other students or collaborators has been outlined above.

Signature: _____

PUBLICATION 4

Polymer-Supported Photosensitizers for Oxidative Organic Transformations in Flow and under Visible Light Irradiation

J. M. Tobin, T. J. D. McCabe, A. W. Prentice, S. Holzer, G. O. Lloyd, M. J. Paterson, V. Arrighi, P. A. G. Cormak, F. Vilela

DOI: 10.1021/acscatal.7b00888

ACS Catal., **2017**, *7*, 4602-4612

Abstract

A 2,1,3-benzothiadiazole (BTZ)–based vinyl crosslinker was synthesized and copolymerized with large excesses of styrene using free radical polymerization to deliver heterogeneous triplet photosensitizers in three distinct physical formats: gels, beads and monoliths. These photosensitizers were employed for the production of singlet oxygen ($^1O_2$) and for the aerobic hydroxylation of aryl boronic acids *via* superoxide radical anion ($O_2^{\bullet -}$) whereby the materials demonstrated good chemical and photo stability. BTZ-containing beads and monoliths were exploited as photosensitizers in a commercial flow reactor, and $^1O_2$ production was also demonstrated using direct sunlight irradiation, with a conversion rate comparable to the rates achieved when using a 420 nm LED module as the source of photons.

Introduction

New advances in photocatalytic processes (including new photocatalysts) have been made in recent years, not only in the production of energy dense materials, as shown in the field of Solar Fuels (with extensive studies on achieving water-splitting and CO_2 reduction), but also in organic synthesis [1-3]. These efforts represent a true advancement in realizing more sustainable, economical and environmentally friendly strategies for a wide-range of chemical processes.

One photocatalytic process that has been under scrutiny is the generation of singlet oxygen ($^1O_2$) through well-known photosensitization reactions [4, 5]. These reactions proceed under mild conditions, requiring only a photosensitizer, a light source and molecular oxygen. Organic dyes such as Rose Bengal, Eosin Blue and Methylene Blue, among others, are some of the most commonly used photosensitizers in this process [6-11]. When irradiated with light of an appropriate wavelength, energy is absorbed by the photosensitizer which is excited electronically to the triplet state through an intersystem crossing mechanism. The excited photosensitizer then transfers this energy to the ground state triplet oxygen ($^3O_2$), resulting in the formation of $^1O_2$ [7]. The electrophilic and oxidizing properties of $^1O_2$ have driven its use as an oxidant and as a synthetic reagent in a wide range of applications, such as organic synthesis [12], water and wastewater treatment[13] and photodynamic therapy for the treatment of cancer [14, 15].

Another area of catalysis that has come to prominence recently is that of photoredox reactions for organic synthesis [16]. Along with the generation of $^1O_2$, photooxidations use molecular oxygen in air as a green reagent, resulting in highly desirable reaction conditions. However, the reactive species for these reactions involve a superoxide radical anion ($O_2^{\bullet-}$), not the aforementioned $^1O_2$. Formation of $O_2^{\bullet-}$ can proceed through a photoredox cycle in the presence of an amine base acting as a sacrificial reductant, a photosensitizer capable of occupying the excited triplet state and molecular oxygen [17].

While both reactive forms of molecular oxygen are generally well-known and have their uses in a variety of applications, many of the photocatalytic materials used rely largely on transition metal complexes or organic dyes, which can lead to several issues. For example, the use of organometallic photosensitizers, while efficient light harvesters

[17-21], tend to be expensive, unsustainable and toxic. Some photosensitizers are also prone to photobleaching, *i.e.*, the degradation of the photosensitizer due to prolonged exposure to light and/or reactivity with $^1O_2$ [7]. This leads to both a reduction in the efficiency and the lifetime of the photosensitizer. Lastly, most of these materials are employed under homogeneous conditions, leading to a cumbersome separation and recovery process of the photosensitizer from the reaction mixture, and ultimately the desired products, which impedes the reusability of the photosensitizer [22]. These disadvantages demonstrate the need to develop metal-free and photostable materials that can act as heterogeneous photosensitizers in a variety of reactions and conditions.

In principle, the use of heterogeneous photosensitizers offers advantages in practical applications when compared to their homogeneous counterparts because they are easy to isolate, recover and recycle. Immobilization of commonly used homogeneous photosensitizers, such as organic dyes [23, 24] and transition metal complexes [25], in polymer matrices has been shown to provide a more photostable material. This is due to the polymer matrix acting as an efficient oxygen diffusion barrier whilst inhibiting photobleaching of the photosensitizer [26]. However, this immobilization technique may lead to a decrease in the quantum yield of $^1O_2$ production and therefore its efficiency as a photosensitizer [7]. Nevertheless, the added benefits of a heterogeneous photosensitizer (ease of recovery, reusability and avoiding contamination of the product) outweigh the lower efficiency of the photocatalytic material.

Recently, we reported the use of conjugated microporous polymers (CMPs) as heterogeneous triplet photosensitizers. Through visible light irradiation, these 2,1,3-benzothiadiazole (BTZ) [27-29] or 4,4-difluoro-4-bora-3a,4a-diaza-s-indacene (BODIPY)-rich [30] CMPs have been shown to be efficient and reusable materials for the production of $^1O_2$. Reports employing heterogeneous photocatalysts for photoredox reactions have begun to emerge, primarily through the use of CMPs [31]. However, along with this work, CMP synthetic strategies largely involve Pd catalysts, resulting in an expensive material that is likely to be contaminated with residual Pd. Residual metal, even at ppb levels, is problematic as it may interfere with catalytic processes or lead to the toxicity of the reaction medium due to leaching. To circumvent this issue, we have developed a photoactive vinyl monomer, based upon the photoactive repeat unit used within the BTZ-CMPs [27-29], which can be incorporated with ease into polymer matrices *via* free radical copolymerization. The BTZ-based monomer contains two

styrene units, which results in an electronic "push-pull" system, in which the BTZ unit acts as the strong electron acceptor and the styrene as a weak electron donor. Similarly to the CMPs, we expected that this system would allow the monomer, and polymers derived from the monomer, to act as photosensitizers for the production of $^1O_2$.

One of the most widely available monomers for the production of polymers is styrene, with over 25 million tons produced globally every year [32]. It is a highly versatile monomer used to prepare a variety of polymer architectures including linear, branched and crosslinked polymers. Various formats of polystyrene have been described, such as foams, gels, beads and monolithic structures [33].

Herein, the synthesis and characterization of a photosensitizing crosslinking monomer and its incorporation into polystyrene structures through free radical copolymerization is presented. A BTZ-based crosslinker was designed with two styrene units (Scheme 1) allowing for its exploitation as a co-monomer together with styrene and/or divinylbenzene (DVB) in traditional, as well as more specialized, free radical polymerization techniques. Using 3-5 mol % only of the BTZ-based crosslinker, three insoluble forms of photoactive polystyrene were synthesized: gels, micrometer-sized polymer beads and monoliths. Computational models of the monomer and polymer repeat unit were investigated to demonstrate their ability to occupy the triplet excited state and thereby act as triplet photosensitizers. To validate these models, both the monomer and corresponding polymers were evaluated for the production of $^1O_2$ in chloroform under both batch and flow conditions under visible light irradiation (420 nm). Furthermore, the same materials were screened as triplet photosensitizers in aerobic hydroxylation of a series of aryl boronic acids *via* the formation $O_2^{\bullet-}$. These materials have been presented as a proof of concept where both computational and catalytic experiments verify them as efficient and stable triplet photosensitizers.

Experimental

General polymer synthesis and photocatalytic procedures will be described henceforth. All other information pertaining to specific experimental methods not presented here can be found in the ESI.

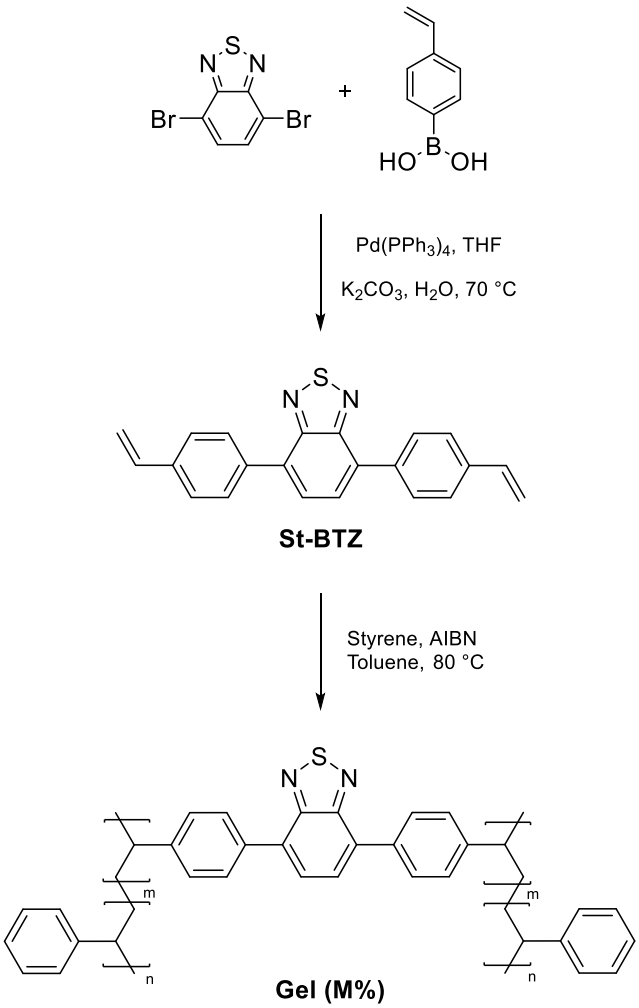

Scheme 1 Reaction schemes for the synthesis of the monomer (**St-BTZ**) and gel-type polymers (**Gel (M%)**).

Synthesis of 4,7-distyrene-2,1,3-benzothiadiazole (St-BTZ). To a dry, 2-necked flask equipped with a magnetic stirring bar and a reflux condenser was added a mixture of 4,7-dibromo-2,1,3-benzothiadiazole (147 mg, 0.5 mmol), 4-vinylphenylboronic acid (148 mg, 1 mmol), and $Pd(PPh_3)_4$ (17 mg, 0.015 mmol). The flask was connected to a Schlenk line, evacuated and back-filled three times with N_2. In the flask whilst under N_2, dry THF (40 mL) was added to dissolve the solid reagents. An aqueous solution (5 mL) was then prepared with K_2CO_3 (140 mg, 1 mmol), degassed for approximately 10 minutes with N_2 and added to the organic solution. The mixture was heated to 70 °C and left overnight, stirring under a N_2 atmosphere. The reaction mixture was allowed to cool to room temperature before adding approximately 40 mL of water and transferring to a separating funnel with 50 mL of dichloromethane. The organic layer was washed three times with deionized water and the collected fractions were dried over Na_2SO_4. The crude mixture was filtered and purified *via* silica gel column

chromatography with hexane:CH_2Cl_2 (4:6) as eluent, yielding a bright yellow colored solid (96 mg, 56%). ^{1}H NMR (300 MHz, $CDCl_3$): δ_{ppm} = 5.36 (d, 1 H), 5.89 (d, 1 H), 6.85 (m, 1 H), 7.63 (d, 2 H), 7.83 (s, 1 H), 8.00 (d, 2 H); ^{13}C NMR (100 MHz, $CDCl_3$): δ_{ppm} = 114.5, 126.5, 127.6, 129.4, 133.0, 136.4, 136.8, 137.7, 154.1.

General synthesis of Styrene-St-BTZ copolymers *via* free radical polymerization (Gel (M%)). Styrene (1 g, 9.6 mmol) was added to a sample vial with a magnetic stirring bar and dissolved in 5 mL of degassed toluene. **St-BTZ** (2, 3 or 5 mol %) and AIBN (16 mg, 0.096 mmol) were added to the solution, allowed to dissolve and degassed with N_2 for 10 minutes. The vial was sealed, heated to 60 °C and left for 16 h to polymerize while stirring. The solution began as a bright, yellow liquid and changed according to the percentage of **St-BTZ** added. The reaction was allowed to cool to room temperature and the product was removed from the vial and worked up as follows: (i) Precipitation of product was performed in 100 mL of MeOH, for soluble copolymers; (ii) Soxhlet extraction was performed for insoluble (crosslinked) copolymers with THF and methanol. All copolymers were dried *in vacuo*. It is noted that only those polymers containing 3 or more mol % of the **St-BTZ** crosslinker produced an insoluble gel. At concentrations lower than 3 mol % a soluble polymer was formed. Product recovery: **Gel (2%)** 367 mg, 37 %; **Gel (3%)** 240 mg, 24 %; **Gel (5%)** 465 mg, 47 %.

Synthesis of Styrene-DVB-St-BTZ copolymer *via* precipitation polymerization (Bead-BTZ). DVB-55 (221 mg, 1.7 mmol), styrene (666 mg, 6.4 mmol), **St-BTZ** (115 mg, 0.3 mmol) (2% w/v total monomer in feed, relative to solvent) and AIBN (41 mg, 0.2 mmol) (2 mol % relative to polymerizable double bonds in monomers) were added to acetonitrile (50 mL) in a Nalgene® bottle (250 mL). Note that the monomer mole ratio employed for this synthesis was 76:20:4 (styrene:DVB-55:**St-BTZ**), providing a good comparative analogue to the gels. The bottle contents were ultrasonicated for 15 minutes. After ultrasonication, N_2 gas was bubbled through the reaction mixture for 15 minutes in an ice-bath. After degassing, the Nalgene® bottle was sealed under N_2 and placed on a low profile roller (Stovall Life Sciences Inc., North Carolina, U.S.A) contained within an incubator (Stuart Scientific, Stone, UK) and rotated slowly about its long axis. The temperature inside the incubator was ramped from ambient temperature to 60 °C over a period of around two hours. The polymerization was allowed to proceed for a further 46 hours to give a milky suspension of polymer particles. The resulting particles were visualized *via* optical microscopy prior to filtration. The product was

filtered by vacuum on a 0.45 μm nylon membrane filter. The particles were then washed with solvent to remove any unreacted monomer or initiator (~100 mL of acetonitrile followed by ~100 mL of toluene, methanol and finally acetone) before being dried overnight *in vacuo* (60 mbar, 40 °C). Product recovery: 120 mg, 12 %.

Synthesis of Styrene-DVB-St-BTZ copolymer *via* high internal phase emulsion polymerization (pHIPE-BTZ). Styrene (0.213 g, 2.04 mmol), DVB-80 (40 mg, 0.29 mmol), **St-BTZ** (25 mg, 0.07 mmol) and Span 80 (0.054 mL) were added to a sample vial and potassium persulfate (18 mg, 0.2 % wt. of water) and sodium chloride (90 mg, 1 % wt. of water) were dissolved in water (9 mL) in a separate vial. Note that the monomer mole ratio was 85:12:3 (styrene:DVB:**St-BTZ**), providing a good comparative analogue to the gels. The organic phase was placed in an electric mixer (Polytron PT 1200 E) and the aqueous solution was added slowly. The addition of the aqueous solution was stopped when the emulsion could no longer be mixed properly due to thickening. Remaining liquid was decanted and part of the emulsion was delivered into a transparent glass column (7 mm inner diameter) equipped with porous frit on both ends *via* syringe. The column was sealed and placed in a 60 °C oven and left for 24 h. The column containing the synthesized polyHIPE was flushed with 100 mL of THF, CH_2Cl_2 and chloroform. The bright yellow monolith (35 mm length x 7 mm diameter) was left in the glass column to be used for flow experiments.

Computational modelling of St-BTZ excited states. Geometry optimization was performed with density functional theory (DFT) using both the CAM-B3LYP and MN12-L functionals, while excited electronic states were computed with time-dependent DFT, utilizing the temporal adiabatic approximation with the same functionals. The 6-311G(d,p) basis set was used for all computations. Analytical Hessian computation was used to confirm optimized stationary geometries as minima. We note only negligible difference between functionals and so discuss the CAM-B3LYP results below (full results for both are given in the supporting information). All computations were performed using Gaussian09 [34].

General procedure for photocatalytic reactions under batch conditions. To a vial containing the required solution (5-10 mL), 5-10 mg of photosensitizing material was added. The mixture was left to stir, whilst open to air, for 10 minutes to allow for proper dissolution or swelling and to aerate the solution. The vial was then placed 7 cm from a

420 nm LED lamp and the lamp was switched on. The reaction was monitored *via* TLC and/or ^{1}H NMR spectroscopy until full consumption of the starting materials was noted, at which time the reaction was stopped and analyzed.

General procedure for photocatalytic reactions in flow employing Bead-BTZ. To a flask containing the required solution (10-15 mL), 5 mg of **Bead-BTZ** was added. The suspension was first sonicated for 2 minutes to ensure an even dispersion of particles. The mixture was then left to stir, whilst open to air, for 10 minutes to aerate the solution. The dispersion was then pumped through the photochemical reactor (Figure S2) at a flow rate of 1 mL.min^{-1}. Concurrently, air was pumped through a second pump at the same flow rate, mixing with the dispersion at a T-junction before entering the photochemical reactor equipped with a 420 nm LED lamp. The dispersion was cycled for the required time and monitored *via* TLC and/or ^{1}H NMR spectroscopy. Upon consumption of the starting materials, the reaction was stopped and evaluated further.

General procedure for photocatalytic reactions in flow employing pHIPE-BTZ. The **pHIPE-BTZ** monolith, fitted to a transparent glass column, was allowed to swell in the required solvent for 16 hours. The solution containing the starting materials (10 mL) was prepared and aerated for 10 minutes open to air. The column was fitted to a light source (Figure S3) and the solution was pumped through the column at 0.5-1.0 mL.min^{-1}. Concurrently, oxygen was pumped through a second pump at the same flow fate, mixing with the solution at a T-junction before entering the column. The operating pressure was kept at 1.3 bar to ensure a steady stream of both the solution and air. The 10 mL solution was pumped through the column and monitored *via* TLC and/or ^{1}H NMR spectroscopy. Upon consumption of the starting materials, the reaction was stopped and evaluated.

Results and Discussion

Monomer Properties

The UV-Vis absorption spectra for **St-BTZ** presented as a broad absorption peak in the range 350 to 450 nm with a maximum absorbance at 400 nm (Figure S13). This falls within the visible spectrum and is comparable to the absorbance characteristics which we have reported for other BTZ-based photosensitizers [27-29]. FT-IR, ^{1}H NMR

and ^{13}C NMR spectroscopic analysis was fully consistent with the structure of **St-BTZ** (see ESI). An X-ray crystal structure and the corresponding analysis data can also be found in the ESI.

By virtue of its polymerizable vinyl groups, **St-BTZ** can be copolymerized with styrene *via* free radical polymerization. Similarly to DVB, **St-BTZ** can act as a branching node and consequently as a crosslinker. Employing the crosslinker at an appropriate concentration in a copolymerization can result in an insoluble, crosslinked polymer that can then be employed as a heterogeneous photosensitizer.

Synthesis and Properties of Gel (M%)

One of the key aims of the work was to minimize the amount of photoactive **St-BTZ** required whilst ensuring the formation of an insoluble polymer with the desired photosensitizing properties. The selection of styrene as co-monomer as the basis for the heterogeneous photosensitizer was influenced by the stability of polystyrene in the presence of $^1O_2$ [35] and the fact that the photoactive monomer also contains styrene units, which leads to a more compatible copolymerization between the co-monomers.

The formation of these polymers (**Gel (3%)** and **Gel (5%)**) suggests that there was sufficient crosslinking of the polymer chains to create an insoluble material. The bright yellow color, similar to that of **St-BTZ**, is also indicative of the integration of the photoactive crosslinker into the polymer network. Most of the solvent used in these reactions was sorbed by the polymers, resulting in bright yellow, swollen gels (Figure 1). A swelling test was performed on dried **Gel (3%),** demonstrating an increase of up to seven times its original volume when added to chloroform (Figure S1).

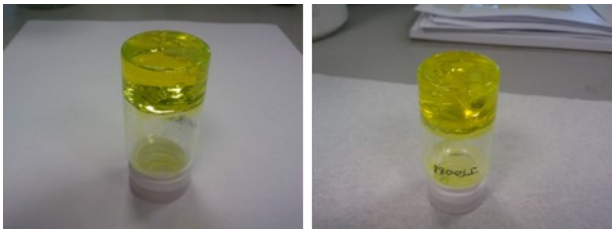

Figure 1 Inverted reaction vials showing **Gel (3%)** (left) and **Gel (5%)** (right) as insoluble gels swollen in chloroform.

UV-Vis absorption spectra of the materials showed a broad absorption band (350-450 nm) with a maximum at 400 nm (Figure S13). FT-IR spectroscopic measurements showed peaks corresponding to **St-BTZ** residues (825 and 887 cm^{-1}), which were not observed in a polystyrene standard (Figure S12). Note that these signals were relatively weak due to the high ratio of styrene to **St-BTZ** within the polymer.

Solid state ^{13}C NMR CP-MAS spectroscopy was also employed to characterize **Gel (3%)**. Whilst aromatic carbons are present primarily, at 128 ppm (C-C) and 146 ppm (C-N), signals in the alkyl region are also identified at 40-45 ppm and correspond to the saturated aliphatic backbone of the copolymer (Figure S18). These observations suggest that **St-BTZ** was incorporated successfully into the polystyrene chains *via* well-established, metal-free, free radical polymerization and that the polymer has the potential to be used a polystyrene-based heterogeneous photosensitizer.

Heterogeneous phase polymerizations (including emulsion, dispersion, precipitation and suspension polymerization) [33] using the same free radical initiator allow us to demonstrate the versatility of the photoactive crosslinker. This versatility arises from the ability of **St-BTZ** to be implemented in a variety of free radical polymerization techniques whilst yielding polymers which retain the photoactive properties of the monomer. For the purposes of this study, precipitation polymerization and high internal phase emulsion (HIPE) polymerization were employed, which allows for the synthesis of the polymers in different physical formats derived from the same monomer set: micron-sized beads from precipitation polymerizations and monolithic structures from HIPE polymerizations.

Precipitation Polymerization (Bead-BTZ)

As seen in Scheme S2, precipitation polymerization utilizing a free radical initiator was used to synthesize particles in the form of micron-sized beads. In order to ensure the production of an insoluble polymer, divinylbenzene-55 (DVB-55) was added as a non-photoactive crosslinker. The incorporation of DVB as a crosslinker also adds rigidity to the structure and good mechanical robustness to the beads. In parallel with the photoactive polymer synthesis, a styrene-DVB copolymer (**Bead**) was synthesized without any photoactive component for comparison.

UV-Vis spectroscopy showed a maximum absorption at ~420 nm for **Bead-BTZ,** which is comparable to the absorbance wavelength of the previously described materials (Figure S15). **Bead** did not display any absorption in the visible region and produced a white product compared to the bright yellow **Bead-BTZ** material. An FT-IR spectrum of **Bead-BTZ** showed the two distinct peaks characteristic of **St-BTZ** (887 and 825 cm^{-1}). These peaks were not observed for **Bead** (Figure S14). Figures 2a and 2b show both bead types together with the corresponding SEM images. These images show the polymer microspheres very clearly, with a bead size range of approximately 1-2 μm for both materials. While **Bead** resulted in better-defined particles, **Bead-BTZ** showed some signs of aggregation and agglomeration. Based on these observations, we concluded that the **St-BTZ** crosslinker was integrated successfully into the polystyrene beads.

High Internal Phase Emulsion Polymerization (pHIPE-BTZ)

The synthesis of **pHIPE-BTZ** was carried out through the free radical polymerization of a high internal phase emulsion (Scheme S3). A UV-Vis spectrum showed a maximum absorption at ~420 nm for **pHIPE-BTZ**, which is comparable to the absorption wavelengths of the other synthesized polymers (Figure S15). An FT-IR spectrum showed only weak bands attributable to **St-BTZ** (887 and 825 cm^{-1}) (Figure S14). Figure 2c shows **pHIPE-BTZ** in the column and the corresponding SEM image. This image demonstrates the high degree of porosity typical of polyHIPEs. Again, DVB was a crucial component to stabilize the structure as attempts with only **St-BTZ** (3-5 mol %) as the crosslinker resulted in amorphous, gel-like polymers.

Given the variety of free-radical polymerization techniques used, the synthesized monomer showed exceptional versatility and stability. By incorporating very limited amounts of the monomer into a polymer matrix, we were able to dilute the amount of photoactive component when compared to more common materials, as previously described. To better understand these materials as potential triplet photosensitizers, computational excited state data were gathered.

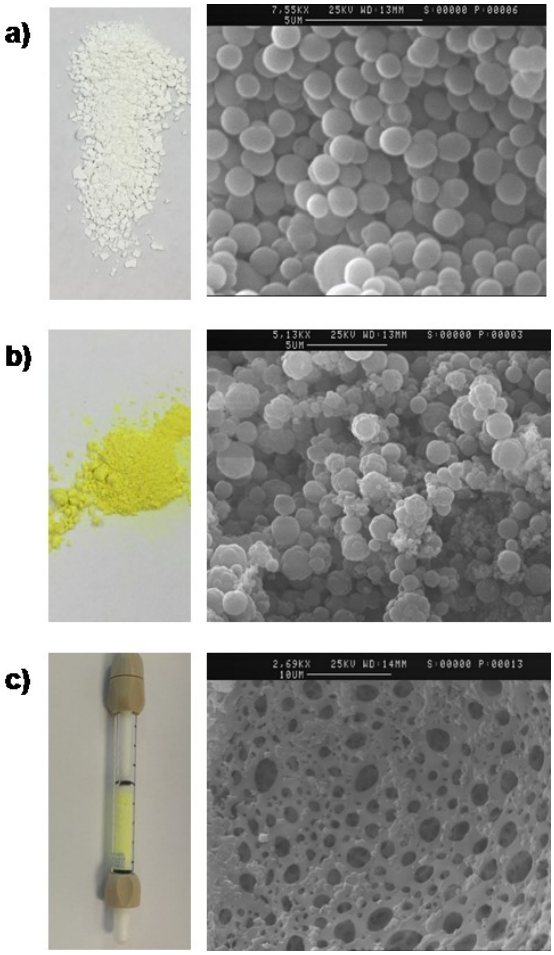

Figure 2 Synthesized copolymers and the corresponding SEM images: a) **Bead** containing no **St-BTZ**; b) **Bead-BTZ** with a yellow color indicating incorporation of **St-BTZ**; c) **pHIPE-BTZ** contained within a column as a stationary material for flow applications.

St-BTZ Excited State Computational Modelling

Computations have been performed to investigate the lowest singlet and triplet state geometries, and a characterization of vertical electronic excited states, for the **St-BTZ** monomer and in the absence of vinyl groups as it would appear in the photoactive polymers. For the systems investigated both C_2 and C_s ground state singlet conformers are found (differing in relative sign of dihedral twist for the benzene rings). Each isomer is essentially isoenergetic and results below are for the C_2 matching the crystal structure (further comparison in ESI). We note generally very good agreement for the S_0 geometry with experiment. For both systems the lowest singlet and triplet states are of the same character, being 94% represented by the HOMO-LUMO orbital transition (Table S1 and S2). This corresponds to charge transfer through the π-system from the styrene-

benzene/isopropyl-benzene groups to the BTZ group as shown in Figure 3 below for the monomer and polymer systems. Finally in Table S3 we give the singlet-triplet energy gap computed at the optimized triplet state geometry for both systems. There is around a 0.8 eV triplet stabilization from the vertical geometry for both systems.

Computational verification of the synthesized materials demonstrated their potential to occupy the triplet excited state. These results showed promise and prompted investigations into their catalytic capabilities. For the purposes of this study, we explored their ability to act as triplet photosensitizers in both the production of $^1O_2$ and $O_2^{\bullet-}$. Furthermore, due to the photoactive component being dramatically reduced within the polymeric materials, it was of great interest to understand if this had any significant effect on their ability to act as photosensitizers.

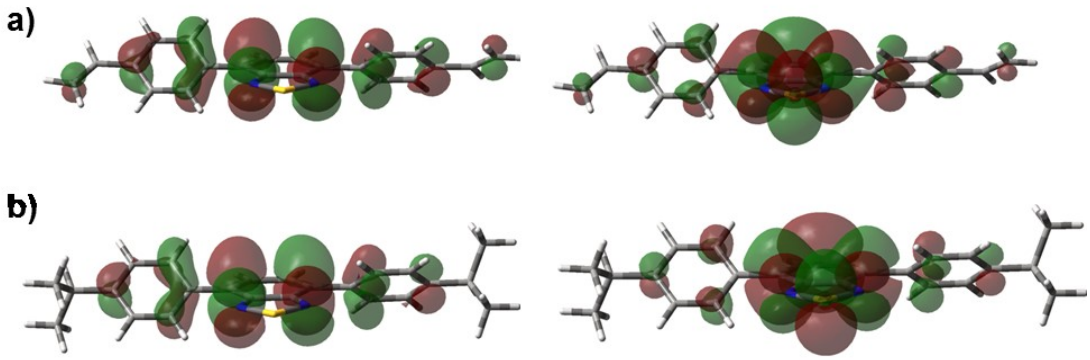

Figure 3 NTO particle-hole representation of a) **St-BTZ** monomer and b) polymer repeat unit T_1 state, computed with TD-CAM-B3LYP/6-311G(d,p).

Homogeneous Photosensitization at 420 nm with St-BTZ

The **St-BTZ** crosslinker was first examined as a homogeneous triplet photosensitizer in the production of $^1O_2$. Scheme 2 shows the Alder-ene reaction, which only proceeds in the presence of $^1O_2$ [36]. The production of $^1O_2$ was monitored by observing the conversion of α-terpinene into ascaridole *via* ^{1}H NMR spectroscopy (Figure S20). Full conversion to ascaridole was observed after 90 minutes of irradiation. However, a sudden decrease in the rate of conversion of α-terpinene to ascaridole was observed after 45 minutes, causing near full conversion to take upwards of 90 minutes.

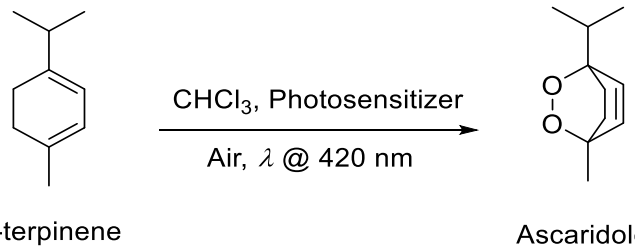

Scheme 2 Synthesis of ascaridole from *α*-terpinene *via* the photosensitization of singlet oxygen under visible light irradiation.

Samples taken at 15-minute time intervals revealed a dramatic color change (Figure S21), prompting further investigations to determine any potential photo-degradation or oxidative effect on **St-BTZ**. ^{1}H NMR spectroscopic analysis for each sample confirmed the degradation of the photosensitizer, where a clear decrease in the characteristic peaks for the monomer was observed (Figure S20).

Unsurprisingly, interactions between $^{1}O_2$ and vinylarenes can result in the production of monoadducts and endoperoxides [37]. The reaction potential of the vinyl groups may also have increased due to the electron withdrawing effects of the BTZ component within the monomer. Along with the known reactivity between vinylarenes and $^{1}O_2$, these observations demonstrate the instability of **St-BTZ** under highly oxidative conditions. Degradation issues aside, we were able to demonstrate the ability of **St-BTZ** to act as a triplet photosensitizer in the production of $^{1}O_2$ under visible light irradiation. However, we have shown in the past that when incorporating BTZ-based building blocks into CMPs, the stability of the resulting CMP upon production of $^{1}O_2$ is increased when compared to the monomeric version of BTZ [27-29]. Therefore, and knowing that polystyrene is largely unaffected by $^{1}O_2$ [35], we postulated that incorporating **St-BTZ** into a polystyrene matrix would mitigate the photo-degradation or oxidative effect on the polymer.

Heterogeneous Photosensitization at 420 nm with Gel (M%)

A procedure similar to that described above for **St-BTZ** (Scheme 2) was employed with a reaction time of 60 minutes. Three control experiments were performed first, as follows: *(i)* in the absence of any photosensitizing material; *(ii)* using a polystyrene standard as the photosensitizer; *(iii)* performing the experiment in the dark

and in the presence of **Gel (3%)**. Each of these controls showed no conversion of *α*-terpinene to ascaridole, and therefore that $^1O_2$ was not produced under these conditions.

As seen in Figure 4, both **Gel (3%)** and **Gel (5%)** showed comparable conversion rates, with close to full conversion achievable after 60 minutes of irradiation. Interestingly, compared to these heterogeneous photosensitization experiments, both homogeneous analogues, **St-BTZ** and **Gel (2%)**, gave significantly reduced conversion rates. The reduction in the rate of $^1O_2$ production with **Gel (2%)** can be explained by a decrease in the level of the photoactive monomer within the material. As the photoactive **St-BTZ** content decreases, there are fewer accessible sites for an energy transfer to $^3O_2$, resulting in reduced production of $^1O_2$. The reduced rate of $^1O_2$ production with **St-BTZ** has been explored as explained above. ^{1}H NMR spectra corresponding to each reaction can be found in the ESI.

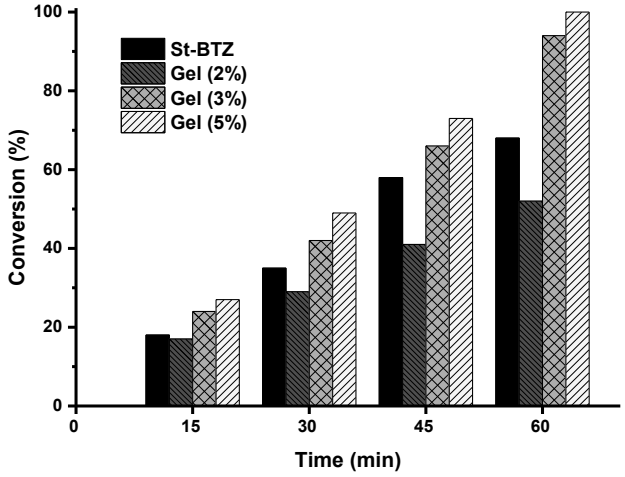

Figure 4 Conversion rates of *α*-terpinene to ascaridole using $^1O_2$ produced from the irradiation of **St-BTZ**, **Gel (2%)**, **Gel (3%)**, and **Gel (5%)** with a 420 nm LED lamp.

Based on these results, it is clear that the insoluble photoactive gels performed more efficiently than their soluble counterparts. While **Gel (5%)** performed slightly better than **Gel (3%)**, it also required a greater amount of the photoactive monomer. The gels also displayed greater stability than **St-BTZ**; no appreciable color change was observed over the reaction period. Most notably, these results demonstrate the generation of $^1O_2$ with a heterogeneous photosensitizer where the main component is polystyrene (95-97%). This is advantageous and cost-effective since it reduces the amount of **St-BTZ** required in the copolymer to produce $^1O_2$ when compared to other heterogeneous

photosensitizers where each repeat unit consist of a BTZ monomer [7, 27-29]. Moreover, self-quenching of the desired triplet state between photocatalytic segments of the polymer can occur if the concentration of the photoactive component is too great. This can greatly hinder the triplet state lifetime, and therefore diminish the effectiveness of the material as a photosensitizer. By reducing the concentration of **St-BTZ** the self-quenching effect is mitigated greatly without compromising the ability of the polymers to act as photocatalysts [8]. These concepts are crucial when investigating routes to both reduce the cost and increase the sustainability and effectiveness of photoactive materials.

Application of Bead-BTZ and pHIPE-BTZ in Continuous Flow

Continuous flow chemistry, as an alternative to standard batch synthesis, offers a flexible route to photochemical reactions, particularly when approaching industrial scales [38]. Reactions using this method allow for streamlined and continuous production of materials along with the potential for work-up and analysis integration [39]. This is critically important within industrial processes as it has the potential to both reduce costs and increase productivity. This is especially true for photochemical transformations as the irradiation of light to a solution is more efficient due to the shorter path lengths when compared to traditional batch processes. On larger industrial scales, photon penetration depth and excessive irradiation can be problematic under traditional batch conditions [40]. Continuous flow addresses these issues through higher surface-to-volume ratios and more efficient heat transfer. This allows for investigations into new synthetic pathways and reaction methodologies [41]. Photochemical reactions have been demonstrated widely using continuous flow methods, even under heterogeneous conditions [29, 41].

While the synthesized gels showed good $^1O_2$ production, post-reaction recovery and continuous flow chemistry was impractical. When attempted in flow, the gel particles aggregated and coagulated within the tubing. For this reason, **Bead-BTZ** and **pHIPE-BTZ** were designed specifically for two distinct continuous flow applications: *(i)* The polymer beads present a spherical shape and a low mean particle diameter (1-2 μm), which allows for facile dispersion throughout a solvent and low susceptibility to aggregation. These properties allow a dispersion of beads within the reaction mixture to flow through a photochemical reactor with greater ease than amorphous gels. This dispersion can be recirculated through the flow reactor for the time required to complete

the reaction; *(ii)* Unlike the beads, a polyHIPE remains as a stationary photosensitizer within a glass column where the reagents flow through the porous structure whilst being irradiated by an external light source. This results in the continuous production of the target product as long as the polyHIPE remains photoactive.

Heterogeneous Photosensitization at 420 nm with Bead-BTZ and pHIPE-BTZ in a Commercial Flow Reactor

The freely dispersible beads were investigated both in batch as well as under flow conditions. A batch experiment was set up identical to that of **Gel (3%)** to compare the production of $^1O_2$. ^{1}H NMR spectroscopy revealed similar conversion rates of *α*-terpinene to ascaridole compared to that of **Gel (3%)** (>95%) (Figure S25). This confirmed the photosensitizing nature of **Bead-BTZ** and showed no appreciable negative effects due to the added DVB-55.

A continuous flow experiment was then carried out with **Bead-BTZ** with the experimental set up depicted in Figure 5a. The dispersion was recirculated through the photochemical reactor for 60 minutes where full conversion to ascaridole was observed *via* ^{1}H NMR spectroscopy (Figure S26). The production rate for the conversion of *α*-terpinene to ascaridole was found to be 136 mg.h^{-1}. In order to relate this to the amount of photoactive component in the beads, the production rate of ascaridole per mg of **St-BTZ** in **Bead-BTZ** needs to be evaluated. This corresponds to 680 mg.h^{-1}.

pHIPE-BTZ was also employed as a photosensitizer under continuous flow conditions. However, the photochemical reactor was replaced with the column containing the trapped photoactive polyHIPE, as described above (Figure 2b). Due to the reduced contact time with **pHIPE-BTZ**, some experimental conditions had to be changed: *(i)* The concentration of the solution was lowered to 0.4 mmol *α*-terpinene in 10 mL of chloroform; *(ii)* air was replaced with pure oxygen; *(iii)* flow rates of both the reaction mixture and oxygen were reduced to 0.5 mL.min^{-1} (Figure 5b). Similarly to the gels, **pHIPE-BTZ** did swell in chloroform. Therefore, the polyHIPE samples were allowed to swell for 16 h in chloroform prior to the introduction of a reaction mixture. These changes were made to allow for a greater opportunity to yield full conversion to ascaridole after a single pass through the irradiated **pHIPE-BTZ** column.

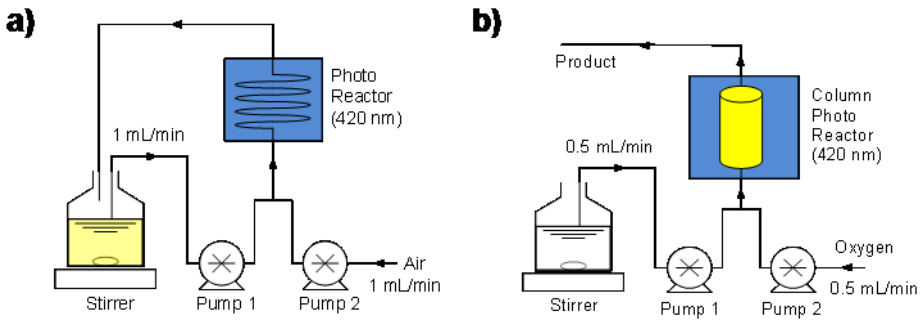

Figure 5 Schematic representation of the experimental set-up using the easy-Photochem flow reactor from Vapourtec Ltd. for a) **Bead-BTZ** and b) **pHIPE-BTZ**.

Under the stated conditions, we observed full conversion of *α*-terpinene to ascaridole after a single pass of the 10 mL solution of *α*-terpinene (0.4 mmol in chloroform) (Figure S27). To investigate the reusability of **pHIPE-BTZ**, a continuous stream of the reaction mixture was allowed to flow through the column, taking measurements in 10 mL increments. After 30 measurements under continuous flow and irradiation, no decrease in the conversion rate was observed (Figure S28). This suggests that the **pHIPE-BTZ** photosensitizer is stable to both light and $^1O_2$ over extended usage periods. Moreover, we note that the same column was employed in the photosensitization of $O_2^{\bullet-}$ for the aerobic hydroxylation of aryl boronic acids (as described below), demonstrating the superior stability of **pHIPE-BTZ** and its potential as a reusable photoactive material.

The production rate for the conversion of *α*-terpinene to ascaridole under **pHIPE-BTZ** conditions was found to be 192 mg.h^{-1}. Thus, both of the continuous flow methods provide specific benefits. The use of **Bead-BTZ** in flow results in good production rates where larger quantities of material are required. However, the use of **pHIPE-BTZ** comprises a method in which no intervention is required to obtain the desired product, such as recovery of the polymer from the reaction mixture. These results demonstrate the potential of these stable and reusable materials in heterogeneous photocatalytic applications.

Production of $^1O_2$ through Photosensitization Reactions under Sunlight Irradiation

To demonstrate further the potential and robustness of these new polymers, a $^1O_2$ production experiment was carried out in batch with **Gel (3%)** and **Bead-BTZ** under

direct sunlight irradiation as an alternative to the 420 nm LED modules. All other parameters were kept the same as described above for the batch reactions. The experimental set-up (Figure 6) demonstrates the ease with which the experiment was carried out. Full conversion was observed after 90 minutes with **Gel (3%)** and after 60 minutes with **Bead-BTZ** (Figure S29 and S30). Under natural sunlight irradiation and aerobic conditions, along with comparable conversion rates, we were able to validate the robustness of the synthesized photosensitizers. The ability to use sunlight as a free source of energy and air as the source of oxygen demonstrates how two of the main components for this photosensitization reaction greatly increase the potential for low environmental impact applications.

Figure 6 Experimental set-up of the conversion of α-terpinene to ascaridole using $^1O_2$ produced from direct sunlight irradiation.

Aerobic Oxidative Hydroxylation of Aryl Boronic Acids

Due to the ability of the described polymers to reach a stable excited triplet state for the generation of $^1O_2$, we successfully demonstrated how these materials compare to our previous work [27-29]. This prompted investigations into the potential of these polymers to act as triplet photosensitizers in other chemical transformations. Materials which can occupy an excited triplet state and subsequently be employed as photocatalysts have been studied in depth and are well known [8]. Within the applications for which triplet photosensitizers can be employed, we envisaged the use of our photoactive polymers for photoredox reactions.

One such reaction that has received much attention recently is the aerobic hydroxylation of aryl boronic acids to phenols. Xiao *et al.* first reported the use of a

visible-light photocatalytic strategy to convert aryl boronic acids to phenols using Ru-based complexes and organic dyes [42]. The large-scale synthesis of phenols is of great importance as they have wide applications in the chemical and pharmaceutical industries. However, the photosensitizers employed for this process are largely transition metal-based materials, which can be problematic when trace amounts of these metals remain in the reaction products, as noted previously. More recently, Zhang *et al.* reported the use of porous carbazole networks as effective visible-light heterogeneous photocatalysts for organic synthesis, including the transformation of aryl boronic acids to phenols [43]. This demonstrates the growing interest for metal-free, heterogeneous photocatalytic materials. In this context, we implemented the synthesized polymers as heterogeneous photosensitizers for the aerobic oxidative hydroxylation of aryl boronic acids.

A standard model reaction was first performed for the oxidation of phenylboronic acid, demonstrating full conversion *via* ^{1}H NMR spectroscopic analysis (see ESI) after 24 h. A series of control experiments were then performed, eliminating either light, air, base or the photocatalyst (Table S6). Each of these controls showed that no reaction occurred, indicating the essential requirement of each component for this photocatalytic reaction. **St-BTZ** was employed as a monomeric comparison to **Gel (5%)**. While photoactive, the monomer was unable to fully convert phenylboronic acid to phenol within 24 h and was therefore less efficient. The focus of this model reaction then turned to optimization of the reaction condition. Upon utilization of different solvents (MeOH, CH_3CN) and bases (Et_3N, 1,8-diazabicyclo[5.4.0]undec-7-ene), we discovered that the initial reaction conditions resulted in the swiftest time to full conversion of the boronic acid.

A scope of reagents for aerobic oxidative hydroxylation of aryl boronic acids is summarized in Table 1. Using the initial optimized reaction conditions, a range of substituted aryl boronic acids were oxidized to the corresponding aryl alcohols until full conversion was demonstrated. A range of electron-neutral, electron-donating and electron-withdrawing substituents were successfully converted to the alcohols. We discovered that among these substrates, those with electron-donating properties (Table 1, Entry 2-3) showed slower conversion rates (40-72 h) compared to phenyl boronic acid. However, those with strong electron-withdrawing substituents (Table 1, Entry 4-6) showed markedly increased conversion rate (18 h) when compared to the other groups. One reagent that did not follow this trend was the ester-substituted phenyl boronic acid

(Table 1, Entry 5), showing full conversion after 48 h. Within this scope, we also extended the use of these reaction conditions for the conversion of phenyl boronic pinacol ester, a derivative of phenyl boronic acid, to phenol. To our surprise, full conversion to the phenol product was seen after 15 h, nearly half the time required for the conversion of phenyl boronic acid (Table 1, Entry 7).

Investigations into the mechanism of this reaction have been discussed within the literature and we believe the above reactions proceed in a similar fashion, through the generation of superoxide radicals *via* an electron transfer mechanism between the triplet photosensitizer and an amine base [42, 43]. By removing the base and subsequent source of superoxide radicals, we have shown that $^1O_2$, which we know is generated, has no effect on the aryl boronic acids. However, we have not found any experimental studies within the literature that investigate the generation of $^1O_2$ along with $O_2^{\bullet-}$ in the presence of a base. To test this, *α*-terpinene, which is well known to react only with $^1O_2$ [36], was added to the model reaction. The resultant ^{1}H NMR spectrum (Figure S45) showed the presence of both the phenol and ascaridole products, confirming the concomitant production $^1O_2$ and $O_2^{\bullet-}$ in the same reaction. While this may not have any particular benefit regarding synthetic procedures, it is important to recognize as a potential issue when reactants or products are particularly susceptible to an unwanted attack by $^1O_2$.

Table 1 Light induced aerobic oxidative hydroxylation of aryl boronic acids.[a]

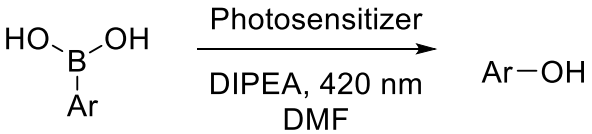

Entry	Photosensitizer	Ar	Time (h)	Conversion (%)[b]
1	Gel (5%)	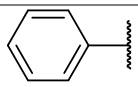	24	>99
2	Gel (5%)	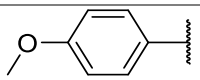	72	>99
3	Gel (5%)	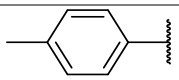	40	>99
4	Gel (5%)	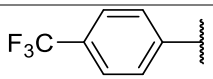	18	>99
5	Gel (5%)	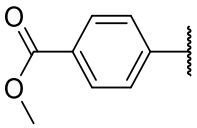	48	>99
6	Gel (5%)	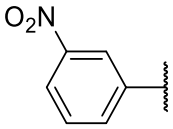	18	>99
7	Gel (5%)	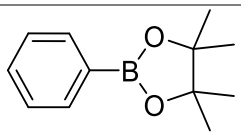	15	>99
8[c]	pHIPE-BTZ	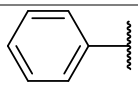	30	>99
9	Bead-BTZ (Batch)	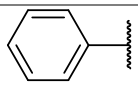	10	>99
10[c]	Bead-BTZ (Flow)	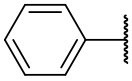	5	>99

[a]Reaction conditions: Aryl boronic acid (0.5 mmol/5 mL DMF), **Gel (5%)** (5 mg), DIPEA (1.0 mmol), DMF (5 mL), 420 nm LED irradiation, air, 24 h. [b]Conversion calculated *via* ^{1}H NMR spectroscopy. DIPEA = *N,N'*-diisopropylethylamine, DMF = *N,N'*-dimethylformamide. [c]Reaction performed under flow conditions.

As a further showcase of the synthesized polymers as versatile heterogeneous triplet photosensitizers, we implemented the optimized model reaction under flow conditions, employing both **pHIPE-BTZ** and **Bead-BTZ**. The use of the immobilized

pHIPE-BTZ resulted in a time of 30 h to reach full conversion (Table 1, Entry 8). While this is a significantly longer reaction time when compared to the model reaction in batch, we note that the total usage of the photoactive polyHIPE at this point was around 80 h. During this time, the polyHIPE was exposed to direct light irradiation, a variety of solvent and chemical systems and harsh oxidative conditions. The fact that **pHIPE-BTZ** continued to display good photocatalytic activity after such an extended and extreme use illustrates the robust and nearly indestructible nature of the material. Implementation of **Bead-BTZ** under both batch and flow conditions was also performed, both resulting in unsurprisingly accelerated conversion rates. Under batch conditions the optimized model reaction required 10 h to show full conversion to the phenol product, more than halving the time required when employing **Gel (5%)** as the photosensitizer. Under flow conditions, the same reaction showed yet another dramatic decrease in reaction time with full conversion occurring after only 5 h. When comparing these results to those of $^1O_2$ generation, a large disparity can be seen with regards to the photoactive capabilities of the polymers under different reaction conditions. While the gels and beads both showed comparable reaction rates for $^1O_2$ generation, we now see a vast difference in effectiveness for the photoredox reaction. This is most likely due to dissimilar physical characteristics between the two materials. While the gels are able to swell greatly, they do not disperse as well as the beads in the same solvent systems. The shape and size of **Bead-BTZ** aids in this as they form well distributed suspensions, which can create a larger surface area by which triplet state interactions can occur. This idea can also be applied to the decreased reaction time required for continuous flow over batch conditions. A suspension can cause light penetration difficulties, resulting in areas of the reaction mixture receiving lower flux and therefore a decrease in triplet state interactions. By applying the same reaction in flow, we negated this issue as demonstrated by the change in the rate of reaction.

Finally, due to the enhanced capabilities of **Bead-BTZ**, we aimed to test both the reusability and productivity of the beads under flow conditions using the same model reaction. We found that beads showed good reusability, with full conversion occurring within the same time as the first run (5 h) after six subsequent uses. Furthermore, and as explained previously, the **pHIPE-BTZ** monolith was used over 30 times for the production of $^1O_2$ and then employed in the light induced aerobic oxidative hydroxylation of aryl boronic acids, showing great photostability, stability towards reactive oxygen species, and that it can be reused easily for both of the reactions. The productivity of the

material was investigated by determining the maximum concentration that can be implemented where full conversion was still achieved after 5 h. From a starting concentration of 0.1 mmol.mL^{-1}, we successfully increased this to 0.4 mmol.mL^{-1} before longer reaction times were required. The dramatic reduction in reaction time, along with reusability and productivity studies, further validates the use of continuous flow technology as a tool for enhancing and optimizing reaction protocols even in heterogeneous photocatalysis.

Conclusion

A novel BTZ-based crosslinking monomer was synthesized and successfully copolymerized with styrene to produce three insoluble polystyrene-based photosensitizers in different formats: gels, beads and monoliths. These materials exhibited absorption wavelengths in the visible spectrum (400-420 nm) and computational data suggested their ability to occupy the triplet excited state. Thereafter, and as a proof of concept, the materials were employed successfully as triplet photosensitizers in the production of $^1O_2$ and $O_2^{\bullet -}$ under different conditions. Whilst the photoactive monomer demonstrated good photosensitizing properties, it was revealed to be unstable in the presence of $^1O_2$. Through its incorporation into a polystyrene matrix, chemical stability was improved dramatically without the loss of its photoactive properties and showed better performance even at low concentrations. While the polymer gels proved to be efficient triplet photosensitizers under batch conditions, they were not suitable for continuous flow chemistry. Both **Bead-BTZ** and **pHIPE-BTZ**, designed for use under continuous flow conditions, were shown to be exceptional photosensitizers. The polyHIPE in particular proved to be an extremely stable and reusable photosensitizer, with total usage time exceeding 80 hours.

These materials have been reported as a proof of concept and through computational and experimental methods, the polymer-supported monomer is clearly demonstrated as a robust triplet photosensitizer. Currently, we are investigating the incorporation of other dyes into polymeric systems through versatile free radical polymerization techniques, particularly within water-compatible polymers for water and waste water treatment [44] and other systems requiring biocompatibility. We acknowledge that photophysical studies are necessary to fully understand the triplet

excited state of these materials. However, the primary scope of this work aims to describe the design and applications of a new class of materials. Whilst photophysical characterization it is not a focus of the current work, it is an aspect we will look to address in the future.

Acknowledgement

We would like to acknowledge Vapourtec Ltd. for their valuable technical support. F. Vilela would like to thank Heriot-Watt University and The Royal Society for financial support (RG140169). G. O. Lloyd would like to thank Heriot-Watt University and The Royal Society of Edinburgh and Scottish Government for support through a RSE/SG Personal Research Fellowship. M. J. Paterson would like to thank the EPSRC for funding through the platform grant EP/P001459/1.

References

[1] Xing, J.; Fang, W. Q.; Zhao, H. J.; Yang, H. G. *Chem. - Asian J.* **2012**, *7*, 642-657.

[2] Habisreutinger, S. N.; Schmidt-Mende, L.; Stolarczyk, J. K. *Angew. Chem., Int. Ed.* **2013**, *52*, 7372-7408.

[3] Xuan, J.; Xiao, W.-J. *Angew. Chem., Int. Ed.* **2012**, *51*, 6828-6838.

[4] Kruk, I. *Environmental Toxicology and Chemistry of Oxygen Species Handbook of Environmental Chemistry*; Springer-Verlag: Berlin, 1998; pp 5-36.

[5] Schweitzer, C.; Schmidt, R. *Chem. Rev.* **2003**, *103*, 1685-1757.

[6] Lamberts, J. J. M.; Neckers, D. C. *Tetrahedron* **1985**, *41*, 2183-2190.

[7] DeRosa, M. C.; Crutchley, R. J. *Coord. Chem. Rev.* **2002**, *233-234*, 351-371.

[8] Zhao, J.; Wu, W.; Sun, J.; Guo, S. *Chem. Soc. Rev.* **2013**, *42*, 5323-5351.

[9] Kamkaew, A.; Lim, S. H.; Lee, H. B.; Kiew, L. V.; Chung, L. Y.; Burgess, K. *Chem. Soc. Rev.* **2013**, *42*, 77-88.

[10] Wu, W.; Guo, H.; Wu, W.; Ji, S.; Zhao, J. *J. Org. Chem.* **2011**, *76*, 7056-7064.

[11] Wu, W.; Zhao, J.; Guo, H.; Sun, J.; Ji, S.; Wang, Z. *Chem. - Eur. J.* **2012**, *18*, 1961-1968.

[12] Kopetzki, D.; Levesque, F.; Seeberger, P. H. *Chem. - Eur. J.* **2013**, *19*, 5450-5456.

[13] Canonica, S.; Tratnyek, P. G. *Environ. Toxicol. Chem.* **2003**, *22*, 1743-1754.

[14] Bonnett, R. *Chem. Soc. Rev.* **1995**, *24*, 19-33.

[15] Awuah, S. G.; You, Y. *RSC Adv.* **2012**, *2*, 11169-11183.

[16] Romero, N. A.; Nicewicz, D. A. *Chem. Rev.* **2016**, *116*, 10075-10166.

[17] Punniyamurthy, T.; Velusamy, S.; Iqbal, J. *Chem. Rev.* **2005**, *105*, 2329-2364.

[18] Connick, W. B.; Gray, H. B. *J. Am. Chem. Soc.* **1997**, *119*, 11620-11627.

[19] Abdel-Shafi, A. A.; Beer, P. D.; Mortimer, R. J.; Wilkinson, F. *Phys. Chem. Chem. Phys.* **2000**, *2*, 3137-3144.

[20] Abdel-Shafi, A. A.; Beer, P. D.; Mortimer, R. J.; Wilkinson, F. *J. Phys. Chem. A* **2000**, *104*, 192-202.

[21] Goethals, A.; Mugadza, T.; Arslanoglu, Y.; Zugle, R.; Antunes, E.; Hulle, S. W.; Nyokong, T.; Clerck, K. *J. Appl. Polym. Sci.* **2014**, *131*, 1-7.

[22] Kuznetsova, N. Sensitization of Singlet Oxygen Formation in Aqueous Media. In *Photosensitizers in Medicine, Environment, and Security*; Nyokong, T. Ahsen, V., Eds.; Springer: Netherlands, 2012; pp 267-314.

[23] Marin, M. L.; Santos-Juanes, L.; Arques, A.; Amat, A. M.; Miranda, M. A. *Chem. Rev.* **2012**, *112*, 1710-1750.

[24] Guo, S.; Zhang, H.; Huang, L.; Guo, Z.; Xiong, G.; Zhao, J. *Chem. Commun.* **2013**, *49*, 8689-8691.

[25] Gerdes, R.; Bartels, O.; Schneider, G.; Wohrle, D.; Schulz-Ekloff, G. *Polym. Adv. Technol.* **2001**, *12*, 152-160.

[26] Carpentier, R.; Leblanc, R. M.; Mimeault, M. *Enzyme Microb. Technol.* **1987**, *9*, 489-493.

[27] Zhang, K.; Kopetzki, D.; Seeberger, P. H.; Antonietti, M.; Vilela, F. *Angew. Chem., Int. Ed.* **2013**, *52*, 1432-1436.

[28] Urakami, H.; Zhang, K.; Vilela, F. *Chem. Commun.* **2013**, *49*, 2353-2355.

[29] Zhang, K.; Vobecka, Z.; Tauer, K.; Antonietti, M.; Vilela, F. *Chem. Commun.* **2013**, *49*, 11158-11160.

[30] Tobin, J. M.; Liu, J.; Hayes, H.; Demleitner, M.; Ellis, D.; Arrighi, V.; Xu, Z.; Vilela, F. *Polym. Chem.* **2016**, *7*, 6662-6670.

[31] Wong, Y. L.; Tobin, J. M.; Xu, Z.; Vilela, F. *J. Mat. Chem. A* **2016**, *4*, 18677-18686.

[32] Global Styrene Production - Merchant Research and Consulting Ltd. http://mcgroup.co.uk/news/20130830/global-styrene-production-exceeded-264-million-tonnes.html (accessed May 1, 2017).

[33] Cowie, J. M. G.; Arrighi, V. *Polymers: Chemistry and Physics of Modern Materials, 3rd Ed.*; CRC Press: Florida, **2008**; pp 1-28, 57-97.

[34] Frisch, M. J.; Trucks, G. W.; Schlegel, H. B.; Scuseria, G. E.; Robb, M. A.; Cheeseman, J. R.; Scalmani, G.; Barone, V.; Mennucci, B.; Petersson, G. A.; et al. *Gaussian 09*, revision D.01; Gaussian, Inc.: Wallingford, CT, 2009.

[35] Geuskens, G.; David, K. In *The Photo-oxidation of Polymers. A Comparison with Low Molecular Weight Compounds,* Plenary Lectures Presented at the Seventh Symposium on Photochemistry, Leuven, Belgium, July 24-28, 1978; Reiser, A., Ed.; Elsevier: London, 1979.

[36] Schenck, G. O.; Ziegler, K. *Naturwissenschaften* **1944**, *32*, 157.

[37] Rabek, J. F. *Photodegradation of Polymers*; Springer-Verlag; Berlin, 1996; pp 51-97.

[38] Baumann, M.; Baxendale, I. R. *Beilstein J. Org. Chem.* **2013**, *9*, 1613-1619.

[39] Levesque, F.; Seeberger, P. H. *Angew. Chem., Int. Ed.* **2012**, *51*, 1706-1709.

[40] Centi, G.; Perathoner, S. Methods and Tools of Sustainable Industrial Chemistry: Process Intensification. In *Sustainable Industrial Chemistry: Principles, Tools and Industrial Examples*; Cavani, F., Centi, G., Perathoner, S., Trifiro, F., Eds.; Wiley-VCH Verlag GmbH & Co. KGaA: Weinheim, Germany, 2009; pp 199-256.

[41] Rubio-Martinez, M.; Batten, M. P.; Polyzos, A.; Carey, K-C.; Mardel, J. I.; Lim, K-S.; Hill, M. R. *Sci. Rep.* **2014**, *4*:5443, 1-5.

[42] Zou, Y.-Q.; Chen, J.-R.; Liu, X.-P.; Lu, L.-Q.; Davis, R. L.; Jorgensen, K. A.; Xiao, W.-J. *Angew. Chem., Int. Ed.* **2012**, *51*, 784-788.

[43] Luo, J.; Zhang, X.; Zhang, J. *ACS Catal.* **2015**, *5*, 2250-2254.

[44] Shen, J.; Steinbach, R.; Tobin, J. M.; Mouro Nakata, M.; Bower, M.; McCoustra, M. R. S.; Bridle, H.; Arrighi, V.; Vilela, F. *Appl. Catal., B* **2016**, *193*, 226-233.

Supporting Information

General Experimental

Instrumentation and Measurements. ^{1}H NMR spectra were recorded on a Bruker AVIII 300 spectrometer at 300.1 MHz at ambient temperature in $CDCl_3$ or Acetone-D_6. ^{13}C NMR measurements were recorded on a Bruker AVIII 400 spectrometer at 100.6 MHz at ambient temperature in $CDCl_3$. Solid state ^{13}C NMR CP-MAS measurements were carried out using a Bruker Advance 400 spectrometer operating at 100.6 MHz for ^{13}C using a Bruker 4 mm double resonance probe-head operating at a spinning rate of 10 kHz. Solution-state UV-Vis spectra were recorded on a Shimadzu UV-2550 system with 10 mm quartz cuvettes. Solid-state UV-Vis spectra were recorded on a PerkinElmer Lambda 25 system using a Labsphere RSA-PE-20 reflectance spectroscopy integration sphere. FT-IR spectra were recorded on a PerkinElmer Spectrum 100 FT-IR Spectrometer. Optical microscopy was carried out on an Olympus VANOX optical microscope. Scanning Electron Microscopy (SEM) was carried out on a Cambridge Instruments Stereoscan 90. Samples were sputter coated with platinum prior to imaging. X-ray crystallography was performed on a Bruker D8 Advanced instrument. A suitable crystal was selected and held in place on the instrument using a cryo-loop and frozen perfluoropolyether. The crystal was crash-cooled to 100K and data collected at this temperature. Photo-catalyzed reactions in batch were carried out by using LED module emitting at 420 nm with 28 W light output and a light intensity of 3.5 $W.cm^{-2}$ (OSA Opto Lights, OLM-018 series, Berlin, Germany) at a distance of 7 cm. Photo-catalyzed reactions under flow conditions were carried out using a commercial photochemical flow reactor equipped with an LED array emitting a wavelength at 420 nm with 61 W light output and a light intensity of 10.2 $W.cm^{-2}$ (easy-Photochem, Vapourtec Ltd.).

Materials. All reagents and starting materials employed in this work were commercially available and used without further purification unless stated otherwise. Styrene was purified before use in polymer synthesis to remove inhibitors. Styrene (120 mL) was washed with 0.1 M NaOH (50 mL) three times and 0.1M HCl once (50 mL). The styrene fraction was then washed with 50 mL aliquots of deionized water until it was shown to be neutral using litmus paper, and then dried over anhydrous $MgSO_4$ and

filtered. Azo*bis*isobutyronitrile (AIBN) was recrystallized from acetone at low temperature to afford white crystals. Tetrakis(triphenylphosphine)palladium(0) ($Pd(PPh_3)_4$) was synthesized *via* literature methods [1].

Experimental Section

Synthesis of Tetrakis(triphenylphosphine)palladium (0) Catalyst

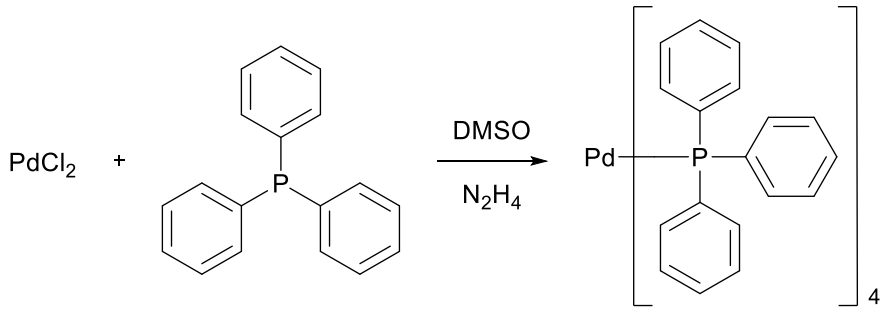

Scheme S1 Synthesis of $Pd(PPh_3)_4$.

Tetrakis(triphenylphosphine)palladium (0) ($Pd(PPh_3)_4$) was prepared *via* modified literature methods [1] by dissolving palladium chloride (350 mg, 2 mmol) and triphenylphosphine (2.62 g, 10 mmol) in 25 mL of anhydrous dimethyl sulphoxide. The mixture was stirred and heated to 140-160 °C under nitrogen until an orange solution was formed and stirring continued for 15 minutes thereafter. Hydrazine hydrate (0.39 mL, 8 mmol) was charged quickly into the orange solution and taken from heat and left to cool to room temperature. During this time, yellow crystals formed and were then filtered through a sintered glass adaptor under nitrogen. The crystals were washed with dry methanol and dry diethyl ether and left to dry under nitrogen. The catalyst was stored at -10 ^{o}C and used without further purification.

Synthetic Scheme of Styrene-DVB-St-BTZ Copolymers (Bead and Bead-BTZ).

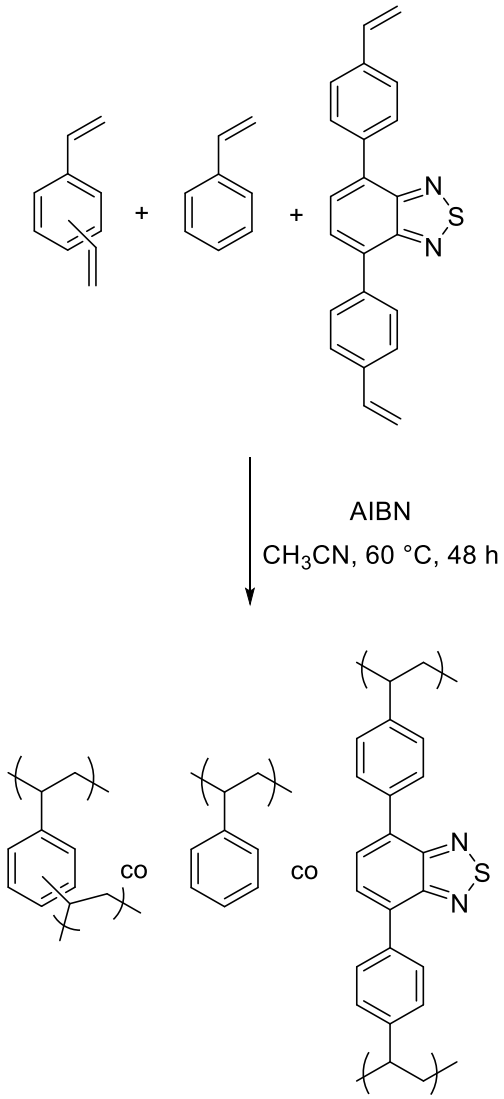

Scheme S2 Synthesis of **Bead** and **Bead-BTZ**.

Synthesis of Styrene-DVB Copolymer via Precipitation Polymerization (Bead)

DVB-55 (296 mg, 2.3 mmol), styrene (705 mg, 6.8 mmol) (2% w/v total monomer in feed relative to solvent) and AIBN (34 mg, 0.2 mmol) (2 mol% relative to polymerizable double bonds in monomers) were added to acetonitrile (50 mL) in a Nalgene® bottle (250 mL). The bottle contents were ultrasonicated for 15 minutes. After ultrasonication, N_2 was bubbled through the reaction mixture for 15 minutes in an ice-bath. After degassing, the Nalgene® bottle was sealed under N_2 and placed on a low profile roller (Stovall Life Sciences Inc., North Carolina, U.S.A) contained within an incubator (Stuart Scientific, Stone, U.K) and rotated along its long axis. The temperature inside the incubator was ramped from ambient temperature to 60 °C over a period of around two hours. The

polymerization was allowed to proceed for a further 46 hours to give a milky suspension of polymer particles. The particles were visualized via optical microscopy prior to filtration The product was isolated by vacuum filtration on a 0.45 μm nylon membrane filter and the particles washed with solvent to remove any unreacted monomer or initiator (~100 mL of acetonitrile followed by ~100 mL of toluene, methanol, and finally acetone) before being dried overnight in vacuo (60 mbar, 40 °C). Product Yield: 116 mg, 11.3%.

Synthetic Scheme of Styrene-DVB-St-BTZ polyHIPE (pHIPE-BTZ)

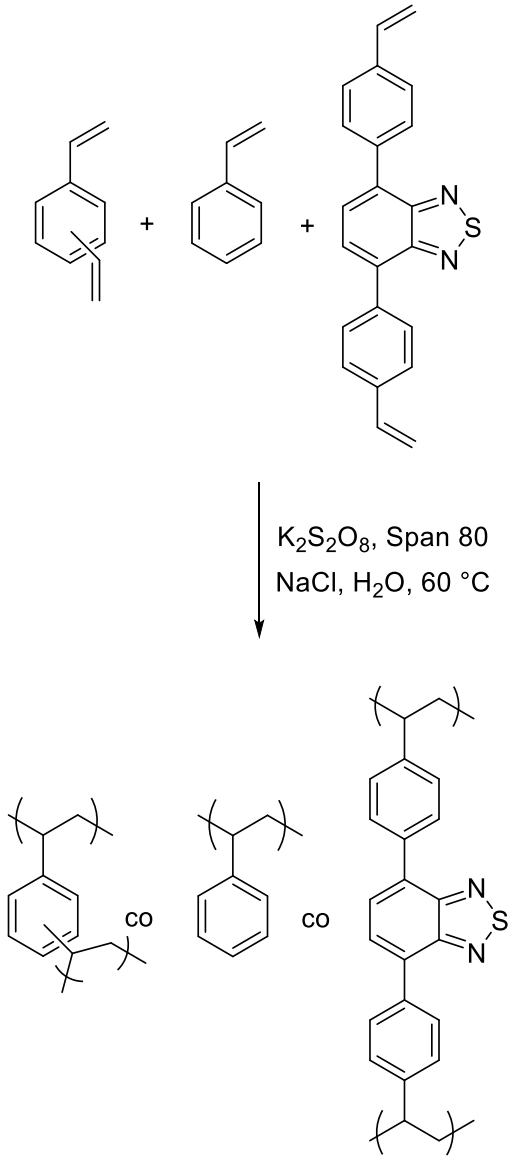

Scheme S3 Synthesis of **pHIPE-BTZ.**

Photocatalytic Reactions

Procedure for Photosensitization of $^1O_2$ Reactions under Batch Conditions

To a vial containing a solution of 136 mg of *α*-terpinene in 10 mL of chloroform, 10 mg of photosensitizing material was added. The mixture was left to stir, whilst open to air, for 10 minutes to allow for proper dissolution or swelling and to aerate the solution. The vial was then placed 7 cm from a 420 nm LED lamp and the lamp was switched on. At 15-minute intervals, 0.5 mL samples were taken from the vial, filtered where appropriate *via* a syringe filter and concentrated *via* rotary evaporation. The residue was then dissolved in deuterated chloroform for ^{1}H-NMR analysis. A typical example of the progression of this reaction *via* ^{1}H-NMR can be found in Figure S19.

Procedure for Aerobic Hydroxylation of Arylboronic Acids and Esters in Batch

To a vial containing a solution of 0.5 mmol of an ayrlboronic acid or ester, 1.0 mmol of diisopropylethylamine (DIPEA) in 5 mL of DMF, 5 mg of **Gel (5%)** was added. The mixture was stirred at room temperature and irradiated at 420 nm using a LED lamp whilst open to air. Monitored by TLC analysis, upon full consumption of the boronic starting material the reaction was stopped and the mixture was filtered *via* syringe filter to remove the photocatalyst. The remaining mixture was then cooled to 0 °C and quenched carefully by aqueous solution of HCl (10%, 5 mL). The resultant mixture was extracted with Et_2O (3 x 10 mL). The combined organic layers were washed with brine (10 mL) and dried over Na_2SO_4. The solution was filtered, concentrated under reduced pressure and the residue diluted in acetone-D_6 for ^{1}H NMR analysis.

Procedure for Photosensitization of $^1O_2$ in Flow Employing Bead-BTZ

To a flask containing a solution of 136 mg of *α*-terpinene in 15 mL of chloroform, 5 mg of **Bead-BTZ** was added. The suspension was first sonicated for 2 minutes to ensure an even dispersion of particles. The mixture was then left to stir, whilst open to air, for 10 minutes to aerate the solution. The dispersion was then pumped through the photochemical reactor (Figure S2) at 1 mL min^{-1}. Concurrently, air was pumped through a second pump at the same flow rate, mixing with the dispersion at a T-junction before entering the photochemical reactor equipped with a 420 nm LED lamp. The dispersion

was cycled for 60 minutes and a 1 mL sample was taken from the flask, filtered *via* a syringe filter and concentrated *via* rotary evaporation. The residue left was then dissolved in deuterated chloroform for ^{1}H-NMR analysis.

Procedure for Aerobic Hydroxylation of Phenylboronic Acid in Flow Employing Bead-BTZ

To a flask containing a solution of 1.0 mmol of phenylboronic acid, 2.0 mmol of DIPEA in 10 mL of DMF, 5 mg of **Bead-BTZ** was added. The suspension was first sonicated for 2 minutes to ensure an even dispersion of particles. The dispersion was then pumped through the photochemical reactor (Figure S2) at 1 mL min^{-1}. Concurrently, air was pumped through a second pump at the same flow rate, mixing with the dispersion at a T-junction before entering the photochemical reactor equipped with a 420 nm LED lamp. Monitored by TLC analysis, upon full consumption of the boronic starting material the reaction was stopped and the mixture was filtered *via* syringe filter to remove the photocatalyst. The remaining mixture was then cooled to 0 °C and quenched carefully by aqueous solution of HCl (10%, 5 mL). The resultant mixture was extracted with Et_2O (3 x 10 mL). The combined organic layers were washed with brine (10 mL) and dried over Na_2SO_4. The solution was filtered, concentrated under reduced pressure and the residue diluted in acetone-D_6 for ^{1}H NMR analysis.

Procedure for Photosensitization of $^{1}O_2$ in Flow Employing pHIPE-BTZ

The **pHIPE-BTZ** monolith, fitted to a transparent glass column, was allowed to swell in chloroform for 16h. A solution of 54 mg (0.4 mmol) of α-terpinene in 10 mL of chloroform was prepared and aerated for 10 minutes in air. The column was fitted to a light source (Figure S3) and the solution was pumped through the column at 0.5 mL min^{-1}. Concurrently, oxygen was pumped through a second pump at the same flow fate, mixing with the solution at a T-junction before entering the column. The operating pressure was kept at 1.3 bar to ensure a steady stream of both the solution and air. The 10 mL solution was pumped through the column, collected and concentrated *via* rotary evaporation. The residue was then dissolved in deuterated chloroform for ^{1}H-NMR analysis.

Procedure for Aerobic Hydroxylation of Phenylboronic Acid in Flow Employing pHIPE-BTZ

The **pHIPE-BTZ** monolith, fitted to a transparent glass column, was allowed to swell in a solution of DIPEA (0.2 mL) in DMF (10 mL) for 16 h. A solution of 0.5 mmol of phenylboronic acid and 1.0 mmol of DIPEA in 5 mL of DMF was then prepared. The column was then fitted to a light source (Figure S3) and the solution was pumped through the column at 1 mL min^{-1}. Concurrently, air was pumped through a second pump at the same flow rate, mixing with the dispersion at a T-junction before entering the column. Monitored by TLC analysis, upon full consumption of the boronic starting material the reaction was stopped and the mixture was then cooled to 0 °C and quenched carefully by aqueous solution of HCl (10%, 5 mL). The resultant mixture was extracted with Et_2O (3 x 10 mL). The combined organic layers were washed with brine (10 mL) and dried over Na_2SO_4. The solution was filtered, concentrated under reduced pressure and the residue diluted in acetone-D_6 for ^1H NMR analysis.

Swelling Experiment with Gel (3%)

To a small vial, 12.7 mg (1 mm) of dried **Gel (3%)** was added (Figure S1a). Approximately 1 mL $CHCl_3$ was added to the vial and the gel was allowed to swell for 1 h. After this time, the height of the gel grew to approximately 7 mm (Figure S1b). The gel was left for a further 24 h but showed no further growth.

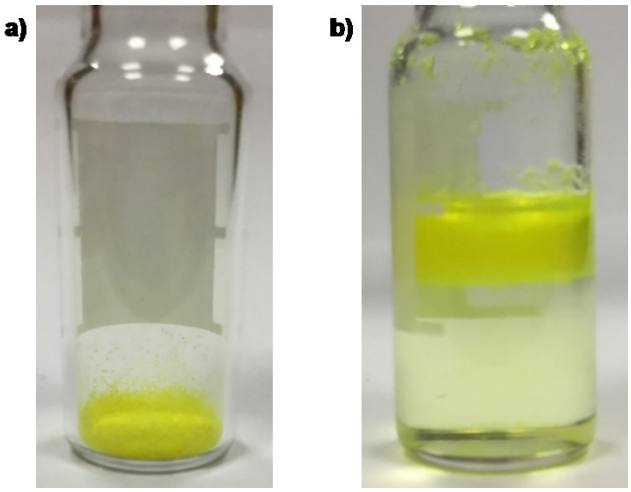

Figure S1 Swelling test showing the (a) initial 1mm dry **Gel (3%)** and (b) subsequent swelling of **Gel (3%)** to approximately 7 mm after the addition of chloroform.

Figure S2 Easy-Photochem flow system from Vapourtec Ltd. equipped with a visible light LED module emitting light at 420 nm.

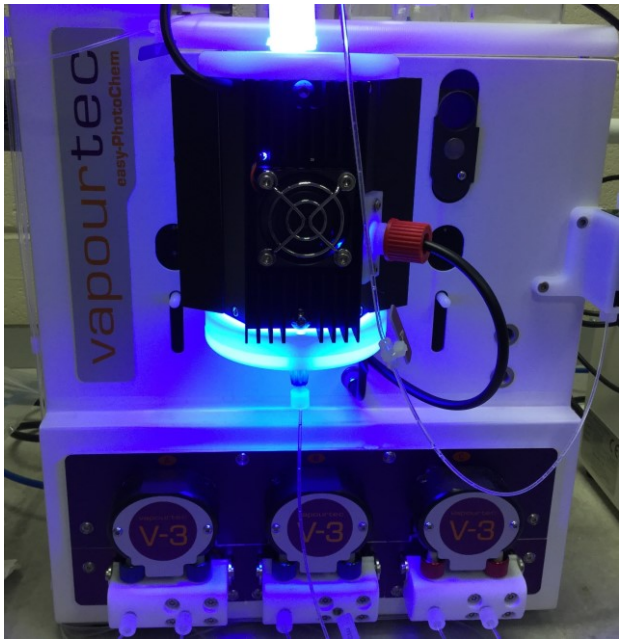

Figure S3 Easy-Photochem flow system from Vapourtec Ltd. equipped with a column photochemical reactor equipped with 420 nm LED lamps.

Properties and Characterization

Crystal Data of 4,7-distyrene-2,1,3-benzothiadiazole (St-BTZ)

Crystal data for **St-BTZ**: $C_{44}H_{44}CoI_2N_8O_6$, M = 1093.60, Yellow Plate, 0.31 x 0.29 x 0.08 mm^3, monoclinic, space group $C2/c$ (No. 15), a = 8.1181(5), b = 24.6486(13), c = 22.3166(12) Å, β = 98.290(2)°, V = 4418.9(4) $Å^3$, Z = 4, D_c = 1.644 g/cm^3, F_{000} = 2180, MoKα radiation, λ = 0.71073 Å, T = 100(2)K, $2\theta_{max}$ = 52.8º, 29100 reflections collected, 4252 unique (R_{int} = 0.0637). Final *GooF* = 1.069, *R1* = 0.0416, *wR2* = 0.0717, *R* indices based on 3264 reflections with I >2sigma(I) (refinement on F^2), 324 parameters, 0 restraints. Lp and absorption corrections applied, μ = 1.843 mm^{-1}. CCDC 1443324.

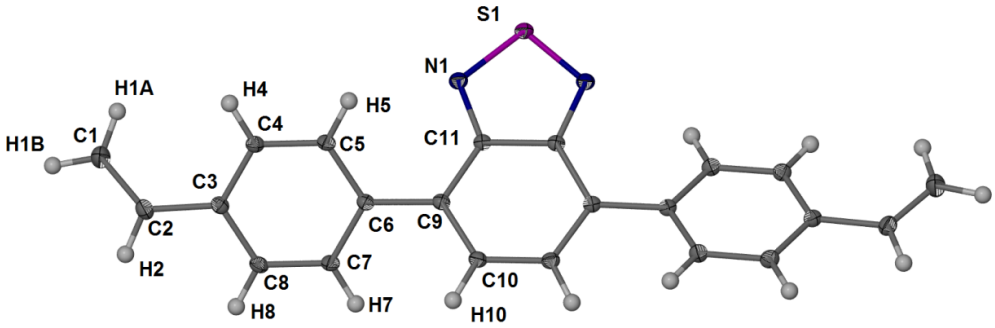

Figure S4 X-ray crystal structure of **St-BTZ** showing its molecular structure and connectivity. The asymmetric unit is only half the molecule with the rest of the molecule generated by the symmetry operation 1-X, Y, 1/2-Z. Atoms are shown as ellipsoids at 50% probability.

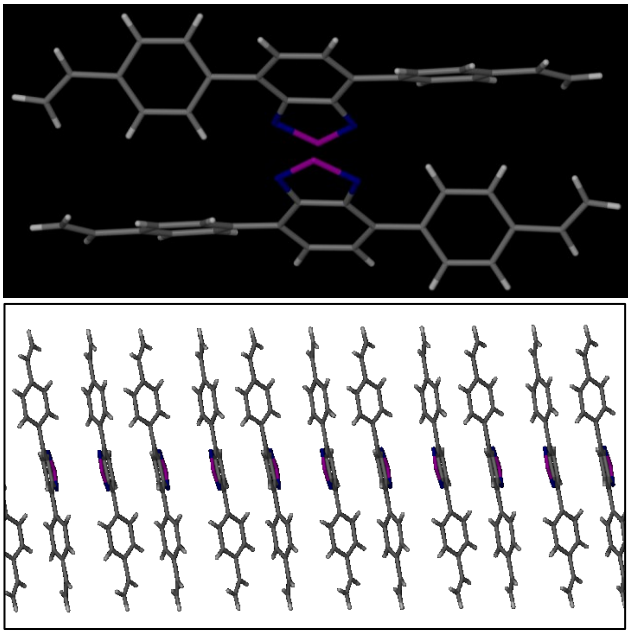

Figure S5 X-ray crystal structure of **St-BTZ** showing the π-π stacking. On the left are shown the Edge-to-Face Pi-Pi interactions between styrene groups. On the right within the box is shown the overall Pi-Pi stacking of molecules in the solid state running along the *c* axis [001] (left to right). 2,1,3-Benzothiadiazole groups are antiparallel stacked with the styrene groups interacting through edge-to-face pi-pi interactions. Pi-Pi stacking distance between 2,1,3-benzothiadiazole groups is half the *c* axis distance which is 1/2 x 7.2194(6) Å.

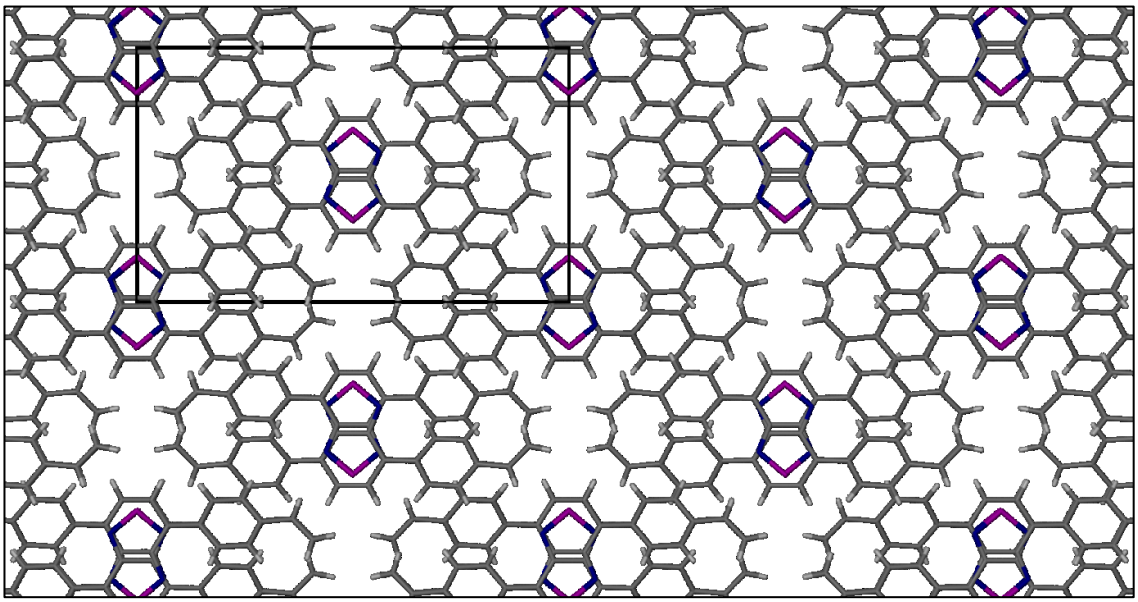

Figure S6 X-ray crystal structure of **St-BTZ**. Packing of molecules in the solid state as viewed down the *c* axis [001]. Black box is the unit cell, *a* axis bottom right to up and *b* axis bottom right to left.

Computational Data

Table S1 Excited state data for **St-BTZ** computed with TD-CAM-B3LYP/6-311G(d,p).

State	Sym.	Excit. Energy (eV)	Wavelength (nm)	Osc. Strength	Maj. Transition	Characterisation
T_1	B	1.8802	659.44	0.0000	H → L (94%)	$\pi \rightarrow \pi^*$ ($CT_{styrene \rightarrow benzim.}$)
T_2	A	2.7214	455.58	0.0000	H → L(+2) (33%)	$\pi \rightarrow \pi^*$ ($CT_{benzim. \rightarrow styrene}$)
T_3	B	2.7927	443.96	0.0000	H → L(+1) (32%)	$\pi \rightarrow \pi^*$
T_4	A	3.2750	378.57	0.0000	H(-5) → L (89%)	$\pi_{benzim.} \rightarrow \pi^*$
S_1	B	3.3738	367.49	0.6424	H → L (98%)	$\pi \rightarrow \pi^*$ ($CT_{styrene \rightarrow benzim.}$)
S_2	A	4.3835	282.84	0.0071	H(-1) → L (80%)	$\pi_{styrene} \rightarrow \pi^*$ ($CT_{styrene \rightarrow benzim.}$)
S_3	B	4.6346	267.52	0.9994	H → L(+1) (79%)	$\pi \rightarrow \pi^*$
S_4	A	4.6390	267.27	0.1472	H(-5) → L (84%)	$\pi_{benzim.} \rightarrow \pi^*$
S_5	A	4.7369	261.74	0.0002	H(-3) → L (42%)	$\pi_{styrene} \rightarrow \pi^*$ ($CT_{styrene \rightarrow benzim.}$)
S_6	B	4.8217	257.14	0.0069	H(-2) → L (42%)	$\pi \rightarrow \pi^*$
S_7	A	4.8825	253.94	0.0157	Mixed	N/A
S_8	B	5.0156	247.20	0.0318	H(-4) → L (53%)	$\pi \rightarrow \pi^*$ ($CT_{sytrene \rightarrow benzim.}$)
S_9	A	5.1166	242.32	0.0051	H → L(+2) (52%)	$\pi \rightarrow \pi^*$ ($CT_{benzim. \rightarrow styrene}$)
S_{10}	B	5.3808	230.42	0.0166	H → L(+3) (22%)	$\pi \rightarrow \pi^*_{styrene}$ ($CT_{benzim. \rightarrow styrene}$)

Table S2 Excited state data for photoactive polymer repeat unit computed with TD-CAM-B3LYP/6-311G(d,p).

State	Sym.	Excit. Energy (eV)	Wavelength (nm)	Osc. Strength	Maj. Transition	Characterisation
T_1	B	1.9247	644.18	0.0000	H → L (98%)	$\pi \rightarrow \pi^*$ ($CT_{iso.\rightarrow benzim.}$)
T_2	A	3.2578	380.58	0.0000	H(-4) → L (79%)	$\pi_{benzim.} \rightarrow \pi^*$
T_3	B	3.3625	368.73	0.0000	H → L(+1) (34%)	$\pi \rightarrow \pi^*$
T_4	A	3.4271	361.78	0.0000	MIXED	N/A
S_1	B	3.4557	358.78	0.4515	H → L (99%)	$\pi \rightarrow \pi^*$ ($CT_{iso.\rightarrow benzim.}$)
S_2	A	4.5760	270.95	0.0183	H(-1) → L (50%)	$\pi_{iso.} \rightarrow \pi^*$ ($CT_{iso.\rightarrow benzim.}$)
S_3	A	4.6651	265.77	0.1570	H(-4) → L (87%)	$\pi_{benzim.} \rightarrow \pi^*$
S_4	A	4.8761	254.27	0.0002	H(-2) → L (40%)	$\pi_{iso.} \rightarrow \pi^*$ ($CT_{iso.\rightarrow benzim.}$)
S_5	B	4.9326	251.36	0.0025	H(-3) → L (72%)	$\pi_{iso.} \rightarrow \pi^*$ ($CT_{iso.\rightarrow benzim.}$)
S_6	A	5.0214	246.91	0.0023	H(-6) → L (36%)	$\sigma \rightarrow \pi^*$
S_7	B	5.0269	246.64	0.7206	H → L(+1) (78%)	$\pi \rightarrow \pi^*$
S_8	B	5.2579	235.81	0.0752	H(-5) → L (72%)	$\pi \rightarrow \pi^*$ ($CT_{iso.\rightarrow benzim.}$)
S_9	B	5.4613	227.02	0.0149	H(-7) → L (24%)	$\sigma \rightarrow \pi^*$ ($CT_{iso.\rightarrow benzim.}$)
S_{10}	A	5.4781	226.33	0.0018	H → L(+2) (32%)	$\pi \rightarrow \pi^*$ ($CT_{benzim.\rightarrow iso.}$)

Table S3 Singlet-triplet energy gap at optimized T_1 geometry computed with CAM-B3LYP/6-311G(d,p).

System	$\Delta E_{S/T}$ at T_1 geom. (eV)
St-BTZ monomer	1.154
Polymer repeat unit	1.225

Table S4 Excited state data for **St-BTZ** computed with TD-MN12-L/6-311G(d,p).

State	Sym.	Excit. Energy (eV)	Wavelength (nm)	Osc. Strength	Maj. Transition	Characterisation
T_1	B	2.0133	615.84	0.0000	H → L (99%)	$\pi \rightarrow \pi^*$ ($CT_{styrene \rightarrow benzim.}$)
S_1	B	2.6186	473.48	0.3638	H → L (100%)	$\pi \rightarrow \pi^*$ ($CT_{styrene \rightarrow benzim.}$)
T_2	A	2.8170	440.12	0.0000	H(-1) → L (81%)	$\pi_{styrene} \rightarrow \pi^*$ ($CT_{styrene \rightarrow benzim.}$)
T_3	B	3.0165	411.01	0.0000	H → L(+1) (55%)	$\pi \rightarrow \pi^*$
S_2	A	3.0615	404.97	0.0007	H(-1) → L (97%)	$\pi_{styrene} \rightarrow \pi^*$ ($CT_{styrene \rightarrow benzim.}$)
T_4	A	3.2803	377.96	0.0000	H → L(+2) (50%)	$\pi \rightarrow \pi^*_{styrene}$ ($CT_{benzim. \rightarrow styrene}$)
S_3	A	3.6529	339.42	0.0010	H(-3) → L (99%)	$\pi_{styrene} \rightarrow \pi^*$ ($CT_{styrene \rightarrow benzim.}$)
S_4	B	3.6642	338.37	0.0255	H(-4) → L (53%)	$\pi \rightarrow \pi^*$
S_5	B	3.7245	332.89	0.7174	H → L(+1) (89%)	$\pi \rightarrow \pi^*$
S_6	B	3.8779	319.72	0.0022	H(-2) → L (48%)	$\pi \rightarrow \pi^*$
S_7	A	3.9510	313.80	0.0015	H → L(+2) (68%)	$\pi \rightarrow \pi^*_{styrene}$ ($CT_{benzim. \rightarrow styrene}$)
S_8	A	4.4451	278.92	0.0561	H(-5) → L (45%)	$\pi_{benzim.} \rightarrow \pi^*$
S_9	A	4.6072	269.11	0.0298	H(-5) → L (26%)	$\pi_{benzim.} \rightarrow \pi^*$
S_{10}	B	4.6171	268.53	0.3266	H(-1) → L(+2) (65%)	$\pi_{styrene} \rightarrow \pi^*_{styrene}$

Table S5 Excited state data for the photoactive polymer repeat unit computed with TD-MN12-L/6-311G(d,p).

State	Sym.	Excit. Energy (eV)	Wavelength (nm)	Osc. Strength	Maj. Transition	Characterisation
T_1	B	2.1105	587.45	0.0000	H → L (100%)	$\pi \rightarrow \pi^*$ ($CT_{iso.\rightarrow benzim.}$)
S_1	B	2.8319	437.82	0.2825	H → L (100%)	$\pi \rightarrow \pi^*$ ($CT_{iso.\rightarrow benzim.}$)
T_2	A	3.3473	370.40	0.0000	H(-1) → L (92%)	$\pi_{iso.} \rightarrow \pi^*$ ($CT_{iso.\rightarrow benzim.}$)
T_3	B	3.5293	351.30	0.0000	H(-5) → L (47%)	$\pi \rightarrow \pi^*$ ($CT_{iso.\rightarrow benzim.}$)
S_2	A	3.5473	349.52	0.0007	H(-1) → L (98%)	$\pi_{iso.} \rightarrow \pi^*$ ($CT_{iso.\rightarrow benzim.}$)
T_4	A	3.5730	347.00	0.0000	H(-2) → L (97%)	$\pi_{iso.} \rightarrow \pi^*$ ($CT_{iso.\rightarrow benzim.}$)
S_3	A	3.6392	340.69	0.0008	H(-2) → L (99%)	$\pi_{iso.} \rightarrow \pi^*$ ($CT_{iso.\rightarrow benzim.}$)
S_4	B	3.6522	339.48	0.0012	H(-3) → L (99%)	$\pi_{iso.} \rightarrow \pi^*$ ($CT_{iso.\rightarrow benzim.}$)
S_5	B	4.2961	288.60	0.1960	H(-5) → L (81%)	$\pi \rightarrow \pi^*$ ($CT_{iso.\rightarrow benzim.}$)
S_6	B	4.3613	284.29	0.6092	H → L(+1) (79%)	$\pi \rightarrow \pi^*$
S_7	A	4.5758	270.96	0.1103	H(-4) → L (71%)	$\pi_{benzim.} \rightarrow \pi^*$
S_8	A	4.7647	260.22	0.0057	H → L(+2) (69%)	$\pi \rightarrow \pi^*_{iso.}$ ($CT_{benzim.\rightarrow iso.}$)
S_9	B	4.8047	258.05	0.0141	H → L(+3) (91%)	$\pi \rightarrow \pi^*_{iso.}$ ($CT_{benzim.\rightarrow iso.}$)
S_{10}	A	4.8583	255.20	0.0005	H(-6) → L (98%)	$\sigma \rightarrow \pi^*$

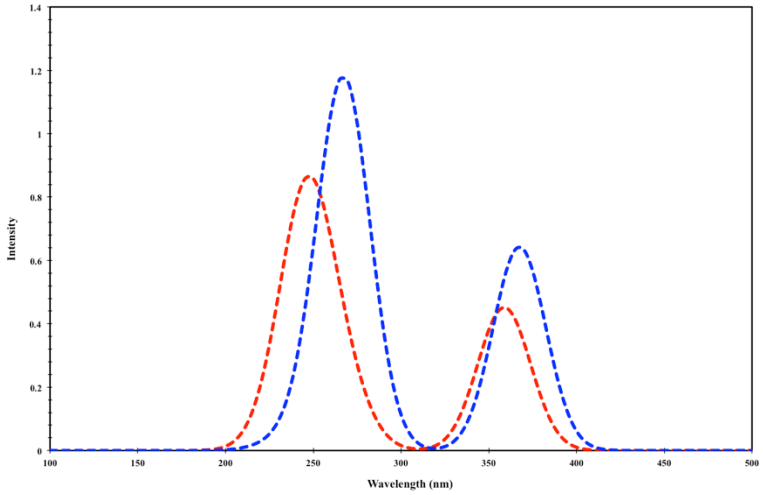

Figure S7 Simulated Absorption Spectra for **St-BTZ** (blue) and the polymer repeat unit (red) at CAM-B3LYP/6-311G(d,p).

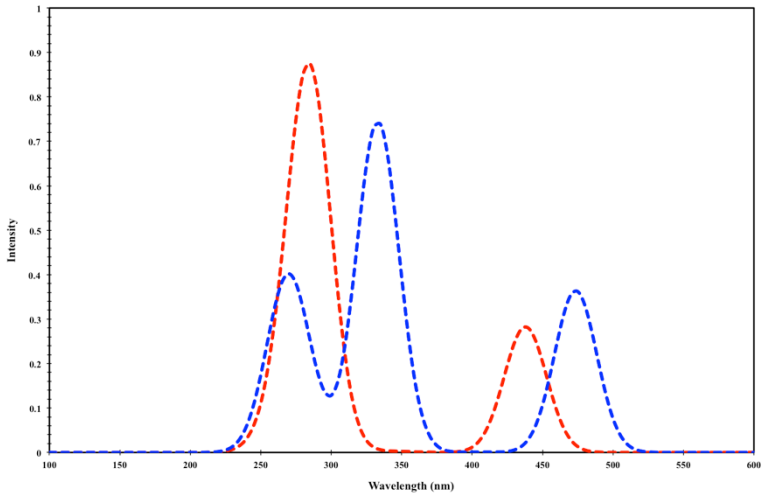

Figure S8 Simulated Absorption Spectra for **St-BTZ** (blue) and the polymer repeat unit (red) at MN12-L/6-311G(d,p).

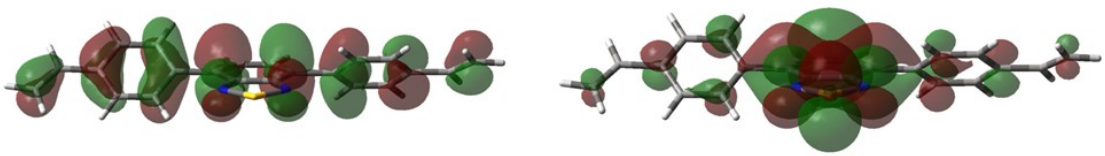

Figure S9 NTO particle-hole representation of **St-BTZ** S_1 state, computed with TD-CAM-B3LYP/6-311G(d,p).

Figure S10 NTO particle-hole representation of the polymer repeat unit S_1 state, computed with TD-CAM-B3LYP/6-311G(d,p).

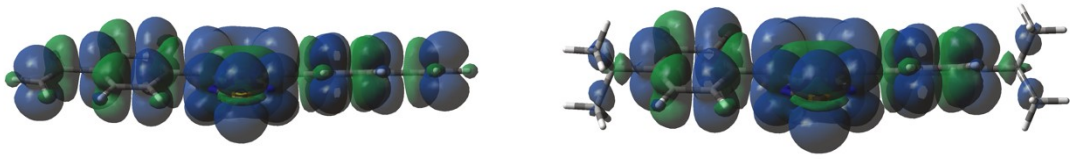

Figure S11 Spin Density of optimised triplet **styrene** and polymer repeat unit geometries respectively, computed at CAM-B3LYP/6-311G(d,p).

FT-IR and UV-Vis Spectra

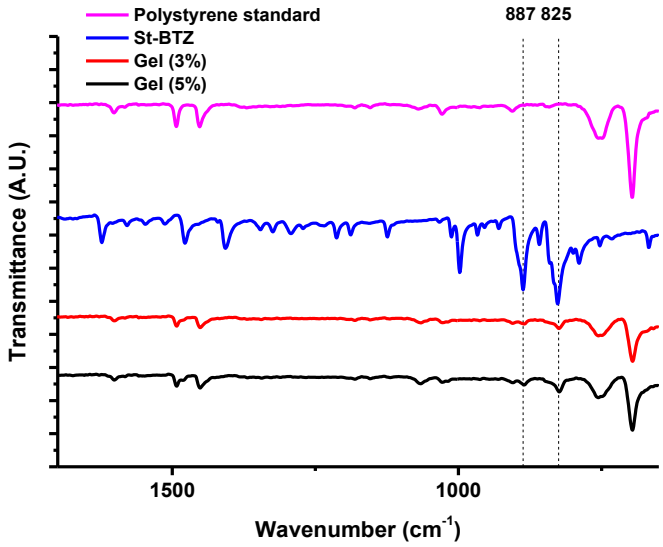

Figure S12 FT-IR Spectra of Polystyrene, **St-BTZ**, **Gel (3%)** and **Gel (5%)**. Characteristic peaks corresponding to BTZ can be seen at 887 and 825 nm.

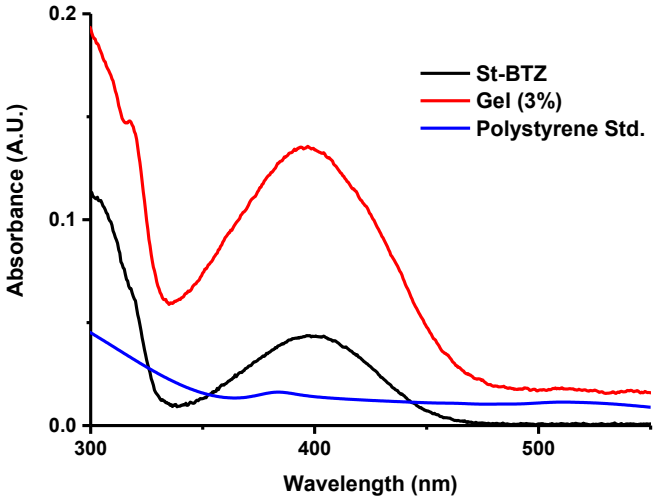

Figure S13 UV-Vis Spectra of a polystyrene standard, **St-BTZ** and **Gel (3%)**. λ_{max} for BTZ-based compounds at 400 nm.

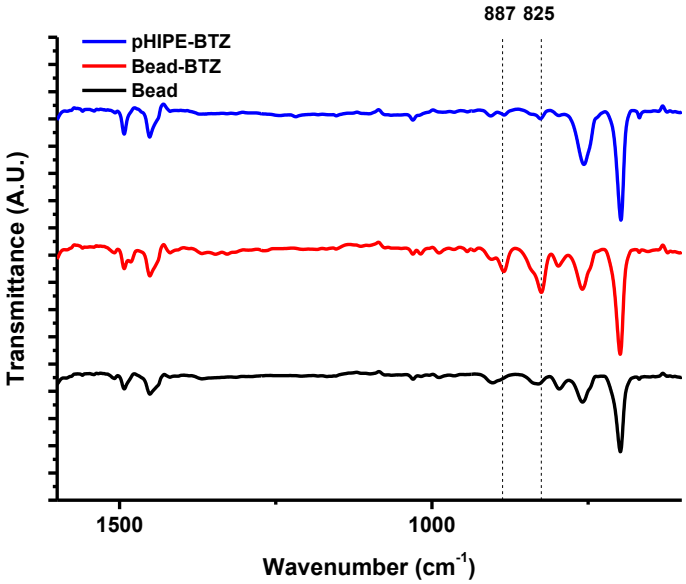

Figure S14 FT-IR Spectra of **Bead**, **Bead-BTZ** and **pHIPE-BTZ**. Characteristic peaks corresponding to BTZ can be seen at 887 and 825 nm.

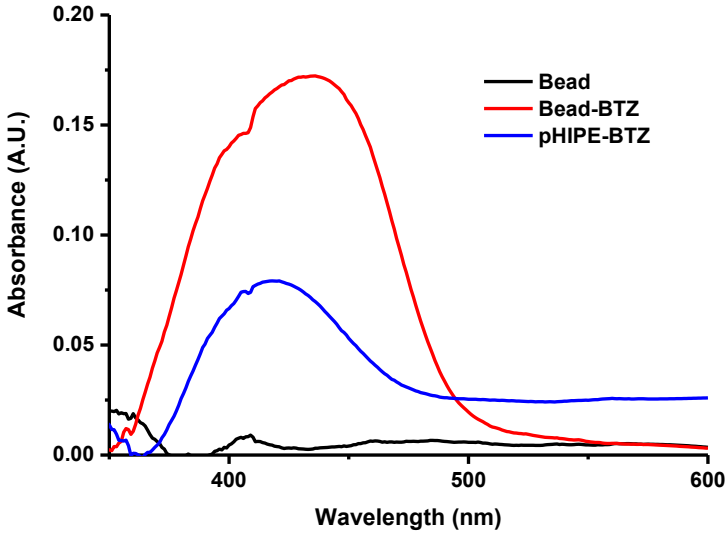

Figure S15 UV-Vis Spectra of **Bead**, **Bead-BTZ** and **pHIPE-BTZ**. λ_{max} for BTZ-based compounds at 425-450 nm.

NMR Spectra

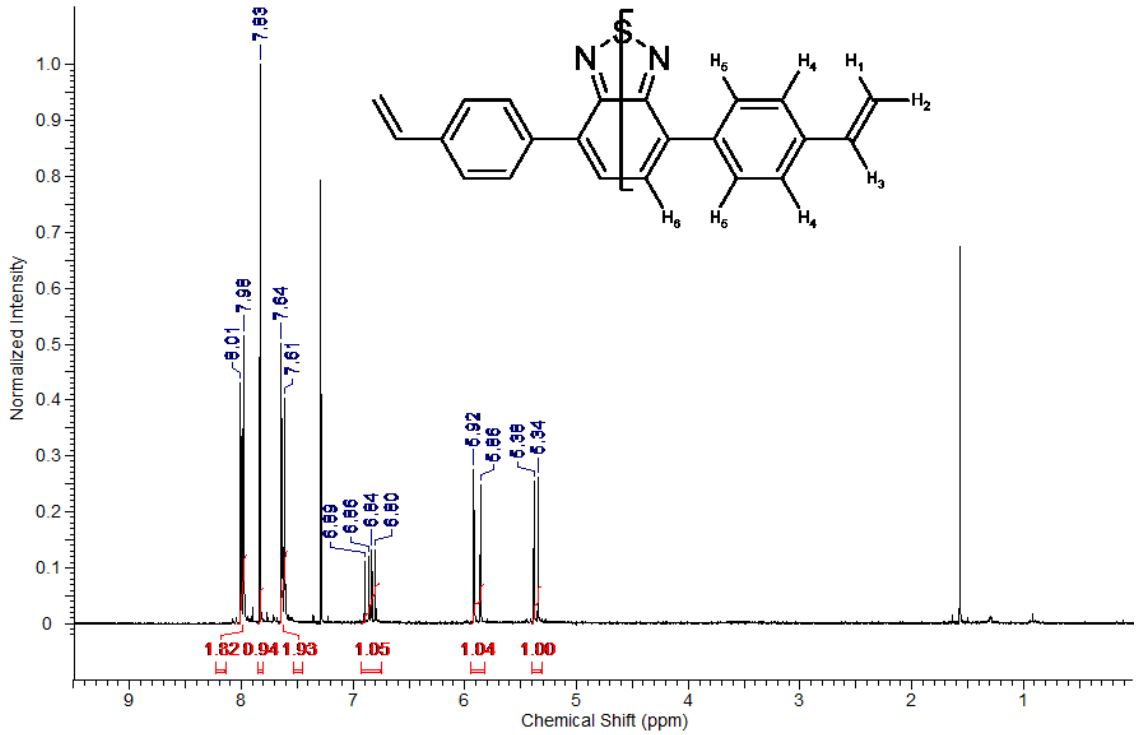

Figure S16 ^{1}H NMR of **St-BTZ** (300 MHz, 30 °C, $CDCl_3$) δ_{ppm} = 5.36 (d, 1 H, H_2), 5.89 (d, 1 H, H_1), 6.85 (m, 1 H, H_3), 7.63 (d, 2 H, H_4), 7.83 (s, 1 H, H_6), 8.00 (d, 2 H, H_5).

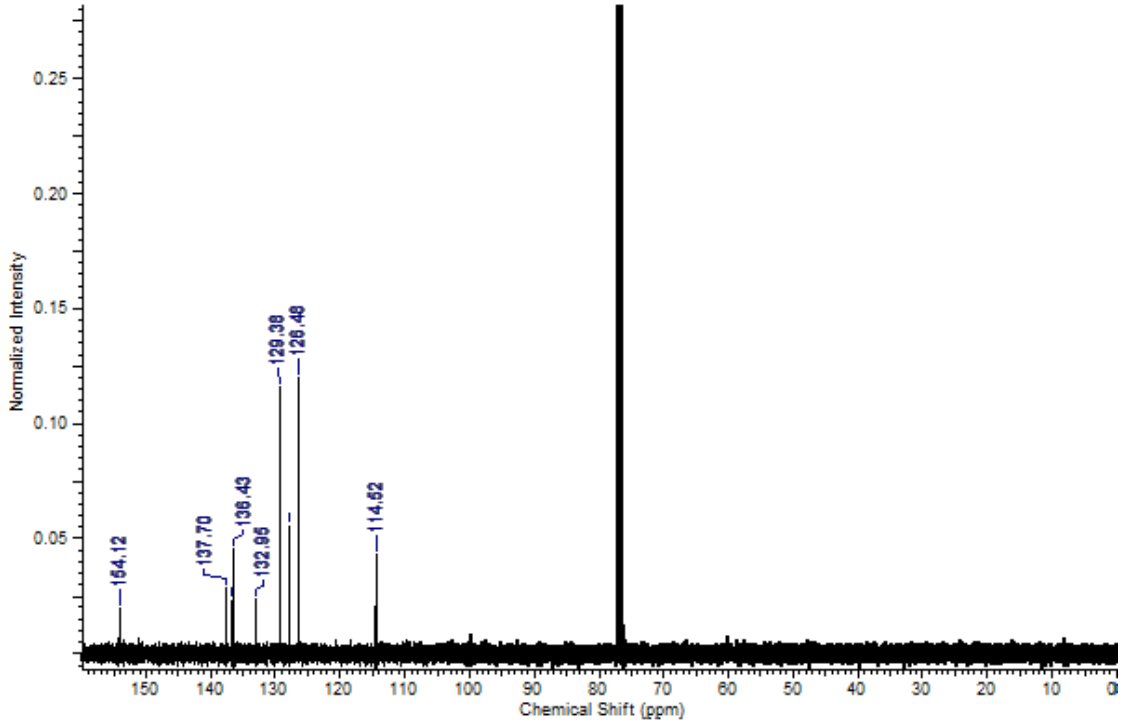

Figure S17 ^{13}C NMR of **St-BTZ** (400 MHz, 30 °C, $CDCl_3$) δ_{ppm} = 114.5 (C_1), 126.5 (C_4), 127.6 (C_5), 129.4 (C_8), 133.0 (C_7), 136.4 (C_2), 136.8 (C_3), 137.7 (C_6), 154.1 (C_9).

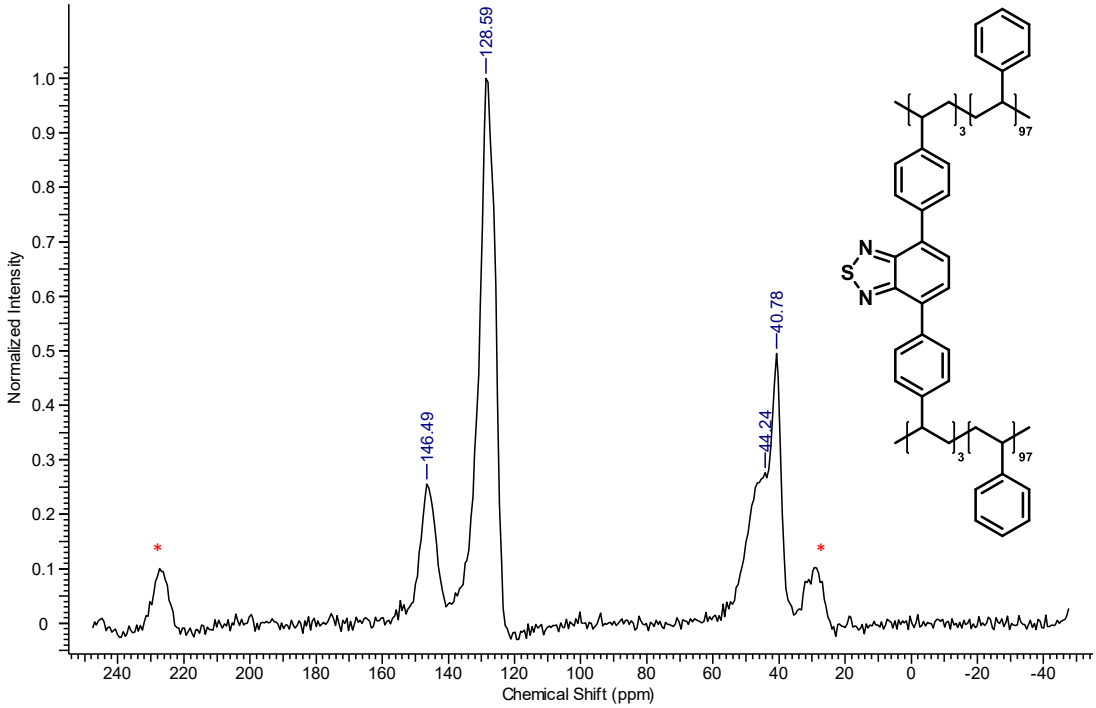

Figure S18 Solid state ^{13}C-NMR analysis of **Gel (3%)**. Aromatic (C-C) carbons can be seen in the δ 128 region and C-N carbons can be seen in the δ 146 region. Alkyl carbons are represented in the δ40-45 region. Peaks denoted by (*) indicate the presence of side bands.

Photooxidation of α-terpinene to ascaridole (^{1}H NMR spectra)

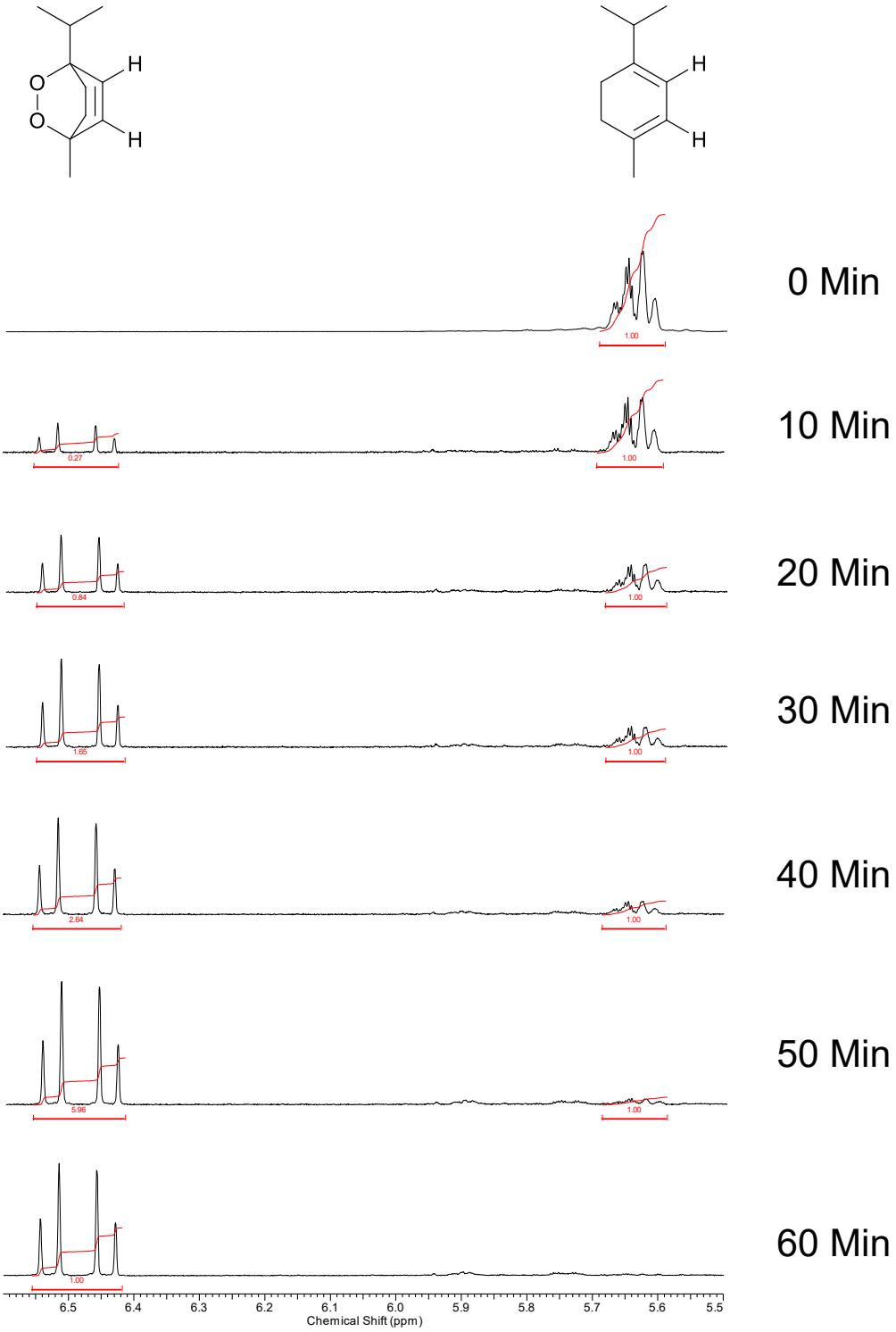

Figure S19 Progress of the typical conversion of *α*-terpinene to ascaridole in chloroform followed by ^{1}H NMR spectroscopy.

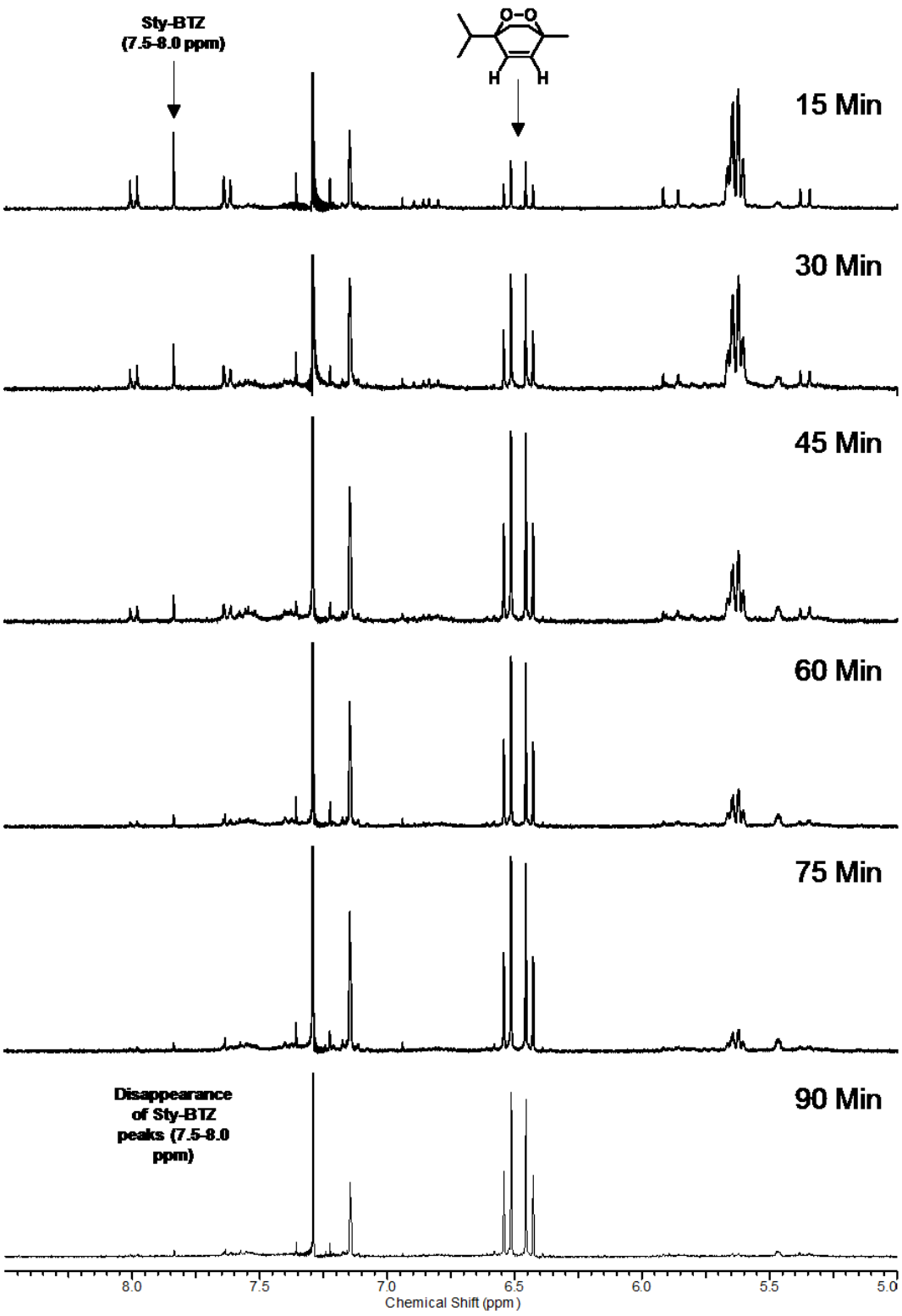

Figure S20 ^{1}H NMR spectrum for the photooxidation of α-terpinene to ascaridole over 90 minutes via irradiation of **St-BTZ** at 420 nm.

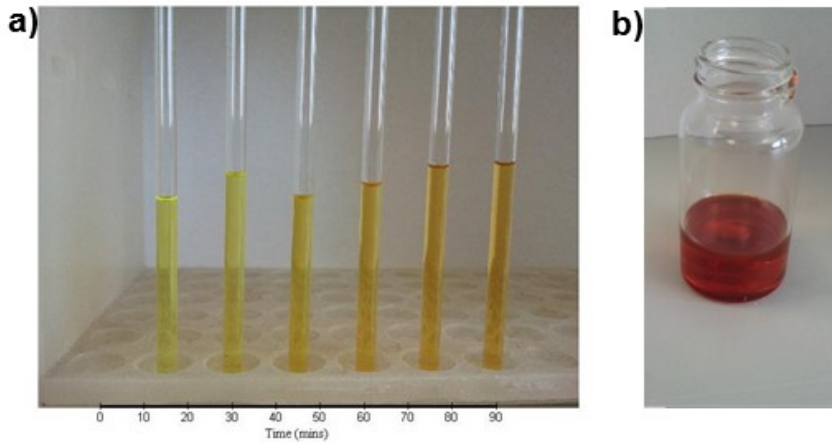

Figure S21 Photodegradation and observed color change of **St-BTZ** over 90 minutes: a) Solution color change of the **St-BTZ** photosensitization experiment at 15-minute intervals; b) Batch solution of the **St-BTZ** photosensitization experiment after 90 minutes showing a change to a deep red color.

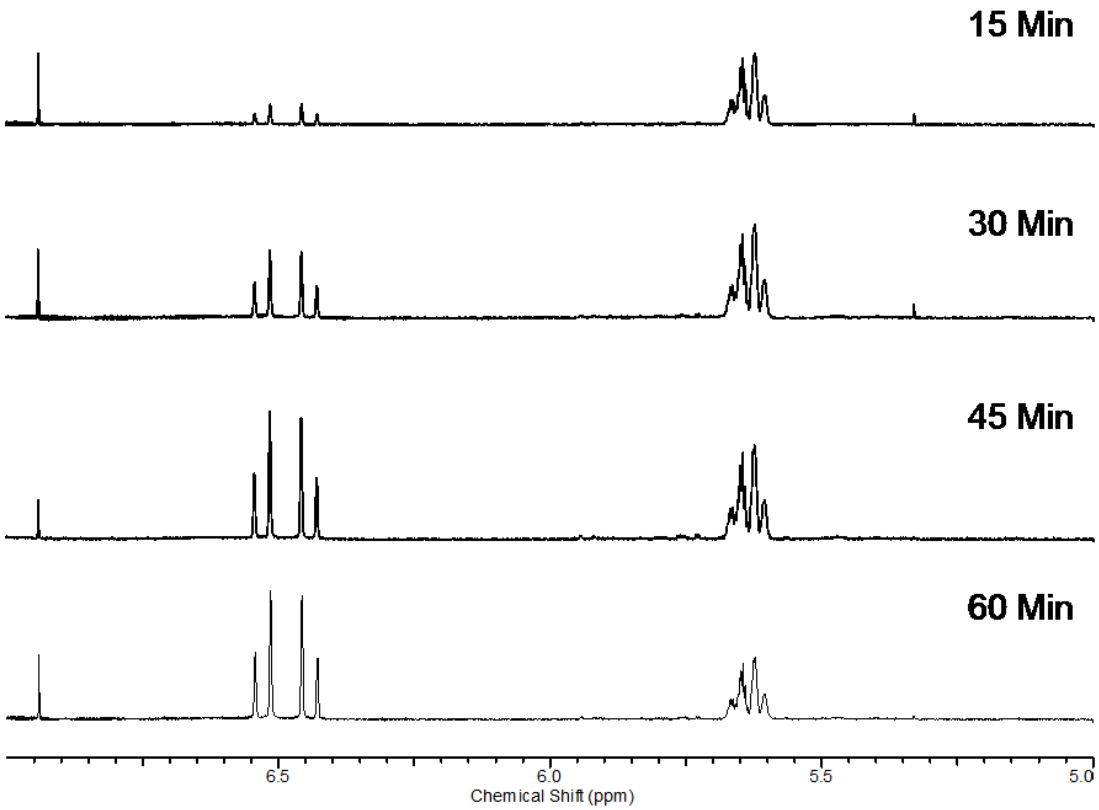

Figure S22 ^{1}H NMR spectrum for the photooxidation of α-terpinene to ascaridole over 60 minutes via irradiation of **Gel (2%)** at 420 nm.

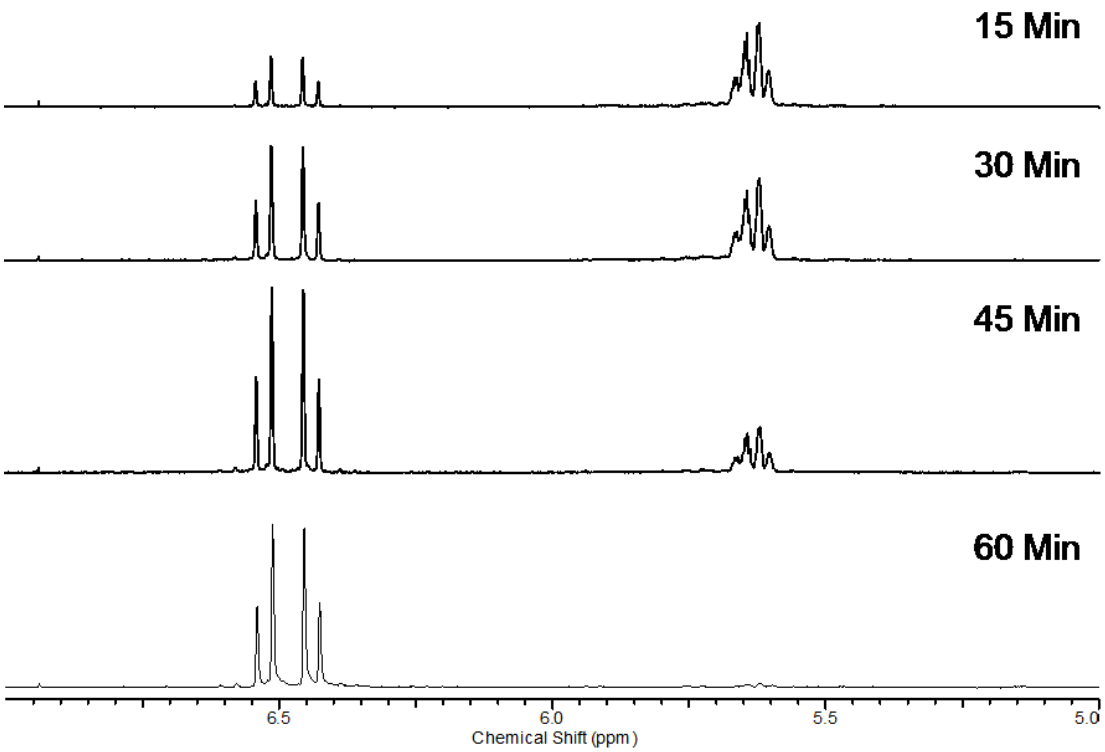

Figure S23 ^{1}H-NMR spectrum for the photooxidation of α-terpinene to ascaridole over 60 minutes via irradiation of **Gel (3%)** at 420 nm.

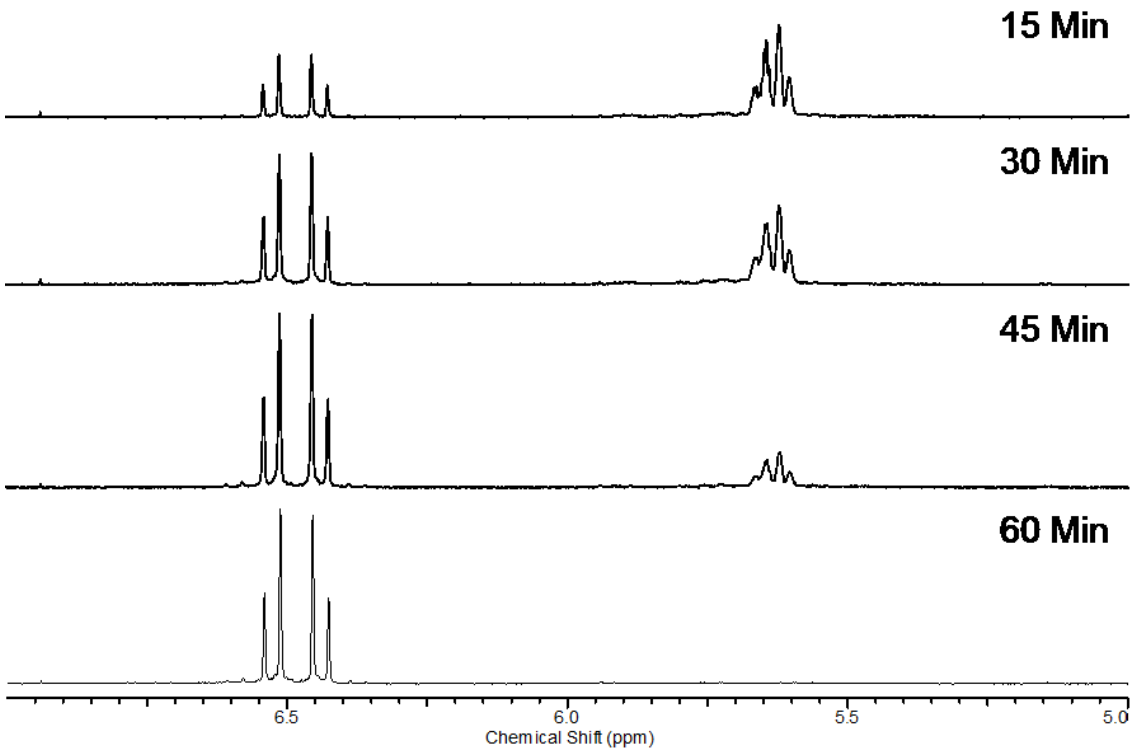

Figure S24 ^{1}H NMR spectrum for the photooxidation of α-terpinene to ascaridole over 60 minutes via irradiation of **Gel (5%)** at 420 nm.

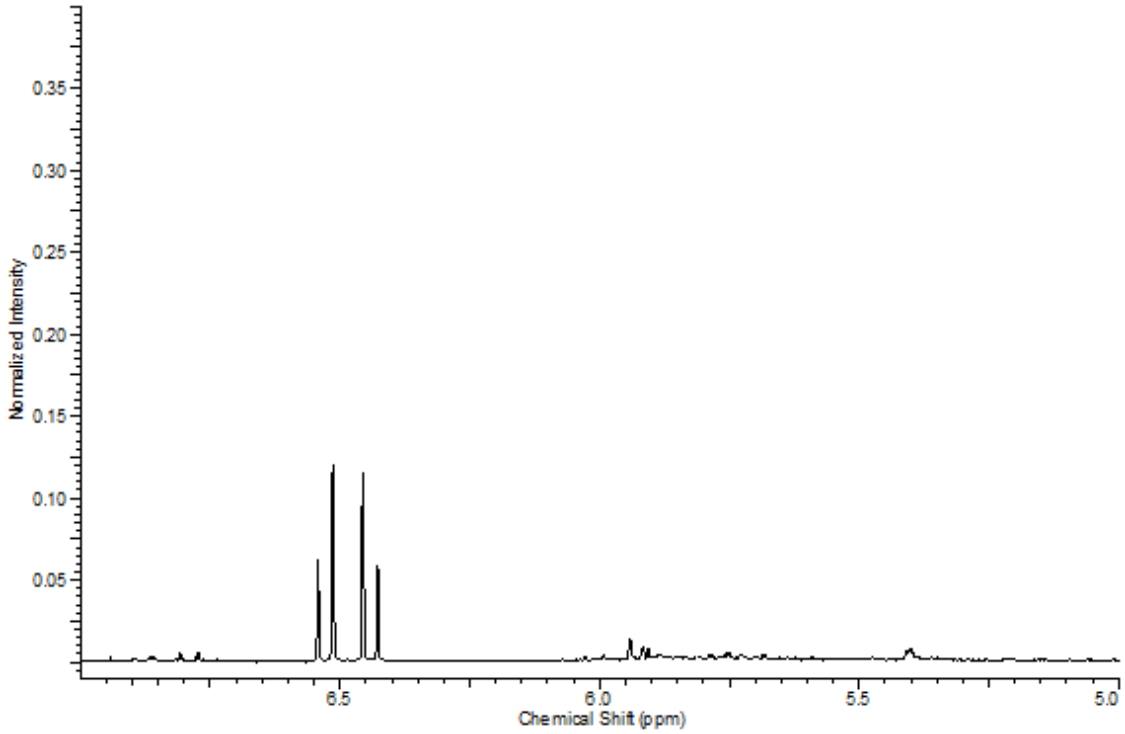

Figure S25 ^{1}H NMR spectrum for the photooxidation of α-terpinene to ascaridole after 60 minutes via irradiation of **Bead-BTZ** at 420 nm under batch conditions.

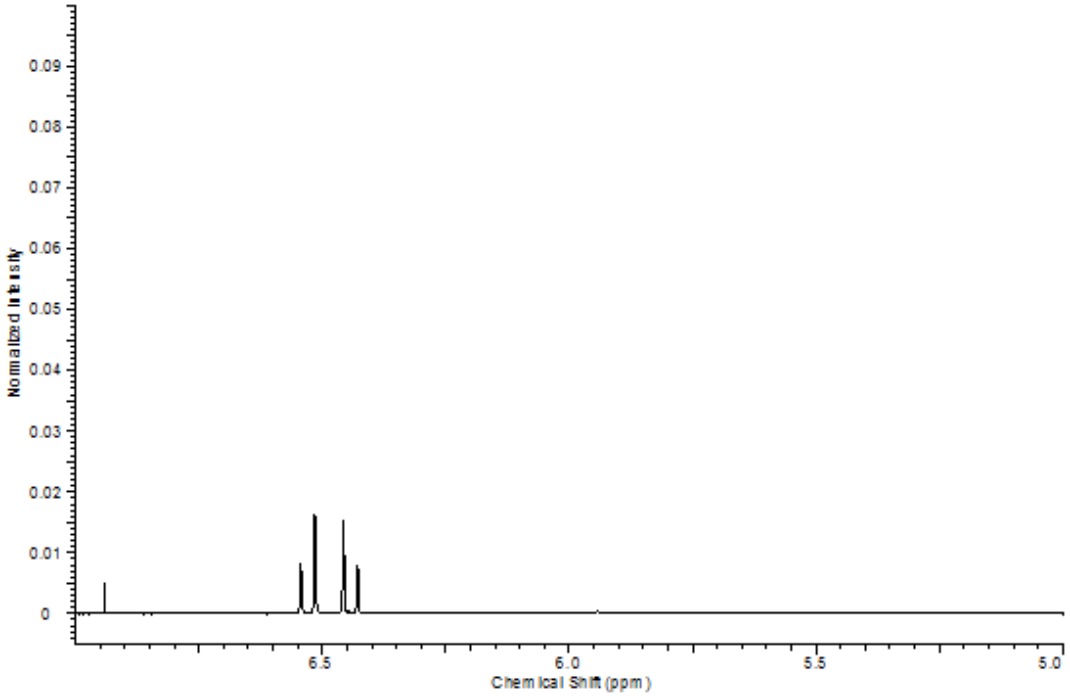

Figure S26 ^{1}H NMR spectrum for the photooxidation of α-terpinene to ascaridole after 60 minutes via irradiation of **Bead-BTZ** in a commercial photochemical flow reactor at 420 nm.

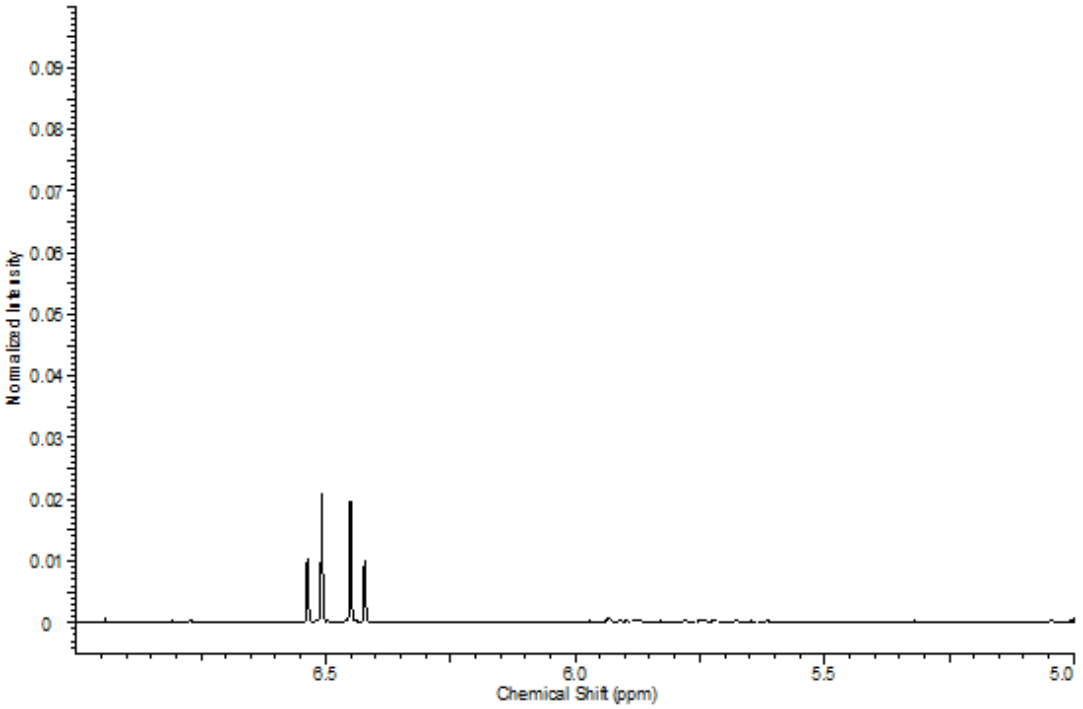

Figure S27 ^{1}H NMR spectrum for the photooxidation of α-terpinene to ascaridole after one pass of a 10 mL solution through a continuous flow column reactor via irradiation of **pHIPE-BTZ** at 420 nm.

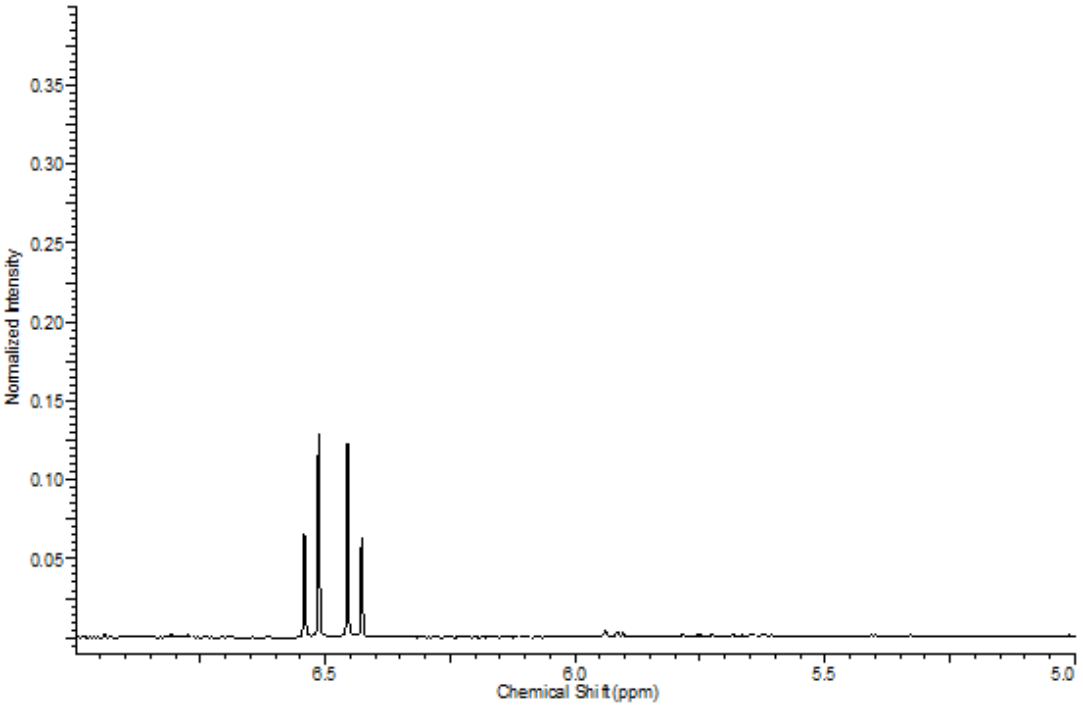

Figure S28 ^{1}H NMR spectrum for the photooxidation of α-terpinene to ascaridole of one pass of a 10 mL solution through a continuous flow column reactor via irradiation of **pHIPE-BTZ** at 420 nm after 6 hours of continuous usage.

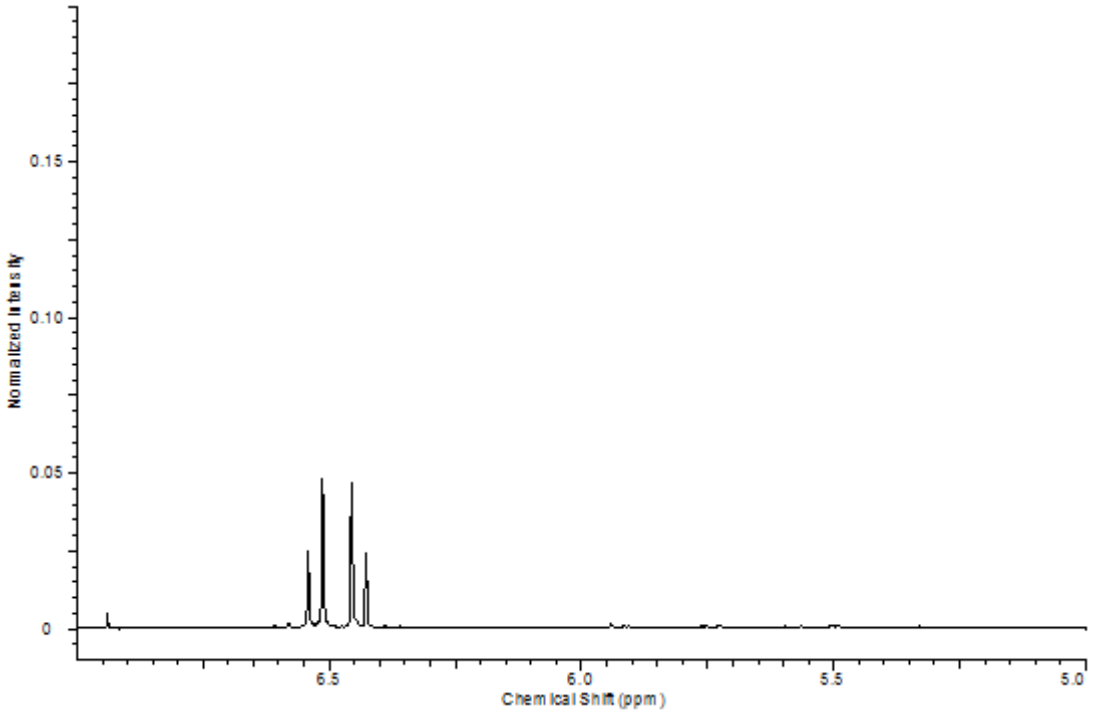

Figure S29 ^{1}H NMR spectrum for the photooxidation of *α*-terpinene to ascaridole after 90 minutes via sunlight irradiation of **Gel (3%)**.

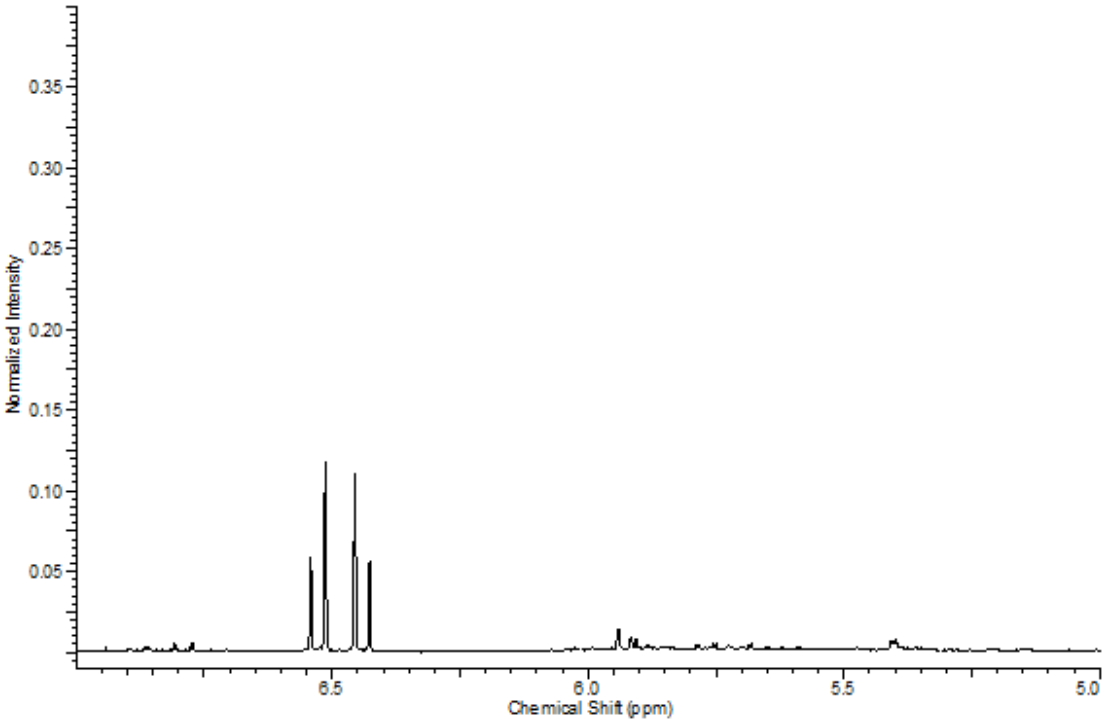

Figure S30 ^{1}H NMR spectrum for the photooxidation of *α*-terpinene to ascaridole after 60 minutes via sunlight irradiation of **Bead-BTZ**.

Aerobic Oxidative Hydroxylation of Aryl Boronic Acids

Table S6 Screening and control experiments.[a]

Entry	Visible light (420 nm)	Photocatalyst	Air	DIPEA	Conversion (%)[b]
1	+	+	+	+	>99
2	-	+	+	+	n.r.
3	+	-	+	+	n.r.
4	+	+	-	+	n.r.
5	+	+	+	-	n.r.

[a]Reaction conditions: Phenyl boronic acid (0.5 mmol), **Gel (5%)** (5 mg), DIPEA (1.0 mmol), DMF (5 mL), 420 nm LED irradiation, air, 24 h. [b]Conversion calculated *via* ^{1}H NMR. DIPEA = diisopropylethylamine, DMF = *N, N'*-dimethylformamide, n.r. = no reaction.

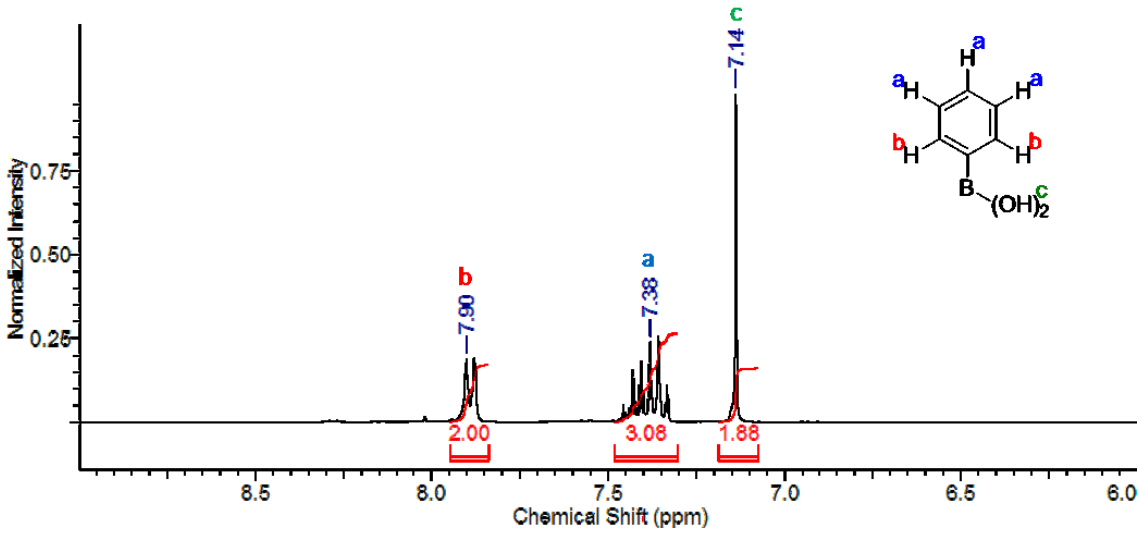

Figure S31 ^{1}H NMR of phenylboronic acid (300 MHz, 30°C C_3D_6O) δ_{ppm} = 7.14 (s, 2 H, H^c), 7.38 (m, 3 H, H^a), 7.90 (d, 2 H, H^b).

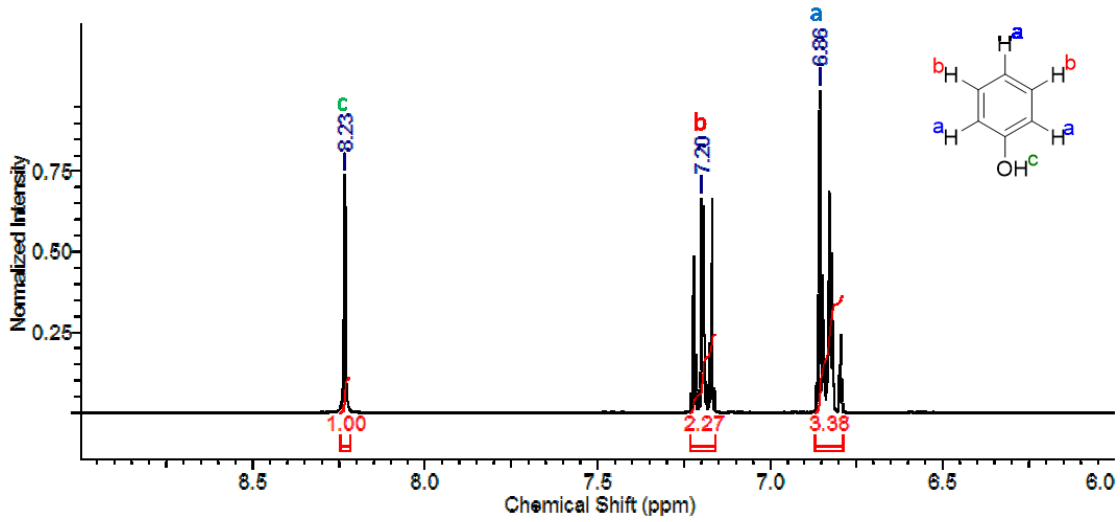

Figure S32 ^{1}H NMR of phenol (300 MHz, 30°C, C_3D_6O) δ_{ppm} = 6.86 (m, 3 H, H^a), 7.20 (m, 2 H, H^b), 8.23 (s, 1 H, H^c).

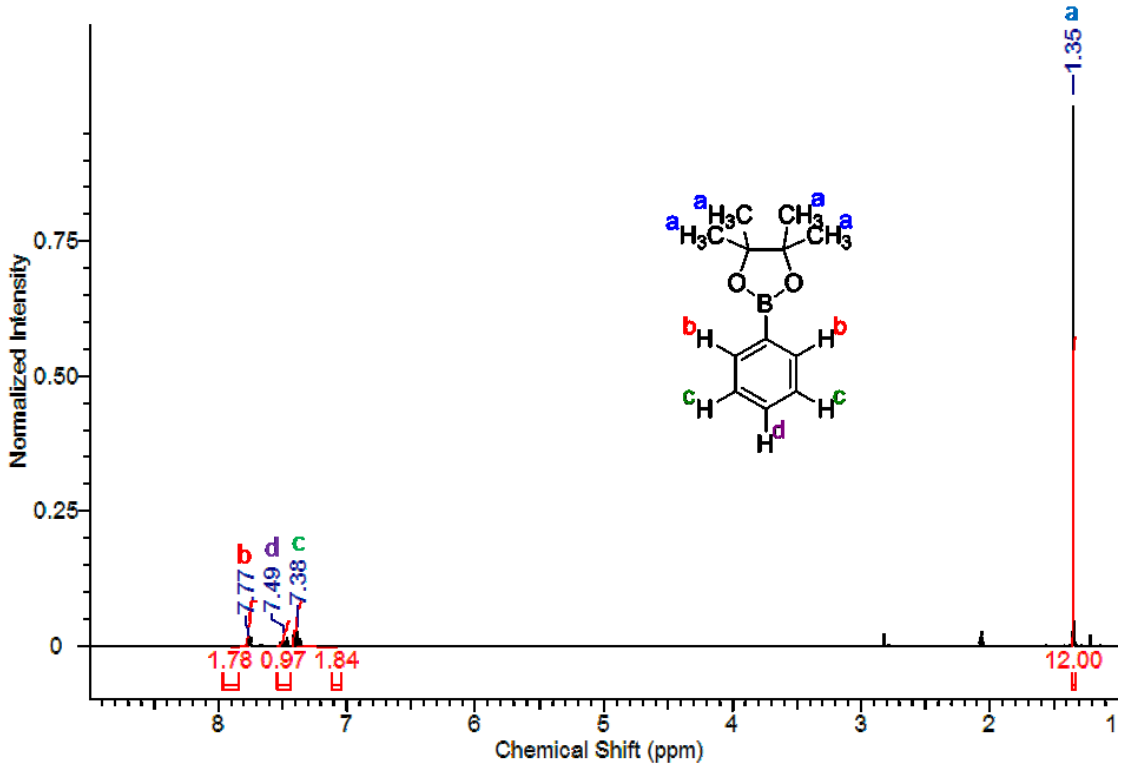

Figure S33 ^{1}H NMR of (4,4,5,5-tetramethyl-1,3,2.dioxaborolan-2-yl) benzene (300 MHz, 30°C, C_3D_6O) δ_{ppm} = 1.35 (s, 12 H, H^a), 7.38 (t, 2 H, H^c), 7.49 (t, 1 H, H^d), 7.77 (d, 2 H, H^b).

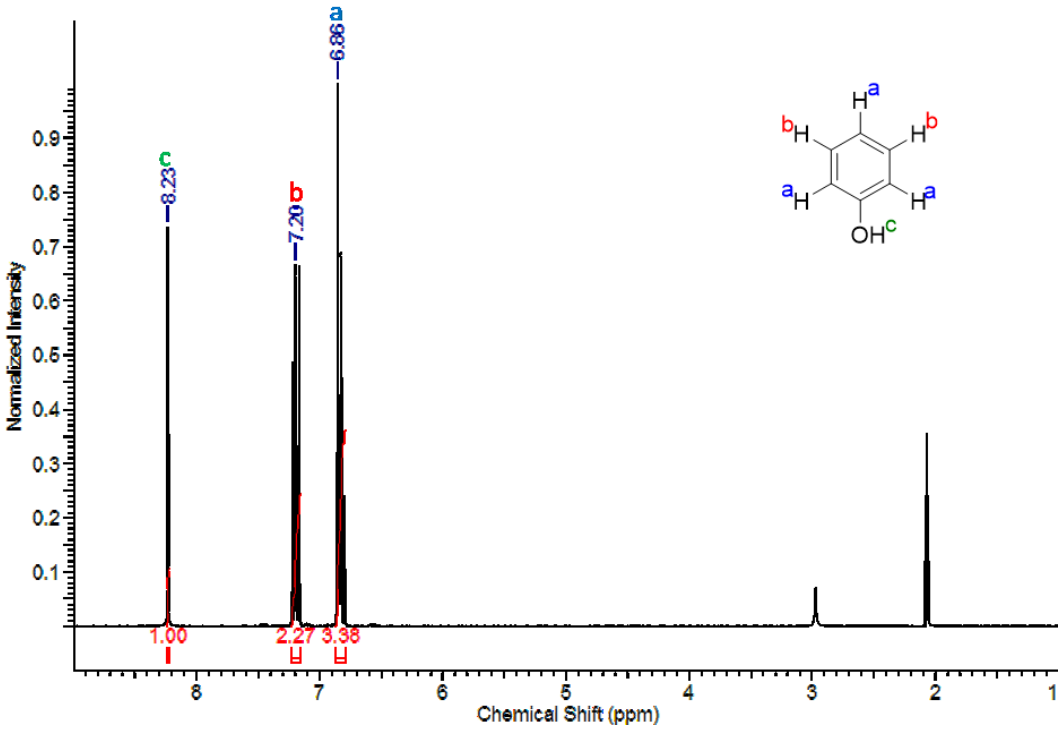

Figure S34 ^{1}H NMR of phenol (300 MHz, 30°C, C_3D_6O) δ_{ppm} = 6.86 (m, 3 H, H^a), 7.20 (m, 2 H, H^b), 8.23 (s, 1 H, H^c).

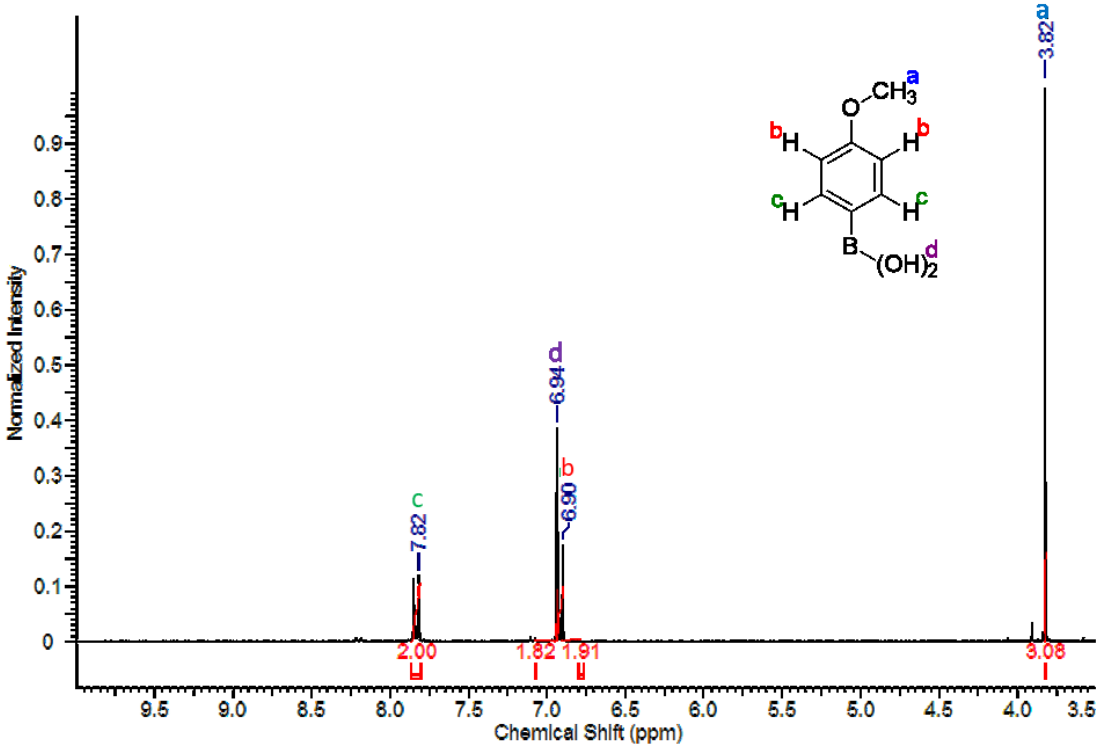

Figure S35 ^{1}H NMR of 4-methoxybenzene boronic acid (300 MHz, 30°C, C_3D_6O) δ_{ppm} = 3.82 (s, 3 H, H^a), 6.90 (d, 2 H, H^b), 6.94 (s, 2 H, H^d), 7.82 (d, 2 H, H^c).

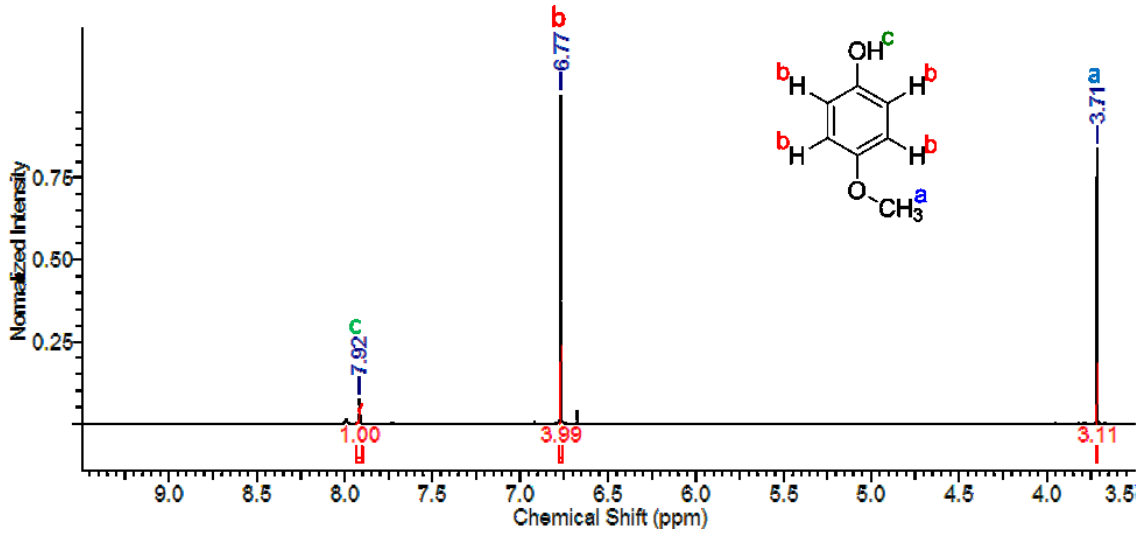

Figure S36 ^{1}H NMR of 4-methoxyphenol (300 MHz, 30°C, C_3D_6O) δ_{ppm} = 3.71 (s, 3 H, H^a), 6.77 (s, 4 H, H^b), 7.92 (s, 1 H, H^c).

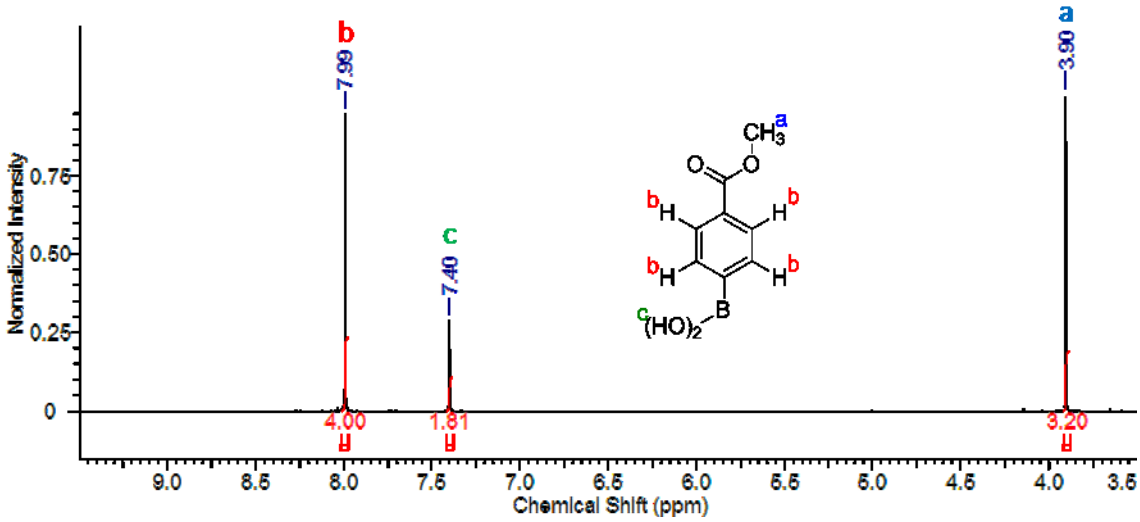

Figure S37 ^{1}H NMR of 4-(methoxycarbonyl)phenylboronic acid (300 MHz, 30°C, C_3D_6O) δ_{ppm} = 3.90 (s, 3 H, H^a), 7.40 (s, 2 H, H^c), 7.99 (s, 4 H, H^b).

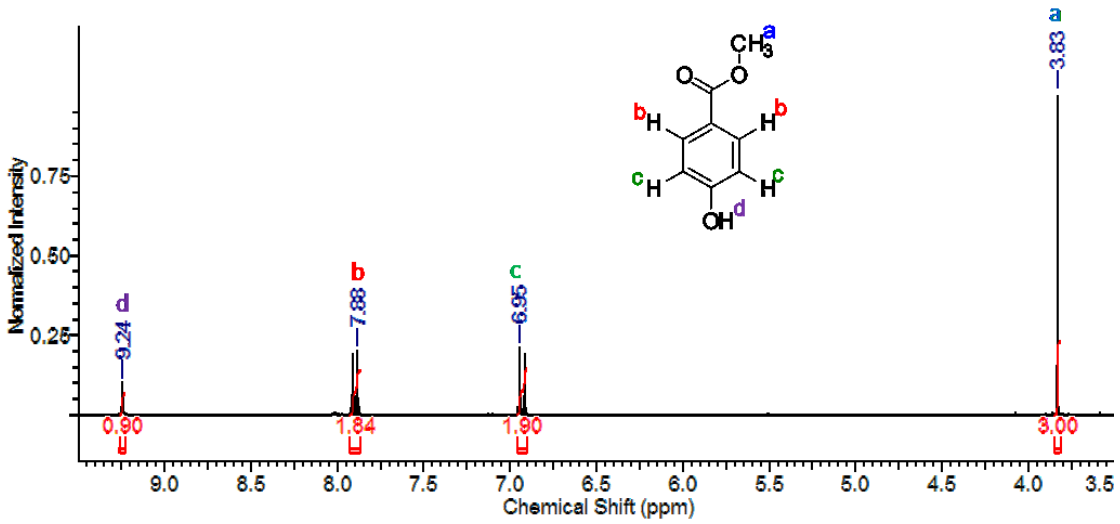

Figure S38 ^{1}H NMR of 4-(methoxycarbonyl)phenol (300 MHz, 30°C, C_3D_6O) δ_{ppm} = 3.83 (s, 3 H, H^{a}), 6.95 (d, 2 H, H^{c}), 7.88 (d, 2 H, H^{b}), 9.24 (s, 1 H, H^{d}).

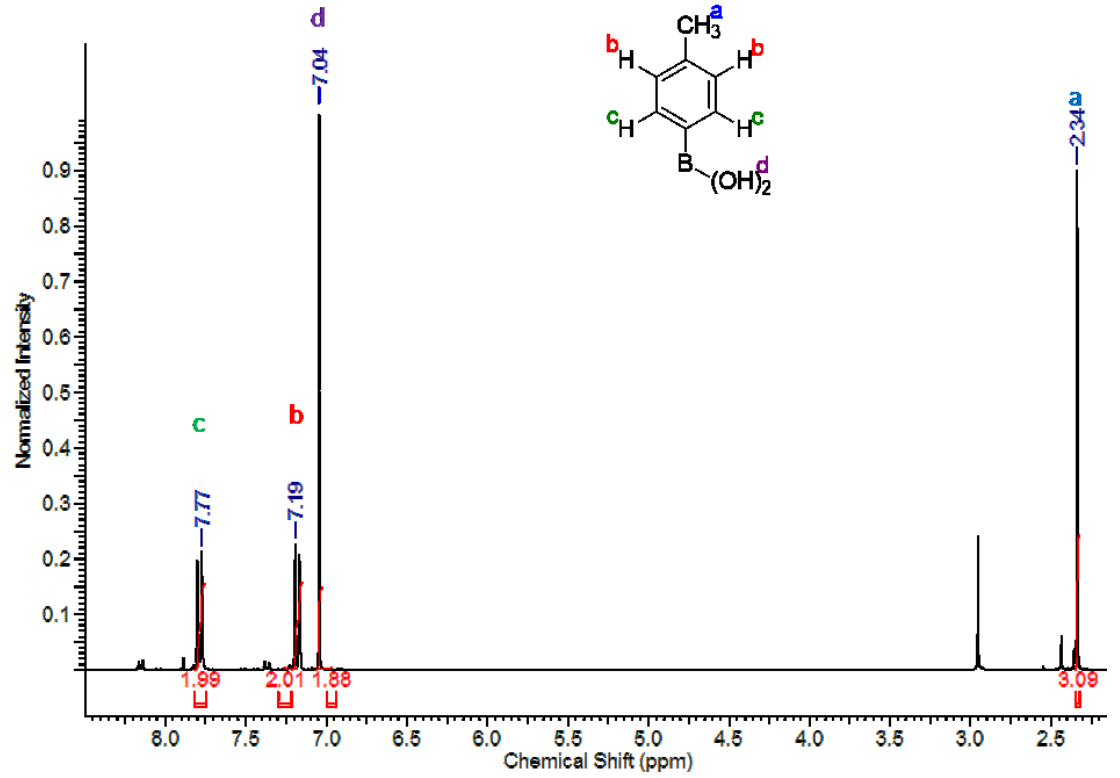

Figure S39 ^{1}H NMR of 4-tolylboronic acid (300 MHz, 30°C, C_3D_6O) δ_{ppm} = 2.34 (s, 3 H, H^{a}), 7.04 (s, 2 H, H^{d}), 7.19 (d, 2 H, H^{b}), 7.77 (d, 2 H, H^{c}).

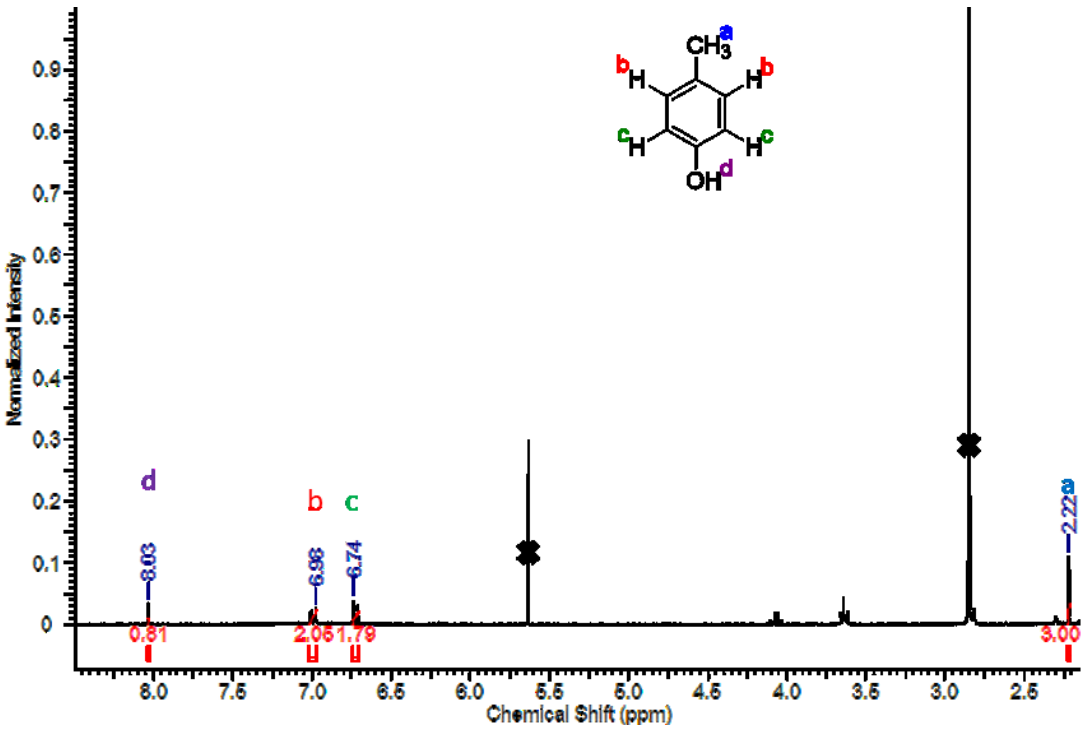

Figure S40 ^{1}H NMR of 4-tolylphenole (300 MHz, 30°C, C_3D_6O) δ_{ppm} = 2.22 (s, 3 H, H^{a}), 6.74 (d, 2 H, H^{c}), 6.98 (d, 2 H, H^{b}), 8.03 (s, 1 H, H^{d}).

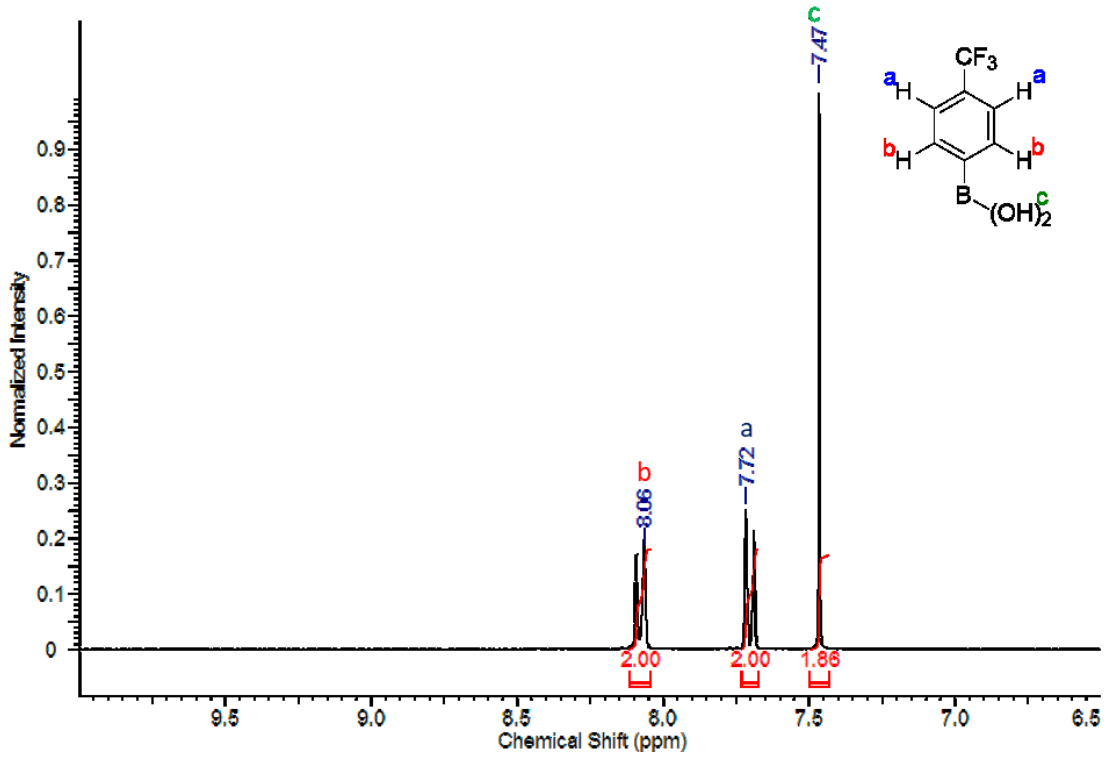

Figure S41 ^{1}H NMR of 4-(trifluoromethyl)phenylboronic acid (300 MHz, 30°C, C_3D_6O) δ_{ppm} = 7.47 (s, 2 H, H^{c}), 7.72 (d, 2 H, H^{a}), 8.06 (d, 2 H, H^{b}).

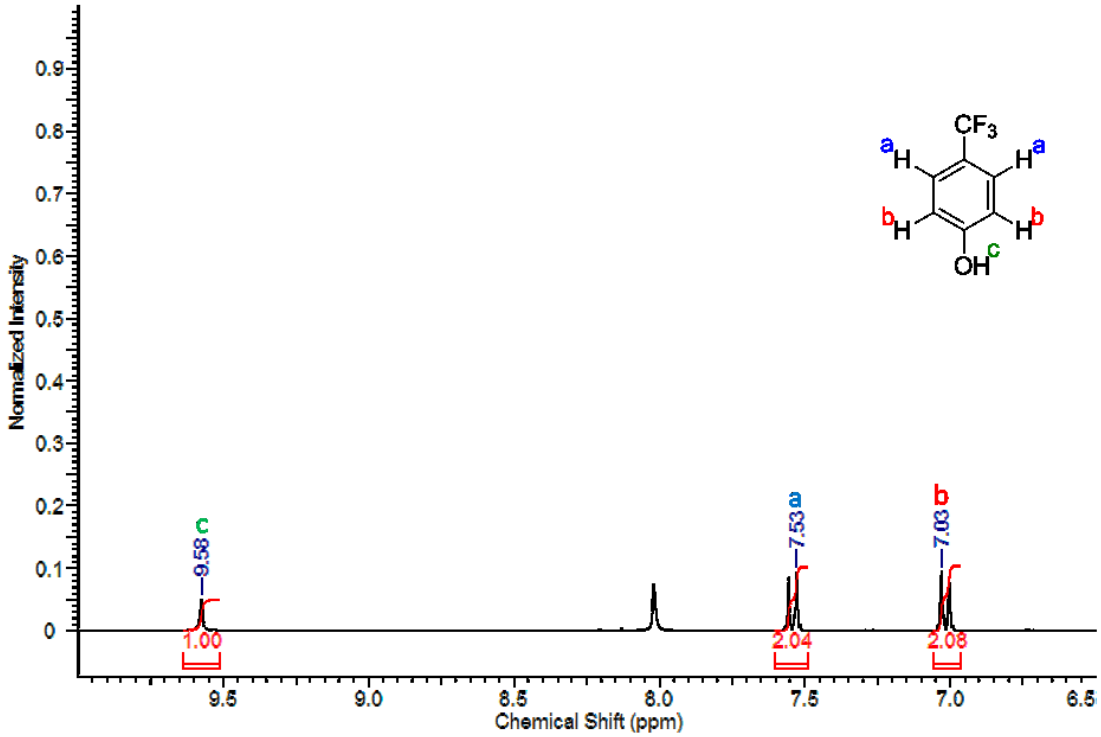

Figure S42 ^{1}H NMR of 4-(trifluoromethyl)phenol (300 MHz, 30°C, C_3D_6O) δ_{ppm} = 7.03 (d, 2 H, H^b), 7.53 (d, 2 H, H^a), 9.58 (s, 1 H, H^c).

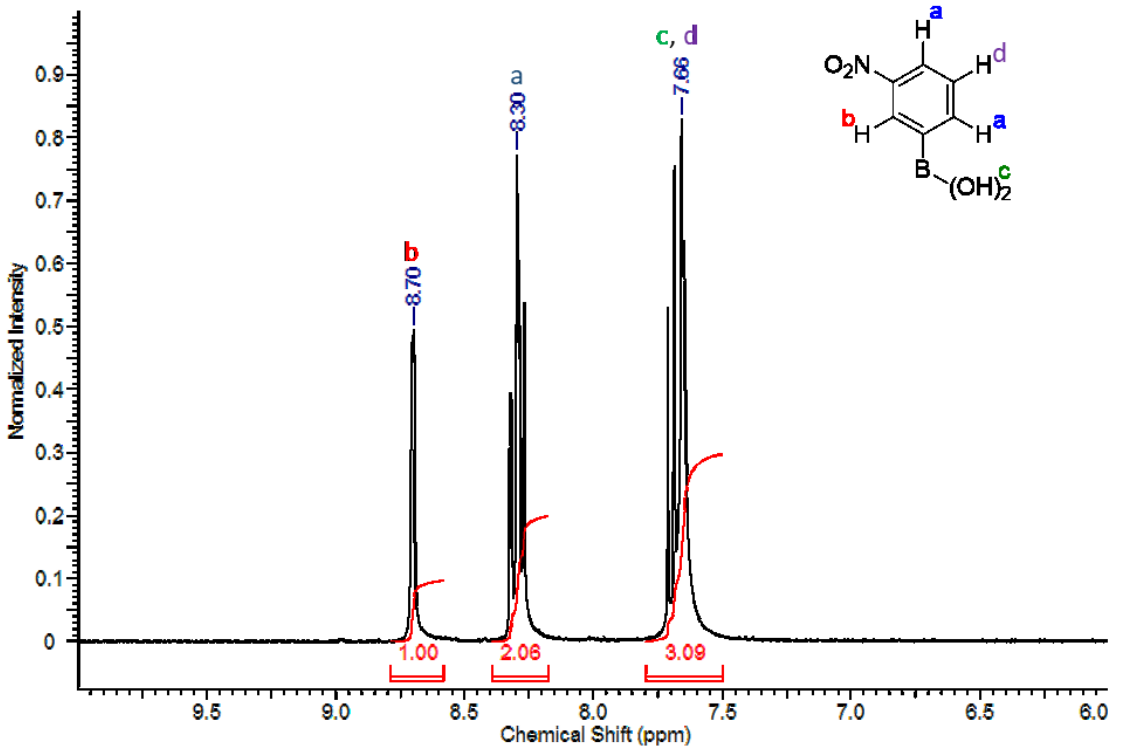

Figure S43 ^{1}H NMR of 3-nitrophenylboronic acid (300 MHz, 30°C, C_3D_6O) δ_{ppm} = 7.66 (d/s, 3 H, H^d/H^c), 8.30 (t, 2 H, H^a), 8.70 (s, 1 H, H^b).

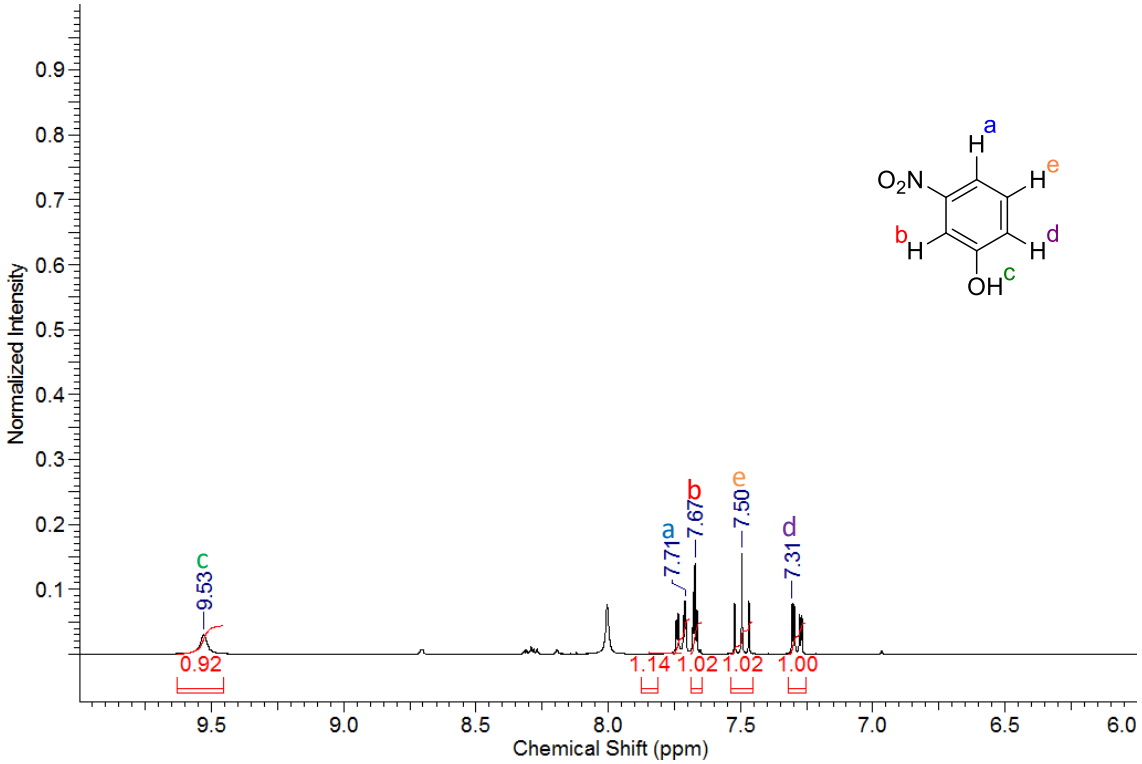

Figure S44 ^{1}H NMR of 3-nitrophenol (300 MHz, 30°C, C_3D_6O) δ_{ppm} = 7.31 (d, 1 H, H^{d}), 7.50 (t, 1 H, H^{e}), 7.67 (d, 1 H, H^{b}), 7.71 (d, 1 H, H^{a}), 9.53 (s, 1 H, H^{c}).

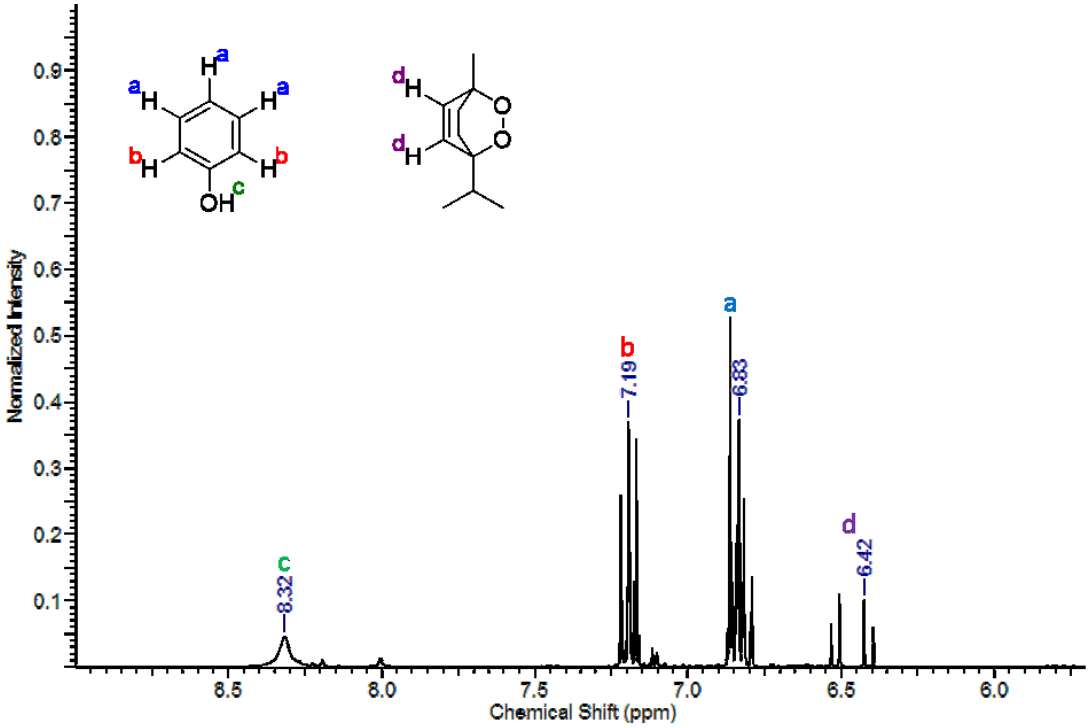

Figure S45 ^{1}H NMR of phenol and ascaridole (300 MHz, 30°C, C_3D_6O) δ_{ppm} = 6.42 (d, 1 H, H^{d}), 6.83 (m, 3 H, H^{a}), 7.19 (m, 3 H, H^{b}), 8.32 (s, 1 H, H^{c}).

References

[1] Ranger, M.; Rondeau, D.; Leclerc, M. *Macromolecules* **1997**, *30*, 7686-7691.

CHAPTER 5: Facile Synthesis of a Conjugated Microporous Polymeric Monolith *via* Copper-free Sonogashira-Hagihara Cross-coupling in Water under Aerobic Conditions (Publication, *Polymer Chemistry*, RSC)

The following section outlines the synthesis of a conjugated porous polymer (CPP) through a simplified copper-free Sonogashira-Hagihara cross-coupling reaction in the absence of a solvent and under aerobic conditions. Furthermore, a post-modification procedure was performed, introducing sulphur moieties into the polymer framework. Both the new and post-modified polymer were fully characterised. Due to the introduction of sulphur groups, the CPP was utilised for metal uptake, with a greater focus on Ag(I). The silver-loaded CPP was then used as a heterogeneous catalyst for the heterocyclisation of 4-pentynoic acid. While the previous chapters have primarily investigated electronic control of polymers for their implementation as photocatalysts, this work centres on morphological control and functionality through the synthesis of a monolithic structure and its synthetic post-modification. Furthermore, immobilisation of a metal catalyst on the CPP surface demonstrates an alternative catalytic material when compared to traditional metal-based catalysts (*i.e.* soluble metal complexes). This chapter will outline and discuss the publication titled '*Facile synthesis of a conjugated microporous polymeric monolith via copper-free Sonogashira-Hagihara cross-coupling in water under aerobic conditions*' which was published in *Polymer Chemistry* and can be found in its entirety (including supporting information) at the end of this chapter. Any contributions and work performed by other students, collaborators or academics are presented throughout the chapter in the appropriate sections.

5.1 Background

A central theme throughout the work presented thus far is the use of polymers as heterogeneous photocatalysts. For CPPs, monomer selection is paramount when applying electronic and/or morphological control. While optoelectronic control can have a significant effect on photocatalytic characteristics and performance, morphological control determines the physical format and other physical properties such as porosity and

surface area of the resultant polymer [5.1, 5.2]. While typical CPPs synthesised through traditional Suzuki-Miyaura and Sonogashira-Hagihara cross coupling tend to result in amorphous powders under normal reaction condition, other synthetic strategies have been investigated to alter the physical format of the product. These other formats include thin films [5.3], monolithic structures [5.4], aerogels [5.5], soluble materials [5.6], and nanoparticles [5.7].

Through careful selection of monomers, functionality can also be introduced into a CPP framework. This is important when examining post-synthetic modification procedures as this is notoriously difficult due to the generally poor solubility of CPPs. The use of Sonogashira-Hagihara cross-coupling reactions have proven to be fruitful in this research as the alkyne backbone present in the repeat unit has been shown as a reactive site for post-synthetic modification [5.8, 5.9]. As described in Chapter 1, there are some reactions where a CPP acting as a photocatalyst does not meet the mechanistic and/or energetic requirements for the reaction to proceed. However, in cases where a metal-based catalyst is employed, CPPs can be used to immobilise the metal species. Through the use of post-synthetic strategies and subsequent functionalisation of a CPP, metal ions can be selectively absorbed and potentially act as an insoluble catalytic site [5.10].

5.2 Aim/Objectives

The primary aim of this study was to showcase the robust nature and versatility of CPPs. Through careful design of the CPP, morphological control and post-synthetic modification can be achieved using specific synthetic routes. The polymer was synthesised under mild conditions *via* a copper-free Sonogashira-Hagihara cross-coupling reaction to yield a monolithic version of the CPP. Furthermore, post-synthetic modification was employed on the alkyne groups through thiol-yne chemistry to yield functional groups with selectivity towards silver ions. With this material, we envisaged its use as reusable catalytic support for the silver-catalysed heterocyclisation of 4-pentynoic acid.

5.3 Synthesis of Materials/Methodology

The methodology used for the preparation and characterisation of the monolithic CPP as well as its use as a heterogeneous catalyst is described in this section. The preparation of the CPP was performed under aerobic conditions through a copper-free Sonogashira-Hagihara cross-coupling reaction in water [5.11]. Post-modification of the CPP was performed using well-known thiol-yne chemistry [5.8, 5.9]. The monolithic CPP was characterised through FT-IR spectroscopy, Raman spectroscopy, solid state ^{13}C NMR CP-MAS spectroscopy, thermogravimetric analysis (TGA), CO_2 gas sorption, energy dispersive X-ray spectroscopy (EDX), and scanning electron microscopy (SEM). The post-modified CPP was loaded with Ag(I) metal ions and employed for the silver-catalysed conversion of 4-pentynoic acid to 5-methylenedihydrofuran-2(3H)-one. ^{1}H NMR spectroscopy of the crude mixture was used to determine the percent conversion to the 5-methylenedihydrofuran-2(3H)-one product. Physical analysis of the CPP was performed by Jie Lui at City University of Hong Kong. All solid state ^{13}C NMR CP-MAS measurements were carried out by Dr David Ellis at Heriot-Watt University.

5.3.1 Synthesis of CPP Monolith (CMP_1)

The synthesis of CMP_1 was employed utilising a copper-free Sonogashira-Hagihara cross-coupling reaction whereby 1,3,5-tribromobenzene, 1,4-diethynylbenzene and $PdCl_2$ were dissolved in pyrrolidine with the aid of a sonication bath. Deionized water was then added to form a large amount of precipitate and then the mixture was sonicated for approximately 2 minutes. The reaction mixture was heated to 85 °C for 24 hours yielding a vial-shaped brown monolithic solid (Scheme 5.1). The monolith was purified *via* Soxhlet extraction with deionised water, methanol, THF, and acetone and subsequently dried *in vacuo* (97 mg, 74 %).

5.3.2 Post-modification of CMP_1 through a Thiol-yne Reaction (CMP_S)

As seen in Scheme 5.2, post-modification of CMP_1 was achieved by introducing the monolith to a solution of $NaSCH_3$ in dimethylformamide (DMF) and heating the mixture to 85 °C for 24 hours. After cooling to room temperature, a 1 % HCl solution was added to achieve a pH lower than 2. The post-modified monolith was then collected, filtered, and washed with deionised water, methanol, and dichloromethane and

subsequently dried *in vacuo*. A monomeric analogue was also synthesised through similar procedures for comparison in metal uptake and catalysis.

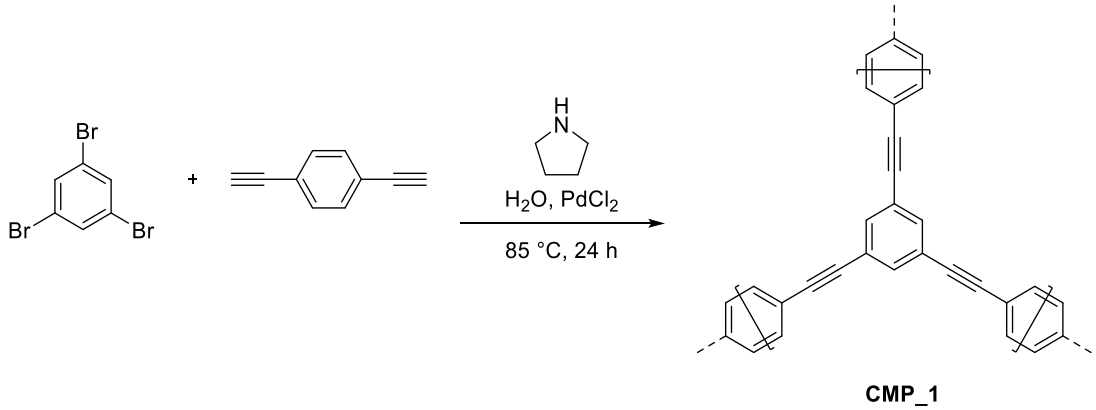

Scheme 5.1 Synthesis and theoretical repeat unit of CMP_1 through a modified Sonogashira-Hagihara cross-coupling reaction.

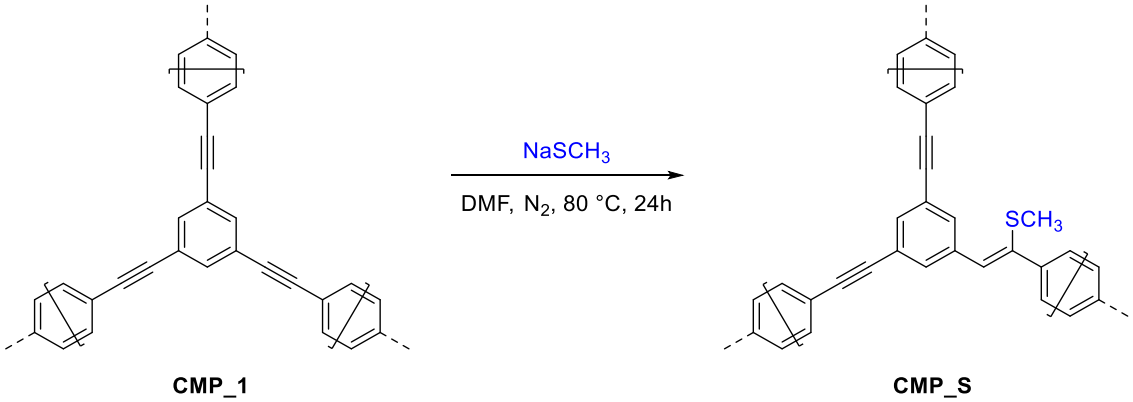

Scheme 5.2 Post-synthetic modification of CMP_1 through thiol-yne chemistry to produce CMP_S.

5.3.3 Uptake of Ag(I) with CMP_S (CMP_S_Ag)

Both the upper limit and selectivity of Ag(I) uptake using CMP_S was examined. The upper limit of Ag(I) uptake was determined by placing CMP_S in an aqueous solution containing excess $AgNO_3$. The mixture was stirred at 80 °C for 24 h and subsequently washed with deionised water to remove unbound Ag(I). The selectivity of CMP_S towards Ag(I) was determined by placing CMP_S in an aqueous mixture of metal salts and stirring overnight. Metal uptake experiments with CMP_S were carried out by Jie Liu, City University of Hong Kong.

5.3.4 Heterogeneous Catalytic Reactions with CMP_S_Ag

To measure the catalytic performance, CMP_S_Ag was added to a solution of 4-pentynoic acid in $CDCl_3$ where the mixture was stirred and heated to 80 °C. After 5 h, the solution was filtered and analysed *via* ^{1}H NMR spectroscopy for the appearance of the hydrofuranone product. Catalytic experiments were carried out by Jie Liu, City University of Hong Kong.

5.4 Results

5.4.1 Synthesis and Characterisation of CMP_1

As CMP_1 can be synthesised under relatively mild reactions conditions, the polymerisation was carried out through a modified procedure. Through the addition of water to the pyrrolidine solution in a reaction vial, rapid formation of a precipitate was initiated. By heating the reaction vial without stirring or agitation, a porous monolithic structure in the shape of the vial (cylindrical) was formed (Figure 5.1). Akin to other CPPs, CMP_1 was insoluble in all conventional solvents.

Analysis of the chemical structure (repeat unit) of CMP_1 was carried out using FT-IR and Raman spectroscopy, solid state ^{13}C NMR spectroscopy, and EDX spectroscopy. Both FT-IR and Raman spectra indicated typical alkyne stretching signals while no signal was present for the terminal C-H found in the starting materials. Solid state ^{13}C NMR spectroscopy indicated the presence of both aromatic and alkyne groups, validating the proposed structure of CMP_1. While EDX spectroscopy primarily exhibited the presence of carbon, bromine was also observed within the sample. This is not uncommon for CPPs as unreacted end groups will always be presented in the final product due to the nature of the synthesis. However, as these end groups are statistically much lower in number when compared to the repeat unit, they can be ignored.

Physical characteristics of CMP_1 were measure *via* TGA, CO_2 gas sorption, and SEM imaging. TGA of CMP_1 demonstrated a highly stable polymer up to 250 °C, as commonly exhibited in CPPs [5.12]. SEM imaging revealed the composition of CMP_1 as hollow fibres, measuring a few hundred nanometres in diameter (Figure 5.2). While

this type of structural formation is unusual for CPPs and not well understood, there have been reports describing this hollow nanofiber formation [5.13, 5.14]. Initial gas sorption experiments were carried out using N_2. However, as no significant sorption was exhibited, the same examination was carried out using CO_2. Using CO_2, a S_{BET} of 374 $m^2\ g^{-1}$ was calculated with an average pore width of 0.48 nm and pore volume of 0.113 $cm^3\ g^{-1}$, indicating microporosity.

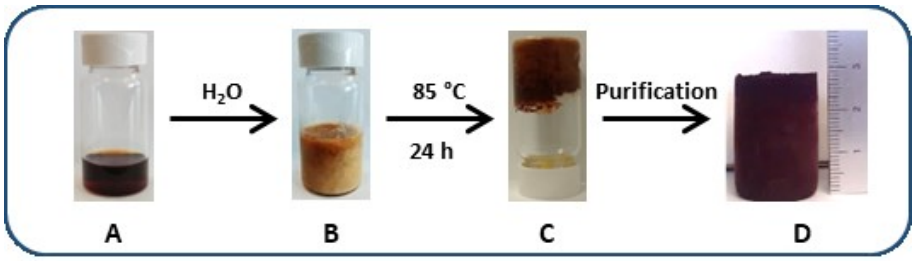

Figure 5.1 Synthetic progress of CMP_1: (A) Reactants dissolved in pyrrolidine; (B) addition of H_2O with precipitate formation; (C) polymer formation and solidification after heating; (D) purification procedure to result in the CMP_1 product.

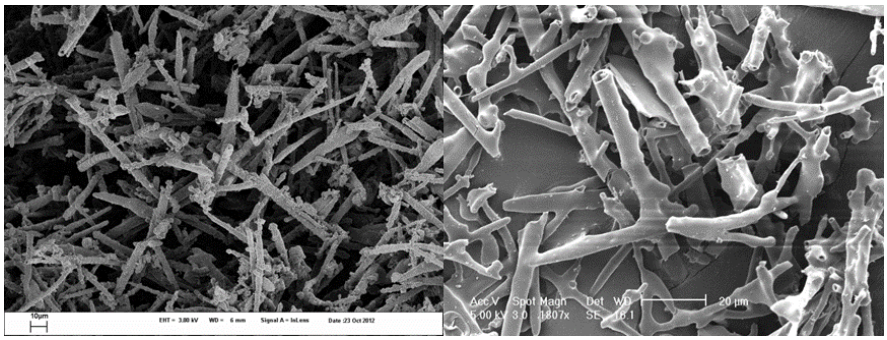

Figure 5.2 SEM images of CMP_1 as hollow fibres.

5.4.2 Post-Synthetic Modification of CMP_1

Thiol-yne chemistry is a well-known method for modifying alkyne groups with a sulphur-containing moiety and has been shown to be an efficient reaction under both homogeneous and heterogeneous conditions [5.8, 5.9]. Therefore, this chemistry was used as a facile method for the post-synthetic modification of CMP_1. Scheme 5.2 depicts the straightforward addition of sulphur methyl ($-SCH_3$) to the alkyne groups within the repeat unit of CMP_1. By introducing a sulphur functionality to the monolith, the potential for metal chelation becomes apparent.

Solid state ^{13}C NMR spectroscopy along with FT-IR and Raman spectroscopy were used to analyse the success of the post-modification procedure. The spectra from all three techniques indicated a largely diminished signal correlating to the alkyne present in CMP_1. Furthermore, EDX measurements showed a new peak corresponding to the presence of sulphur. These results indicate that the addition of SCH_3 to CMP_1 was successful.

5.4.3 Selectivity and Effective Uptake of Ag(I)

The post-synthetically modified CMP_S offered a new functionality to the polymer for the uptake of metal species. CMP_S was first analysed for its ability to selectively chelate metal ions from an aqueous solution. Metal ions (in the form of metal salts) were added to an aqueous mixture at a concentration of 10 ppm which included Cu^{2+}, Zn^{2+}, Co^{2+}, Ag^{+}, Cd^{2+}, Ni^{2+} and Pb^{2+}. Each mixture also contained either CMP_1 (Figure 5.3a) or CMP_S (Figure 5.3b) as the adsorbent. The mixture was stirred in the absence of light and the solution measured at specified time intervals *via* ICP-MS to determine the concentration of metal ions unbound to the polymers. For comparison, the unmodified CMP_1 was used in the same experiment to help reinforce the requirement of the sulphur functionality as a metal chelator.

Both polymers showed significant uptake of metal ions within two hours. In both cases, Ag(I) showed the greatest decrease in concentration within the solution. However, CMP_S demonstrated a much greater ability to uptake Ag(I) ions with 95 % removed from the solution after 20 h while CMP_1 showed only a 50 % decrease in concentration after the same duration of time. While many of the other metal ions remained unchanged in concentration, it should be noted that both Cu(II) and Pb(II) concentrations showed a significant decrease over this time. As silver is a transition metal which is generally found in natural environments mixed with other metal ores such as copper, nickel, zinc, and lead, separation of the Ag(I) species from a mixture is of great industrial importance [5.15].

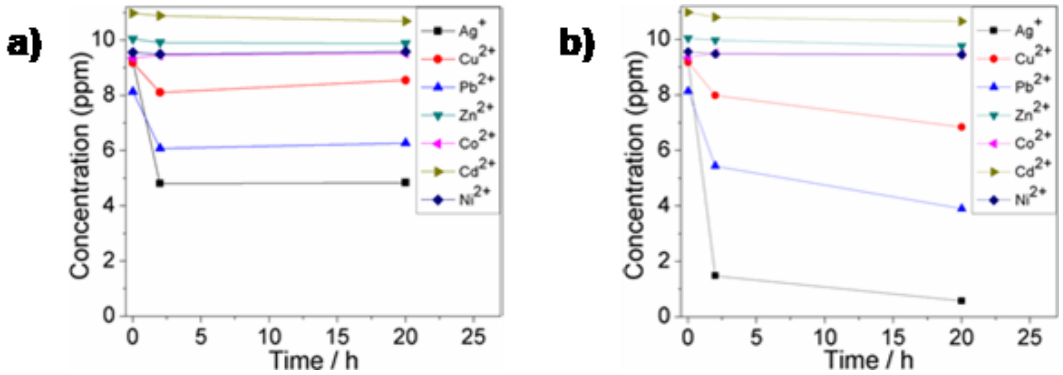

Figure 5.3 Uptake of metal ions from an aqueous solution after 20 h with (a) CMP_1 and (b) CMP_S.

To better understand the uptake of Ag(I) to the polymers, both CMP_1 and CMP_S polymers were mixed with an aqueous solution containing excess $AgNO_3$. After mixing and heating at 80 °C for 1 day, both polymers were washed thoroughly to remove unbound metal salts. Analysis *via* EDX and ICP-MS indicated a substantial difference in Ag(I) content with CMP_S at 8.75 % and CMP_1 at 5.8 %. These result shows that while not fully selective, the presence of the sulphur moiety in CMP_S greatly enhances the chelation properties of the monolithic polymer.

5.4.4 Heterogeneous Silver-Catalysed Heterocyclisation of 4-Pentynoic Acid

As CMP_S showed excellent affinity for the uptake of Ag(I), we chose to investigate silver-catalysed heterocyclic reactions due to their importance in the literature [5.16]. Although the cyclisation of alkynols and acetylenic acids have been reported using silver salts [5.17, 5.18], this type of homogeneous catalyst requires the careful removal of metal ions from the reaction mixture. By chelating the metal catalysts to an insoluble framework, in this case the Ag(I) loaded CMP_S_Ag, the same reaction can be performed with a heterogeneous catalyst whereby a simple filtration is required to remove the metal-loaded polymer.

The catalytic activity of the silver-loaded monolith was examined by heating a mixture of 4-pentynoic acid and CMP_S_Ag in $CDCl_3$ (Scheme 5.3). After 5 hours, full conversion to 5-methylenedihydrofuran-2(3*H*)-one was observed *via* ^{1}H NMR spectroscopy. The same reaction performed with $AgNO_3$ showed very poor conversions, even after extended reaction times (24 h). As CMP_S_Ag can be easily recovered and washed, the same polymer sample was reused over 5 cycles where no loss in catalytic

activity was observed. Furthermore, the silver content found in CMP_S_Ag did not change over the 5 cycles, indicating a highly stable and reusable heterogeneous silver catalyst.

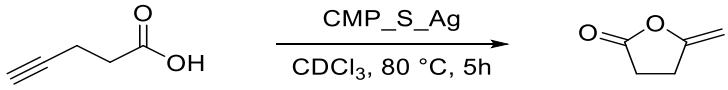

Scheme 5.3 Cyclisation of 4-pentynoic acid *via* the CMP_S_Ag heterogeneous catalyst.

5.5 Conclusion

Through the facile approach presented, we have demonstrated a unique method for both the morphological control and post-synthetic modification of a CPP. Morphological control allowed the formation of a monolithic solid CPP while an efficient post-synthetic modification technique proved useful for adding a sulphur group to create a functionalized CPP. Furthermore, exploitation of the functional sulphur moiety allowed for selective Ag(I) uptake and subsequent use as a heterogeneous silver catalyst for the heterocyclisation of 4-pentynoic acid. This work only begins to explore the potential of CPPs and has helped create new avenues of research into their form, function and application.

5.6 Impact on Literature and Research

This research has continued to provide new possibilities for CPPs regarding both morphological control and post-synthetic modification techniques. Furthermore, applications exploring immobilised metal-based catalysis offer green and sustainable alternatives to traditional homogeneous catalytic materials. To date, this paper has been cited 12 times, denoting the impact and continued interest in this field. By demonstrating the ability to form a solid mass rather than a loose powder, the use of CPPs under immobilised conditions becomes an interesting avenue of research. Employing the silver-loaded monolith under continuous flow conditions becomes more attractive as the target molecule can be synthesised effortlessly without the need to separate the catalyst from reaction mixture.

Although post-synthetic modification of CPPs has been demonstrated in a similar fashion to that described above, it does not diminish the impact of this work. While past work has utilised the sulphur functionality to generate a water-compatible CPP [5.8], more recent studies have used a CPP post-synthetically modified with a *N*-acetylcysteine moiety (Scheme 5.4) for the separation of uranium from radioactive waste sources [5.19]. Through the single concept of a thiol-yne reaction, we have seen multiple ways in which the structure of the thiol can be altered for an end application. It can be envisaged that the methodologies used for the synthesis and modification of CMP_1 may be explored further for applications such as wastewater treatment or heterogeneous catalysis.

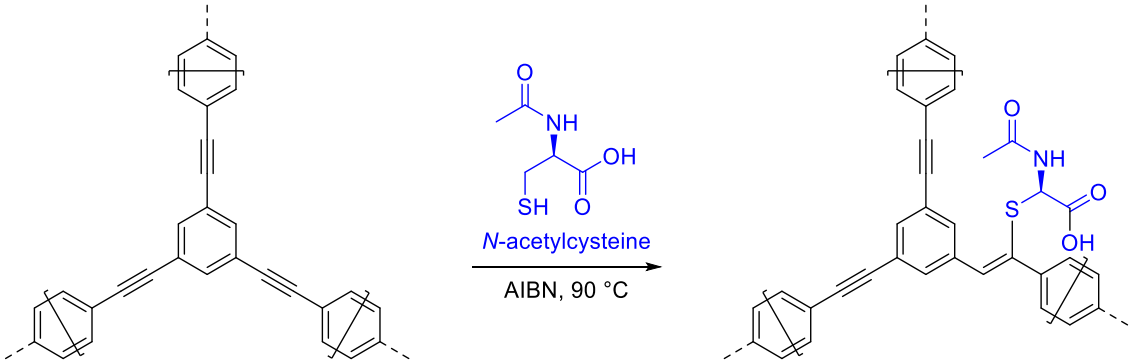

Scheme 5.4 Post-synthetic modification of a CPP through the addition of *N*-acetylcysteine to an alkyne using thiol-yne chemistry [5.19].

5.7 References

[5.1] R. Dawson, A. Laybourn, R. Clowes, Y. Z Khimyak, D. J. Adams, A. I. Cooper, *Microporous Poly(tri(4-ethynylphenyl)amine) Networks: Synthesis, Properties, and Atomistic Simulation*, Macromolecules, **42**, 8809-8816 (2009)

[5.2] D. Cortizo-Lacalle, C. T. Howells, S. Gambino, F. Vilela, Z. Vobecka, N. J. Findlay, A. R. Inigo, S. A. J. Thomson, P. J. Skabara, I. D. W. Samuel, *BODIPY-based conjugated polymers for broadband light sensing and harvesting applications*, J. Mater. Chem., **22**, 14119-14126 (2012)

[5.3] K. Zhang, B. Tieke, J. C. Forgie, F. Vilela, P. J. Skabara, *Donor–Acceptor Conjugated Polymers Based on p- and o-Benzodifuranone and Thiophene Derivatives: Electrochemical Preparation and Optical and Electronic Properties*, Macromolecules, **45**, 743-750 (2012)

[5.4] K. Zhang, Z. Vobecka, K. Tauer, M. Antonietti, F. Vilela, *π-Conjugated polyHIPEs as highly efficient and reusable heterogeneous photosensitizers*, Chem. Commun., **49**, 11158-11160 (2013)

[5.5] R. Du, N. Zhang, H. Xu, N. Mao, W. Duan, J. Wang, Q. Zhao, Z. Liu, J. Zhang, *CMP Aerogels: Ultrahigh-Surface-Area Carbon-Based Monolithic Materials with Superb Sorption Performance*, Adv. Mater., **26**, 8053-8058 (2014)

[5.6] G. Cheng, T. Hasell, A. Trewin, D. J. Adams, A. I. Cooper, *Soluble conjugated microporous polymers*, Angew. Chem., Int. Ed., **51**, 12727-12731 (2012)

[5.7] B. C. Ma, S. Ghasimi, K. Landfester, F. Vilela, K. A. I. Zhang, *Conjugated microporous polymer nanoparticles with enhanced dispersibility and water compatibility for photocatalytic applications*, J. Mater. Chem. A, **3**, 16064-16071 (2015)

[5.8] H. Urakami, K. Zhang, F. Vilela, *Modification of conjugated microporous poly-benzothiadiazole for photosensitized singlet oxygen generation in water*, Chem. Commun., **49**, 2353-2355 (2013)

[5.9] B. Kiskan, J. Weber, *Versatile Postmodification of Conjugated Microporous Polymers Using Thiol-yne Chemistry*, ACS Macro Lett., **1**, 37-40 (2012)

[5.10] J.-X. Jiang, C. Wang, A. Laybourn, T. Hasell, R. Clowes, Y. Z. Kimyak, J. Xiao, S. J. Higgins, D. J. Adams, A. I. Cooper, *Metal–Organic Conjugated Microporous Polymers*, Angew. Chem., Int. Ed., **50**, 1072-1075 (2011)

[5.11] B. Liang, M. Dai, J. Chen, Z. Yang, *Copper-Free Sonogashira Coupling Reaction with $PdCl_2$ in Water under Aerobic Conditions*, J. Org. Chem., **70**, 391-393 (2005)

[5.12] Y. Xu, S. Jin, H. Xu, A. Nagai, D. Jiang, *Conjugated microporous polymers: design, synthesis and application*, Chem. Soc. Rev., **42**, 8012-8031 (2013)

[5.13] X. Feng, Y. Liang, L. Zhi, A. Thomas, D. Wu, I. Lieberwirth, U. Kolb, K. Mullen, *Synthesis of Microporous Carbon Nanofibers and Nanotubes from Conjugated Polymer Network and Evaluation in Electrochemical Capacitor*, Adv. Funct. Mater., **19**, 2125-2129 (2009)

[5.14] J. Chun, J. H. Park, J. Kim, S. M. Lee, H. J. Kim, S. U. Son, *Tubular-Shape Evolution of Microporous Organic Networks*, Chem. Mater., **24**, 3458-3463 (2012)

[5.15] W. Lee, C. Kim, J. Yi, *Selective recovery of silver ions from aqueous solutions using modified silica beads with Adogen 364*, J. Chem. Technol. Biotechnol., **77**, 1255-1261 (2002)

[5.16] J.-M. Weibel, A. Blanc, P. Pale, *Ag-Mediated Reactions: Coupling and Heterocyclization Reactions,* Chem. Rev., **108**, 3149-3173 (2008)

[5.17] P. Pale, J. Chuche, *Silver-Catalyzed Cyclization of Acetylenic Alcohols: Synthesis of Functionalized 2-Methylene-oxolanes*, Eur. J. Org. Chem., **6**, 1019-1025 (2000)

[5.18] V. Dalla, P. Pale, *Silver-catalyzed cyclization of acetylenic alcohols and acids: a remarkable accelerating effect of a propargylic C–O bond*, New J. Chem., **23**, 803-805 (1999)

[5.19] X. Han, M. Xu, S. Yang, J. Qian, D. Hua, *Acetylcysteine-functionalized microporous conjugated polymers for potential separation of uranium from radioactive effluents*, J. Mater. Chem. A, **5**, 5123-5128 (2017)

DECLARATION

As secondary author of this publication, I can confirm a significant portion of the work to be my own. Work carried out by other students or collaborators has been outlined above.

Signature: _____

PUBLICATION 5

Facile synthesis of a conjugated microporous polymeric monolith *via* copper-free Sonogashira-Hagihara cross-coupling in water under aerobic conditions

J. Liu, J. M. Tobin, Z. Xu, F. Vilela

DOI: 10.1039/c5py00772k

Polym. Chem., **2015**, *6*, 7251-7255

Abstract

A conjugated microporous polymer was synthesized via a modified Sonogashira–Hagihara cross-coupling reaction under aerobic conditions in water and in the absence of copper. These conditions allowed the directing of the CMP format during synthesis into a monolithic structure. Post-modification of the polymer with thiol–yne chemistry followed by Ag(I) uptake led to a catalytically active material for a heterocyclization reaction.

Introduction

Development of conjugated microporous polymers (CMPs), as first described by Andrew Cooper *et al*. [1], has attracted interest in the search for materials for energy storage and conversion [2]. These extended π–π conjugated materials are known to demonstrate properties such as photoactivity, insolubility, high surface area and microporosity. Given these properties, applications such as heterogeneous (photo)catalysis [3, 4], gas storage and separation [5], and light harvesting [6] have been recently explored. Functionality within the monomers implemented in a CMP is a key component with regard to most of these specific applications since it allows for both electronic and morphological control of the CMP [7].

Along with the chemical design of CMPs, there is scope for improvement with regard to the difficult post-reaction processability resulting from their generally poor solubilities. Several synthetic strategies have been explored to help forge the product format during synthesis of these CMPs. These include electropolymerization (thin films) [8], emulsion polymerization (monoliths) [9], aerogels [10] and even soluble materials [11]. However, these strategies are still under-explored with a large scope for further development.

The ability to tailor CMPs into different physical forms, along with the functional flexibility of the monomers, underpins the rich potential that CMPs offer for catalysis and many other applications. Homogeneous catalysis is used widely in commercial and industrial applications, as well as under smaller laboratory conditions [12]. However, implementation of heterogeneous catalysis in place of its homogeneous counterpart has added benefits, especially within industrial settings. These include easy recovery and reusability of the catalyst, and application in continuous flow processes, which minimizes time and the cost of the overall catalytic reaction and potentially increases productivity. There is therefore a need to develop, in a sustainable fashion, catalytically active materials in different forms and formats.

CMPs are mainly synthesized using palladium-mediated Suzuki–Miyaura and Sonogashira–Hagihara cross-coupling reactions [2]. Both of these methodologies provide different levels of control in designing a material. Suzuki–Miyaura has proven

to be compatible with emulsion polymerization [9], whereas Sonogashira–Hagihara allows for easy post-modification of CMPs at the alkyne moiety [13].

While a major characteristic of CMPs is their metal-free composition, post-synthetic strategies allow for the addition of functional groups, including metals [14]. Judicious post-modification strategies also allow access to further applications such as sorption of specific metal ions, which in turn can potentially enhance the CMP material performance in heterogeneous (photo)catalysis.

Herein a versatile synthetic strategy in the development CMPs is described via a copper-free Sonogashira–Hagihara cross-coupling reaction in water under aerobic conditions [15]. These conditions provide a more sustainable route for the facile synthesis of monolithic CMPs. Further post-modification of the monolith using thiol–yne chemistry gives rise to a material with selectivity to silver ions. Finally, the silver-rich CMP is shown to have enhanced catalytic activity and reusability.

Facile Synthesis

Given the flexible reaction conditions we chose to carry out the polymerisation for 24 h at 85 °C in a 7.5 mL vial without any form of stirring or agitation. The monomer building blocks chosen are commercially available: 1,3,5-tribromobenzene (TBB) and 1,4-diethynylbenzene (DEB). This methodology led to the formation of a brown material with a cylindrical monolithic structure shaped by the reaction vessel (Scheme 1, Fig. 1). As expected, the monolithic CMP_1 is insoluble in all conventional solvents investigated ($CHCl_3$, CH_2Cl_2, THF, MeCN, EtOH, MeOH, H_2O and acetone).

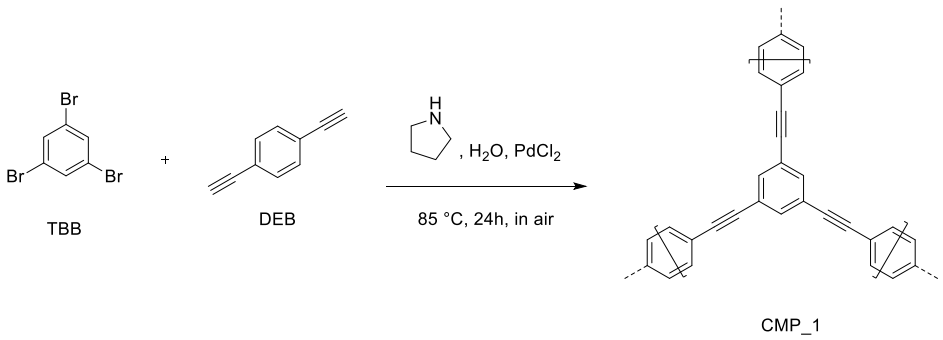

Scheme 1 Synthetic scheme for the conjugated microporous polymer monolith (CMP_1).

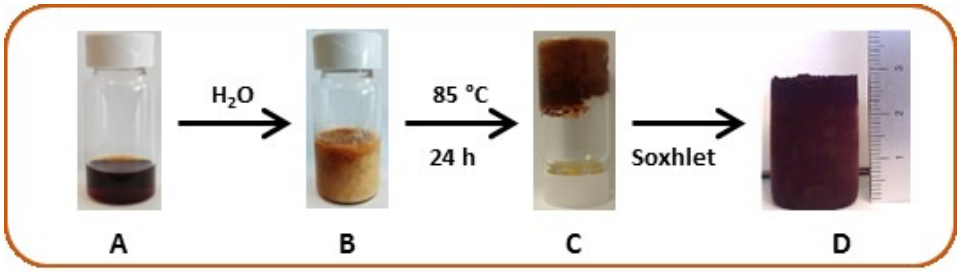

Fig. 1 Synthetic evolution of CMP_1: (a) TBB, DEB and $PdCl_2$ dissolved in pyrrolidine; (b) addition of water and subsequent precipitate formation; (c) solidification of monolith after heating; (d) purified and dried monolithic CMP_1.

The polymer was characterised by solid-state ^{13}C-NMR, thermogravimetric analysis (TGA), FTIR spectroscopy, SEM imaging, Raman spectroscopy, CO_2 gas sorption and energy dispersive X-ray spectroscopy (EDX). TGA (Fig. S2) of the monolithic polymer reveals no weight loss up to 250 °C, indicative of the non-volatile polymeric nature of the product. In the FTIR spectra (Fig. S9), C–H stretching mode (terminal alkynes) from the starting material (1,4-diethynylbenzene) at 3263 cm^{-1} is absent in the resulting CMP; the typical C≡C stretching mode at about 2200 cm^{-1} can be observed both in FTIR and Raman spectra (Fig. S9).

The monolithic polymer sample exhibits no significant N_2 sorption at 77 K. Nevertheless, at 273 K, CO_2 sorption does take place (pressure range: from 8×10^{-3} to 780 mmHg) with reproducible isotherms indicating a BET surface area of 374 m^2 g^{-1}. Such different sorption behaviour towards N_2 and CO_2 is often seen in porous polymers, wherein the pores blocked at 77 K become more accessible (e.g., to CO_2 gas) at higher temperatures due to stronger thermal motions [16]. DFT analysis (fitting error, 0.055%) on pore size distribution and pore volume (Fig. S5) of the CO_2 adsorption isotherms indicates an average pore width of 0.48 nm and a micropore volume of 0.113 cm^3 g^{-1}. EDX (Fig. S3) shows that there is still a small amount of bromine in CMP_1, indicating potential unreacted sites of the TBB monomer. Solid state ^{13}C-NMR (Fig. S1) shows the aromatic nature of the material and the presence of the alkyne groups, which can be used for the postmodification of CMP_1, as we have previously demonstrated.

Scanning electron microscopy (Fig. S6) reveals in detail the microstructure of the polymer network. CMP_1 is primarily composed of hollow fibres with diameters in the range of a few hundreds of nanometers. The formation of these tubular shapes is most

likely induced via the cross-coupling reaction and directed by a self-assembly mechanism of the aromatic building-blocks during synthesis. Although this phenomenon is not new, there are only a few reports describing the formation of tubular-shaped nanofibers of conjugated networks, with very little details on their mechanism of formation [17].

Post-modification of the Monolithic CMP_1

Thiol–yne chemistry was employed for the post-modification of CMP_1 as it generally results in a high yielding reaction under both homogeneous (Scheme S1) and heterogeneous conditions [13]. Furthermore, with the introduction of a sulfur moiety, when using this strategy, arises the possibility of metal chelation for different applications.

As shown in Scheme 2, the addition of sulfur methyl (–SCH3) to alkyne groups was performed on a monolithic polymer by simply treating the insoluble solid with sodium methanethiolate in DMF under a N_2 atmosphere.

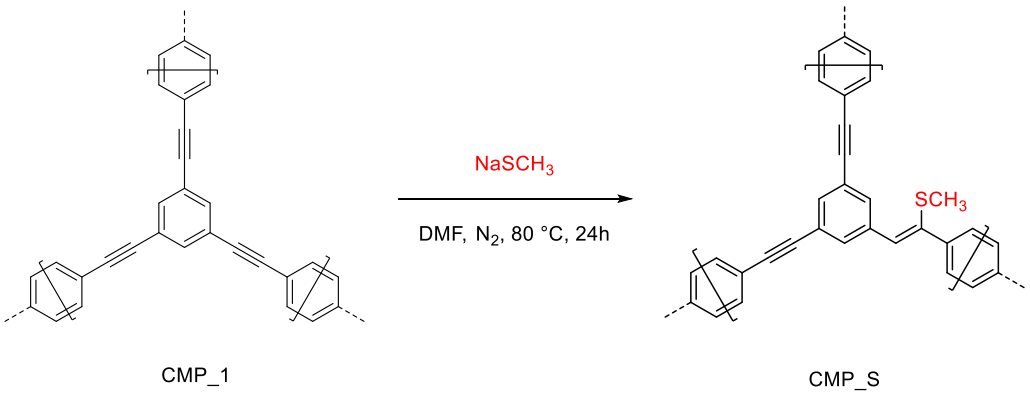

Scheme 2 Post-modification of CMP_1 monolith using a thiol–yne reaction to produce CMP_S.

The typical C≡C stretching mode at about 2200 cm^{-1} of CMP_S is largely diminished in both the FTIR and Raman spectra (Figure S9) when compared to the original CMP_1. Solid state ^{13}C-NMR (Figure S7) also confirms the reduction of the alkyne signal, indicating that the thiol-yne reaction was successful. Furthermore, this post-modification strategy is confirmed by EDX (Figure S8) where sulfur can be readily seen.

Selective Ag(I) Uptake

Silver as a precious metal often occurs naturally in mineral forms together with ores of copper, nickel, zinc and lead. Separation of Ag(I) from these base metal species is of great industrial importance [18]. With a view to assess the chelating ability of the sulfur rich CMP_S, we applied this material in the separation of different metal ions in solution. The concentration of each of the metal ions was set at 10 ppm (Tables S1 and S2) by dissolving $AgNO_3$ and the following: $Cu(NO_3)_2 \cdot 3H_2O$, $Zn(NO_3)_2) \cdot 6H_2O$, $Co(NO_3)_2 \cdot 2H_2O$, $Cd(NO_3)_2 \cdot 4H_2O$, $Ni(NO_3)_2 \cdot 6H_2O$, $Pb(NO_3)_2$ in water. CMP_S (10 mg, 0.03 mmol of the desired repeat unit) was placed in 10 mL of the above solution, which contains about 0.1 mg (9.2×10^{-4} mmol) Ag^+ and a total of 8.4×10^{-3} mmol of metal ions. The mixture was then stirred in the absence of light and sampled at different times (0 h, 2 h and 20 h) in order to monitor the concentrations of the metal species present in the solution. As a control experiment, the original monolithic CMP_1 was also tested under similar conditions (see ESI for details).

Fig. 2 shows for both CMPs that within the first 2 hours, Ag(I) ions rapidly decrease in concentration, whereas concentrations of the other ions present remained the same, with the exception of Cu(II) and Pb(II). By the 20th hour, 95% of Ag(I) ions in solution were removed by the CMP_S monolith (Fig. 2b), whilst more than 50% of the Ag(I) ions were still present in solution when using the control CMP_1 (Fig. 2a). These results show that the selectivity towards Ag(I) is largely enhanced by the sulfur present in CMP_S. Generally speaking, the strong selective binding of Ag(I) is possibly driven by the higher (less negative) Gibbs free energy of hydration for silver ions than other metal ions, as well as by the kinetics/liability of the coordination properties of Ag(I).

Effective Ag(I) Uptake

To quantify the effective Ag(I) uptake of CMP_S (40 mg, 0.13 mmol of the desired repeat unit), it was placed in an aqueous solution containing excess $AgNO_3$ (156 mg, 0.92 mmol) in 3 mL of water. After the mixture was stirred for 1 day at 80 °C in the absence of light, the resulting solid was separated by filtration and washed repeatedly with water (5 × 10 mL) to remove residual unbound Ag^+ salts. EDX (Fig. S10) showed the appearance of silver in the CMP_S_Ag sample, ICP indicated Ag content to be 8.75%.

This Ag(I) uptake demonstrated by this sulfur rich porous polymer is found to be substantial compared to CMP_1 (Ag content is about 5.8%), under the given conditions.

.

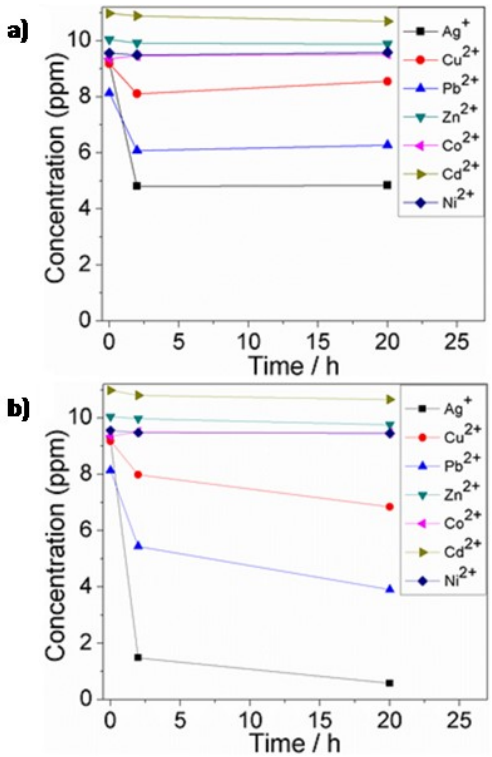

Fig. 2 Uptake of individual metal ions from a solution over a 20 h period using (a) CMP_1 and (b) CMP_S.

Heterogeneous Silver-catalysed Heterocyclization of 4-pentynoic acid

Silver-catalysed heterocyclization reactions have been widely investigated [19]. The cyclization of alkynols and acetylenic acids can be readily catalysed by silver salts as reported by Pale *et al*. [20]. The catalytic activity of the $AgNO_3$ treated CMP_S (CMP_S_Ag) was tested under normal conditions for the cyclization of 4-pentynoic acid by simply heating the reactants and CMP_S_Ag (Ag/substrate molar ratio: 5%) in $CDCl_3$ (Scheme 3).

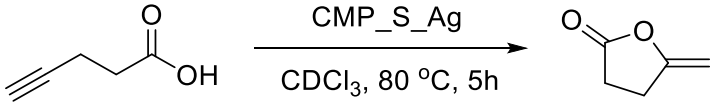

Scheme 3 CMP_S_Ag mediated cyclisation of 4-pentynoic acid.

It was found that 4-pentynoic acid can be readily converted to 5-methylenedihydrofuran-2(3H)-one in quantitative yield within 5 hours. The recyclability

of this CMP_S_Ag heterogeneous catalyst was tested over 5 cycles showing no loss in efficiency (Fig. 3) and the Ag content in the solids after the 5 catalytic cycles remained unchanged. The isolated supernatant exhibits no catalytic activity under similar reaction conditions (as verified by the NMR data in Fig. S11).

As a comparative study to highlight the effective catalytic activity of CMP_S_Ag, AgNO3 salt was employed under similar conditions (Ag/substrate molar ratio: 5%) for the cyclization of 4-pentynoic acid. Very low conversions were measured via ^{1}H-NMR, even after 24 hours (Fig. S12).

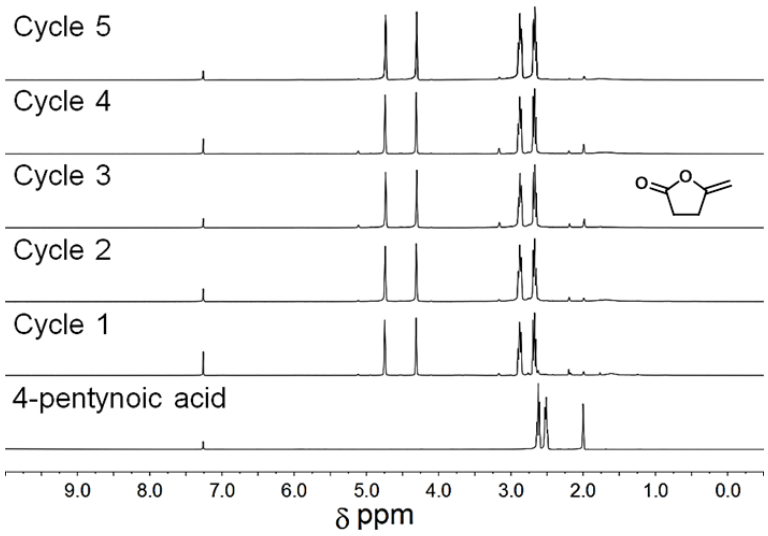

Fig. 3 ^{1}H NMR of 4-pentynoic acid and the converted 5-methylenedihydrofuran-2(3H)-one after 5 cycles using CMP_S_Ag as the catalyst.

Conclusions

Taken together, these exercises have opened new grounds in the research of CMPs—by means of a unique and broad combination that include the convenient synthesis of the monolithic polymer solid, and the efficient post-synthetic reaction between the thiolate guest and the phenylalkyne backbone in the polymer host. The substantial post-synthetic modification serves to highlight the structural robustness of the polymer backbone as well as its functional flexibility. Such flexibility is further exploited in the selective Ag(I) uptake that is enabled by the thioether donors thus installed, and in the effective, recyclable catalysis of the heterocyclization tests. The rich potential for further exploration is underpinned by the large array of phenylacetylene-based polymer

frameworks and by the wide variety of the incoming thiolate molecules (e.g., cysteine and cysteamine).

Synthesis of the Monolithic CMP_1 *via* Copper-free Sonogashira–Hagihara Cross-coupling

1,3,5-Tribromobenzene (157.5 mg, 0.50 mmol), 1,4-diethynylbenzene (95.0 mg, 0.75 mmol) and $PdCl_2$ (1.25 mg, 0.007 mmol) were dissolved in pyrrolidine (2.0 mL) with the aid of a sonication bath in a 7.5 mL sintering vial to get a clear dark brown solution. DI water (3.0 mL) was then added resulting in a milky suspension. The mixture was then sonicated for a further 2 minutes. The reaction mixture was heated at 85 °C in a heating block for 24 hours, after which a deep brown monolithic solid was formed. The monolith was washed with DI water and methanol for several times. The recovered material was calculated at 73.5%.

Acknowledgements

This work was supported by the Research Grants Council of HKSAR (GRF Project 11303414).

References

[1] J.-X. Jiang, F. Su, A. Trewin, C. D. Wood, N. L. Campbell, H. Niu, C. Dickinson, A. Y. Ganin, M. J. Rosseinsky, Y. Z. Khimyak and A. I. Cooper, *Angew. Chem., Int. Ed.,* 2007, **46**, 8574-8578.

[2] F. Vilela, K. Zhang and M. Antonietti, *Energy Environ. Sci.,* 2012, **5**, 7819-7832.

[3] J.-X. Jiang, Y. Li, X. Wu, J. Xiao, D. J. Adams and A. I. Cooper, *Macromolecules,* 2013, **46**, 8779-8783.

[4] K. Zhang, D. Kopetzki, P. H. Seeberger, M. Antonietti and F. Vilela, *Angew. Chem., Int. Ed.,* 2013, **52**, 1432-1436.

[5] X. Liu, S. A, Y. Zhang, X. Luo, H. Xia, H. Li and Y. Mu, *RSC Adv.,* 2014, **4**, 6447-6453.

[6] Y. Xu, S. Jin, H. Xu, A. Nagai and D. Jiang, *Chem. Soc. Rev.,* 2013, **42**, 8012-8031.

[7] *(a)* R. Dawson, A. Laybourn, R. Clowes, Y. Z. Khimyak, D. J. Adams and A. I. Cooper, *Macromolecules,* 2009, **42**, 8809-8816; *(b)* D. Cortizo-Lacalle, C. T. Howells, S. Gambino, F. Vilela, Z. Vobecka, N. J. Findlay, A. R. Inigo, S. A. J. Thomson, P. J. Skabara and I. D. W. Samuel, *J. Mater. Chem.,* 2012, **22**, 14119-14126; *(c)* K. Zhang, D. Kopetzki, P. Seeberger, M. Antonietti and F. Vilela, *Angew. Chem., Int. Ed.,* 2013, **52**, 1432-1436.

[8] K. Zhang, B. Tieke, J. C. Forgie, F. Vilela and P. J. Skabara, *Macromolecules,* 2012, **45**, 743-750.

[9] K. Zhang, Z. Vobecka, K. Tauer, M. Antonietti and F. Vilela, *Chem. Commun.,* 2013, **49**, 11158-11160.

[10] R. Du, N. Zhang, H. Xu, N. Mao, W. Duan, J. Wang, Q. Zhao, Z. Liu and J. Zhang, *Adv. Mater.,* 2014, **26**, 8053-8058.

[11] G. Cheng, T. Hasell, A. Trewin, D. J. Adams and A. I. Cooper, *Angew. Chem., Int. Ed.,* 2012, **51**, 12727-12731.

[12] *(a)* E. Alberico and M. Nielsen, *Chem. Commun.,* 2015, **51**, 6714-6725; *(b)* M. Aresta, A. Dibenedetto and A. Angelini, *Comprehensive Inorganic Chemistry (Second Ed.)*, Elsevier, Oxford, 2013, pp. 563-586; *(c)* C. Martin, G. Fiorani and A. W. Kleij, *ACS Catal.,* 2015, **5**, 1353-1370.

[13] *(a)* H. Urakami, K. Zhang and F. Vilela, *Chem. Commun.* **2013**, 49, 2353-2355; *(b)* B. Kiskan and J. Weber, *ACS Macro Lett*., 2012, *1*, 37–40.

[14] J-X. Jiang, C. Wang, A. Laybourn, T. Hasell, R. Clowes, Y. Z. Kimyak, J. Xiao, S. J. Higgins, D. J. Adams and A. I. Cooper, *Angew. Chem., Int. Ed.,* 2011, **50**, 1072-1075.

[15] B. Liang, M. Dai, J. Chen and Z. Yang, *J. Org. Chem.,* 2005, **70**, 391-393.

[16] *(a)* J. Liu, K.-K. Yee, K. K.-W. Lo, K. Y. Zhang, W.-P. To, C.-M. Che and Z. Xu, *J. Am. Chem. Soc*., 2014, **136**, 2818; *(b)* J. Jeromenok and J. Weber, *Langmuir*, 2013, **29**, 12982.

[17] *(a)* Kang, N. *et al*., *Angew. Chem., Int. Ed*., 2012, **51**, 6626-6630; *(b)* X. Feng, Y. Liang, L. Zhi, A. Thomas, D. Wu, I. Lieberwirth, U. Kolb and K. Mullen, *Adv. Funct. Matter.,* 2009, **19**, 2125-2129; *(c)* J. Chun, J. H. Park, J. Kim, S. M. Lee, H. J. Kim and S. U. Son, *Chem. Mater.,* 2012, **24**, 3458-3463.

[18] W. Lee, C. Kim and J. Yi, *J. Chem. Technol. Biotechnol.,* 2002, **77**, 1255-1261.

[19] J-M. Weibel, A. Blanc and P. Pale, *Chem. Rev.,* 2008, **108**, 3149-3173.

[20] *(a)* P. Pale and J. Chuche, *Euro. J. Org. Chem.,* 2000, **6**, 1019-1025; *(b)* V. Dalla, P. Pale, *New J. Chem.,* 1999, **23**, 803-805.

Supporting Information

Physical Measurements

FT-IR spectra were measured using a Nicolet Avatar 360 FT-IR spectrophotometer. **FT-Raman** spectra were obtained using a FT-IR, NIR-FT-Raman Perkin–Elmer Spectrum 2000 instrument equipped with a diode pumped Nd:YAG laser PSU and using the standard Spectrum v2.0 software. **Solution ^{1}H NMR** spectra were recorded on a 400 MHz Bruker superconducting-magnet high-field NMR spectrometer at room temperature, with tetramethylsilane (TMS) as the internal standard. **Thermogravimetric analyses** (TGA) were carried out in a nitrogen stream using PerkinElmer Thermal analysis equipment (STA 6000) with a heating rate of 5 °C/min, with an empty Al_2O_3 crucible being used as the reference. **Porosity and surface area analysis** was performed using a Quantachrome Autosorb iQ gas sorption analyzer. Each sample was outgassed at 0.03 torr with a 2 °C/min ramp to 100 °C and held at 100 °C for 12 hours. The sample was then held at vacuum until the analysis was run. Pore analysis was performed using CO_2 at 273 K (P range of 8×10^{-3} to 780 mmHg). The amounts of the metal ions were determined by using a PerkinElmer Optima™ 2100 DV **ICP optical emission spectrometer**. **Scanning Electron Microscope** (SEM) was carried out on Philips XL30 Esem-FEG, (FEI Company, the Netherlands) equipped with an **energy-dispersive x-ray microanalysis** (EDX) system (EDAX Phoenix system, EDAX Inc., Mahwah NJ, USA). **Solid State ^{13}C {1H} CP-MAS** measurements were carried out using a Bruker Avance 400 spectrometer operating at 100.6 MHz for ^{13}C using a Bruker 4 mm double resonance probe-head operating at a spinning rate of 10 kHz.

Experimental Section

Staring materials, reagents and solvents were purchased from commercial sources (pyrrolidine from Merck, palladium chloride from J&K and the others from Aldrich) and used without further purification.

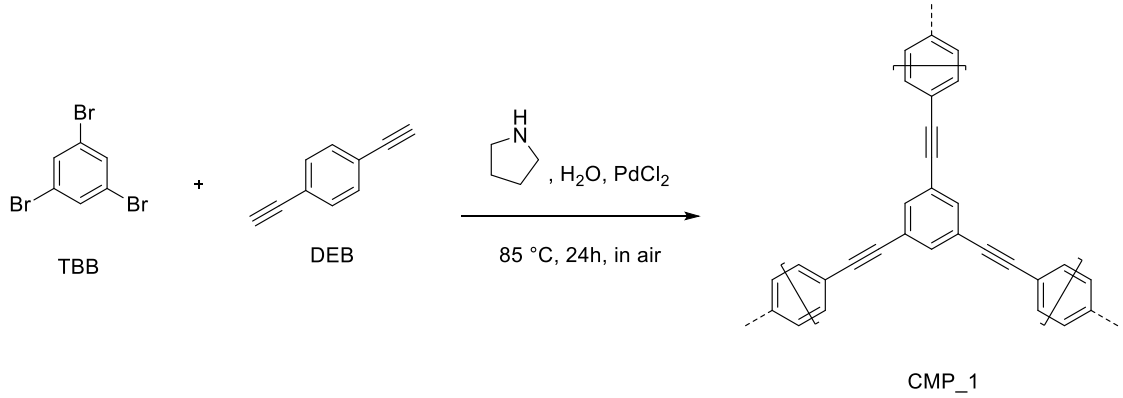

Scheme 1 Synthetic scheme for the CMP monolith (CMP_1).

Synthesis of the Monolithic Polymer (CMP_1)

1,3,5-Tribromobenzene (157.5 mg, 0.50 mmol), 1,4-diethynylbenzene (95.0 mg, 0.75 mmol) and $PdCl_2$ (1.25 mg, 0.007 mmol) were dissolved in pyrrolidine (2.0 mL) with the aid of a sonication bath in a 7.5 mL sintering vial to get a clear dark brown solution. DI water (3.0 mL) was then added (a large amount of precipitate was formed), and then the mixture was sonicated for about 2 minutes. The reaction mixture was heated at 85 °C in a heating block for 24 hours, and a deep brown monolithic solid was formed. The monolith was washed with deionised (DI) water and methanol for several times.

Purification of the Monolithic CMP_1

A thimble (e.g., made from folding filter paper) containing the monolithic polymer sample was loaded into the main chamber of a Soxhlet extractor. The Soxhlet extractor was connected onto a 250-mL round bottom flask containing methanol (150 mL), and then equipped with a condenser. The solvent is heated at 100 °C by an oil bath for 6 hours. Afterwards similar steps of extraction--lasting also 6 hours--were conducted by using tetrahydrofuran (150 ml) and acetone (150 mL) in lieu of the methanol. The filter paper was then taken out and the solid was dried in vacuum to give the purified monolithic CMP sample (97 mg, yield: 73.5%).

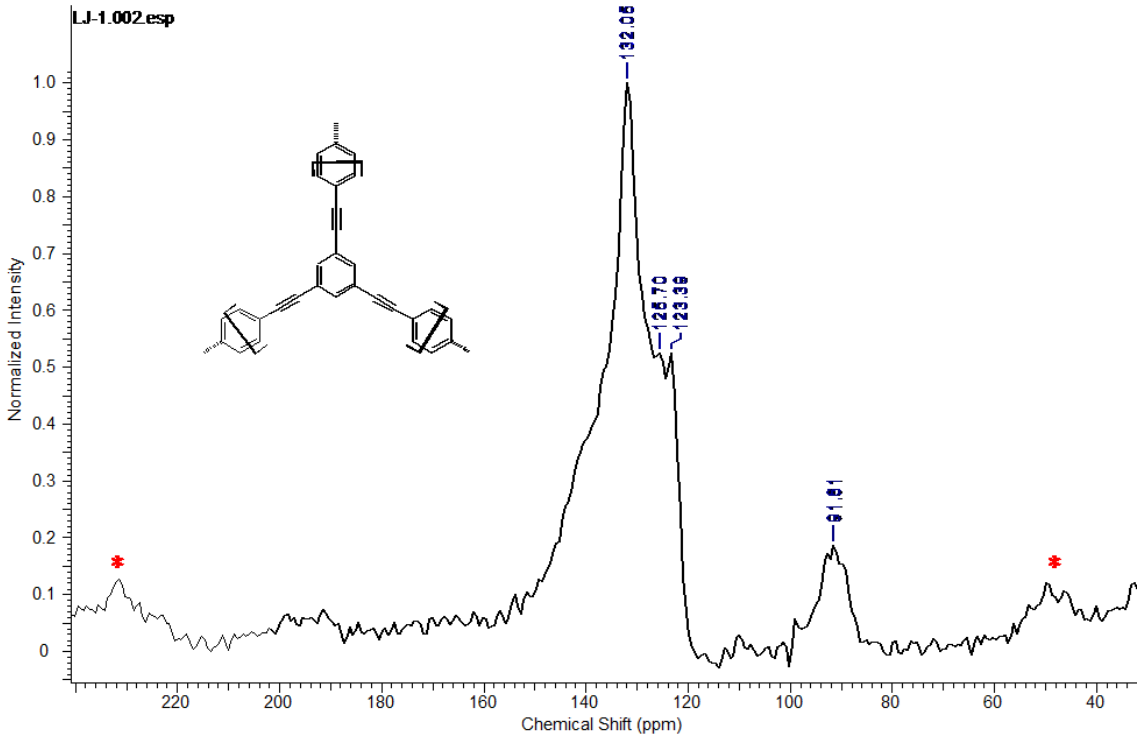

Figure S1 Solid state ^{13}C-NMR analysis of the monolithic CMP_1. Aromatic carbons can be seen in the δ 123-132 region while the alkyne singal can be seen at δ 91.61. Signals denoted by (*) indicate the presence of side bands.

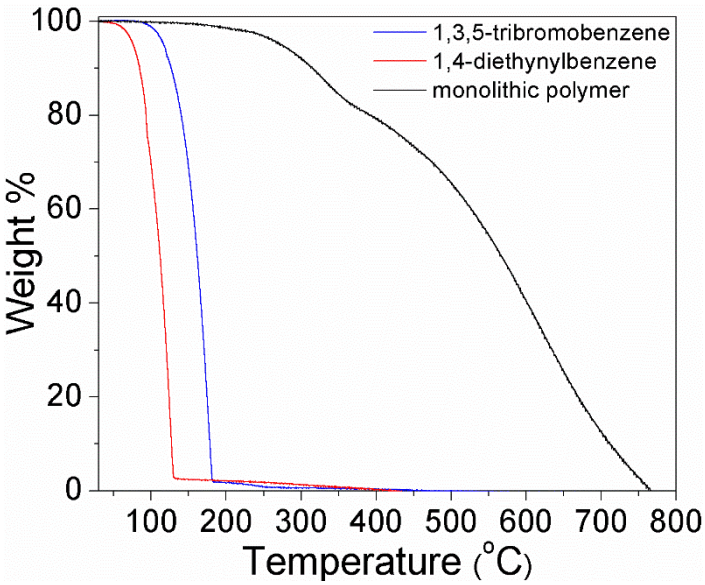

Figure S2 Thermogravimetric analysis (TGA) plots of 1,3,5-tribromobenzene (blue line), 1,4-diethynylbenzene (red line) and monolithic CMP_1 (black line).

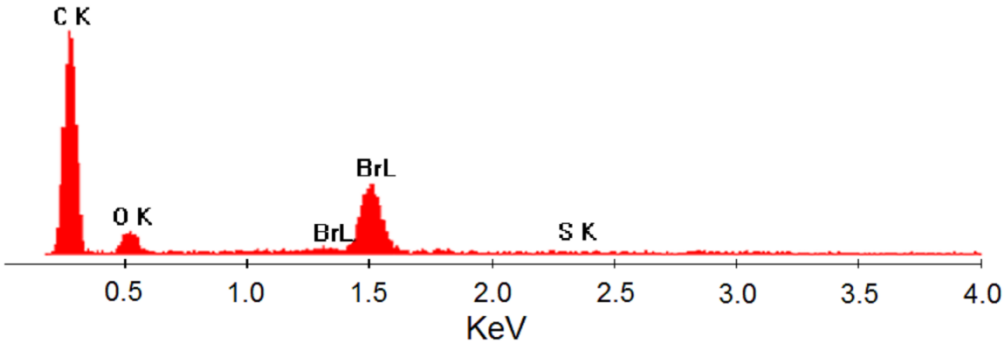

Figure S3 An energy-dispersive X-ray (EDX) spectrum of monolithic CMP_1 sample.

Gas Sorption

Pore analysis of the activated monolithic polymer sample was performed using CO_2 at 273 K (P range of 8×10^{-3} to 780 mmHg). Initial data analysis was done using the AS1Win and QuadraWin 5.05 software (both of Quantachrome instruments). NLDFT analysis (Pore Size Distribution and Pore Volume, Figure S4) of the CO_2 adsorption isotherm (273 K) was done using a commercialized model (CO_2 at 273 K on carbon; NLDFT model). The PSD and pore volume of CO_2 showed us an average pore width of 0.48 nm and a micropore volume of 0.113 cm^3/g.

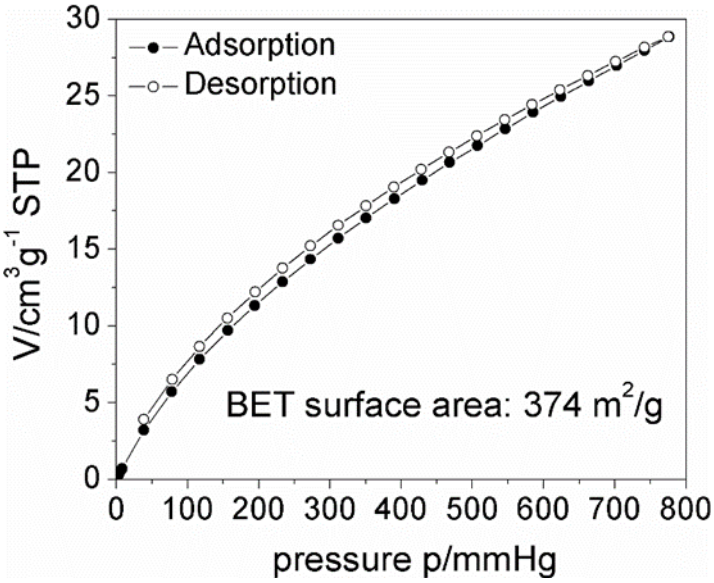

Figure S4 CO_2 sorption isotherm at 273 K for the monolithic CMP_1 (113.4 mg, activated by evacuating at 100 °C for 12 hours).

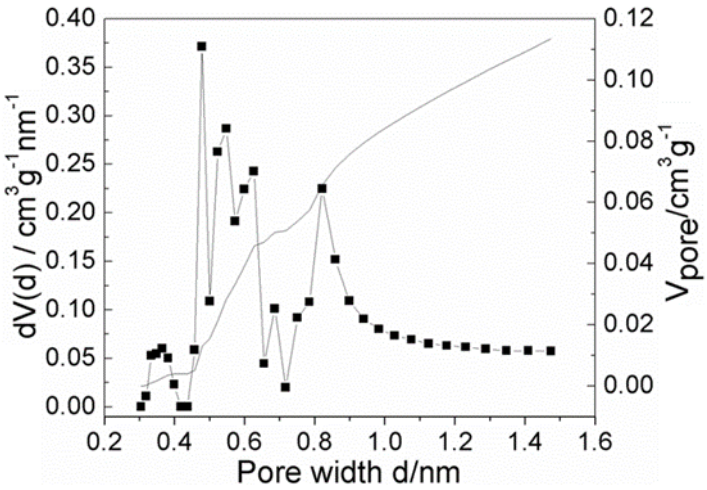

Figure S5 Pore size distribution and Pore volume of the monolithic CMP_1 (CO_2 gas at 273 K; NLDFT model).

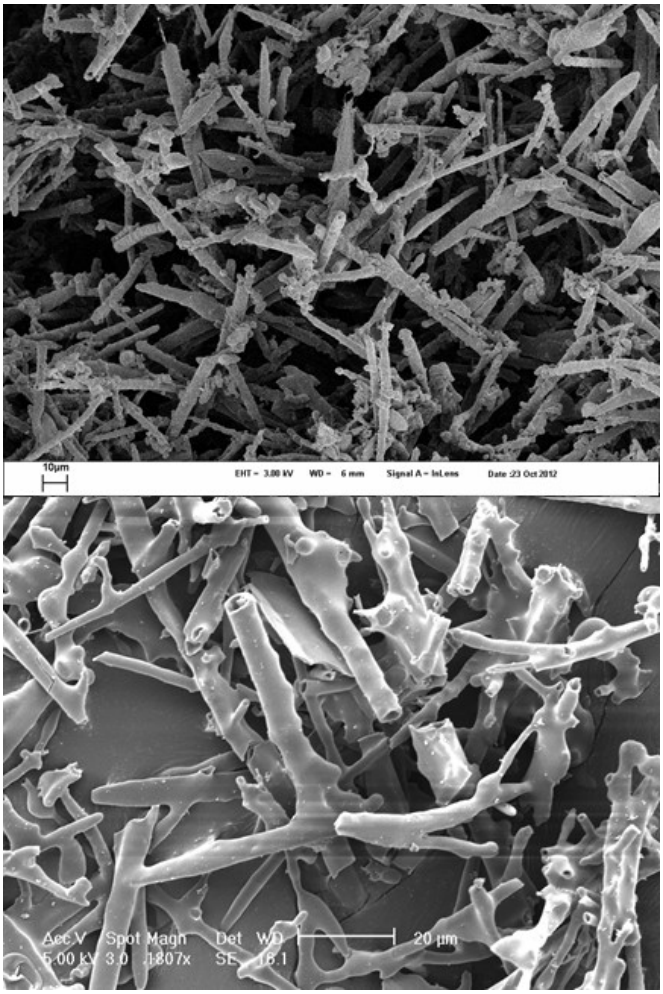

Figure S6 SEM imaging reveals that CMP_1 is primarily composed of hollow fibres with diameters in the range of a few hundred of nanometers.

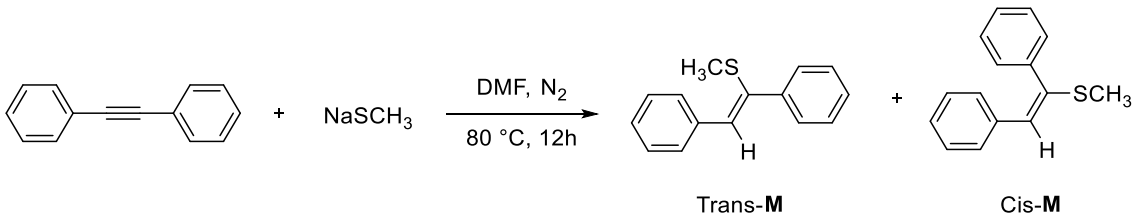

Scheme S1 Synthesis of homogeneous M molecule using a thiol-yne reaction.

Diphenylacetylene (100 mg, 0.56 mmol) and $NaSCH_3$ (94 mg, 1.34 mmol) were added into a 10-mL, two-neck, round-bottom flask equipped with a magnetic stirring bar. Dimethylformamide (5 mL), previously deaerated by N_2, was then transferred into the round-bottom flask. The flask was placed in an oil-bath, stirred and heated at 80 °C for 12 hours. Upon cooling to room temperature, 1% HCl was then slowly added into the reaction mixture with vigorous stirring. After the pH value of the mixture was lower than 2, the mixture was poured into DI water (15 mL) and extracted by ethyl acetate (2 x 10 mL). The combined organic layer was then washed by DI water (3 x 10 mL), dried over $MgSO_4$, evaporated *in vacuo*. The crude product (yellow oil) was further purified by a silica gel column (with CH_2Cl_2/hexane 1:10 as the eluent) to provide light yellow oil (118.4 mg, 0.26 mmol, yield: 93.2%). ^{1}H NMR (400 MHz, $CDCl_3$) *trans*-**M** δ 7.07-7.69 (m, 10H, aromatic), 6.77 (s, 1H, =CH), 1.98 (s, 3H, SCH_3); ^{1}H NMR (400 MHz, $CDCl_3$) *cis*-**M** δ 6.91-7.69 (m, 10H, aromatic) 6.51 (s, 1H, =CH), 2.25 (s, 3H, SCH_3).

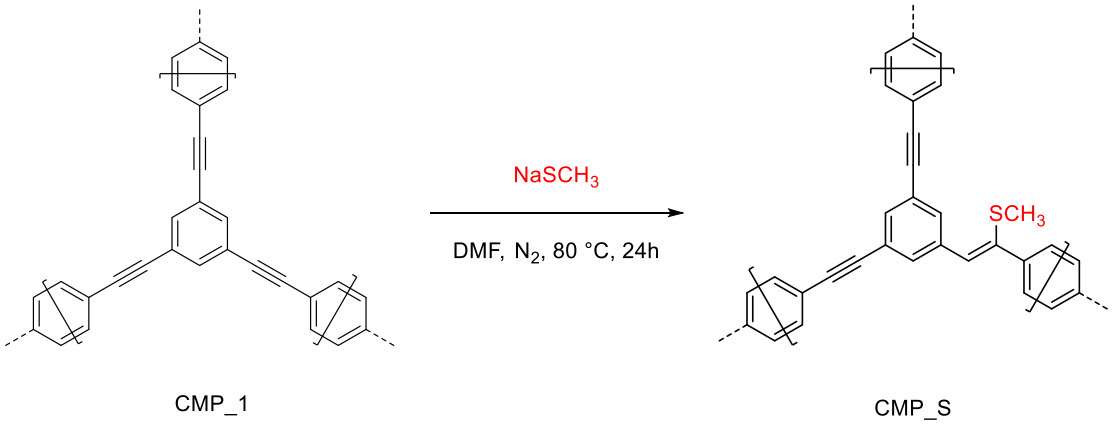

Scheme 2 Post-modification of the CMP_1 monolith using a thiol-yne reaction.

Typical Conditions for Modification of the Monolithic CMP_1 by $NaSCH_3$

The polymer (repeat unit~261.3 g/mol, 65 mg, ~ 0.75 mmol of alkyne) and $NaSCH_3$ (126 mg, 1.8 mmol) were added into a 25-mL, two-neck, round-bottom flask equipped with a

magnetic stirring bar. Dimethylformamide (10 mL), previously degassed by N_2, was then transferred into the round-bottom flask. The flask was placed in an oil-bath, stirred and heated at 80 °C for 24 hours. Upon cooling to room temperature, 1 % HCl was then slowly added into the reaction mixture with vigorous stirring. After the pH value of the mixture was lower than 2, the brownish-red solid was collected by suction filtration and washed with water (until pH=7), methanol (2x10 mL) and dichloromethane (2x10 mL). The CMP_S monolith was then dried under vacuum at room temperature for 24 hours.

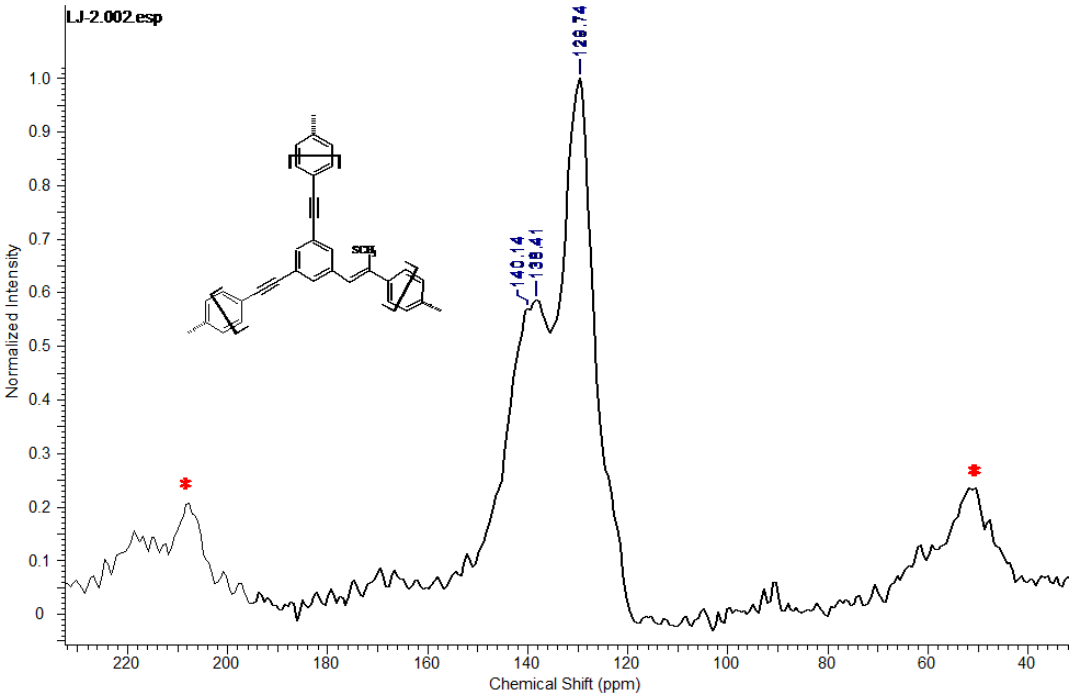

Figure S7 Solid state ^{13}C-NMR analysis of the monolithic CMP_S. Aromatic carbons can be seen in the δ 129-140 region while the alkyne peak has receded. Peaks denoted by (*) indicate the presence of side bands.

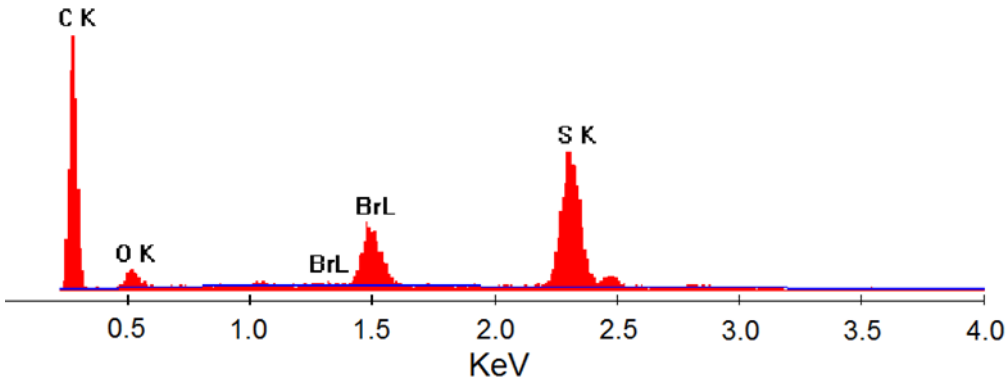

Figure S8 An energy-dispersive X-ray (EDX) spectrum of CMP_S sample.

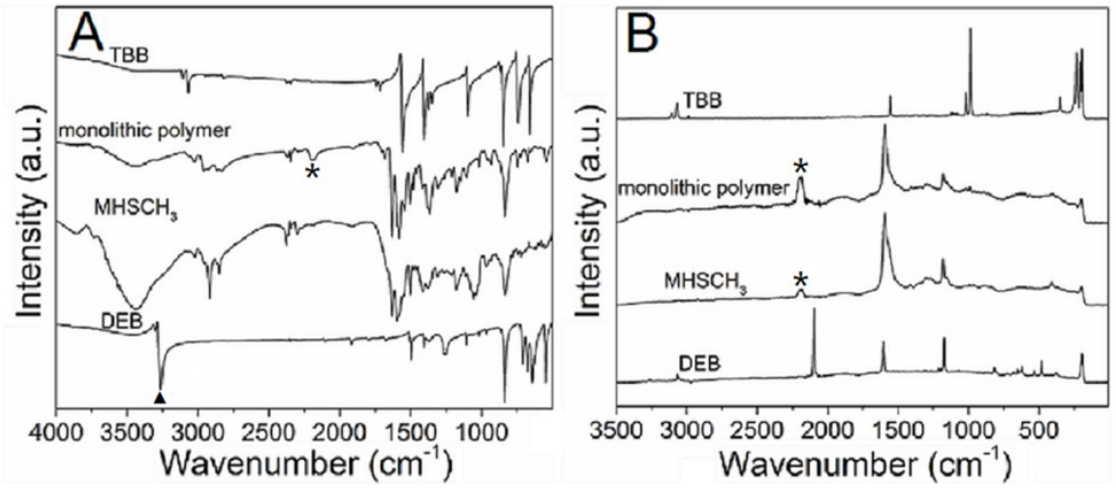

Figure S9 The IR (A) and Raman (B) spectra of 1,3,5-tribromobenzene (TBB), monolithic CMP_1, CMP_S and 1,4-diethynylbenzene (DEB). (▲: C-H stretching mode of terminal alkynes; stars: typical C≡C stretching mode).

Ag(I) Uptake by CMP_S

To probe the upper limit of Ag(I) uptake, the CMP_S solid (40 mg, 0.16 mmol of the desired repeat unit) was placed in an aqueous solution containing excess $AgNO_3$ (156 mg, 0.92 mmol) in 3 mL DI water. After the mixture was stirred for 1 day at 80 °C in the dark (with the vial wrapped by aluminum foil), the resultant solid was separated by filtration and washed repeatedly by DI water (5 x 10 mL) to remove residual unbound Ag(I) species and dried under vacuum for overnight. Ag(I) content of the $AgNO_3$ treated sample was then measured by ICP, which indicated that Ag content to be 8.75%.

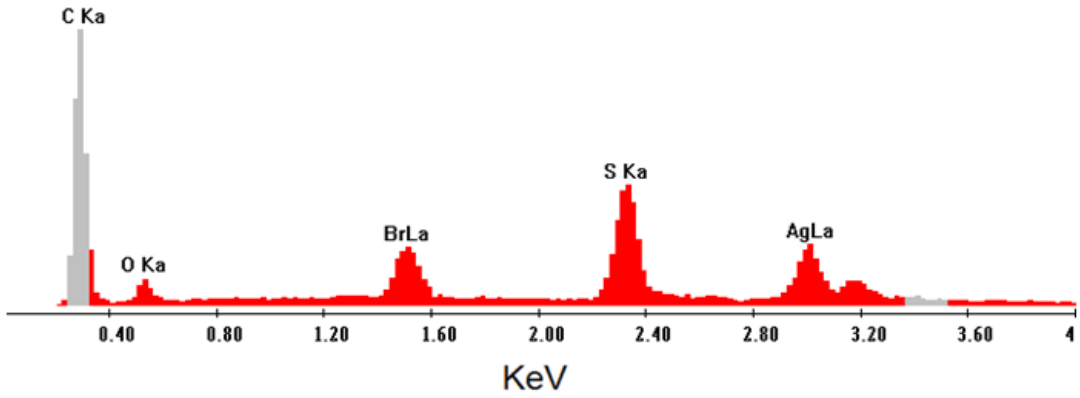

Figure S10 An energy-dispersive X-ray (EDX) spectrum of CMP_S_Ag sample.

Selective Ag(I) Uptake

Monolithic CMP_1 (10 mg, 0.04 mmol of the repeat unit) and CMP_S (10 mg, 0.16 mmol of the repeat unit) were separately added into two aqueous solutions (each was 10 mL) of a mixture of $AgNO_3$, $Pb(NO_3)_2$, $Cd(NO_3)_2{\cdot}4H_2O$, $Zn(NO_3)_2{\cdot}6H_2O$, $Cu(NO_3)_2{\cdot}3H_2O$, $Ni(NO_3)_2{\cdot}6H_2O$ and $Co(NO_3)_2{\cdot}2H_2O$, with the concentration each metal ion being set at about 10 ppm (see Table S1 and S2 for the specific figures). The mixtures were then stirred in the dark and small portions of the solution was taken out at different times (0h, 2h and 20 h) for determining the concentrations of the remaining metal species

Table S1 The concentrations (ppm) of the individual metal ions in a mixture solution at different hours after being mixed with monolithic CMP_1.

ions / time	Pb^{2+}	Cd^{2+}	Cu^{2+}	Ni^{2+}	Zn^{2+}	Co^{2+}	Ag^{+}
0 h	8.14	10.9	9.18	9.56	10.0	9.46	9.23
2 h	6.08	10.9	8.11	9.50	9.92	9.45	4.81
20 h	6.57	10.7	8.55	9.59	9.88	9.50	4.84

Table S2 The concentrations (ppm) of the individual metal ions in a mixture solution at different hours after being mixed with the monolithic CMP_S.

ions / time	Pb^{2+}	Cd^{2+}	Cu^{2+}	Ni^{2+}	Zn^{2+}	Co^{2+}	Ag^{+}
0 h	8.14	10.9	9.18	9.56	10.0	9.46	9.23
2 h	5.44	10.8	7.99	9.48	9.97	9.50	1.48
20 h	3.90	10.7	6.84	9.46	9.76	9.47	0.57

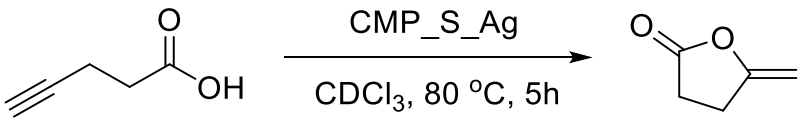

Scheme 3 CMP_S_Ag mediated cyclisation of 4-pentynoic acid.

Typical Conditions for Heterogeneous Catalytic Reactions (Synthesis of 5-methylenedihydrofuran-2(3H)-one) by $AgNO_3$ treated CMP_S (CMP_S_Ag)

4-Pentynoic acid (10 mg, 0.10 mmol) was dissolved in $CDCl_3$ (0.5 mL) in a 3.5 mL glass vial equipped with a magnetic stirring bar. CMP_S_Ag (6.2 mg, Ag/substrate molar ratio: 5%) was added into the mixture, the reaction mixture was then heated at 80 °C in a heating block with stirring. After 5 hours, the clear solution (obtained by centrifugation of the reaction mixture) was directly analyzed by ^{1}H NMR. The solid (catalyst) was used for at least another 4 cycles after washing by $CHCl_3$ and drying under vacuum. ^{1}H NMR (400 MHz, $CDCl_3$) δ 4.75 (s, 1H, =CH), 4.31 (s, 1H, =CH), 2.86-2.90 (t, 2H, CH), 2.65-2.67 (t, 2H, CH). ^{13}C NMR (100 MHz, $CDCl_3$) δ 175.09, 155.83, 88.94, 28.19, 25.27.

Catalytic Activity Test of the Reaction Supernatant

After the catalytic reaction was completed (monitored by ^{1}H NMR), the catalyst was removed by simple filtration. The supernatant was collected and a new batch of reactant (4-pentynoic acid) was added to the supernatant. 0.1 mL of this solution was added to 0.5 mL $CDCl_3$ for ^{1}H NMR measurement. The remaining solution was heated at 80°C for 5 hours. The mixture was cooled to room temperature and 0.1 mL of this solution was taken out and added to another 0.5 mL $CDCl_3$ for ^{1}H NMR measurement. The ratio between 5-methylenedihydrofuran-2(3H)-one and 4-pentynoic acid was unchanged after heating at 80°C for 5 hours, suggesting no catalytic activity for the isolated supernatant.

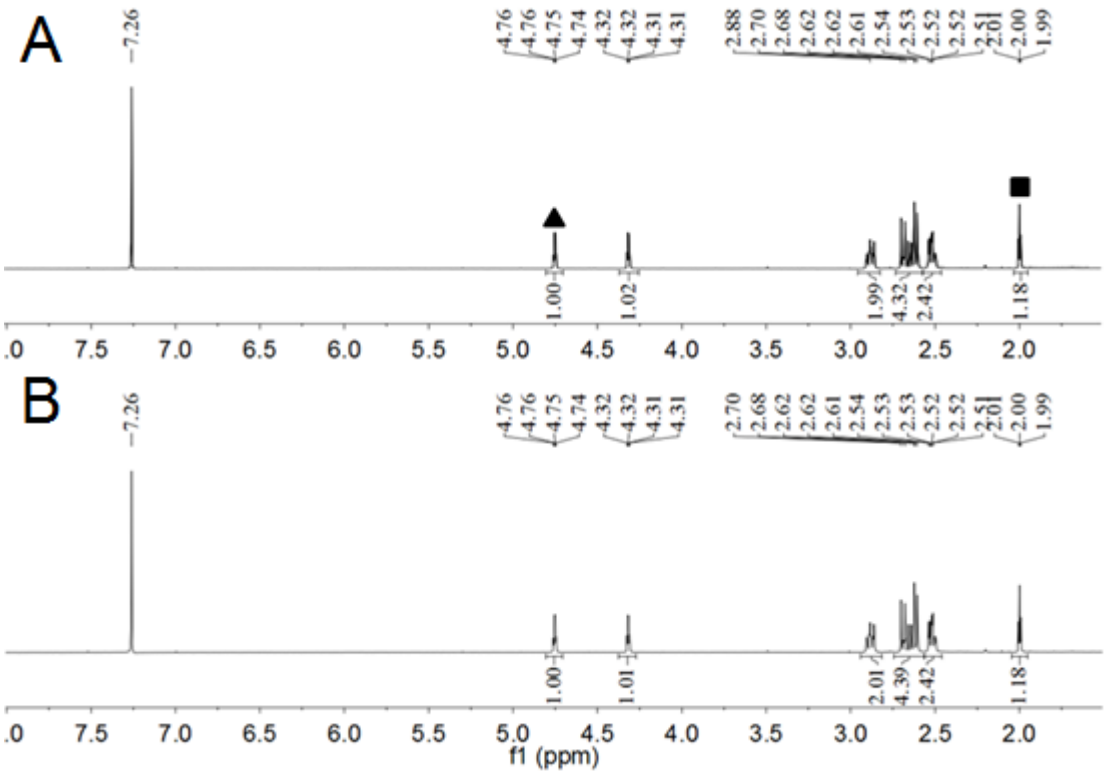

Figure S11 Solution ^{1}H NMR spectra of the reaction supernatant (a) before and (b) after stirring at 80°C for 5 hours. Characteristic peak labelling: ▲, 5 -methylenedihydrofuran-2(3H)-one; ■, 4-pentynoic acid.

Typical Condition for Heterogeneous Catalytic Reaction of 4-pentynoic acid by $AgNO_3$ salt

4-Pentynoic acid (10 mg, 0.10 mmol) was dissolved in $CDCl_3$ (0.5 mL) in a 3.5 mL glass vial equipped with a magnetic stirring bar. $AgNO_3$ salt (0.85 mg, Ag/substrate molar ratio: 5%) was added into the mixture, the reaction mixture was then heated at 80 °C in a heating block with stirring. After overnight reaction, the clear solution (obtained by centrifugation of the reaction mixture) was directly analyzed by ^{1}H NMR.

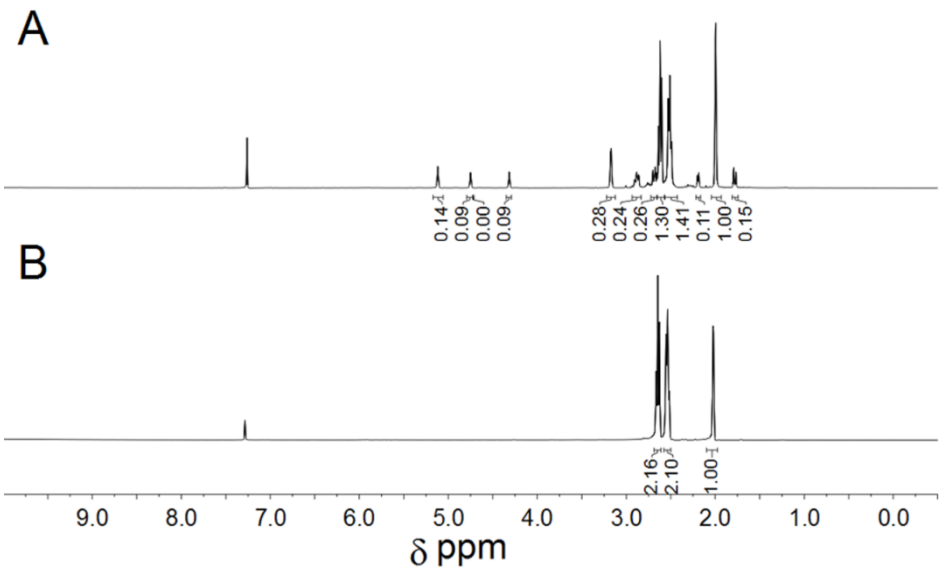

Figure S12 ^{1}H NMR of 4-pentynoic acid (B) and the clear reaction solution (A) after being stirried with $AgNO_3$ salt overnight.

CHAPTER 6: Conclusion and Future Work

This final chapter will summarise and conclude the work presented throughout this thesis. Furthermore, the potential for advancements in material design and applications moving forward will be discussed, including preliminary work as well as unexplored ideas.

6.1 Conclusions

The primary aim of this thesis was to develop novel polymeric materials for photocatalytic applications. This approach utilised monomers in an alternating strong electron acceptor/weak electron donor motif through which electronic control can be implemented. Furthermore, metal chelation and heterogeneous catalysis were also explored to exhibit the versatility of functionalisation and morphological form that can be found in CPPs.

A general introduction to photocatalysis and polymers was presented in Chapter 1. Conjugated porous polymers (CPPs) were described in more detail within this framework as a relatively new class of materials with intriguing properties such as high S_{BET} and light harvesting capabilities. Due to these properties, CPPs were examined further through a literature review for their employment as heterogeneous photocatalytic materials. While the literature presented a wide scope of materials and applications, the field is still in its infancy with considerable room for growth. This is particularly true for the development of new materials through metal-free synthetic procedures as we strive to explore more sustainable alternatives to the materials currently used for photocatalytic applications. Furthermore, electronic control of CPPs is also important as it allows for tailored absorbance values in the visible spectrum. This is a key concept as movement away from the need for highly energetic UV light has become more desirable, particularly when harnessing sunlight as a source of photons. We also surmised that while CPPs have shown excellent photocatalytic capabilities, there are instances where photocatalysis is either unfeasible or impractical. In this case, the use of metal-based catalysts combined with a CPP support structure can offer a practical solution by immobilising the metal species and allowing for facile recovery and reuse of the catalytic material.

Both metal-free synthesis and electronic control were explored in Chapter 2 through the development of two new BODIPY-based CPPs, building upon two of the key factors that were discussed for the progression of CPPs. The incorporation of BODIPY into the repeat unit of the conjugated polymers resulted in a bathochromic shift in absorbance (~530 nm) when compared to current photocatalytic materials. The polymers exhibited excellent photocatalytic capabilities, along with high photo and chemical stability, when employed as heterogeneous photosensitisers for $^1O_2$ production under continuous flow conditions. Moreover, the combination of metal-free synthesis and band gap tuning within a singular material (PHTT_BDP) offered a shining example for the future of CPPs as it did not negatively affect the ability of the CPP to act as a photocatalyst.

The concept of metal-free synthetic methodologies for the synthesis of CPPs was further expanded in the development of HOTT-HATN, as described in Chapter 3. Through a combination of alternating nitrogen and oxygen-rich monomers, electronic control resulted in a material with a broad absorption spectrum. This offered another example of a CPP synthesised in the absence of a metal catalyst showing excellent photocatalytic activity and stability through the photooxidation of benzylamines under continuous flow chemistry using broad spectrum white light ($\lambda > 400$ nm). Furthermore, the inclusion of bipyridyl groups in the polymer backbone allowed for its use as both a heterogeneous catalyst for Knoevenagel reactions and a chelating material for the removal of Pb from a water source. As a CPP, this degree of 'green' characteristics and scope of applications is unprecedented and introduces a potential avenue for the continued development of these materials.

In Chapter 4, the scope of material design shifted from fully conjugated polymers towards the more common polystyrene as a polymer support. Using the knowledge of CPP design, a well-known photoactive CPP repeat unit was synthesised (St-BTZ) as a crosslinker for use as a comonomer in the polymerisation of styrene. Due to the versatility of both St-BTZ and styrene, three different physical formats were synthesised using free radical polymerisation techniques: gels, beads, and a monolithic polyHIPE. Both the photoactive monomer and the subsequent polymers exhibited absorbance in the visible spectrum (400 – 450 nm). While the monomer degraded under photocatalytic conditions, the three polystyrene-based photosensitisers demonstrated excellent photocatalytic activity in the formation of reactive oxygen species ($^1O_2$ and $O_2^{\cdot -}$). Again, continuous

flow chemistry was employed in the case of the beads and polyHIPE where they showed enhanced performance and photo/chemical stability.

In the final chapter, we return to CPPs whilst moving away from photocatalysis. Here, the versatility of physical form and functionality possible in CPPs was addressed through the design and synthesis of a monolithic polymer. A facile Sonogashira-Hagihara cross-coupling reaction allowed for morphological control while available alkyne units in the polymer backbone provided a route for post-synthetic modification using thiol-yne chemistry. Utilising the sulphur moiety within the modified CPP, selective Ag^{I} uptake was conducted. The silver-loaded material was then used as a heterogeneous silver catalyst for the heterocyclisation of 4-pentynoic acid, hereby addressing the need for easily recoverable and reusable immobilised metal catalysts where photocatalytic methods are not appropriate.

The entirety of this thesis addresses the three main concepts regarding the scope of CPP development: *i*) optoelectronic control and consequent bathochromic shift in maxima wavelength absorbance; *ii*) metal-free synthesis; *iii*) immobilisation of metals for heterogeneous catalysis. Not only has this work increased our understanding of CPPs as photocatalytic materials, it shows their versatility and robust nature. Furthermore, the use of continuous flow chemistry in most studies illustrates a novel and efficient method for introducing CPPs into commercial or industrial settings. As CPPs continue to gain a foothold as sustainable and efficient photocatalytic materials, a complete understanding of their properties and catalytic mechanisms is imperative to fully realise their potential.

6.2 Future Work

Much of the work presented in this thesis offered qualitative measurements to demonstrate the photocatalytic activity (*i.e.* generation of $^{1}O_{2}$) of a given material. This is a very useful tool, particularly when investigating new photocatalytic mechanisms and reaction pathways. However, without quantitative measurements (*i.e.* photophysical properties and quantum yield measurements) it is difficult to compare separate materials without gauging their relative catalytic performance in a given reaction. While computational methodologies were presented in Chapter 4, further physical characterisation of the photocatalytic polymers presented is the next step forward in fully

understanding their capabilities. For example, transient-absorption spectroscopy and time-resolved fluorescence spectroscopy can be used to determine quantum yields and singlet/triplet state lifetimes [6.1, 6.2].

While the work presented demonstrates a degree of electronic control through alteration of the strong electron acceptor (SA), band gap manipulation continues to be an important factor in the design and synthesis of CPPs. Similar control can also be implemented by changing the weak electron donator (WD). Many CPPs in literature utilise benzene as a WD which is likely due to its stability and availability as a substituted aromatic compound [6.3, 6.4]. As a result, we have performed preliminary investigations into other hydrocarbon-based aromatic compounds as the WD monomer in CPPs. Using a known benzothiadiazole-benzene system for comparison (Ph-BTZ) [6.5], the benzene monomer was systematically replaced with pyrene (Py), tetraphenylethylene (Tpe) or spirobifluorene (Sp) (Figure 6.1). These polymers were synthesised through traditional Suzuki-Miyaura cross-coupling methods.

The results from this were immediately apparent as the observed colour of the resultant polymers differed between the four samples (Figure 6.2). Along with the colour changes, solid state UV-Vis measurements show a shift in absorbance values and optical band gaps (Figure 6.3). While Ph-BTZ has a λ_{max} around 425 nm, a bathochromic shift is observed in the other polymers each with a λ_{max} around 500 nm. Furthermore, a broadening effect can also be seen which can be attributed to a decrease in the optical band gap. Although this is a small range of potential combinations, large libraries of CPPs investigating electronic control can be envisaged.

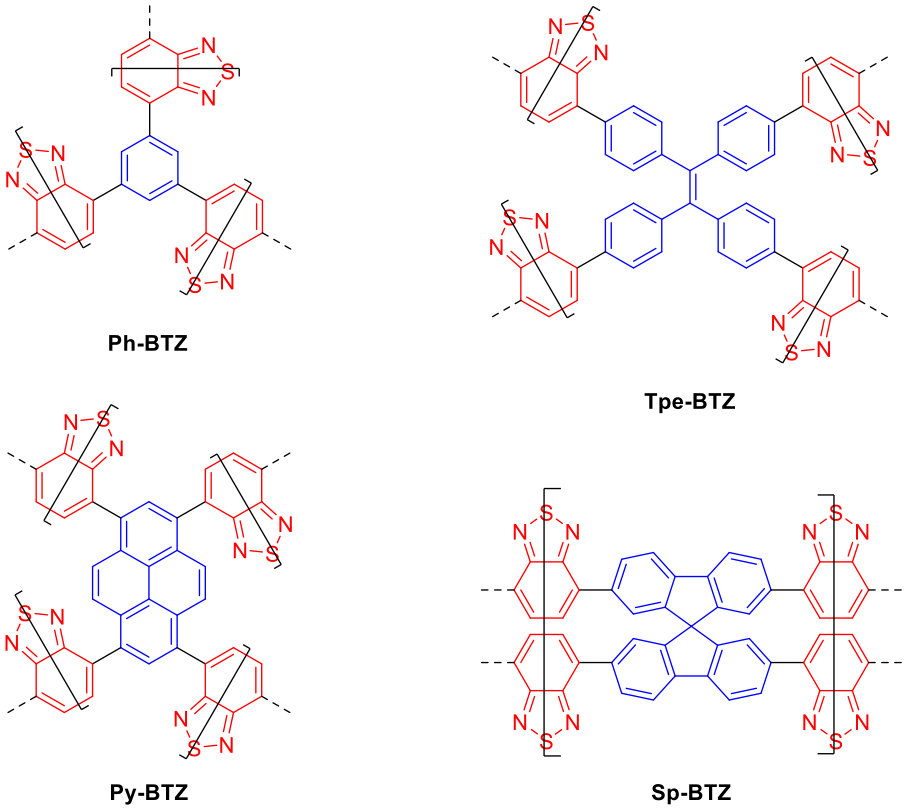

Figure 6.1 A selection of CPPs based on BTZ as a SA (red) and different aromatic cores as the WD (blue). Brackets indicate the polymer repeat unit.

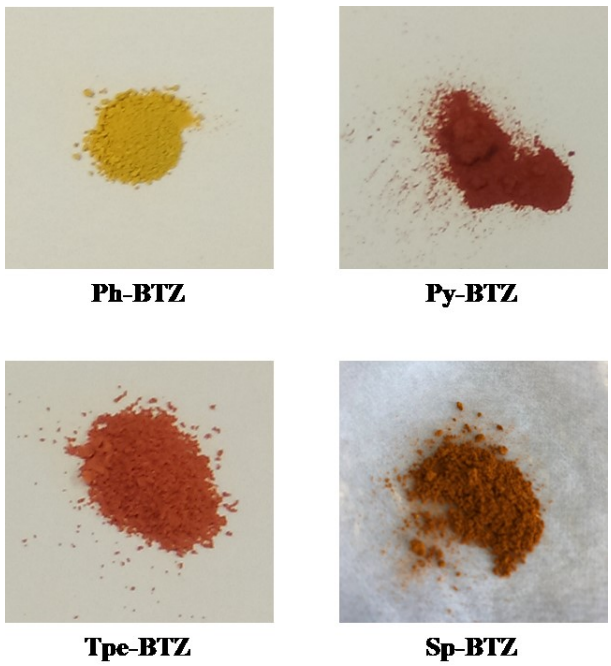

Figure 6.2 Visual comparison between four CPPs with different aromatic core WD groups.

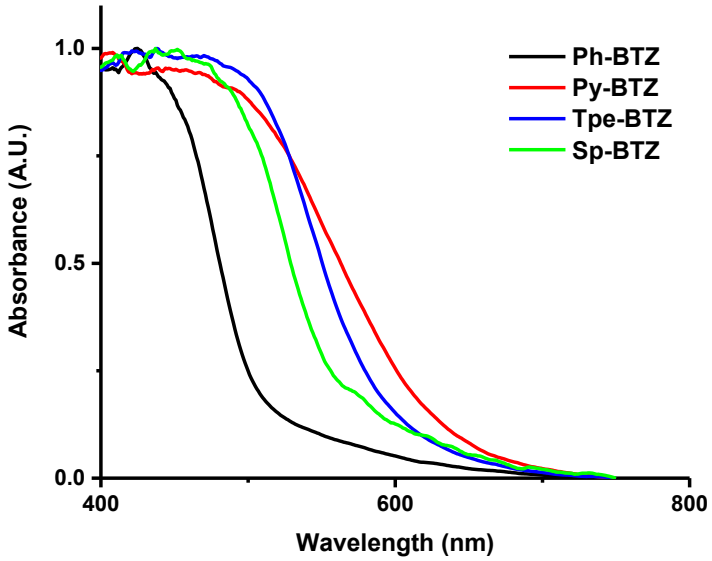

Figure 6.3 UV-Vis absorption spectra of four CPPs with different aromatic core WD groups.

As the majority of this thesis has focused on the development of new heterogeneous (photo)catalytic materials, it is prudent to also continue broadening the scope of applications. This idea can range from specific organic reactions which use common metal-based homogeneous (photo)catalysts to more expansive concepts such as size exclusion [6.6] and gas phase (photo)catalysis [6.7], as well as materials for energy storage [6.8]. These concepts would benefit greatly from the use of CPPs due to their inherent microporosity as well as high thermal and chemical stability.

Recently, our group has started to explore new organic photocatalytic reactions, which have only employed homogeneous photocatalysts. Scaiano *et al*. recently reported the use of methylene blue for photocatalytic radical trifluoromethylations of heteroarenes as well as terminal alkenes and alkynes [6.9]. Molecules containing CF_3 groups are highly topical as many new pharmaceutical drugs contain this group within the molecular structure. Preliminary studies used the materials described in Figure 6.1 as the photocatalysts along with different CF_3 sources and 3-methylindole as the target substrate (Scheme 6.1). Out of the CF_3 sources presented in Figure 6.4, Umemoto's reagent presented with the greatest yields reaching as high as 61 % *via* ^{19}F NMR spectroscopy and HPLC.

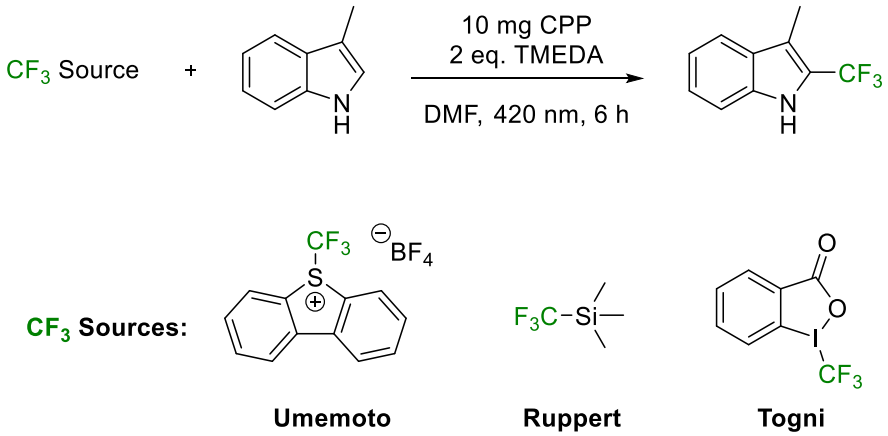

Scheme 6.1 Typical reaction scheme for the photocatalytic trifluoromethylation of 3-methylindole. TMEDA = *N,N'*-tetramethylenediamine.

Another interesting photocatalytic process was presented by Glorius *et al.* introducing a method for the decarboxylative C-H functionalisation of heteroarenes using iridium-based photocatalysts [6.10]. Again, one of the primary uses of this chemistry is for easier and more sustainable access to high-value pharmaceuticals. Our early studies have a used a selection of photocatalytic CPPs to drive the decarboxylation of cyclohexane carboxylic acid to allow for the addition of cyclohexane to lepidine (Scheme 6.2). At present, Ph-BTZ demonstrated the highest activity with full conversion occurring after 24 h *via* ^{1}H NMR. Both photocatalytic processes presented above utilise a single electron transfer mechanism whereby a base is necessary as a sacrificial electron donor. While CPPs using this mechanism have not been explored in depth, their use as photocatalytic material continue to show great promise.

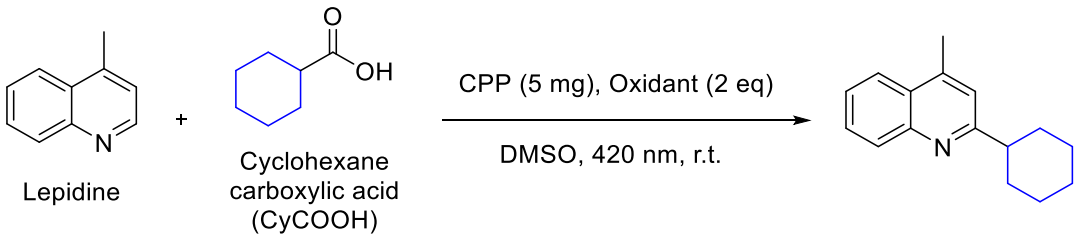

Scheme 6.2 Typical reaction scheme for the decarboxylative C-H functionalisation of lepidine.

Finally, as we look towards the future, expanding interest and adoption of continuous flow chemistry is an intriguing trend, indicating a great potential for growth [6.11]. Much of the work presented throughout this thesis utilised continuous flow chemistry for photocatalytic applications. However, when investigating potential

methods regarding more efficient and streamlined synthesis of CPPs, continuous flow (as opposed to traditional batch) conditions may introduce a more effective method for their production. Furthermore, this methodology has the potential to alter the physical properties of CPP when compared to the same materials produced through traditional batch synthesis. This level of control is not unprecedented as literature has shown something as simple as solvent choice can have a significant effect on the surface area and pore size of CPPs containing identical repeat units [6.12].

Continued development of not only CPPs but polymeric materials in general could have a profound effect on many (photo)catalytic processes ranging from laboratory to industrial implementation. By choosing efficient, recoverable, and reusable materials along with the appropriate reaction conditions, the sustainability and 'green' characteristics of these processes will only continue to rise.

6.3 References

[6.1] K. Masuda, S. Ohmori, T. Arai, *Triplet-State Lifetime Measured by Time-resolved Luminescence from 1O2 Generated by PDT under High-Intensity Pulsed Excitation*, Laser Lett., **34**, 447-449 (2006)

[6.2] B. Bonillo, R. S. Sprick, A. I Cooper, *Tuning Photophysical Properties in Conjugated Microporous Polymers by Comonomer Doping Strategies*, Chem. Mater., **28**, 3469-3480 (2016)

[6.3] Y. L. Wong, J. M. Tobin, Z. Xu, F. Vilela, *Conjugated porous polymers for photocatalytic applications*, J. Mat. Chem. A, **4**, 18677-18686 (2016)

[6.4] F. Vilela, K. Zhang, M. Antonietti, *Conjugated porous polymers for energy applications*, Energy Environ. Sci., **5**, 7819-7832 (2012)

[6.5] B. C. Ma, S. Ghasimi, K. Landfester, F. Vilela, K. A. I. Zhang, *Conjugated microporous polymer nanoparticles with enhanced dispersibility and water compatibility for photocatalytic applications*, J. Mater. Chem. A., **3**, 16064-16071 (2015)

[6.6] J. Kou, C. Lu, J. Wang, Y. Chen, Z. Xu, R. S. Varma, *Selectivity Enhancement in Heterogeneous Photocatalytic Transformations*, Chem. Rev., **117**, 1445-1514 (2017)

[6.7] N. Chaoui, M. Trunk, R. Dawson, J. Schmidt, A. Thomas, *Trends and challenges for microporous polymers*, Chem. Soc. Rev., **46**, 3302-3321 (2017)

[6.8] Y. Liao, H. Wang, M. Zhu, A. Thomas, *Efficient Supercapacitor Energy Storage Using Conjugated Microporous Polymer Networks Synthesized from Buchwald–Hartwig Coupling*, Adv. Mater., **30**, 1705710 (1-10) (2018)

[6.9] S. P. Pitre, C. D. McTiernan, H. Ismaili, J. C. Scaiano, *Metal-Free Photocatalytic Radical Trifluoromethylation Utilizing Methylene Blue and Visible Light Irradiation*, ACS Catal., **4**, 2530-2535 (2014)

[6.10] R. A. Garza-Sanchez, A. Tlahuext-Aca, G. Tavakoli, F. Glorius, *Visible Light-Mediated Direct Decarboxylative C–H Functionalization of Heteroarenes*, ACS Catal., **7**, 4057-4061 (2017)

[6.11] M. B. Plutschack, B. Pieber, K. Gilmore, P. H. Seeberger., *The Hitchhiker's Guide to Flow Chemistry*, Chem. Rev., **117**, 11796-11893 (2017)

[6.12] R. Dawson, A. Laybourn, Y. Z. Khimyak, D. J. Adams, A. I. Cooper, *High Surface Area Conjugated Microporous Polymers: The Importance of Reaction Solvent Choice*, Macromolecules, **43**, 8524-8530 (2010)

APPENDIX A: Publication

Application Note 58: Visible-Light Singlet Oxygen Generation using Heterogeneous Photosensitisers in Continuous Flow

J. M. Tobin, F. Vilela

Application Note 58 – Visible Light Singlet Oxygen, 2018, Vapourtec Ltd., https://www.vapourtec.com/flow-chemistry-resource-centre/application-note-58-visible-light-singlet-oxygen/

DECLARATION

As primary author of this publication, I can confirm this work to be my own with editing from Dr. Filipe Vilela.

Signature: _____

Abstract

A selection of polymeric materials designed as heterogeneous photosensitisers for the production of singlet oxygen under continuous flow conditions is described. The photosensitisers all absorb in the visible spectrum (420 – 530 nm) and were employed either as a dispersion within the reaction mixture or immobilised in a transparent glass column. The studies demonstrate the efficiency of these materials and the ability to use them in complex flow streams consisting of solid, liquid and gas components.

Background

Heterogeneous Photosensitisers in Flow

Singlet oxygen ($^1O_2$) is a highly energetic electronic state of oxygen which has been studied extensively for over 100 years. Due to its wide range of synthetic, environmental and biological applications, $^1O_2$ continues to be examined and the materials and methods used to produce it improved upon [1]. The production of $^1O_2$ in continuous flow was first reported in 2002 using Rose Bengal as a homogeneous photosensitiser [2]. In fact, the vast majority of literature employing flow chemistry for $^1O_2$ production has continued to use similar homogeneous materials (organic dyes and metal complexes) [2-4]. While heterogeneous photosensitisers, such as immobilised dyes and fullerenes, have been implemented in flow, only small scale microphotoreactors (or microfluidic chips) were utilised [3]. These reactors typically have a volume <1 mL resulting in lower productivity as there are upper limits to how much reactant, and subsequent product, can pass through the system. In order to increase this productivity, flow systems with greater volume (larger scale) can be used. Therefore, these issues have spurred the development of new heterogeneous photosensitisers for flow systems at a larger scale.

Generation of $^1O_2$ using heterogeneous photosensitisers has clear advantages such as ease of recovery and subsequent reusability. However, due to photon penetration depth and excessive irradiation, the significance of these advantages is lessened at larger scales [5]. Continuous flow addresses these issues through higher surface area to volume ratios and more efficient light penetration due to shorter path lengths compared to batch procedures.

Herein we present a range of polymeric materials that have been successfully employed as heterogeneous photosensitisers for the production of singlet oxygen ($^1O_2$) in flow using the **Vapourtec easy-Photochem E-series** apparatus or a bespoke continuous flow set up. We demonstrate these materials to be photoactive in the visible spectrum and outline the use of synthetic design to alter the conditions under which they are utilised as photosensitisers. As depicted in Figure 1, production of $^1O_2$ was indirectly detected through a chemical reaction whereby α-terpinene was converted to ascaridole. This reaction was chosen as it only proceeds in the presence of $^1O_2$ and is inert to other reactive oxygen species [6].

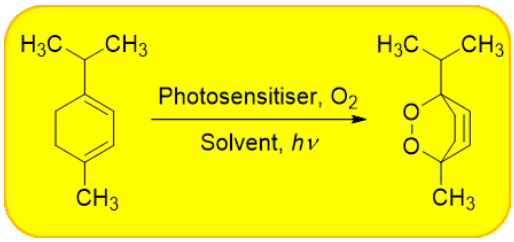

Figure 1 Synthesis of ascaridole from α-terpinene via the photosensitisation of $^1O_2$ under visible light irradiation.

Setup

All of the reactions were carried out using a Vapourtec easy-Photochem E-series (or equivalent instrument) in one of two ways: (*i*) as a heterogeneous suspension through a UV-150 photochemical reactor equipped with an LED module irradiating light at the appropriate wavelength (Figure 2a); (*ii*) as an immobilised photosensitiser trapped in a transparent glass column fitted to a photochemical reactor through which the reaction mixture is allowed to flow (Figure 2b). The PTFE tubing used within the systems had a 1 mm bore and oxygen was provided from either ambient air or from an oxygen cylinder equipped with a low-pressure regulator. The reagent mixture generally consisted of a 1.0 M solution of the target molecule and was stirred continuously to ensure even distribution of the reagent and a uniform suspension. The mixture was pumped at a constant flow rate (0.1 – 1.3 mL min^{-1}) through the photoreactor. Air (or oxygen) was pumped at the same (or higher) flow rate (0.1 – 10.0 mL min^{-1}) and met the reaction mixture at the T-junction prior to entering the photoreactor. For suspension reactions, the mixture was cycled through the photoreactor until full conversion of the starting material was observed. For reactions utilising an immobilised photosensitiser, the solution was allowed to flow

through the column (not cycled) after which no starting material remained. The product was collected manually and analysed *via* ^{1}H NMR spectroscopy to determine conversion to the desired product.

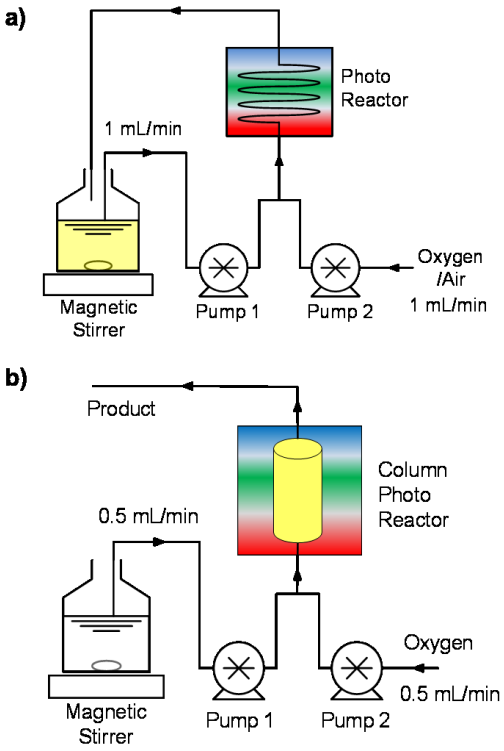

Figure 1 Schematic representation of the experimental flow setup for (a) a heterogeneous suspension of the photosensitiser and (b) an immobilised photosensitiser.

Results

BTZ-based Conjugated Microporous Polymers

Conjugated microporous polymers (CMPs) are fully crosslinked polymer networks characterised by their extended π-conjugation and high surface area. Due to their insoluble nature and ability to act as light harvesters, they make ideal candidates as heterogeneous photocatalysts [7]. Two CMPs based around an electronic 'push-pull' system between benzene (weak electron donor) and 2,1,3-benzothiadiazole (BTZ, strong electron acceptor) were designed as depicted in Figure 3. These materials were fully characterised and subsequently implemented as heterogeneous photosensitisers under continuous flow conditions combined with a visible light LED module as the source of photons.

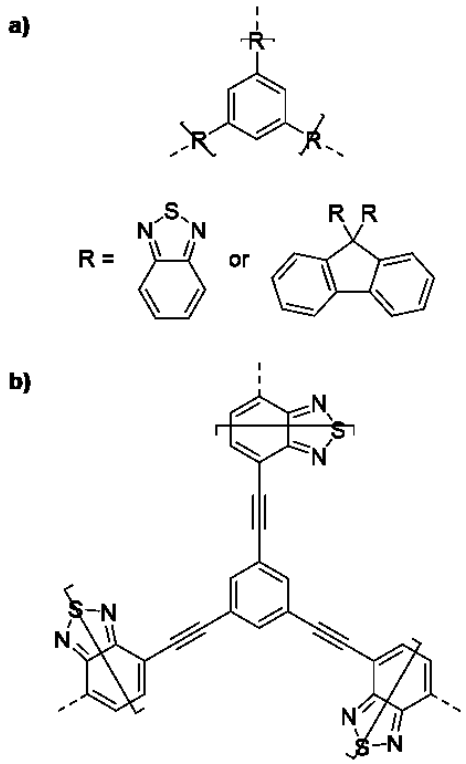

Figure 3 Representative repeat units for two BTZ-based CMPs synthesised via (a) Suzuki and (b) Sonogashira cross coupling.

The first of these materials was synthesised *via* palladium-catalysed Suzuki-Miyaura cross-coupling reaction as a polymerised high internal phase emulsion (polyHIPE, Figure 3a). This strategy enabled the production of a monolithic photoactive polymer that can be used as an immobilised photosensitiser for the production of $^1O_2$ (See Figure 4a) [8]. The highly porous CMP-HIPEs were placed in a glass column where a solution of α-terpinene (0.1 M in 10 mL $CHCl_3$), mixed with oxygen, was allowed to flow through the column whilst irradiated at 420 nm. Under these conditions, full conversion to the ascaridole product was observed *via* ^{1}H NMR spectroscopy, up to a flow rate of 30 mL h^{-1}. As flow rates increased, contact time between α-terpinene and the $^1O_2$ generated within the column decreased, resulting in lower conversion rates as depicted in Figure 4b. Calculations based on these results translated to a reaction time of approximately 2 minutes. Furthermore, the immobilised polyHIPE showed exceptional photoactivity and photostability as continuous flow of the reagent (10 repeat experiments) at 20 mL h^{-1} resulted in no decrease in conversion to the ascaridole product.

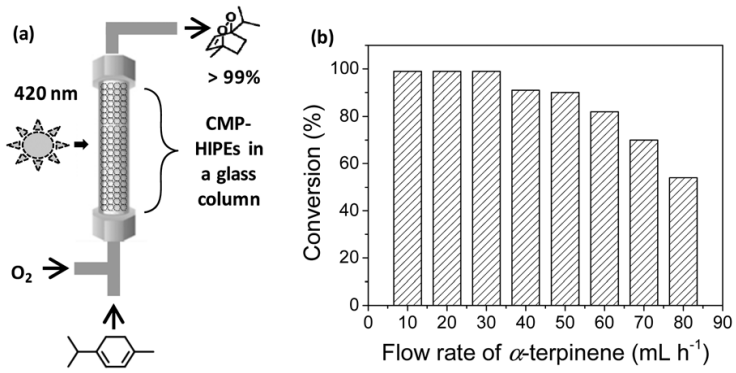

Figure 4 (a) Schematic representation of the continuous flow setup; (b) ascaridole conversion at different flow rates of α-terpinene solution. Reproduced from Ref. 8 with permission from The Royal Society of Chemistry.

The second of these CMP-based materials was designed in a similar fashion. However, in this instance palladium-catalysed Sonogashira-Hagihara cross-coupling was employed resulting in an alkyne spacer between the BTZ and benzene in the repeat unit (Figure 3b) [9]. This study focuses on the photoactivity between structurally identical materials of varying surface areas. Therefore, in order to control for surface area, the polymers were synthesised in the presence of silica nanoparticles and subsequently employed as heterogeneous photosensitisers.

Whilst the reaction flow setup was bespoke, Figure 2a offers a general representation. Since these materials formed insoluble powders, they were used as a dispersion (1 mg mL^{-1}) in a solution of α-terpinene (0.1 M in $CHCl_3$) rather than an immobilised photosensitiser. Again, the reaction mixture was mixed with oxygen, irradiated at 420 nm and allowed to flow at 1 mL min^{-1}. The lowest conversion (26 %) was observed using the untemplated polymer with a relatively low BET surface area (CMP_0, 270 m^2 g^{-1}) while the polymer with the highest surface area (CMP_60, 660 m^2 g^{-1}) presented with near full conversion to the ascaridole product (96 %). Materials with surface areas between these two extremes showed increased photoactivity when compared to the unaltered polymer, but quickly plateaued until CMP_60. Upon doubling the flow rate, the same trend is observed albeit with lower conversions, as expected from the reduced residence time.

While surface area did seem to play a role in the photoactivity of the different materials, this was not the only benefit observed from the templating strategy. Interestingly, the silica templating not only affected the surface areas, but also the

mesostructure of the polymers, resulting in distinct morphologies. The more spherical structures showed a greater ability to disperse and were less prone to aggregation, allowing them to be more suitable heterogeneous materials under continuous flow conditions.

BODIPY-based Conjugated Microporous Polymers

In an attempt to develop materials absorbing at less energetic wavelengths, two CMPs incorporating BODIPY (4,4-difluoro-4-bora-3a,4a-diaza-s-indacene) were designed and synthesised, the final products of which are shown in Figure 5 [10]. Designing photocatalytic materials that absorb light at higher wavelengths mitigates issues surrounding the use of highly energetic (UV) light such as photodecomposition of the starting materials and/or products or unwanted side reactions. While both exhibited similar physical properties, their syntheses differed as BDP_CMP used a traditional palladium-catalysed Suzuki-Miyaura cross-coupling route while PHTT_BDP was post-synthetically modified through a metal-free process. It is important to note that the starting material used to synthesise PHTT_BDP was also made through a metal-free procedure [11].

As these CMPs showed good dispersion in organic solvents (Figure 6), each polymer was added (0.33 mg mL^{-1}) to a solution of α-terpinene (1 mmol in 15 mL $CHCl_3$). Each dispersion was mixed with air, irradiated at 530 nm and allowed to flow at 1 mL min^{-1}. Within 1 hour of circulation, full conversion to ascaridole was observed for both materials. Both also demonstrated a high level of photo and chemical stability, where PHTT_BDP showed only a minor decrease in photoactivity after 6 hours.

Due to the compatibility of both polymers in a variety of organic solvents, the same photosensitisation reactions were performed for a selection of common solvents as well as a few ‘green’ solvents (dimethyl carbonate and 2-methylTHF). Each showed comparable conversion to ascaridole, supporting the versatility of these materials under flow conditions. Furthermore, as PHTT_BDP demonstrates nearly identical photoactivity and stability to BDP_CMP, a clear benefit can be ascertained to using PHTT_BDP. As the synthesis of PHTT_BDP contains no metals throughout the entirety of the process, increasing both environmental and economic sustainability. Any effects

regarding photocatalytic performance and toxicity from residual metals is also negated, solving often cited criticisms posed to CMPs used as photocatalytic materials.

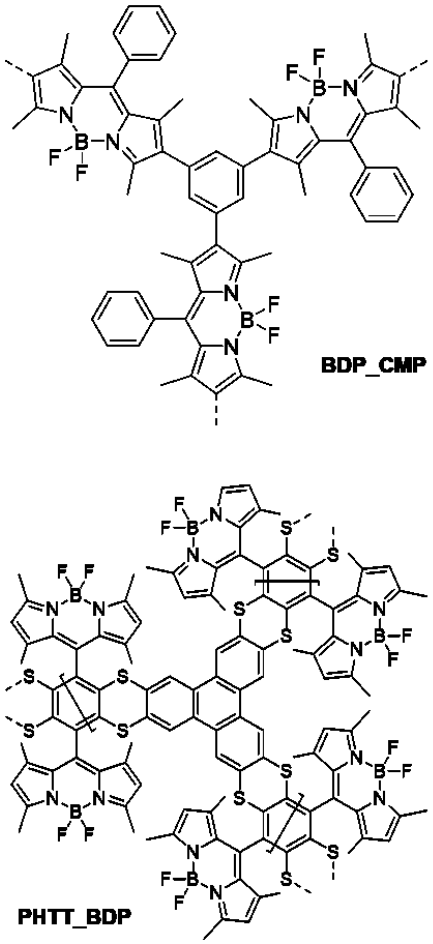

Figure 5 BDP_CMP (top) and PHTT_BDP (bottom) as a powder and dispersed in a solvent.

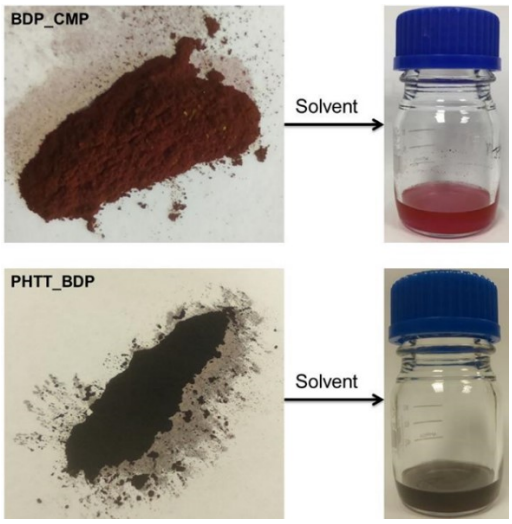

Figure 6 BDP_CMP (top) and PHTT_BDP (bottom) as a powder and dispersed in a solvent. Reproduced from Ref. 10 with permission from The Royal Society of Chemistry.

The CMPs presented above have been shown as effective and reusable heterogeneous photosensitisers, particularly when employed under continuous flow conditions. While the potential for further exploration of these polymers as photocatalysts is strong, photoactive materials (photosensitiser) designed through different synthetic methodologies, such as free radical polymerisation, have proven useful.

Polymer Supported Photosensitisers

Applying the photocatalytic properties and ideas from the BTZ-based CMPs discussed above, two repeat units were designed based on these polymers (Figure 7). These repeat units, either diamine or divinyl-based, were then implemented as photoactive crosslinkers in polyamides or polystyrenes. Furthermore, only a small mol % of monomer was used in each of the polymerisations in order to determine the efficacy of the newly synthesised materials with lower concentrations of photoactive material. It should also be noted that these specific polymers do not display the same physical characteristics as the aforementioned CMPs. Most importantly, this means they do not contain extended π-conjugation beyond the photoactive monomer.

The first of the two materials utilised the divinyl monomer (R = $HC{=}CH_2$) which was first tested for photocatalytic performance as a homogeneous photosensitiser [12]. While the monomer did show full conversion to ascaridole after extended reaction times, it was unstable in the highly oxidative environment. In order to use this monomer in a heterogeneous fashion, it was incorporated as a crosslinker into a polystyrene synthesis at 3-5 mol % *via* free radical polymerisation, resulting in an insoluble gel. While the gel demonstrated a marked improvement in both stability and conversion when compared to the monomer, due to physical limitations this material was not being suitable for implementation in flow chemistry.

To combat this, well-defined polymer beads (Figure 8, top) and a polyHIPE (Figure 8, bottom) were also synthesised using precipitation and emulsion polymerisation techniques, respectively, whilst incorporating the photoactive monomer. This resulted in two materials that were used under flow conditions: (*i*) beads were dispersed in $CHCl_3$ and allowed to flow through the reactor (Figure 2a); (*ii*) polyHIPE was trapped in a

transparent column and used as a stationary photosensitiser through which the solution was allowed to flow, similar to the CMP-HIPEs present above (Figure 2b).

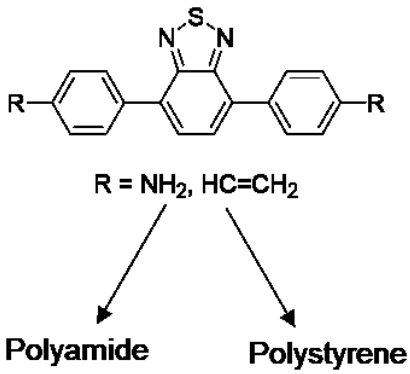

Figure 7 Monomer design for the synthesis of photoactive polyamide and polystyrene materials.

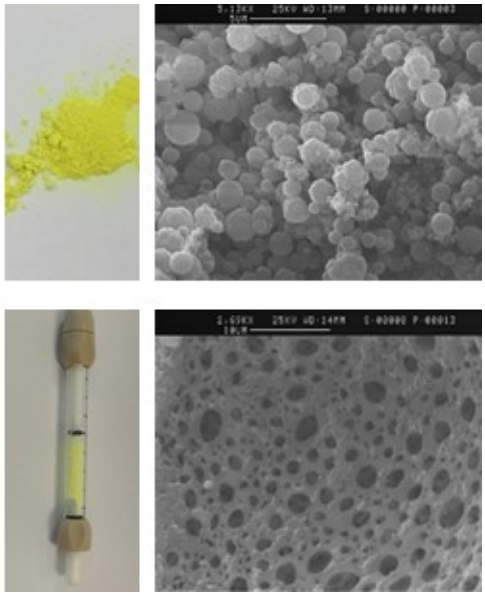

Figure 8 Synthesised polystyrene copolymers and their corresponding SEM images: (top) beads; (bottom) polyHIPE. Adapted with permission from Ref. 12. Copyright 2017 American Chemical Society.

Due to their spherical shape, the polystyrene beads demonstrated excellent physical properties as they were easily dispersed (1 mg mL^{-1}) and showed no tendency to aggregate. In a solution of α-terpinene (1 mmol in $CHCl_3$), the dispersion was mixed with air, irradiated at 420 nm and allowed to flow at 1 mL min^{-1}. Within 1 hour of circulation, full conversion to ascaridole was observed.

The polyHIPE also showed good photocatalytic activity, however due to the short path and subsequent residence time, the flow parameters needed some adjustment. This included a decrease in concentration of α-terpinene (0.4 mmol in 10 mL $CHCl_3$) and flow rate (0.5 ml min^{-1}) as well as the use of pure oxygen. These changes aided in demonstrating full conversion to ascaridole after a single pass through the polyHIPE. Moreover, the production rate of ascaridole under these parameters was found to be 192 mg h^{-1} or 1.1 mmol h^{-1}.

It should be noted that determination of flow parameters for the polyHIPE underwent many iterations, largely regarding the source of irradiation. Initially a single LED module was used but proved inadequate. After discussing the issue with Vapourtec Ltd., we tested a set up consisting of 3 modules surrounding the column. This resulted in a great increase in efficiency and was reported back to Vapourtec Ltd. With this data, it aided in the design of a new column photochemical reactor in which the polyHIPE was ultimately employed (Figure 9).

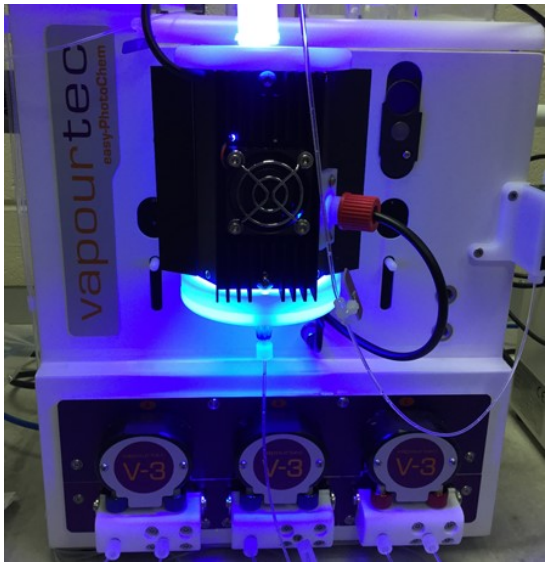

Figure 9 Easy-Photochem flow system from Vapourtec Ltd. equipped with a column photochemical reactor equipped with 420 nm LED lamps. Reprinted with permission from Ref. 12. Copyright 2017 American Chemical Society.

To further demonstrate the versatility of the polystyrene materials as triplet photosensitisers under flow conditions, the aerobic hydroxylation of arylboronic acids to phenols was investigated (Figure 10). While the reaction conditions were nearly essentially identical to that of the $^1O_2$ reactions, there were two changes to the reactants.

Firstly, phenylboronic acid replaced α-terpinene as the acceptor for the reactive oxygen species. Secondly, an organic base (*N,N'*-diisopropylethylamine) was added to facilitate the formation of a super oxide radical anion ($O_2^{\bullet -}$) as opposed to $^1O_2$.

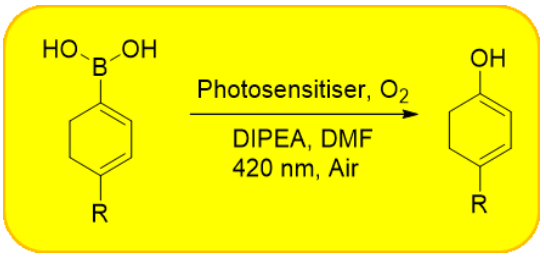

Figure 10 Synthesis phenols from arylboronic acids via the photosensitisation of $O_2^{\bullet -}$ under visible light irradiation.

As seen in Table 1, a scope of aryl boronic acids were tested under batch conditions (Entry 1-6) whereby the reaction time to reach full conversion varied greatly depending on the substituted functional groups present. When performing the model reaction (phenylboronic acid) with the polymer beads in batch, a dramatic decrease in reaction time was observed (Entry 8). Applying this same reaction to continuous flow, the reaction time required for full conversion was cut in half (Entry 9) compared to the same reaction in batch. The polyHIPE was also employed for the same reaction showing good performance (Entry 7), albeit a somewhat longer reaction time required than that of the batch reactions.

Table 1 Light-Induced Aerobic Oxidative Hydroxylation of Arylboronic Acids.[a] Adapted with permission from Ref. 12. Copyright 2017 American Chemical Society.

Entry	R Group	Photosensitiser	Time (h)
1	H	Gel	24
2	OCH_3	Gel	72
3	CH_3	Gel	40
4	CF_3	Gel	18
5	$COOCH_3$	Gel	48
6	NO_2[b]	Gel	18
7[c]	H	PolyHIPE	30
8	H	Beads	10
9[c]	H	Beads	5

[a]*Reaction conditions: arylboronic acid (0.5 mmol/5 mL DMF), photosensitiser (5 mg), DIPEA (1.0 mmol), DMF (5 mL), 420 nm LED irradiation, air. All reactions reached full conversion as calculated via ^1H NMR spectroscopy. Abbreviations: DIPEA = N,N'-diisopropylamine, DMF = N,N'-dimethylformamide.* [b]*NO_2 at the meta position.* [c]*Reaction performed under flow conditions.*

The versatility of polystyrene in conjunction with the photoactive monomer is demonstrated through the ability to make highly photoactive polymeric materials for specific reaction conditions in flow. Furthermore, both materials showed tremendous photo and chemical stability. In particular, the polyHIPE was employed for over 80 hours and showed little to no degradation in photocatalytic ability.

The second material used was a photoactive diamine monomer (Figure 5, R=NH_2) [13]. Again, while the monomer worked as a photosensitiser under homogeneous conditions, photodegradation was observed. Therefore, the monomer was incorporated into a polyamide polymer matrix in varying concentrations (5 – 75 mol %) through a metal-free polycondensation reaction. Initially, the range of polyamides were added (0.5 mg mL^{-1}) into a 0.1 M α-terpinene $CHCl_3$ solution. The dispersion was mixed with air, irradiated at 420 nm and allowed to flow at 2 mL min^{-1}, recirculating for 120 minutes. The conversion to ascaridole under the stated conditions for each polyamide presented with an upward trend in conversion as the percentage of the photoactive monomer used increases. However, beyond 25%, diminishing returns were observed, particularly when comparing the increase in monomer required for a small increase in conversion.

Unlike most CMPs and the polystyrene described above, these polyamide materials were compatible with water, making them more attractive for both environmental and biological applications. Utilising their ability to generate $^1O_2$, PA-ABT (25 %) was used for the degradation of two environmental pollutants, bis-phenol A and cimetidine, under the same flow conditions. Furthermore, the neutralisation of Cryptosporidium, a chlorine-resistant water-borne pathogen, was also performed. However, due to technical limitation this could not be performed under flow conditions.

It should be noted that all of the polymer supported photosensitisers presented above were synthesised through metal-free methodologies. As we continue to design and create new photosensitising materials, it is important to consider both synthetic sustainability and desired applications. By removing metals from these processes, new industrial avenues emerge such as pharmaceutical development, where even trace metal species can be catastrophic.

Conclusion

Using the **Vapourtec easy-PhotoChem**, along with other continuous flow apparatus', it has been possible to implement a host of insoluble photoactive polymers for the photosensitisation of oxygen under visible light irradiation. The use of two pumps allows for precise control of both the dispersion mixture and introduction of air/oxygen into the system, particularly when compared to more tradition batch methods. As a result, faster conversion rates have been noted along with the potential for scale up procedures. It should also be noted that prior to this work, no literature could be found describing suspension-based photosensitisation under continuous flow conditions at this scale.

By pumping the dispersions with air/oxygen through the photochemical reaction module, a greater ratio of surface area to volume is formed, resulting in higher conversion rates. The control afforded with this method allows for fine tuning of the reactions which cannot be easily achieved through other means. Control of the light source (narrow wavelength or broad spectrum) further aids in both material design and optimisation of reaction conditions.

While dispersions only require filtration and washing to be reused, the inclusion of a column photoreactor elevates the versatility of this system. Design and implementation of immobilised photosensitisers introduces another layer of ease to the process. A system whereby the only output from a photochemical process is the desired product is highly coveted within industry.

Comparisons between the work presented here and other flow systems utilising heterogeneous photosensitisers is rather difficult, primarily due to the difference in scale. While microscale reactions have demonstrated extremely rapid conversion rates (1-2 minutes for full conversion) [3], it is unknown if similar results would be observed on a greater scale with the same materials. However, when comparing the conversion rates of these heterogeneous materials between batch and flow methods, it is clear that the use of continuous flow techniques has a distinct advantage. This advantage is largely due to the Beer-Lambert law whereby the absorbance of a material is directly proportional to its path length. The irradiation of light through a solution is more efficient under flow conditions due to the shorter path lengths when compared to traditional batch processes. This application note demonstrates the versatility of the E-series, photochemical and column

photoreactors which have made possible the use of these polymers as photosensitisers under flow conditions. As the materials continue to develop, they do so with an aim towards further flow applications.

Acknowledgements

Vapourtec wish to thank Dr Filipe Vilela and Mr John M. Tobin at Heriot-Watt University for conducting the experimental work and providing additional information for this application note.

References

[1] M. C. DeRosa, R. J. Crutchley, *Coord. Chem. Rev.*, 2002, **233-234**, 351-371.

[2] D. Cambie, C. Bottecchia, N. J. W. Straathof, V. Hessel, T. Noel, *Chem. Rev.*, 2016, **116**, 10276-10341.

[3] A. A. Ghogare, A. Greer, *Chem. Rev.*, 2015, **116**, 9994-10034.

[4] M. B. Plutschack, B. Pieber, K. Gilmore, P. H. Seeberger, *Chem. Rev.*, 2017, **117**, 11796-11893.

[5] G. Centi, S. Perathoner, Methods and Tools of Sustainable Industrial Chemistry: Process Intensification. *In Sustainable Industrial Chemistry: Principles, Tools and Industrial Examples*; F. Cavani, G. Centi, S. Perathoner, F. Trifiro, Eds.; Wiley-VCH: Weinheim, Germany, 2009, 199−256.

[6] G. O. Schenck, K. Ziegler, *Naturwissenschaften*, 1944, **32**, 157.

[7] Y.-L. Wong, J. M. Tobin, Z. Xu, F. Vilela, *J. Mater. Chem. A.*, 2016, **4**, 18677-18686.

[8] K. Zhang, Z. Vobecka, K. Tauer, M. Antonietti, F. Vilela, *Chem. Commun.*, 2013, **49**, 11158-11160.

[9] K. Zhang, D. Kopetzki, P. H. Seeberger, M. Antonietti, F. Vilela, *Angew. Chem. Int. Ed.*, 2013, **52**, 1432-1436.

[10] J. M. Tobin, J. Liu, H. Hayes, M. Demleitner, D. Ellis, V. Arrighi, Z. Xu, F. Vilela, *Polym. Chem.*, 2016, **7**, 6662-6670.

[11] J. Liu, J. Cui, F. Vilela, J. He, M. Zeller, A. D. Hunter, Z. Xu, *Chem. Commun.*, 2015, **51**, 12197-12200.

[12] J. M. Tobin, T. J. D. McCabe, A. W. Prentice, S. Holzer, G. O. Lloyd, M. J. Paterson, V. Arrighi, P. A. G. Cormack, F. Vilela, *ACS Catalysis*, 2017, **7**, 4602-4612.

[13] J. Shen, R. Steinbach, J. M. Tobin, N. M. Mouro, M. Bower, M. R. S. McCoustra H. Bridle, V. Arrighi, F. Vilela, *Appl. Catal. B*. *Environ*, 2016, **193**, 226-233.

APPENDIX B

The following section describes the synthesis and characterisation for the polysquaraine-based CPPs as presented in Chapter 3. Surface area and porosity analysis was carried out by the Xu Group at City University of Hong Kong.

B1 Experimental Methods

B1.1 Synthesis of 1,3,5-tris(2,3,3-trimethyl-3H-indol-5-yl)benzene (1)

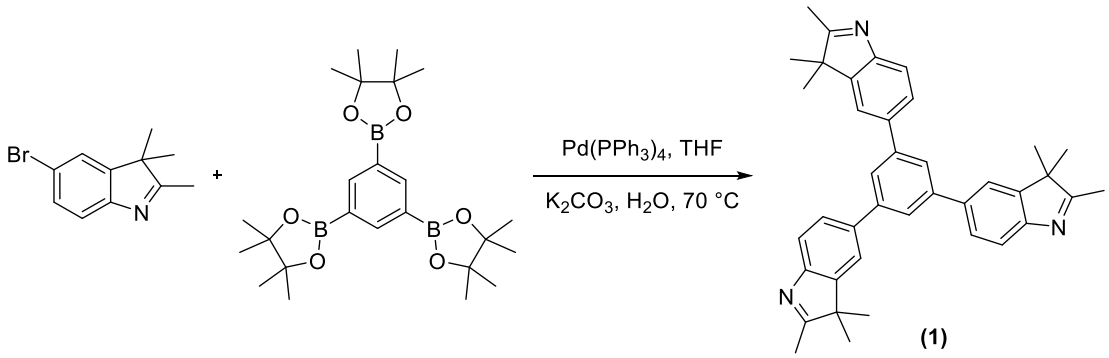

5-Bromo-2,3,3-trimethyl indole (1.67 g, 7 mmol), 1,3,5-tris(4,4,5,5-tetramethyl-1,3,2-dioxaborolan-2-yl)benzene (910 mg, 2 mmol), and $Pd(PPh_3)_4$ (58 mg, 0.05 mmol) were dissolved in 160 mL of previously degassed THF in a 2-necked round bottom flask (oven dried) connected to a condenser. The mixture was further degassed with a flow of N_2. K_2CO_3 (1.66 g, 12 mmol) dissolved in 20 mL of deionised water was degassed for approx. 15 minutes and added through a syringe to the organic solution. The solution was heated to 70 °C and stirred overnight. The reaction mixture was allowed to cool to room temperature and then diluted with 50 mL CH_2Cl_2 and filtered over Celite® S. The filtrate was washed 3x with water and brine and the organic layers were dried over Na_2SO_4 and filtered. The solvent was rotoevaporated and afforded 2.04 g of crude product. The crude product was purified by silica gel column chromatography (EtOAc) to yield a pale yellow solid (715 mg, 65%). ^1H NMR (300 MHz, $CDCl_3$): δ_{ppm} = 1.41 (s, 18H), 2.36 (s, 9H), 7.62 (d, 3H), 7.68 (s+d, 6H), 7.80 (s, 3H).

B1.2 Synthesis of polysquaraine CPP (PSQ)

1,3,5-Tris(2,3,3-trimethyl-3H-indol-5-yl)benzene (300 mg, 0.545 mmol), squaric acid (94 mg, 0.82 mmol), and quinoline (20 mg, 0.11 mmol) were dissolved in a butanol/toluene mixture (20 mL, v/v 1:1) and deoxygenated with N_2 for 10 min. The flask was fitted with a Dean-Stark condenser with molecular sieves (3Å). The reaction was heated up to 130 °C and left to react over 3 days. After this time, a dark, insoluble solid had formed. The precipitate was filtered and washed with H_2O, acetone and THF. The resulting polymer was purified *via* Soxhlet extraction with toluene (24 h) and chloroform (24 h) and dried *in vacuo* to afford 350 mg (96 %) of a metallic red powder.

B1.3 Synthesis of polycroconaine CPP (PCR)

1,3,5-Tris(2,3,3-trimethyl-3H-indol-5-yl)benzene (300 mg, 0.545 mmol), croconic acid (116 mg, 0.82 mmol), and quinoline (20 mg, 0.11 mmol) were dissolved in a butanol/toluene mixture (20 ml; v/v 1:1) and deoxygenated with N_2 for 10 min. The reaction flask was equipped with Dean-Stark condenser containing molecular sieves (3A). The reaction was heated up to 130 °C and left to react over 3 days. After this time, a dark, insoluble solid had formed. The precipitate was filtered and washed with H_2O, acetone and THF. The resulting polymer was purified *via* Soxhlet extraction with toluene (24 h) and chloroform (24 h) and dried *in vacuo* to afford 330 mg (85 %) of a metallic green powder.

B1.4 Synthesis of polyrhodizaine CPP (PRH)

1,3,5-Tris(2,3,3-trimethyl-3H-indol-5-yl)benzene (300 mg, 0.545 mmol), rhodizonic acid (169 mg, 0.2 mmol), and quinolone (16 mg, 0.11 mmol) were dissolved in a butanol/toluene mixture (20 mL; v/v 1:1) and deoxygenated with N_2 for 10 min. The flask was fitted with a Dean-Stark condenser with molecular sieves (3A). The reaction was heated up to 130 °C and left to react over 3 days. After this time, a dark, insoluble solid had formed. The precipitate was filtered and washed with H_2O, acetone and THF. The resulting polymer was purified *via* Soxhlet extraction with methanol (24 h) and THF (24 h) and dried *in vacuo* to afford 442 mg (97 %) of a dark blue powder.

B2 Spectroscopic Analysis

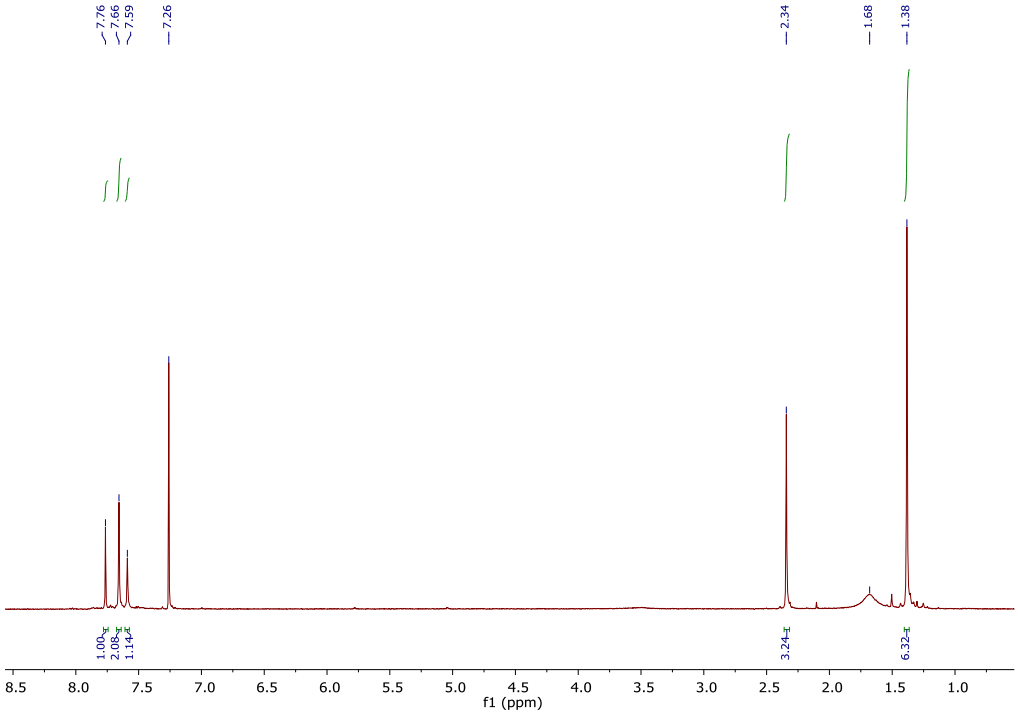

Figure B1 ^{1}H NMR of compound **1** (300 MHz, 30 °C, $CDCl_3$) δ_{ppm} = 1.38 (s, 6 H), 2.34 (s, 3 H), 7.59 (s, 1 H), 7.66 (s, 2 H), 7.76 (s, 1 H).

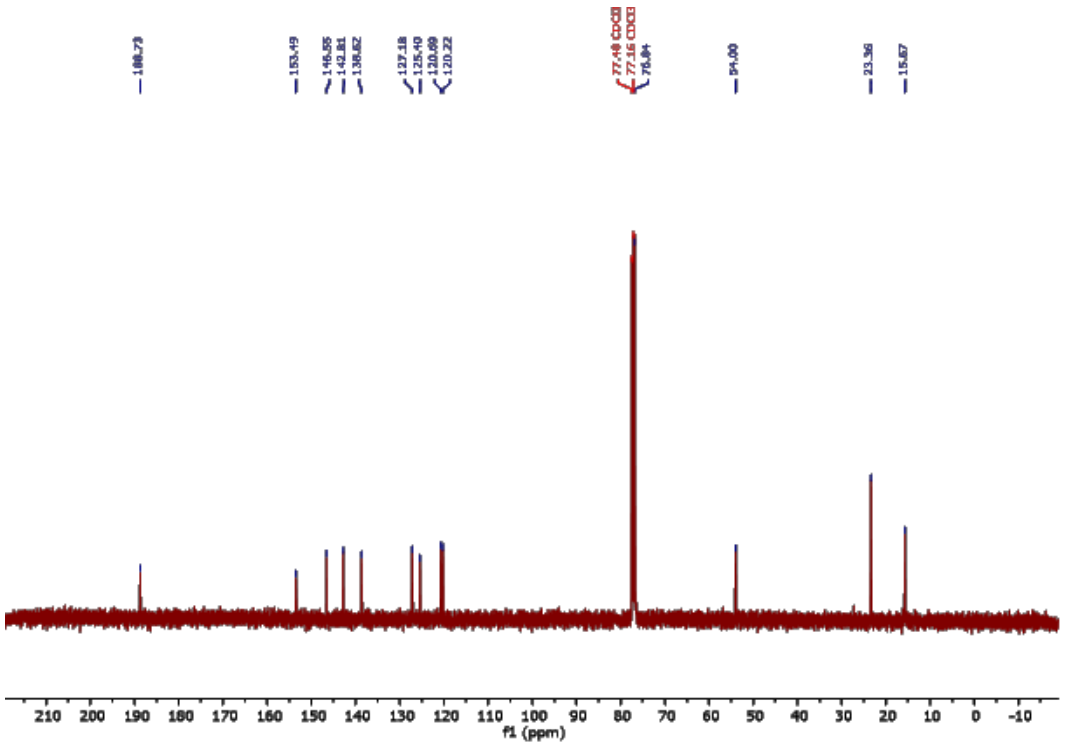

Figure B2 ^{13}C NMR of compound **1** (300 MHz, 30 °C, $CDCl_3$) δ_{ppm} = 15.7, 23.4, 54.0, 120.2, 120.7, 125.4, 127.2, 138.6, 142.8, 146.6, 153.5, 188.8.

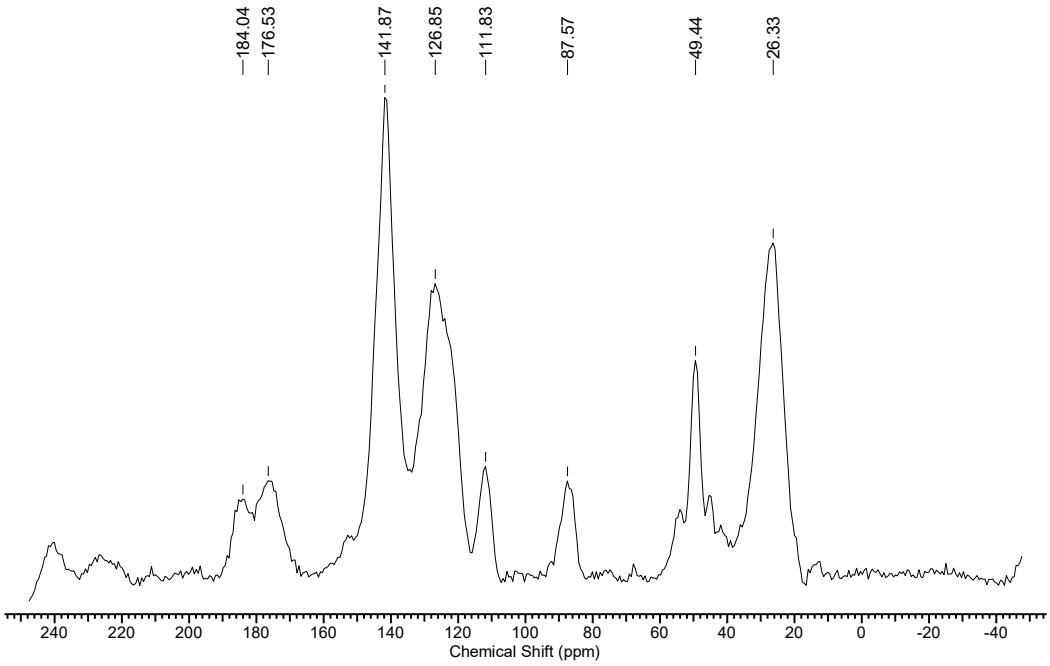

Figure B3 Solid state ^{13}C NMR of **PSQ**. Aromatic (C-C) carbons can be seen in the 112-129 ppm region and C-N carbon at 141.9 ppm. The ketone functionality is represented by the two signals at 178-184 ppm while the C-O carbon bond is indicated at 87.5 ppm. Lastly, non-aromatic C-C bond is seen at 49.4 ppm while methyl carbons are indicated at 26.3 ppm.

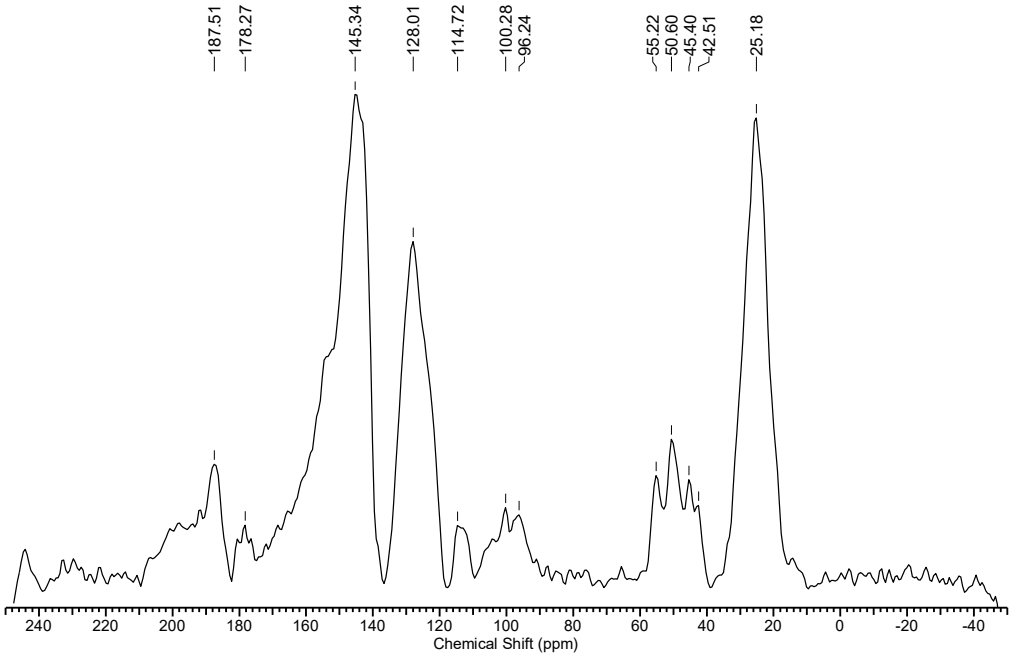

Figure B4 Solid state ^{13}C NMR of **PCR**. Aromatic (C-C) carbons can be seen in the 114-128 ppm region and C-N carbon at 145.3 ppm. The ketone functionality is represented by the two signals at 178-188 ppm while the C-O carbon bond is indicated at 96.2 ppm. Lastly, non-aromatic C-C bond is seen at 45-55 ppm while methyl carbons are indicated at 25.2 ppm.

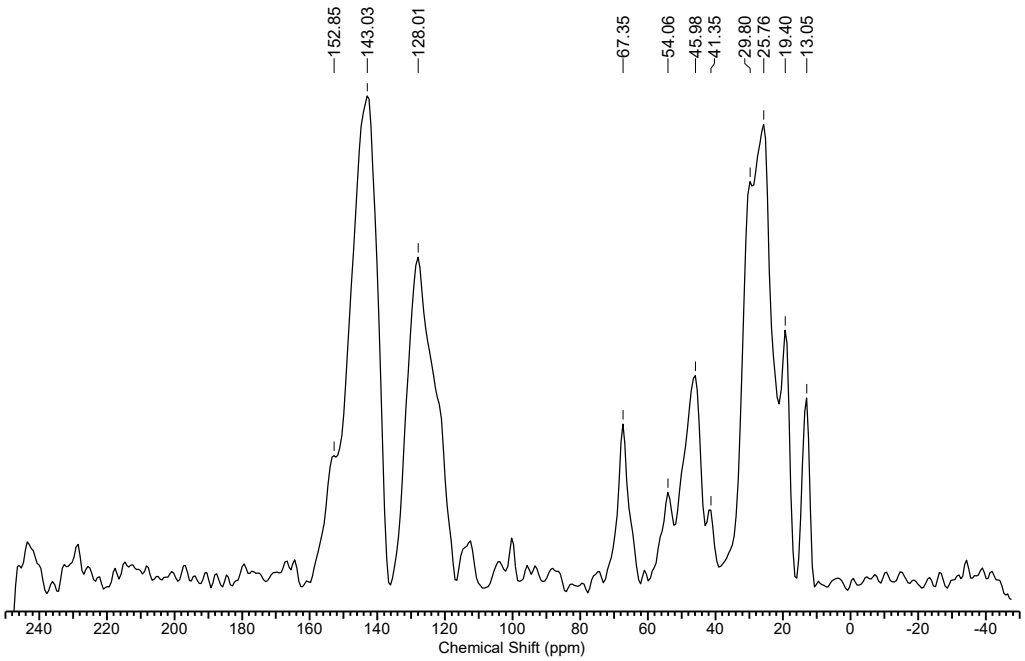

Figure B5 Solid state ^{13}C NMR of **PRH.** Aromatic (C-C) carbons can be seen at 128 ppm and C-N carbon at 143.0 ppm. The ketone functionality is not represented in this spectrum while the C-O carbon bond is indicated at 67.4 ppm. Lastly, non-aromatic C-C bond is seen at 45-54 ppm while methyl carbons are indicated at 25.8 ppm.

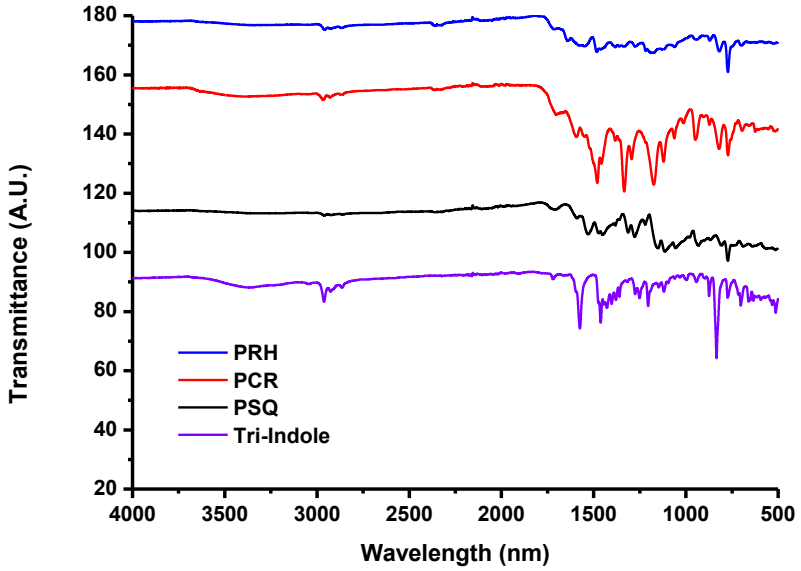

Figure B6 FT-IR of the tri-substituted indole (1) and the three CPPs: PSQ, PCR, and PRH. The reduced peak in the polymers at 2960 cm^{-1} indicates the disappearance of a methyl stretch found at the 2-position of the indole.

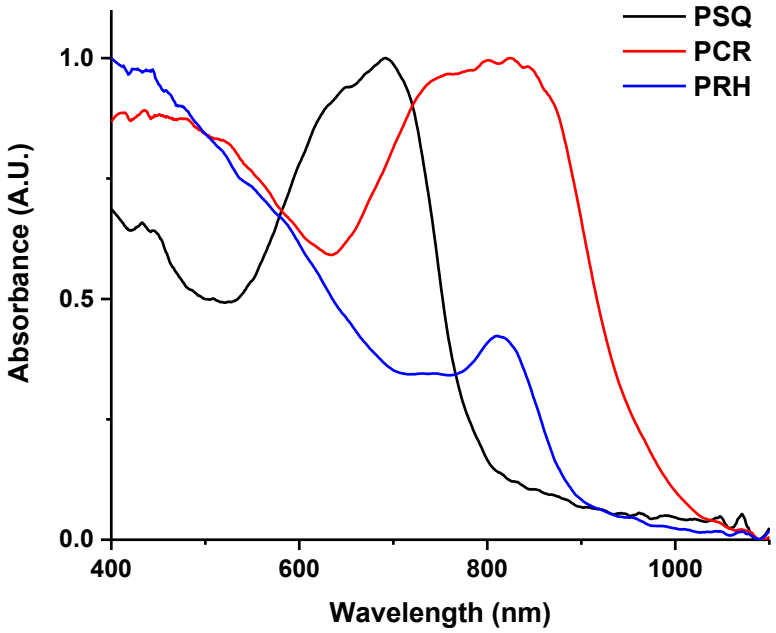

Figure B7 Solid state UV-Vis absorption spectra of PSQ, PCR and PRH with local maximum absorbance values at 690, 850 and 810 nm, respectively.

B3 Surface Area Analysis

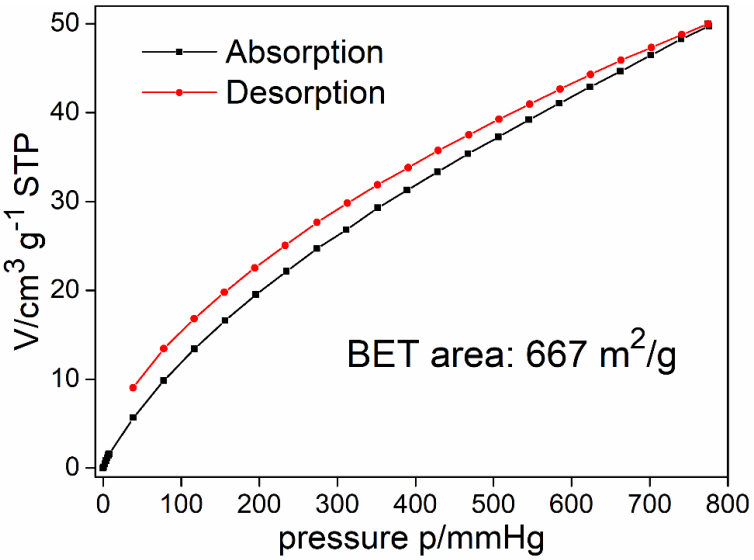

Figure B8 CO_2 sorption isotherms at 273 K for a sample of PSQ (39.1 mg). Inset: the corresponding Brunauer–Emmett–Teller (BET) surface area of 667 m^2/g.

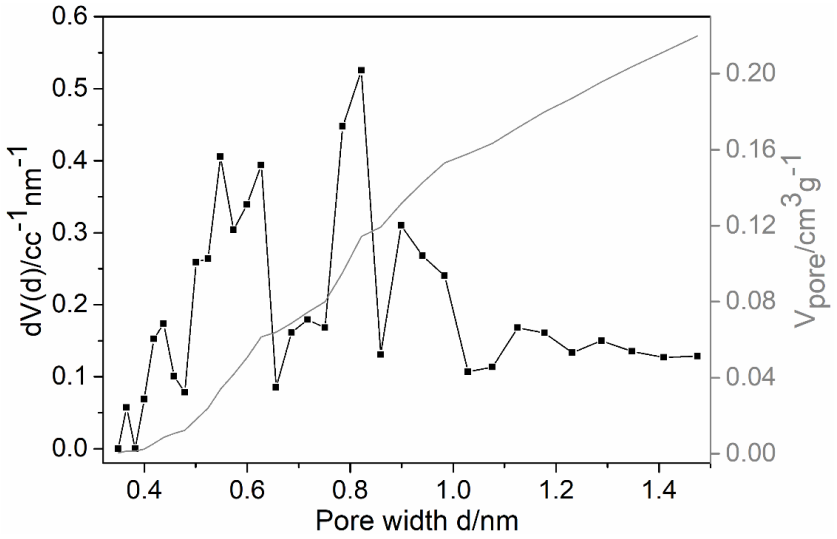

Figure B9 Pore size distribution and pore volume of a sample of PSQ (CO_2 gas at 273 K; Monte-Carlo model). The average pore width 0.822 nm, the pore volume 0.220 cm^3/g.

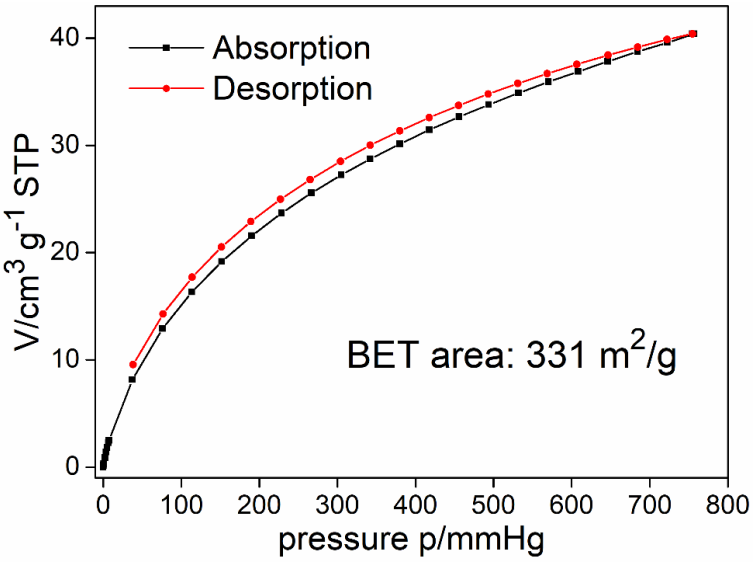

Figure B10 CO_2 sorption isotherms at 273 K for a sample of PCR (110.2 mg). Inset: the corresponding Brunauer–Emmett–Teller (BET) surface area of 331 m^2/g.

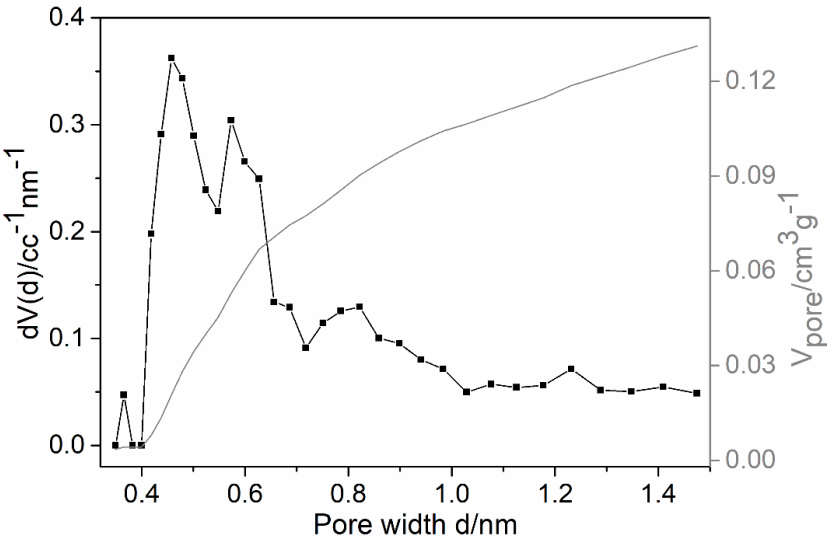

Figure B11 Pore size distribution and pore volume of a sample of PCR (CO_2 gas at 273 K; Monte-Carlo model). The average pore width 0.458 nm, the pore volume 0.131 cm^3/g.

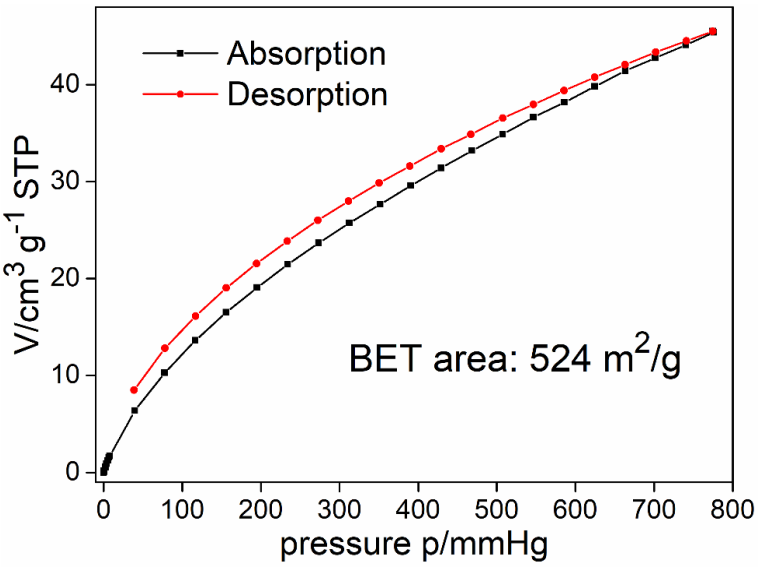

Figure B12 CO_2 sorption isotherms at 273 K for a sample of PRH (58.9 mg). Inset: the corresponding Brunauer–Emmett–Teller (BET) surface area of 524 m^2/g.

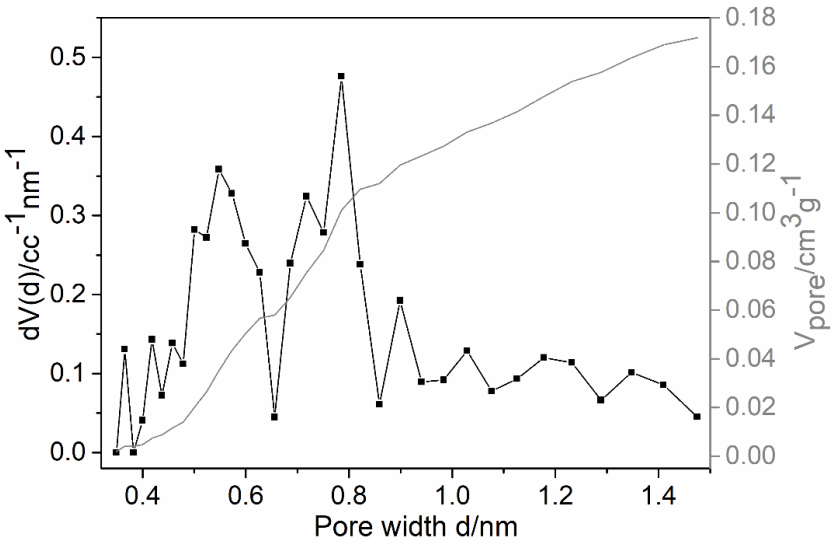

Figure B13 Pore size distribution and pore volume of a sample of PRH (CO_2 gas at 273 K; Monte-Carlo model). The average pore width 0.785 nm, the pore volume 0.172 cm^3/g.